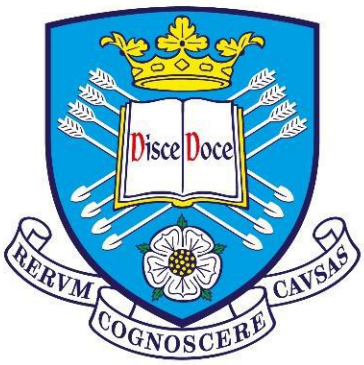

The University Of Sheffield.

Stress, microstructure, and morphology: The relationship between surface finish and the initiation of corrosion in stainless steel intermediate level waste containers.

Joe Pawley

A thesis submitted in partial fulfilment for the degree of Doctor of Philosophy

Immobilisation Science Laboratory

Department of Materials Science and Engineering

The University of Sheffield

Sponsored by EPSRC and Sellafield Ltd as part of the Next Generation Nuclear CDT

November 2020

Abstract

The corrosion of stainless steel is of crucial interest to a wide range of industries, from construction to nuclear. Nuclear waste disposal involves temporary storage for around 100 years in Intermediate Level Waste (ILW) containers made from 304L stainless steel. Storage conditions such as chloride contamination, material stress, temperature, and humidity fluctuate, making Atmospheric Stress Corrosion Cracking (ASCC) and under-droplet pitting known vulnerabilities. This Thesis investigates the effect surface finish has on corrosion initiation in ILW containers.

Detailed characterisation of the surface and subsequent in-depth analysis of the surface topography highlighted specific features brought about during manufacturing that cause corrosion vulnerabilities. Novel techniques such as openness mapping and differential imaging with in-situ corrosion measurements revealed that features such as the etched grain boundaries on rolled surfaces and folded over regions of ground and brushed surfaces contribute to localised aggressive conditions. This was confirmed with outdoor exposure tests. This work allows for the identification of other enclosed locations that are vulnerable to corrosion initiation.

Surfaces were mapped with Atomic Force Microscopy (AFM) and Vertical Scanning Interferometry (VSI) providing data for analytical models of surface stress concentration (the Neuber model and the Arola and Ramulu model). Finite Element Analysis (FEA) was used to corroborate these findings. Using 3D modelling, shotblast craters were shown to have the depths, and the low valley radii, required to form very high stress concentrations of 5 and above. Additionally, stress was shown to concentrate at valley minima on ground and brushed surfaces. ASCC trials revealed the influence the distribution of stress had on crack development. Crystallographic data gathered by Electron Backscatter Diffraction (EBSD) demonstrated that grain damage could be caused by surface finishing processes. The parameter of grain shape was used alongside grain misorientation to estimate residual grain stress.

Acknowledgements

I would like to acknowledge my supervisor, Dr Claire Corkhill, and the labs used, the Immobilisation Science Laboratory, the Sorby Centre for Electron Microscopy, and the Next Generation Nuclear CDT. This work was funded by EPRSC and Sellafield Ltd in equal measure, so I would like to thank them for supporting this research. Thank you, Pat Liddicott (Sellafield Ltd) and Lisa Hartley (NNL) for suggesting and helping with the outdoor trial at the Sellafield site and Andy Backhouse (Outukumpu, Sheffield) for providing samples.

I would very much like to thank my friends and colleagues at The University of Sheffield who provided constant support and advice. A special thanks goes to Dr James Vigor for introducing me to Python, and patiently helping me to learn it for no gain to himself.

I would like to thank the university support for thesis writing, Lynne Newcombe for optimism and support, and the Disability and Dyslexia Support Service for the practical support without which I would have struggled greatly.

Tas Khatra, thank you for your support and your faith that I would not be a student forever.

Contents

Chapter 1. Introduction

Since the 1940s, the UK has accumulated a large inventory of Intermediate Level nuclear Waste (ILW) with the majority produced through nuclear power generation, weapons production and research [1]. At present, 163,000 m^3 of this hazardous waste is stored in various facilities at nuclear licenced sites such as at Sellafield Ltd., and it is anticipated that a further 335,000 m^3 will be generated through ongoing reprocessing and decommissioning operations [2]. The baseline treatment plan for ILW is encapsulation in cement within stainless steel containers. The current plan for England and Wales involves long term storage of these containers in interim storage facilities for up to 100 years, or until a Geological Disposal Facility (GDF) becomes available. This facility, which will allow final disposal of ILW in a deep underground environment, will be constructed and operated by RWM Ltd. (Radioactive Waste Management) once a suitable site and willing host community are located [3]. The key principle of the GDF is the multi barrier system. This consists of the wasteform, the container, backfill material and the host rock. The performance of the ILW containers during the anticipated prolonged storage period, in addition to the environment in the disposal facility, post emplacement, is critical to the safe management of ILW.

In the ~100 years prior to being emplaced in a GDF [4], the containers will remain in interim storage facilities, near the UK coast, where chloride-containing aerosols, are able to come into contact with container surfaces, often in humid conditions and with little temperature control. Due to the presence of chloride contamination on the containers currently in storage, and those yet to be stored, and the propensity for stainless steel to corrode both by Atmospheric Stress Corrosion Cracking (ASCC) and by under-droplet pitting, corrosion is a phenomenon that is closely monitored by the waste producers and the NDA (Nuclear Decommissioning Authority) [5].

To facilitate contamination removal and to address some of the corrosion concerns during storage, the surface specification of the stainless steel used for ILW containers is relatively high and, therefore, expensive. It is anticipated, for example, that the price of one $3m^3$ box for ILW encapsulation will cost on the order of £40k. Given the fact that a large number of containers are yet to be produced, and that the UK Government's Nuclear Sector Deal states that a 20% reduction in decommissioning costs must

be achieved by 2030, it is prudent to investigate whether such high surface specification is required [6]. Numerous techniques exist for treating the surface of stainless steel, and *some* of their effects on corrosion initiation are already known, as discussed in the literature review presented in Chapter 2. These techniques vary in cost and complexity and affect surfaces both physiochemically and microstructurally. The research presented in this Thesis provides an underpinning scientific understanding of the mechanisms by which surface finish can affect corrosion initiation, such as through stress concentrations or through affecting near-surface diffusion. The conclusions drawn may be used to inform future container manufacture, further research or the development of new surfaces.

The Thesis is structured as follows:

Chapter 2 is a review of the relevant literature on Intermediate Level Waste containers, the conditions in which they are stored and the planned development of these environments. It outlines the theory behind corrosion in stainless steel and its specific relevance to ILW containers. The body of research on the effect of surface finish on corrosion is presented and its relevance in the context of this Thesis is investigated. Finally, the phenomenon of surface stress concentration and how surface finish influences the localisation of stress is explained, which underpins the experimental work carried out in Chapter 6. The experimental methods for the results chapters are outlined in Chapter 3. This includes the methods used for sample preparation, in-situ corrosion trials (Chapter 4), Electron Backscatter Diffraction (Chapter 5), and ASCC trials (Chapter 6).

A thorough characterisation of the morphology of a range of common surface finishes applied to stainless steel is presented in Chapter 4. This involved using Atomic Force Microscopy (AFM) and Vertical Scanning Interferometry (VSI) methods to characterise and quantify surfaces by height, surface area, fractal behaviour, and by using spatial, hybrid and functional parameters. Additionally, novel parameters such as openness were presented and mapped. An in-situ accelerated corrosion trial using VSI showed the effect of specific features on corrosion rate around key features on the surfaces. Results supported the use of openness mapping as a tool to predict locations of corrosion initiation and as a parameter for overall surface performance.

Chapter 5 investigates the impact of surface finish on the microstructure of stainless steel for ILW containers. It uses crystallographic data from Electron Backscatter Diffraction (EBSD) to estimate strain through misorientation profile analysis and damage through grain refinement. The Chapter presents a calculation of grain stress that considers grain shape through a measurement of grain length and width. The finding of high levels of residual stress in ground and shotblasted surfaces supports previous literature that suggests these surfaces can undergo SCC with little or no applied stress [7].

Chapter 6 considers the implications of stress concentrations brought about by the morphology of characteristic surface features on ASCC. Surface morphology was found to affect the distribution of stress, creating stress concentrations around certain surface features such as valley minima. These concentrations can be many times higher than an applied stress, creating a critical cracking stress in a material that would otherwise maintain its integrity. Analytical models (the Neuber model and the Arola and Ramulu model) for estimating the magnitude of the stress concentration factor caused by surface finish were applied to topographic data gathered by AFM and VSI. The results of these were compared with Finite Element Analysis (FEA) modelling using the same data. ASCC trials on U-bend corrosion specimens showed *surface-finish-caused* stress concentrations to influence crack development.

Finally, Chapter 7 presents the results arising from an in-situ corrosion experiment performed at the Sellafield site. Stainless steel samples with different surface finishes were exposed to the coastal salt-rich aerosol environment for 8 months, so that comparison could be made between “real-life” corrosion environments and those accelerated experiments performed in the earlier chapters in this Thesis. Analysis of the extent of corrosion of the different surface finishes is presented, in addition to a detailed quantification of pitting corrosion, performed by VSI methodology. These results highlight the complexity of uncontrolled “real-life” experiments and serve to demonstrate corrosion behaviours predicted in previous chapters such as pitting preference in valley minima.

Chapter 2. Literature Review

2.1. Intermediate Level Waste in the UK

2.1.1. Intermediate Level Waste

Intermediate Level Waste (ILW) is the term used to describe all nuclear wastes produced in the UK that are not sufficiently radioactive to be heat producing but a significantly higher radioactivity than Low Level Waste (LLW) such that it exceeds 4 giga-becquerel (GBq) per tonne of alpha activity, or 12 GBq per tonne of beta/gamma activity [8]. It includes a broad range of materials, including, but not limited to, steels, graphite, concrete, cement and sand, sludges, ion exchange resins and flocculants. Radioactive waste is produced by the manufacture of nuclear fuel, the operation and decommissioning of nuclear power stations, reprocessing of spent nuclear fuel, nuclear R&D, nuclear weapons production, research, medicine, and industrial users [1].

The baseline treatment plan for ILW is encapsulation in cement within stainless steel containers. The waste is placed in 500 L drums made from 316L and 304L stainless steel and two types of 3 m^3 boxes made from 2205 duplex stainless steel; one of these boxes is designed to hold pile fuel cladding silo

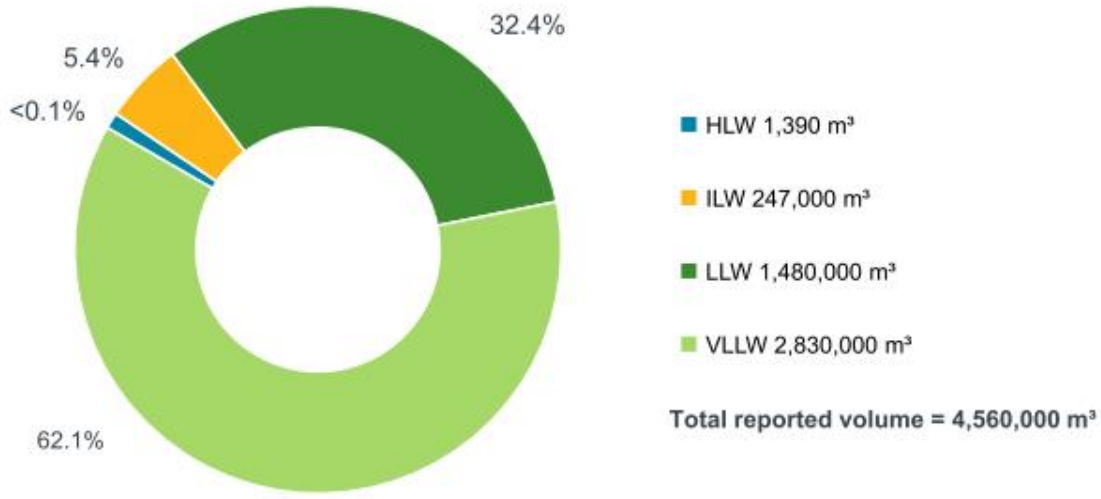

Figure 2.1 Waste volume by type, including: Very Low Level Waste (VLLW); Low Level Waste (LLW), Intermediate Level Waste (ILW) and High Level Waste (HLW).

waste and the other one to hold Magnox swarf. ILW currently makes up 5.4% of the UK's nuclear waste stockpile, with a total volume (including future arisings) of 247,000 m^3 as shown in Figure 2.1 [1]. This value has reduced by 15% between 2017 and 2019 due to reassessment of wastes, mostly into lower categories.

A rough estimate shows that approximately 500,000 containers of 500 L volume will be required to store 247,000 m^3 of waste; as of 2017, NDA reported there are 60,000, meaning that 440,000 are still required to be manufactured [9].

At present, this waste is stored in various facilities at nuclear licenced sites such as Sellafield. The current plan for England and Wales involves long term storage in interim storage facilities, and final disposal in a Geological Disposal Facility (GDF) constructed and operated by RWM Ltd (Radioactive Waste Management). This facility, due to be built by 2075, would isolate the waste from the biosphere in specially built tunnels and vaults between 200 m and 1000 m deep in a stable rock form underground, while the radioactivity decays [5]. The basis for RWM's current design work considers high strength rock, sedimentary rock (clay) and evaporites (salt) as potential rock types [10]. It is expected that the containers will remain in interim storage for around 100 years before being moved to a GDF [4]. The location, or specific type of engineering to be used for the GDF has not yet been decided. The UK government are currently appealing for a community to volunteer to host the facility. The Scottish government have no plans to build a GDF, instead opting for near surface disposal [11].

2.1.1.1. Intermediate Level Waste Containers and Surface Finish

ILW containers must fulfil several key requirements, as follows [12]:

- Mechanical strength to withstand stacking forces;
- Perform well against impact;
- Perform well against fire;
- Resist corrosion for an adequate period;
- Be cost effective.

This has led to the use of 304L stainless steel as it tends to have extremely low corrosion rates, and is strong, ductile, and readily available.

Unshielded ILW containers include 500 L drums, 3 m^3 boxes and 3 m^3 drums. The 500 L drum is the primary focus of this Thesis and is shown in Figure 2.2. These drums are manufactured from stainless steel sheet or plate. The walls and lid are 2.33 mm thick and the base is thicker, at 2.93 mm. The lifting flange is thicker still, and can be either 15 mm or 30 mm. The total size of a container is 1200 mm high with a diameter of 800 mm [13].

Figure 2.2 A 500 L Intermediate Level Waste container [13]

The surface finish of the 500 L container has a tightly constrained, high specification, which is costly to produce. The steel used in the manufacture of the drums is wet bead blasted; either Vaqua or aqua blast [14]. This process involves an ultra-high pressure (140 MPa) waterjet carrying glass beads that strike the surface of the steel. This deforms and stretches the surface, leaving a compressive stress. The process also cleans the surface and provides a desirable surface finish for SCC protection [13]. However, this process can be costly and for other containers such as the 3 m^3 box, rolled finishes such as 1D are employed. The rolled finish is cheap, matte, and smooth. Alternatively, the surface could be ground with silicon carbide grit or brushed with wire brushes to apply a directional finish. If these finishing techniques are found to be as effective as shotblasting, they could be used to dress areas such as weld seams.

2.1.2. Intermediate Level Waste Container Storage Conditions

Intermediate level waste containers will be subject to a variety of conditions and environments throughout their long service life. They are stored above ground in specialist interim storage facilities, before experiencing transport, emplacement within vaults in a GDF pre-closure and finally, surrounded by a buffer material in a GDF post-closure. Each one of these stages will have unique conditions and will pose different risks to the container integrity, so corrosion at each stage must be considered in the design. The containers will reside in their current location, in interim storage in specialist facilities, for around 100 years [4]. Early conditions for a stainless steel surface are known to impact lifetime performance of the surface [15]. The time spent in interim storage will be critical to the longevity of ILW container surfaces while at the same time, the performance of a relatively young material such as stainless steel over 100 year timescales is difficult to predict. The transportation of ILW brings higher corrosion risks since defects can be induced by manual handling, such as scratches or other damage, or by contamination. It is at this time when it is most important that ILW containers retain their integrity.

Though interim storage facilities have been well optimised for their purpose, there are several conditions present that can contribute to the risk profile. The conditions that affect corrosion and are considered in this Section are:

- Temperature
- Humidity, including humidity flux
- Surface contamination, composition and rate of deposition
- Surface stress and residual stress

2.1.2.1 Container lifetime

The lifetime of ILW containers, and the associated temperature is presented in Figure 2.3. The interim phase is expected to last 100 years, during which time the storage temperature will be 1 to 24°C [4]. During the emplacement phase, which is expected to last 100 years, the temperature in the GDF rises to around 35°C [16]. The temperature is expected to rise to 80°C for around 10 years during backfilling [16]. Post-closure, a calculated stable temperature of 35°C is expected to be reached and maintained for 100,000 years [16].

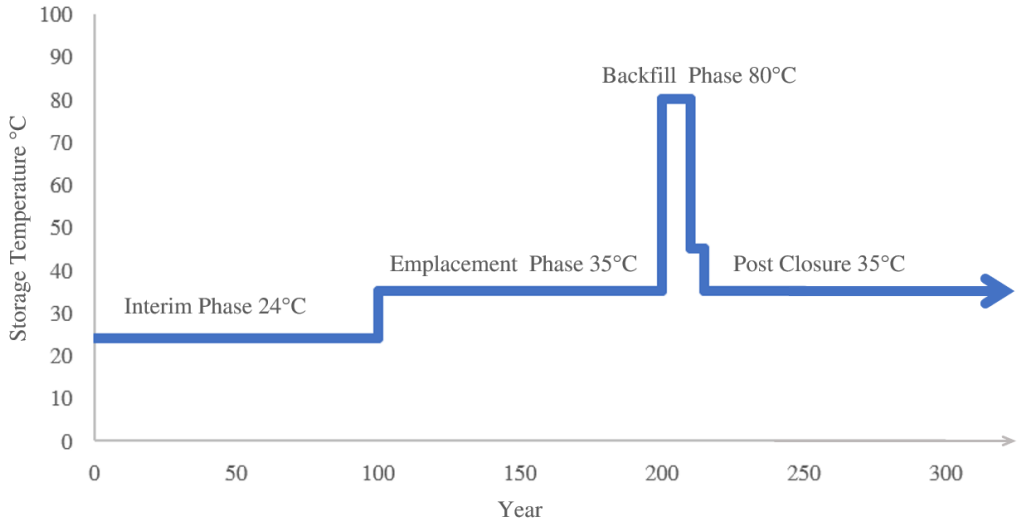

Figure 2.3 ILW container timescale with temperature conditions.

2.1.2.2. Temperature

Current monitoring of ILW container interim storage facilities has found that the temperature fluctuates seasonally between 1°C and 24°C and a temperature difference of 6-12°C was detected between the top and bottom of the storage facility [17]. These fluctuations indicate there is little control of temperature in these facilities. Since ASCC has been shown to occur at 25°C, and temperature fluctuations may reach 25°C, this indicates that this type of corrosion may occur in ILW containers in interim storage, especially considering the long timescales [14].

A heat distribution study, intended to model the pre-closure temperatures of a GDF using the Nirex GDF design, found that for a ventilated, fan-cooled repository, a stable temperature of 30°C was likely. For an unventilated repository, or for a ventilated repository with dysfunctional fans, temperatures of 43°C would be reached [18]. ASCC has been shown to occur well below both of these temperatures. This study used a waste-heating rate of 3.5 W/m^3 with an average of 18780 m^3 of waste per vault, giving a heat load of 65.75 kW. These values could change depending on the repository design.

Post closure, NDA technical specifications give 80°C as an acceptable temperature for the first 5 years of a facility that uses a cementitious backfill. The backfill itself is also somewhat heat generating during the curing process [19]. After the cement curing heat source has reduced significantly, radioactive heating and geothermal effects were considered and these gave a long term GDF temperature of 50°C [19]. Corrosion will significantly increase at these temperatures. The initiation of corrosion mechanisms such as pitting and cracking require more aggressive conditions than their continuation, meaning the cooling to 50°C may not halt corrosion that initiates at 80°C.

Effect of Temperature

Temperature is a critical factor in both ASCC and for pitting corrosion. There is an increased corrosion rate with temperature, discussed further in Section 2.2.1.2., and a critical temperature for both ASCC and for pitting corrosion, below which this corrosion type will not occur [20]. For a given material this temperature is extremely reproducible.

At temperature below the critical pitting temperature, there are extremely high breakdown potentials, which, instead of being indicative of localised corrosion, instead correspond to transpassive dissolution. Just above this temperature, pitting corrosion can occur at much lower potentials. There is a weak relationship between temperature and pitting potential from here, with lower pitting potentials occurring at higher temperatures [20].

ASCC at low temperature in an austenitic stainless steel similar to 304L (302) has been observed at 40°C under zinc chloride deposits [21].

ASCC has been shown to occur in types 304L and 316L stainless steels under ambient conditions, for example, under ambient conditions ASCC occurred at 7-10 mol/dm^3 Cl^- for 304L and 8.5-10 mol/dm^3 Cl^- for 316L at the equilibrium RH [21]. $MgCl_2$ was used as the source of chloride ions and it was concluded that $MgCl_2$ was the constituent of sea water responsible for low temperature SCC [21]. This shows that ASCC can occur at low temperatures (25°C was the lowest observed in these papers), showing that current interim storage of ILW is very close (24°C) to the temperature range that allows ASCC. Additionally, GDF pre and post closure will both be in the temperature range for ASCC, as shown in Section 2.1.

Critical pitting temperatures for stainless steels have been found in the rage of 10-100°C [22]. For 304 grade stainless steel, pitting has been observed below 20°C, showing ILW containers to be within this range [23].

2.1.2.3. Humidity

Humidity within interim storage facilities is not controlled. During regular monitoring it has been found to vary between 21% and 94% RH [17]. Since relative humidity and temperature are closely related it is highly likely that the smaller fluctuations in temperature cause the much larger fluctuations in humidity. It has been suggested that humidity fluxes causing repeated deliquescence and recrystallization of salt particles on the container surface could consequently coalesce multiple salt droplets to create larger, more corrosive droplets or individual droplets with higher local chloride

concentrations [24]. In this way humidity cycles during interim storage can be harmful. The most vulnerable range for humidity is close to the deliquescence point for a given contaminant. These ranges have been established by Greenspan (1976) [25].

Prior to being filled, the target relative humidity ranges for the Nirex generic repository is 40 – 60% RH [26]. This has been shown to be near the optimal range for $MgCl_2$ driven SCC. Although these are the targets, models have shown it is unlikely that they will be achieved. The predictions showed that the RH would fall below 40%, even closer to the optimal SCC range for $MgCl_2$ driven SCC of 32.7% [18][27]. $MgCl_2$ has been shown to be the driver of low temperature ASCC [28]. At other times, prior to closure, predictions showed humidity would reach as high as 70%, nearing the range for NaCl driven ASCC, which optimises at 75.1% RH [18][27]. This means that ILW containers are stored in the vulnerable rage regarding humidity.

Effect of pH on Corrosion

In a study using 0.2 M NaCl solution, the corrosion rate of 304L stainless steel has been show to increase with decreasing pH [29]. It was noted that this was consistent with the pH dependence of the breakdown potential of the passive film, which is well established. The pitting potential, however, has been shown to be independent of pH [20].

2.1.2.4. Surface Contamination, Composition and Rate of Current Deposition

During interim storage ILW containers are under semi-controlled conditions. The atmosphere is filtered, and the temperature and humidity are monitored. However, contamination from the air still finds its way to the surface of these containers, possibly due to periodic monitoring. With the majority of containers stored at Sellafield, located on the NW coast of the UK, and others at decommissioned nuclear power stations, which tend to reside next to the sea, this contamination will contain sea-borne aerosol particles, which are salt-rich. For example, the outside chloride deposition rate at Sellafield has been measured at between 15 – 75 $\mu g/cm^2/d$ NaCl [30].

The composition of deposits on the surface of ILW containers may also consist of particles acquired before storage, filling, or during transit, depending on the cleaning procedures. Additionally, it should be considered that unless a cleaning stage occurs between interim storage and disposal, contamination collected during storage will build and then exist on the surface for the lifetime of the container.

In a report to the NDA on conditions in ILW stores it was found that the surface chloride concentration measured as high as 13 μg/cm^2 in locations considered to be representative of containers, including on a dummy drum [17]. This value is both above the density required for ASCC and the suggested maximum density of 1 μg/cm^2 at ambient temperature [31]. If the surface stresses are high enough, it is highly likely that ASCC will occur in ILW containers in interim storage. In general, horizontal surfaces gather much more chloride contamination than vertical surfaces [17].

Compositions of particulate contamination were found to be broadly similar in a range of stores from Culham, Harwell, and Winfrith. Cations sampled by amount were Na>Ca>K≈Mg, with traces of Ba, Sr, Fe, Cu, Mn, Al, Cr, Ni, Si. Other chemicals measured included sulphate (up to 20 μg/cm^2), nitrate (up to 3.9 μg/cm^2) and carbonate [17]. The sodium to magnesium ratio detected was between 6 and 21 [17]. This lowers the critical corrosion humidity into the current target humidity of the interim ILW stores. With this ratio, high humidity would reduce the corrosion rate as it would dilute the chloride concentration on the surface. During storage design it is important to consider that the critical corrosion humidity range depends on the composition of the contamination and is not necessarily the case that higher humidity is worse. The amount of chloride present on the surface of containers has been found to be affected by human activity, partly because some of the chloride stems from 'dermal detritus' and in part is attributed to the disturbance caused by people. Typical indoor deposition rates have been measured to be 1 μg/cm^2/yr but can rise to 5 μg/cm^2/yr during peaks in human activity [32]. In a separate series of measurements on a 4m^3 box at Culham/Harwell the chloride deposition rate was found to be between 1 – 4 μg/cm^2/yr [17].

In a waste package specification and guidance document it was reported that there is a risk of pitting and rust staining at 25°C ambient temperature and a RH of 50 - 70% above a surface chloride concentration of 10 μg/cm^2 [30]. This shows that interim storage facilities are already entering the risk zone for ASCC. Currently ASCC has not been detected on an ILW container in an interim store, however it is known that induction times associated with ASCC can be long and show large variability [33]. The current amount of chloride on ILW containers is sufficient for ASCC, and the annual deposition rate is high.

While salt-induced corrosion is a particular concern for the longevity of interim storage, geological disposal relies upon the slow corrosion of the container by groundwater and high pH cement backfill to maintain reducing conditions (by the generation of hydrogen gas in the corrosion mechanism), thus lowering the solubility of radionuclides in the waste. The key principle here is that the corrosion should occur slowly, to maintain reducing conditions for as long as possible. Although most grouted ILW

containers do not contain extremely high concentrations of chlorides, a limited fraction may do so. Furthermore, radiochloride (^{36}Cl) is one of the decay products of graphite waste and is expected to be present in significant quantities in a UK GDF. As such, there is a concern that the high concentrations of chloride in the pore water of any encapsulant grouts, or cement backfill, might promote localised corrosion of container materials [34]. This is also a concern for interim storage when considering the materials encapsulated within steel drums; chloride-driven corrosion from the inside of a container is a risk, as wastes can contain relatively high concentrations of chloride and grouting is not effective at stopping the chloride driven corrosion of steel.

Effect of Chloride Deposition Density

It has been suggested that a minimum chloride deposition density is required for ASCC to occur. One study on 304 stainless steel, using NaCl at 50°C, found a critical chloride deposition density for cracking of 1 μg cm^{-2} [35]. Albores-Silva *et al.* investigated the critical chloride density for 316L, and found 10 and 25 μg/cm^2 for 50 and 30°C, respectively, at the equilibrium RH of $MgCl_2$ [21]. In a study that used an inkjet printer to dispense low levels of $MgCl_2$ onto a 304 plate, a chloride density of 3.5 μg/cm^2 was found to cause pitting at 45% RH at room temperature in just 24hrs [36].

These studies also showed that the critical chloride deposition density, i.e., the minimum density required to initiate cracking, is highly dependent on both the temperature and also the chloride source, with $MgCl_2$ being more aggressive than NaCl. As such, Magnox have proposed safety limits for surface chloride concentration that match the critical chloride density in the literature. They have suggested a maximum of 1 μg/cm^2 at ambient temperature and 0.1 μg/cm^2 at 50°C [31].

2.1.3. The Sources of Stress in ILW Containers

Stress occurs in when non uniform forces act on an object. It is defined as the ratio between the force to the cross sectional area (Equation 2.1) such that it describes the distribution of the force across the object.

$$\sigma = \frac{F}{A} \qquad \textit{Equation 2.1}$$

Strain describes the proportional change in dimension of an object that has resulted from an applied stress and is defined by Equation 2.2.

$$\varepsilon = \frac{\Delta L}{L_0} \qquad \textit{Equation 2.2}$$

Figure 2.4 shows the typical relationship between stress and strain. Below a certain amount of stress, the yield point, the material behaves elastically and will return to its original dimensions with the removal of the stress. The curve is linear in this range. At greater stresses, the material undergoes plastic deformation, dislocations in the material change the microstructure so that the material permanently changes shape. The curve becomes flatter, meaning greater stress increases are required to produce the same amount of strain increase. This is known as strain hardening. The ultimate strength represents the greatest amount of stress a material will undergo before necking and fracture occur.

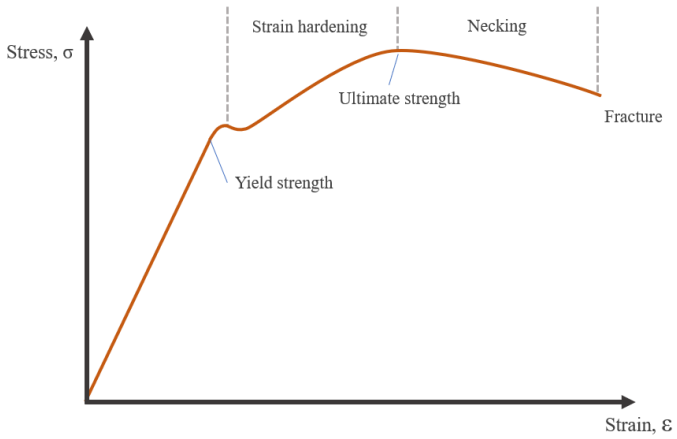

Figure 2.4 The stress-strain curve.

The state of stress on the surface of an ILW container is the summation of a range of factors. Stresses are applied operationally, from transporting, filling and stacking, and exist residually from container manufacturing and surface finishing. Residual stress is a well-known effect of some surface finish procedures. For instance, shotblasting produces a strong compressive stress [37], while grinding can impart tensile stress [38]. Since SCC requires a surface tensile stress, a residual surface compressive stress can be beneficial as it reduces corrosion as in the case of shotblasting. In contrast, residual tensile stresses imparted by grinding or machining can be detrimental, because it can promote SCC and have microstructural or phase altering effects [39].

Pitting has been shown to occur more in ground surfaces than milled surfaces, even when the Ra (Roughness) value is lower [38]. This is thought to be an effect of the higher tensile residual stress caused by grinding. Crack formation has been found to occur perpendicular to the machining direction [40]. This is in opposition to the stress concentration theory that would expect cracks to run along the bottom of valleys. Instead, it was found that the machining process imparted a tensile stress in the machining direction, as cracks form perpendicularly to the direction of stress, in this case they cut across the valleys instead of along them.

Stress makes up one of the three required components of SCC. Stress itself is made of two components, residual stress from manufacturing process and operational stress, as detailed below [41].

2.1.3.1. Operational Stresses

Operational stresses tend to be small and unlikely to contribute to ASCC. In comparison, stresses caused by manufacturing and surface finishing are an order of magnitude larger. This section presents the main operational stresses and their calculation.

Operational stress loads on the 500 litre drums will arise due to lifting and stacking operations. Calculations have previously been carried out to determine the stresses in the drum and these are summarised in Table 2.1 [13]. Tensile stress is presented as a positive number, and a range of values for the stacking stress have been calculated for multiple different assumptions.

Table 2.1 Operational Stresses in Intermediate Level Waste Containers

Loading	Stress
Lifting	+ 5 MPa
Stacking	-20 MPa
	-11 MPa
	-42 MPa

Stacking

ILW containers must be designed to withstand a minimum stacking load, according to the Nirex Waste Package Specification [30]. The 500 L drum package is usually stored in stillages that provide support, that do not use lower drums in a stack to support upper drums, however they can be stacked up to 7 high without stillages, relying solely on the drum structure to carry loading [13]. It is important to note that the drum structure is designed to carry the load, rather than the wasteform itself, to ease the wasteform criteria [42].

For a maximum drum weight of 2,000 kg this amounts to an additional 12,000 kg resting on the lowest container to support through a 0.005 m^2 cross section of material [42]. This gives a compressive stress of 23.5 MPa. Previous literature has asserted that since this is a compressive stress, it will act to mitigate the corrosive effects of tensile stress and benefit the container [13]. However, this compressive stress is vertical, and the largest applied stress (hoop stress) is horizontal and so they do not add. Additionally, from Poisson's ratio this creates a horizontal tensile stress of 7 MPa which is the largest operational tensile stress.

Overall, the stress due to stacking is the cause of the highest tensile stress in the containers and makes them more vulnerable to ASCC. This can be made worse by uneven load distribution at the interface between adjacent containers or imperfect alignment between containers in a stack. The current recommendation is that the worst expected alignment would be around 25 mm off-set [42].

Lifting

When a container is lifted by its flange it experiences both a hoop stress induced by the pressure differential (during grouting) and a cylinder stress caused by tension induced by the weight of the contents resting on the base plate [42].

The entire weight of the container and contents is held by a 0.005 m^2 cross section of the container. Since the maximum allowed loading of the container is 2000 kg, this gives a (fully loaded) vertical tensile stress of approximately 200-400 KPa [43]. This is an achievable mass should the waste consist of, for example, grout containing 30% steel.

It is also well known that a tensile stress in one direction will also produce a stress in the transverse direction. The ratio of transverse to longitudinal stress is given by Poisson's ratio which is shown by Equation 2.3 [44].

$$\varepsilon_x = \varepsilon_y = -v\varepsilon_z = \frac{-v\sigma_y}{E} \qquad \textit{Equation 2.3}$$

Where ε_x and ε_y are transverse strains caused by a longitudinal strain ε_z. v is Poisson's ratio and σ_y is an applied stress and E is the Young's Modulus. Poisson's ratio for stainless steel is between 0.27 -0.30 [45].

This suggests that the tensile vertical tensile stress of 400 kPa would impart a tensile horizontal stress of 120 kPa, adding to the stress already present at the surface. This stress would be transient and only exist during lifting, reducing its effect on ASCC vulnerability.

Filling

ILW containers contain waste that has been encapsulated using a liquid grout, which imparts a pressure onto the walls of the container. These walls get their strength from the excellent tensile properties of steel. 500 L of grout at 1800 kg/m^3 weighs 900 kg. The column of grout inside a container is around 1.1 m high which creates a pressure at the bottom of the drum of around 20 kPa.

For a thin wall cylindrical vessel, Equation 2.4 is used to calculate the hoop stress.

$$\sigma_\theta = \frac{Pr}{t} \qquad \textit{Equation 2.4}$$

P is the internal pressure; *r* is the radius of the cylinder (400 mm) and *t* is the thickness of the walls (2.3 mm). This equation gives a circumferential tensile hoop stress of 3.5 MPa near the bottom of the container. This pressure is exerted during the grouting process, however after this the grout sets and shrinks the pressure is greatly reduced.

The stacking tensile stress of 7 MPa will add to the hoop stress of 3.5 MPa in some circumstances. If the interior grouting had not set, or if it were to relax while stacked, these stresses add to a maximum tensile stress of 10.5 MPa.

2.1.3.2. Residual Manufacturing Stresses

Forming Process

The dimensions of an ILW container are shown in Figure 2.5. The manufacturing process for 500 L ILW containers involves bending sheet metal around rollers to form the drum before autogenously seam welding. The drum is then swaged to improve its structural strength. The base is formed by drawing with a press and is then machined to size and welded onto the body.

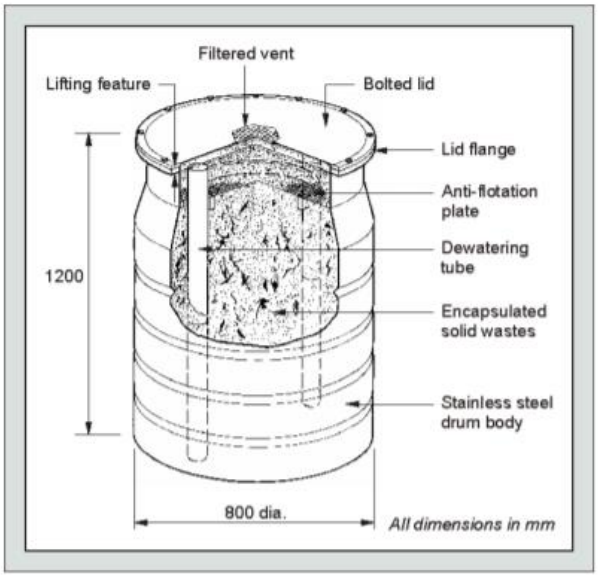

Figure 2.5 A 500 L ILW container [46].

The flange is made from a flat bar section, which is ring rolled into a circle with the correct diameter, and welded to the body. This weld and previous welds are then machined to the correct tolerance. Drums are then cleaned by Vaqua blast for visual inspection which uses a non-destructive dye penetrant test method [46].

The drums are then moved on to final assembly where drum internals may be added (paddles, grout tubes, filters, welded lids). The drums/lids and filters are then tested for leakage before each container is blasted with a fine glass bead to provide a consistent and decontaminable external surface finish.

The manufacturing processes used can be broadly defined by cold working (rolling, pressing), machining (cutting, grinding), welding (autogenous, flash butt) and surface treatment (finishing). Each of these processes results in residual stresses which may be detrimental to the long term integrity [13].

Welding Stress

The container parts are joined by TIG welding. Two pieces are brought together and heated by an electrical arc from a tungsten electrode. A melted pool of metal joins them requiring no filer material. This metal cools, solidifies, and contracts creating high residual stresses. Heat treatment can reduce these stresses though no heat treatment is known to be applied to ILW containers [47].

A tensile surface stress of 400 MPa has been measured 50 mm from ILW container welds and a 500 MPa compressive stress 50 mm into the material [47].

2.1.3.3. Residual Stresses Due to Surface Finishing

Shotblasting

Shotblasting involves conditioning the surface of steel high speed particles known as shot. These can be glass balls, in a high pressure water jet, or steel particles in air. Their impact on the surface of the material deforms it, leaving a crater. These impacts increase the number of dislocations near the surface due to the large amount of plastic deformation. These defects store elastic energy, creating residual stress, and creating work hardening [48].

With depth, the stress induced by a single shot is compressive, however in the transverse direction the crater has a tensile centre and a compressed ring of material surrounding it [49]. The superposition of stress rings caused by many shots will cause there to be a residual compressive stress across the entire surface. The compressive stress created by shotblasting has been shown to reach from 0.4 mm to 0.15 mm into the material [37][50].

Industry research has found compressive stresses of 500-760 MPa [41]. It has also been shown that this stress can be extremely effective at stopping SCC [41].

Modelling of the shotblasting process has suggested there to be a large variability in the residual stress distribution, potentially caused by incomplete coverage or variations in the shapes of the shot [51]. This means that the ability of this process to protect from SCC may not be conferred to the entire surface.

Grinding

Grinding has also been found to impart residual stress into steel. This effect is different depending on whether the material has been ground longitudinally according to its rolling direction, or transversely. A study that used X-ray fluorescence to measure the residual stress present in the top 10 μm of stainless steel found a residual stress of 200 MPa in both the longitudinal and transverse directions of a longitudinally ground surface, but for a transversely ground surface, the stress was higher in the transverse direction at 400 MPa compared to 250 MPa in the longitudinal direction [38]. This suggests that the grinding process imparts a tensile stress in the direction of grinding and a compressive stress laterally, both of with interact with the residual stress already present in a rolled sheet. This study also found a large variation of between 100 – 200 MPa for each condition. Very close to the surface, the tensile residual stress was very high (approaching 1000 MPa). This is likely to encourage crack

initiation. It was deduced that these high residual stresses were accommodated by either local work hardening or by a significant reduction in grain size.

Machining

Machining steel imparts a tensile residual stress in the machining direction. It has been shown that this stress ranges from 190 to 700 MPa [40]. Machining of 304L has been shown to impart heavy plastic strain near the surface (150 μm deep), which is found with a high number of slip bands, deformation, and grain refinement [39].

2.1.3.4. Summary of Stress Environment

Table 2.2 presents the sources of stress and their magnitudes for a 500 L ILW containers. The magnitudes are all the maximum tensile stress caused by each source.

Table 2.2 Summary of Container Stresses

	Source of Stress	Magnitude of Stress
Operational	Stacking	7 MPa
	Lifting	0.4 MPa
	Filling	3.5 MPa
Manufacture	Welding	400 MPa
Surface Finish	Shotblasting	-800 MPa
	Grinding	1000 MPa
	Machining	700 MPa

304L stainless steel has a yield stress of 210 MPa and an ultimate strength of 560 MPa [52]. That the measured residual stresses can be above these numbers suggests that these processes create a large amount of work hardening and phase transformation. The high level of stress known to be present, makes the material vulnerable to SCC.

2.1.3.5. Dislocations in Metals

Metals tend to form crystalline solids [53]. This means atoms within individual grains form in a periodic arrangement. In real materials, this arrangement is often disrupted by imperfections that come in a

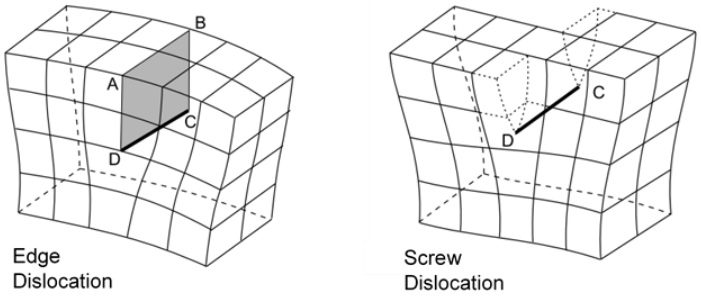

Figure 2.6 The effects of an edge dislocation and a screw dislocation on a crystal lattice [55].

number of types. Figure 2.6 shows two ways in which a crystal lattice can be disrupted. These are linear imperfections: edge and screw dislocations. Not shown in this figure are point defects, such as vacancies and interstitials which also play a role. These disruptions have a strong influence on the physical and mechanical properties of metals [54].

Edge dislocations can be visualised as the insertion of an extra half plane of atoms in the middle of a crystal. This causes the surrounding planes to bend around the edge of the extra plane, analogous to the insertion of half a sheet of paper into a stack of paper.

In a screw dislocation a path spirals around a dislocation line penetrating through otherwise individual planes. An example could be formed by the crystal lattice being cut into and the regions separated by the cut being shifted by one atom, and reattached.

Dislocation Motion

With the application of stress, bonds around dislocations stretch, break and reform, resulting in the movement of dislocations. This allows planes of atoms to slide over each other at significantly lower stress than the ideal strength. This process is known as glide or slip [55]. Through this mechanism, dislocations allow the movement of large number of atoms and are responsible for plastic deformation.

A slip occurs above a certain stress on the slip plane, called the critical resolved shear stress (CRSS), which is directly related to the mechanical strength of the metal. This critical resolved shear increases as plastic deformation increases, this is known as work hardening.

Crystal Plasticity

Dislocation motion occurs along a particular direction and over a particular plane, these are called the slip direction and slip plane [53]. The combination is called a slip system. These planes are usually the most densely packed planes in a crystal. In FCC metals slip planes correspond to the {111} close-packed planes, while slip directions correspond to the <110> close-packed directions [54].

To summarise, plastic deformation in metals takes place by the slip of crystal planes. This occurs at lower shear stresses than for an ideal crystal structure because the motion of imperfections (dislocations) in the lattice allow slip to occur at significantly lower stress levels.

2.2. Corrosion in ILW Containers

The NDA (Nuclear Decommissioning Authority) considers corrosion of ILW containers to be a major potential threat to the integrity of waste packages during storage [12][30][56]. Some containers have already been stored for 60 years, and since the GDF is not anticipated to start accepting waste packages until at least 2040 (and more likely in 2075), a considerable amount of storage time remains [57][30]. A range of specific conditions must be in place for corrosion to occur, and of all the different types of corrosion, including Atmospheric Stress Corrosion Cracking (ASCC) and pitting corrosion, and especially under-droplet pitting, are a major concern for ILW containers. Considered in Section 2.2.1. is corrosion theory, with specific detail on ASCC and pitting corrosion, including a discussion on the effect that factors including stress, heat, chloride, pH, and inclusions have on these forms of corrosion. This Section begins with an explanation of the theory behind corrosion and passivation in stainless steels, and the corrosion mechanisms relevant to ILW containers.

2.2.1. Corrosion

2.2.1.1. Basic Corrosion Theory

Corrosion is a thermodynamically driven electrochemical process. For corrosion to occur, four requirements must be fulfilled. There must be:

1. An electrified interface between the metal and the electrolyte solution.
2. Transfer of positive charge from the bulk metal in the form of positive metal ions leaving the surface with consequent oxidation of the metal ions to a higher valence state.
3. Transfer of positive charge from the solution to the metal with consequent reduction of a species in solution (an electron accepter) to a lower valence state.
4. Transfer of charge through both the solution and corroding metal [58].

Corrosion can proceed with very simple chemistry or can take more convoluted routes. However, with all routes these features are consistent.

2.2.1.2. Basic Electrode Reactions

Oxidation (the loss of electrons) and reduction (the gain of electrons) can occur thermodynamically spontaneously, meaning that more energy is released than is required to initiate. On the surface of a metallic material containing iron atoms there are two different reactions defining the corrosion process. The main oxidation process in the corrosion of iron is given by Equation 2.5. This occurs at the anode.

$$Fe^{2+} + 2e^- \rightleftharpoons Fe \qquad \textit{Equation 2.5}$$

The sign of the reduction potential sets the direction in which the electrode reaction will proceed. Equation 2.5 has a reduction potential of -0.44 V, meaning the process is driven in the oxidising direction [59]. The main reduction process in the corrosion of iron is given by Equation 2.6 which occurs at the cathode.

$$O_2 + 2H_2O + 4e^- \rightleftharpoons 4OH^- \qquad \textit{Equation 2.6}$$

This has a reduction potential of +0.40 V, making the reaction spontaneous in the reducing direction. This gives the redox reaction an Emf of +0.84 V, this is also known as the corrosion potential or open circuit potential and is what drives the corrosion process. These electrode reactions and can occur apart from each other, with electrons transported through the bulk iron and ions transported through the electrolyte. An applied voltage of -0.84 V would counter the corrosion potential and halt the corrosion reaction. Conversly, the application of a positive voltage would increase the reaction rate, in accordance with the Nernst equation (Equation 2.7) which relates the reduction potential to the electrode potential, temperature and activities of the reactants.

$$E = E_o - \frac{RT}{nF} \ln Q \qquad \textit{Equation 2.7}$$

Where:

E = Reduction potential

E_0 = Standard potential

R = Universal gas constant

T = Temperature (Kelvin)

n = Ion charge

F = Faraday constant

Q = Reaction quotient

2.2.1.2. Passivation Theory

It is understood that, "*The study of corrosion is essentially the study of the nature of the metal reaction products (corrosion products) and their influence on reaction rate*" [58]. It is well known that stainless steel owes its corrosion-resistant properties to its chromium content, although the mechanism by which this works is far from simple, or settled [60]. Stainless steel forms a thin passive layer of relatively inert chromium oxide on its surface upon exposure to oxygen. Unlike the iron oxide layer formed on steel, chromium oxide has a comparable lattice constant, and adheres well with the bulk material. This passive layer does not readily react and so protects the bulk material from corrosion and rust by at least one of several mechanisms, which are described in more detail in this Section.

It is important to consider the various routes by which the passive layer could be formed, as surface finishing processes may affect the surface film differently depending on how it is formed, and exactly how it is formed has not been agreed. In common stainless steels, chromium makes up 18% of the mass and is a substitutional alloying element. Therefore 1 in 5.5 atoms in stainless steel are chromium. One theory suggests that as iron has a much higher diffusion rate in the passive film, an average of 4.5 surface iron atoms can diffuse leaving only the chromium enriched in the passive film [61]. This is supported both by percolation theory and by the fact that iron preferentially dissolves into the electrolyte about 8 times faster than chromium [61]. Should the diffusion of iron from the surface be the rate limiting step for the passivation process, this would affect different surface finishes differently. It could be expected that iron at surface peaks would readily defuse, forming a strong passive film in exposed areas, and weaker films at more closed locations.

An alternative theory is that chromium ions are attracted to the surface of steel and will either move from the near surface to the surface, or once dissolved precipitate back [62]. Should the diffusion of chromium from the bulk to the surface be the rate limiting step for the passivation process, it would be expected that strong passive films would form in valleys where there was greater chromium accessibility, and weaker more vulnerable films would be found at peaks. The different passive film growth models are described below.

Place Exchange Mechanism: Sato and Cohen proposed a model in which a layer of oxygen is adsorbed to the surface and then exchanges, possibly through rotation, with the underlying metal. This process is then repeated by a second layer of oxygen adsorbing to the surface, and the two M-O pairs rotate simultaneously. The oxygen required to form a passive film can be gained from H_2O [63]. In this manner, a passive metal oxide film grows *into* the bulk as shown in Figure 2.7 [62]. This process may be affected by the extreme curvatures of some surfaces.

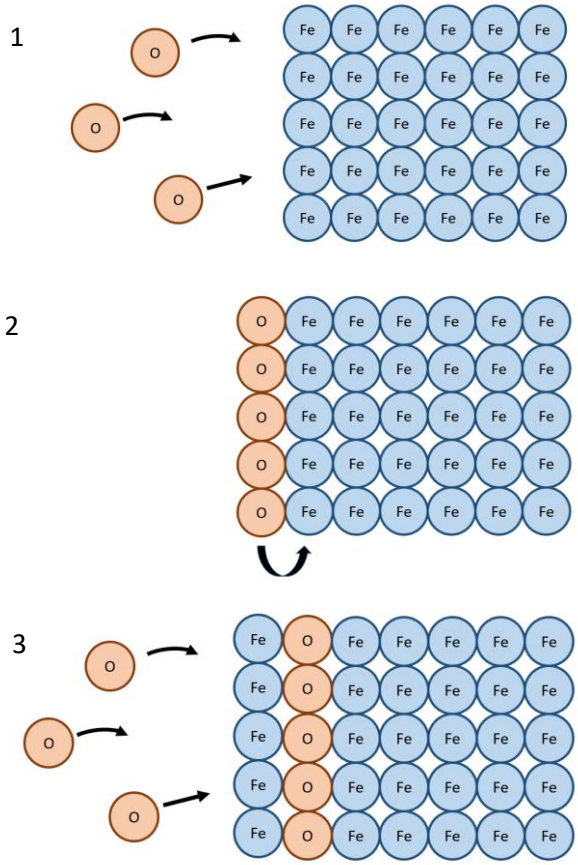

Figure 2.7 Film formation by The Place Exchange Mechanism

Metal Ion Migration: Mott and Cabrera proposed that film growth is due to the migration of metal cations through the film to the film-solution boundary, where they react with the electrolyte as shown in Figure 2.8. There is a strong, uniform electric field inside the film which encourages this [62].

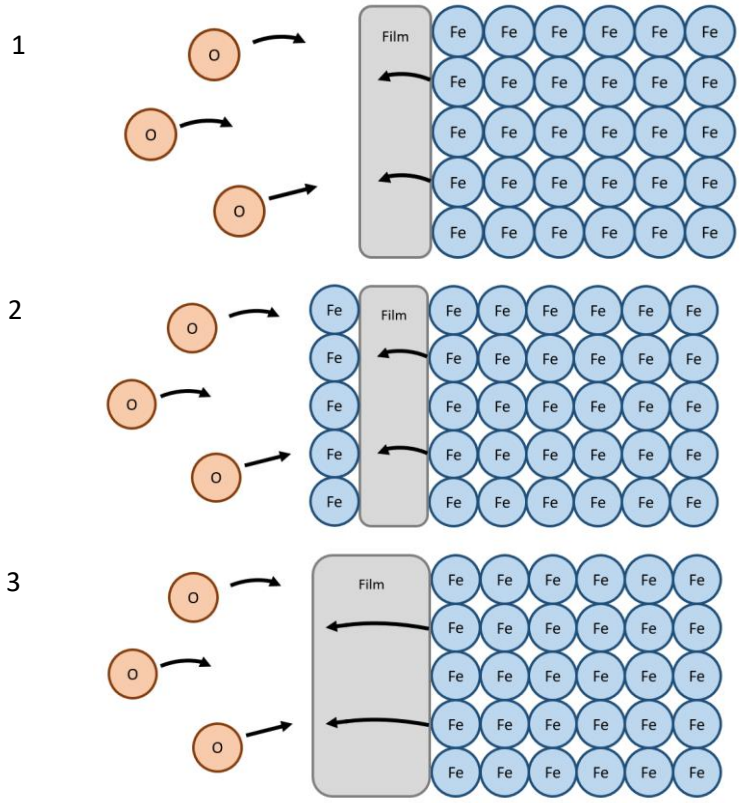

Figure 2.8 Film formation through metal ion migration

Anion Diffusion: Fehlner and Mott proposed another model in which anion diffusion is responsible for film growth. In this model an oxide network grows inwards by oxygen diffusion. The emission of an anion is the rate limiting step and this rate decreases proportional to the thickness of the film [62]. This model is comparable to the metal ion migration model shown in Figure 2.8, but with oxygen crossing the film and reacting with the bulk material, instead of metal ions crossing the film.

2.2.1.3. Pitting Corrosion

A common type of corrosion for stainless steel is pitting corrosion. This is characterised by the creation of small holes or pits in the surface as shown in Figure 2.10. The passive film is broken down in a localised area exposing the depassivated bulk material to the electrolyte, allowing the oxidation of iron. The geometry of the pits slow the diffusion of corrosion products from the site and of oxygen to the site [64]. This leads to pits developing a local chemistry distinct from the bulk electrolyte which can become highly acidic [65]. Oxygen consumed in the normal corrosion process becomes depleted in the pit. Iron ions hydrolyse water to produce iron hydroxide and protons which lower the pH. This local environment

is highly acidic causing an increased corrosion rate. The accumulation of positive charge in the pit attracts negative ions such as chloride and hydroxide which diffuse into the pit to maintain a minimum potential energy. Metal chloride is formed and undergoes hydrolysis, lowering the local pH, increasing corrosion rate and preventing repassivation [66]. Under droplet pitting is a subset of pitting in which the aggressive environment is a droplet, often formed by the deliquescence of a salt particle in a humid environment as shown in Figure 2.9 [67].

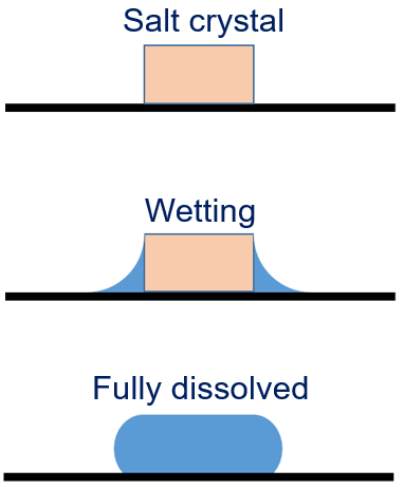

Figure 2.9 Deliquescence of a salt particle.

The initial breakdown of the passive film is required for pitting to occur. This process can be forced to occur by the application of a potential across the surface. This potential is known as the pitting potential and is dependent on the composition of the metal and the nature of the environment, it is lowered, for instance, in acidic medium [22].

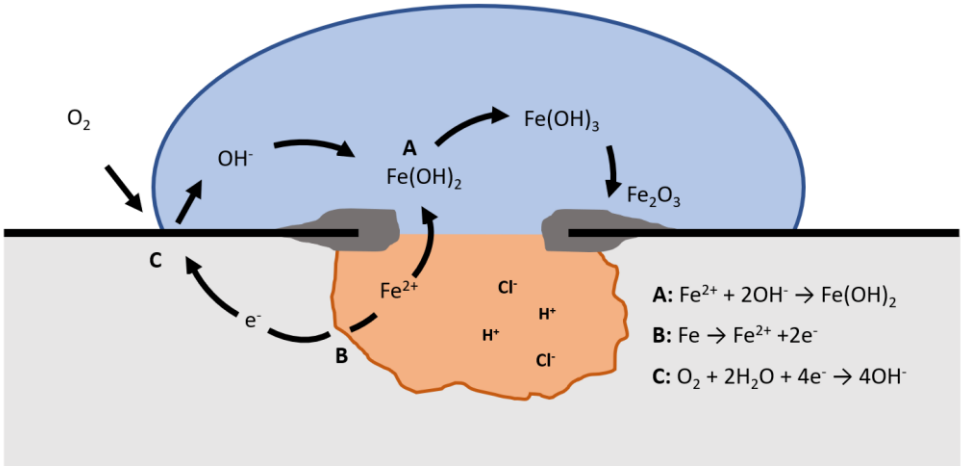

Figure 2.10 Basic process of under droplet pitting

2.2.1.4. Atmospheric Stress Corrosion Cracking

Stress Corrosion Cracking (SCC) is a corrosion mechanism that forms cracks in a susceptible material in the presence of an aggressive environment and tensile stresses. As with pitting, the lack of diffusion inside the crack allows the formation of an aggressive localised environment. This combined with a high stress concentration at the crack tip drive crack propagation. These tensile stresses can arise from residual stresses, induced, for example, from welding or machining, or they can be applied during component use. Either type may be concentrated by surface morphology into local areas of high stress [68].

Under normal conditions the passive oxide layer that forms on stainless steel is stable and protects the bulk. However, in the presence of an aggressive environment (e.g. a chloride containing one), localised breakdown of this passive film can occur, leading to pitting and micro cracking. An appropriate medium, an aggressive environment and a tensile stress must all be present as the absence of one of these factors will halt SCC [13]. Cracks can initiate at pits due to the aggressive local environment and the concentration of stress as explained in Section 2.2.1.5. The next section describes the crack growth mechanism.

2.2.1.5. Crack Growth Mechanism for SCC

The progression of a crack occurs by cyclical film rupturing, especially in sensitized austenitic stainless steels where cracks follow chromium depleted paths adjacent to grain boundaries [69]. The explanation of the theory that this process is cyclical is as follows:

- Stress concentrates and builds up at the crack tip, where slip bands cause the sudden rupture of the passive film.
- This exposes material which immediately begins to re passivate.
- The exposed area decreases over time, which can create very high current densities.
- Quickly, the whole surface is repassivated and stresses at the crack tip begin to build up again, hence restarting the cycle [69].

2.2.1.6. Depassivation Due to Chloride Theory and the Point Defect Model

Chloride induced corrosion: Corrosion begins with the breakdown of the protective passive film. This occurs above the breakdown potential (Eb) and becomes stable above the pitting potential (Ep). These potentials are heavily influenced by the concentration of chloride ions in an electrolyte, with a minimum chloride concentration required for any film breakdown to occur, though the mechanism by which the chloride enhances the corrosion is not fully understood [70][16].

It is established that in an aggressive chloride-containing environment, at the film/electrolyte interface, aggressive ions such as chloride ions compete with hydroxyl ions for adsorption [60]. Here, the passive film can locally dissolve and become thin. Adsorbed chloride ions cause a localised mode of film dissolution, rupturing the film leaving the bulk vulnerable to pitting corrosion [70]. How this localised film dissolution occurs can be explained using three models, as described below.

The point defect model: The point defect model describes passive film breakdown in the presence of chloride ions. It suggests that chloride ions adsorb onto the surface of a passive film and create cation vacancies that migrate through the film and collect at the film-metal boundary as shown in Figure 2.11. These chloride ions may be individual ions of chloride complexes [60].

These cation vacancies at the metal/film layer interface prevent the film from growing into the metal substrate [71]. This then causes the passive film to blister and burst, exposing unprotected bulk material to the electrolyte [72]. This model is considered to be one of the currently prevailing models [70].

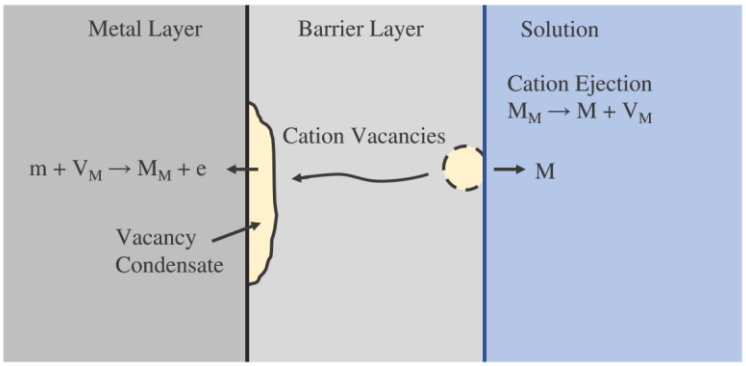

Figure 2.11 The point defect model [71].

The point defect model has also been used to explain passive film growth in the absence of chloride ions [73][74].

A criticism of the point defect model is that it is basically deterministic, which opposes the observation of the stochastic distribution of pitting. This has been explained in more recent generations of the model by considering the normal distribution of cation diffusivity in the passive film [75].

Since this process involves three main steps: (i) the adhesion of chloride ions at the film surface; (ii) the transport of cation vacancies through the film and; (iii) the settling of vacancies at the film-metal boundary, the location of film breakdown could be influenced by factors that affect any of these processes. Surface finishing processes may influence any or all of these processes.

It has been proposed that the penetration of chloride ions occurs predominantly at the inter-grain boundary sites [76].

Electronic Point Defect Model: This model deviates from the point defect model in that it assumes the injection of an electronic defect in the film electrolyte boundary. It has been suggested that this causes quasi-metallisation resulting in local film dissolution. Above a critical potential pores form in the film. This model also predicts a critical potential at which the passive film is electrochemically unstable and the pores lead to film breakdown [77]. Surface finishing processes change the electrical properties of the film, both by affecting the thickness of the film and the shape. In this way surface properties due to finishing processes could affect the process behind the electronic point defect model.

Metal Chloride Salt Model: Burstein and Mattin proposed that chloride ions could travel through the film to form metal chloride salt islands on the film-metal boundary. These islands would then act in a similar way to the vacancy clusters in the point defect model, preventing film growth and blistering the film [78].

2.2.1.7. The Causal Link Between Pits and Crack Initiation

ASCC and pitting corrosion happen in very similar environments. When in the absence of a tensile stress, but still in the presence of an aggressive environment, 304L stainless steel will pit. With the application of stress, it will undergo SCC instead. This raises a few questions:

- Do cracks propagate from pits?
- Can cracks initiate without pitting?

It has been proposed that pitting corrosion may create sites with a high potential for SCC [75]. Pits create a localised aggressive environment that could encourage crack initiation, as well as providing features that may cause stress concentrations to induce crack initiation at pit sites. Since pitting has been shown to occur in specific locations, such as work hardened areas and inclusion sites, it may be this initial feature that causes cracks to form at the same location as pits, rather than the pits themselves.

It is common to regard stress corrosion cracks as being associated with pitting. It has been shown that in conditions that allow both pitting and cracking to occur, there is competition between pitting rates and cracking rates. Additionally, it has been shown that at a critical length, pits will transition from deepening to crack propagation [79].

In one study, cracks were found to initiate along chains of pits, forming what is described as “necklaces”. This relationship was found to occur at higher temperatures, and not at all at lower temperatures or humidities, possibly because of a lack of pits in these conditions. At lower temperatures cracking still occurred although the cracks were not associated with pits. It was also suggested that cracks would form at either side of the mouth of a pit, not from the base, as shown in Figure 2.12 [79]. This gives weight to the theory that the pit providing an area of stress concentration, rather than an aggressive local environment, is the bigger factor.

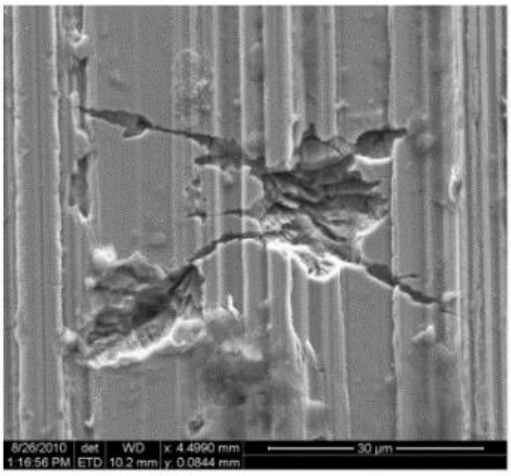

Figure 2.12 Showing stress corrosion cracks emanating from a pit mouth [79].

Studies have modelled the evolution from a pit to a crack [80][81]. These models concluded that the influence of pitting on cracking was due to the combination of the local aggressive chemistry and the stress concentrating morphology [82].

In a study on the effect of grinding and machining on corrosion resistance, 304 stainless steel was subjected to a four-point bend stress, with a droplet of $MgCl_2$ at 45% RH and 60°C. SEM analysis showed clear evidence of small cracks propagating from pits. Small embryonic pits growing from the pit mouth were observed, however, larger cracks were visible inside pits. This suggested that cracking may have started inside the pit, nearer the base than the mouth as shown in Figure 2.13. No cracks were found without an associated pit [38]. The process of crack initiation is important to consider, since if

cracks must initiate at pits, then factors that influence pitting, such as surface morphology or inclusions, will also affect cracking.

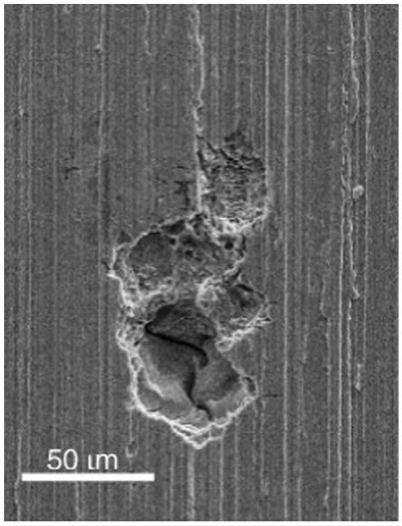

Figure 2.13 Stress corrosion cracks emanating from a pit base [38].

The link between pitting and cracking is usually made from an instantaneous assessment of an SEM or optical image rather than a longitudinal observation of individual pit and crack growths. This can slightly obscure the causal link, and in fact some studies have instead suggested a causal link between cracking and pitting [38].

A study into the mechanism behind pitting found that pits as small as 0.01 µm could have the required current density (over 1 A/cm^2) to fulfil pit initiation conditions. At this scale, a crack in the passive film would create a feature with a diffusion path long enough to reach the critical pH [83]. In this manner, small cracks in the passive film provide the geometric shape (width and depth) required to reach the concentration gradient necessary for pitting. These pits could then lead to SCC cracks in a crack – pit – crack regime. If stress induced micro-pits regularly initiate pits, then there is a link between stress and pitting, which has had very little investigation. This would also suggest that surfaces that can withstand greater stresses before micro-cracking will not develop pits as readily.

2.3. The Effect of Surface Finish on Corrosion

This Section will describe how surface finish is characterised and investigated in ways relevant to this Thesis. It will then evaluate the available literature that investigates the effect of surface finishing on the material, and how these changes influence the corrosion performance of the surface.

2.3.1. Surface Characterisation Techniques

2.3.1.1. The Measurement of Roughness

Rough

> "*Not even or smooth*." [84]

Surface roughness can be described using many units, making it difficult to define in itself. Roughness in language describes a deviation from a more perfect, or finished, state. This style of definition is carried into physical roughness, making it difficult to define in science, as it is effectively a measure of the deviation from a particular state, rather than a measure of a property inherent to a surface.

Technical definitions of roughness tend to describe the deviation from a smooth surface or flat plane, with industry predominantly using the average deviation in the form of an Ra value [48]. Further, more involved definitions focus on microscopic rather than macroscopic features. These are the features of interest when talking about roughness, although the distinction is made distinctly for each application [85].

The generic deviation from a flat plane definition fails to consider the sharpness of a surface. For example, sandpaper with sharp sand will feel rougher than that with a softer, rounder sand, when, if the grain size is consistent, the deviation from a flat plane will be consistent.

2.3.1.2. The Units Associated with Roughness

The basic units of surface roughness are calculated from the distribution of surface heights, some of these are shown on the line profile in Figure 2.14.

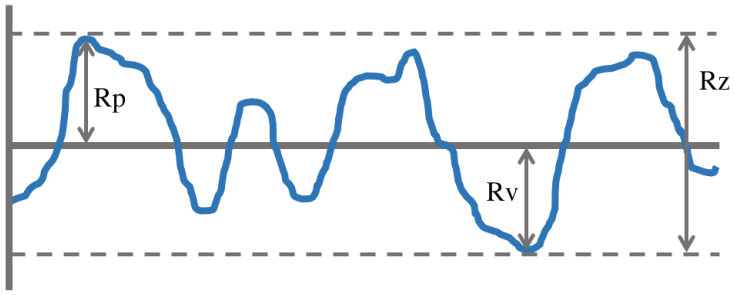

Figure 2.14 The calculation for basic height parameters from a line profile.

Table 2.3 The parameters of roughness

Parameter	Description	Equation
Ra	Arithmetical mean deviation of the assessed profile [86].	$Ra = \frac{1}{n}\sum_{i=1}^{n}\lvert y_i\rvert$
Rq, Rms	Root mean squared [86].	$Rq = \sqrt{\frac{1}{n}\sum_{i=1}^{n}\lvert y_i^2\rvert}$
Rv	Maximum valley depth [86].	$Rv = \lvert min\, y_i\rvert$
Rp	Maximum peak height [86].	$Rp = \max y_i$
Rz, Ry	Maximum height of the profile [86].	$Rz = Rp + Rv$
Ssk	Skewness [86].	$Ssk = \frac{1}{nRq^3}\sum_{i=1}^{n} y_i^3$
Sku	Kurtosis [86].	$Sku = \frac{1}{nRq^4}\sum_{i=1}^{n} y_i^4$
RzDIN, Rtm	Average distance between highest peak and lowest valley for an area [87].	$RzDIN = \frac{1}{s}\sum_{i=1}^{s} Rt_i$
RzJIS	Japanese Industrial Standard for based on the five highest peaks and lowest valleys [88].	$RzJIS = \frac{1}{5}\sum_{i=1}^{5} Rp_i - Rv_i$
Sdq	Mean slope angle [89].	$Sdq = \sum_{i=1}^{n}\lvert\nabla f\rvert$
Svi	Valley fluid retention index [89].	$Sv_i = \left(\frac{V_v(h_{0.80})}{A}\right)/Sq$
Sds	Mean summit density [89].	$Sds = \frac{Number\ of\ Peaks}{Area}$
Ssc	Mean summit curvature [89]. $Ssc = \frac{1}{N}\iint_{Summit-Area}\left(\frac{\partial^2 z(x,y)}{\partial x^2}\right) + \left(\frac{\partial^2 z(x,y)}{\partial y^2}\right) dxdy$	

As shown in Table 2.3, a wide range of units are used depending on the application. The Ra value is the simplest and most widely used. It is the average deviation from a flat plane, meaning surfaces with sharp spikes or deep pits can have the same Ra as one with more rounded features. It makes no distinction between peaks and valleys. It has been found to be a poor predictor of corrosion compared with other units such as skewness and valley depth [90].

The average deviation from the average surface height is a useful starting point for surface characterisation, but it does not provide detail on the shape of the surface. Larger Ra values tend to be given to surfaces with naturally large wavelengths, such as shotblasted surfaces, and do not consider

surface gradients or peak sharpness that can be considered an important part of roughness and that affect corrosion resistance. Surfaces with sharp spikes or deep pits can have the same Ra as those with more rounded features since it makes no distinction between peaks and valleys. It has been found to be a poor predictor of corrosion compared with other units such as skewness and valley depth [90].

Rq is the root mean square roughness. This is the square root of the mean average of the squared distance from a flat plane. This is also referred to as **SD** i.e. the standard deviation of the surface. Since a surface would be expected to have a normal distribution of heights, areas of the surface at extremes are given a higher weighting for this parameter.

Sp denotes maximum peak height from the average surface and **Sv** gives maximum valley depth as a negative number. **Sz** is the difference between the two and gives the height range, or maximum height of the surface.

Ssk is the skewness of the surface. It is the mean cubed height divided by Rq cubed as described in Table 2.3. This gives an indication of how much the distribution of surface heights deviates from Gaussian as shown in Figure 2.15. Since the odd power preserves the sign of the value, a positive Ssk indicates that the surface contains a predominance of peaks, while a negative Ssk indicates the predominance of valleys. For a normal distribution of surface heights, Ssk would be 0.

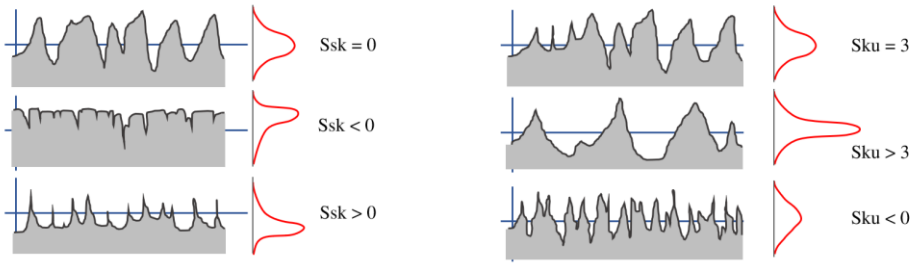

Figure 2.15 Skewness and kurtosis in surfaces

Sku describes the kurtosis of the surface. This is the mean height to the fourth power divided by Sq to the fourth as described in Table 2.3. The value of Sku can indicate the presence of inordinately large peaks or valleys since extreme values are greatly amplified by the power of four.

Sdq gives a good general impression of what the average slope of a surface is and can be very useful when comparing surfaces of similar roughness. Sdq is strongly related to the wettability of a surface which has an important influence on the overall rate of corrosion in under droplet conditions [91]. In general, the Sdq heavily influences the behaviour of fluids on the surface which is likely to have an

impact on corrosion processes such as pit initiation where the diffusion behaviour of the liquid very near the surface is a critical factor [92][93].

The **Sds** parameter gives the summit density, or the number of peaks per area. This is parameter influences the tribological function of the surface, i.e., how a surface wears and may experience stress concentrations. It also impacts the appearance of the surface. Summits are defined as points that are higher than all 8 neighbouring points (on a square grid), at least 5% of the total height range over the mean surface height, and are separated from each other by at least an arbitrary distance, usually 1% of the measurement area. As a parameter, Sds influences the wear behaviour of a surface, and its deformation behaviour during loading, both elastic and plastic. The density of peaks affects the localised stress concentrations a surface will experience, which could affect stress and pitting corrosion [89].

The parameter **Ssc** is the mean summit curvature. It is a measure of the curvature of the summits which are defined as for the Sds. It is effectively the average of the rate of change of gradient of the summits. It is related to how sharp the summits are and is closely related to the Sds and has very similar applications.

The functional parameters describe the nature of the extremes of the surface height; they are pertinent to how fluids such as lubricants are likely to interact with the surface. **Sk**, **Spk** and **Svk** are defined by the distribution of surface heights in the surface bearing curve, as shown in Figure 2.16. This curve is drawn in the same manner as the cumulative probability density curve, but inverted. A straight line is

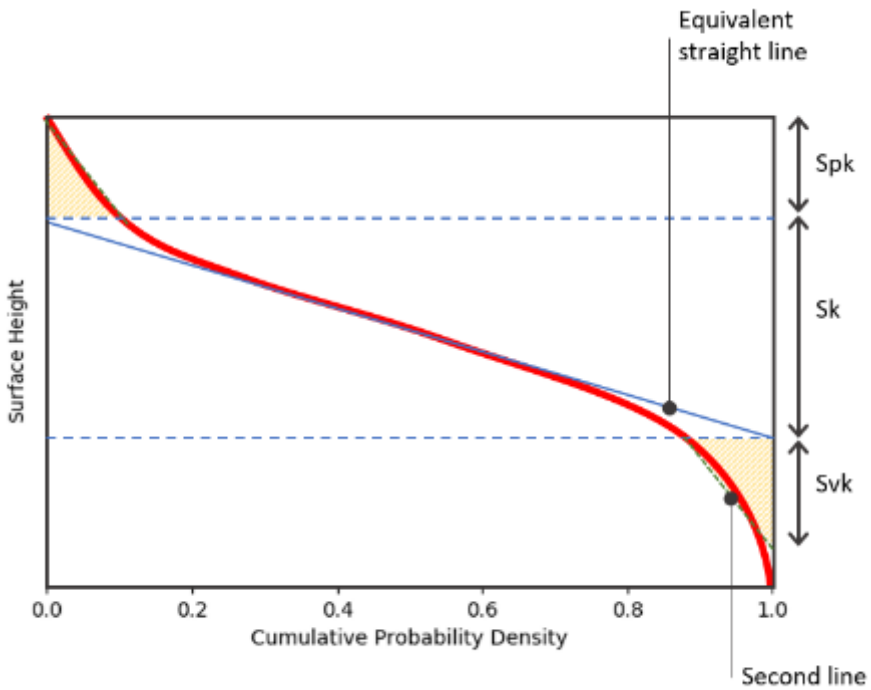

Figure 2.16 Demonstration of the calculation of Spk, Sk and Svk.

drawn along the curve, with a least-squares fitting over the flattest 40%. This line is then extended to the full x-range of the bearing curve where a point is drawn. The reciprocal point on the bearing curve at the same y value is found and a second line drawn from this to a point with a y value equal to the maximum y value of the curve. This line is drawn in such a way that the area formed between it and the curve is equal on both sides of the line so that the area of the right angled triangle formed is the same as that of the peak area, as shown in Figure 2.16[94].

The area between the second line and the curve is equal both above and below the line. This serves to give a more reasonable estimation of the extremities of the surface. If only a few points of the surface are at extreme locations, the curve will be very steep, and these points will be cut off to give a value that more closely represents the surface.

The surface bearing parameters give an indication of the volume of a surface that is made up by the peaks, core and valleys. **Sbi**, the surface bearing index, was developed to evaluate how fluids such as lubricants behave on surfaces. Corrosion occurs under a fluid and is completely dependent on the diffusion properties of this fluid. These diffusion properties are themselves strongly affected by the nature of the surface at the microscopic scale, meaning that this index could be a strong indicator of the corrosion resistance properties of a surface. These parameters would certainly strongly influence the clean-ability and resistance to contamination of a surface.

To calculate the surface bearing parameters, the surface bearing index curve is drawn and is divided up into three sections, the highest 5% of the surface is defined as the peak zone as shown in Figure 2.17. The deepest 20% of the surface is defined as the valley zone and the area between is defined as the core zone. A horizontal line is drawn through the curve at these points. The area above this line and below the curve in the peak zone is known as the peak area, and the equivalent in the valley zone is the valley area.

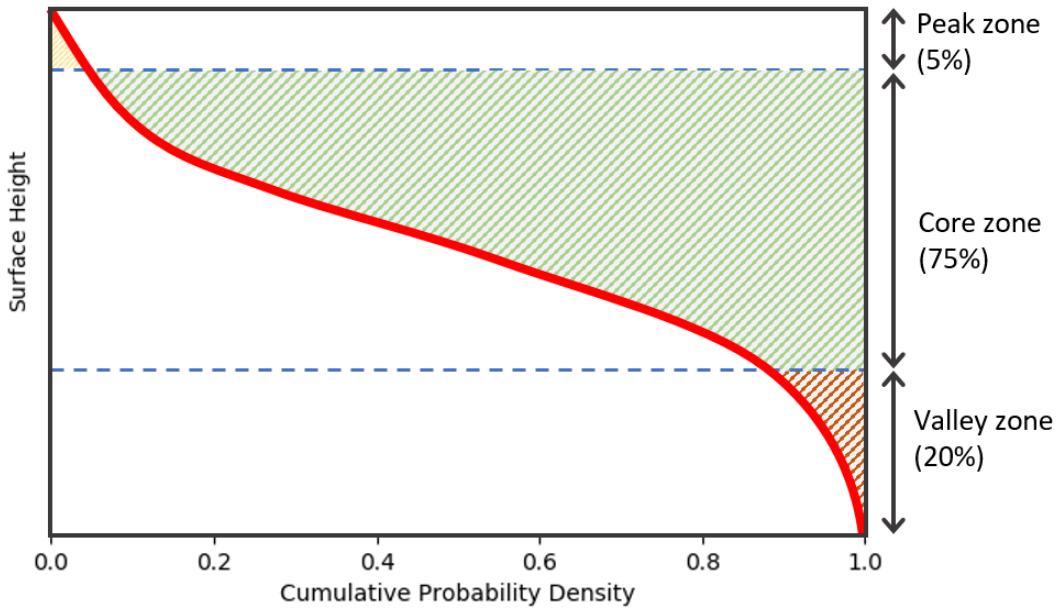

Figure 2.17 Surface bearing index calculation.

The surface bearing index (Sbi) is calculated by dividing Sq by the distance between the top of the sample and the core zone. The surface core index (Sci) is the difference between peak and valley areas divided by the surface area and Sq, and finally, the surface valley index (Svi) is the valley area divided by the area and Sq.

2.3.1.3. Roughness Values and Grit Size

Table 2.4 The effect of grit size on roughness [85]

Grit grade	Grit size um	Ra (um)
80	200	1.8
120	125	1.32
150	100	1.06
180	80	0.76
240	60	0.38
320	46	30
500	30	0.18
600	26	0.13

For a ground surface, the size of the grit used affects the roughness of the material. Larger grains will create larger valleys which contribute to the average deviation of the surface. The depth of the valley is also dependent on the force on the grain by the grinding device, whether that device is a grinding wheel, a flap wheel, or a spinning grinding pad. Larger grains have a larger surface area and so will be under a greater force than smaller ones, consistent with the fact that a larger grit size will always cause a rougher surface.

2.3.1.4. The Measurement of Surface Profile

Roughness can be measured with a number of devices using a range of technologies, from handheld profile gauges to white light interferometry and Atomic Force Microscopy (AFM). The different methods are detailed herein.

Stylus profilometry: The most commonly used roughness measurement, stylus profilometry, involves dragging a stylus across a surface and measuring its displacement with horizontal position. Because of its simplicity and low cost, it has become the industry standard. It can only take linear scans, so the amount of data gathered is less than for 3D techniques, and it can measure different results in different directions along a surface. The resolution is limited by the size of the probe, which at 2 μm is larger than for other methods [85].

Atomic Force Microscopy: AFM is a form of stylus profilometry that measures atomic forces between the stylus and the surface. The probe tip radius can be as low as 5 nm and so this technique gives the best resolution. It has been used effectively on very smooth surfaces with a surface area ratio as low as 1.03 [95]. It is usually used in a raster scan pattern so can gather data across a 3D area. It is limited in the Z direction by the size of the cantilever and cannot measure Ra values over around 6 μm.

Linear Laser Scan: Height data for a straight line across a surface can be measured and used to calculate roughness with a device such as a Nanofocus Confocal C4S machine [48].

Vertical Scanning Interferometry: VSI can be used to map large areas of a surface with an extremely high vertical resolution of around 1 nm. From this, Ra value and a range of other values can easily be calculated [90]. The horizontal resolution is not as good as an AFM, but it can be used on rough surfaces and relatively quickly.

2.3.2. Physiochemical Surface Finish Effects

Separate to the shape of a surface, the nature of the material itself affects a surface's resistance to corrosion. The material can be changed by surface finishing processes. Its crystallographic phase can be altered, as can the structure of grains that steel forms at the micro level. Both of these can impact the corrosion process.

2.3.2.1. Effect of Specific Surface Finishes on Corrosion

Pitting and cracking corrosion are known to nucleate at imperfections, flaws, or dislocations in the material surface. Grains that are broken will present more imperfections and dislocations to the surface, which could increase the initiation of pitting [70]. Roughness has been found to have a major influence on the nucleation of metastable pitting and pitting potential. The nucleation rate of metastable pits has been shown to increase with roughness in 304 stainless steel, while pitting potential has been shown to decrease. This was linked to the number of potential pitting sites of a surface being increased with increased surface area ratio [96].

Crack propagation has been shown to be affected by grinding grooves on the surface. In a study that found that cracks primarily correlated orthogonally to the direction of tensile stress, it was also found that surface features could direct them along grooves [38]. Similarly, surface machining has been shown to reduce the initiation time for cracks to appear by a factor of 3.5. This has been attributed to the formation of a work hardened layer, and a high density of martensite on the surface. Since the corrosion resistance of martensite is much lower than austenite, this allows for micro-cracks to initiate and propagate along grain boundaries [39].

In situ AFM studies of electrically accelerated pitting have shown a preference for pit initiation sites to be located at mechanically polished areas. It was suggested that these areas had been strain hardened [97]. A study on the effect of surface roughness on pitting potential found increasing surface roughness would drastically decrease pitting potential. The peak to peak roughness values measured were from 5 μm for the 80 grit paper to 0.03 μm for the 3 μm diamond paste. The roughest surfaces had a pitting potential of 135 mV vs SCE and the smoothest surfaces had a pitting potential of 216 mV vs SCE, clearly showing a beneficial effect in terms of reducing roughness. This effect was independent of preparation method, i.e. whether the sample was mechanically or chemically prepared. This study

concluded that pit initiation occurred at austenite/sulphide interfaces and that rougher surfaces had more of these potential sites [98].

It is intuitive to think that smoother surfaces resist corrosion better, and this is largely consistent. However, there are a series of studies that have found the opposite to be true in certain circumstances. For example, one study found the breakdown potential to decease as the surface roughness of 316L stainless steel increases. With the breakdown potential decreasing, the corrosion rate would increase, however it was also found that this effect was reversed for mild steel, where improving the surface finish lead to a higher corrosion rate [99]. Another study linked the rate of nucleation of metastable pits to surface roughness and found them to be positively correlated. However, it was also found that the growth rate in of pits in the smoother surfaces was increased [96].

In a study that compared the effects of electropolishing and micro-undulation with cold rolled 2B steel, it was found that the surface finishing procedures significantly impacted the roughness of cold-rolled 316L stainless steel as well as the corrosion resistance and repassivation ability, with the rolled surface performing the worst in these areas [100]. These tests were performed in NaCl media on standard rolled surfaces, some of which underwent a secondary treatment. Electropolishing provided a highly smooth surface while micro-undulation produced a surface very similar to a shotblasted one. A high degree of twinning indicative of plastic deformation was observed on the micro-undulated surface and therefore a high degree of grain refinement was concluded. No differences were measured in the pitting potentials of the three surfaces, and they were found to exhibit almost identical impedance spectroscopy. Despite this, the rolled surface developed significantly deeper pits. This was explained by a significantly higher capacitance for the rolled surface, which indicated poorer corrosion resistance properties since capacitance is directly proportional to active surface area.

In work focused on 316L steel in simulated PWR water at 350°C it was found that cracks on highly polished surfaces initiated sooner and grew deeper than those on ground surfaces [101]. A manually ground (500 grit) surface with an Ra value of 0.032 μm was compared with a 1 μm diamond paste polished surface with an Ra value of 0.005 μm. Despite the smoothness of the polished surface, it was found that cracks initiated from the remaining machining grooves. Maximum crack depth on the polished surface was around double that found on the ground surface. It was concluded that the polished surface had a lower threshold stress with cracks penetrating completely through the oxide layer.

One study linked an increase in roughness with a decrease in the pitting potential of 304L stainless steel in 3.5% NaCl solution and concluded that openness in the surface was a cause [102]. The study used

cyclic polarization to compare 120 and 1000 grit finishes (roughness values of 1.47 and 0.06 μm respectively) and found the rougher surfaces pitted more readily; at a lower potential.

The passive film on stainless steel exhibits breakdown and repassivation events well below the pitting potential, this is known as metastable pitting. It was concluded that rougher surfaces increase the incidence of metastable pitting by increasing the number of appropriate sites available. The deeper micro-crevices on the rougher surfaces were identified as features with low openness that stabilize pits by reducing the diffusion of corrosion products. This was evidenced by the observation that fast growing metastable pits in smoother surfaces were quickly passivated.

An electrochemical study on 304L stainless steel wires, ground with 600 and 4000 grit, found that raising an applied potential could increase the pit nucleation rate [103]. This was attributed to new, more open, nucleation sites becoming available at higher potentials, showing pitting probability for a location being a function of both the applied potential and the openness. This supported the theory that fluctuations in passive current in enclosed regions could cause unstable increases in solution acidity, creating the conditions required for pit initiation.

A different study used long term (5 year) exposure in a marine environment to assess the effects of metal composition and surface finish on corrosion [104]. Ground surfaces were compared with those that had been rolled, shotblasted or electropolished, all of which were affixed to outdoor exposures rigs in shielded and non-shielded free weather conditions. The shotblasted surfaces showed the worst visual degradation. This was attributed to the accumulation of chloride and other contaminates on the rougher surfaces, where regular rainfall was insufficient to effectively clean. This theory was partly corroborated by the excellent performance of the electropolished surface, which was by far the smoothest. It was noted that the differences in surface finish mainly affected the corrosion behaviour in the initial stages of exposure, with bulk factors such as composition dominating long term behaviour.

A different study on the effect of machining on 304 stainless steel found a significant impact on crack development [7]. A fine machined surface (Ra = 0.50 μm) was compared with a rough machined surface (Ra = 0.90 μm) and an electropolished surface (likely Ra < 0.20 μm [105]) under SCC conditions and it was found that the rougher surface was more susceptible to intergranular cracking and tended to develop the longest cracks. This was, in part, linked to strain induced martensitic transformation which has previously been shown to increase the susceptibility to SCC [39]. Additionally, it was found that residual stresses are sufficient to cause cracking in the absence of an applied stress.

It was also suggested that the local geometry of damaged grain boundaries acted as enclosed regions affecting pH and solution concentration and also affecting the local stress concentrations. The effect of geometry on openness is investigated in Chapter 4 and the effect of geometry on stress concentration is investigated in Chapter 6.

It is clear from these studies that surface finish has a significant impact on corrosion resistance of a surface, with the prevailing relationship being that rougher surfaces will corrode more readily. Pitting and cracking nucleate at imperfections, and roughness can provide these sites, reducing the pitting potential and increasing metastable pitting. Further, openness has been shown to play a role in the local environment and likely affects the pitting probability.

Crack initiation has been linked to work hardened layers brought about by surface finishing such as grinding. Additionally, cracking has been shown to initiate on features such as grooves, and the propagation has been shown to be affected by grinding grooves.

Even the surface interaction with the environment at the more macro scale has been shown to be important, with the reduced cleanability of shotblasted surfaces having been shown to encourage degradation.

However, it is also clear that the relationship is not straightforward, with additional factors having an influence; importantly, residual compressive stress works to prevent corrosion and work hardening encourages it. Occasionally, smoother surfaces are shown to corrode faster, though when the initiation rate of pitting is decreased by the reduction of potential sites, growth rate of individual pit can be increased, making the relationship between roughness and vulnerability to corrosion complicated.

2.3.2.2. Surface Finish Effects on Crystallography and Microstructure of Steel

Some manufacturing processes that affect the surface finish also have an effect on the underlying microstructure of the surface of the material. Surface finishing processes can cause such strain to the material that the crystallographic phase changes. 304L is almost completely austenitic (FCC), and with enough strain it work-hardens and becomes martensitic (BCT). The process that brings about a change in phase may, or may not, also cause a change in microstructure; as such, it is important to consider these effects both together and independently. 304L, as well as most other austenitic stainless steels, also contains a small percentage of delta ferrite (BCC). Delta ferrite in austenitic stainless steel welds increases its resistance to SCC [106].

Using the phase detection capability of Electron BackScattered Diffraction (EBSD), the phase distribution of 304L samples have been mapped as a function of depth [65]. Machined surfaces and those ground by a grinding wheel were compared and martensitic transformation was found in a high volume fraction in a deformed layer at the surface as shown in Figure 2.18. Additionally, the martensitic phase was found to extend into the bulk material by over 50 µm along grain boundaries [107]. It has been shown that such a phase change induced by the surface finish process can have an effect on the corrosion resistance of the surface [39]. The formation of martensite at the surface of steel is detrimental, since martensite is far more permeable to hydrogen, and more susceptible to hydrogen embrittlement [108].

Another study found significant martensitic transformation caused by lathe-machining in the top 50 µm of a 304L steel surface. This was linked to volume expansion in the strained surface layers [39]. Since the phase change accompanies changes in the strain and microstructure, it is difficult to isolate whether phase, or microstructure, has the greater influence on corrosion. This study did directly link the machining process to the shallow nature of cracking in machined stainless steels, with the unaffected bulk halting cracking.

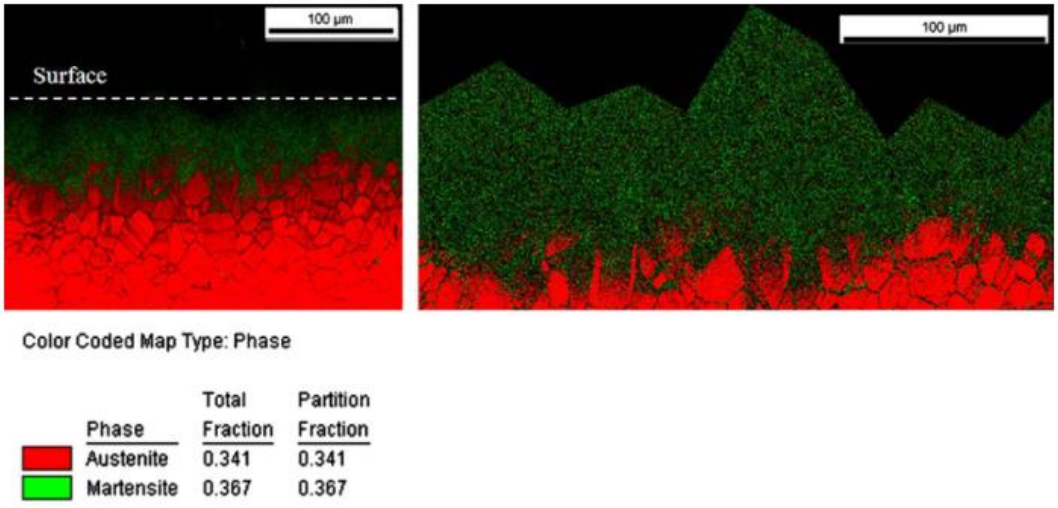

Figure 2.18 Cross sectional EBSD map of a 304L surface showing phase transformation due to grinding in 304L stainless steel [39].

In addition to phase transformation, grain fragmentation is also caused by certain surface finishing techniques. As a result of the induction of severe distortion or breaking grains into nanocrystalline domains, the indexing rate of 304L steel surfaces subjected to grinding and milling surfaces of 304L by EBSD has been found to be poor close to the surface [38].

Figure 2.19 shows extensive grain fragmentation of a 304L stainless steel surface machined specimen that was subjected to machining by 0.5 mm using a lathe. Using EBSD it was found that extensive grain

refinement (<0.5 µm from 60 µm) occurred to a depth of 150 µm. Additionally, a high density of deformation twins was found up to 1 mm deep. These findings were coupled with a higher susceptibility to SCC, thought to be caused by the formation of the work hardened layer, increased tensile stress, and the presence of martensite. The authors did not comment on whether the grain size change could have exacerbated the susceptibility to SCC but listed it as an effect of the machining [39].

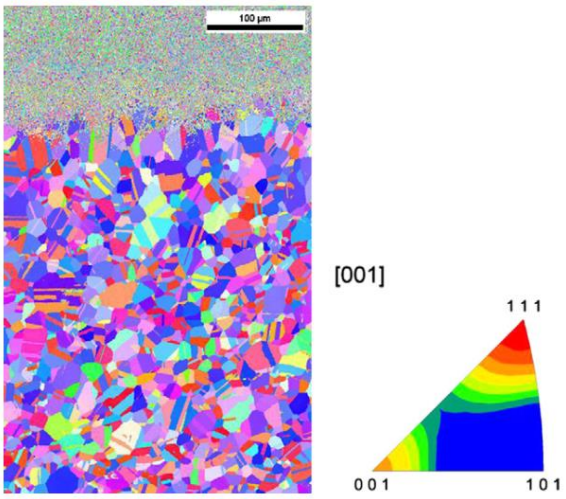

Figure 2.19 Cross-sectional EBSD map of a ground 304L stainless steel. showing poor indexing near the surface [39].

In summary, these studies describe both grain fragmentation and phase transformation near the surface of stainless steels resulting from surface working such as machining and grinding. This has been found to affect a surface layer up to 150 µm deep. Both effects have a detrimental impact regarding corrosion, with grain fragmentation presenting more potential sites for corrosion initiation, and martensitic transformation, at times extending along grain boundaries, making the surface layer more vulnerable to cracking.

2.3.3. Morphological Surface Finish Effects

2.3.3.1. Morphological Effects in General

As well as differences in surface roughness, different surface finishes create different surface features. These specific features may have a larger impact on the performance of a surface than the difference in roughness, or of microstructure. For example, in one study on 304 steel, pits were observed growing at a peak on a ground sample. The sample was under longitudinal stress (to the direction of grinding) and was under a droplet of concentrated $MgCl_2$ at 60°C after 500 hrs.

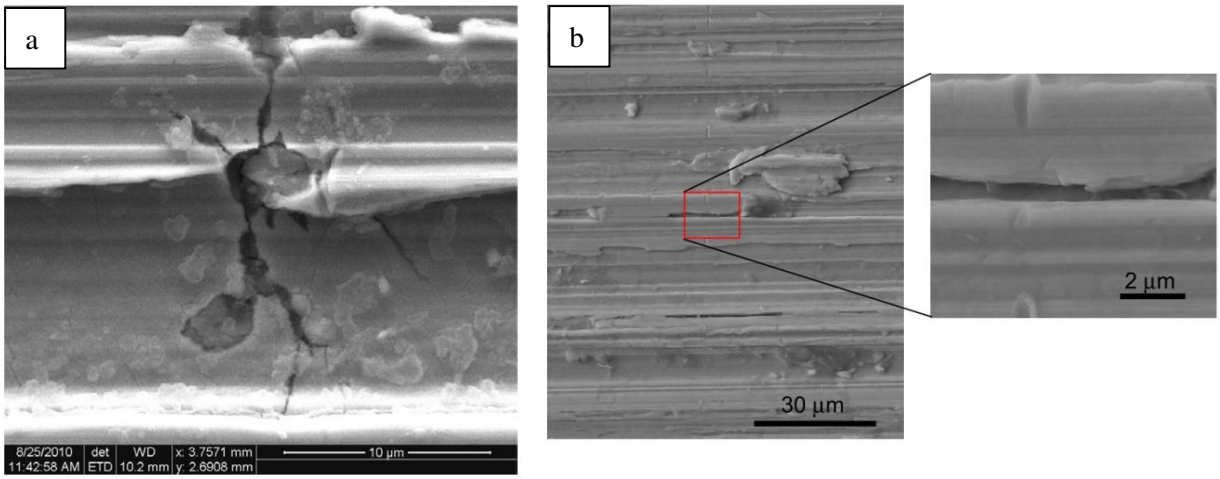

Figure 2.20 SEM image showing: A, pit growth at a machining mark, B, local deep grooving caused by folded over material formed during the grinding process.

The same study assessed the machined surface as having the defects that are inherent in any machining or grinding process. Specifically, deep grooving and folded overlaps were described and are shown in Figure 2.20a. It was suggested that these sites could cause local chemistry changes (such as acidification, the increase of chloride ions, the decrease of oxygen and the increase of corrosion products) and provide the precursors to crack initiation [38]. Other studies have also observed the folding over effect of grinding, this is shown in Figure 2.20b [109].

In a comparison of the corrosion resistance of two surfaces with similar Ra values, one was found to corrode much faster. Analysis of this surface found a predominance of deep valleys on the corrosion-prone stock. Several geometric variables such as skewness and valley depth were used to quantify these deep values, and were found to correlate well with the tendency for corrosion [90].

From these studies it is apparent that unwanted, accidental surface features will be present as a result of grinding processes, and likely other surface finishing processes also. It is clear that these features are likely to be a major factor in the performance of a surface, and that they are quantifiable with several geometric variables.

2.3.3.2. Surface Geometry and Aspect Ratio

Surface finishing techniques such as grinding, brushing, rolling and shotblasting affect the geometry of the surface. While it is well accepted that the geometry of a surface will affect corrosion behaviour for an already corroding stable pit, its role in pit initiation, and in the passivation state of re-passified pits is less well understood, though there is a growing body of evidence suggesting aspect ratio has a large influence on pit initiation. The aspect ratio hypothesis suggests that for a surface, and between different

surfaces, the openness or closedness of a site varies with position and surface. More closed sites may begin to have the self-sustaining nature of a corrosion pit. This affects the development of metastable pits on such sites and may influence pit initiation.

The self-sustaining nature of pit growth relies on the local stabilisation of an acidic corrosive medium. This local environment induces dissolution of the metal, which in turn causes further acidification due to hydrolysis reactions. The continuation of this process therefore relies on diffusion in the electrolyte being slow enough to maintain the acidic local environment [65]. Retardation of dissolution in mature pits is caused by the structure and shape of the pit itself, and so it is possible that surface features could themselves slow dissolution and cause pitting in the first instance.

Figure 2.21 shows a representation of ion concentration gradients for a pit (A) and a valley (B). The concentration gradient shown in Figure 2.21A is consistent with current understanding, while the gradient shown in Figure 2.21B is a suggestion of the aspect ratio hypothesis. If a valley can sustain a concentration gradient similar to that found in a pit, as shown in Figure 2.21, it could be responsible for the onset of pitting.

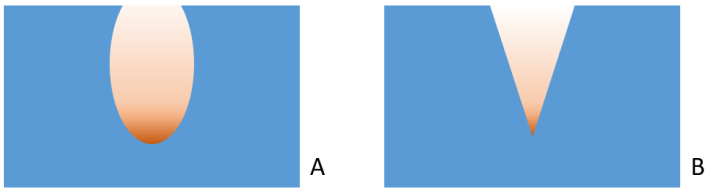

Figure 2.21 Ion concentration gradients.

Galvele found that the deeper a metastable pit, the less current density was required to activate it [83]. The current density manifests an ion concentration gradient, where the highest concentration occurs at the base of the pit. A deeper pit allows a greater concentration of ions at the pit bottom to build and stabilise. Additionally, as well as ion concentration being dependant of geometry, current density is also dependent on surface geometry [110]. A criterion for stable pit depth has been presented by Pistorius and Burstein, who state that the product of pit depth and current density must exceed a certain minimum value [111]. From this it can be taken that for a given current density, pit depth determines the pit stability.

It has been proposed that stable pit growth requires a pit stability product (product of current density and pit radius) which exceeds 3 mA/cm [112]. It has been further suggested that the aspect ratio (shown in Figure 2.22) of surface features such as grooves is a suitable and useful measure of openness. Aspect

ratio has been shown to affect pit nucleation in a study that found a negative correlation between pit nucleation and aspect ratio [96].

A critical aspect ratio of surface valleys for pitting has been observed [96]. This is a clear link between

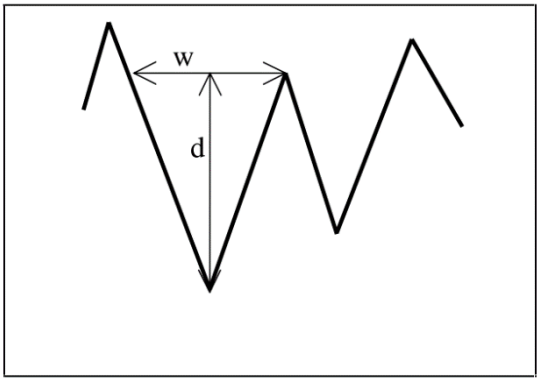

Figure 2.22 Aspect ratio (the ratio between width w, and depth d)

the topography of a surface and its susceptibility to pitting. Additionally there is a propensity for pitting to occur in deeper grooves, which could be due to the shape of the groove [38]. It was also observed that naturally occurring cracks and pits were large enough to act as aspect ratios, increasing the ionic concentration and leading to acidification. It was found that the necessary acidification for stable pit growth could be obtained in pits as small as 10^{-6} cm [83].

In one experiment, the average pit geometry was thought to become more open at more anodic potentials. It was suggested that pitting occurred initially in more closed sites, and that under more aggressive, anodic potentials the number of potential pitting sites increased to include more open sites [110]. For pit nucleation that is driven by surface inclusions, for rougher surfaces there would be a higher likelihood of an electrochemically active inclusions being associated with a particularly geometrically closed region of the surface that is deep enough to support metastable pitting. This means that a greater surface roughness should increase the number of available pit sits, even when the distribution of inclusions is identical [113].

It was found that pits initiated at inclusion sites, and it was originally thought that this would mean that there should be no difference in pit nucleation rate for different surfaces, since the distribution of surface breaching inclusions should be identical for different surface finishes. However, it was found that for rougher surfaces the pit nucleation rate was higher; this effect was attributed to the inclusion sites on the rougher surfaces being less open on average due to surface geometry, thereby providing more potential pitting sites. Additionally, it was suggested that more open pits grow from more open sites, and grow more readily than closed pits when under higher current densities [112]. This shows that the optimal geometric conditions for corrosion change with current density. While more open pits corrode

faster in high current density conditions, more closed ones grow in low current density conditions when open pits cannot.

2.4. The Effect of Surface Finish on Stress Concentration

2.4.1. Introduction

Surface morphology affects the distribution of stress, creating stress concentrations (intensities) around certain features on a surface. These concentrations can be many times higher than an applied stress, creating a critical cracking stress in a material that would otherwise maintain its integrity.

Historically, these stress concentrations have been studied in notched samples. This simple analogy is easy to measure and can also be solved analytically. By contrast, it has been suggested that the surface morphology that is applied by surface finishing acts in similar ways, however the characteristics of a real surface are both much harder to measure, and the stress concentrations are much harder to solve analytically.

It has been shown that the surface morphology of machined surfaces with Ra > 0.1 μm has a strong influence on surface stress distribution, while for Ra > 2.5 μm, residual stress becomes a more signification factor [114]. It is suggested that since critical crack stress is heavily influenced by the morphology of the sample around it, this effect influences crack initiation at the surface. Some surfaces, such as ground ones, that contain valleys, act to concentrate stress in the lowest points. This would reduce the applied stress required to reach a critical cracking stress at the surface.

Stress is a necessary component of SCC and so the stress concentrations on a surface are critical to its propensity for SCC. In Chapter 6 multiple models are used to estimate the stress concentration distribution for four surface finishes, which is then compared with experimental data.

2.4.2. The Effect of Surface Finish on the Mechanical Properties of a Surface

It has been shown that surface finish affects the fatigue behaviour of a material. One mechanism for this is the formation of stress concentrations on the surface by the geometry of the surface finish. Since surface stress behaviour is a key factor in stress corrosion cracking, the effect of surface finish on the mechanical properties of the surface can provide insights into possible cracking behaviour. During fatigue tests under a range of stresses from 400 MPa to 2000 MPa, ground surfaces with a surface roughness of Ra = 1.58 μm performed worse than polished surfaces Ra = 0.32 μm [115]. This effect has been attributed to stress concentrations forming on rough surfaces and decreasing their endurance limit.

In general fatigue strength decreases with an increase in surface roughness [116]. Features on the surface such as valleys raise the stress concentration at a microscopic level. Surface roughness, i.e. the average height of features on the surface, has been shown to determine stress concentration and lead to fatigue failure [117].

One study found that the fatigue life of stainless steel was surface texture dependent, and that it decreased with increased surface roughness [118]. Grooves from machining have been shown to act as points for crack initiation, in a study that conducted fractography on cracked specimens [117]. Additionally, with finite element analysis it was shown that these points were areas of high stress concentration. The key determinate of stress concentration was identified as the depth of the feature so *Ry*, the maximum depth of valleys, was identified as a key predictor.

Numerical analysis modelling a real brushed surface found that the surface morphology dominated the stress distribution compared with polycrystalline effects. Stress concentrations were shown to occur in valleys on the surface that were 3X higher than at peaks. A drastic change in the localization patterns was also observed when comparing the results on flat and brushed surfaces, where plastic strain tends to localize at the bottoms of valleys [119].

Other experimenters have found no evidence that surface condition affects initial crack location and suggest therefore that there is no localisation of high stress concentrations, or that it has little effect. It has been found that when intermetallic inclusions are present, crack initiation always occurs on these, implying either a much lower stress is required to initiate cracking at these points, or a much higher stress concentration is created by the inclusion [68]. In either case, the stress at these inclusions will be

heavily influenced by the macro shape of the surface around them, for example an inclusion at the bottom of a sharp valley would be under a greater stress and therefore fail faster than an inclusion on a flat surface.

In general, multiple studies have shown surface morphology to concentrate stress in features such as the bottoms of valleys and that these stress concentrations behave differently on different types of surface. This has been clearly linked to the mechanical properties of surfaces, with much evidence for a reduction in fatigue life, and some evidence linking stress concentrations to stress corrosion cracking. Specifically, machining and grinding grooves are identified as sites directly linked to crack initiation, having a greater effect on stress distribution than the polycrystalline structure. Chapter 6 attempts to map these stress concentrations, and experimentally show their effect on corrosion cracking for 304L stainless steel.

2.4.3. Fracture Mechanics

2.4.3.1. Basic Theory

It is known that the morphology of a surface has a large influence on the transmission of stress. Shapes like notches, crack, or tears can concentrate stresses at their tips. This can lead to crack propagation at bulk stresses much lower than the stress required to initiate a crack.

The stress intensity factor (K_I) is a gives the magnified stress due to the shape of the cracking scenario in question. A minimum value of (K_I) that propagates a crack can be derived and is referred to as the critical fracture toughness (K_{IC}). For work in the present Thesis on ASCC, it is assumed that all cracking originates at the surface of a material and propagates through the material via a crack tip. For a crack tip to progress, it must be over a critical stress.

Calculations to standardise stress intensity factors were presented by Irwin, and shown in Equation 2.8, which is the stress at a crack tip for a crack of depth a, [120].

$$K_I = \sigma\sqrt{\pi a} \qquad \textit{Equation 2.8}$$

Where K_I is the stress intensity factor (MPa/m$^{1/2}$) and σ is the applied stress. This shows that the stress amplification is proportional to the square root of the length of the crack.

2.4.3.2. Estimating the Increase in Stress Concentration

The ratio between the applied stress and the concentrated stress is known as the stress concentration factor K_t. A ground surface, with its series of valleys can be thought of as a series of notches in a fracture model. For the surface finish example, the feature has a non-zero width, r, and a root radius. It is dissimilar to a crack in these regards and must be modelled differently. Notches to represent surface features can be modelled as ellipses, as shown in Figure 2.23. The stress concentration of these can be analytically derived to give Equation 2.9 [121].

$$K_t = 1 + \frac{2a}{b} = 1 + 2\sqrt{\frac{t}{\rho}} \qquad \textit{Equation 2.9}$$

Where K_t is the stress concentration factor, a is the half length of the ellipse, b is the half width of the ellipse, ρ is the root valley radius, and t is the thickness of the material.

This equation acknowledges the width of the ellipse and shows that it is possible to calculate stress concentrations for features that do not contain sudden discontinuities as a crack does. An important inclusion is the root radius. Here, it is calculated from the equation of an ellipse. This is a safe assumption when the feature in question is similar to an ellipse both at the deepest, sharpest, point and at the widest.

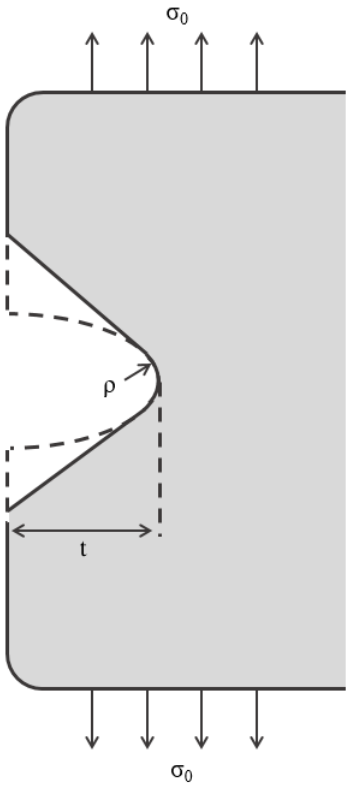

Figure 2.23 The parameters associated with an elliptical hole.

Another deviation from the ideal models used to predict stress concentrations is the existence of multiple features. An important effect is that additional notches reduce the amount of tensile stress transmitted to the notch in question, hence reducing its stress intensity factor [122]. While stress can be transferred to a single notch along the surface, for a series of notches less stress can be transmitted since the surface is effectively removed either side of the notch. This means that the number of stress intensities is higher, but the stress intensity at each one is lower.

2.4.4. Models of Surface Finish

Neuber proposed a semi empirical expression for the estimation of stress concentration factor caused by surface finish, as shown in Equation 2.10 [123].

$$K_t = 1 + \mathrm{n}\sqrt{\lambda\frac{\mathrm{R_z}}{\rho}} \qquad \textit{Equation 2.10}$$

Where ρ is the mean root radius of valleys; n is the state of stress ($n = 1$ for shear stress, $n = 2$ for tensile stress); Rz is the surface height range (as shown in Figure 2.14); and λ is the ratio between spacing and depth of the features, which can be considered to be the openness ratio.

This method considers the effect similar adjacent features have on the local stress. The λ term conveys the frequency of features, and so is linked to the distance to the next one. Additionally, it is related to the steepness of the valley sides, and so is linked to the sharpness of the feature.

In this equation, K_t is roughly proportional to the square root of the width of the spacings divided by the root radius. Here, there is a deviation from the equation of the stress concentration factor for an ellipse, which is proportional to the square root of the depth divided by the root radius. It highlights the reducing effect neighbouring features have on the local stress, and therefore the stress concentration. Less stress is transmitted to the feature if there are equally deep features on either side.

Arola and Ramulu suggested the stress concentration factor induced by surface roughness could be estimated more accuracy with the expression shown in Equation 2.11 [11].

$$K_t = 1 + n\left(\frac{R_a}{\rho}\right)\left(\frac{R_y}{R_z}\right) \qquad \textit{Equation 2.11}$$

Where Ry is the maximum valley height as shown in Figure 2.14. In this equation, K_t is roughly proportional to the depth of the feature divided by the root radius. Interestingly, this has not been square rooted as in Equation 2.9 and Equation 2.10. Additionally, the width of the feature has been replaced with the depth as the factor considered to have a greater influence.

This model was investigated experimentally by Arola who found a maximum error of 2%, valley radius was measured with a "best-fit circle" gauge applied to critical valleys [118]. It was also found that the Neuber model and the Arola and Ramulu model could make significantly different stress concentration predictions in some circumstances [118].

These models estimate the maximum stress concentration factors that could be found on a surface, based on averages of surface height, openness and root radius. These parameters are distributed around the average and so without a factor to account for this, these models would be expected to predict the average stress concentration factor, hence underestimating the maximum. However, these models generally agree with experimental data and finite element analysis. For this reason, it is expected that the application of these models to individual features would overestimate stress concentration.

2.4.5. Finite Element Analysis

2.4.5.1. The use of Finite Element Analysis to Model Surfaces

The aforementioned analytical models can provide a good amount of accuracy in estimating stress concentration factors in surfaces, when surfaces are consistently, predictably, repetitive. Real surfaces are not. Ground surfaces bear the imprint of grinding particles that are effectively randomly arranged, and shotblasted surfaces show the superposition of a random distribution of incident shots, similarly the grain boundaries of the rolled surface and the valleys of the brushed surface are formed in a stochastic manner.

It is considered to be almost impossible to theoretically analyse the stress concentration distribution of real complex surface topography because of unique features and geometric non-repeatability and so finite element analysis (FEA) is used [124][125]. This involves building a computer model of a surface, either from real data from scanning or profilometry, or of a generated surface designed to have identical surface parameters. A mesh of nodes with links are distributed throughout the model and are programmed to interact according to relevant rules of physics and materials science. On this model, a stress can be applied which is transmitted through the links, as it is through a real surface, and, like a real surface, stress concentrations are created and can be measured. The accuracy of this technique relies on the accuracy of the model to the real surface, the resolution of the mesh and the selection and understanding of the relevant rules. FEA is considered a good standard to which to test and compare analytical methods [124].

In one FEA study the effect of surface roughness on fatigue behaviour was investigated. Surface topography was characterised mechanically by profilometry and did not use surface parameters such as Ra or root radius. By interpolating between measurement points with a spline function, FEA was successfully used to calculate the stress concentration factor and it was concluded that this provided a

reliable method to predict the effect surface finish has on fatigue life [68]. In this study, and others, 1D profiles were measured, and used to estimate stress concentrations [126].

Finite Element Analysis (FEA) has been used to measure the size of stress concentrations formed on machined surfaces. One study used 3D data gathered by a coordinate measuring machine (CMM) to compute the stress concentrations formed on an additive manufactured metallic surface with a machined surface [127]. It was found that the smoother machined surface had smaller stress concentrations and a resultingly higher yield strength.

Another study used FEA to validate a proposed analytical model developed to predict stress concentration factors in 3D surfaces formed by machining [128]. This study used an optical profilometer to gather 3D data on an aluminium surface used to create the 3D model for FEA. It was found that the maximum stress concentrations were not located in the deepest valleys, but in the most extreme changes of height (valley to peak). In places, high stress concentration factors were measured, greater than 10.

A different study used VSI with a 20x objective lens to gather 3D data on a machined nickel based super alloy [117]. This data was then used to produce a 3D model used for FEA. It was found that machining features such as turning grooves and pits acted as crack initiation sites. This had the secondary effect of reducing the overall fatigue life of the material. The highest stress concentration factors reported were around 2.

To summarise, FEA allows for the analysis of stress concentrations of real complex surface topography and has been used for this purpose a few times. Methods have involved data collection methods such as 1D profiling, 3D VSI profiling, and CMM devices. Stress concentrations have been identified in areas with extreme changes of hight as well as in valleys, grooves, and pits. These concentrations, measured between 2 and 10, have also been found to reduce fatigue life.

Overall, there is very little literature regarding the use of FEA to investigate stress concentrations in surfaces at the micro scale. There is a complete absence of research using FEA to measure the size of stress concentrations formed by rolled, shotblasted, ground or brushed surfaces, with only surfaces formed by machining or additive manufacturing being studied thus far. Chapter 6 uses FEA in on models produced by VSI to compute the effect of surface finish on stress concentration for a range of previously untested surfaces.

2.4.5.2. Notch Sensitivity Factor

For the study of fatigue cracking, the concept of the notch sensitivity factor was developed. This material parameter explains how the link between elastic and plastic behaviour at a crack tip affects the stress concentration.

Very near to the tip of a stressed crack, deformation occurs which changes the shape of the tip, and therefore the root radius which decreasing the stress concentration. The effective stress concentration factor K_e can be defined as the ratio between the fatigue strength of an object with a smooth surface, and of an object with a surface roughness with characteristic valley radius ρ. Its magnitude is shown by Equation 2.12.

$$1 \leq K_e \leq K_t \qquad \textit{Equation 2.12}$$

The ratio between the effective stress concentration K_e and the geometric stress concentration factor K_t is known as the notch sensitivity, q. This can be rearranged for K_e, shown in Equation 2.13, which shows that the effective stress concentration factor is a product of both the stress concentration factor and q.

$$q = \frac{K_e - 1}{K_t - 1} \quad or \quad K_e = q(K_t - 1) + 1 \qquad \textit{Equation 2.13}$$

q is shown by Equation 2.14 and Equation 2.15 to be a product of both the yield strength and the valley root radius. This means that the effective distribution of stress is dependent on the material qualities as well as the geometric qualities of the surface in question.

$$q = \frac{1}{(1 + \gamma/\rho)} \qquad \textit{Equation 2.14}$$

$$\gamma = 0.025 \left(\frac{2070\ MPa}{\sigma_u}\right)^{1.8} mm \qquad \textit{Equation 2.15}$$

Where σ_u is the ultimate tensile stress (MPa). The notch sensitivity factor includes the ultimate strength of the material, showing that this behaviour is material dependant. In a perfectly elastic material, stress concentration distribution is solely determined by morphology, but with high enough stresses, this assumption does not hold and the notch sensitivty is used [118].

The effect of surface roughness on notch sensitivity has been investigated, and no correlation found. This indicates that valley radii are process-dependent rather than dependent on surface roughness [118].

2.4.5.3. Minimum Feature Size

A minimum size of feature is required to create surface stress concentrations. At smaller roughness values, in materials with larger grains, the positions of high stress concentration are determined by subsurface grains over surface shape. The minimum size of feature is given by Equation 2.16 and Equation 2.17 [124][129].

$$c_{min} = \frac{\sqrt{area_c}}{\sqrt{10}} \qquad \textit{Equation 2.16}$$

$$\sqrt{area_c} = \left[\frac{1.43(Hv + 120}{1.6Hv}\right]^6 \qquad \textit{Equation 2.17}$$

Where Hv is the Vickers Hardness and $area_c$ is the minimum cross-sectional area. This area is the cross sectional area perpendicular to the direction of stress and has been used to estimate the minimum depth required for cracking. Features such as valleys can have massive cross-sectional areas in this regard, owing to their length. While the area of a hole can be roughly square-rooted to give a characteristic depth, features such as valleys cannot be. For a 2 µm deep valley to fulfil the requirement of 220 µm^2 it would need to be over 100 µm long. Valleys far longer than this are observed, so, though this method would normally predict no stress concentrations would be possible, with the application of more appropriate geometrical parameters it has been shown that stress concentrations up to the threshold required for cracking are possible.

A distinction between macro-topography and micro-topography has been made [130]. It was suggested that features belonging to these levels influence crack formation in different ways, for macro-topography (250 – 1000 μm), elastic stress concentration effects are of importance, whereas for micro-topography (5 – 50 μm), plastic strain is more influential [130].

FEA has shown that micro-topographic features such as micro-pits and "jut-ins" give the greater contribution to local stress concentrations [130]. These features are often caused by stochastically distributed corrosion and so can move the maximum stress concentrations away from obvious macro-sites such as pits, this causes cracks to form away from these regions in some circumstances.

2.4.6. Conclusion

It is well known that on structures under load, certain morphologies serve to concentrate stresses at a point [131]. Just as a pre-crack in a crack test sample provides a location for the initiation of a crack, a valley in a surface could act in the same way.

Some surface finishes are shaped in such a way as to mimic crack tips, with an applied stress concentrating at the tip and having a far worse effect. This should have the biggest effect on those finishes comprised of valleys with the smaller aspect ratios, such as ground finishes rather than polished or shot peened. It would be expected that the most stress would be found at the bottom of the valley as it resembles a crack tip. This amplified stress fulfils one of the three requirements for SCC and so stress concentrations can allow SCC in conditions otherwise not disposed to it or accelerate it in those that are.

2.5. References

[1] Poyry Energy Ltd and Wood Nuclear Ltd, “2019 UK Radioactive Waste Inventory,” 2019.

[2] Nuclear Decommissioning Authority, “UK Radioactive Waste Inventory, reported volumes,” 2019.

[3] BEIS, “Consultation: Working With Communities, Implementing Geological Disposal,” no. January, 2018.

[4] T. W. Hicks *et al.*, “Concepts for the geological disposal of intermediate-level radioactive waste,” vol. 44, no. 1572, pp. 1–66, 2008.

[5] NDA, “Geological Disposal: An overview of the generic disposal system safety case,” 2010.

[6] Department for Business Energy & Industrial Strategy, “Nuclear Sector Deal,” 2018.

[7] S. Rahimi, K. Mehrez, and T. J. Marrow, “Effect of surface machining on intergranular stress corrosion cracking (IGSCC) in sensitised type 304 austenitic stainless steel,” *Corros. Eng. Sci. Technol.*, vol. 51, no. 5, pp. 383–391, 2016.

[8] UKRWI, “What are the main waste categories? | UK Radioactive Waste Inventory,” 2020.

[9] NDA, “Waste in stock, UK Radioactive Waste Inventory.” 2019.

[10] Nuclear Decommissioning Authority, “NDA Report no DSSC/412/01 - Geological Disposal: Generic disposal facility design,” 2016.

[11] APS Group Scotland, “Scotland’s higher activity radioactive waste policy,” 2011.

[12] RWM, “Geological disposal guidance on the application of the waste package specifications for unshielded waste packages,” 2014.

[13] M. Row, “A review of manufacturing processes used in stainless steel intermediate level waste containers to evaluate the presence of residual stresses report to NDA,” *Serco Rep. to NDA*, no. 3, pp. 1–42, 2009.

[14] O. E. Albores-Silva, E. a Charles, and C. Padovani, “Effect of chloride deposition on stress corrosion cracking of 316L stainless steel used for intermediate level radioactive waste containers,” *Corros. Eng. Sci. Technol.*, vol. 46, no. 2, pp. 124–128, 2011.

[15] G. Wranglen, “The ‘rustless’ iron pillar at Delhi,” *Corros. Sci.*, vol. 10, no. 10, pp. 761–770, 1970.

[16] H. Godfrey and G. Cann, “Effect of chloride on magnox corrosion with respect to carbon-14 release post closure,” *NNL, Risley*, vol. 18, no. 6, 2015.

[17] AMEC, “Characterisation of environmental conditions in an ILW store,” 2012.

[18] S. C. Boden and G. Hulme, “Nirex phased disposal concept: further analysis of the environment within UILW vaults,” 2003.

[19] NDA, “Geological disposal: generic disposal system technical specification,” 2010.

[20] R. Qvarfort, “Critical pitting temperature measurements of stainless steels with an improved electrochemical method,” *Corros. Sci.*, vol. 29, no. 8, pp. 987–993, 1989.

[21] A. B. Cook *et al.*, “Assessing the risk of under-deposit chloride-induced stress corrosion cracking in austenitic stainless steel nuclear waste containers,” *Corros. Eng. Sci. Technol.*, vol. 49, no. 6, pp. 529–534, 2014.

[22] Frankel G. S., “Pitting corrosion of metals, a review of the critical factors,” *J. Electrochem. Soc.*, vol. 145, no. 6, p. 2186, 1998.

[23] N. J. Laycock and R. C. Newman, “Temperature dependence of pitting potentials for austenitic stainless steels above their critical pitting temperature,” *Corros. Sci.*, vol. 40, no. 6, pp. 887–902, 1998.

[24] A. B. Cook *et al.*, “Atmospheric-induced stress corrosion cracking of austenitic stainless steels under limitted chloride supply,” *Proc. 18th Int. Corros. Congr.*, pp. 1–11, 2011.

[25] L. Greenspan, “Humidity fixed points of binary saturated aqueous solutions,” *J. Res. Natl. Bur. Stand. Sect. A Phys. Chem.*, vol. 81A, no. 1, p. 89, 1977.

[26] S C Boden, “Nirex vault environment feasibility study: summary report,” 2002.

[27] J. Young, “Humidity control in the laboratory using salt solutions – a review,” *J. Appl. Chem.*, vol. 17, no. 9, pp. 241–245, 1967.

[28] T. Prosek, A. Iversen, C. Taxén, and D. Thierry, “Low-temperature stress corrosion cracking of stainless steels in the atmosphere in the presence of chloride deposits,” vol. 65, no. 2, pp. 105–117, 2009.

[29] F.-R. F. F. and A. J. Bard, “In situ scanning tunneling microscopic study of the corrosion of type 3041. stainless steel in aqueous chloride media,” *Electrochem. Soc.*, vol. 77, no. 9, pp. 1268–1270, 2013.

[30] NDA, “Waste package specification and guidance documentation,” 2008.

[31] Serco, “Review of environmental conditions for storage of ILW radioactive waste containers,” 2010.

[32] N. Drew, “Analysis of chloride deposition rates relevant to ILW stores,” 2005.

[33] A. B. Cook *et al.*, “Under-deposit chloride-induced stress corrosion cracking in austenitic stainless steels: aspects associated with deposit type, size and composition,” *ECS Trans.*, vol. 58, no. 29, pp. 25–39, 2014.

[34] Serco, “Review of effect of chloride on corrosion of stainless steels in cementitious environments,” 2010.

[35] T. Moriyasu, H. Kimura, and H. Kusanagi, “The amount of chloride contamination for prevention of stress corrosion cracking in sensitised type 304 stainless steel,” *Corros. Sci. 25(8/9), 837-844,* 1985.

[36] N. Mi, M. Ghahari, T. Rayment, and A. J. Davenport, “Use of inkjet printing to deposit magnesium chloride salt patterns for investigation of atmospheric corrosion of 304 stainless steel,” *Corros. Sci.*, vol. 53, no. 10, pp. 3114–3121, 2011.

[37] S. Wang, Y. Li, M. Yao, and R. Wang, “Compressive residual stress introduced by shot peening,” *J. Mater. Process. Technol.*, vol. 73, no. 1–3, pp. 64–73, 1998.

[38] A. Turnbull *et al.*, “Sensitivity of stress corrosion cracking of stainless steel to surface machining and grinding procedure,” *Corros. Sci.*, vol. 53, no. 10, pp. 3398–3415, 2011.

[39] S. Ghosh and V. Kain, “Microstructural changes in AISI 304L stainless steel due to surface machining: Effect on its susceptibility to chloride stress corrosion cracking,” *J. Nucl. Mater.*, vol. 403, no. 1–3, pp. 62–67, 2010.

[40] W. Zhang, K. Fang, Y. Hu, S. Wang, and X. Wang, “Effect of machining-induced surface residual stress on initiation of stress corrosion cracking in 316 austenitic stainless steel,” *Corros. Sci.*, vol. 108, pp. 173–184, 2016.

[41] I. Kritzler, J, Metal Improvement Company, “Effect of shot peening on stress corrosion

cracking on austenitic stainless steel," 1995.

[42] NIREX, "Waste Container Design," 2003.

[43] ISM, "Submarine dismantling - packaged waste container selection combined report," 2010.

[44] National Physical Laboratory, "Determination of residual stresses by X-ray diffraction, a national measurement good practice guide," 2005.

[45] EFunda.Inc, "eFunda: Properties of Stainless Steel AISI Type 316," 2013.

[46] RWM, "Geological disposal guidence on the production of encapsulated wasteforms," 2015.

[47] Y. J. Janin, "Characterisation of residual stress and investigation of environmental effects on atmospheric-induced stress corrosion cracking of austenitic stainless steel nuclear waste containers," *PhD Thesis, Univ. Manchester*, 2012.

[48] S. L. Clitheroe, "The physical and microstructural properties of peened austenitic stainless steel," *PhD Thesis, Univ. Manchester*, 2011.

[49] M. Kobayashi, T. Matsui, and Y. Murakami, "Mechanism of creation of compressive residual stress by shot peening.," *Trans. Japan Soc. Mech. Eng. Ser. A*, vol. 63, no. 5, pp. 1226–1230, 1997.

[50] M. A. S. Torres and H. J. C. Voorwald, "An evaluation of shot peening, residual stress and stress relaxation on the fatigue life of AISI 4340 steel," *Int. J. Fatigue*, vol. 24, no. 8, pp. 877–886, 2002.

[51] S. A. Meguid, G. Shagal, J. C. Stranart, and J. Daly, "Three-dimensional dynamic finite element analysis of shot-peening induced residual stresses," *Finite Elem. Anal. Des.*, vol. 31, no. 3, pp. 179–191, 1999.

[52] D. Peckner and I. M. Bernstein, *Handbook of Stainless Steels*. 1977.

[53] N. Vasios, "Crystal Plasticity, a Rate Independent Constitutive Model," 2015.

[54] G. N. Haidemenopoulos, *Physical Metallurgy: Principles and Design*. 2018.

[55] S. Li and G. Wang, *Introduction to Dislocation Theory*. 2018.

[56] Nirex, "Nirex Report: generic repository studies, generic waste package specification - justification," 2007.

[57] NDA, “Sellafield Plan,” 2011.

[58] L. L. Shreir, *Corrosion Volume 1*. London: Newnes-Butterworths, 1965.

[59] C. Padovani, R. J. Winsley, N. R. Smart, and P. A. H. Fennell, “Corrosion control of stainless steels in indoor atmospheres,” *Corros. Vol. 71 issue 5*, 2015.

[60] N. Sato, “An overview on the passivity of metals,” *Corros. Sci.*, vol. 31, no. C, pp. 1–19, 1990.

[61] C. O. A. Olsson and D. Landolt, “Passive films on stainless steels - Chemistry, structure and growth,” *Electrochim. Acta*, vol. 48, no. 9 SPEC., pp. 1093–1104, 2003.

[62] C. Y. Chao, L. F. Lin, and D. D. MacDonald, “A Point Defect Model for Anodic Passive Films,” *J. Electrochem. Soc.*, vol. 128, no. 6, p. 1187, 1981.

[63] J. W. Schultze and M. M. Lohrengel, “Stability, reactivity and breakdown of passive films. Problems of recent and future research,” *Electrochim. Acta*, vol. 45, no. 15–16, pp. 2499–2513, 2000.

[64] B. Baroux, “The kinetics of pit generation on stainless steels,” *Corros. Sci.*, vol. 28, no. 10, pp. 969–986, 1988.

[65] B. Baroux, *The Pitting Corrosion of Stainless Steels (Further insights)*. 1995.

[66] N. Rashidi, S. Alavi-soltani, and R. Asmatulu, “Crevice corrosion theory, mechanisms and prevention methods,” *Proc. 3rd Annu. GRASP Symp.*, pp. 215–216, 2007.

[67] J. Wintle *et al.*, “Investigations on the susceptibility to atmospheric-induced stress corrosion cracking of austenitic stainless steel nuclear structures,” in *SMiRT-22*, 2013.

[68] M. Suraratchai, J. Limido, C. Mabru, and R. Chieragatti, “Modelling the influence of machined surface roughness on the fatigue life of aluminium alloy,” *Int. J. Fatigue*, vol. 30, no. 12, pp. 2119–2126, 2008.

[69] D. D. MacDonald and M. Urquidi-MacDonald, “A coupled environment model for stress corrosion cracking in sensitized type 304 stainless steel in LWR environments,” *Corros. Sci.*, vol. 32, no. 1, pp. 51–81, 1991.

[70] N. Sato, *Basics of Corrosion Chemistry*. 2011.

[71] D. D. MacDonald, “The history of the Point Defect Model for the passive state: A brief review of film growth aspects,” *Electrochim. Acta*, vol. 56, no. 4, pp. 1761–1772, 2011.

[72] D. D. Macdonald, “The Point Defect Model for the Passive State,” *J. Electrochem. Soc.*, vol. 139, no. 12, p. 3434, 1992.

[73] B. Krishnamurthy, R. E. White, and H. J. Ploehn, “Simplified point defect model for growth of anodic passive films on iron,” *Electrochim. Acta*, vol. 47, no. 20, pp. 3375–3381, 2002.

[74] B. Krishnamurthy, R. E. White, and H. J. Ploehn, “Non-equilibrium point defect model for time-dependent passivation of metal surfaces,” *Electrochim. Acta*, vol. 46, no. 22, pp. 3387–3396, 2001.

[75] T. Shibata, “Stochastic studies of passivity breakdown,” *Corros. Sci.*, vol. 31, no. C, pp. 413–423, 1990.

[76] P. Marcus, V. Maurice, and H. H. Strehblow, “Localized corrosion (pitting): A model of passivity breakdown including the role of the oxide layer nanostructure,” *Corros. Sci.*, vol. 50, no. 9, pp. 2698–2704, 2008.

[77] N. Sato, “Anodic breakdown of passive films on metals,” *J. Electrochem. Soc.*, vol. 129, no. 2, p. 255, 1982.

[78] M. P. Ryan, “The pitting behavior of iron-chromium thin film alloys in hydrochloric acid,” *J. Electrochem. Soc.*, vol. 145, no. 5, p. 1566, 1998.

[79] D. T. Spencer, M. R. Edwards, M. R. Wenman, C. Tsitsios, G. G. Scatigno, and P. R. Chard-Tuckey, “The initiation and propagation of chloride-induced transgranular stress-corrosion cracking (TGSCC) of 304L austenitic stainless steel under atmospheric conditions,” *Corros. Sci.*, vol. 88, pp. 76–88, 2014.

[80] A. Turnbull, L. Mccartney, and S. Zhou, “Modelling of the evolution of stress corrosion cracks from corrosion pits,” *Scr. Mater.*, vol. 54, no. 4, pp. 575–578, 2006.

[81] A. Turnbull, L. N. McCartney, and S. Zhou, “A model to predict the evolution of pitting corrosion and the pit-to-crack transition incorporating statistically distributed input parameters,” *Environ. Crack. Mater.*, vol. 48, pp. 19–45, 2008.

[82] A. Turnbull, L. Wright, and L. Crocker, “New insight into the pit-to-crack transition from finite element analysis of the stress and strain distribution around a corrosion pit,” *Corros. Sci.*, vol. 52, no. 4, pp. 1492–1498, 2010.

[83] J. R. Galvele, “Transport processes and the mechanism of pitting of metals,” no. April, pp.

464–474, 1976.

[84] Cambridge University, “Cambridge Dictionary | English Dictionary, Translations & Thesaurus,” *Cambridge University Press*. 2018.

[85] R. Leach, “Optical measurement of surface topography,” *Springer Sci. Bus. Media*, pp. 1–7, 2011.

[86] ISO, “Geometrical product specifications - Surface texture : Profile method - Terms, definitions and surface texture parameters,” 1997.

[87] AMSE, “Surface Texture Symbols,” 1996.

[88] “Surface roughness drawing indications of surface texture (JIS B 0601-2001),” 1998.

[89] “Michigan metrology - 3D surface texture measurement,” *Michigan Metrology*, 2020. [Online]. Available: www.michmet.com.

[90] Z. Mike, “Characterizing surface quality: why average roughness is not enough,” *Bruker*, 2000.

[91] K. J. Kubiak, M. C. T. Wilson, T. G. Mathia, and P. Carval, “Wettability versus roughness of engineering surfaces,” *Wear*, vol. 271, no. 3–4, pp. 523–528, 2011.

[92] I. S. Cole, T. H. Muster, N. S. Azmat, M. S. Venkatraman, and A. Cook, “Multiscale modelling of the corrosion of metals under atmospheric corrosion,” *Electrochim. Acta*, vol. 56, no. 4, pp. 1856–1865, 2011.

[93] a. Cook *et al.*, “Atmospheric-induced stress corrosion cracking of austenitic stainless steels under limited chloride supply,” *18th Int. Corros. Congr. 2011*, vol. 2, no. February 2017, pp. 1438–1449, 2011.

[94] G. Bitelli, A. Simone, F. Girardi, and C. Lantieri, “Laser scanning on road pavements: A new approach for characterizing surface texture,” *Sensors (Switzerland)*, vol. 12, no. 7, pp. 9110–9128, 2012.

[95] M. J. Graham, “The application of surface techniques in understanding corrosion phenomena and mechanisms,” *Corros. Sci.*, vol. 37, no. 9, pp. 1377–1397, 1995.

[96] Y. Zuo, H. Wang, and J. Xiong, “The aspect ratio of surface grooves and metastable pitting of stainless steel,” *Corros. Sci.*, vol. 44, no. 1, pp. 25–35, 2002.

[97] F. A. Martin, C. Bataillon, and J. Cousty, “In situ AFM detection of pit onset location on a 304L stainless steel,” *Corros. Sci.*, vol. 50, no. 1, pp. 84–92, 2008.

[98] P. E. Manning, D. J. Duquette, and W. F. Savage, “Effect of test method and surface condition on pitting potential of single and duplex phase 304L stainless steel.,” *Corrosion*, vol. 35, no. 4. pp. 151–157, 1979.

[99] L. Abosrra, A. F. Ashour, S. C. Mitchell, and M. Youseffi, “Corrosion of mild steel and 316L austenitic stainless steel with different surface roughness in sodium chloride saline solutions,” *Electrochem. Process Simul. Iii*, vol. 65, pp. 161–172, 2009.

[100] L. B. Coelho *et al.*, “Mechanical and corrosion characterization of industrially treated 316L stainless steel surfaces,” *Surf. Coatings Technol.*, vol. 382, no. September 2019, p. 125175, 2020.

[101] A. Hojna, M. Zimina, and L. Rozumova, “Effect of the surface grinding on the environmentally assisted crack initiation of 316 L steel in simulated pressurized water reactor water,” *J. Nucl. Eng. Radiat. Sci.*, vol. 5, no. 3, 2019.

[102] H. Ezuber, A. Alshater, S. O. Nisar, A. Gonsalvez, and S. Aslam, “Effect of surface finish on the pitting corrosion behavior of sensitized AISI 304 austenitic stainless steel alloys in 3.5% NaCl solutions,” *Surf. Eng. Appl. Electrochem.*, vol. 54, no. 1, pp. 73–80, 2018.

[103] E. Hosni and R. C. Newman, “Critical factors in localized corrosion,” *Electrochem. Soc. Proc. Ser.*, no. October, 1992.

[104] A. Burkert, T. Müller, J. Lehmann, and J. Mietz, “Long-term corrosion behaviour of stainless steels in marine atmosphere,” *Mater. Corros.*, vol. 69, no. 1, pp. 20–28, 2018.

[105] P. J. Núñez, E. García-Plaza, M. Hernando, and R. Trujillo, “Characterization of surface finish of electropolished stainless steel AISI 316L with varying electrolyte concentrations,” *Procedia Eng.*, vol. 63, pp. 771–778, 2013.

[106] V. Kain, *Stress corrosion cracking (SCC) in stainless steels*. 2011.

[107] S. G. Acharyya, A. Khandelwal, V. Kain, A. Kumar, and I. Samajdar, “Surface working of 304L stainless steel: Impact on microstructure, electrochemical behavior and SCC resistance,” *Mater. Charact.*, vol. 72, pp. 68–76, 2012.

[108] J. W. Fielder, B. A. Hobson, and M. L. Pickett, “The stress corrosion cracking behaviour of

stainless steel at temperatures below 50 C," *EUR*. European Commission.

[109] T. Nguyen, I. Zarudi, and L. C. Zhang, "Grinding-hardening with liquid nitrogen: Mechanisms and technology," *Int. J. Mach. Tools Manuf.*, vol. 47, no. 1, pp. 97–106, 2007.

[110] P. C. Pistorius and G. T. Burstein, "Growth of corrosion pits on stainless steel in chloride solution containing dilute sulphate," *Corros. Sci.*, vol. 33, no. 12, pp. 1885–1897, 1992.

[111] P. C. Pistorius and G. T. Burstein, "Detailed investigation of current transients from metastable pitting events on stainless steel - the transition to stability," *Mater. Sci. Forum*, vol. 111–112, pp. 429–452, 1992.

[112] V. Ouvrir, "Stability and metastability of corrosion pits on stainless steel," no. August, pp. 1–3, 2018.

[113] G. T. Burstein and P. C. Pistorius, "Surface roughness and the metastable pitting of stainless steel in chloride solutions," *Corrosion*, vol. 51, no. 5, pp. 380–385, 1995.

[114] D. Novovic, R. C. Dewes, D. K. Aspinwall, W. Voice, and P. Bowen, "The effect of machined topography and integrity on fatigue life," *Int. J. Mach. Tools Manuf.*, vol. 44, no. 2–3, pp. 125–134, 2004.

[115] O. Obiukwu, M. Nwafor, B. Okafor, and L. Grema, "The effect of surface finish on the low cycle fatigue of low and medium carbon steel," *Int. Conf. Mech Ind. Engg*, pp. 14–15, 2015.

[116] E. Zahavi, *Fatigue design: life expectancy of machine parts*. 1997.

[117] D. T. Ardi, Y. G. Li, K. H. K. Chan, L. Blunt, and M. R. Bache, "The effects of machined topography on fatigue life of a nickel based superalloy," *Procedia CIRP*, vol. 13, pp. 19–24, 2014.

[118] D. Arola and C. L. Williams, "Estimating the fatigue stress concentration factor of machined surfaces," *Int. J. Fatigue*, vol. 24, no. 9, pp. 923–930, 2002.

[119] Y. Guilhem, S. Basseville, F. Curtit, J. M. Stéphan, and G. Cailletaud, "Numerical analysis of the effect of surface roughness on mechanical fields in polycrystalline aggregates," *Model. Simul. Mater. Sci. Eng.*, vol. 26, no. 4, 2018.

[120] D. P. Rooke and D. J. Cartwright, *Compendium of Stress Intensity Factors*, vol. 80. 1976.

[121] Y. Murakami, *Theory of Elasticity and Stress Concentration*. 2017.

[122] A. Manan, “Fracture mechanics analysis of multiple edge cracks,” *PhD Thesis, Univ. Coll. London*, no. February, 2008.

[123] H. Neuber, *Kerbspannungslehre: Theorie der Spannungskonzentration. Genaue Berechnung der Festigkeit*. 2001.

[124] Z. Cheng and R. Liao, “Effect of surface topography on stress concentration factor,” *Chinese J. Mech. Eng. (English Ed.*, vol. 28, no. 6, pp. 1141–1148, 2015.

[125] Y. Aono and H. Noguchi, “Fatigue limit reliability of axisymmetric complex surface,” *Int. J. Fract.*, vol. 131, no. 1, pp. 59–78, 2005.

[126] S. Kyrre Ås, B. Skallerud, and B. Wathne Tveiten, “Surface roughness characterization for fatigue life predictions using finite element analysis,” *Int. J. Fatigue*, vol. 30, no. 12, pp. 2200–2209, 2008.

[127] W. Everhart, E. Sawyer, T. Neidt, J. Dinardo, and B. Brown, “The effect of surface finish on tensile behavior of additively manufactured tensile bars,” *J. Mater. Sci.*, vol. 51, no. 8, pp. 3836–3845, 2016.

[128] I. Perez, A. Madariaga, P. J. Arrazola, M. Cuesta, and D. Soriano, “An analytical approach to calculate stress concentration factors of machined surfaces,” *Int. J. Mech. Sci.*, vol. 190, no. August 2020, p. 106040, 2020.

[129] Yukitaka Murakami, *Metal Fatigue: Effects of Small Defects and Nonmetallic Inclusions*. 2002.

[130] J. T. Burns, J. M. Larsen, and R. P. Gangloff, “Driving forces for localized corrosion-to-fatigue crack transition in Al-Zn-Mg-Cu,” *Fatigue Fract. Eng. Mater. Struct.*, vol. 34, no. 10, pp. 745–773, 2011.

[131] G. R. Irwin, “Analysis of stresses and strains near the end of a crack traversing a plate,” *Journal of Applied Mechanics*, vol. 24, no. September. pp. 361–364, 1957.

Chapter 3. Methods and Materials

This Chapter details the methods and materials used in this Thesis. Firstly, the range of analytical techniques and their associated data analysis methods are described. It should be noted that almost all of the data analysis performed in Chapters 4 and 5 used a self-developed Python code, since the commercial software available was not able to provide sufficient flexibility to fully, and accurately, quantify surface morphology and stress. This code is briefly herein. Secondly, a description of the stress corrosion testing apparatus and methodology are detailed. It was deemed appropriate that for specific applications of some methodologies, for example, in-situ corrosion testing by AFM, discussed in Chapter 4, that the detailed methods are described within the relevant Chapters.

3.1. Scanning Electron Microscopy and Energy Dispersive Spectroscopy

EDS (Energy Disperse X-Ray Spectroscopy) analysis measures composition at a sample surface and paired with an SEM provides a high resolution surface map of composition. EDS was used as a second measurement of composition. The surface mapping feature of this method provided a measure of the variation of composition found across the surface of the sample. This was applied to cross-sectionally mounted samples to investigate how composition changes with depth into the sample.

Area maps were taken alongside SEM images to allow for the comparison of compositional changes with surface features. Point EDS measurements were taken for composition analysis.

For SEM and EDS analysis, samples of stainless steel were cut from a 1 mm thick sheet using a ferrous cut-off blade. They were then sectioned down into 10 mm squares and mounted in conductive Bakelite at 150ºC and 290 MPa for 2 minutes. Some samples were also prepared in cross-section using plastic ring-forming tabs. For cross sectional analysis the samples were then coarsely ground until the surface was removed, and the bulk material was revealed. Subsequently, a series of finer grinding papers were used, followed by polishing using 0.3 μm diamond suspension on a Texmet C cloth pad, and finally a 0.1 μm colloidal silica suspension on a ChemoMet soft pad at pH 5.

For examination of the initial surface, no mounting or grinding was required. Samples were cut to size and degreased with isopropanol before being attached to SEM stubs with carbon sticky tabs.

3.2. X-Ray Fluorescence Analysis

X-Ray Fluorescence (XRF) analysis works by repeatedly exposing a sample to an incident X-Ray beam, exciting electrons in the material, before switching it off and observing the fluorescence spectra caused by electron relaxation. Since the gap between energy shells is unique for each element, the fluorescence spectra gives the composition of the material [1][2].

Typically, XRF is used on powdered crystalline or amorphous materials but due to the polycrystalline nature, no sample preparation other than sectioning with a ferrous cut-off blade and degreasing with isopropyl alcohol was necessary. Samples were cut to squares larger than 10 mm in width to completely cover the 10 mm diameter aperture.

A series of measurements were taken for each sample used to calculate the variance for each element. The Panalytical Zetium XRF instrument outputs measurements as percentages, typically summing to 106%. These were normalised with no weighting, before being reported. Calibration was performed using an Omnian standard calibration piece, no longer than one week before the scans were completed. Each set of scans were performed within a one-day time slot to reduce the effects of long-term calibration drift. To reduce the unwanted fluorescence effects found when using a copper X-ray source with iron-rich samples, a rhodium source was used with a kα2 energy of 20073.6 eV and a kα energy of 20216.12 eV.

3.3. Vertical Scanning Interferometry (VSI)

Vertical Scanning Interferometry (VSI) provides data sets covering large areas of a given surface at a range of magnifications. In comparison with Atomic Force Microscopy (AFM, see Section 3.4.), which was also used in this Thesis, it provides lower horizontal and vertical resolution (Table 3.1).

Table 3.1 The spatial resolutions of AFM and VSI

	AFM	VSI
Horizontal Resolution	0.01 μm	0.1 μm
Vertical Resolution	0.001 μm	0.01 μm

3.3.1. General Explanation

Vertical Scanning Interferometry (VSI) was used to map the height of the sample surfaces. VSI works through the physical phenomena of interferometry, which was first used to measure distance by Albert A. Michelson [3]. A coherent beam of laser light is split along two paths, where one path is incident on, and reflected by, the sample surface, with the other reflected by a mirror of similar path-length. The two reflected beams are brought back together and interfere with each other before their image is measured by a CCD as shown in Figure 3.1. These interference patterns reveal path length differences, and therefore surface height differences, at the order of a fraction of the wavelength of the light.

For a continuous surface, fringes are formed. For a flat but sloped surface these fringes appear as stripes of positive (light) and negative (dark) interference and run perpendicular to the directionality of the slope. For a large hill or mound, these fringes form a circular pattern. The detecting of these fringes allows the computation of relative surface heights.

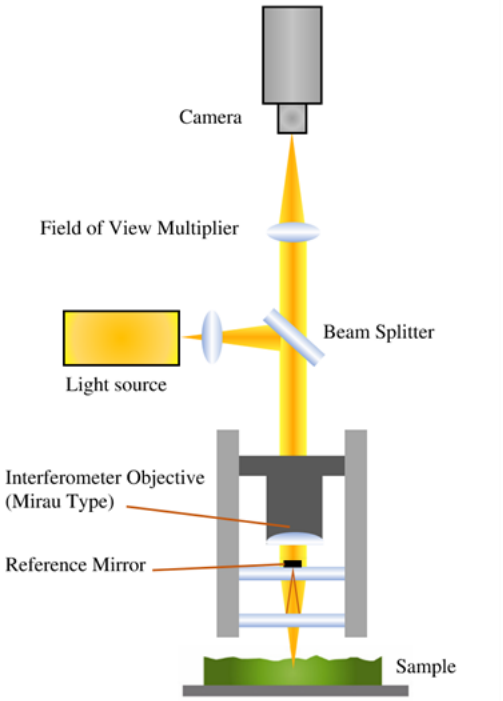

Figure 3.1 Surface height measurement by interferometry.

3.3.2. Practical Method

Very little sample preparation was required for this method. Basic cleaning and degreasing of the stainless steel coupons in isopropyl alcohol was sufficient. Samples that did not rest in a stable manner were held with plasticine. Sample surfaces were levelled using a manual levelling stage by eye, using fringe interference patterns. Any remaining small slopes were then removed using software. The instrument used was a Bruker Contour GT VSI with a 50X objective.

3.3.3. Data Analysis Technique Development

Proprietary software provided with the Contour GT VSI had a range of useful functions to provide quantities measured values of surface properties, such as surface roughness, although it provided no explanation as to how these values were calculated. Additionally, the handling of NaN (Not a Number) values raised concerns; the default setting was to zero these values, but since the average surface height measured was nonzero this artificially inflated roughness values so much as to obscure their true value. This made it difficult to calculate a reasonable error measurement. For this reason, analysis of surface height data was performed using a series of self-developed, purpose-made, python scripts. This allowed for control and open publication of the calculation method of these values, making the measurements more reproducible, and comparable with AFM measurements of the same surfaces. Self-handling of the

data allowed for an increased range of functions to be used and designed. These included measurements of the surface area, the fractal behaviour of the surface and a measure of the openness of the surface.

Measurements like surface area and the fractal behaviour of the surface (see Section 4.3. for more detail) immediately fed into electrochemical tests (not included in the scope of this Thesis, but discussed in Section 4.8.), providing an opportunity to normalise and control for these features. The openness mapping measurement gives an indication of local pitting prevalence based on geometry alone.

Analysis was completed in Python using the Jupyter Notebook Integrated Development Environment (IDE) [4]. The "matplotlib", "math" and "numpy" libraries were used. Data was imported from .dat files in surface height data array format.

Missing data points were filled with an average of their nearest neighbours. Tilt was removed by computing the tilt of a flat plane with nearest average tilt and this was removed from the dataset to flatten it. It was then zeroed by removing the average from each point.

3.4. Atomic Force Microscopy (AFM)

3.4.1. General Explanation

To improve the resolution of the geometric characterisation, Atomic Force Microscopy (AFM) was also employed. The VSI used had a maximum lateral resolution of 0.1 μm compared to the 0.01 μm resolution of the AFM (Table 3.). This allowed for greater magnification of the surface, as well as comparison of the two techniques where the resolutions overlapped.

AFM uses a photolithography-produced probe with a very sharp tip of radius around 10 nm. This tip sits on a cantilever with a reflective backing on which a laser is incident as shown in Figure 3.2. The tip is scanned across the sample, vibrating by a piezoelectric oscillator to "tap" the surface. This motion is affected by atomic forces such as Van der Waals forces, dipole-dipole interactions, and electrostatic forces. This deflection is detected by the reflected laser beam and an evaluation is made to quantify the deflective force and plot a force curve [5]. This is then used to estimate the height of the sample.

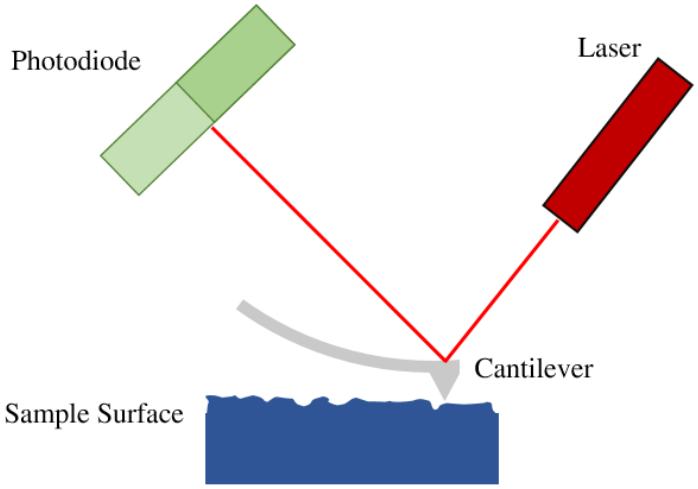

Figure 3.2 Operation of an Atomic Force Microscope (AFM)

3.4.2 Practical Method

Square samples of each the four different surface finishes, 6 mm in size, prepared by waterjet cutting (as described in Section 3.5.3.), were used. Samples were cleaned in isopropyl alcohol and dried with air. These were scanned with a Bruker Multimode AFM with a ScanAsyst-Air A-Frame cantilever using Nanoscope 9.2 software. The probe tip and cantilever model used are shown in Figure 3.3.

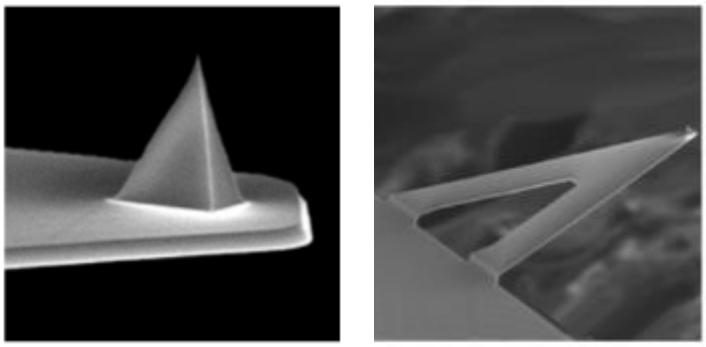

Figure 3.3 ScanAsyst-Air probe tip and A-Frame cantilever.

The following parameters, shown in Table 3.2, were used with the method parameters shown in Table 3.3.

Table 3.2 AFM Probe Parameters

Parameter	
T, Thickness of cantilever	650 nm
L, Length of cantilever	115 µm
W, Width of cantilever	25 µm
f_0 , Frequency	70 kHz
K, Spring constant	0.4 N/m

Table 3.3 AFM Method Parameters

Parameter	
Scan size (Square)	10 - 100 µm
Aspect Ratio	1
Scan Rate	0.100 Hz
Samples/ Line	256 - 1024
Lines	256 -1024
Feedback Gain	40
Peak Force Set point	4.980 nN
Peak Force Frequency	4 kHz
Z Limit	5.376 µm

Due to the relative roughness of the ground, brushed and shotblasted samples compared with samples usually used in AFM, the scan rate was lowered to avoid damage of the tip, so that each image tended to take over one hour to collect.

3.5. Electron Backscatter Diffraction

3.5.1. Technical Explanation

Electron Backscatter Diffraction (EBSD) is conducted with a Scanning Electron Microscope (SEM). The sample in the SEM is rotated to 70°, this is the angle at which the best diffracted Kikuchi bands appear; Figure 3.4 shows a diagram of the system. A phosphor screen detector is moved close (<10 mm) to the sample to detect diffracted electrons. An incident electron beam with an energy of 20 kV penetrates 1-5 μm into the sample surface [6]. These electrons are inelastically scattered by a high angle. Those that are scattered in a direction satisfying the Bragg diffraction condition for a particular crystal plane are channelled with similar electrons to form intensity cones with very high semi-apical angles (near 90°). This is non 90° due to the 1% energy loss of the inelastic scattering. These cones form disks that widen from the centre; the disks form along crystal planes and stereographically project a Kikuchi band pattern on a sphere centring on the pattern point source. The intensity of the bands is captured on a flat phosphor screen, close to the sample. This forms an Electron Back-Scattering Pattern (EBSP) consisting of many intersecting linear-appearing features, which consist of strips that are brighter than the background, bound by two edges (one from each cone, caused by an individual plane). These are recorded by a low light camera and then automatically analysed to detect crystal structure, quality, and orientation.

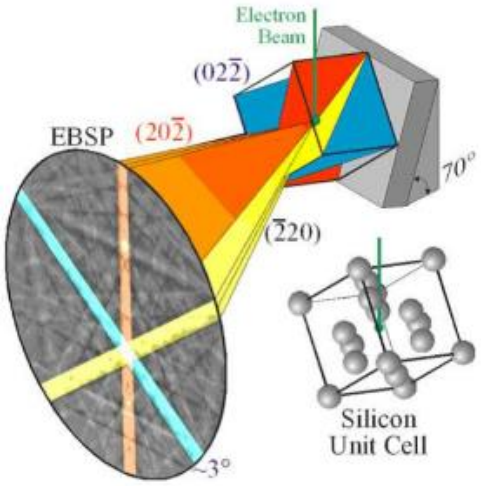

Figure 3.4 Kikuchi bands diagram [18].

The analysis of a Kikuchi band involves assigning indices to bands and band intercept areas (zones) as shown in Figure 3.5. These zones represent crystallographic directions. This process is automated, but with a large number of user input parameters.

3.5.2. The Formation of Kikuchi Band Projections from a Primary Cube

In Figure 3.6a, the vertical grey cross is projected by the (100), (010) and (001) planes. These are the planes that would segment the unit cube into eight smaller cubes. The dark central cross is projected by the (110) and ($\bar{1}$10) planes. These planes would segment the above cube along the diagonals visible in the shown orientation. The four remaining dark lines are projected by the (01$\bar{1}$) and (011) pair (top and bottom) and the (101) and ($\bar{1}$01) pair (two sides). These planes are described later.

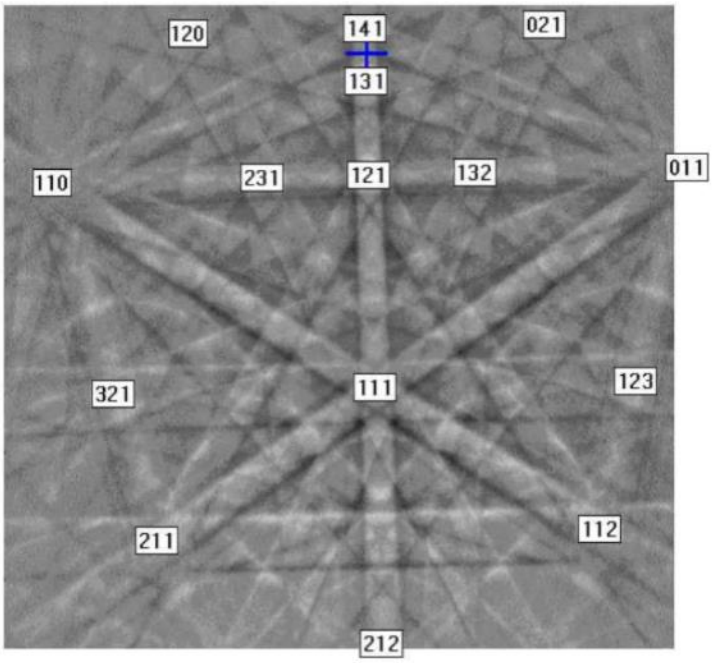

Figure 3.5 Showing the indexing of Kikuchi bands.

In Figure 3.6b the vertical dark line is projected by the (10$\bar{1}$) plane. The two dark lines that cross it are from the same family of planes, they are the ($\bar{1}$10) and (01$\bar{1}$) planes. These are the planes that segment the primary cube along two edges and two faces each and which pass through the corner closest to the reader. The three lighter grey lines forming an upright triangle are formed by the (100), (010) and (001) planes. The dark lines forming the upside-down triangle are formed by the (101), (110) and (011) planes.

These are the planes that segment the primary cube along two edges and two faces each and which do not pass through the corner closest to the reader.

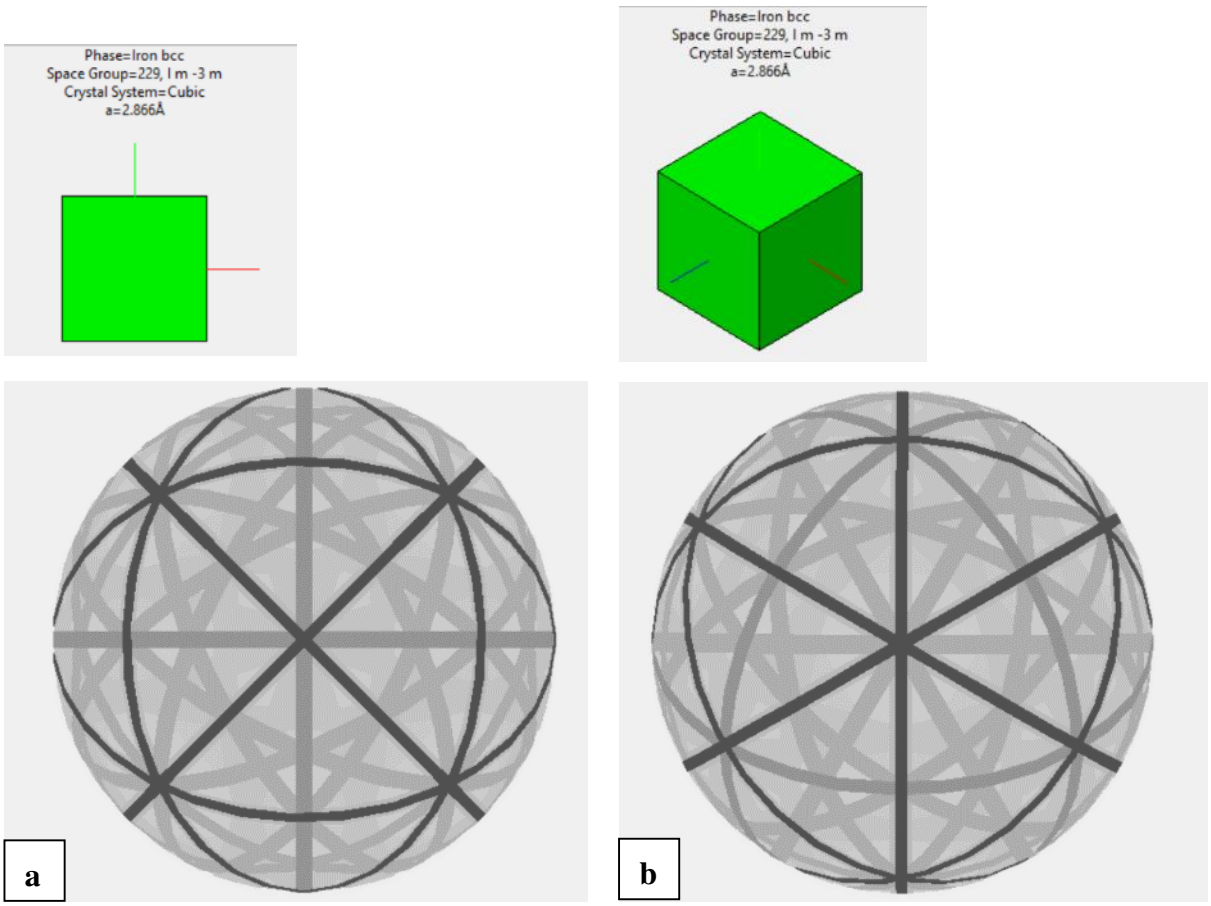

Figure 3.6 Kikuchi band projections of two orientations of cubic lattice

3.5.3. Sample Cutting

Of particular interest was crystallographic characterisation performed cross-sectionally, to show effects of surface finishing. Samples sectioned with ferrous cut-off blades, which even at relatively slow rates with a precision cut-off wheel, showed signs of cutting-heat induced oxidation near the cut site. This showed itself as a coloured oxidation pattern, similar to weld oxide discolouration. To avoid this detrimental effect, a water-jet cutting method was used using a high pressure waterjet carrying abrasive grit. This had the advantages of being rapid, keeping the temperature low, and allowed the manufacture of highly reproducible tokens.

3.5.4. Adhesion and Mounting

Application of ProbeMet conductive metallic mounting compound resulted in adhesion to the sample edges without a gap. It was found to preserve the sample edges during grinding and polishing with the minimum of edge-rounding.

The samples were cross sectionally mounted using plastic ring-clip sample holders in ProbeMet conductive mounting compound. These were cut roughly to shape by ferrous cut off wheel. They were then ground by hand on a rough grit grinding wheel to cylinders of 14 mm by 19.5 mm radius (required by the EBSD sample holder) before the sample side was ground and polished by the standard method finalising with a 0.3 μm diamond suspension.

This method provided a durable sample form that allowed repeat grinding and polishing between EBSD scans. This meant that if a scan failed due to insufficient sample preparation, or if the surface had aged too much, or if multiple measurements were required, they could be quickly re-ground and polished. The cylinder mount is shown in Figure 3.7.

The cylinders were then attached to SEM stubs by Silver DAG electrode paste and left for ten minutes to form a dry set. This was done before ion milling to limit the time spent outside a vacuum after milling.

Figure 3.7 A Cylindrically mounted sample in ProbeMet, affixed to an SEM stub with silver DAG and with plastic ring clip covered with conductive ink.

3.5.5. Ion Milling

These cylinders, once polished, were subjected to ion-milling using a Gatan Precision Etching Coating System (PECS) device. This subjected the surface to an argon ion beam at 5.00 keV for 2 hrs. Two beams were used with a gun current of 26-29 μA and an argon gas flow of 0.1 sccm (standard cubic centimetres per minute) each. Care was taken to centre the ion milling on the main area of interest. This was not the centre of the sample, but the edge of it. Once milled, the sample was removed from the device and immediately transported to the EBSD SEM (Inspect F50). The total time not in a vacuum between being milled and being scanned was kept below a minute to minimise oxidation.

The plastic ring-clip sample holders were flush with, and showed at, the top of the mount. In SEM this was liable to cause charging. To counter this, these areas were coated with a Pilot Super Color Marker ultra-fine pen which worked well at stopping charging and was precise enough to not contact the sample.

3.5.6. EBSD Instrument and Parameters

An Inspect F50 SEM was used. An EBSD scanning software called Flamenco from the HKL suite was used to set up scans. The parameters detailed in Table 3.4 were used to program scans.

Table 3.4 Parameters used in the setup of EBSD scans.

Timing/Frame	11
# Frames	64
Dynamic background	On
Operation	Subtract
Enhancement	Dynamic Structure
Noise reduction #Frames	20
Binning	4x4
Gain	High
Band detection method	Edge
#Bands	3-6
Run Time	15 hrs

- **Timing/Frame**, represents the time taken, in milliseconds, to scan each frame, this needs to be high enough to produce a good image, but too high can over-saturate the image.
- **# Frames**, is the number of frames that will be taken for each measurement.
- **Dynamic background** refers to in-software image enhancement. This removes the background using image diffusion and offset algorithms, increases the contrast, and produces a much clearer image.
- **Operation** is the method by which the background is removed, with 'divide' being an alternative, potentially slower, option.
- **Enhancement** is a method used to account for artefacts resulting from the 70° tilt required in the specimen.
- **Noise reduction #Frames.** This is the number of frames used as an average to reduce noise**.**
- **Binning** is effectively the resolution used for the Kikuchi band measurement and is a compromise between speed and accuracy.
- **Gain** amplifies the signal from the camera sensor, a high gain will increase the sensitivity of the camera but can introduce more noise.
- **Band detection method.** Band centres or edges can be detected, with edges being more productive when the edges are sharp and clear.
- **#Bands** refers to the minimum and maximum number of Kikuchi bands used to calculate an index solution with numbers giving slower, more reliable indexing, but potentially producing more zero solutions.
- **Run Time** is the time taken to complete measurement of a whole area.

3.6. Stress Application for Corrosion Testing

U-Bend tokens were produced according to ASTM G38 to the form shown in Figure 3.8 [7]. The tokens were cut using water jet cutting to forms designed on AutoCAD, as shown in Figure 3.9.

Figure 3.8 A complete U-Bend specimen.

Figure 3.9 Dimensions of an unbent U-Bend token.

The U-Bend tokens were pre-bent using a custom-made laser-cut Perspex pressing die, designed to work with a tabletop hand vice as shown in Figure 3.10. This ensured consistent bending while avoiding over-bending and easy application of the tightening screw. Without the tightening screw the tokens would relax to a 30° angle. This meant that once the token was tightened until the ends were parallel, a constant strain was imparted, which was focused on the centre of the curved area.

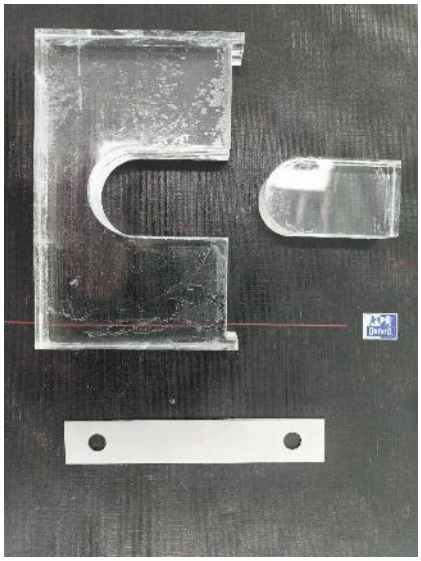

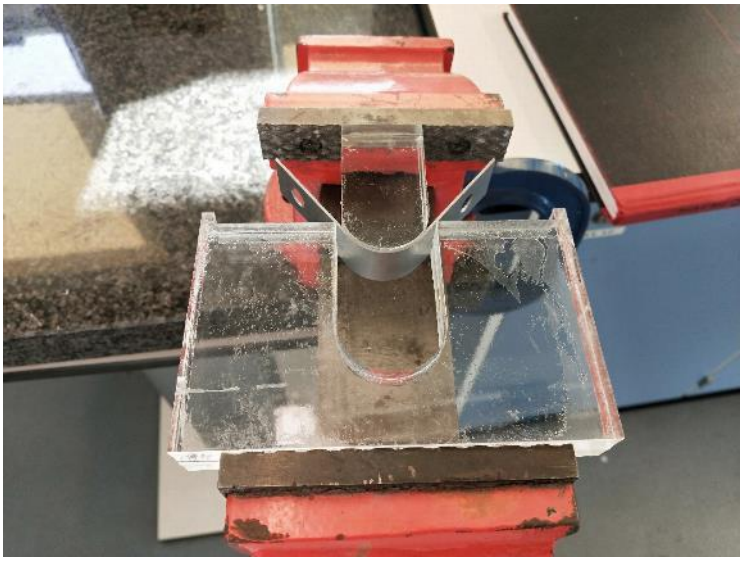

Figure 3.10 Operation of a Bending Die.

3.7. Materials

3.7.1. Introduction to Investigated Surface Finishes

Samples of four surface finishes applied to 1 mm sheets of 304L stainless steel were kindly provided by Andy Backhouse from Outokumpu, Sheffield. The surface finishes are described in Table 3.5.

Table 3.5 Surface finish naming conventions

Industry Standard	**Description**
2B	Rolled. A cold rolled surface, it is smooth and moderately reflective. It is finished by a final cold roll between large diameter polished rolls.
RAP 2E	Shotblasted. A surface that has been blasted with glass beads from a high pressure waterjet, leaving it with a matter, rougher finish.
Phoenix™	Brushed. A surface brushed in a single direction by wire brush in a propriety Outukumpu technique, leaving it with a bright finish.
240 Grit	Ground. A surface ground with 240 Grit silicon carbide, leaving it with a bright finish.

The “rolled” surface was cold rolled, heat treated, pickled and skin passed. It is a smooth surface with low gloss. The “shotblasted” surface was cold rolled, heat treated, mechanically descaled by shotblasting, and then pickled. It is a relatively rough finish and is unreflective and dull. The “brushed” or Phoenix™ surface is a propriety Outukumpu finish that is produced by wire brushing. It is bright and glossy and has a directional finish. The “ground” surface was dry belt polished with 240 grit silicon carbide. It is bright but rougher than the brushed surface.

3.7.2. General Description of the Surface Morphology

Topographical surface characteristics were initially examined at the micro-scale with an Inspect F50 Scanning Electron Microscope (SEM). This provided a qualitative impression of the sample surfaces as a foundation for further quantitative investigations of morphology, such as openness, surface inclusions, microstructure damage and valley angle, as described in Chapter 4. An accelerating voltage of 15 kV was used to examine features down to a 2.5 K magnification. Figure 3.11 to Figure 3.15 show the SEM images acquired for each of the surface finishes.

Figure 3.11 shows the morphology of the brushed sample surface. In contrast to the ground surface, the valleys on the brushed sample are narrower, at around 2 μm wide, and they do not continue uninterrupted. In addition to ledges running in the direction of brushing, some ledges are found to be perpendicular. This suggests a shorter dragging distance of the mechanical finishing device, which is a wire brush. This surface shows deep cracks. Some smearing is seen in the ground surface and is also evident in the brushed surface. Where in the ground surface it exists as overhanging ledges, in the brushed surface is appears as cracks, as though sections of the surface did not adhere to each other during the smearing process.

The brushing process has a “smearing” effect, which results in portions of the surface being missed in the brushing process. In the central area of Figure 3.12 a 30 μm wide area showing the underlying grain structure is seen. Since the surface is as resistant to corrosion as its weakest area, this implies that the brushed surface cannot have a better corrosion resistance than a rolled surface. Nine individual grains were observed in this region; these match the likeness of the cold rolled sample, indicating that this sample was pickled in a similar manner prior to being brushed. Large cornices were observed on the bottom of the missed-area, and much smaller ones on the top. This suggests an upwards brushing motion (relative to the orientation of this image). This also exposes crevices, in both the area underneath the cornices and in the grain boundaries.

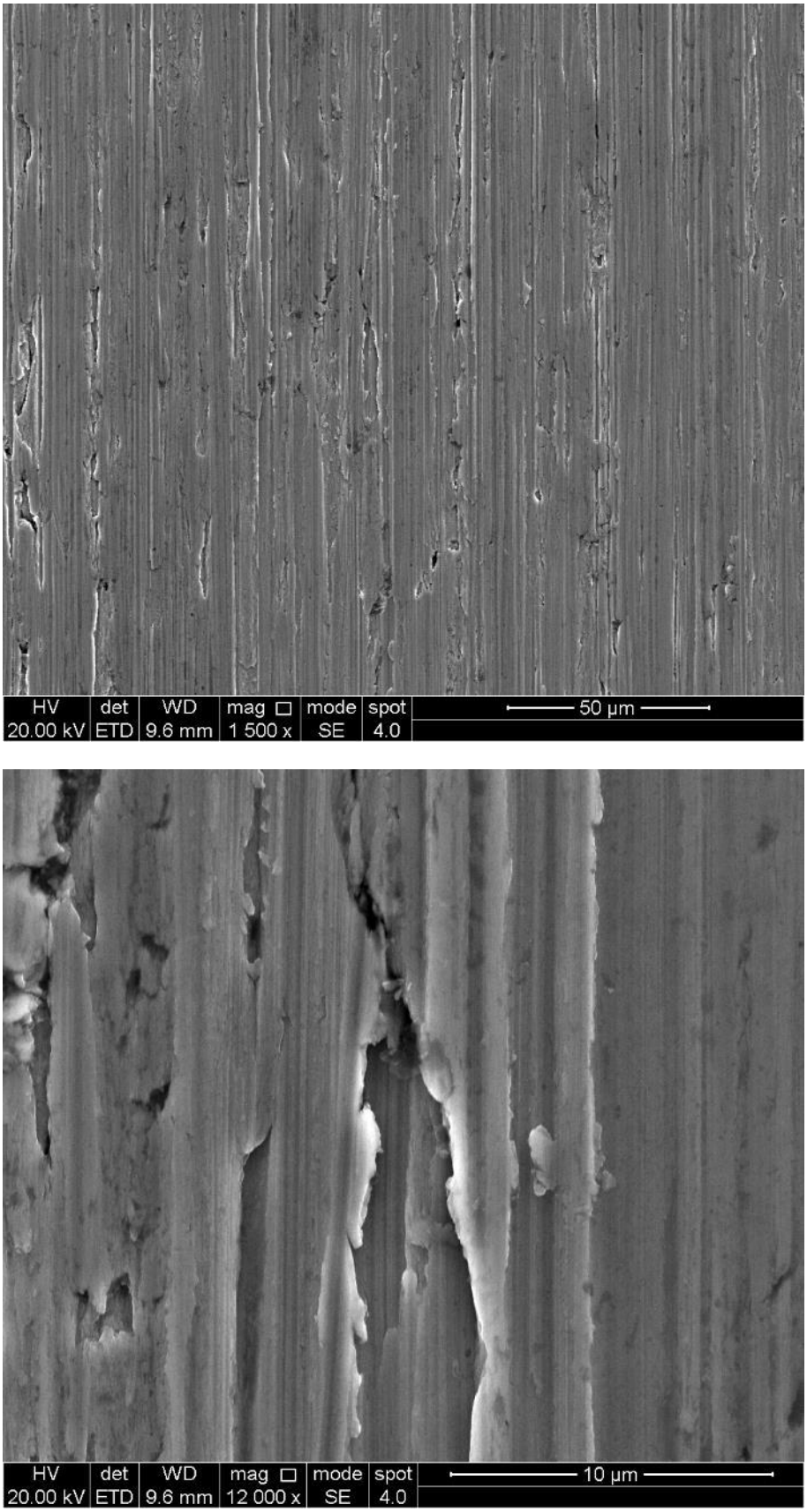

Figure 3.11 SEM micrographs showing a brushed surface.

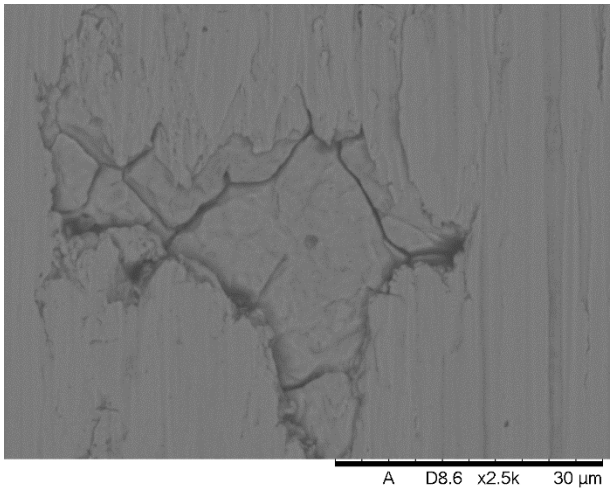

Figure 3.12 A "missed area" feature of the brushed surface.

Figure 3.13 shows the 240 grit ground surface investigated. Long continuous grooves were observed across the entire surface. The valleys of these grooves are around 5 µm wide and have been made with a 50 µm silicon grit,[8] indicating the low pressure dry belt grinding process. Some valleys are extremely uniform in the vertical direction showing the result of an efficient ploughing, or else a smearing, grinding mechanism. Other valleys are heavily affected by a turn-over smearing affect. This leaves the surface sharper in these edge areas.

Figure 3.14 shows the surface of the rolled sample. It is very flat and is characterised by its visible surface grains. This surface has been pickled to remove oxide scale and expose the substrate material. Some intergranular corrosion is seen, etching grain boundaries, which makes it possible to see individual grains. In the magnified image, the rolling direction can be discerned by the linear marks running diagonally.

The shot-blasted sample surface is shown in Figure 3.15, this surface has also been pickled. The surface undulates greatly and is made up of a series of impact craters. The surface is also characterised by visible grains similar to the rolled surface, which were chemically etched during the pickling process. In some areas these surface grains are unaffected by the shot-blasting, while in other areas they are spread and warped by up to five times their original length. There is no overall directionality to this warped surface which show the beads used in the shot-blasting impacted the surface with random direction. The peaks on this surface have been flattened by a final rolling process.

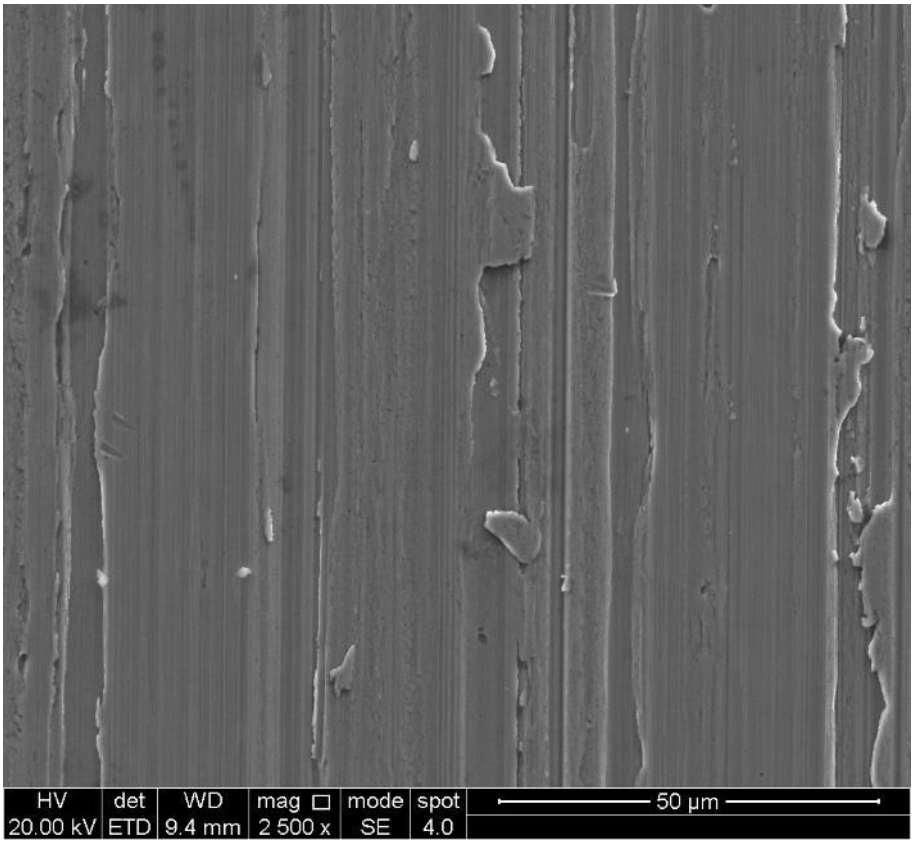

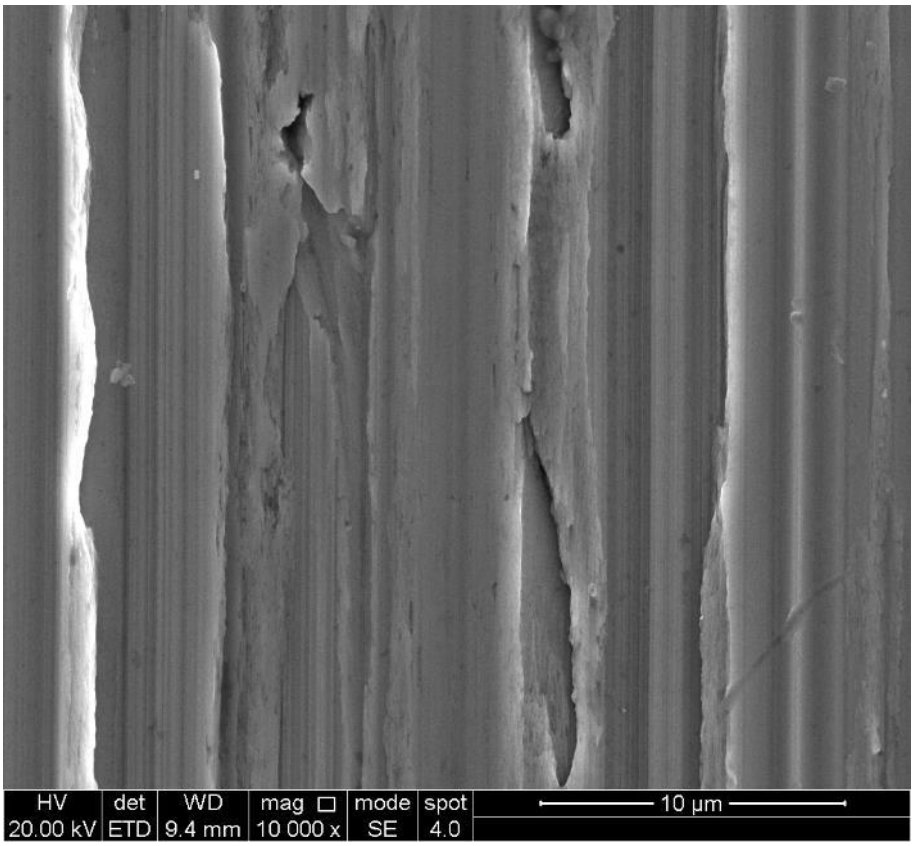

Figure 3.13 SEM micrograph showing a ground surface.

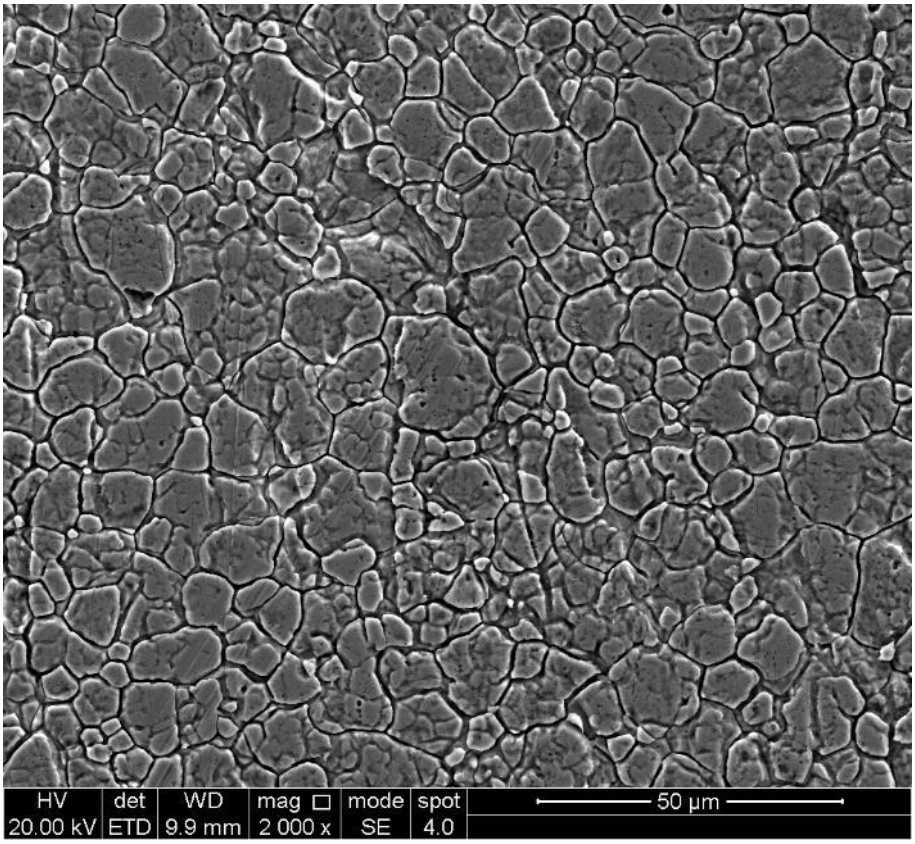

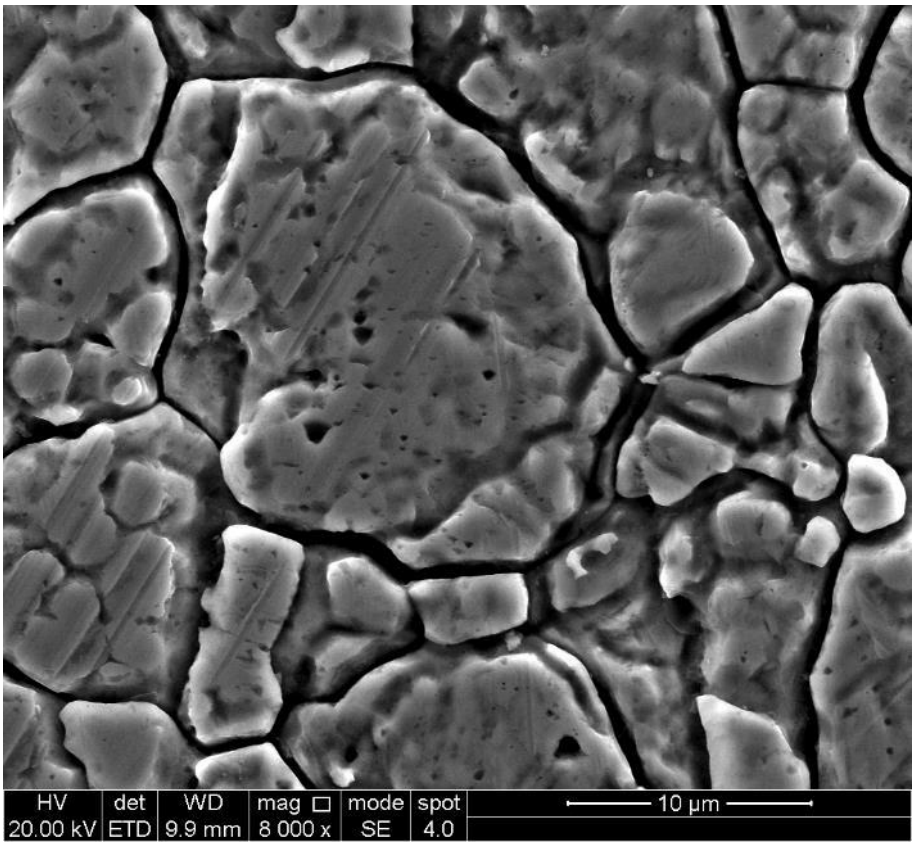

Figure 3.14 SEM micrographs showing a rolled surface.

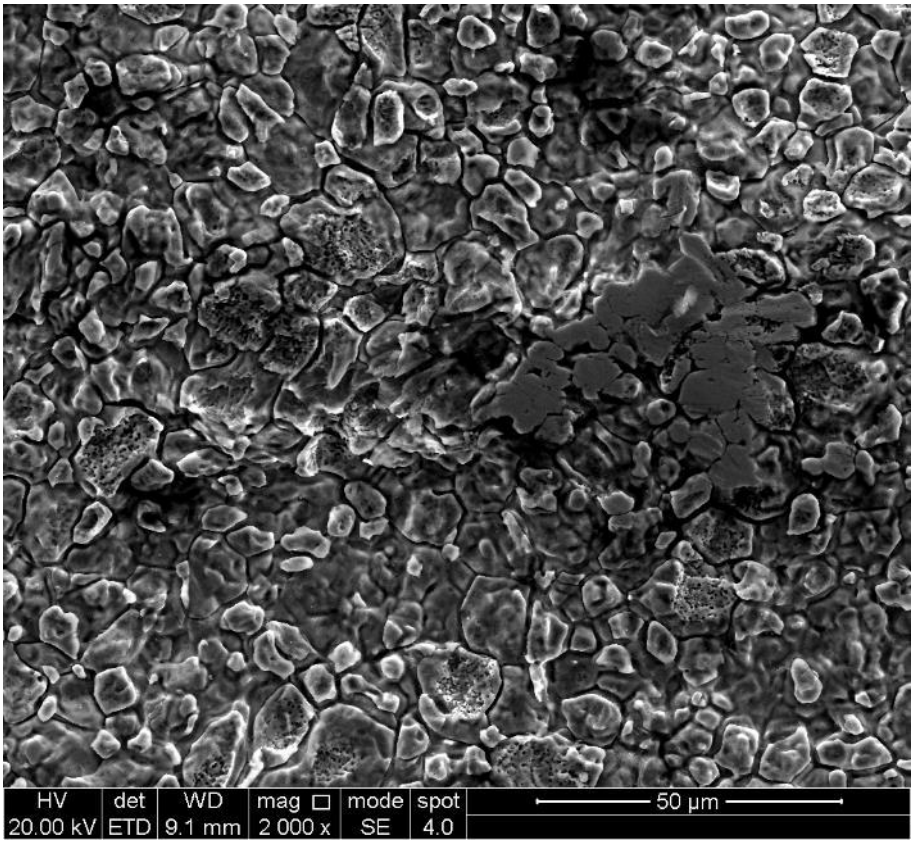

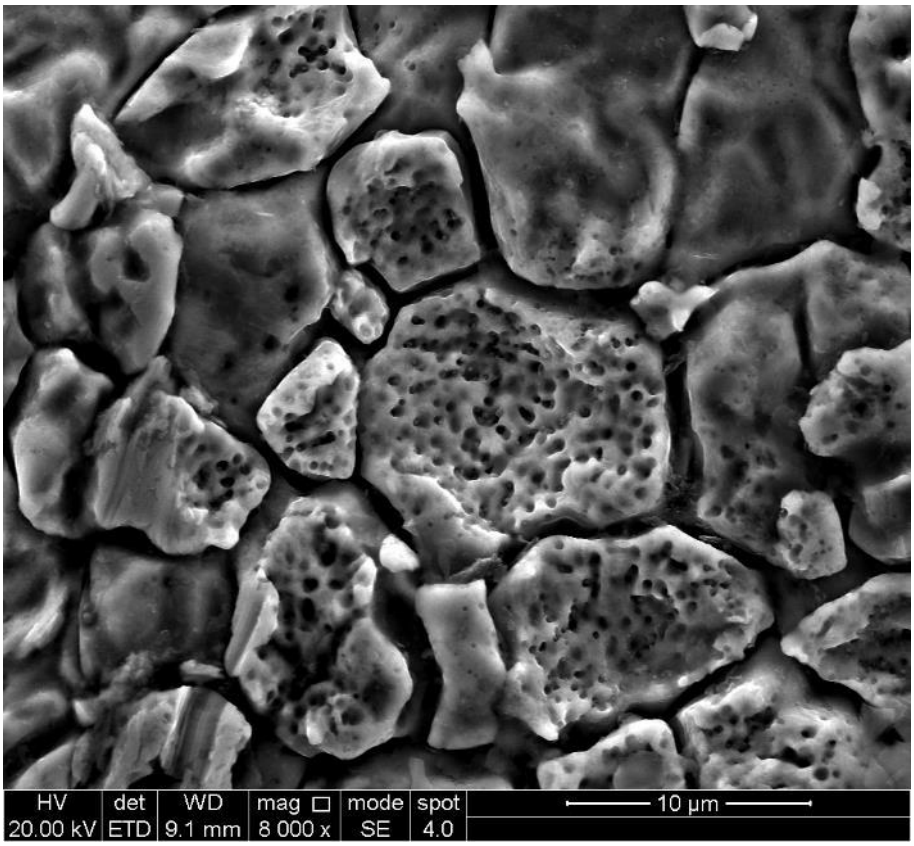

Figure 3.15 SEM micrographs showing a shotblasted surface.

3.7.3. General Description of the Surface Composition

The commonly used SAE (Society of Automotive Engineers) International grading system, which uses designations such as 304L or 2205, is applied in defining the composition of stainless steel. This grading system is used jointly with European EN steel numbers and British BS grades. These grades are well used in industry and commerce and give a clear indication of the type of stainless steel to be used. However, it is known that there is a large amount of variation within individual grades. This has led to introduction of the addition of the "High Quality" tag for particular batches that are especially low in undesired contaminating elements. This reveals that for scientific research this grading system is an insufficient source of composition.

For pitting corrosion in stainless steel, MnS inclusions are considered to play an important role [9]. It is thought that they dissolve much faster than the surrounding material, providing features similar in shape to small pits. Such a geometry allows for the concentration of corrosion products, such as iron ions and hydroxides, as well as the attraction of hydrogen and chloride ions, which leads to an aggressive environment and a steep ion concentration gradient. The conditions under which pitting initiates are crucial to understanding the surface's resistance to corrosion since, once pitting begins, propagation is inevitable and is maintained in less aggressive conditions. The reported quantity of sulphur varies greatly within individual grades of stainless steel, being measured anywhere between 0.002 wt.% and 0.3 wt.% [10], [11]. In this range, a very small increase in the quantity of sulphur will define the mode by which the material surface fails and corrodes.

Additionally, intergranular corrosion cracking can be driven by sensitisation in a material. Here, the effect of heat from, for example, a nearby weld causes chromium near grain boundaries to form chromium carbides at the grain boundaries, leaving a chromium depleted zone. This zone is especially prone to corrosion cracking due to its lack of the passivating element chromium, the chromium carbides offer no protection against corrosion [12]. This has led to the development of very low carbon grades of stainless steel such as 316L and 304L which resist sensitisation. Despite the impact of carbon on corrosion, within these grades the quantity varies.

For these reasons it is inadequate to assume that the manufacturer's composition is the true composition. Instead, for this work, composition has been measured by two corroborating techniques, and at multiple locations and depths for each sample. Firstly, X-ray fluorescence (XRF) analysis was used as an initial method to check bulk composition. The penetration depth of 100-200 μm gives a relatively good measure of bulk composition which is not too skewed by the thin 1-10 nm passive film [13]. Secondly, Energy Dispersive Spectroscopy analysis was used for a confirmatory method to measure surface

composition. The penetration depth of <1 μm is affected by the material surface, giving a more representative composition of the surface of the material that is exposed interacts with the environment. The mapping feature allows for an analysis of the variation of surface composition.

XRF analysis of each of the steel samples, as a function of surface finish, are shown in Table 3.6. The differences in compositions for the different surface finishes is well within the expected error margin of this technique, therefore, it can be stated that the samples studied in this thesis are of the same material, and that the surface finishing process does not cause any compositional changes. Although not reported in Table 3.6, sulphur was detected for the shotblasted sample only, but only on one scan, and at a normalised percentage of 0.014%. This is well below the error margin, and it is highly likely that this anomalous result is an error, possibly due to contamination during sample preparation, therefore, it was disregarded.

Table 3.6 XRF Composition by surface finish. (wt.%)

SS 304L	**Fe**	**Cr**	**Ni**	**Mn**	**Cu**	**Mo**	**Si**	**Co**
Shotblasted	70.2 ± 1.50	18.8 ± 0.30	8.1 ± 0.15	1.3 ± 0.06	0.5 ± 0.01	0.4 ± 0.02	0.3 ± 0.01	0.3 ± 0.01
Brushed	69.3 ± 1.45	17.9 ± 0.25	7.8 ± 0.15	1.2 ± 0.06	0.5 ± 0.01	0.3 ± 0.03	0.3 ± 0.01	0.5 ± 0.03
Ground	70.4 ± 1.50	19.0 ± 0.30	7.9 ± 0.15	1.2 ± 0.05	0.4 ± 0.01	0.3 ± 0.02	0.4 ± 0.01	0.2 ± 0.01
Rolled	70.8 ± 1.50	18.4 ± 0.25	8.2 ± 0.15	1.2 ± 0.05	0.4 ± 0.01	0.3 ± 0.02	0.3 ± 0.01	0.2 ± 0.01

The average sum of the compositions of all measurements was 107.25%. This could suggest an error of around ±8%; however once individual compositions are normalised according to their separate sums, the variance in composition for each element across the separate samples falls to below one percent. Therefore, the higher sum of compositions is not a true error and can be calculated out. The error presented is the standard deviation over four trials.

Point EDS measurements were performed with a 10 KeV beam to determine the surface composition (as opposed to the bulk, as determined by XRF), due to the shallow (<1 μm) penetration depth of the electron beam, as shown in Figure 3.16. It also allowed spatial determination of the following elements of interest:

1) Mn and S. The detrimental effect of MnS inclusions, as described above, make the detection of these elements a priority.

2) C. The amount of carbon in a low carbon grade of stainless steel will be critical to its resistance to sensitisation.

3) Cr. The percentage composition of Cr affects the passivity of the surface and critical pitting potential, specifically any localised concentrations, or deprived areas will be prone to intergranular corrosion cracking.

4) Si. Silicon will indicate the level of surface contamination caused by the sample preparation process, since it is used in the grinding and polishing phases.

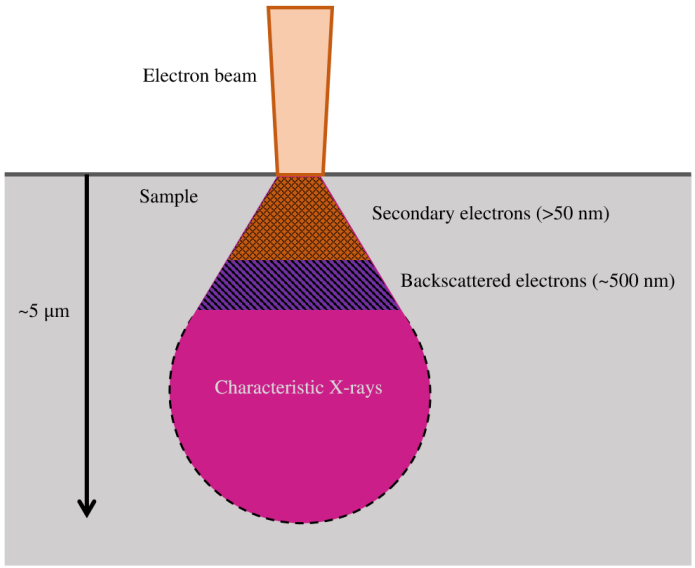

Figure 3.16 Penetration of an EDS electron beam.

The penetration depth, and interaction volume, of the EDS technique increase with a higher accellerating voltage and decrease with the atomic number of the specimen. The penetration depths for iron are shown in Figure 3.17, these were calculated with the Kanaya-Okayama depth penetration formula [14]. These volumes have a distinctive pear like shape, with a higher energy deposition rate near to the impact point. Higher accelerating voltages allow for greater resolution, but can also result in unclear surface sturctures, greater edge effects and greater charging and surface damage. Lower accelerating voltages suffer less from these effects, however lower resolutions are possible.

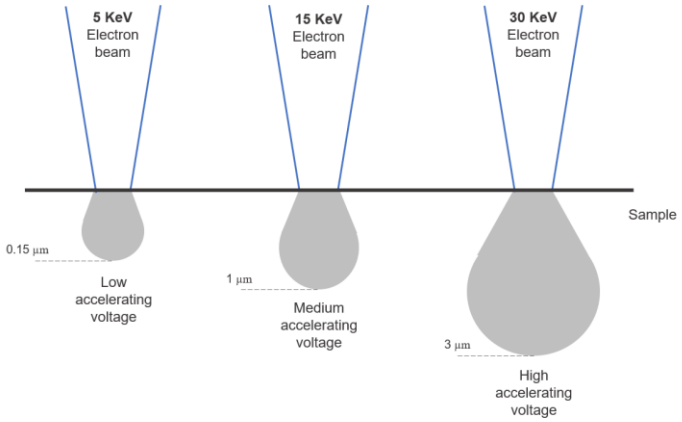

Figure 3.17 The effect of accelerating voltage on interaction depth for iron.

Table 3.7 shows that surface composition measured by EDS differed from that in the bulk, as determined by XRF. Oxygen was measured at 30 ± 4 wt.% by EDS for all surfaces. The passive film, is expected to be 1–10 nm thick [13], this indicates that the EDS technique is not measuring oxygen in this film. Instead it is likely measuring an iron rich oxide film which, have previously been measured up to 2 µm thick [15].

Table 3.7 EDS Composition by surface finish.

	Rolled		Ground		Brushed		Shotblasted	
Element	Mean wt.%	O Removed	Mean wt.%	O Removed	Mean wt.%	O Removed	Mean wt.%	O Removed
C	3.19	4.58	3.2	4.58	3.73	5.41	5.27	7.96
O	30.25	-	30.11	-	31.09	-	33.78	-
Al	0.59	0.85	-	-	0.23	0.33	0.14	0.21
Si	0.18	0.26	0.34	0.49	0.22	0.32	0.19	0.29
S	-	-	-	-	0.06	0.08	-	-
Cr	12.55	17.99	12.67	18.12	12.35	17.92	11.72	17.70
Mn	1.1	1.58	1.11	1.58	1.08	1.57	1.05	1.58
Fe	47.15	67.59	47.17	67.49	46.2	67.04	43.15	65.17
Ni	4.83	6.93	5.02	7.19	4.97	7.21	4.54	6.85
Mo	0.17	0.24	0.19	0.28	0.17	0.24	0.19	0.28
Total:	100	100	100	100	100	100	100	100

To compare differences in composition between the surface and the bulk, the "O Removed" column is presented in Table 3.7, where oxygen was removed, and all of the remaining elements were normalised back to 100%. The same was done for carbon, which was not detected at all by XRF in the bulk material. Figure 3.18 shows the EDS measured composition, next to the EDS measured composition adjusted by the removal of oxygen and carbon. This is compared in the same diagram with the XRF measured composition.

With oxygen and carbon removed, the EDS surface composition is consistent with the XRF measurement of the bulk material as shown in Figure 3.18. This shows that the only compositional change in the surface is the introduction of oxygen and carbon. Since the proportion of chromium does

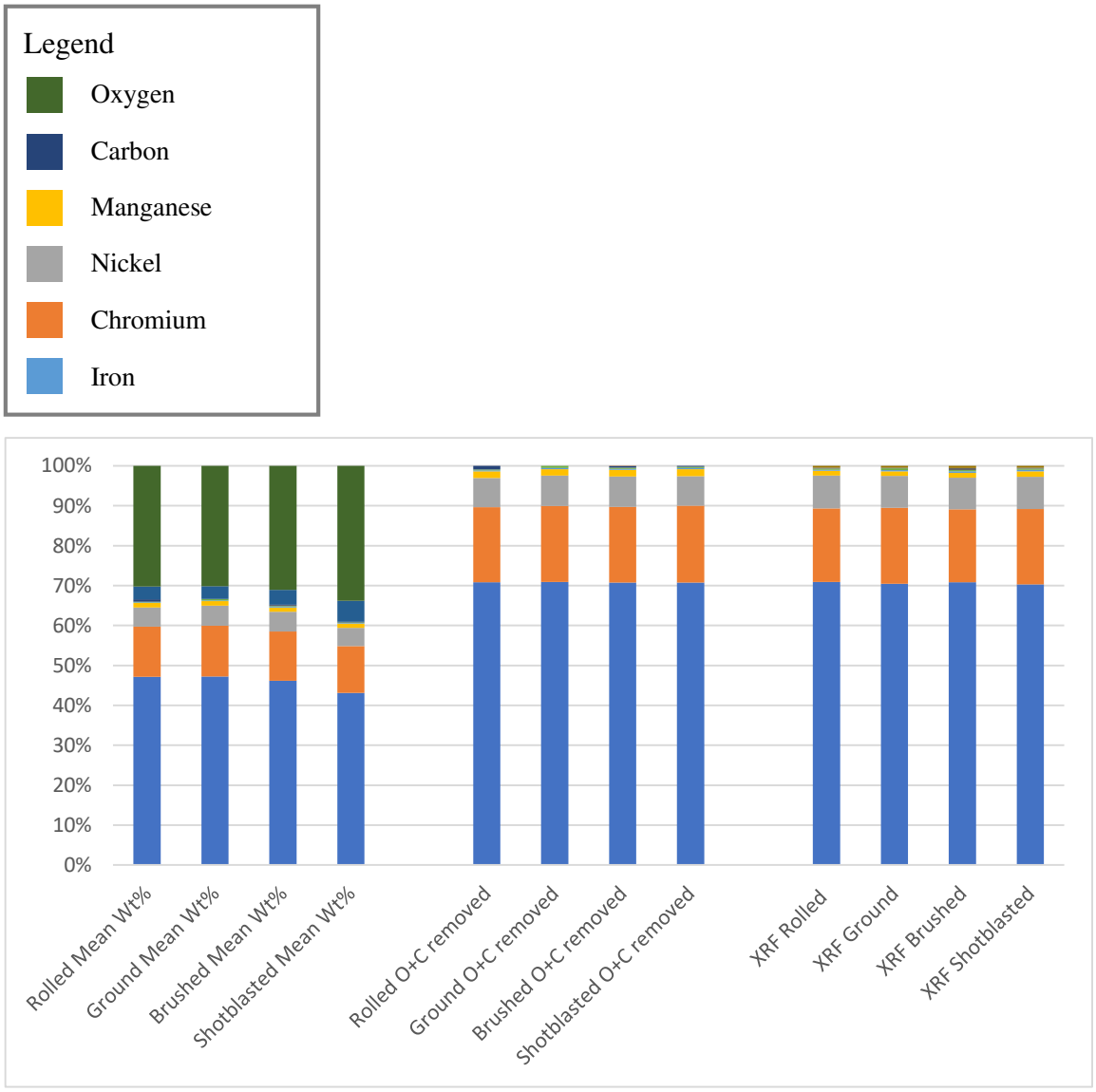

Figure 3.18 Composition measurement comparisons between EDS and XRF.

not increase in the EDS measurements, the majority of the oxygen increase measured cannot be in the form of chromium oxides. Instead, it likely indicates an iron oxide rich surface region.

EDS is considered less accurate compared to XRD, with analytical accuracies commonly around ±2% and <0.1% respectively. Despite this, Figure 3.18 shows that, once oxygen is removed, results from the two techniques align closely. EDS was chosen for its surface mapping capability, while bulk composition measurements were taken from the XRF measurements.

Conventionally, EDS has been considered to have poor reliability and accuracy when measuring oxygen, although modern equipment has improved on this issue significantly [16]. The low atomic number of oxygen and carbon make both more difficult to determine accurately. Figure 3.23 to Figure 3.26 show EDS measurement can reliably detect oxygen at the surface band across multiple locations and specimens. Since these plots indicate higher counts for oxygen in a thin band for all surfaces, and do not detect this elsewhere across the sample cross-section, these measurements are reliable and considered correct. The oxygen recorded in Figure 3.18 is the result of the EDS measurement picking up on this oxygen enriched thin band at the surface.

Even with the low (or below detection limit) quantity of S detected by XRF and EDS, it is possible that MnS inclusions were formed in the steel samples. Sulphur was detected in only 2 of the 16 EDS spots measured, at a Wt.% of only 0.05%. All of these measurements were made on the brushed surface. Should S be present at this percentage in this surface, it is possible that MnS inclusions could form, and despite the very low level, few would be needed to critically change the critical pitting potential.

To further assess whether these features were present, or if there were any other local distribution of elements at the steel surfaces, EDS surface mapping was performed with a 10 KeV beam. Figure 3.19 - Figure 3.22 show the elemental distribution of key elements present in the rolled, ground, brushed and shot-blasted surfaces.

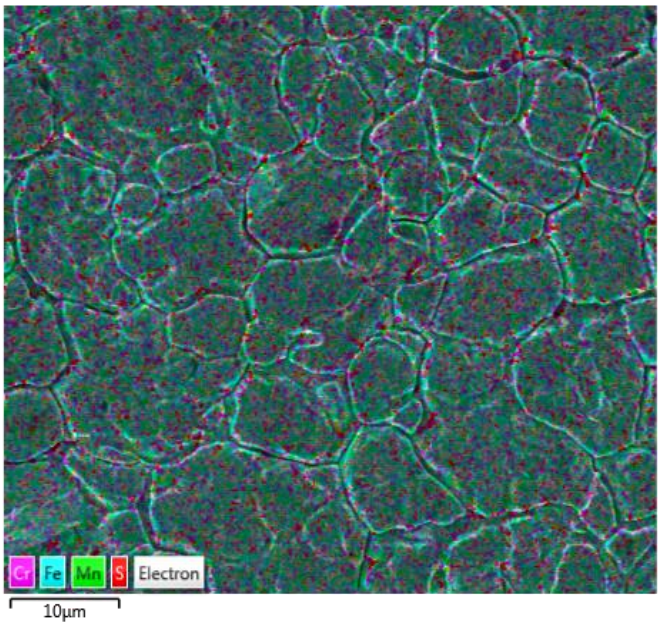

Figure 3.19 SEM micrograph of a stainless steel rolled surface finish, with overlaid EDS composition map.

The distribution of elements across the surfaces showed some evidence of being affected by the grain structure, with the shapes of grains becoming apparent for the ground and the brushed surfaces, even through the valleys and ridges. There was an apparent increase in the concentration of elements at the edges of morphological surface features (e.g., grain boundaries and grooves), however, this is considered an artefact of the SEM and not representative of any change in composition.

In the shotblasted surface shown in Figure 3.22, a localised distribution of chromium (pink in EDS maps) can be observed.

There was a pore-like structure in some of the grains, likely formed during the pickling (shown previously in Figure 3.15). These were also seen in all other surfaces. From the lack of colour differentiation in these in the EDS maps it is unclear whether these are due to inclusions. It is possible that they could have been formed by inclusions that were subsequently plucked out, or otherwise dissolved to leave no trace of the inclusion composition.

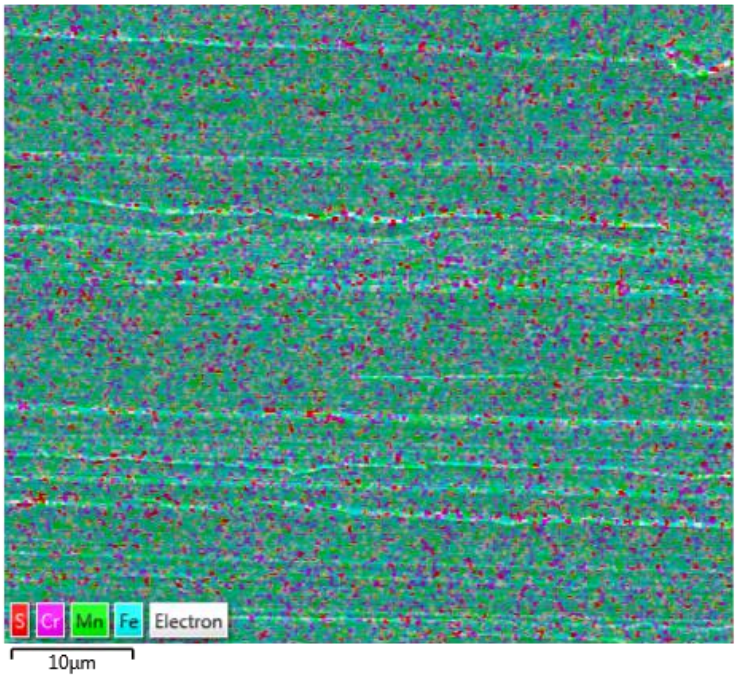

Figure 3.20 SEM micrograph of a stainless steel ground surface finish, with overlaid EDS composition map.

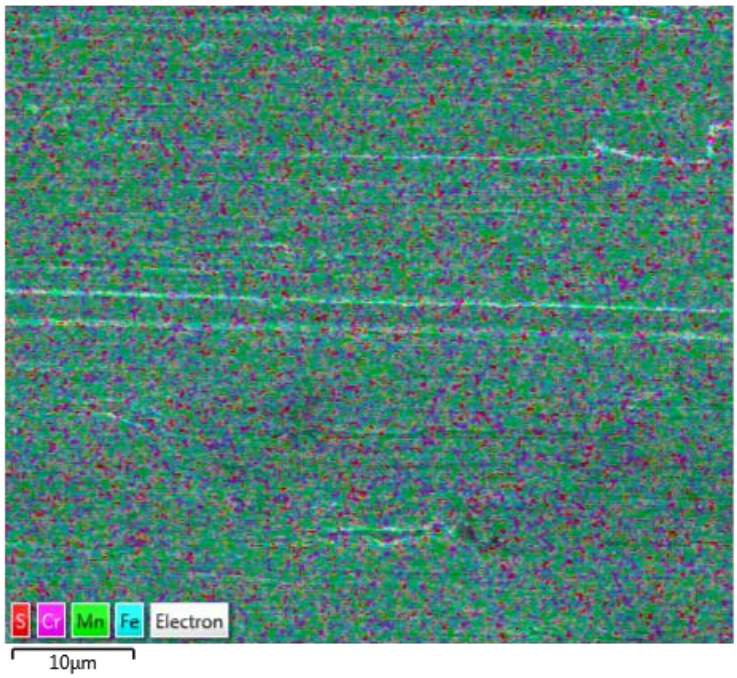

Figure 3.21 SEM micrograph of a stainless steel brushed surface finish, with overlaid EDS composition map.

There is a single localised concentration of Mn in Figure 3.22 (shown in green), however this does not correlate with an increase in S (red).

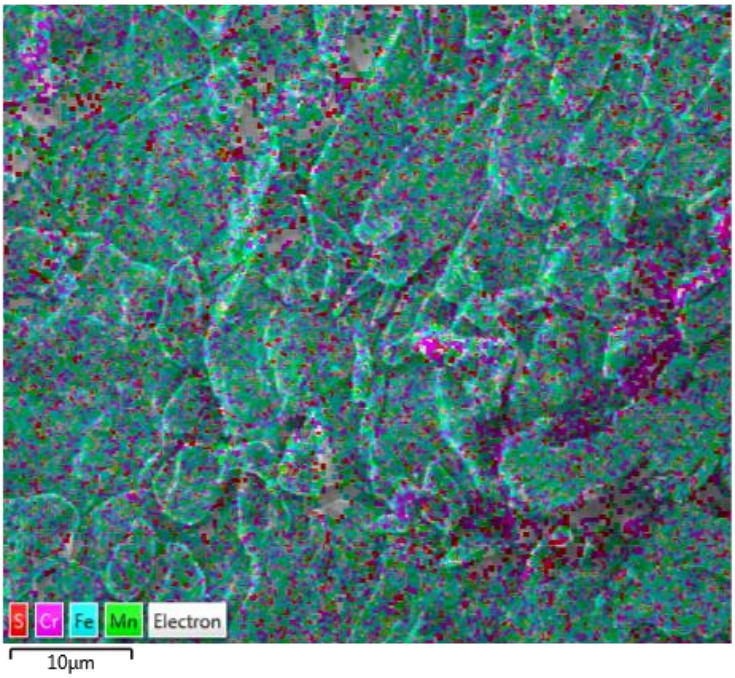

Figure 3.22 SEM micrograph of a stainless steel shotblasted surface finish, with overlaid EDS composition map.

3.7.4. Compositional Measurement with Depth using Cross-Sectional EDS Imaging

Cross sectional EDS scans were performed at 30 KeV to reduce the detection of surface oxides. 10 µm line scans were performed: these covered a large section of the bulk material, the surface layer, and the mounting compound and are shown in Figure 3.23 to Figure 3.26.

Figure 3.23 shows the location of such a linescan on an SEM image of a brushed surface, as well as the counts of oxygen, chromium, and iron. The left hand side of the line is over the mounting compound and, moving left to right, it passes over the surface layer and then over the bulk material. The SEM image and the line scan annotation are at the same scale as the graphs presented below it. The y-axes of these graphs denote the numbers of counts for each element. These axes are normalised for each element so that the shape of the line can be clearly displayed. This means that these axes are not consistent.

Figure 3.23 shows an increase in oxygen near the surface for the brushed surface. This is consistently high for a 1.25 µm band before trailing off exponentially into the bulk. This exponential reduction of oxygen with depth is consistent across all surfaces and is characteristic of the permeation of an element into a material. The thickness of the oxygen rich band is consistent with previous research [17].

In Figure 3.24 the oxygen rich band for the ground surface can also be seen to also be around 1.25 μm deep. Also for the rolled surface (Figure 3.25), the surface is higher in oxygen than the bulk, which still shows around a 1.25 μm thickness of oxygen ingress. The shotblasted surface in Figure 3.26 also shows a similar thickness near the surface.

All surfaces showed an oxygen rich band at the surface, all with similar thicknesses. In these surface bands, the ratio of iron to chromium remains roughly the same. This indicates that these surface bands contain both iron and chromium oxides, as supported from the data shown in Figure 3.18.

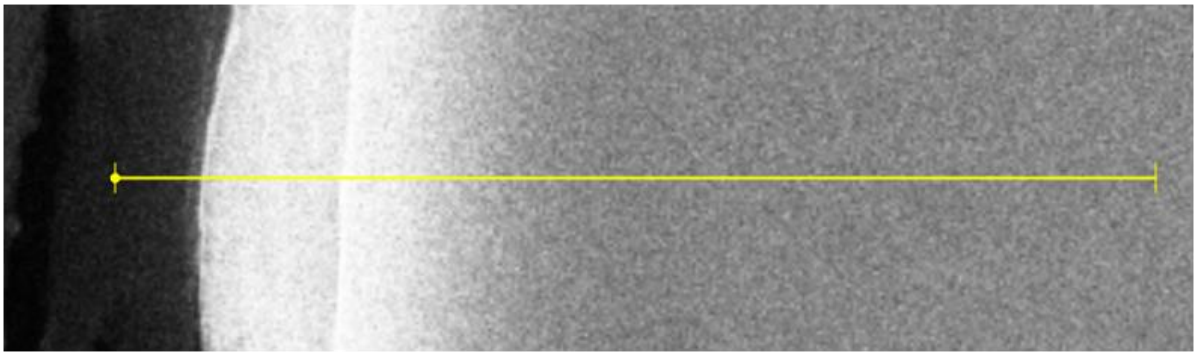

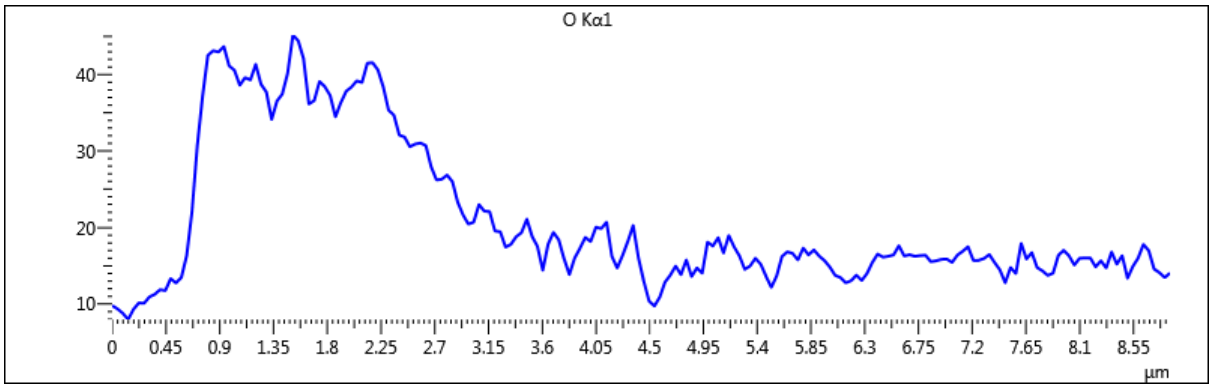

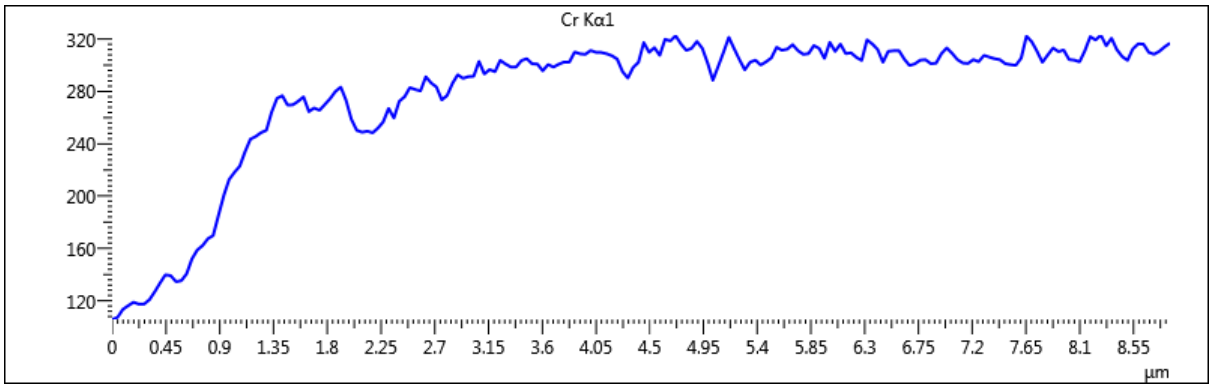

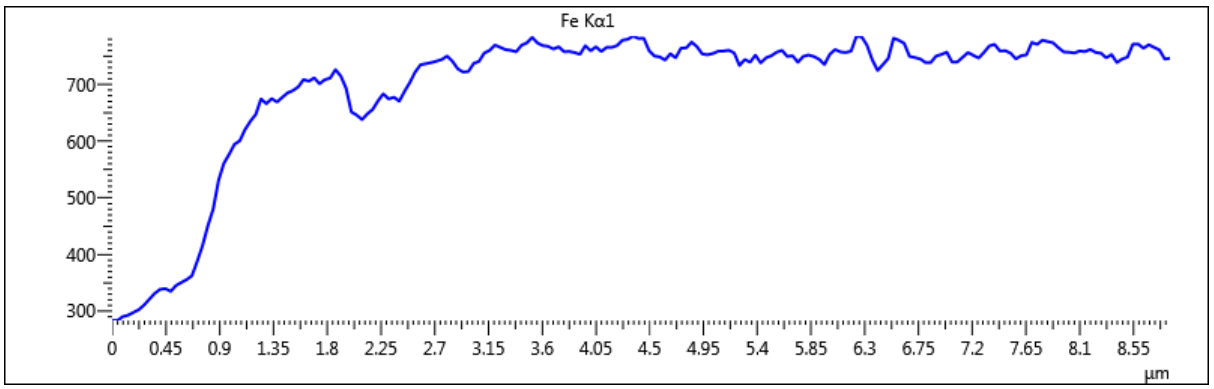

Figure 3.23 EDS line-scan of a cross-sectionally mounted brushed sample, showing O, Cr and Fe counts with increasing depth.

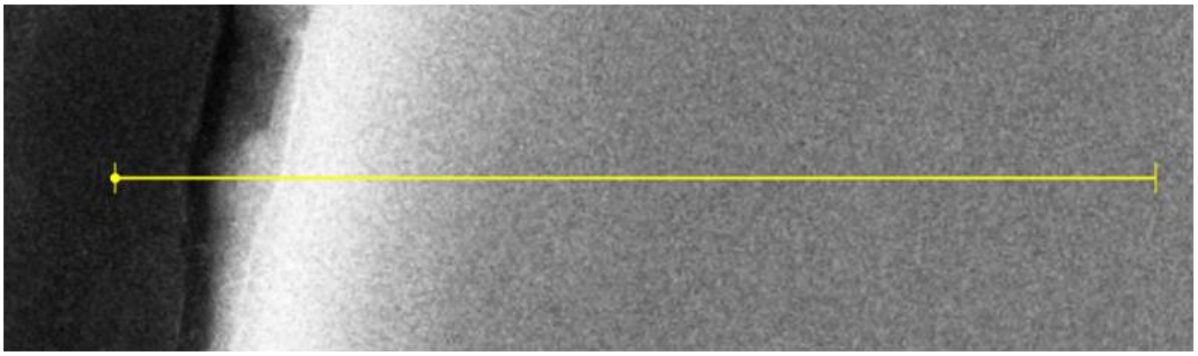

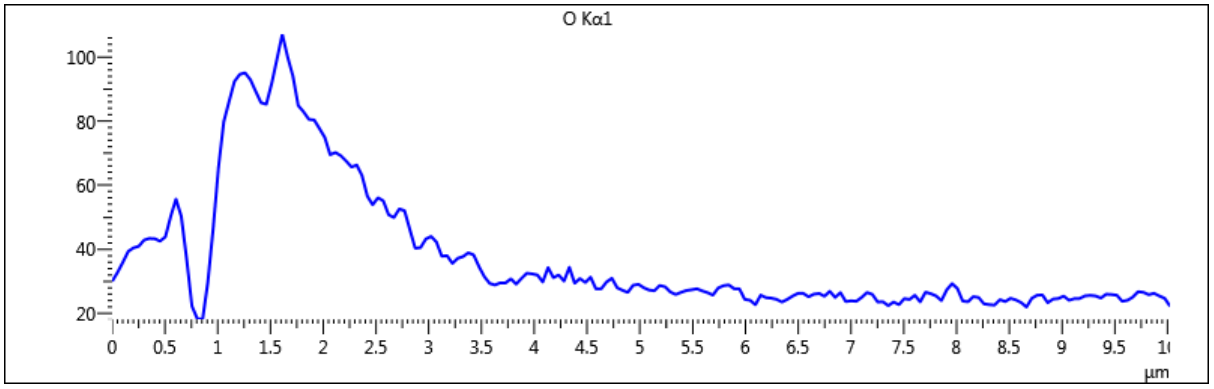

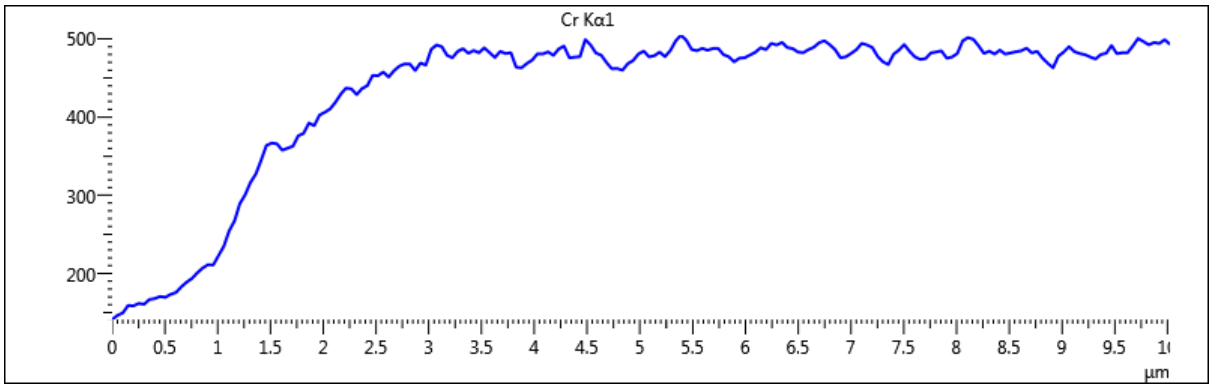

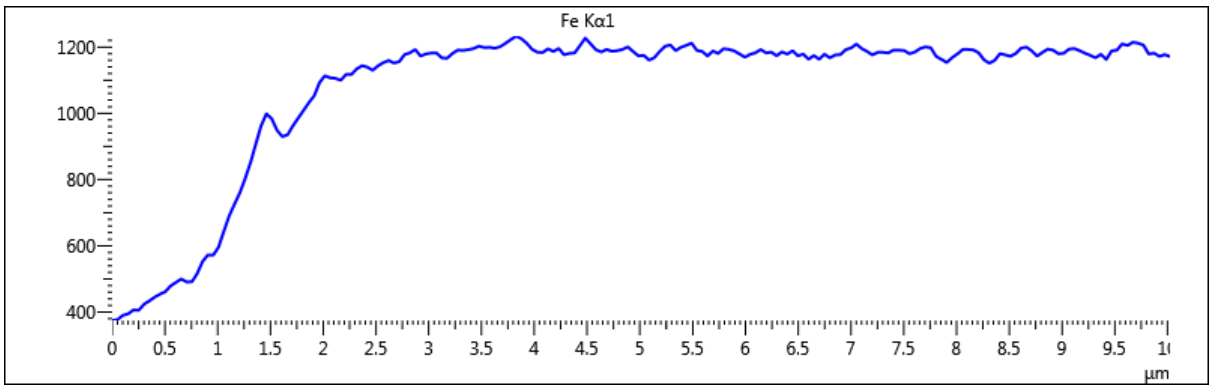

Figure 3.24 EDS line-scan of a cross-sectionally mounted ground sample, showing O, Cr and Fe counts with increasing depth.

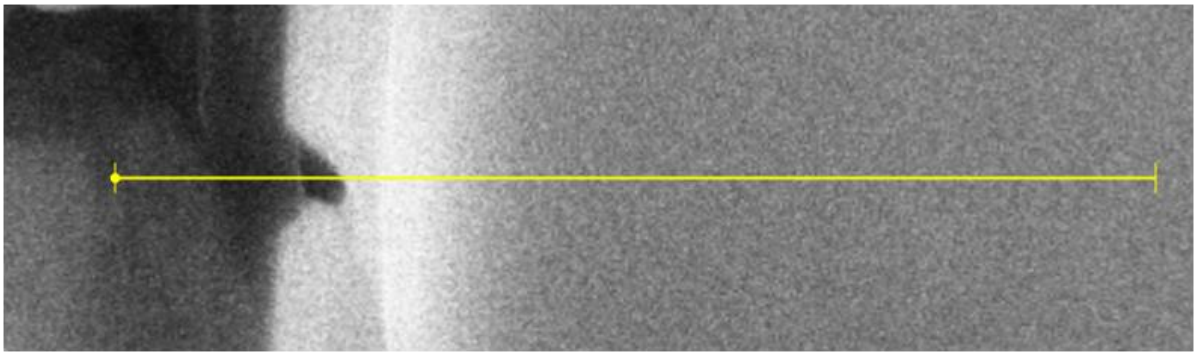

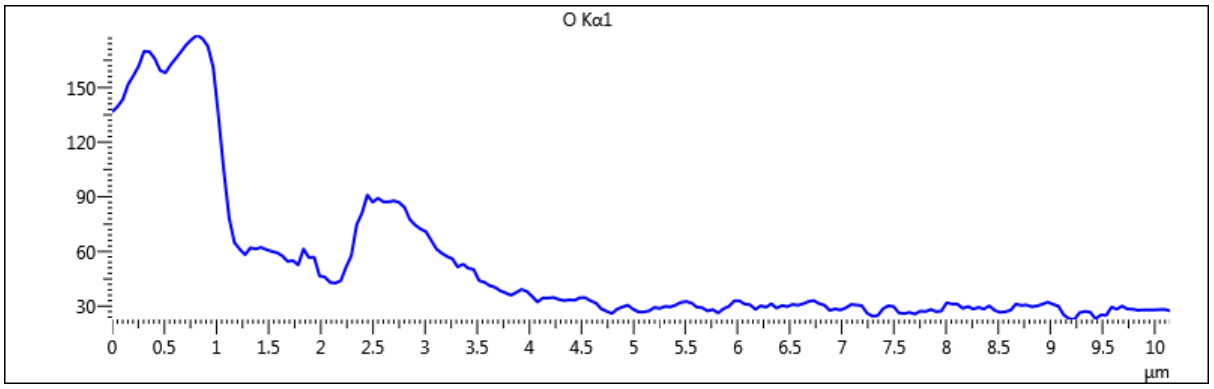

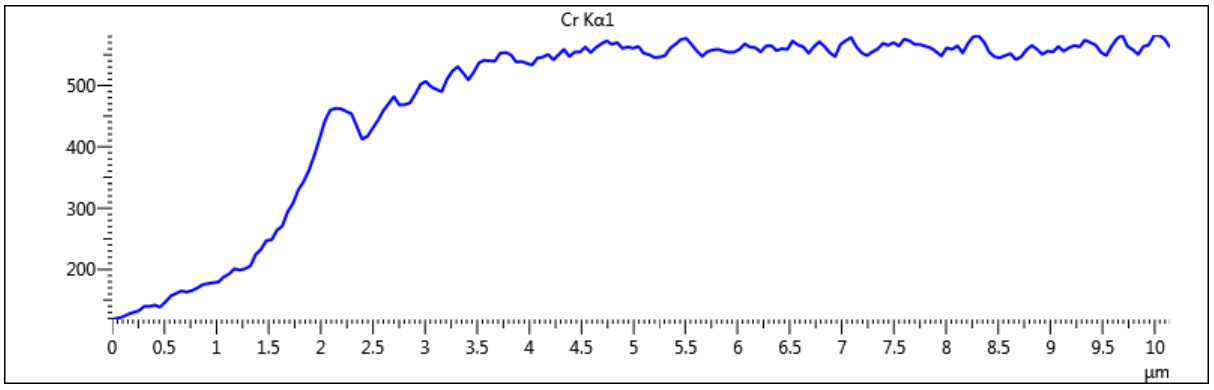

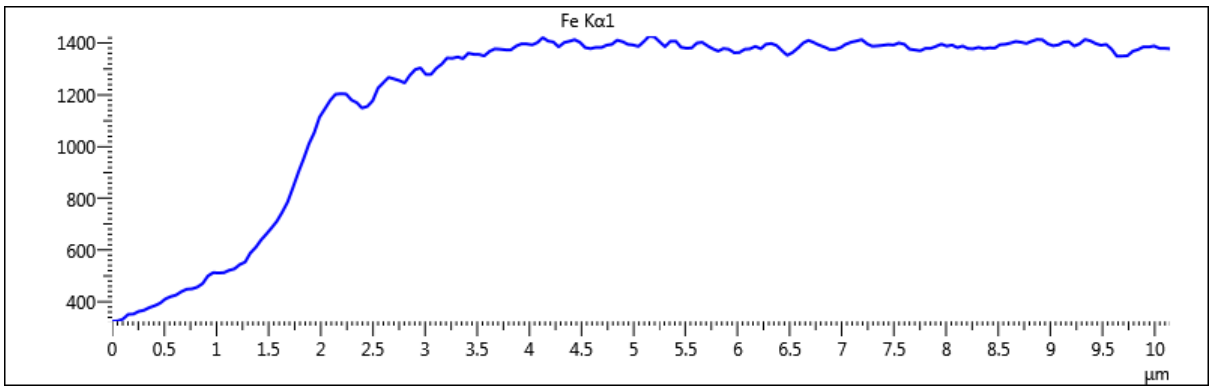

Figure 3.25 EDS line-scan of a cross-sectionally mounted rolled sample, showing O, Cr and Fe counts with increasing depth.

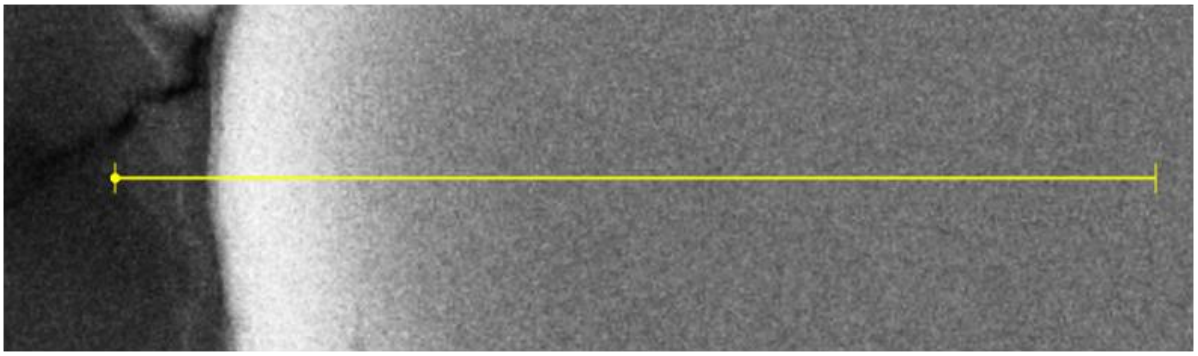

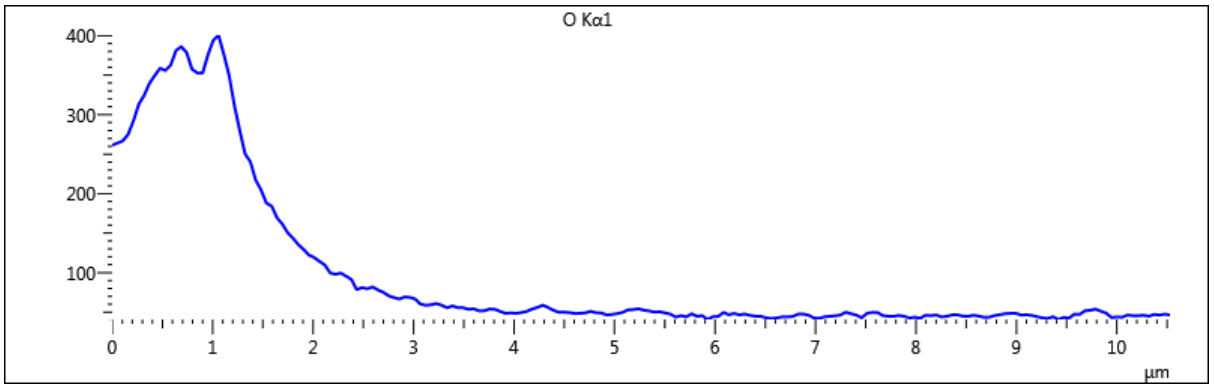

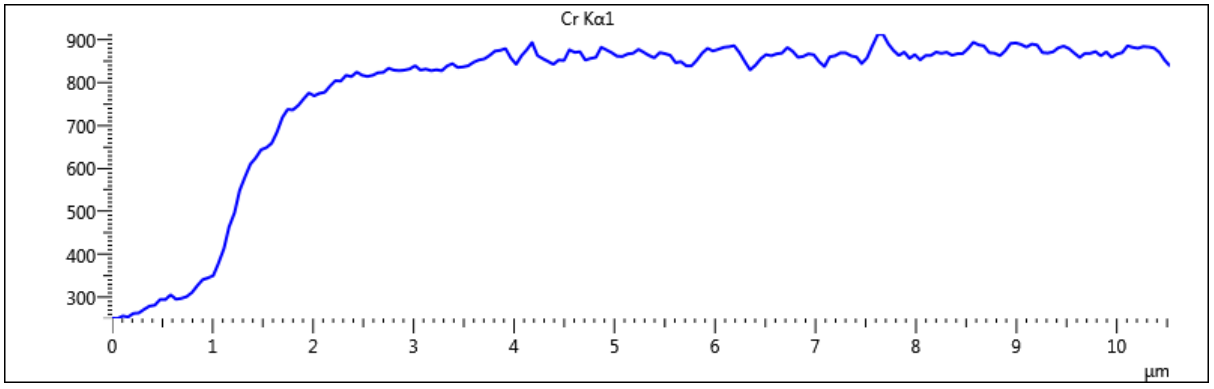

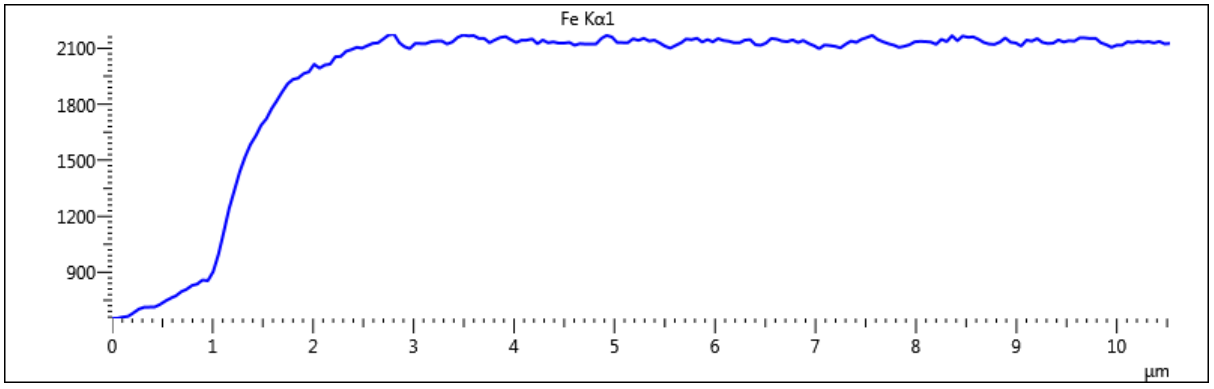

Figure 3.26 EDS line-scan of a cross-sectionally mounted shotblasted sample, showing O, Cr and Fe counts with increasing depth.

3.8. Processing of Topographic Data

3.8.1. Surface Area Measurement Technique

A method of surface area measurement was developed that utilised the python numpy.gradient function. Using the gradient maps created for the calculation of slope for the hybrid parameters in Section 4.4., an algorithm was developed to estimate the surface area using the slope of the surface. By changing the number of points used to calculate local gradient, from just neighbouring points to the width of the entire measurement area, surface area could be calculated over a greater range of resolutions, as described below.

The gradient of the array of the height data was calculated with the numpy.gradient function. With this array, the adjusted surface area resulting from the slope was calculated with the proceeding method.

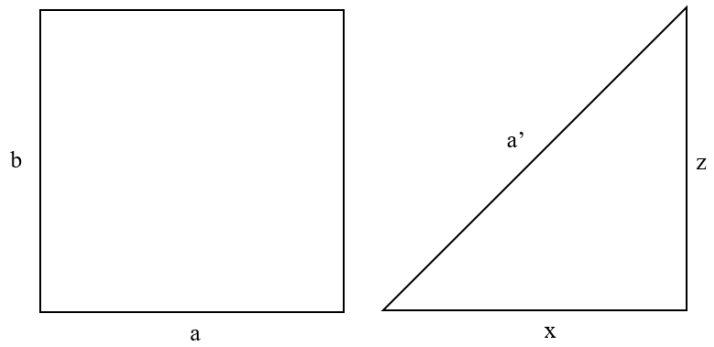

Figure 3.35 Estimating the change in area linked to gradient

Figure 3.35 shows a representation of a small square area of a surface, where *a* and *b* are the horizontal resolution. The height data is collected in a square grid, so squares are used to measure area in this method. For a flat surface the surface area of this piece is given by Equation 3.1.

$$A = a \times b \qquad \textit{Equation 3.1}$$

The change in surface area is attributed to the surface having a non-zero gradient; this gradient ($\frac{dz}{dx}$) increases *a* and *b* to *a'* and *b'* and changes the surface area to *A',* according to Equation 3.2.

$$A' = a' \times b' \qquad \textit{Equation 3.2}$$

a' and *b'* are calculated by the Pythagorean theorem as shown in Equation 3.3.

$$a' = \sqrt{(z^2 + x^2)} \qquad \textit{Equation 3.3}$$

The height is found terms of the horizontal spacing and the gradient as shown in Equation 3.4.

$$z = \frac{dz}{dx}x \qquad \textit{Equation 3.4}$$

This gives the new hypotenuse *a'* or *b'* for that side, shown in Equation 3.5.

$$a' = \sqrt{(\frac{dz}{dx}x)^2 + x^2} \qquad \textit{Equation 3.5}$$

The new area, *A'*, that includes the slope is given by Equation 3.6 which combines Equation 3.5 and Equation 3.2. This is calculated for each square across the surface.

$$A' = \sqrt{(\frac{dz}{dx}a)^2 + a^2} \times \sqrt{(\frac{dz}{dy}b)^2 + b^2} \qquad \textit{Equation 3.6}$$

To investigate the effect that resolution has on the surface area, the resolution was varied by changing *a* and *b,* which increases the size of the square being assessed. The gradient array is then recalculated, providing a slightly lower resolution gradient map, and the surface area is recalculated. This is done for all resolutions up to the width of the entire measurement area.

The geometric surface area is that of a perfectly flat plane spanning the same distance. The measured surface area is always greater than this since it takes more surface detail into account. The ratio between the two is the surface area ratio.

3.8.2. The Openness Calculation Method

The level of openness of each point across the four surface finishes was calculated in the following manner. A Python script was written to analyse each point on the surface in turn (Appendix 1). For each point the angle made between that point, and the points immediately to the left and right of that point, as demonstrated in Figure 3.., were measured. This measurement was performed for the neighbouring points with a sample size of 100 points. This was repeated in the vertical direction, and the lowest angle measured was designated at that point in the surface, creating a map of the openness.

The resolution, or the magnification of the image, affects the distance from each point that the open angle is considered for. 100 points was chosen as this forms a long distance to consider, even at the highest magnification. This equated to 10 μm for the 100 μm measurement area.

Openness values were calculated and plotted for each surface. At each point on the surface the height of the near surface, or horizon, was considered and the average angle made recorded. This angle is shown in Figure 3..

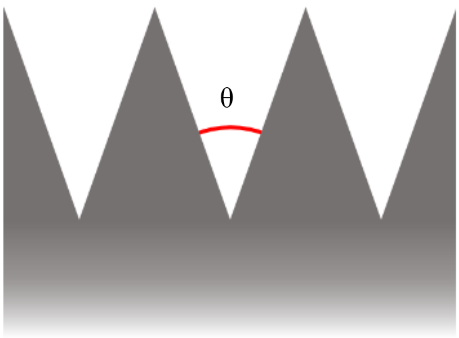

Figure 3.36 The openness of a valley.

3.9. References

[1] E. M. Elmahi, "Studies of some alloys using X-Ray Fluorescence," *PhD Thesis, Univ. Khartoum*, no. January, 1997.

[2] S. Boakye-Yiadom, A. K. Khan, and N. Bassim, "A systematic study of grain refinement during impact of 4340 steel," *Mater. Sci. Eng. A*, vol. 605, pp. 270–285, 2014.

[3] E. Morley and A. Michelson, "On the relative motion of the earth and the luminiferous ether," *American Journal of Science*. 1887.

[4] T. Kluyver *et al.*, "Jupyter Notebooks—a publishing format for reproducible computational workflows," *Position. Power Acad. Publ. Play. Agents Agendas - Proc. 20th Int. Conf. Electron. Publ. ELPUB 2016*, pp. 87–90, 2016.

[5] P. Fajnor, T. Liptáková, and V. Konstantová, "Influence of AISI 316Ti stainless steel surface treatment on pitting corrosion in various solutions," *Mater. Eng.*, vol. 17, no. 3, pp. 21–27, 2010.

[6] J. I. Goldstein, "Electron Beam – Specimen Interaction," *Pract. Scanning Electron Microsc.*, 1975.

[7] ASTM, "ASTM G38: Standard practice for making and using C-ring stress-corrosion test specimens," 2014.

[8] Washington Mills, "Particle size conversion - ANSI." 2018.

[9] P. Schmuki, H. Hildebrand, A. Friedrich, and S. Virtanen, "The composition of the boundary region of MnS inclusions in stainless steel and its relevance in triggering pitting corrosion," *Corros. Sci.*, vol. 47, no. 5, pp. 1239–1250, 2005.

[10] S. Cissé, L. Laffont, B. Tanguy, M. C. Lafont, and E. Andrieu, "Effect of surface preparation on the corrosion of austenitic stainless steel 304L in high temperature steam and simulated PWR primary water," *Corros. Sci.*, vol. 56, pp. 209–216, 2012.

[11] T. L. Wijesinghe, L. Sudesh, and D. J. Blackwood, "Characterisation of passive films on 300 series stainless steels," *Appl. Surf. Sci.*, vol. 253, no. 2, pp. 1006–1009, 2006.

[12] C. Padovani, R. J. Winsley, N. R. Smart, and P. A. H. Fennell, "Corrosion control of stainless

steels in indoor atmospheres," *Corros. Vol. 71 issue 5*, 2015.

[13] B. Krishnamurthy, R. E. White, and H. J. Ploehn, "Simplified point defect model for growth of anodic passive films on iron," *Electrochim. Acta*, vol. 47, no. 20, pp. 3375–3381, 2002.

[14] F. A. Lukiyanov, E. I. Rau, and R. A. Sennov, "Depth range of primary electrons, electron beam broadening, and spatial resolution in electron-beam studies," *Bull. Russ. Acad. Sci. Phys.*, vol. 73, no. 4, pp. 441–449, 2009.

[15] D. R. Baer, "Protective and non-protective oxide formation on 304 stainless steel," vol. 7, 1981.

[16] J. Konopka, "Quantitative differentiation of three iron oxides by EDS," *Microsc. Microanal.*, vol. 19, no. S2, pp. 1046–1047, 2013.

[17] X. Huang *et al.*, "Oxidation behavior of 316L austenitic stainless steel in high temperature air with long-term exposure," *Mater. Res. Express*, vol. 7, no. 6, 2020.

[18] HKL Technology, "Channel5," *(Manual)*, 2001.

Appendix 1

Script to produce openness surface maps.

```
import numpy as np
import numpy.ma as ma
import math
import os
from numpy import loadtxt
from numpy import savetxt

#horizontal openness
opennessi = np.zeros((height,width))
for ii in range(0, height):

    for jj in range(0, width1):
        samplesize = 100 #size of area considered for openness measurement
        array = np.zeros(samplesize)
        for kk in range(0,samplesize):
            if ii<(height1-samplesize):

                a = 90 - np.degrees(np.arctan((grid[ii+(1+kk),jj]-grid[ii,jj])/(p*(1+kk)))) #measures the openness
                b = 90 - np.degrees(np.arctan((grid[ii-(1+kk),jj]-grid[ii,jj])  /(p*(1+kk))))

                array[kk] = a + b

            else: #edge avoidance
                x = int(height-1)-ii
                a = 90 - np.degrees(np.arctan((grid[ii+x,jj]-grid[ii,jj])  /(p*(1+x))))
                b = 90 - np.degrees(np.arctan((grid[ii-(1+kk),jj]-grid[ii,jj])  /(p*(1+kk))))

                array[kk] = a + b

        opennessi[ii,jj] = np.min(array) #takes the most enclosed value

#vertical openness
opennessj = np.zeros((height1,width1))
for ii in range(0, height1):
    print('2nd ii is')
    print(ii)
    for jj in range(0, width1):
        array = np.zeros(samplesize)
        for kk in range (0,samplesize):
            if jj< (width1-samplesize):
```

```
            a = 90 - np.degrees(np.arctan((grid[ii,jj+(1+kk)]-grid[ii,jj])  /(p*(1+kk)))) #measures the openness
            b = 90 - np.degrees(np.arctan((grid[ii,jj-(1+kk)]-grid[ii,jj])  /(p*(1+kk))))

            array[kk] = a + b

        else:#edge avoidance
            x = int(width-2)-jj
            a = 90 - np.degrees(np.arctan((grid[ii,jj+x]-grid[ii,jj])  /(p*(1+x))))
            b = 90 - np.degrees(np.arctan((grid[ii,jj-(1+kk)]-grid[ii,jj])  /(p*(1+kk))))

            array[kk] = a + b

    opennessj[ii,jj] = np.min(array) #takes the most enclosed value

for ii in range(0, height1): #takes the most enclosed value
    for jj in range(0, width1):
        if (opennessi[ii,jj] < opennessj[ii,jj]):
            opennessj[ii,jj] = opennessi[ii,jj]


print(opennessj)

np.savetxt(name+"openness.dat", opennessj)
```

Chapter 4. The Geometry of Different Surface Finishes and their Relationship to Corrosion

4.1. Introduction

In this Chapter the characterisation of the surface of the different stainless-steel surface finish types, based on surface height measurements, is described. There are a wide range of parameters that can be calculated from surface height data, and their method and purpose are described. The implication of these parameters to the corrosion of these surfaces is shown by experiment in Section 4.7.

4.1.1. The Appearance of Surface Finish

Figure 4.1 shows photographs of the four surface finishes taken with a macro lens. The aesthetic effect of each surface, which is a driver in many industries, can be seen. The photographs also demonstrate the nature of the surfaces at the macro scale.

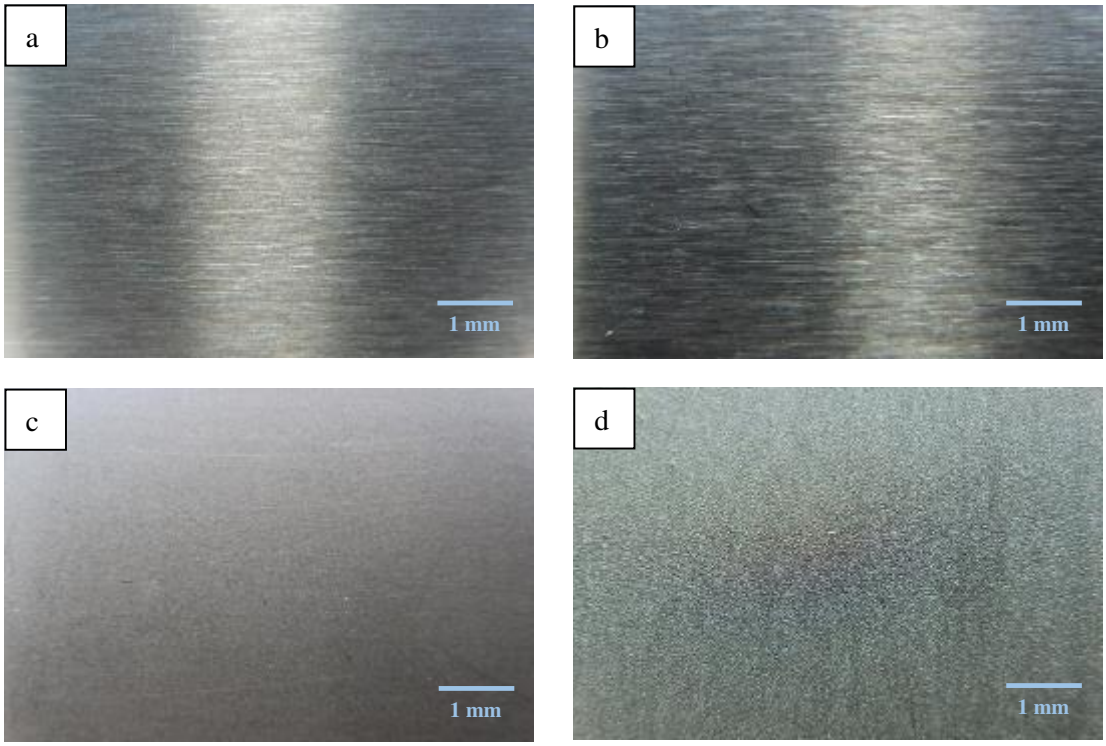

Figure 4.1 Photographs of surface finishes. A brushed, B ground, C rolled, D shotblasted.

The brushed and the ground surfaces (Figure 4.a and Figure 4.b) are similar. They both have a lustrous shine and reflect a light well. The brushed surface appears slightly finer than the ground surface. The rolled surface (Figure 4.c) appears very smooth, and has a shine to it, but does not reflect objects clearly. The shotblasted surface (Figure 4.d) is matte and its roughness can be seen by eye.

4.2. Surface Height Analysis

4.2.1. Surface Height Mapping

Figure 4.2 shows Vertical Scanning Interferometry (VSI) surface height maps of representative areas of the four different surface finishes. These were produced to characterise surface relief at the microscale. The colour bar to the right of each plot denotes the surface height range for the measurement area which range from 2 μm for the brushed surface to 20 μm for the shotblasted surface. A brighter, yellower colour on the map indicates high points on the surface while a darker, red colour indicates lower points on the surface. The resolution of each measurement was kept constant, with images taken at 50 times magnification. Data is normalised so that the average hight is set to 0. 10 other locations were imaged, and the data used to calculate surface parameters. The brushed (Figure 4.2a) and the ground (Figure 4.2b) surfaces look similar at this magnification, as they also do by eye (Figure 4.). The long ridges and valleys are of similar depth and height, with a range of around 2.4 μm.

The VSI image also shows the grain boundaries of the rolled surface (Figure 4.2c), which are omnidirectional. The direction of rolling can still be discerned from the horizontal patterns visible in this image. For the shotblasted surface (Figure 4.2d), multiple craters dominate the relief, where grain boundaries can also be seen.

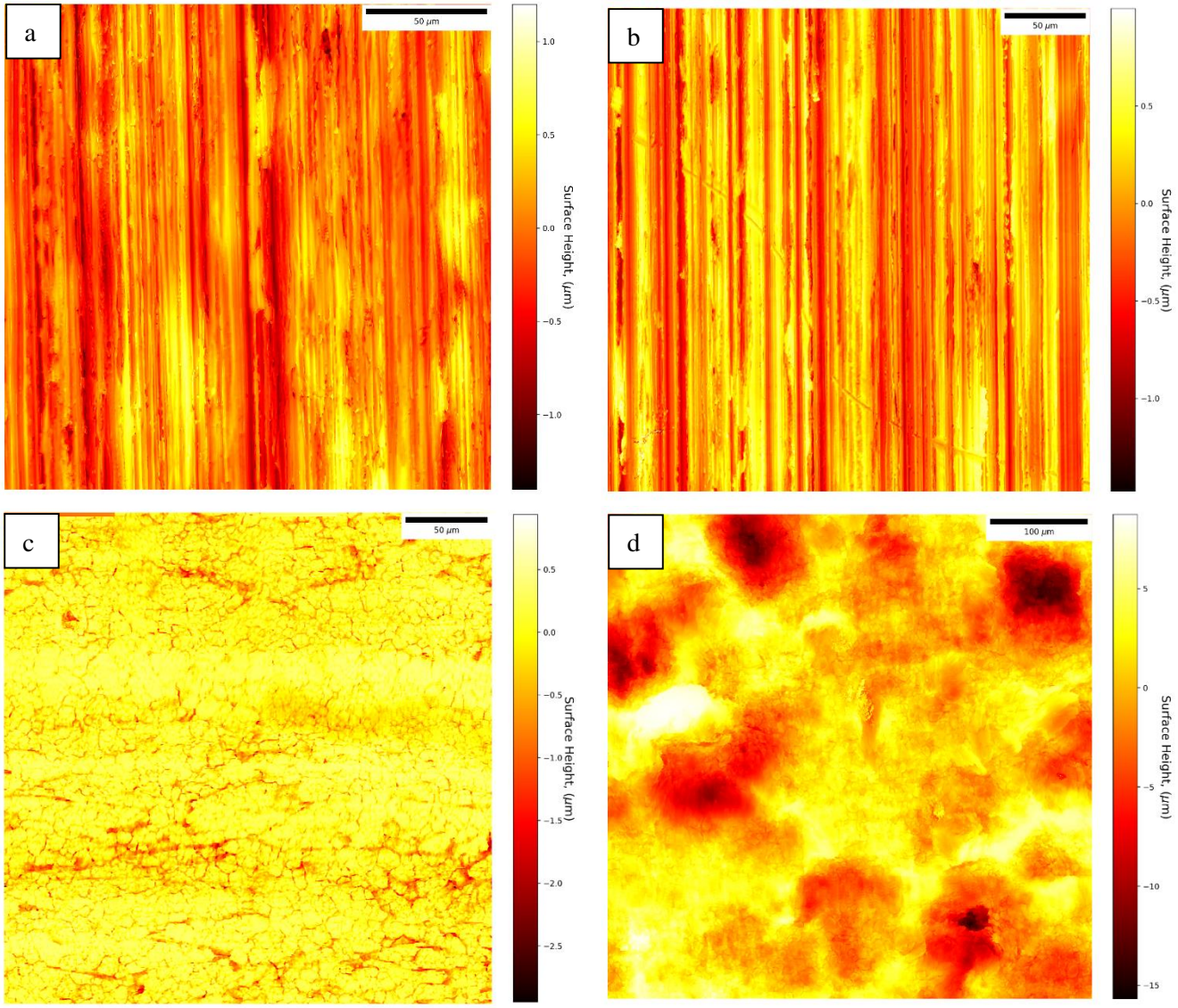

Figure 4.2 VSI Surface height maps for: A brushed, B ground, C rolled, D shotblasted surfaces.

The cumulative probability density distributions for the heights of the four surface finishes, as obtained by VSI, are shown in Figure 4.3. These describe how height is distributed across each surface; where a short curve would indicate a small height range and vice versa. The gradient of the curve at a given point is indicative of the proportion of the surface that is at that particular height, with more gradual areas of the curve showing heights that are less represented in the surface. Additionally, the symmetry of the curve can be assessed, with asymmetrical curves showing skewness in the surface. It is immediately observable that the shotblasted surface (d) has a far larger range of surface heights than the other three surfaces.

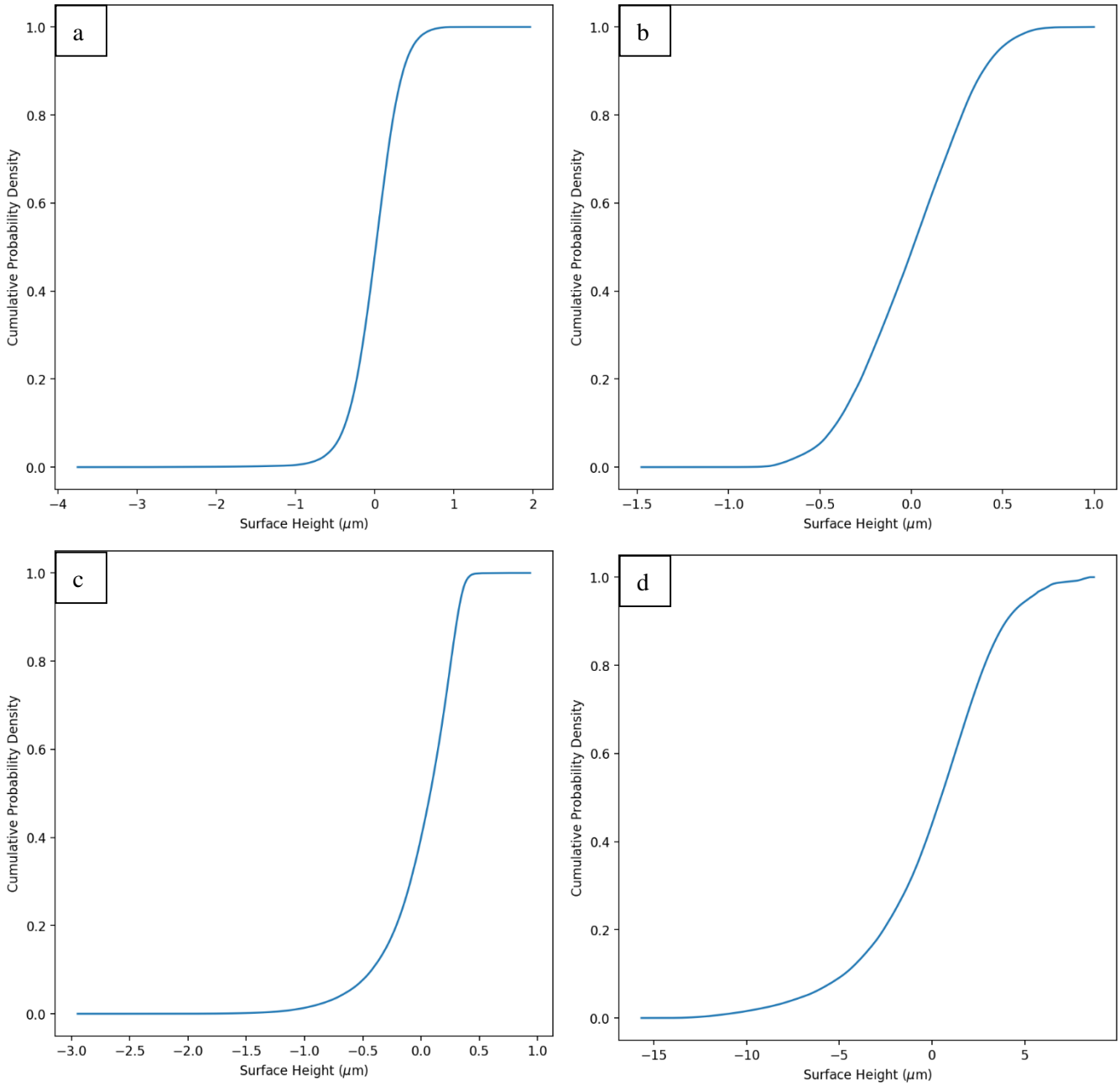

Figure 4.3 VSI Cumulative Probability Density plots for the surface height of: A brushed, B ground, C rolled, D shotblasted surfaces. From VSI data.

Of particular note is the difference in the head and tail of the height distribution of the rolled surface (Figure 4.3c). Consistent with the corresponding data taken with AFM, there is a sharp arrival at a cumulative probability density of 1, indicating that very little of the surface is comprised of peaks or other features with a positive height distribution. This contrasts heavily with the tail of the same sample, which had a longer, more gradual, slope to zero. This indicates that the surface has a predominance for negative height features; this characteristic is described by the skewness (Ssk) parameter. The magnitude of this value is largest and is most negative, compared with the other surfaces, for the rolled

surface at -1.51. This shows that a sizable portion of the rolled surface lies beneath the average surface height. Since these areas are likely to be more favourable to pitting corrosion than peaks, this increases this surface's vulnerability to this type of corrosion.

Figure 4.4 shows the surface height maps collected by AFM for the four surface finishes. Each map is of a 100 μm square measurement area. The colour bar to the right of each plot denotes the surface height range for this measurement area which range from 2160 nm for the brushed surface to 8720 nm for the shotblasted surface. Considering the horizontal span of the features, it is certain that the height range of the whole shotblasted surface is much greater than that measured for this small area, with both taller and deeper features existing outside of this area. Whereas for the other surfaces it is likely that the representative hight range has been measured.

The brushed surface (Figure 4.4a) has shorter grooves that are interrupted by both particles and gaps. This contrasts with the grooves on the ground sample which are long, continuous, and uniform (Figure 4.4b). They are far less interrupted by surface imperfections.

The arrows on Figure 4.4 are where, on both the ground and brushed surfaces, deep holes in the surface are observed. Both of these surfaces are formed by action along the surface and so it is likely that these features are formed by the smearing of surface material [1]. These areas are likely to be more prone to pitting initiation, and so these features will likely reduce the surface's ability to withstand conditions that encourage pitting corrosion [2].

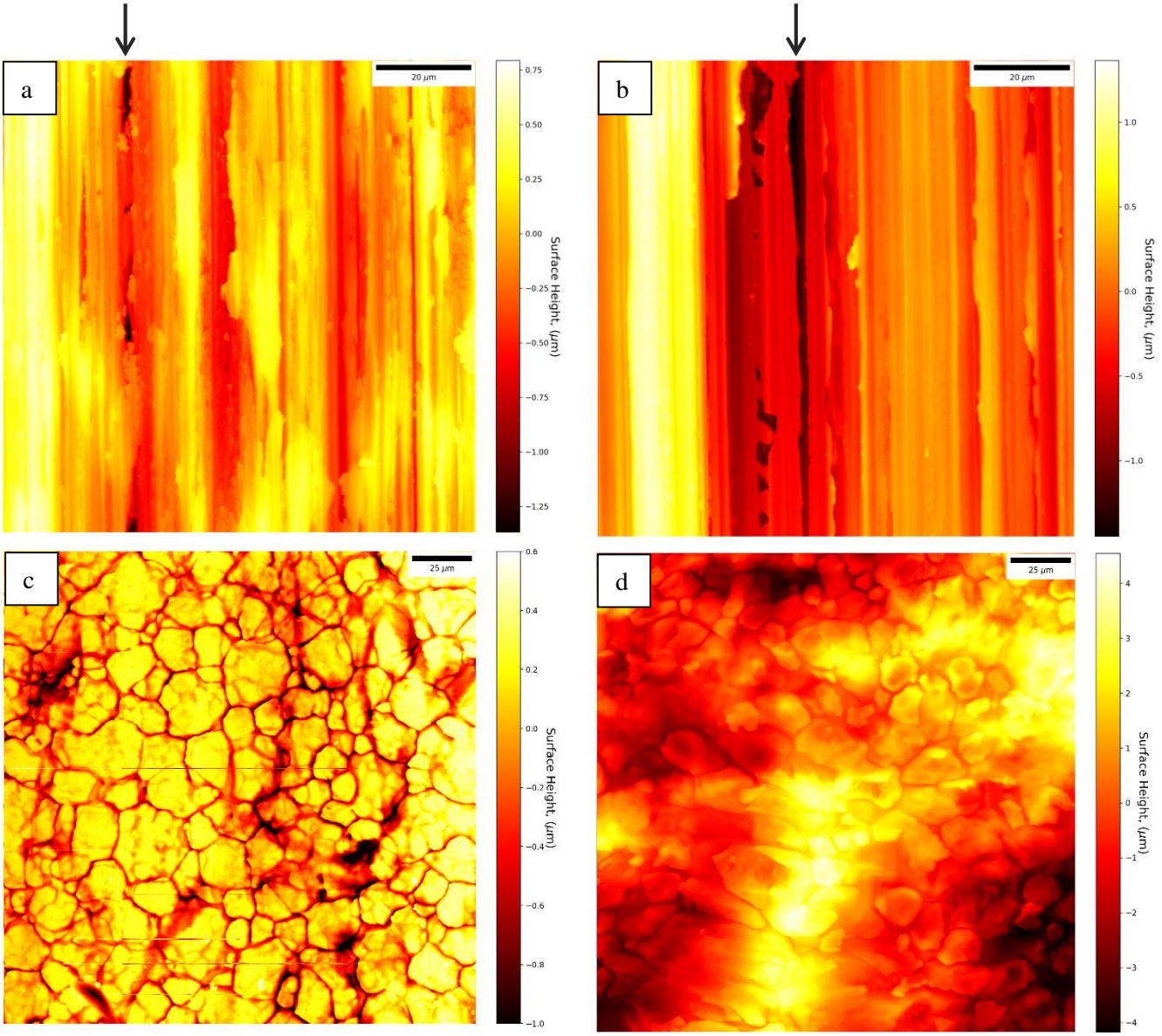

Figure 4.4 AFM Surface height maps for: A brushed, B ground, C rolled, D shotblasted surfaces.

The shotblasted surface has the largest height range at 10 µm. The ground sample has the second highest height range at 3.4 µm and the rolled sample the smallest at 1.9 µm. The brushed sample is more comparable with the ground sample with a 2.8 µm range.

The undulating, cratered nature of the shotblasted surface is clearly displayed in Figure 4.4d. It has no predominant directionality. As well as larger features that resemble craters and peaks caused by the incident shots of the finishing process, smaller undulations are observed. These are likely to be surface grains and are of the same size as the grains seen on the rolled surface. Those seen on the shotblasted surface, however, are not as flat as the rolled surface since they have not been rolled flat. Some grains

at the shotblasted surface are elongated and warped; this could be the effect of multiple collisions on a single grain, or by collisions at an angle with a high horizontal velocity.

The craters are relatively flat on the bottom (the material immediately below an impact is not moved horizontally) and the rounded edges of the craters are relatively tall and contribute to a very high roughness value. One peak can be seen with a flat top.

On the ground surface, repeating ridge and valley features are seen at two distinct magnitudes. The larger one is responsible for the taller 1 μm ridge seen in Figure 4.4b while the smaller ridge and valley like features run parallel with the directionality of the surface and the large ridge and exist as a very small order waviness with an amplitude of around 0.1 μm.

The larger valleys are made by grit grains ploughing the surface while the smaller waviness may be made by grains having a smaller force on the surface. Alternatively, the shape of this smaller waviness may be caused by variation in the shape and size of individual grains and their layout is responsible for the texture of the small magnitude waviness.

While the ground surface is made up of perfectly straight ridges and valleys, the brushed surface has ridges and valleys that meander slightly as shown in Figure 4.4a. This indicates that the brushing media are free to move amongst themselves unlike grit grains on a grinding device. The conventional distinction between grinding and polishing is that the abrasive material in grinding is fixed to the grinding media, whereas the abrasive material used in polishing is free. In this way wire brushing is more akin to polishing and has in fact produced a shinier surface in the surfaces investigated in this Thesis.

At the etched grain boundaries on the rolled surface, minima features can be seen that have a very low aspect ratio (width/height) [3]. “Minima features” refer to low points on the surface, such as valley bottoms or other dips. These valleys are potentially areas where film breakdown and pit initiation could occur. This effect is discussed in Section 4.6.

The surface height maps in Figure 4.5 show the same data as presented in Figure 4.4. The magnification is much higher and a lighting affect has been applied using the Nanoscope Analysis software that reveals surface texture.

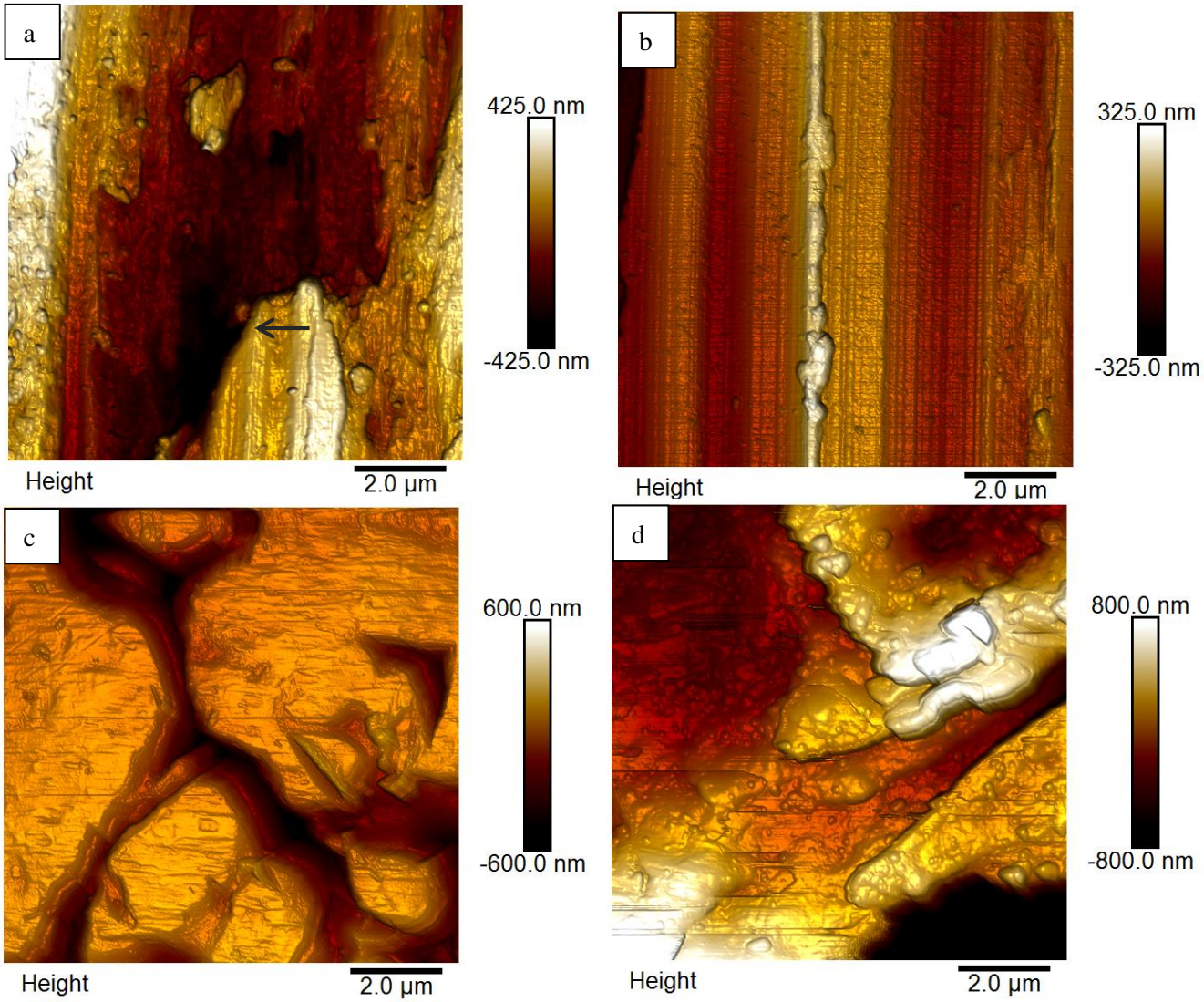

Figure 4.5 AFM Surface height maps for: A brushed, B ground, C rolled, D shotblasted surface.

The depth of the grooves between grains are apparent in the rolled surface (Figure 4.5c), also revealed is the texture of each of the flat faces of the grains. These lines are caused by the rolling process and are imprinted by the final roller. They show the direction of rolling (horizontal).

At this magnification, the difference between the brushed and the ground surfaces is most apparent. Particles on the brushed surface have been removed from elsewhere on the surface and re-adhered during the finishing process; they are not compositionally distinct, as has been shown in Chapter 3. Another difference is the presence of folded-over ridges (Figure 4.5a, arrow). This smearing causes overhanging materials to form which likely have a very low aspect ratio and so are likely to be vulnerable to corrosion since this will slow diffusion near the surface [3]. The actual angle of the aspect ratio cannot be measured using VSI or AFM as it is not normal to the surface. This is discussed in Section 4.6.

4.2.2. Surface Height Parameters

The surface height parameters calculated according to data acquired from both VSI and AFM are summarised in Table 4.1 and Table 4.2 respectively. These are the mean values taken from 10 locations on the surface, with 95% confidence intervals given. Their calculation is described in Section 2.3.1.

Table 4.1 Surface height parameters calculated from VSI data. (95% CI)

	Brushed	Ground	Rolled	Shotblasted
Ra nm	230 (217,243)	246 (241, 251)	204 (184, 225)	2710 (2400, 3040)
Rq nm	291 (273, 309)	298 (293, 304)	272 (247, 297)	3490 (3170, 3810)
Sp nm	1140 (10108, 1270)	953 (926, 981)	802 (751, 853)	7590 (6770, 8400)
Sv nm	-1320 (-1420, -1220)	-1180 (-1300, -1070)	-1900 (-2010, -1780)	-11350 (-11960, -10730)
Sz nm	2460 (2240, 2670)	2140 (2020, 2260)	2700 (2570, 2830)	18940 (17770, 20100)
Ssk	-0.24 (-0.32, -0.17)	-0.11 (-0.14, -0.08)	-1.54 (-1.72, -1.36)	-0.59 (-0.86, -0.31)
Sku	3.04 (2.94, 3.15)	2.50 (2.45, 2.55)	6.74 (5.67, 7.81)	3.35 (2.67, 4.02)

Table 4.2 Surface height parameters calculated from AFM data. (95% CI)

	Brushed	Ground	Rolled	Shotblasted
Ra nm	236 (222, 250)	404 (396, 412)	221 (199, 243)	1440 (1270, 1610)
Rq nm	297 (279, 315)	520 (510, 530)	286 (260, 312)	1750 (1580, 1910)
Sp nm	793 (701, 885)	1360 (1320, 1400)	776 (726, 826)	4550 (4060, 5040)
Sv nm	-1370 (-1470, -1270)	-1450 (-1590, -1310)	-2210 (-2340, -2090)	-4170 (-4390, -3950)
Sz nm	2160 (1970, 2350)	2810 (2650, 2970)	2990 (2850, 3140)	8720 (8180, 9270)
Ssk	-0.18 (-0.21, -0.14)	0.34 (0.25, 0.43)	-1.20 (-1.34, -1.06)	0.02 (0.01, 0.02)
Sku	3.03 (2.62, 3.44)	3.05 (2.68, 3.42)	4.84 (4.07, 5.61)	2.38 (2.02, 2.74)

Ra gives the roughness of the surface. This is simply the mean deviation from a flat plane and is the most commonly used roughness parameter. The Ra values measured show the shotblasted surface as the roughest, at 2710 nm compared with the ground surface at 250 nm, the brushed surface at 230 nm and the rolled surface at 205 nm. The Ra values for the brushed, ground and shotblasted surface measured with AFM confirm this, while the Ra value calculated for the shotblasted surface is much smaller for the AFM measurement at 1440 nm. This shows the effect of the measurement area being too small to contain an area of the surface spanning the entire height range; for this reason, the VSI value is taken to be the correct one.

Ssk is the skewness of the surface. It is the mean cubed height divided by Rq^3. The surfaces all give negative Ssk indicating that their surfaces are predisposed to valleys rather than peaks. This is particularly apparent for the rolled surface which has an Ssk value of -1.54. The gaps between grains form steep, deep valleys that contribute highly to Ssk due to their depth but are also too narrow to greatly increase the Ra value.

Sku describes the kurtosis of the surface. This is the mean height to the fourth power divided by Sq^4. The value of Sku can indicate the presence of inordinately large peaks or valleys since extreme values are greatly amplified by the power of four. For a normal distribution of surface heights, Sku would be 3. Surfaces with an Sku of less than 3 are considered gradually varying, smooth and with very few sharp peaks as shown in Figure 4.6.

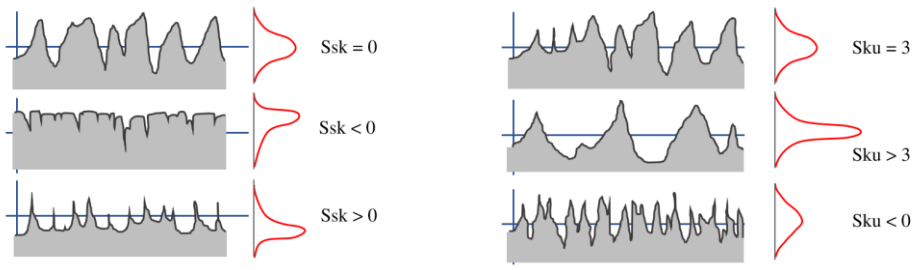

Figure 4.6 Skewness and kurtosis in surfaces

The ground surface has an Sku (kurtosis) of 2.5, indicating the distribution of its surface heights has slightly thinner tails than a normal distribution. This means the surface height distribution has few extreme values such as very high peaks or valleys. The shotblasted surface has an Sku of 3.4 showing that its height distribution has slightly more extreme values than a normal distribution indicating that a larger proportion of this surface is either part of a peak or a low point. The rolled surface has an Sku of

6.7 the surface height distributions has the thickest tails and the most extreme values for height and depth [5].

Some difference in skewness would be expected for the same surface as measured by AFM or VSI due to a distortion effect inherent in AFM. The probe tip has a 10 nm radius that interacts with the surface, which is around 5% of the Ra value for some surfaces used. When passing over sharp peaks, as shown in Figure 4.7, the measured value tends to become rounded. When passing over valleys however, the probe tip cannot reach to the deepest point since it interacts with the opposite slope. This reduces the recorded depth of the valley and records a sharp root valley radius. Overall, this increases the measurement of peaks and decreases the measurement of valleys increasing the positive skewness of the measurement.

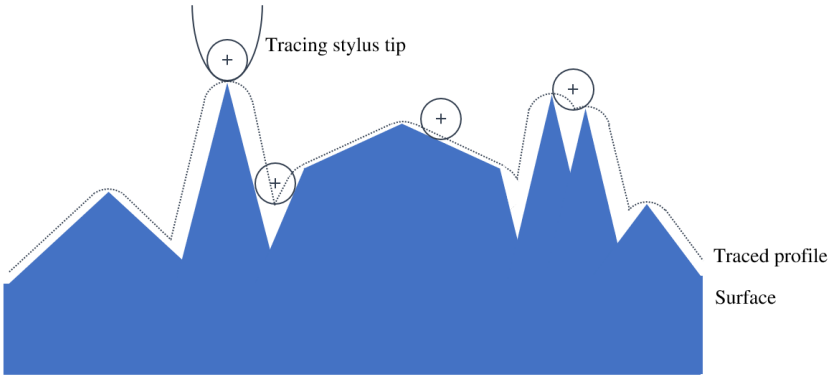

Figure 4.7 Distortion due to size of AFM probe tip.

Sp denotes maximum peak height from the average surface and **Sv** gives maximum valley depth as a negative number. **Sz** is the difference between the two and gives the height range, or maximum height of the surface. These values, shown in Table 4. and Table 4.2, indicate the greater depth of features in the shotblasted surface and its overall greater range of surface height.

For these parameters, the range for the 95% CI is below 10% of the mean, and largely under 5%. This range is smaller than the measured differences between the parameters when they described here as different.

4.3. Surface Area and Fractal Analysis

As detailed in Chapter 2 of this Thesis, surface area is an important factor in corrosion science and is often controlled for in experiments; however, it can be difficult to measure due to its variance with resolution. The surface area exposed to an environment affects how much material will corrode in a given time. Corrosion rates, and dissolution rates, are often given as a function of surface area. Additionally, the triggers for corrosion initiation such as specific surface geometries or the presence of inclusions, have surface densities. These densities increase if the surface roughness is high and so more of these vulnerable points are exposed for a given geometric surface area.

Surface area and fractal characteristics are closely linked and support one another; in this Section they are presented adjacently. It was found that detail in the surface was present over the range of 0.01 μm (the smallest resolution measured) to around 50 μm. This makes the measurement of surface area challenging as it is dependent on resolution. This effect is better understood by investigating the fractal behaviour of the surface, as is presented here.

4.3.1. Surface Area Analysis Results

Using VSI, a 300 μm square of each surface was imaged. This square was broken down into 1516 / 1516 separate measurement points, giving a horizontal resolution of 0.2 μm. An explanation of the method is detailed in Section 3.8.1.

Figure 4.8 shows the change of surface area ratio with resolution for the four surface finishes. The shotblasted surface has the largest surface area ratio at all resolutions, maximising at 1.42. This means that the surface area is 42% larger when measured with a 0.2 μm resolution than at 100 μm. The rolled surface has the second highest surface area ratio, maximising at 1.19, compared with around 1.06 for the ground and the brushed surfaces. It is expected that the curve grows with a x^n relationship where ($0<n<0.5$) [6].

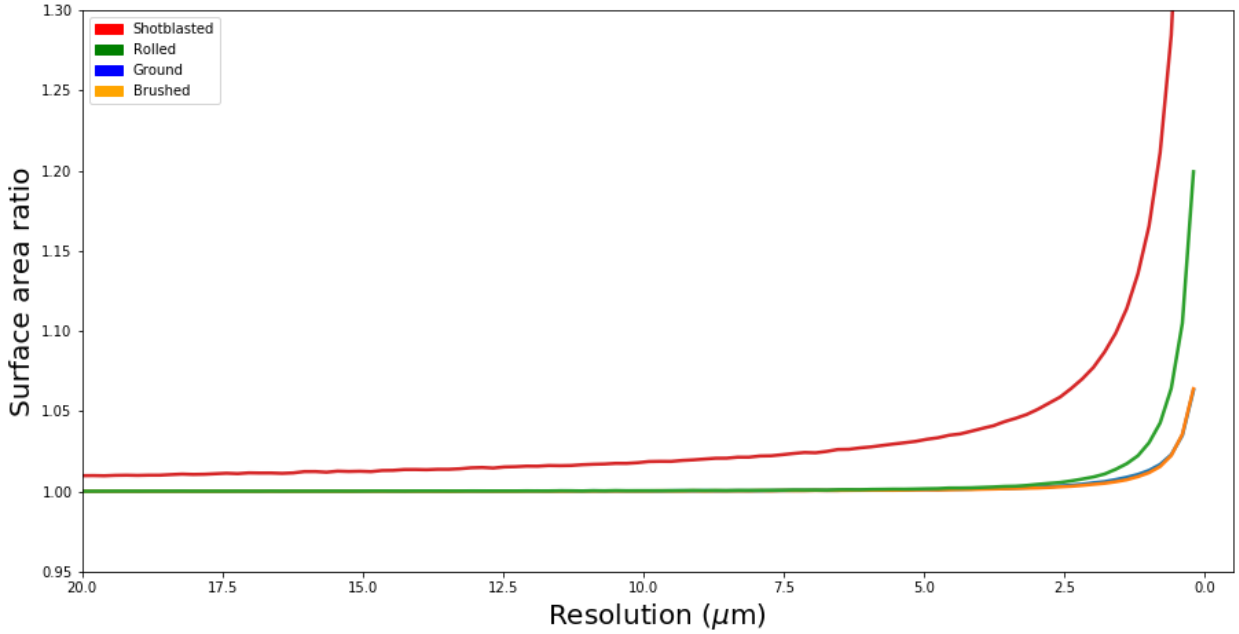

Figure 4.8 Surface area ratio with resolution for the four surface finishes. (VSI). The ground surface is in line with the brushed surface.

The measurement area for AFM was a 100 µm square. This was divided into 1024 /1024 measurement points, giving a horizontal resolution of 98 nm. This resolution was later improved to 9.8 nm for a smaller 10 µm square.

Figure 4.9 shows how surface area changes with resolution for the AFM data. Consistent with the VSI data, the shotblasted surface had the largest surface area ratio throughout. The surface area ratio maximised at 1.30 at the resolution of 98 nm. This curve could be expected to plateau at higher resolution, although whether it would do this before the actual position of the surface becomes difficult to define is unknown.

It should be noted that the surface area ratio is not the ratio of surface area at one resolution, to the correct geometric surface area, but is the ratio between one resolution and a different, much larger resolution e.g. 0.2 µm to 100 µm.

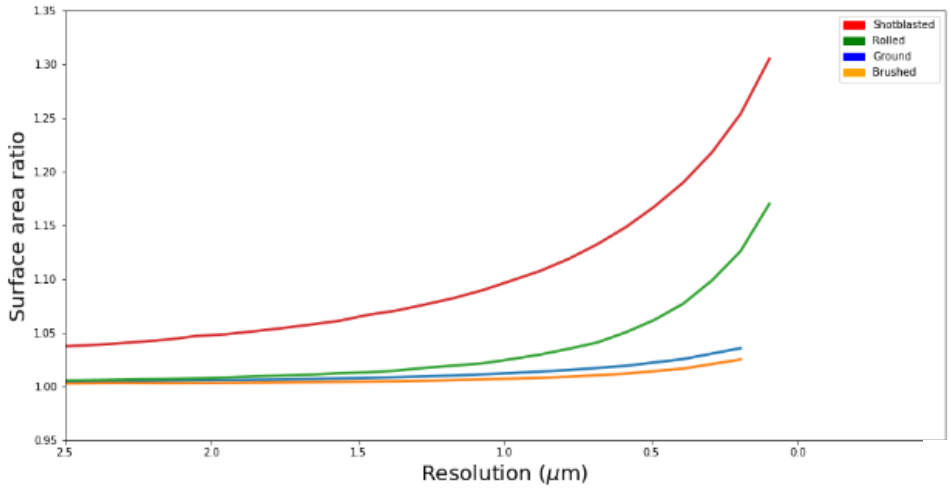

Figure 4.9 Surface area ratio with resolution for the four surface finishes. (AFM)

The surfaces with larger surface area ratios may be impacted by having higher corrosion rates since more surface is presented per cm^2. Further, a greater surface density of inclusions, imperfections or vulnerable surface geometries will be found on these surfaces. For example, for the shotblasted surface, with a surface area ratio of 1.30, the surface density of inclusions should be expected to be higher by this proportion, since this is how much more surface area is exposed to the environment. This effect would be expected to be consistent even given identical inclusion densities by volume for other surface finishes.

4.3.2. Fractal Analysis Technique

Fractals exhibit self-similarity across resolution. For some cases this is manifest by similar structures being observable at multiple magnifications. To be fractal it is not required that identical features reappear at multiple magnifications; further intricacy being present at higher magnification is sufficient.

Fractal behaviours are seen throughout the physical world but are often ignored to enable measurement. Physical measurements are rounded to a finite number of significant figures which creates inaccuracy and only allows estimates to be made. Fractal analysis has been proven useful in meteorology before spreading to a wider range of applications [7]. It is recognised that features like wind and clouds are

fractal in nature, and that considering this in calculations has allowed for more accurate predictions without large increases in the computing power required.

An accurate measurement and description of surface area, and its fractal behaviour, serves to be useful for electrochemistry and other applications such as stress concentration estimation. Currently, it is standard practice in electrochemistry to grind and polish a surface to a flat mirror finish to control for the effects of the surface area ratio. This denies the option to do electrochemistry on real surfaces by effectively reducing the fractal dimension of the surface from its real world number to close to two.

Additionally, an investigation of the surface that considers the surface detail at all resolutions will provide the opportunity to reveal at which scale certain processes occur and are influenced. Passive film growth, for instance, occurs at scales of tens of nm and below, meaning it is the surface at this resolution that matters for this process.

To calculate the fractal dimension of the surfaces the surface area ratio with resolution curve was used. When this curve is plotted on logarithmic axis for both variables, the gradient is the power of the surface area ratio to resolution curve at that point and is related to the fractal dimension of the surface by Equation 4.1, where β is the gradient and D is the fractal dimension.

$$D = 2(1 - \beta) \qquad \textit{Equation 4.1}$$

For a surface with a uniform fractal dimension the log curve would be a straight line, and the gradient fixed. It was found that, for the surfaces investigated, this curve was not fixed but had some upward inflection. Rather than fit a straight line to this, the gradient was taken across the full range of the resolution, and the fractal dimension was calculated across the full resolution and plotted.

4.3.3. Fractal Analysis Results

Figure 4.10 Shows the fractal dimension for each surface acquired from the VSI data, with regard to resolution. All of the surfaces investigated are roughly 2D above a resolution of 1 μm. Below this, the fractal dimension rapidly increases to 2.03 for the brushed and ground surfaces, 2.10 for the rolled surface and 2.28 for the shotblasted surface. These sit within ranges already measured for aluminium (2.1 – 2.6) [8].

The fractal behaviour displayed in these surfaces could influence corrosion in a number of ways. The passive film, vital to performance of the stainless steel surface, must cover the entire surface to successfully protect the bulk material. Since it is 1 - 10 nm thick [9], the shapes and features of the surface at this resolution should be inspected. The shape of the surface at this resolution in particular defines the morphology of the film. It is at this resolution that the shapes and angles the film forms are defined.

MnS inclusions are thought to be of the order of 1 μm in size; the holes that remain when these are dissolved will be of a similar size [10]. When considering the increased number of exposed MnS inclusion sites caused by the increased surface area, it can only be increased with surface area ratios above this resolution, i.e., a large amount of waviness with wavelength below 1 μm will increase the surface area but cannot expose more 1 μm inclusions. Additionally, it is thought that the holes that these MnS inclusions leave when dissolved, are amplified by surrounding geometry, thus increasing local acidification during pitting corrosion [3]. From the surface area ratio graphs, it can be seen how much of the surface is at this resolution and can have this amplifying affect. The smallest size that stable pitting can occur is 0.1 μm [11]. Features below this size can be discounted when considering the effect of surface geometry on local acidification.

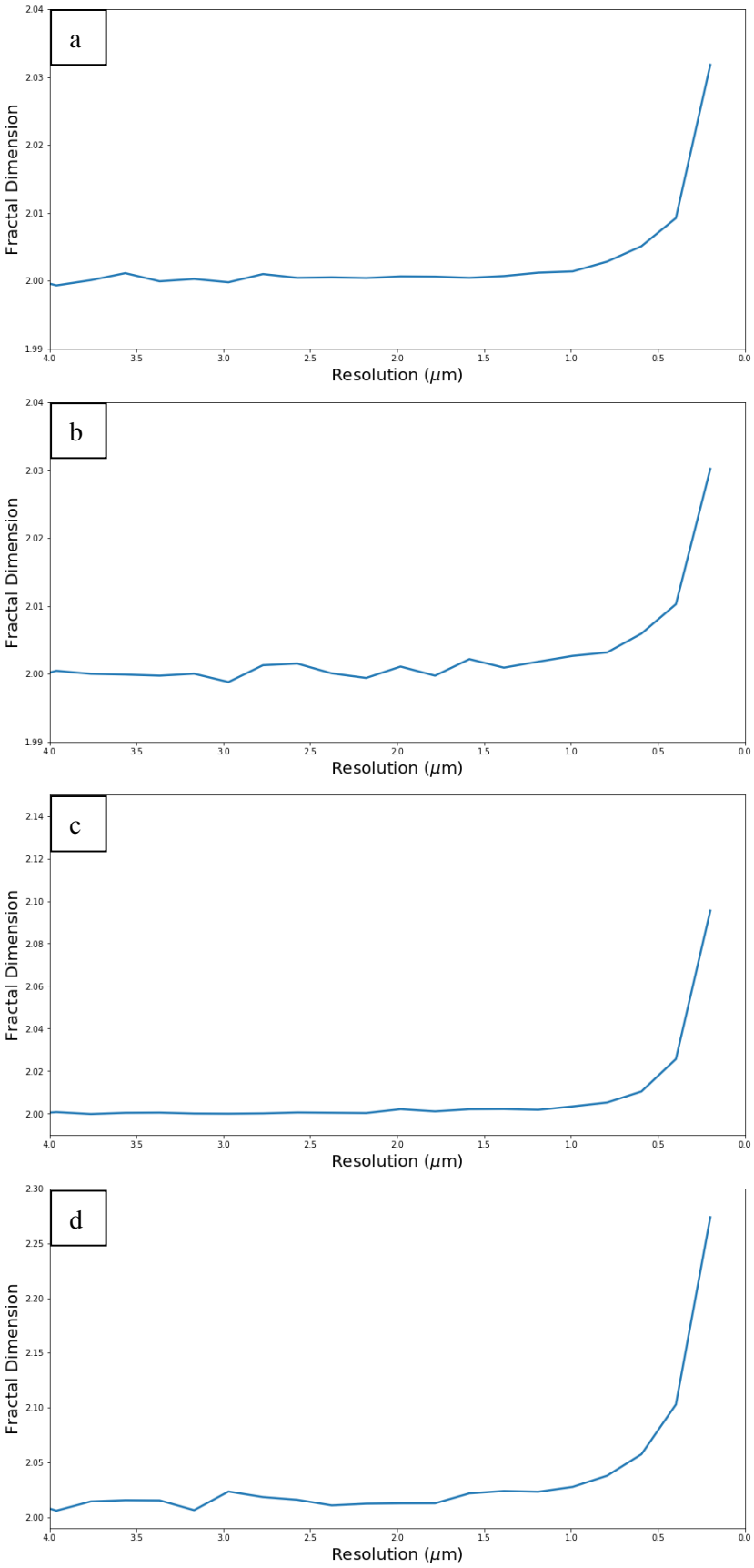

Figure 4.10 How fractal dimension changes with resolution for: A brushed, B ground, C rolled, D shotblasted surfaces. (VSI)

It was found that the rolled surface, despite being flatter and less rough than the brushed and ground surfaces, had the second highest surface area ratio. This is a result of the rolled and the shotblasted surfaces consisting of features such as etched grain boundaries that are intricate at very small resolutions. By comparison, the ground and the brushed surfaces are rougher than the rolled surface at larger resolutions, but from Figure 4.10 it was deduced that they are smoother at very small resolutions. This is as though the surface finishing action of wire or grain across the surface creates large grooves with sides that are themselves very smooth. This highlights a known drawback in traditional stylus measurements and in commonly used roughness parameters such as Ra, which both fail to describe surfaces which are rough, but only at high resolutions [12].

From optical microscopy and from the SEM analysis of the surfaces shown in Chapter 3, all four surfaces considered here have shown some intrinsic self-similarity. Given the increased fractal dimension at increasing resolution, the standard units that describe surface area may be unsuitable [13]. For example, the surface area of a piece of stainless steel at higher resolutions could be given in units of $\mu m^{5/2}$ since this more closely reflects the nature of the surface.

4.4. Hybrid and Inverse Hybrid Parameter Analysis

4.4.1. Hybrid Parameter Analysis

The topology of a stainless-steel surface consists of peaks, ridges, valleys, and holes; connecting these features are slopes. The hybrid parameters describe the nature of the gradients of the surface, both of the slopes and of the maxima and minima of the surfaces. Steep surface valleys could encourage pit initiation, discourage corrosion product diffusion and could encourage contaminate particle adhesion [15].

To visualise this, the maximum gradient in any direction for each point was plotted, as shown for AFM data in Figure 4.11. In these diagrams, surface gradient is shown in colour, with steeper slopes shown in a lighter, more yellow colour. This demonstration highlights the parts of the surface which are steepest. The brushed and ground surfaces (Figure 4.11a and b) look similar to their height maps, ableit around a quarter phase shifted; as from a sinusoidal model it could be expected that the steepest points on these surfaces would be at zero height. For the rolled surface (Figure 4.11c) it is clear that the etched

grain boundaries are the cause of the vast majority of the surface slope. The centre of these surface grains are almost all at 0 gradient, showing that this surface is extremely flat except at the corroded grain boundaries. The edges of craters are visible in the shotblasted surface (Figure 4.11d), showing that these features contribute to the average slop of the surface. Additionally, the etched grain boundaries also found on the rolled surface are present. The flat-topped peaks are highlighted in this image with a gradient of 0 and solid colour, indicating their flattness. The same process was applied to the data gathered with VSI for the analysis of hybrid features.

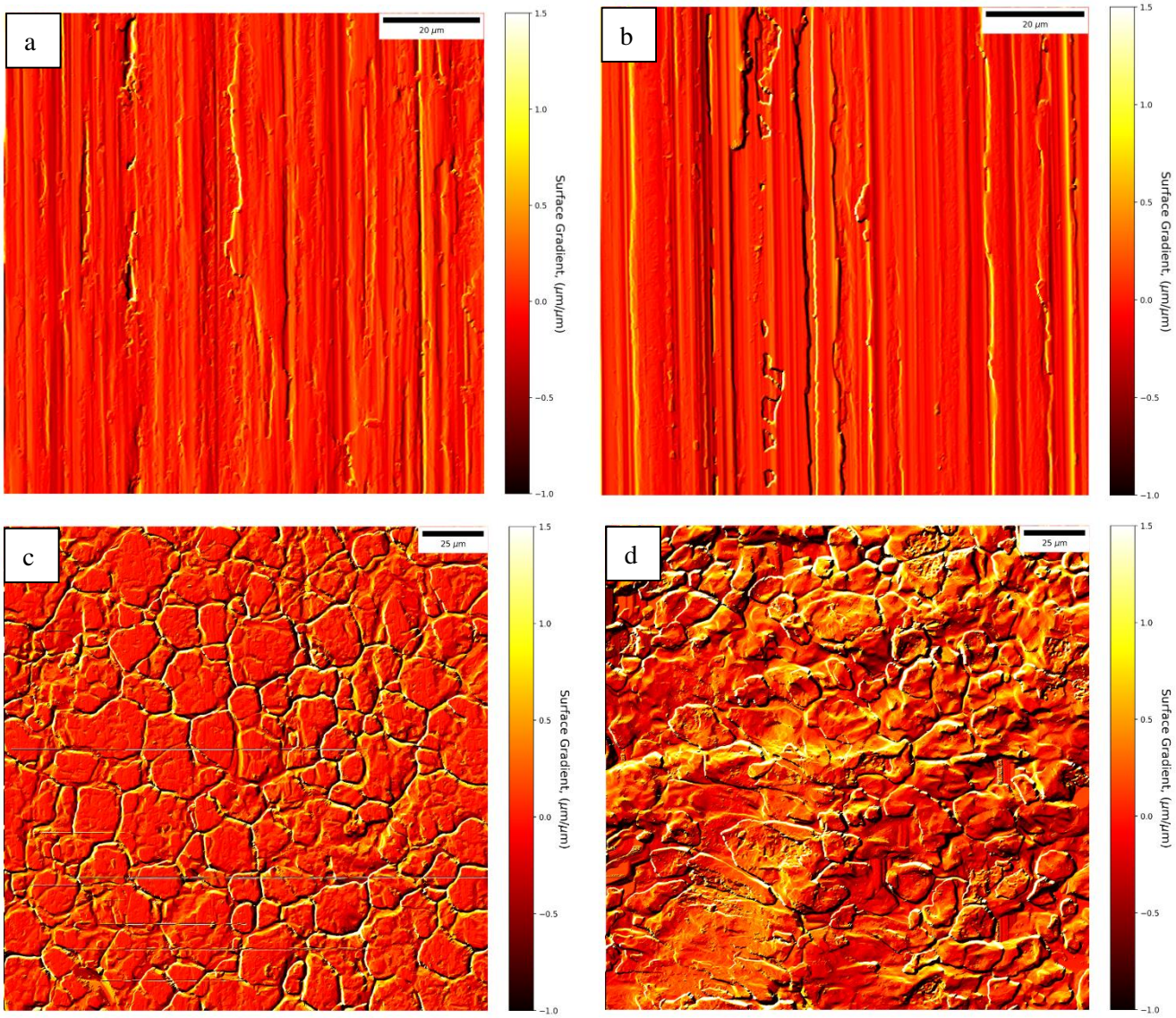

Figure 4.11 Surface Gradient Plots A brushed, B ground, C rolled, D shotblasted surfaces. (AFM).

The gradient plots look as though they were lit by a light source from the top left. This is because of the convention of arrays being positive in the right direction and the downwards direction, meaning that a slope increaseing in these directions is seen as having a positive gradient and vice versa. Most hybrid parameters take the absolute value for gradient, so this is effect is of no concern.

The values in these plots were then squared and divided by their amount before being square rooted to give the **Sdq**, which represents the root mean square surface slope, as described in Section 2.3.1. The Sdq for the four surfaces are shown in Table 4.3 for the VSI data and Table 4.4 for the AFM data. These are the mean values taken from 10 locations on the surface, with 95% confidence intervals given.

Table 4.3 Calculated Hybrid Parameters from VSI data. (95% CI).

	Brushed	Ground	Rolled	Shotblasted
Sdq °	19 (18, 20)	20 (19, 21)	30 (28, 33)	53 (51, 56)
Sds µm^{-2}	0.15 (0.15, 0.15)	0.18 (0.17, 0.19)	0.05 (0.04, 0.06)	0.17 (0.15, 0.18)
Ssc µm^{-1}	0.23 (0.20, 0.25)	0.21 (0.18, 0.23)	0.37 (0.32, 0.42)	0.71 (0.59, 0.83)
ISdq °	19 (18, 20)	20 (19, 21)	30 (28, 33)	53 (50, 56)
ISds µm^{-2}	0.17 (0.16, 0.18)	0.18 (0.17, 0.19)	0.20 (0.18, 0.21)	0.20 (0.17, 0.22)
ISsc µm^{-1}	0.24 (0.21, 0.27)	0.23 (0.20, 0.25)	0.71 (0.66, 0.76)	0.78 (0.69, 0.86)
Radius µm	5.8 (5.5, 6.1)	5.5 (5.2, 5.8)	5.4 (5.0, 5.8)	5.3 (4.5, 6.2)

Table 4.4 Calculated Hybrid Parameters from AFM data. (95% CI).

	Brushed	Ground	Rolled	Shotblasted
Sdq °	14 (13, 14)	17 (15, 16)	31 (28, 33)	51 (49, 53)
Sds µm^{-2}	0.10 (0.10, 0.11)	0.10 (0.10, 0.11)	0.08 (0.07, 0.09)	0.1 (0.09, 0.11)
Ssc µm^{-1}	0.11 (0.10, 0.12)	0.09 (0.08, 0.10)	0.34 (0.29, 0.39)	0.86 (0.72, 1.00)
ISdq °	14 (13, 14)	17 (15, 16)	31 (28, 33)	51 (49, 53)
ISds µm^{-2}	0.12 (0.19, 0.21)	0.12 (0.11, 0.13)	0.18 (0.17, 0.19)	0.14 (0.12, 0.16)
ISsc µm^{-1}	0.20 (0.19, 0.21)	0.20 (0.19, 0.21)	0.82 (0.75, 0.89)	0.56 (0.48, 0.64)
Radius µm	5.0 (4.7, 5.3)	5.0 (4.7, 5.3)	1.2 (1.1, 1.3)	1.8 (1.5, 2.1)

Table 4.3 and Table 4.4 shows that the ground and the brushed samples have a lower Sdq than the rolled and shotblasted surfaces. This was unexpected since the ground and brushed surfaces are entirely made up of ridges and valleys. As the measurement is root mean squared, it gives higher weighting to the larger values on a surface. This could be why the rolled surface and the shotblasted surface have higher Sdq values at around 30° and 50° than the brushed surface and ground surface at 15° - 20°. The rolled surface has steep, deep features between grains which have high slope angles. From Figure 4.11, these areas are steeper than a gradient ratio of 1.5, or 56°. The shotblasted surface has a rough surface at a resolution much smaller than the shotblasting craters. These features contribute highly to the average Sdq while the rather uniform and repeating slope distribution of the brushed and ground surfaces is lower than the extremes of the other two surfaces. As surface slope is linked to there being more closed, sheltered, locations, a higher Sdq is likely to indicate a higher propensity for corrosion.

The Sds values shown in Table 4.3 and Table 4.4 are broadly similar across the four surfaces with the exception of the rolled surface, which has a lower summit density, although there is also significant difference between the two measurement techniques. It is thought that summits are very dense, and that the requirement for them to be spaced out more than 1% of the measurement area has a large influence on the Sds parameter. Since summits have to be spaced further than 1% of the measurement area apart, for the 100 μm AFM measurement, a maximum of 250 summits could fit. This would limit the Sds to below 0.25 μm^{-2}. Considering also that the summits are not uniformly distributed, the maximum Sds is likely to be 0.1 μm^{-2}, which explains the calculated value for the AFM data.

Furthermore, this requirement is somewhat arbitrary since different size measurement areas could be made, potentially at a consistent resolution. Different Sds results would then be calculated for multiple images of one surface compared with one large, stitched image. Overall, this parameter, in this form, gives little use in comparing these surfaces with these constraints.

To calculate Ssc, curvature maps were calculated by taking the gradient of the gradient maps. The lists of summits calculated according to the rules used for the Sds parameter were then used to identify the locations of summits and record the curvature at each of these points before the mean average was taken. The shotblasted surface had the greatest Ssc at 0.86 μm^{-1} for the AFM data and 0.71 μm^{-1} for the VSI data. This value is dominated by the edges of grains rather than the larger curvature of the main peaks, since the gradient is calculated extremely locally for nearest neighbours only. This may explain why the rolled surface has the second largest Ssc of 0.34 μm^{-1} and 0.37 μm^{-1}. The ground and brushed samples both have much lower Ssc. This suggests that their peaks are more gradual compared with those created by etched grain boundaries.

4.4.2. The Inverse Hybrid Parameter

The standard hybrid parameters are used for tribology and sealing applications; however, the impact of these on corrosion is limited to the stress that may be experienced by sharper peaks influencing SCC. Since pitting corrosion is known to favour deeper, more enclosed areas it was more important to be able to characterise these areas rather than the surface peaks. The hybrid parameters applied to an inverted surface does this.

The **ISsc** (Inverse Summit Curvature) is the average curvature of the minima of the surface. Compared with Ssc, which likely has little to no bearing on corrosion, the curvature of the lowest points of the surface will likely have a great effect since this parameter directly affects local diffusion properties. Higher numbers indicate a faster changing curve with a smaller radius; in fact, the radius is equal to the inverse of the curvature and this is how valley root radius is calculated in Chapter 6.

Figure 4.12 shows the inverted height maps for the four surface finishes from the VSI data. These were used to calculate the inverse versions of Sds and Scc. Normally used for characterising the peaks of a surface, when inverted, these parameters characterise the lowest points of the surface, that is the minima or valley bottoms. For the height-inverted maps shown in Figure 4.12 and Figure 4.13, the minima and valleys become the peaks and high points of the surface, so that the parameters used to quantify peaks can be applied to these areas.

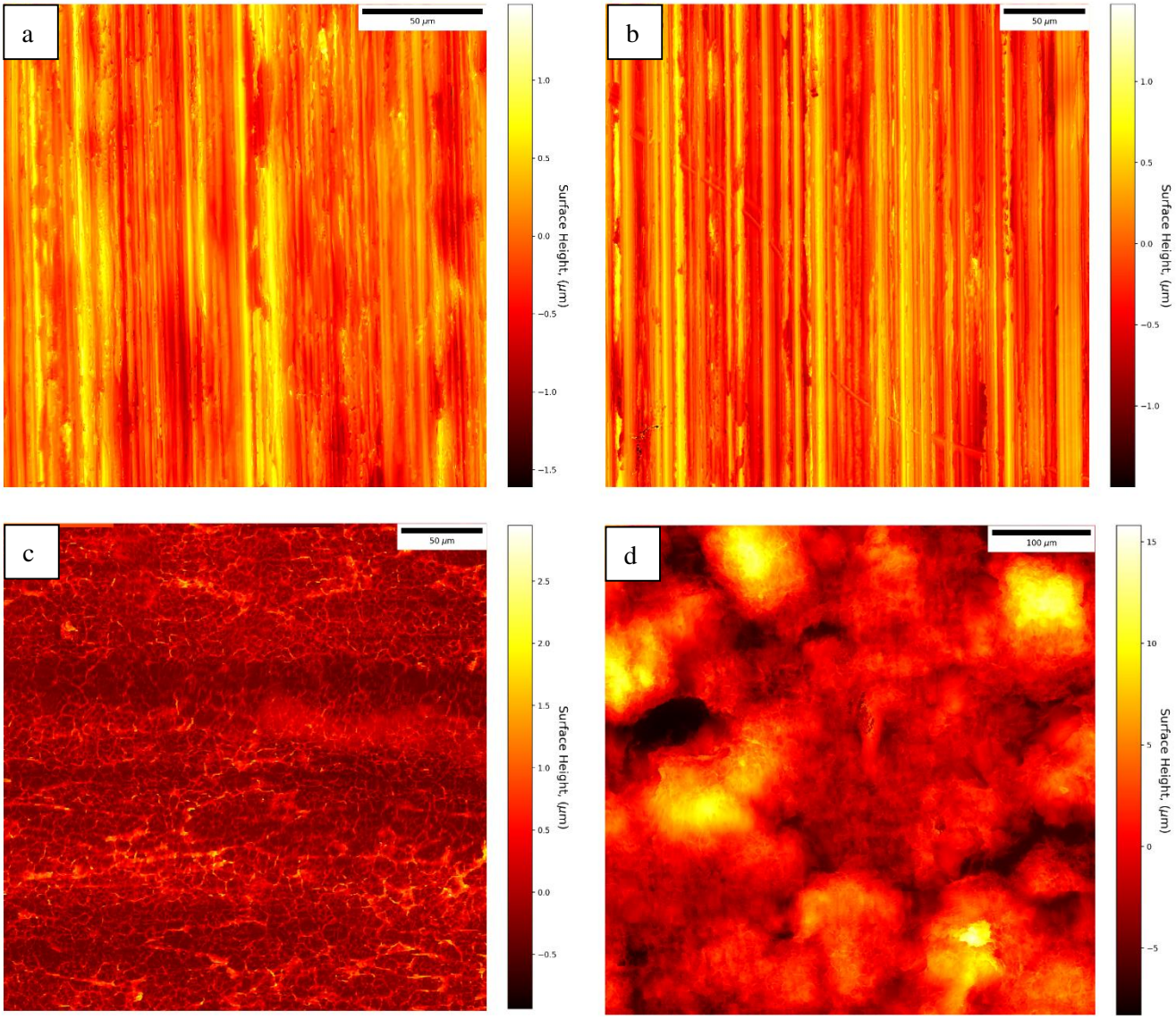

Figure 4.12 Inverted surface height maps for: A brushed, B ground, C rolled, D shotblasted surfaces.

Figure 4.13 shows the inverted height maps for the four surface finishes from the AFM data. Here, as in Figure 4.12, the bright areas denote the deepest points in the surface such as the spaces between surface grains on the rolled surface.

It can be seen that the inverted Sdq, the ISdq**,** for the inverted surface area are identical to that of the original surface Table 4.3. For any given point on the surface, the direction of the gradient will be flipped but the magnitude will be unchanged. The Sdq is a root mean square value, so only considers the magnitude of the slope.

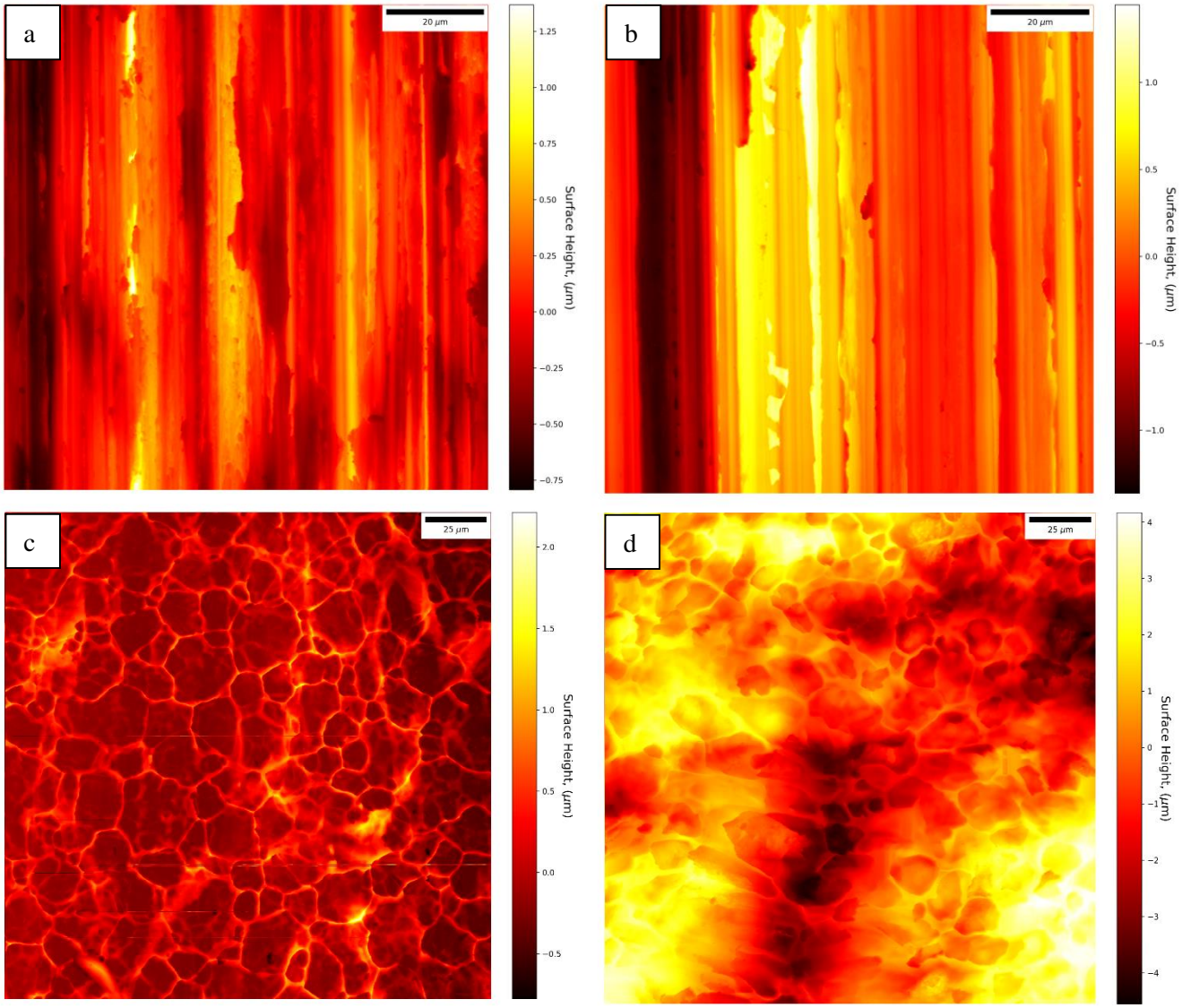

Figure 4.13 Inverted surface height maps for: A brushed, B ground, C rolled, D shotblasted surfaces.

The **ISds** (Inverse Summit Density) shows the density of minima of a given surface. It is calculated in the same way as the Sds; however, the calculation is performed on the inverted dataset. This means that low points on the surfaces, that are lower than their eight nearest neighbours, and spread at least 1% of the measurement area apart, are recorded in the ISds. For this parameter, the rolled surface is highest at 0.18 μm^{-2} for the AFM data in Table 4.4, 50% higher than the other surfaces. This contrasts with the Sds for the rolled surface, which is the lowest of the four surfaces, and this shows that this particular surface is better described as having a high density of minima rather than by the density of its peaks. These features are vulnerable points for pitting initiation and, coupled with a random distribution of inclusions such as MnS, a greater ISds will increase the chance of there being a vulnerable point in a given area of surface.

The inverse summit curvature (**ISsc**) value is greatest for the shotblasted and rolled surfaces. The rolled surface has an ISsc of 0.71 μm^{-1} for the VSI data and 0.82 μm^{-1} for the AFM data. The shotblasted surface has an ISsc of 0.78 μm^{-1} for the VSI data and 0.56 μm^{-1} for the AFM data showing a difference between the two methods. Despite this difference, it can be concluded that the ISsc is still much larger for the rolled surface and the shotblasted surface than the ground surface or the brushed surface.

The ISsc measures a characteristic that is similar to valley angle, or openness (discussed in Section 4.6.) and in most cases these values will correlate. However, there is an important distinction. The openness angle measures the maximum observable solid angle between two opposite horizons at a point on the surface, it can be affected by points far away, as long as they belong to the same feature. By comparison, the surface curvature considers only neighbouring points and so is extremely localised. The difference is highlighted in Figure 4.14 where two features with identical valley angle and openness have different curvatures at their minima. Figure 4.14b has a very sharp valley floor, whereas Figure 4.14a has a more rounded valley floor. It is likely that for locations with similar openness, the surface curvature will have a deciding impact on which will be more prone to corrosion.

Figure 4.14 Valley root radius.

The ISsc can be used to calculate the valley radius at the low points of the surface. Modelling a valley as a circle, the second derivative at the base of the valley is equal to the inverse of the radius. The brushed and ground surfaces have the largest radii (in their lowest points) at 5 µm Table 4.4. Despite having rough, sharp looking surfaces, the bottoms of valleys of these surfaces tend to be rounded; this might offer some protection from corrosion initiation.

The rolled surface has the smallest measured average radii at 1.2 µm with the shotblasted surface second at 1.8 µm Table 4.4. Both of these are due to the valleys found between grains, with these features overshadowing the larger craters of the shotblasted surface. These features are likely to encourage pit

initiation since they shelter the surface and slow diffusion. Additionally, these features could act as sites for stress concentrations, which is described in Chapter 6.

4.5. Functional Parameter Analysis

Functional parameters describe the nature of the extremes of the surface height; they are pertinent to how fluids such as lubricants are likely to interact with the surface. The calculation of these parameters is described in Section 2.3.1.

Figure 4.15 shows the bearing curves for the AFM data with Sk calculation markings for the four surface finishes. The curved blues lines denote the bearing curves, which present the surface height distribution. The straight solid black line on each diagram represents the flattest 40% of the curve, from which the line is extended to calculate Sk, Spk and Svk.

Table 4.5 and Table 4.6 show the results of the functional parameter analysis for each of the surface finishes, comparing VSI and AFM analysis methods. 95% confidence intervals are calculated from 10 measurements, these are relatively wide, but small enough to differentiate between surfaces.

The most pertinent of the functional parameters are those that measure the proportion of the valleys and other deep features of the surface. These features are Svi and Svk. For Svk, the shotblasted surface is significantly greater than the others, but this is only because the Sk parameters are in μm and are not normalised in the same way the surface bearing parameters are.

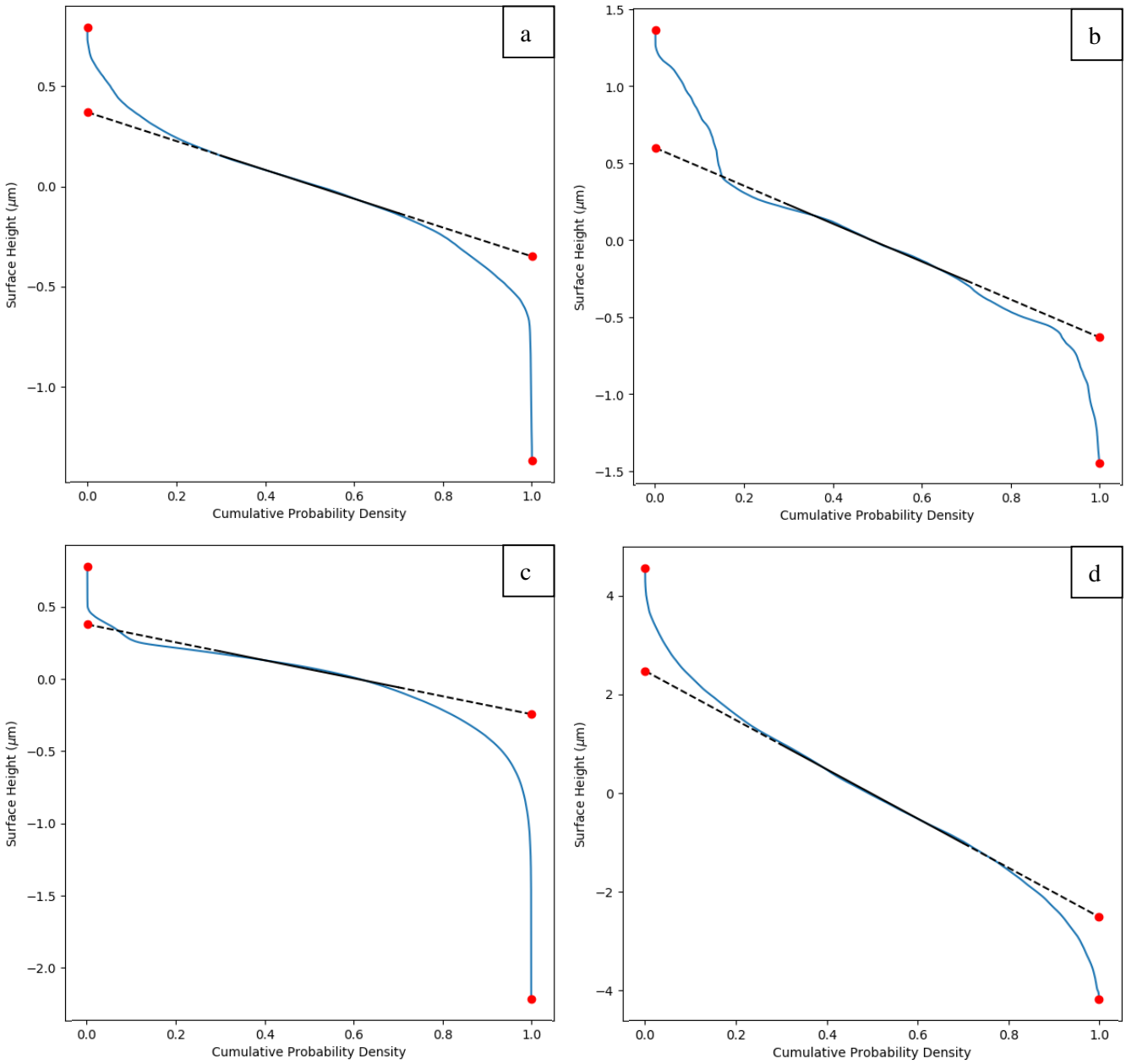

Figure 4.15 Bearing curves with Sk calculation markings for: A brushed, B ground, C rolled, D shotblasted surfaces. AFM data.

Table 4.5 Calculated Functional Parameters for each of the surface finishes, calculated from VSI data. (95% CI)

	Brushed	Ground	Rolled	Shotblasted
Sbi	0.22 (0.18, 0.26)	0.3 (0.26, 0.33)	0.54 (0.50, 0.58)	1.13 (1.10, 1.17)
Sci	0.02 (0.00, 0.06)	0.09 (0.00, 0.13)	0.18 (0.00, 0.21)	0.14 (0.00, 0.18)
Svi	0.03 (0.00, 0.06)	0.11 (0.07, 0.15)	0.19 (0.16, 0.22)	0.16 (0.13, 0,19)
Spk (µm)	0.3 (0.26, 0.74)	0.21 (0.17, 0.25)	0.08 (0.05, 0.11)	2.83 (2.80, 2.86)

Sk (µm)	0.76 (0.72, 0.80)	0.89 (0.86, 0.92)	0.73 (0.70, 0.77)	7.91 (7.88, 7.94)
Svk (µm)	1.2 (1.17, 1.23)	0.9 (0.86, 0.93)	1.2 (1.16, 1.24)	11 (10.97, 11.04)

Table 4.6 Calculated Functional Parameters for each of the surface finishes, calculated from AFM data. (95% CI)

	Brushed	Ground	Rolled	Shotblasted
Sbi	1.04 (1.01, 1.08)	1.77 (1.74, 1.81)	0.71 (0.67, 0.74)	1.07 (1.05, 1.10)
Sci	0.11 (0.07, 0.15)	0.07 (0.03, 0.11)	0.16 (0.13, 0.10)	0.09 (0.06, 0.13)
Svi	0.12 (0.08, 0.15)	0.08 (0.05, 0.10)	0.17 (0.14, 0.21)	0.1 (0.08, 0.12)
Spk (µm)	0.27 (0.24, 0.30)	0.73 (0.70, 0.76)	0.09 (0.06, 0.12)	1.22 (1.19, 1.25)
Sk (µm)	0.72 (0.68, 0.75)	1.23 (1.19, 1.26)	0.62 (0.59, 0.65)	4.98 (4.95, 5.00)
Svk (µm)	0.3 (0.27, 0.34)	0.5 (0.46, 0.54)	0.5 (0.49, 0.55)	1.2 (1.18, 1.24)

The relatively flat 40% line of the rolled surface shown in Figure 4.15 shows that the majority of the surface lies within a very narrow height range compared with the total range of the surface heights. This is consistent with previous descriptions of the surface: that it is a very flat, relatively smooth surface with deep valleys between grains. The rolled surface has an Spk of around 0.1 µm which is very small. This shows that peaks on the surface do not reach far from the core roughness range of Sk = 0.6 – 0.7 µm. Contrary to this, the reduced valley depth, Svk, is large at 0.5 – 1.2 µm. This is indicative of surface features such as valleys that are deep and have steep sides that slow the diffusion of aggressive ions, potentially creating the conditions for pit initiation and stable pitting.

For Svi, the rolled surface has the greatest value. This parameter quantifies the proportion of the empty space enclosed by the surface, and it shows that proportionally, the rolled surface has more of its surface as features that enclose space below the average surface height. This parameter also describes how well a surface holds fluids and, by extension, potentially its tendency for under-droplet corrosion. This may also increase the number of potential pitting sites by increasing the chance that a MnS inclusion is found exposed in a valley. This would be expected to increase the density of pitting, however the Svi gives little indication of what the nature of these valley sites are, for instance how open they are to the

environment, which has an important effect. The other surfaces have lower, but more similar Svi's around 0.1, as shown in Table 4.5.

The surface-bearing curve for the shotblasted surface is steep, indicating that the surface varies relatively evenly and consistently. The Spk and Svk are higher compared to the other surfaces, but as a proportion of Sk they are smaller.

4.6. Surface Openness Analysis

It has been suggested that the openness of features on a surface contribute to pitting potential, with more closed surfaces consisting of steeper gradients being more prone to corrosion [11], [20]. This effect is either due to the features attracting or retaining more aggressive ions or by slowing mass diffusion in the same manner as a pit.

4.6.1. Openness Mapping and Surface Distribution Results

Figure 4.16 shows the openness map for the brushed surface, with the height map for comparison. In this graph, the surface openness is displayed in degrees by colour according to the scale bar. Perfectly flat regions have an openness of 180° and are displayed as a pale yellow. The more enclosed regions are darker with red regions having an openness of around 110° and black regions 80° and below. The most closed regions of the surface lie at the bases of valleys and so the diagram looks similar to that of a height map. Longer wavelength surface height deviation is removed by this process. The larger valleys and ridges are removed showing that the smaller deviations have a greater impact on the openness at a given point. High points on the surface have an openness of 180°, and at these points diffusion in the electrolyte is uninhibited by surface morphology. Aggressive concentrations of Cl and oxygen scarcity caused by small fluctuations in potential and pH will be unstable and diffuse quickly. Aggressive corrosion conditions are unlikely to develop here and so these areas are somewhat protected by their location.

The deepest points in the brushed surface shown in Figure 4.16 are the holes found in the deep groove (features indicated by arrows). These low points are 1.25 μm below the average surface height and are also the points most enclosed at 80 - 100°. These are actually the most open of the most extreme points

over the four surfaces. It is possible that the full depth of the holes has not been probed by the AFM probe in this measurement area. If the probe reached as far as its z-range allowed and recorded that value across the width of the hole, it is possible for there to be a large underestimation of the enclosedness.

The other type of feature that contributes to the enclosedness of the surface is the folded over regions. These areas register as more closed than average at 100 - 120°. AFM, like VSI, only measures with a top down method and so features that bend over horizontally may be much more closed when viewed from the side and are therefore underestimated by this method.

Figure 4.17 is a magnified section of Figure 4.16 (shown by the black box in Figure 4.16), which shows the particles present on the brushed surface. They appear to have been transported from elsewhere on the surface and register very low openness around them. This is an important result since these particles will overhang somewhat and therefore could be responsible for the most closed areas of the surface. The estimation of the magnitude of the openness at these points is difficult since modelling these particles as cuboid would give angles of 90° and modelling as spheroidal would give angles of 0°.

Figure 4.18 shows the openness distribution for the ground surface. Like the brushed surface, this surface contains folded over regions that are responsible for the most extremely enclosed regions. Both have a very similar distribution of openness with only a small portion of the surface registering as very closed (<120°).

It was initially predicted that the valleys caused by grinding or brushing, whether formed by the removal of material, or by the ploughing of material, would be the source of the most enclosed areas. From these diagrams it can be seen that these features have an openness of 160°. This is not particularly closed, especially compared with the rest of the surface. Both surfaces have openness values as low as 90 – 100°, which are not found at the bottom of valleys but at the edges of smeared, folded over, or transported material. The openness of these areas is also highly likely to be underestimated due to their horizontality.

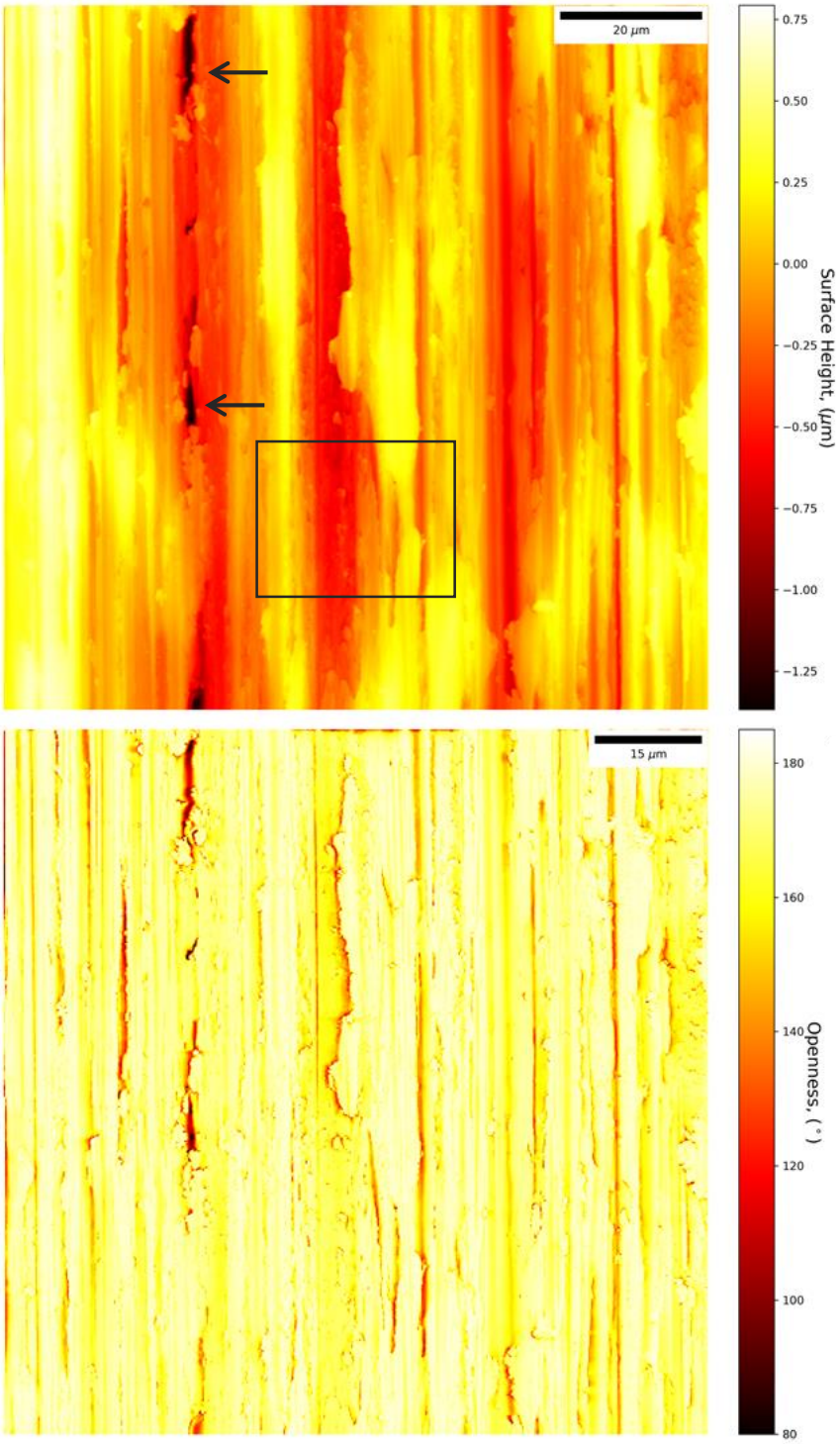

Figure 4.16 Surface height map (top) and corresponding openness map (bottom) for a brushed surface, AFM data.

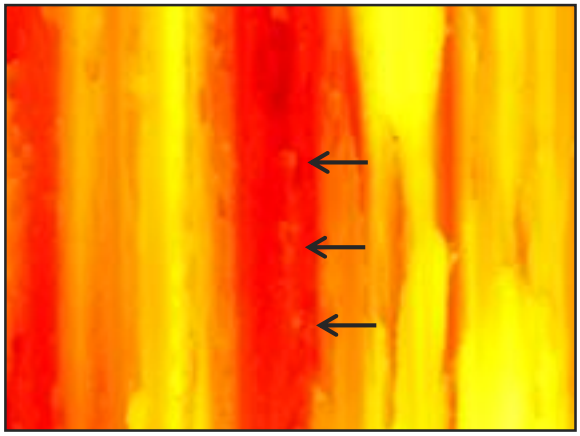

Figure 4.17 Particles on a brushed surface.

Figure 4.19 shows the openness distribution for the rolled surface. Highly enclosed areas are common across the surface between grains. These areas on this surface frequently have openness values below 90°, making it, at this scale, far more enclosed than the brushed or ground surfaces. It is clear that pickling has an important influence on the openness of the surface.

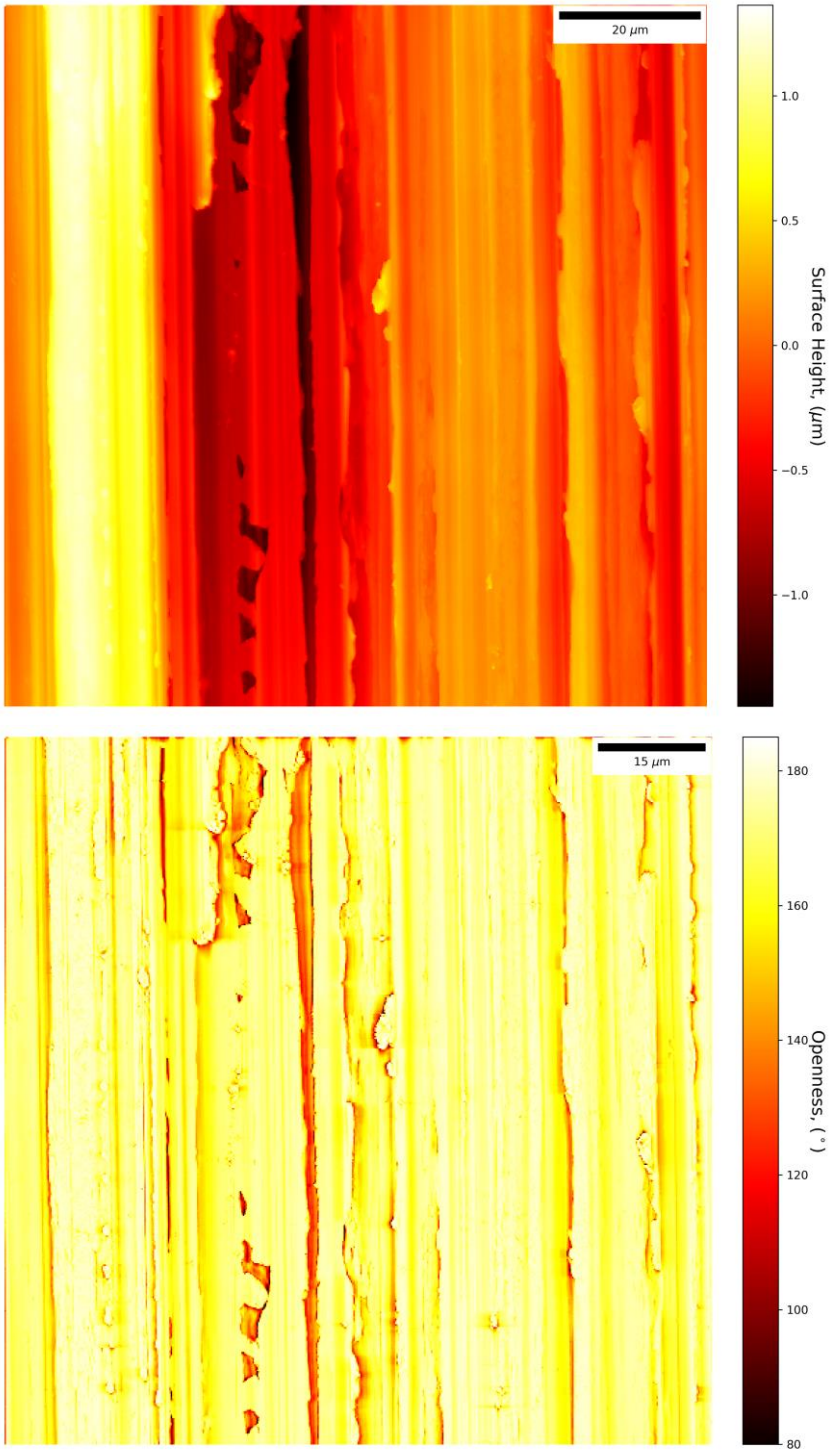

Figure 4.18 Surface height map (top) and corresponding openness map (bottom) for a ground surface, AFM data.

On some of the grain boundaries shown in Figure 4.19, small indents are observed with openness angles of around 100°. These features possess the same magnitude of openness as the grooves on a ground or brushed surface.

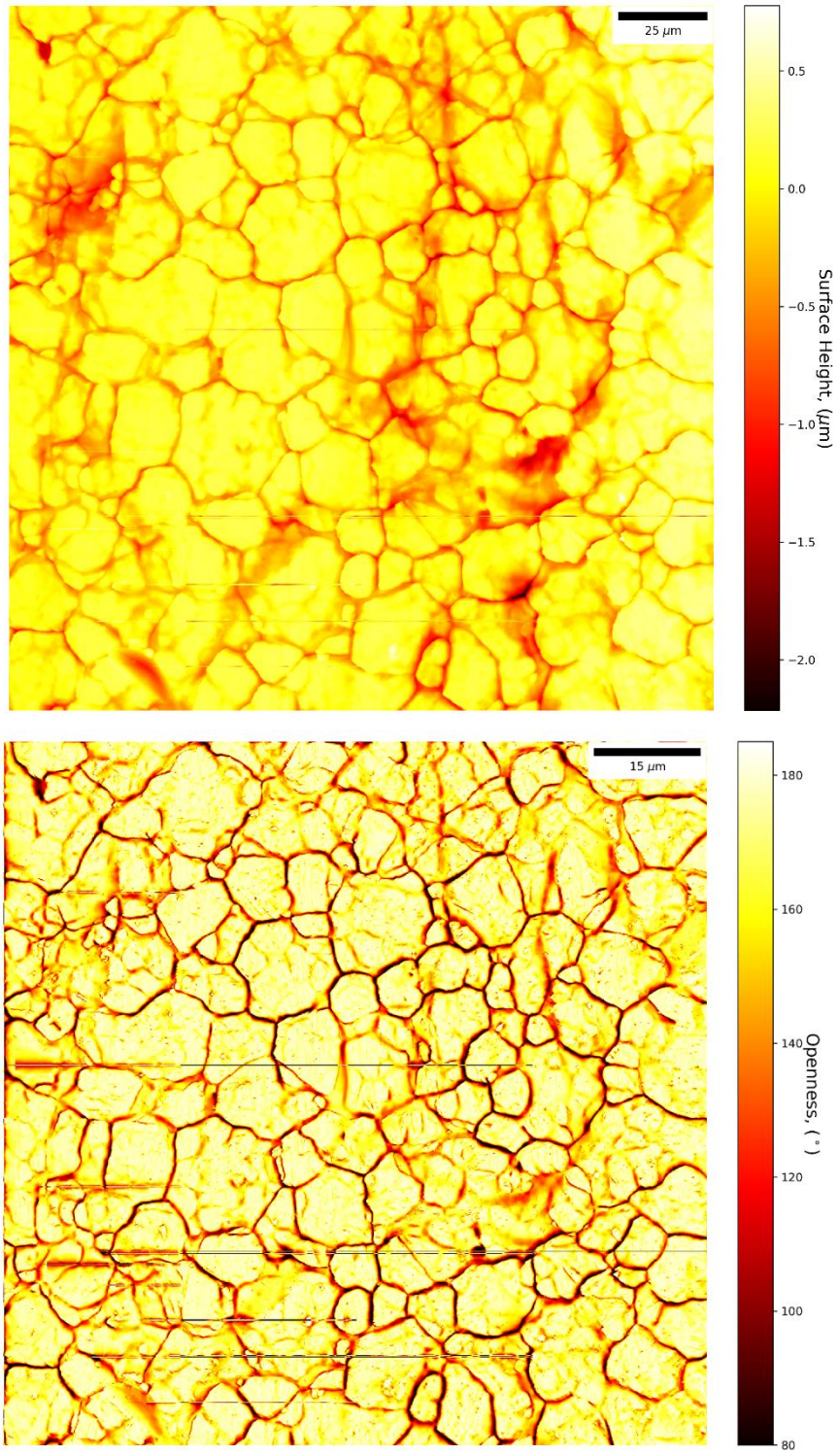

Figure 4.19 Surface height map (top) and corresponding openness map (bottom) for a rolled surface, AFM data.

The openness distribution for the shotblasted surface is shown in Figure 4.20. This surface is more varied than the others, with some areas etched grain boundaries while others do not, and the nature of the surface grains can be somewhat distorted. The initial observation is that the major features on the shotblasted surface caused by the shotblasting, i.e. the craters, are not apparent in the openness diagram.

At a macroscopic-scale the craters cause the surface to be matte, and from the height map, it can be seen that they are considerably deep, at -4 μm compared to features around -1 μm for the other surfaces. However, they are also quite wide at >50 μm. Since openness as defined here is the ratio of the two, the contribution from the craters is minor. Instead, the surface openness distribution is dominated, much as the rolled surface, by the etched grain boundaries. These have been warped and compressed by the shotblasting process and so the gaps between grains can be narrower than for the rolled surface, leading to much more enclosed areas on this surface at around 60°.

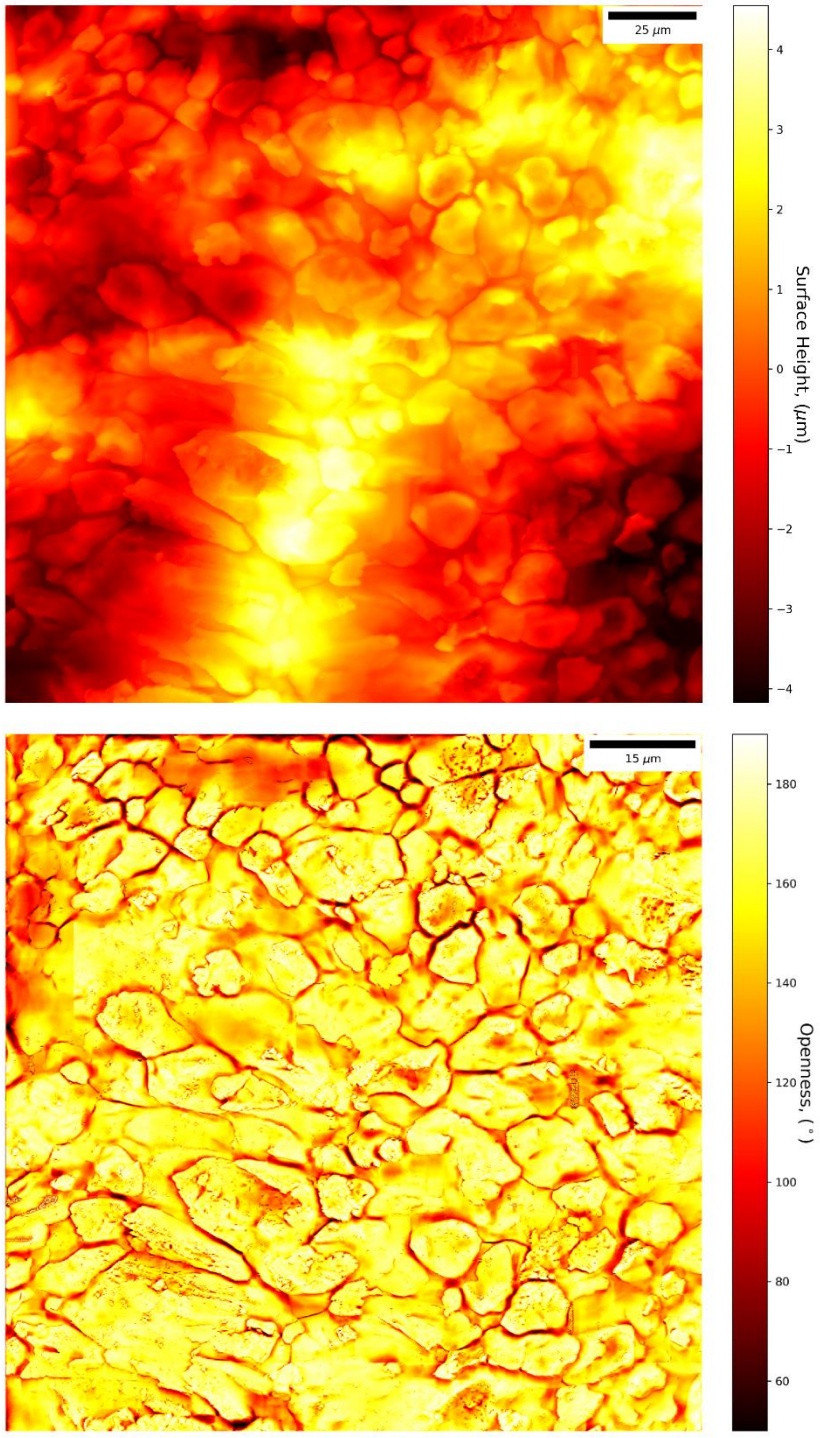

Figure 4.20 Height map (top) and corresponding openness map (bottom) for a shotblasted surface, AFM data.

Should openness play an important role in corrosion initiation and the transition to metastable pitting, the surface density of closed areas is likely unimportant compared to the range of the openness distribution. If one surface has many fairly closed areas, and another has fewer, much more closed, areas, the later will be expected to pit first, and reach metastable pitting faster. For this reason the openness distributions obtained from AFM data are displayed in Figure 4.21. The rolled and the shotblasted surfaces (Figure 4.21c and d) have much thicker tails indicating the presence of more enclosed regions. The peak for the shotblasted surface is at a lower angle, at 170°, whereas openness for the other surfaces tend to peak much closer to 180°.

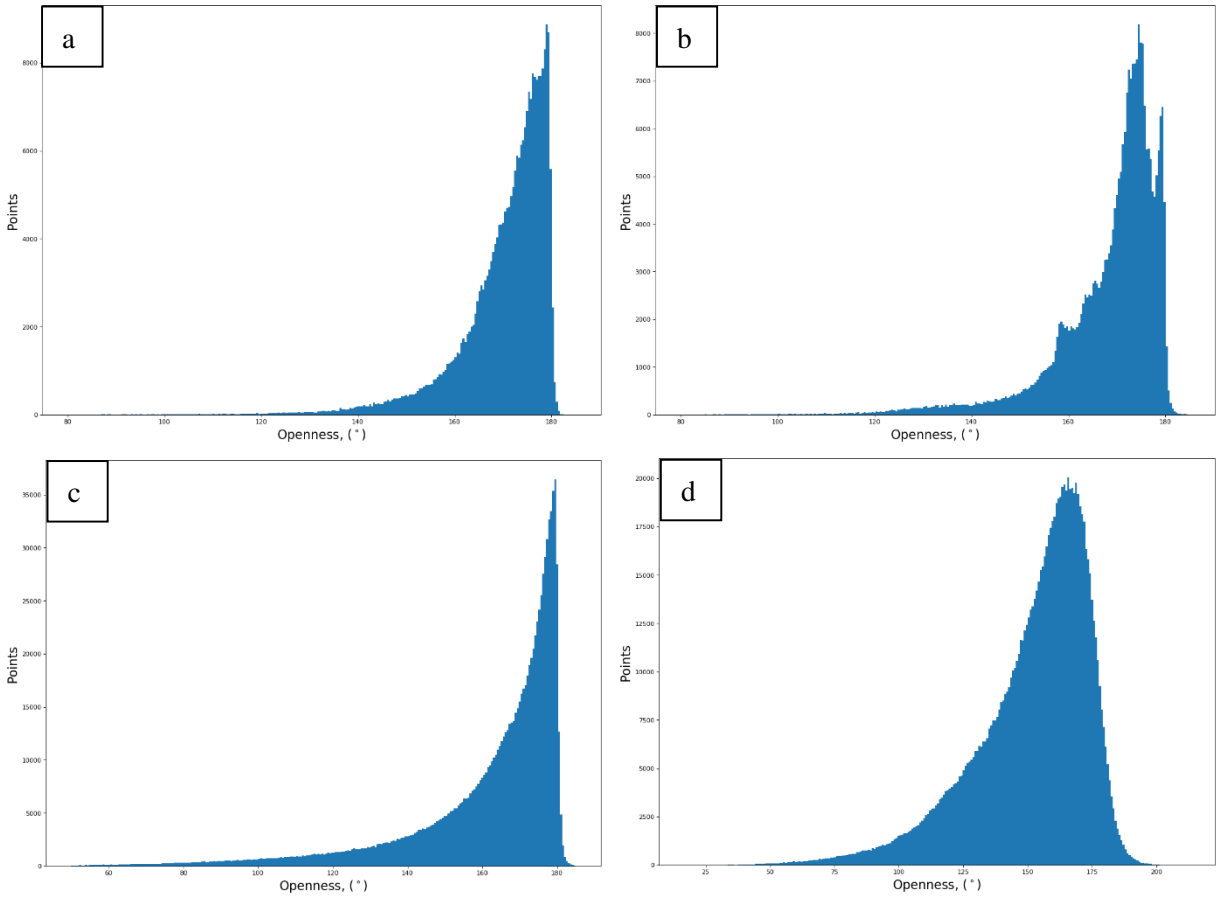

Figure 4.21 Distributions of surface openness values for: A brushed, B ground, C rolled, D shotblasted.

The openness parameter is distinct from the gradient, as shown in Section 4.4., in a few ways. Firstly, the maximas and minimas for each type of map is offset by half a phase. For instance, the largest gradients will appear on steep slopes, which needn't be very enclosed at all. In comparison, the most enclosed areas, and the most open areas, are at surface minima and maxima respectively, where the gradient is zero for both.

Additionally, while steep slopes do increase the likelihood that a surface will contain more enclosed areas, they do not guarantee it. The rolling surface of the shotblasted sample has steep slopes around shotblast craters, however these are well exposed and do not register nearly as enclosed as the etched grain boundaries of the rolled surface.

4.7. In-Situ Corrosion Study

4.7.1. In-Situ Corrosion Method

To test the hypotheses developed throughout this Chapter, regarding the potential role of surface parameters on the corrosion behaviour of the four different surfaces, surface retreat during pseudo-in-situ surface corrosion was quantified using VSI.

Samples of the four surface finishes were sectioned by water-jet into 6mm square pieces and affixed with superglue onto glass microscope slides as described in Chapter 3. Small bolts (M3 X 10mm) were affixed to the sample stage of the Contour GT VSI. This allowed for the repeatable positioning of the glass slides onto the stage with identical location and rotation. This enabled differential imaging to be conducted. Samples were imaged in position by VSI before being removed from the stage, replaced back onto the stage, and reimaged. This allowed for the estimation of the magnitude of image difference caused by small changes in sample position, which would be used as an estimation of the error associated with the differential imaging technique.

Samples were corroded by pipetting 0.1 ml of 37% HCl onto the surface, forming droplets. The contact time was 5 mins, after which time the sample was rinsed in deionised water, air dried, replaced onto the VSI stage and re-imaged. HCl was chosen as previous trials had showed it measurably corrodes stainless steel within a reasonable timescale and does not allow large amounts of corrosion product to form on the surface, which would obscure the surface height measurements. Additionally, it did not degrade the glass slide or the superglue that affixed the sample. Optical microscopy analysis (data not shown) indicated that surface discolouration should be expected to occur at around 10 mins of exposure and recognisable corrosion at 20 mins. For this reason, measurements were taken at 7 time points, each separated by 5 mins, adding up to 30 mins of exposure. The expected anodic reaction was the oxidation

of iron to Fe^{2+}, and the cathodic reaction was the reduction of H^{+}. In addition, it was expected that iron would also be oxidised to form iron chloride and then undergo hydrolysis.

To repeatedly find identical surface location after each exposure, images were taken of the surface at a range of magnifications. This allowed for the matching of the location at higher magnifications, using the previous images as a map, before increasing the magnification, finally completing the scans with the 50X objective. Since the surface structure was affected by corrosion and changed between each measurement, these images were retaken at each time interval as the surface was recognisable to itself 5 mins prior, but not past 15 mins. This method allowed for a very high degree of accuracy, with < 3 μm of sample movement between scans.

4.7.2. In-Situ Corrosion Differential Imaging

To analyse the data, relief maps were plotted highlighting the difference in surface height before and after corrosion. To calculate the difference in height between two time points (i.e. the retreat rate), the surface heights were normalised by normalising the average peak height (top 5% of the surface) to zero for all measurements. This method assumes that corrosion on the surface will not be uniform, and that the surface will only be in retreat, and not advance, through the formation of corrosion products. It also assumes that around 5% of the surface will not retreat at all. This was necessary as no standard height reference was used.

Figure 4.22 shows the effect of corrosion on the brushed surface. Figure 4.22a and b show retreat across large areas of the surface, albeit missing some of the highest points. Additionally, the surface becomes rougher as quantified in Section 4.7.4. Figure 4.22c shows the openness parameter of the surface, highlighting that the most enclosed regions lie in the bottoms of valleys and especially along folded-over parts of the surface, which suggested these regions would be most vulnerable to corrosion. Figure 4.22d shows the surface height difference between Figure 4.22 a and b. This shows a surface retreat of around 3 μm for the worst affected areas. Figure 4.22d shows corrosion occurring across the whole surface, with an increased amount found to occur in deeper areas. This map correlates with the openness map in many areas, but there are clearly some enclosed areas visible in Figure 4.22c that are not greatly affected by corrosion.

This surface was largely unrecognisable after 30 mins. The corrosion craters seen in Figure 4.22b indicate that this surface has corroded quickly compared to the other surfaces. While corrosion has occurred more in the deeper regions, the areas of greatest corrosion do not correlate with any features visible in the initial height map or openness map. They are likely the result of increased corrosion around underlying grain boundaries, the location of which cannot be predicted by the surface morphology.

Figure 4.23 shows the corrosion of the ground surface. After 30 mins much of the original surface structure is still recognisable, although it is rougher and highly damaged. Overall, corrosion is largely uniform across the surface, as shown by Figure 4.23d, although some features have clearly corroded more rapidly than others. For instance, central to the measurement area is a groove that appears to have missed the grinding process: it is deeper than the surrounding material and is partly covered by smeared material. Despite being deeper, it has not corroded at a faster rate. Instead, the overhanging smeared material is corroded in the direction of the groove. This has resulted in the largest amount of corrosion on this surface at a retreat rate of 1.5 µm / 30 mins, which is the depth of this feature.

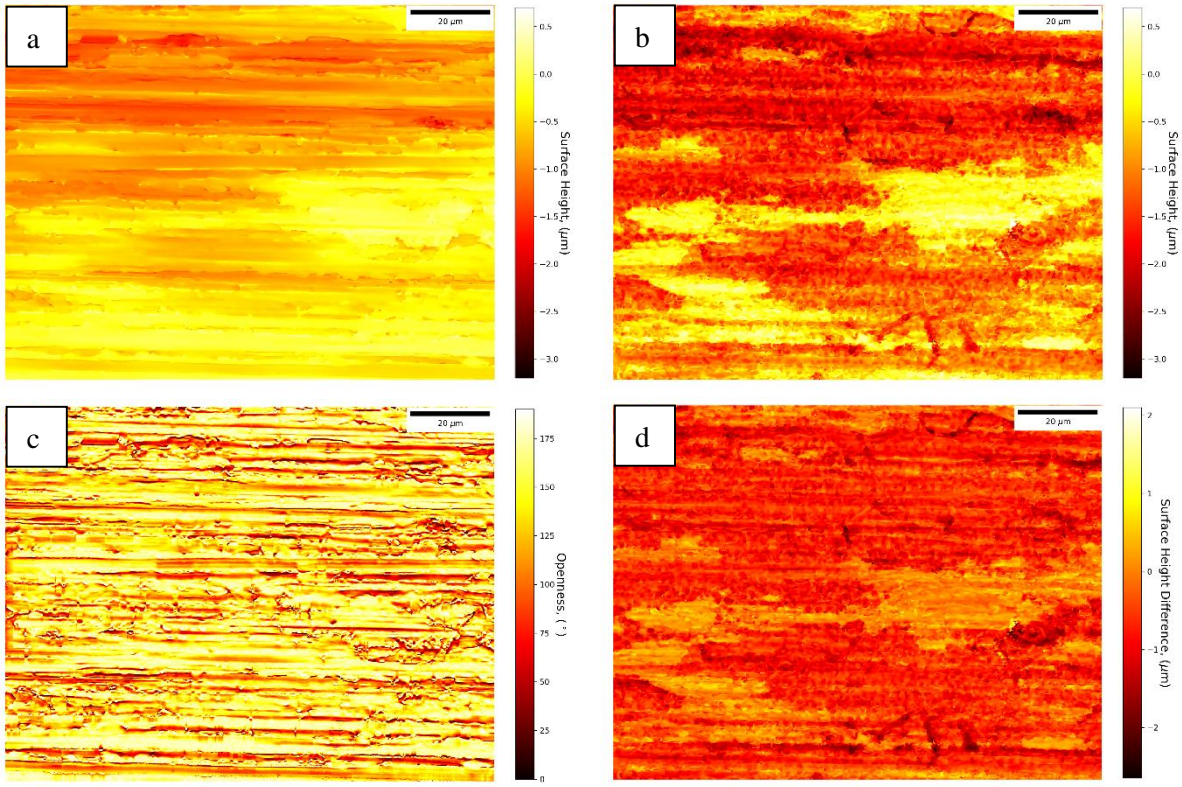

Figure 4.22 VSI images of a brushed sample, before (a) and after (b) 30mins exposure to 37% HCl. The openness parameter of the surface (c) and the surface height difference (d) are shown.

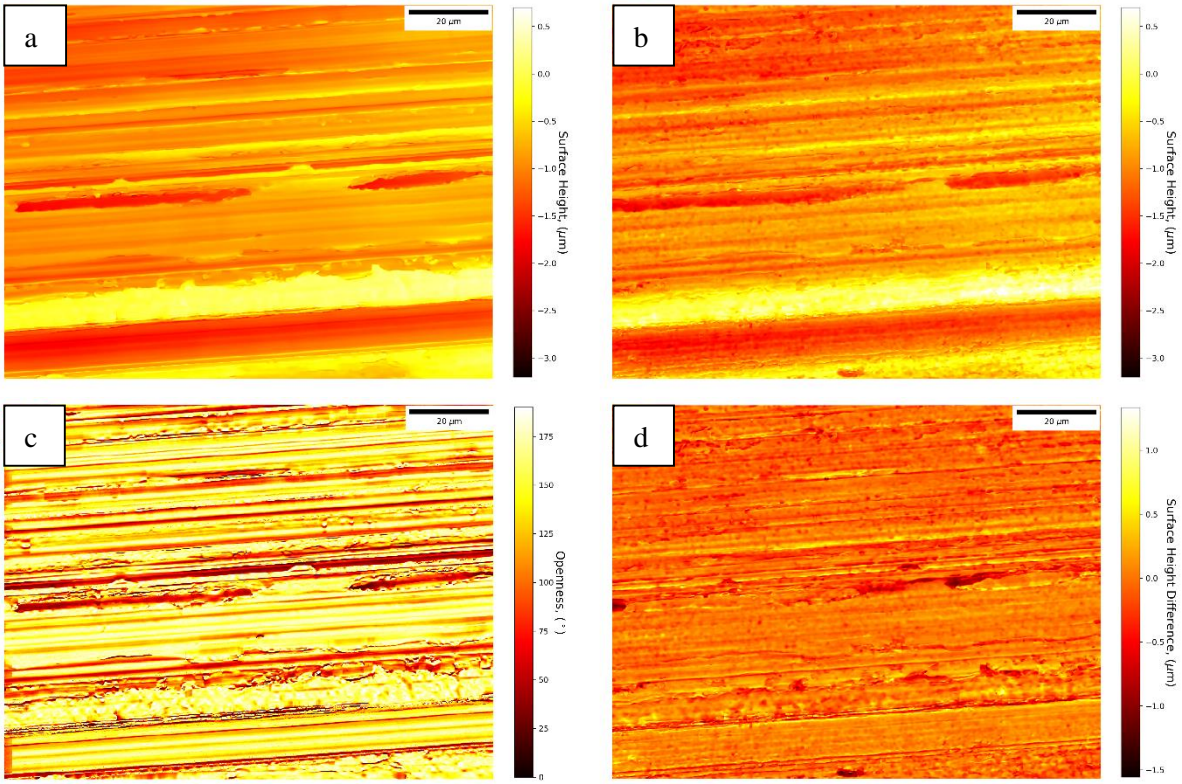

Figure 4.23 VSI images of a ground sample, before (a) and after (b) 30mins exposure to 37% HCl. The openness parameter of the surface (c) and the surface height difference (d) are shown.

Figure 4.25 shows the corrosion of the rolled surface. Corrosion, as quantified in Figure 4.25d is mostly limited to grain boundaries, which may indicate a chromium depleted layer. These features deepen and widen faster than the surrounding surface retreats, indicating intergranular corrosion and potentially supporting the hypothesis that the more enclosed features highlighted in Figure 4.25c accelerate corrosion.

Figure 4.24 shows the corrosion of the shotblasted surface. Similar to the rolled surface, preferable corrosion is observed at grain boundaries, the most corrosion, however, is found on the edge of the central flat peak feature. It is likely that this area of highly localised corrosion was an overhanging feature made of thin material.

Deductions made from plotting the openness suggested that the large craters (14 µm deep) found in the shotblasted surface in this measurement area would not contribute to an increase in corrosion in these areas since they were far too open when compared to the smaller features. This is consistent with the surface height retreat observed since these craters are not discernible in Figure 4.24d.

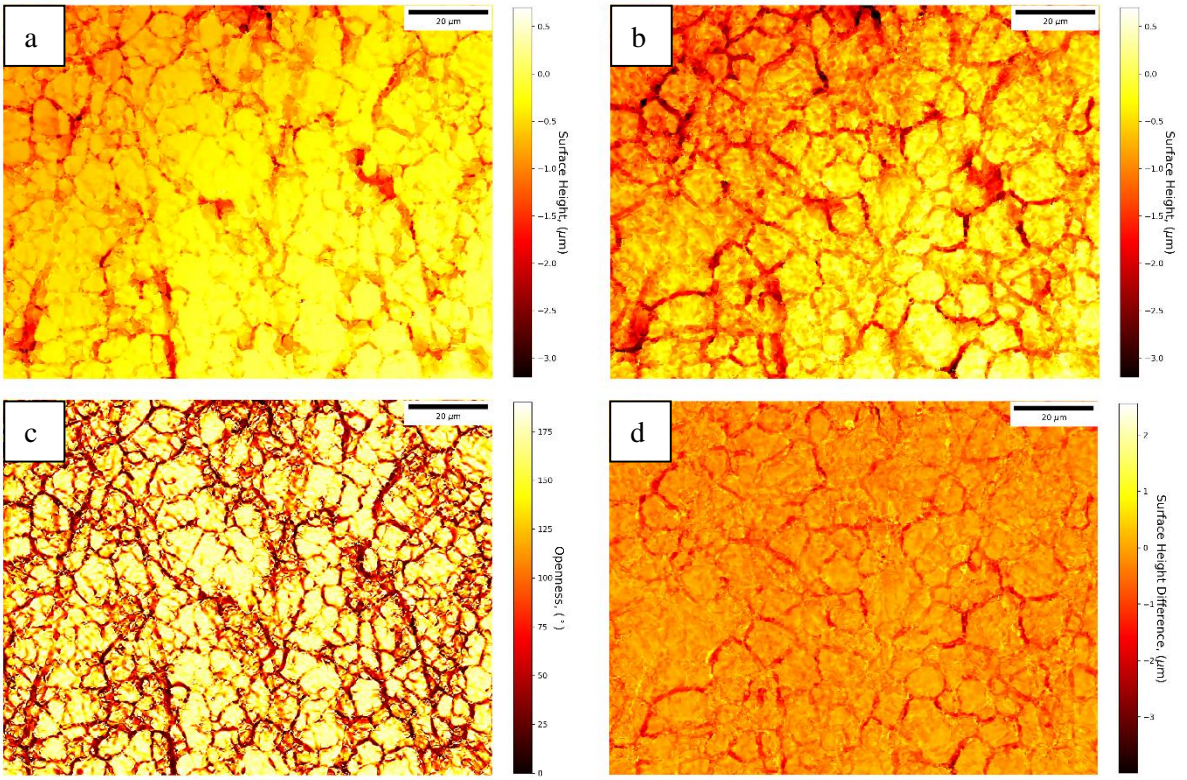

Figure 4.25 VSI images of a rolled sample, before (a) and after (b) 30mins exposure to 37% HCl. The openness parameter of the surface (c) and the surface height difference (d) are shown.

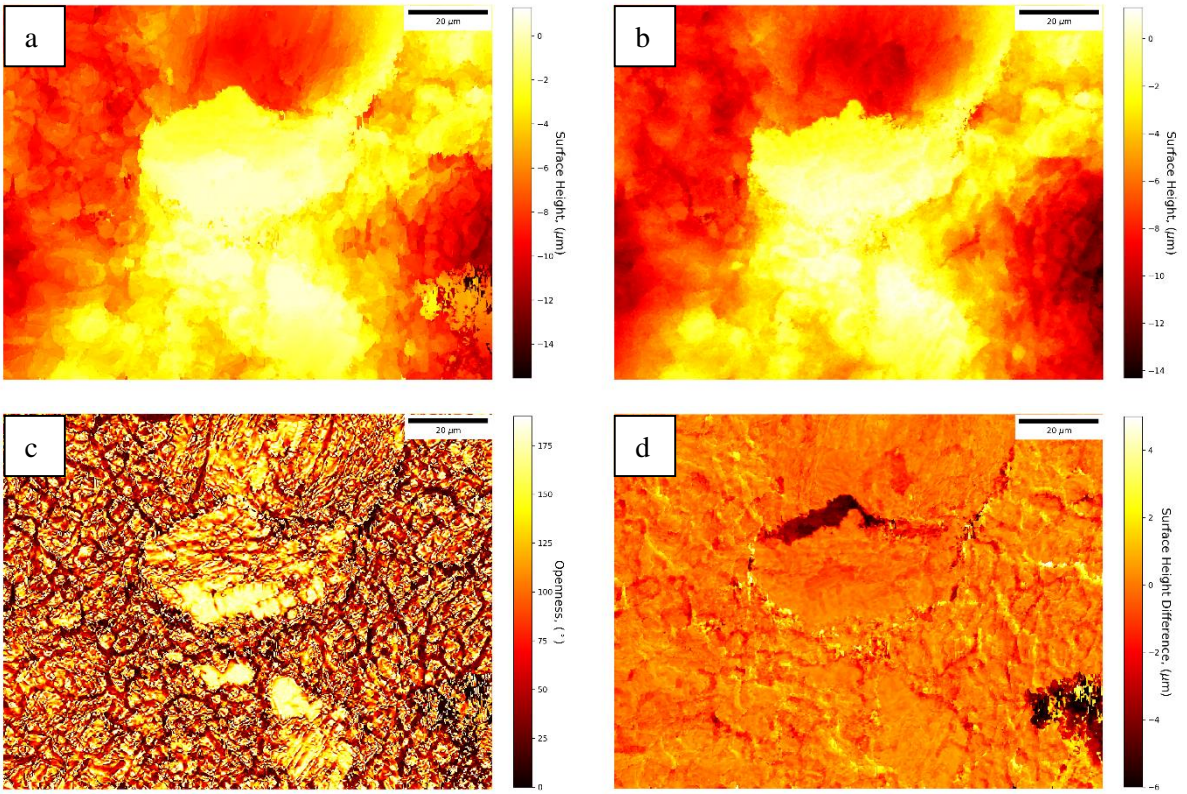

Figure 4.24 VSI images of a shotblasted sample, before (a) and after (b) 30mins exposure to 37% HCl. The openness parameter of the surface (c) and the surface height difference (d).

4.7.3. In-Situ Corrosion Rate Quantification

Figure 4.26 shows the surface volume loss rate for each surface finish. Volume is presented with regard to a 100 µm / 100 µm (10,000 µm^2) square section of the material. A steeper line indicates faster corrosion. In general, the straight lines show constant volume loss rates with time. The brushed surface lost the most material at 5,300 µm^3, around double that of the rolled and the shotblasted surfaces at 2,500 and 1,700 µm^3, respectively. The ground surface showed the minimum volume loss at around 200 µm^3.

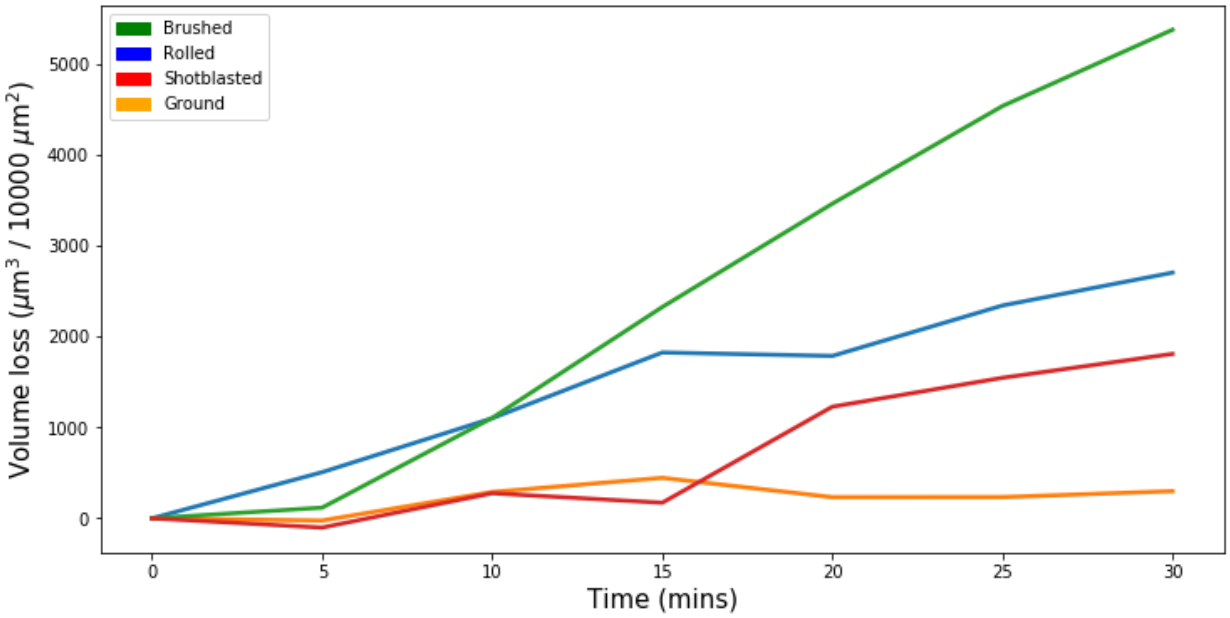

Figure 4.26 Volume loss over time for four surface finishes.

The corrosion rate of each surface was obtained by calculating the gradient of each volume loss curve for the whole duration of the experiment. The results are given in Table 4.7, in nm per min. The rates increase in the order: Ground < Shotblasted < Rolled < Brushed. A higher rate indicates faster corrosion, for example Table 4.7 shows that the brushed surface corroded at an average rate of 18 nm into the surface each minute.

Table 4.7 Corrosion rates of surface finishes in HCl

	Rolled	Ground	Brushed	Shotblasted
Corrosion rate (nm/min)	8.3	0.67	18	5.7

Figure 4.27 shows the development of corrosion on the brushed surface and the ground surface for each of the time intervals. Side by side they facilitate comparison. The ground surface is smoother and more continuous than the brushed surface, and it remains this way for far longer.

Overall, corrosion in HCl is shown to be general, attacking the whole surface simultaneously. This makes it useful for identifying morphological and physiochemical effects. One such effect shown here is the preferential corrosion at grain boundaries which be seen in the brushed surface from 15 min onwards in the form of short, curved, lines appearing on the surface. The corrosion of the surface progresses from an initial surface corrosion phase where the original surface is recognisable to a secondary phase where bulk corrosion develops. From this trial it can be seen that the ground surface remains in this initial phase for longer, affording better protection to the underlying material.

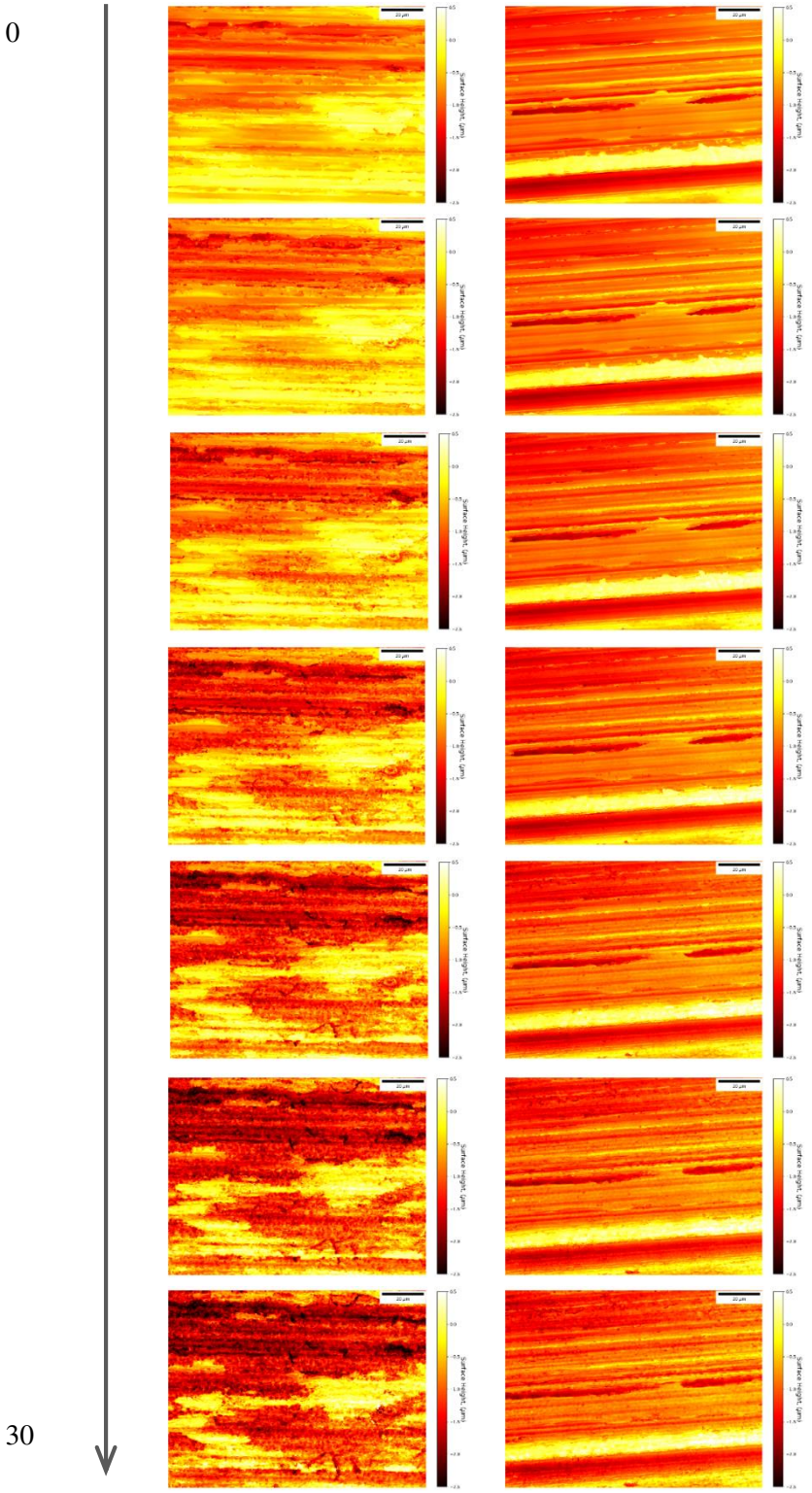

Figure 4.27 Surface retreat under HCl for a brushed surface (left) and a ground surface (right). Measurements taken in 5min intervals starting from 0 mins (top) to 30 mins (bottom).

Figure 4.28 shows how the surface corrosion developed for the rolled and the shotblasted surfaces. The intergranular corrosion of the rolled surface is clearly apparent. Additionally, presented incrementally, the constant rate of corrosion is apparent, as there are no sudden increases between time increments. The etched grain boundaries consistently become deeper and wider, while the flat areas show little to no sign of corrosion at all.

For the shotblasted surface in Figure 4.28 the state of the intergranular corrosion is more difficult to determine since the height of the peaks and depth of the craters dominates the figure. The sideways corrosion of the flat topped peak from the top of the image is clear. Other than this, the state of the flat top and the state of the crater shows little change.

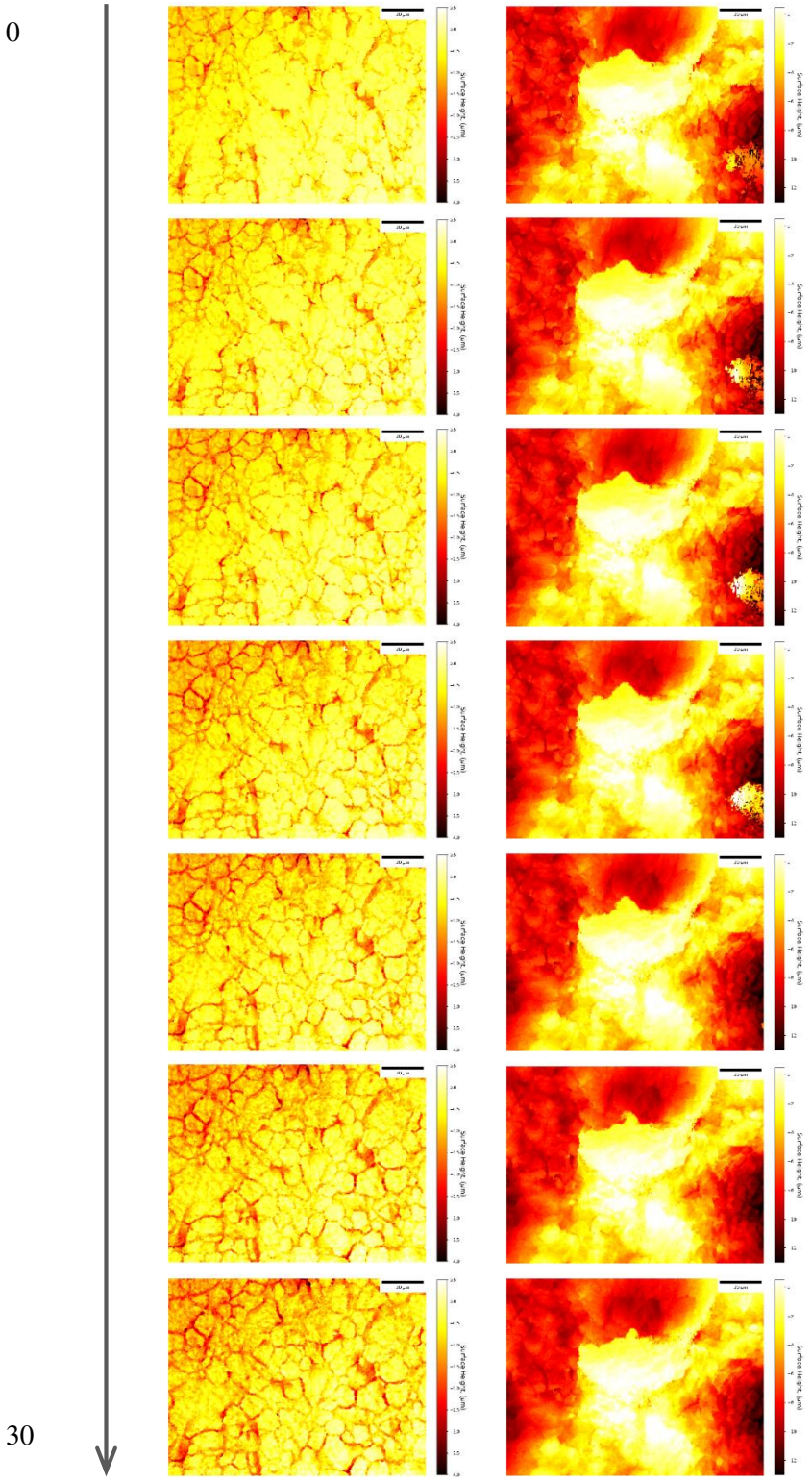

Figure 4.28 Surface retreat under HCl for a rolled surface (left) and a shotblasted surface (right). Measurements taken in 5min intervals starting from 0 mins (top) to 30 mins (bottom).

4.7.4. Corrosion Surface Profiles

Figure 4.29 shows the development of a 1D 20 µm line profile across the brushed surface with respect to exposure time. The rear line profile shows the initial surface state which is relatively flat with some grooves. Moving forward through the plot to later profiles it can be seen that small grooves grow into much larger grooves, suggesting preferential corrosion in these areas. The greatest surface retreat is around 3 µm of depth while some areas of the surface do not retreat by a measurable amount. Additionally, the line profile becomes rougher with longer exposure.

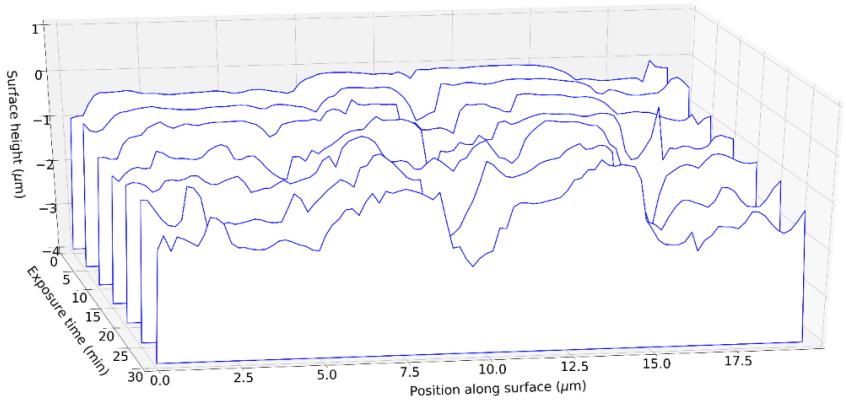

Figure 4.29 Waterfall plot showing development of a 1D line profile for a brushed surface.

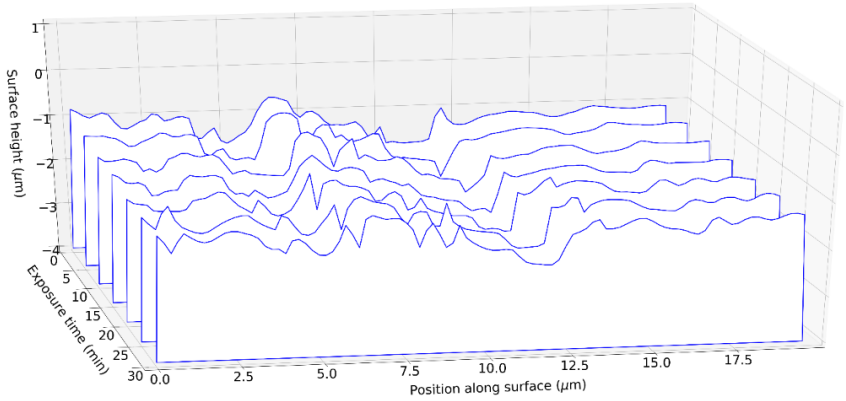

Figure 4.30 Waterfall plot showing development of a 1D line profile for a ground surface.

Compared to the brushed surface, the HCl has had little effect ground surface, shown in Figure 4.30. Similar to the brushed surface, the central groove deepens with exposure. The flat area of the plot becomes wavier, and the higher regions become rougher.

The initial very flat surface of the rolled sample, with the characteristic narrow, steep valleys between grains are seen in Figure 4.31. It is clear here that these features corrode the fastest. They become deeper with longer exposure, retreating by around 2 µm and they become wider, growing from around 1 µm to 2.5 µm wide. This indicates either a corrosive environment develops in these regions, or that the material is naturally more vulnerable in these areas. This could be because of the formation of a weaker passive film or because a higher surface area ratio in these areas exposes more material, or potentially indicative of a chromium depleted layer due to sensitization.

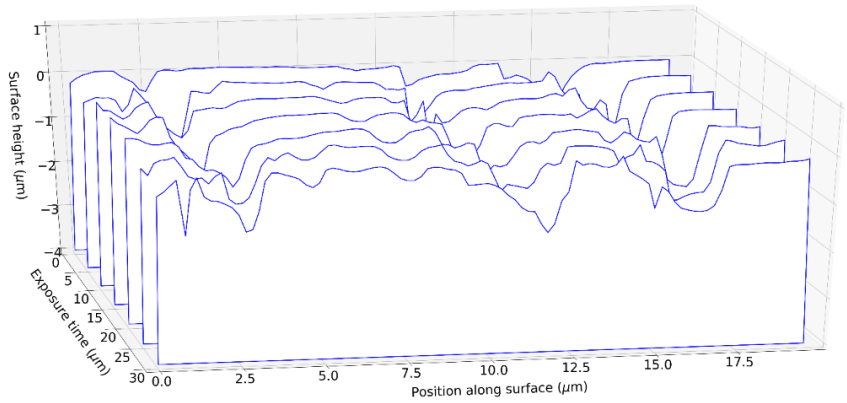

Figure 4.31 Waterfall plot showing development of a 1D line profile for a rolled surface.

Figure 4.32 shows the development of the shotblasted surface. As greater height ranges are present in this surface, the Z-range for this graph is much larger. Almost no surface retreat into the surface is discernible in this graph. Instead, a large amount of horizontal retreat is observed. The single major cliff found at this location separates two areas at different heights. This cliff-like feature is around 5 µm tall. It retreats horizontally by around 5 µm during the 30 min exposure, which is the fastest corrosion rate

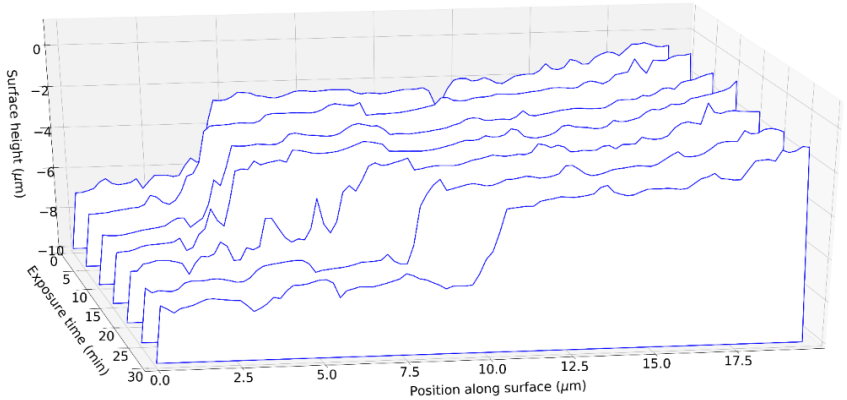

Figure 4.32 Waterfall plot showing development of a 1D line profile for a shotblasted surface.

observed. Rather than corrode uniformly, which would have the effect of smoothing out prominent features, the shape of the cliff is maintained. As shown by the VSI imaging in Figure 4.28 the positioning of each line profile is correct, and it is not the case that this effect is caused by a continual steady shift in measurement position. This suggests that the cliff feature was more vulnerable to corrosion. It is unlikely that a locally more corrosive environment is created as this feature is large and exposed to the bulk solution.

A limitation of the VSI method is that it measures height in a top-down manner. This means that any overhanging features are seen as cliffs with 90° walls. Since the initial state of this surface is similar to this description, it is possible that the retreating cliff is actually a retreating overhang. Further supporting this is the fact that an overhang would be expected to corrode more quickly since it would be exposed on two sides. On the other hand, the cliff seen in this graph is not at 90° but a slope has been measured, indicating the presence of material below this feature.

4.7.5. Relationship Between Surface Parameters and Corrosion

4.7.5.1. Effect of Corrosion on Roughness

Figure 4.33 shows the effect of surface corrosion on the roughness of the surface finishes. As expected, for each surface finish the roughness increased as a function of corrosion time. The ground surface shown in Figure 4.33b showed the smallest increase in surface roughness of 0.015 μm over the 30 minutes, an insignificant value. This is consistent with the observed corrosion process presented in Figure 4.27 where the ground surface appears to be fairly unaffected.

The rolled and shotblasted surfaces show similar roughness increases of 0.12 μm and 0.10 μm, respectively, while the brushed surface showed the greatest increase at 0.20 μm. The increase for the brushed and the rolled surface are most significant, since they represent a 75% and a 40% increase in roughness respectively, leaving the surfaces visibly very different. Interestingly, the increase in surface roughness was not related to the initial roughness value since the surfaces initially had different roughness values. Instead, the increase was proportional to the exposure time.

It is interesting to note that although the roughness increased for each surface, this had no effect on the corrosion rate which was shown to not change with time.

The roughness measurement is considered very reliable for this measurement area as it uses a large number of data points, each with a very small error, and repeatedly calculated the same value for this surface, showing very little corrosion occurring. This matches what is observed in the in-situ imaging. It is more difficult to generalise this result to other areas of the same surface, since only one in-situ corrosion trial was done, however it is noted that the measurement area includes a large number of features, over 20 valleys and ridges for the brushed and the ground surfaces, which were selected with microscopy to be representative of the surface.

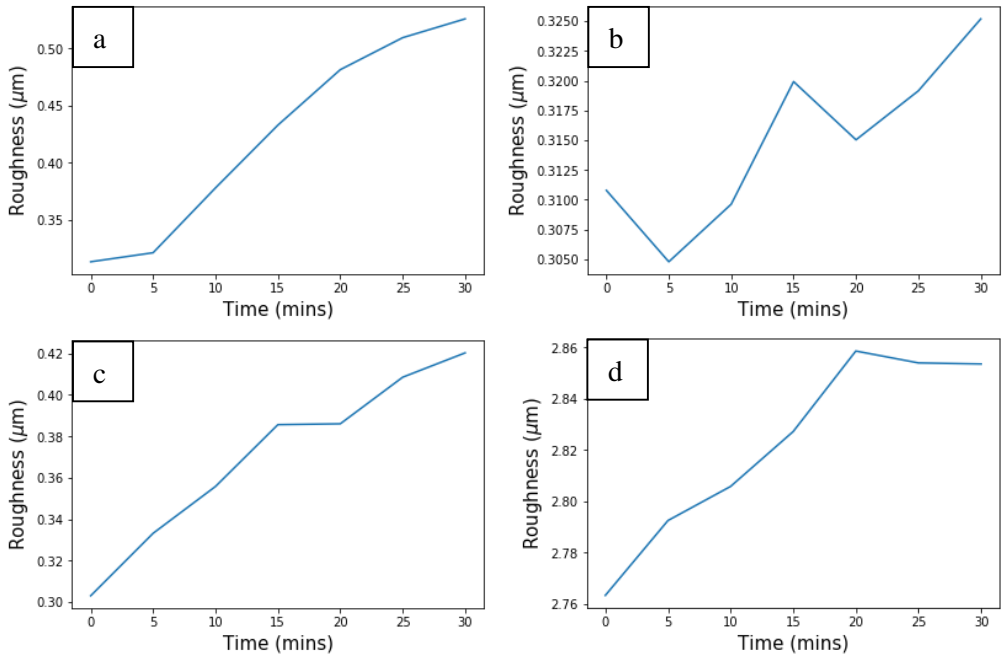

Figure 4.33 The effect of corrosion on surface roughness for: A brushed, B ground, C rolled, D shotblasted surfaces.

Figure 4.34 shows the effect of corrosion on surface bearing. Each plot shows the distribution of surface height for each sample, and how that changed with exposure to HCl. The shotblasted surface (Figure 4.34d) shows no change in surface height distribution as corrosion progresses, this means that the surface retreats a a similar rate at the peaks and the valleys and troughs. The ground surface (Figure 4.34b) shows similar behaviour, with the majority of the surface corroding at similar rates, as demonstrated by the parallel nature of the series of cumulative probability density lines. That they are not overlapping, as they are for the shotblasted surface, but instead are decreasing, shows that the peaks of this surface are not retreating as fast as the rest of the surface. Aside from the peaks, the rest of the surface retreats uniformly for both of these surface finishes.

This behaviour is in contrast to that observed for the brushed (Figure 4.34a) and the rolled (Figure 4.34c) surfaces. The gradient of the surface bearing curve decreases with exposure for both of these surfaces. Together the series form a wedge shape with the thick end on the right side of the graph. This indicates clearly that the deeper features are corroding faster, with the effect being proportional to depth. This is in contrast to the hypothesis made earlier in this Chapter which predicted that deeper features would be much more prone to corrosion, such that corrosion would be isolated to these regions. Instead, there is a propensity for corrosion to increase with even moderate reduction of surface height and continues proportionally.

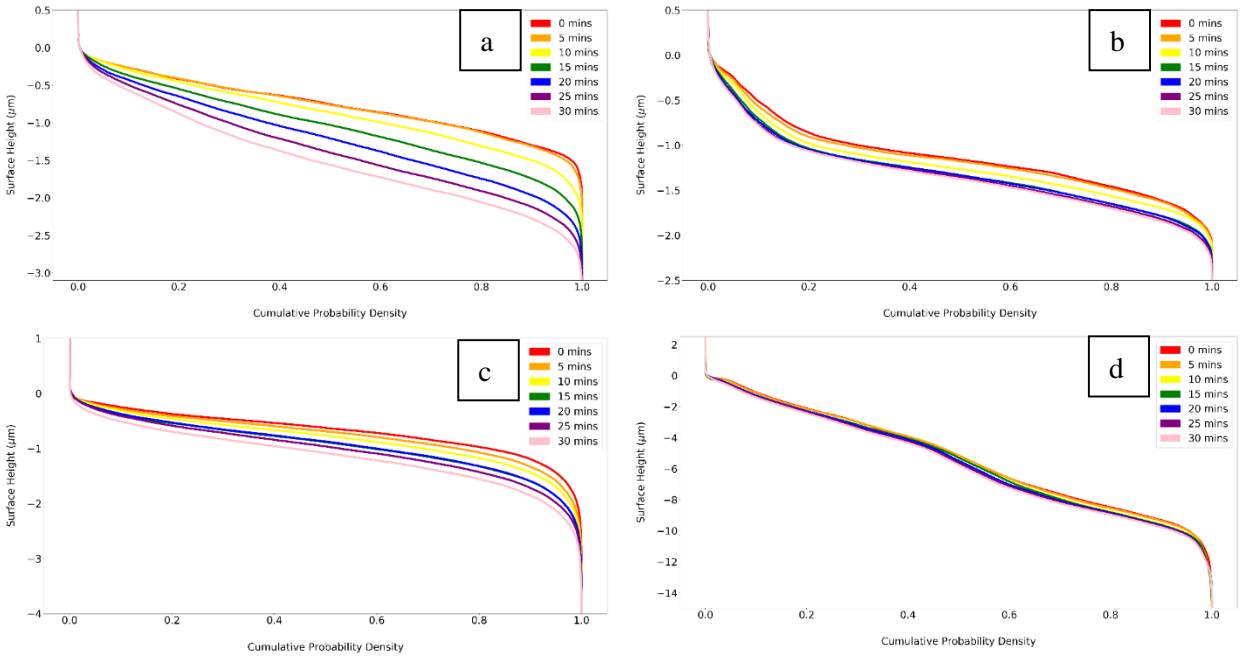

Figure 4.34 The effect of corrosion on surface bearing for: A brushed, B ground, C rolled, D shotblasted surface finishes.

4.8. Discussion

4.8.1. Summary of Surface Finish Parameters

4.8.1.1 Key Surface Parameters of Each Surface

The brushed surface was shown to have a roughness of Ra = 230 nm, similar in magnitude to the ground and rolled surfaces. The analysis of the functional parameters and the surface bearing curve showed the brushed surface had very limited valleys deeper than 1 µm.

The measured kurtosis in the brushed surface was 8.33, higher than has been measured on some metal surfaces (1.5 – 4) [5] but within the range measured by other studies (4 – 16) [23]. Across many parameters the brushed surface resembles the ground surface, the difference in kurtosis differentiates the two. This surface performed poorly in the in-situ corrosion trial, under HCl. Additionally, kurtosis has also been highlighted as a parameter that could influence stress concentration and increase the risk of SCC [24].

The ground surface was shown to have a roughness of Ra = 250 nm. The deepest valleys were measured at Sv = -1.2 µm. Similar to the brushed surface, the functional parameters showed the ground surface to have a low percentage of valleys deeper than 1 µm. The measured kurtosis in the ground surface was 2.5, well within that already measured in metals [5] (1.5 – 4), showing a slightly narrower than normal distribution of surface height.

The rolled surface had a roughness of Ra = 205 nm, in rough agreement with existing research (0.3 – 0.5 nm)[25] and had the deepest valleys measured at Sv = -1.9 µm. Despite being the smoothest surface, the functional parameters showed the rolled surface to have a much larger percentage of valleys deeper than 1 µm than the brushed or the ground surfaces. The measured kurtosis in the rolled surface was 6.2, reasonably high, but in agreement with that found in existing literature (3 – 6) [14].

The shotblasted surface was shown to have a roughness of Ra = 2710 nm due to the large, deep craters on the surface. This is lower than some existing Ra measurements on shotblasted surfaces that have recorded roughness values around 4,000 nm [26]. The maximum valley depth was measured at Sv = -11.4 µm during the analysis of the functional parameters. This method of surface finish has previously been shown to produce deeper valleys around 20 µm deep [26], though this is the result of a high degree of waviness in the surface.

For the functional parameters, the shotblasted surface was shown to be more evenly represented across its whole height range due to its lack of sharp peaks or small radii valley minima. This also meant that the percentage of the surface at greater depths was the highest for this surface, though these areas were also very open due to the gradual nature of the shotblast surface.

The measured kurtosis in the shotblasted surface was 3.9, close to a normal distribution and within that already measured in other metals (1.5 – 4) [5], additionally, it was much lower than that measured by other shot blasting techniques (6 – 8) [27]. A relatively low kurtosis of 3.9 suggests that, compared with the brushed and the rolled surfaces, and though the height range of the shotblasted surface is wide, it is less greatly represented at the extremes.

4.8.1.2 Surface Area and Openness

All the surfaces, above a resolution of 1 μm, were 2D. Below this, the fractal dimension rapidly increases to 2.03 for the brushed and ground surfaces, 2.10 for the rolled surface and 2.28 for the shotblasted surface. These values are in agreement with ranges previously calculated with a similar method for aluminium surfaces (2.1 – 2.6) [8]. This showed that the majority of surface detail in all the surfaces lay below the 2 μm length scale.

Despite consisting of valleys, the openness mapping showed the brushed and the ground surfaces to be relatively open. The valleys were some of the least open features found on these surfaces with values below 100°. Openness analysis of the rolled surface revealed that the etched grain boundaries have the largest influence on the openness. Areas between grains were found to be highly enclosed (<80°). The etched grain boundaries of the shotblasted surface resulted in a similar openness distribution with the addition of a few small indents into the surface with openness also < 80°.

The openness of grinding valleys has been measured previously as the aspect ratio and has been found to range between 35° and 106° at the valley minima, with less open valleys corresponding to lower peak metastable pit currents though no literature on the openness of brushed, rolled or shotblasted surfaces has been found [3].

Furthermore, the openness analysis revealed some previously unnoteworthy features as being potential areas for pitting initiation. The etched grain boundaries on the rolled and shotblasted surfaces, indent marks on the shotblasted surface and folded over regions on the brushed and the ground surfaces were highlighted as especially enclosed features. Openness mapping has shown to be a useful method for analysing a surface for individual features that may encourage pitting initiation.

Openness was shown to be a good predictor of corrosion location as shown in Section 4.7. Deeper, more enclosed features such as folded over regions on the brushed and ground surfaces and the gaps between grains on the rolled and shotblasted surfaces were seen to both retreat and widen. While aspect ratio has been shown to promote overall pitting on ground surfaces before [3], the in-situ method has highlighted specific surface features responsible for causing corrosion. This result has built on existing research that has suggested that the openness parameter in a surface could cause corrosion [30].

4.8.2. Application to Intermediate Level Waste Containers

This study has found the ground surface to perform better at resisting corrosion under aggressive HCl conditions. This is attributed to the smoothness of the surface at the microscale; though the Ra value of 250 nm indicates a reasonably rough surface, at very small resolutions there are few imperfections that form features of low openness, as shown in Figure 4.35c. As a result, it is likely that the good corrosion resistance of this surface is due to good diffusion properties near the surface and an inability of aggressive local concentration gradients to stabilise. For this reason, grinding is a suitable method of surface finishing for 304L stainless steel intermediate level waste containers.

Future consideration of new types of surface finish should seek to measure Sv and kurtosis to ensure the surface has as few deep valleys and sharp minima as possible. Additionally, openness can be assessed with non-destructive VSI and characteristic features on the surface can be investigated with this method with the goal of identifying more open surfaces.

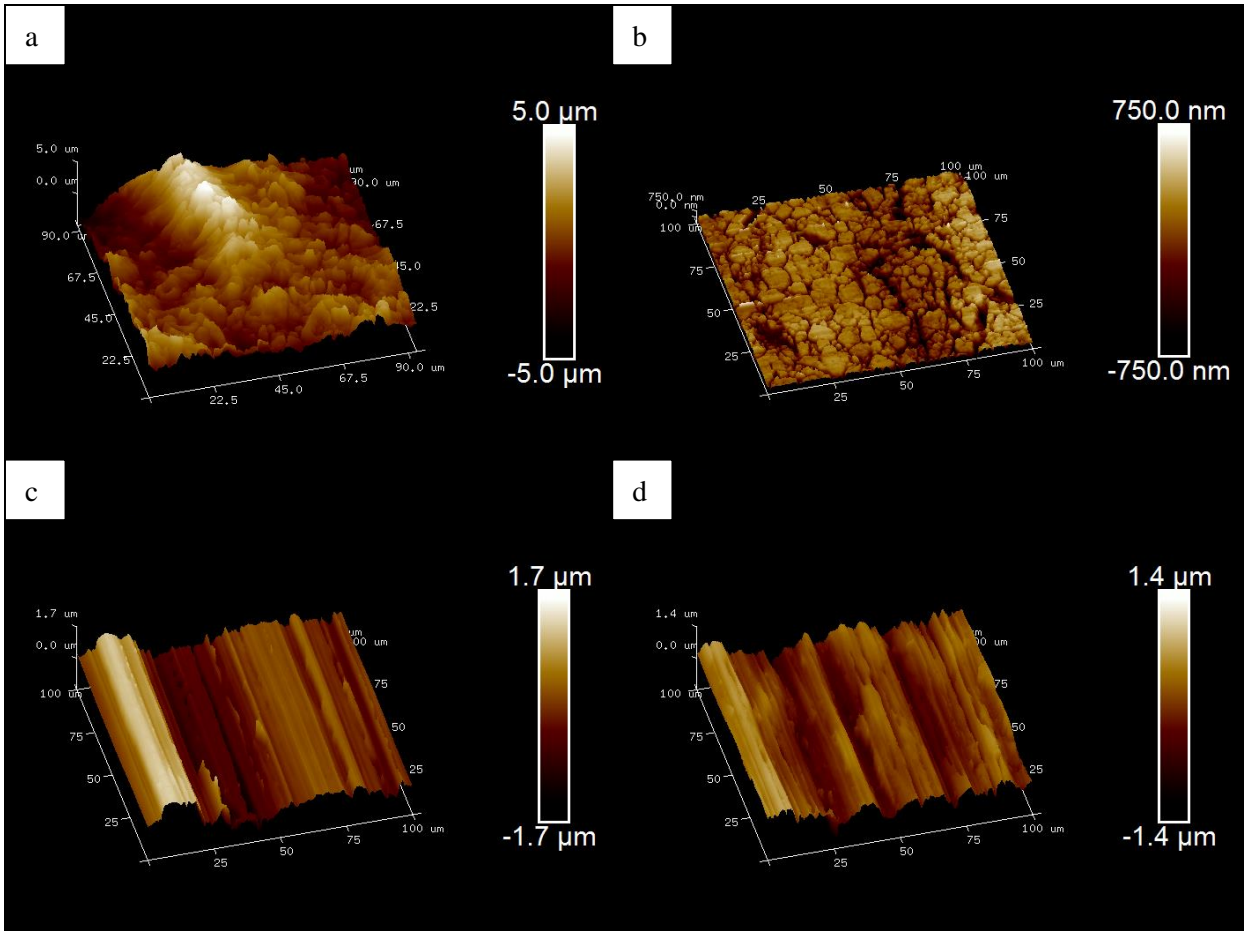

Figure 4.35 AFM Height maps for: A shotblasted, B rolled, C ground, D brushed surface.

4.8.3. Limitations of AFM

AFM relies on the sharpness of the probe tip for its resolution. The quality of the tip changes on each repeat scan as it wears during normal use. This can have the effect of obscuring data at smaller resolutions, since a rounded tip will blur the image and reduce the ability to resolve smaller features. This must be considered when comparing factors such as surface area ratio between samples. Since surface area ratio is plotted here with regard to resolution, it can be seen at what resolutions the tip remains appropriate for each sample. No sharp stopping of the increase in surface area ratio occurs in any sample, so it is thought that these measurements have not reached the resolution limit of the probe.

The quality of the tip will not affect roughness measurements since the height data that contributes to the Ra value is of a large-scale and can still be measured well at a poorer resolution. Openness measurements will be affected faster, especially for smaller features.

4.8.4. Applications of Fractal Behaviour Analysis

The examination of the fractal behaviour of these surfaces follows as a natural continuation of the calculation of surface area. Surface area was calculated as a way of characterising the surface to identify parameters that affect corrosion, and as an aid to electrochemistry to normalise results between different surface finishes. Applications for the understanding of the fractal behaviour of surfaces are suggested in this section but are not exhaustive.

Coatings.

Micaceous Iron Oxide containing epoxy is used to coat stainless steel surfaces to protect from corrosion with a layer between 30 – 50 µm thick [31]. Polyvinylidene fluoride (PVDF) is applied in layers of 17 µm [32]. Chemical Vapour Deposition (CVD) methods used on stainless steel form protective layers down to 100 nm [33]. With such a wide range of thicknesses of coatings and paint layers commercially available, the fractal behaviour of a surface will affect each application differently.

For a 304L ILW container, the geometric surface area is around 4m^2. However, this will vary wildly with the surface finish applied, and on the resolution considered. At a 100 nm resolution, the shotblasted surface has 1.5 times its geometric area, and 1.4 times the area of the other surfaces analysed. This will affect the amount of material required to effectively coat the surface [33]. Figure 4.36 shows the 3D AFM height maps for the four surfaces at a higher resolution. In this image it is the smooth nature of the ground surface at high magnification is clear compared with the rough nature of the brushed surface, despite very similar Ra values.

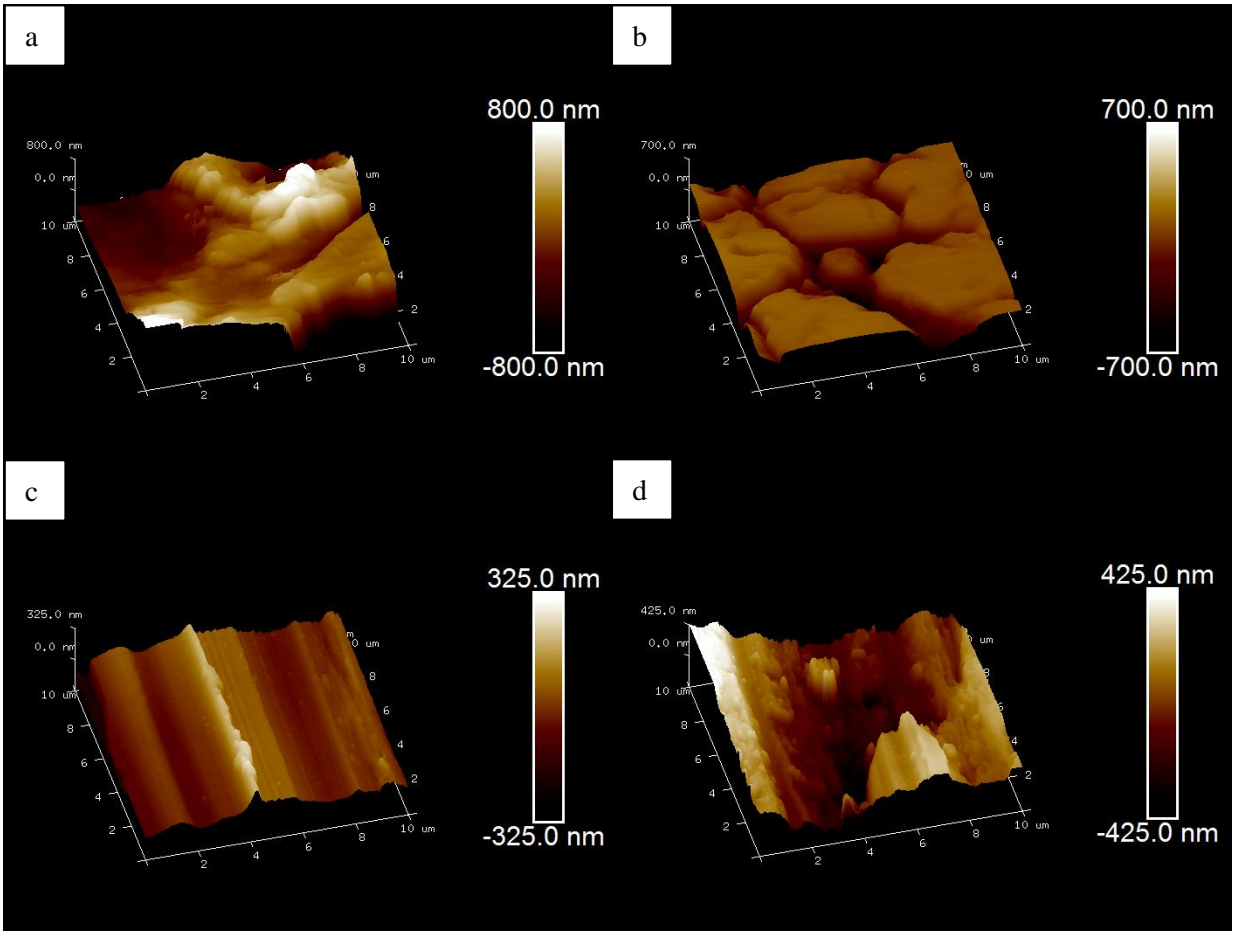

Figure 4.36 AFM height maps for: A shotblasted, B rolled, C ground, and D brushed surface.

This is relevant in not all applications, so for instance, considering the painting of ILW containers, the amount of paint required would be independent of the applied surface finish. The thickness of the layer of paint is in the flat area of the surface area ratio curve, and so it is too thick to be greatly affected by the slight differences in surface area at this resolution.

Electrochemistry Experiments.

Conventionally, surface area is tightly controlled in electrochemical experiments so as to accurately measure properties such as current density across an electrode [34]. Working electrodes are ground and polished flat so that their surface area closely resembles their geometric area. This is not ideal when the area of research is the surface finish itself. With an appreciation of the relationship between surface area and resolution, the surface area of these electrodes can be normalised to each other and real surfaces can be compared which have the same geometric area, but different real surface areas. This means that experiments can be performed on different surface finishes without the requirement for grinding and polishing.

Electron transfer at an electrode is a molecular-scale process. The local potential difference can be over 1 V across a distance of just a fraction of a nm, meaning very high potential gradients ($>10^7$ Vcm^{-1}) can be reached. This potential attracts oppositely charged ions and dipoles in the electrolyte to the surface forming an electrical double layer of the scale of a few nms. If the surface area is incorrectly measured, the calculated potential gradient will be affected. The current density recorded by the potentiostat could be corrected by a better estimation of the surface area at this resolution.

For surface processes that are limited by size of reaction area, or number of surface sites, this change in surface area should be considered during electrochemistry experiments. For processes limited by mass transfer, no such effect should be seen as this step is not affected by the surface area. From this example, an accurate knowledge of the surface area could be used to determine the nature of rate limiting processes.

Pitting corrosion.

A fluid's viscosity acts as though it were proportionally higher at smaller scales [35]. Pitting corrosion relies on the surface geometry slowing the diffusion of corrosion products to maintain a concentration gradient and an aggressive environment. Since diffusion is also proportionally slowed by viscosity, the scale of the diffusion-slowing features is extremely important. A feature shape that promotes pitting may not do so if it were enlarged; as at a larger scale the fluid enclosed by it would move more freely and so diffusion would happen more readily. This also suggests that large closed features would have to be much more enclosed than smaller features to promote pitting. As pitting is a major risk in ILW containers, this is a potentially useful application of this method [36].

Glass dissolution.

A glass dissolution test, Product Consistency Test (PCT) is used to determine chemical durability of nuclear, hazardous, and mixed waste glasses [37]. To normalise surface area of crushed glass particles, they are assumed to be spherical. They are not exactly spherical, nor any other exact shape so an approximation must be made. The fractal behaviour of the particles is, however, likely to be consistent across particles and so could be used to correct the approximation.

4.8.5. Applications of Openness Behaviour Analysis

Corrosion in Industry and Research.

The process of mapping openness across a surface allows for the prediction of probable pitting sites using non-destructive efficient scanning techniques such as VSI. This has applications in industry in identifying vulnerable areas in engineering surfaces, such as folded over areas, or even pits. Additionally, this method provides an opportunity to compare different corrosion mechanisms for an individual surface. The propensity for pitting for a material surface due to its geometry can be compared with its PREN (Pitting Resistance Equivalence Number) for instance [38].

Flow Behaviour.

Many applications of stainless steel in the nuclear industry involve fluids, making the effect of surface finish on fluid dynamics relevant [22]. In fluid mechanics, the surface roughness of a pipe is known to affect flow. To calculate the effect of this, the mean surface height is used, but the function chosen depends on the type of roughness found. If surface features are spaced further apart than they are tall, k-type behaviour is achieved [39]. If surface features are spaced a shorter distance than they are tall, the behaviour of eddy currents around these features abruptly changes and d-type behaviour is achieved. A distinction is made between the two behaviours with different functions being used to explain the effect the surfaces have on flow.

The deciding factor is the ratio of the width to the height, which is how openness is calculated. This means the openness mapping technique could also be used to estimate the behaviour of flow across a

surface. Specifically, the two different flow behaviours impact the amount of flow in the lowest parts of the surface, the areas most vulnerable to corrosion.

4.9. Conclusions

4.9.1. Surface Characterisation Summary

A thorough characterisation of the morphology of brushed, ground, rolled and shotblasted stainless steel was produced. This allowed for the comparison with corrosion behaviour and the linking of certain characteristics to corrosion and pit initiation.

Legacy and height parameters were analysed which showed the magnitude of the skewness of the rolled surface to be greatest and most negative. This indicated a sizable portion of the rolled surface lies beneath the average surface height, creating areas more favourable to pitting corrosion than peaks, increasing corrosion vulnerability.

Holes caused by the smearing of surface material were found on both the ground and the brushed surfaces. These areas were found to be deeper and more enclosed, making the surface more prone to pitting initiation.

The surface area ratio was calculated and described for each surface, highlighting the difficulty of defining surface area for a fractal surface. The surface area ratio was found to increase with resolution, with the greatest effect being found with the shotblasted surface, which, at a resolution of 0.2 μm, had a 40% larger surface area than its geometric area as demonstrated by Figure 4.10.

Additionally, the ground and the brushed surfaces were found to be rougher than the rolled surface at larger resolutions, but from Figure 4.10 it can be deduced that they are smoother at very small resolutions. This showed a drawback in traditional stylus measurements and in commonly used roughness parameters such as Ra, both of which fail to describe surfaces which are rough, but only at high resolutions and highlighted the benefit of using surface area ratio curves.

The hybrid parameters, describing the nature of slopes on the surfaces, were calculated. These highlighted the effect the exposed grain boundaries had on the rolled and the shotblasted surfaces, making them far steeper than the ground and brushed surfaces, despite the rolled surface having the

lowest Ra value. Steeper surface slopes were linked to the existence of more closed, sheltered, locations, and a higher propensity for corrosion.

Ssc was used to quantify the curvature of peaks for the four surfaces. A novel method to invert this parameter (creating ISsc) to describe the curvature of surface minima was demonstrated. It was found that the rolled surface and the shotblasted surface had the highest IScc, showing they had the smallest radii minima, an outcome likely caused by the presence of the etched grain boundaries. The surface curvature at minimas will have a deciding impact corrosion initiation since these features shelter the surface and slow diffusion. Additionally, these features could act as sites for stress concentrations which is described in Chapter 6.

Openness as a surface parameter was described and a method of calculating it across a surface and forming descriptive maps over large areas was demonstrated. This method revealed properties of the surfaces which did not stand out by standard height mapping. The flatness of the flat topped peaks of the shotblasted surface (Figure 4.20) was found. At these points diffusion would be uninhibited by surface morphology and aggressive conditions are unlikely to develop, making these areas somewhat protected by their location. Additionally, small indents into the shotblasted surface were found to stand out with openness < 80°. These were barely visible on the height map but stood out strongly out when openness was plotted.

The distribution of openness across each surface was plotted (Figure 4.21) showing the rolled and the shotblasted surfaces to have much thicker tails indicating the presence of more enclosed regions.

4.9.2. Conclusions from Differential Imaging

The ground surface showed the least corrosion under HCl. From analysis of the time-interval imaging it was seen that this surface remained smooth the longest. Small features that provided discontinuities corroded quickly on this surface, while the majority of it corroded very slowly, as shown in Figure 4.27. In comparison, the initial surface of the brushed finish had many of these features which allowed corrosion to set in at many locations across the surface. This was likely the cause of the disparity in volume loss.

Figure 4.34 showed that for the brushed and the rolled surfaces corrosion rate was proportional with surface depth, with deeper areas corroding faster. This behaviour was consistent with areas of the

surface above average surface height, with any reduction in height bringing about an increase in corrosion. This is good evidence that surface morphology acts to shelter the surface and can allow aggressive environments to form.

4.10. References

[1] T. Nguyen, I. Zarudi, and L. C. Zhang, “Grinding-hardening with liquid nitrogen: Mechanisms and technology,” *Int. J. Mach. Tools Manuf.*, vol. 47, no. 1, pp. 97–106, 2007.

[2] A. Turnbull *et al.*, “Sensitivity of stress corrosion cracking of stainless steel to surface machining and grinding procedure,” *Corros. Sci.*, vol. 53, no. 10, pp. 3398–3415, 2011.

[3] Y. Zuo, H. Wang, and J. Xiong, “The aspect ratio of surface grooves and metastable pitting of stainless steel,” *Corros. Sci.*, vol. 44, no. 1, pp. 25–35, 2002.

[4] Z. Mike, “Characterizing surface quality: why average roughness is not enough,” *Bruker*, 2000.

[5] R. Horváth, Á. Czifra, and Á. Drégelyi-Kiss, “Effect of conventional and non-conventional tool geometries to skewness and kurtosis of surface roughness in case of fine turning of aluminium alloys with diamond tools,” *Int. J. Adv. Manuf. Technol.*, vol. 78, no. 1–4, pp. 297–304, 2015.

[6] M. Hasegawa, J. Liu, K. Okuda, and M. Nunobiki, “Calculation of the fractal dimensions of machined surface profiles,” *Wear*, vol. 192, no. 1–2, pp. 40–45, 1996.

[7] S. Lovejoy and B. B. Mandelbrot Ibm, “Fractal properties of rain, and a fractal model,” *Tellus A Dyn. Meteorol. Oceanogr.*, vol. 37, no. 3, pp. 209–232, 1985.

[8] C. Zhai, Y. Gan, D. Hanaor, G. Proust, and D. Retraint, “The role of surface structure in normal contact stiffness,” *Exp. Mech.*, vol. 56, no. 3, pp. 359–368, 2016.

[9] C. O. A. Olsson and D. Landolt, “Passive films on stainless steels - Chemistry, structure and growth,” *Electrochim. Acta*, vol. 48, no. 9 SPEC., pp. 1093–1104, 2003.

[10] P. E. Manning, D. J. Duquette, and W. F. Savage, “Effect of test method and surface condition on pitting potential of single and duplex phase 304L stainless steel.,” *Corrosion*, vol. 35, no. 4. pp. 151–157, 1979.

[11] J. R. Galvele, “Transport processes and the mechanism of pitting of metals,” no. April, pp. 464–474, 1976.

[12] A. Majumdar and C. L. Tien, “Fractal characterization and simulation of rough surfaces,”

Wear, vol. 136, no. 2, pp. 313–327, 1990.

[13] D. M. Mark and P. B. Aronson, “Scale-dependent fractal dimensions of topographic surfaces: An empirical investigation, with applications in geomorphology and computer mapping,” *J. Int. Assoc. Math. Geol.*, vol. 16, no. 7, pp. 671–683, 1984.

[14] B. Ma, A. K. Tieu, C. Lu, and Z. Jiang, “An experimental investigation of steel surface characteristic transfer by cold rolling,” *J. Mater. Process. Technol.*, vol. 125–126, pp. 657–663, 2002.

[15] E. S. Gadelmawla, M. M. Koura, T. M. A. Maksoud, I. M. Elewa, and H. H. Soliman, “Roughness parameters,” *J. Mater. Process. Technol.*, vol. 123, no. 1, pp. 133–145, 2002.

[16] K. J. Kubiak, M. C. T. Wilson, T. G. Mathia, and P. Carval, “Wettability versus roughness of engineering surfaces,” *Wear*, vol. 271, no. 3–4, pp. 523–528, 2011.

[17] I. S. Cole, T. H. Muster, N. S. Azmat, M. S. Venkatraman, and A. Cook, “Multiscale modelling of the corrosion of metals under atmospheric corrosion,” *Electrochim. Acta*, vol. 56, no. 4, pp. 1856–1865, 2011.

[18] a. Cook *et al.*, “Atmospheric-induced stress corrosion cracking of austenitic stainless steels under limited chloride supply,” *18th Int. Corros. Congr. 2011*, vol. 2, no. February 2017, pp. 1438–1449, 2011.

[19] G. Bitelli, A. Simone, F. Girardi, and C. Lantieri, “Laser scanning on road pavements: A new approach for characterizing surface texture,” *Sensors (Switzerland)*, vol. 12, no. 7, pp. 9110–9128, 2012.

[20] J. R. Galvele, “Transport processes in passivity breakdown .2. full hydrolysis of the metal-ions,” *Corros. Sci.*, vol. 21, no. 8, pp. 551–579, 1981.

[21] C. Padovani, R. J. Winsley, N. R. Smart, and P. A. H. Fennell, “Corrosion control of stainless steels in indoor atmospheres,” *Corros. Vol. 71 issue 5*, 2015.

[22] S. B. Lyon, “Overview of Corrosion Science,” *Nucl. Corros. Sci. Eng.*, pp. 1–24, 2012.

[23] M. Sedla ek, B. Podgornik, and J. Vižintin, “Correlation between standard roughness parameters skewness and kurtosis and tribological behaviour of contact surfaces,” *Tribol. Int.*, vol. 48, pp. 102–112, 2012.

[24] W. Grzesik, “Prediction of the functional performance of machined components based on

surface topography: state of the art," *J. Mater. Eng. Perform.*, vol. 25, no. 10, pp. 4460–4468, 2016.

[25] R. Leach, "Optical measurement of surface topography," *Springer Sci. Bus. Media*, pp. 1–7, 2011.

[26] S. L. Clitheroe, "The physical and microstructural properties of peened austenitic stainless steel," *PhD Thesis, Univ. Manchester*, 2011.

[27] S. Bagherifard, R. Ghelichi, and M. Guagliano, "Numerical and experimental analysis of surface roughness generated by shot peening," *Appl. Surf. Sci.*, vol. 258, no. 18, pp. 6831–6840, 2012.

[28] T. Hong and M. Nagumo, "Effect of surface roughness on early stages of pitting corrosion of Type 301 stainless steel," *Corros. Sci.*, vol. 39, no. 9, pp. 1665–1672, 1997.

[29] L. Abosrra, A. F. Ashour, S. C. Mitchell, and M. Youseffi, "Corrosion of mild steel and 316L austenitic stainless steel with different surface roughness in sodium chloride saline solutions," *Electrochem. Process Simul. Iii*, vol. 65, pp. 161–172, 2009.

[30] H. Ezuber, A. Alshater, S. O. Nisar, A. Gonsalvez, and S. Aslam, "Effect of surface finish on the pitting corrosion behavior of sensitized AISI 304 austenitic stainless steel alloys in 3.5% NaCl solutions," *Surf. Eng. Appl. Electrochem.*, vol. 54, no. 1, pp. 73–80, 2018.

[31] "Two pack high build epoxy MIO," *Firwood Manuf.*, vol. 44, no. 207861, pp. 2–3, 2010.

[32] BSS, "Specialist coil coated stainless steel," *BS Stainl.*, 2018.

[33] SilcoTek, "Why it is important for CVD coatings to have a thickness range," *AZO Mater.*, 2019.

[34] D. Pletcher, *A First Course in Electrode Processes*. 2019.

[35] A. Kapustin, *Scaling laws in hydrodynamics*. 2016.

[36] F. King, "Container materials for the storage and disposal of nuclear waste," *Corrosion*, vol. 69, no. 10, pp. 986–1011, 2013.

[37] ASTM, "Standard methods for determining chemical durability of nuclear, hazardous and mixed waste glasses and multiphase glass ceramics: the product consistency test (PCT)," vol. 02, no. Reapproved 2008, pp. 1–23, 2008.

[38] F. King, “Corrosion resistance of austenitic and duplex stainless steels in environments related to UK geological disposal,” *A Rep. to NDA RWMD*, no. April, 2009.

[39] S. Leonardi, P. Orlandi, and R. A. Antonia, “Properties of d- and k-type roughness in a turbulent channel flow,” *Phys. Fluids*, vol. 19, no. 12, 2007.

Chapter 5. The Relationship Between Surface Finish, Grain Microstructure, Stress and Strain in Stainless Steel

5.1. Introduction

5.1.1. Background

Surface finishing processes such as grinding, polishing, rolling and shotblasting have been shown to impart near-surface areas of stainless steel with microstructural changes [1]. These changes are of grain area, orientation, residual stresses, texture, and phase in nature. Each of these likely has an effect of a surface's resistance to SCC. These changes are quantified in this Chapter, and their potential effects on SCC, studied in further detail in Chapter 6, are discussed.

This Chapter utilises Electron Back-Scatter Diffraction (EBSD), described in Chapter 3, to provide an unrivalled picture of the crystallographic structure of the different surface finishes at a high resolution. The data acquired can be used to plot images of the granular structure and can be used to reveal in-grain orientation changes characteristic of in-grain stresses. EBSD is excellent at differentiating between grains, since adjacent grains always have different orientations or phases in a totally crystallized material such as in 304L stainless steel. This makes EBSD perfect for grain analysis techniques as pixels belonging to a particular grain are identifiable by orientation as distinct to those in the adjacent grain.

A proportional relationship between the force applied in a surface finishing process and the extent of microstructure grain damage was expected, and this is hypothesised to vary with depth, with the most damage occurring at the surface. For the surfaces investigated in this thesis, the horizontal dragging that occurs in grinding and brushing applies both compressive and tensile lateral stresses to the surface. Additionally, these techniques apply a vertical compressive stress [2]. These stresses damage the surface, breaking larger grains into smaller grains. It was expected that this effect would be recognisable in the distribution of grain area, with the surface having a higher proportion of smaller grains. Since these grains have been broken, there should be some deviation from the natural standard shape of grains. A large deviation from the expected grain edge angle distribution to much smaller grain edge angles would be expected in damaged regions, near the surface.

It was expected that the shotblasting process would impart a residual compressive lateral stress in the surface [3]. This would be detectable in the misorientation profile of the material, with a higher degree of misorientation in samples that are under higher stress, a phenomena long observed in both EBSD and X-Ray diffraction [4]. It was expected that the grinding process would leave a tensile stress in the direction of grinding [2]. Both of these stress profiles were expected to depend on depth.

For the shotblasted surface, the size of the pellets used in the process should be calculable from the radius of the craters, although some elastic relaxation off the centre of the craters may be seen that artificially increases this radius. From the depth of the stress profile the kinetic energy of the pellet may be estimable.

5.2. Microstructure Damage Analysis

5.2.1. Grain Structure Analysis

Samples were cut and mounted cross-sectionally so that microstructure below the surface could be assessed. Once mounted and milled by PECs, EBSD was performed using an Inspect F50 SEM, programmed using Flamenco from the HKL suite. The parameters detailed in

Table 5.1 were used to program scans. With the samples on their side, the sample surfaces are near the top of the following EBSD images with grains lower in the image being deeper into the sample.

Some mounting material above the surface of the sample was incorrectly indexed. These features required manual removal, before extrapolating wild spikes (individual pixels that varied greatly with all those around them) and then extrapolating data to fill the zero solutions. This noise reduction process was performed for all samples. All further diagrams in this Chapter follow the same format, being cross sectional images of the surface of the material with the surface at the top and the bulk forming the majority of the image.

Table 5.1 Parameters used for the collection of EBSD scans.

Timing/Frame	11
# Frames	64
Dynamic background	On
Operation	Subtract
Enhancement	Dynamic Structure
Noise reduction #Frames	20
Binning	4x4
Gain	High
Band detection method	Edge
#Bands	3-6
Run Time	15 hrs

5.2.1.1. Grain Boundary Determination

Grain boundary determination was completed by calculating local misorientation profiles across the surfaces. Where misorientation exceeded 7°, a grain boundary (solid black line) was drawn, as shown in Figure 5.1. Since this alone did not form perfectly enclosed grains, automatic boundary completion down to 0° was used.

The analysis software defined a grain as a 2D area completely enclosed by a grain boundary. Correct grain detection was required for further analysis to be accurate. Multiple critical misorientation angles were tested and 7° was found to be optimal, with lower values creating artificial sub-grains and with higher degrees tending to join grains up incorrectly into larger sets of grains. This value captured both high and low angle grain boundaries and so 7° was used for all samples. The boundaries of each grain were visible in the EBSD patterns and so it was clear when correct grain boundary determination was achieved.

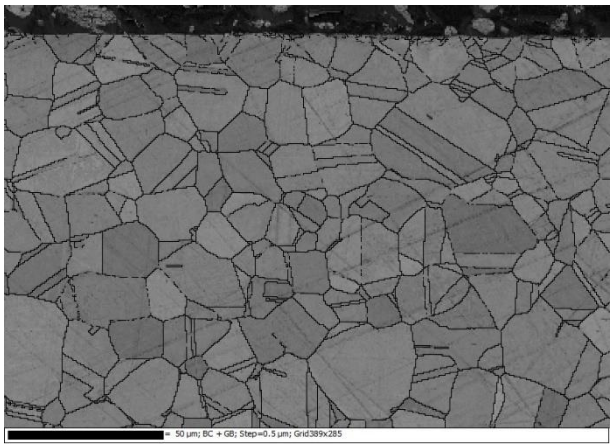

Figure 5.1 Grain boundary detection for a brushed sample.

5.2.1.2. Euler Angle Mapping

Euler angles represent the three rotations of a 3D object required to transform its orientation to match a different orientation. For these images the Bunge convention for the choice of axes and angles has been used. The three Euler angles: ϕ_1, Φ, ϕ_2 (phi_1, Phi, phi_2) represent the following rotations:

1. A rotation of ϕ_1 about the z-axis followed by,
2. A rotation of Φ about the rotated x-axis followed by,
3. A rotation of ϕ_2 about the rotated z-axis.

Euler colouring for Figure 5.2 denotes orientations (ϕ_1, Φ, ϕ_2) to Red Green Blue (RGB) colour values with Equation 5.1.

$$Red = 255 \cdot \frac{\phi_1}{360}, \quad Green = 255 \cdot \frac{\Phi}{360}, \quad Blue = 255 \cdot \frac{\phi_2}{360} \qquad \textit{Equation 5.1}$$

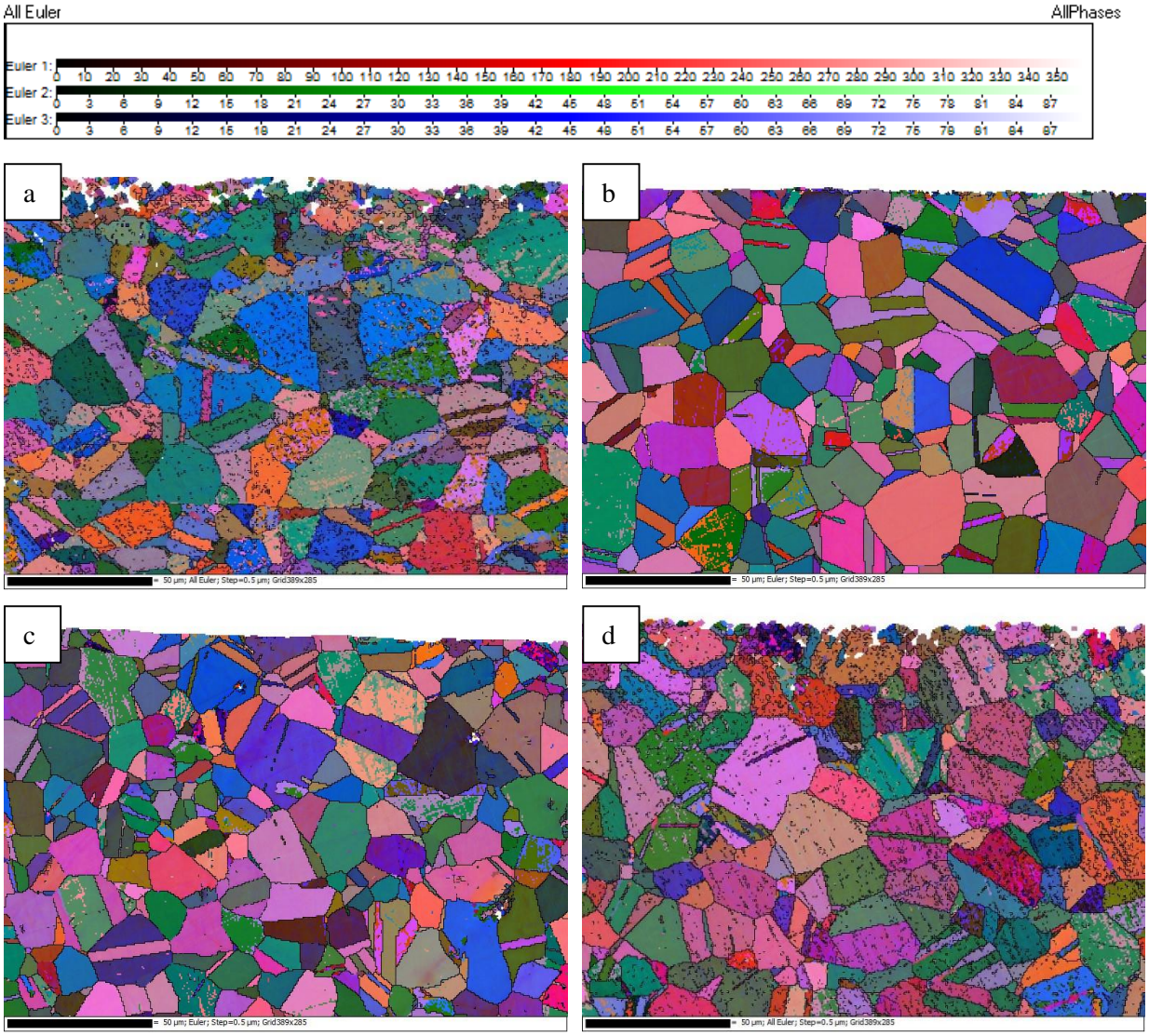

Figure 5.2 Grain orientation Euler Colour maps for: A shotblasted surface, B brushed surface, C rolled surface, D ground surface

Figure 5.2 displays grain orientation by Euler angles. These correspond to the combination of colours shown in the key at the top of Figure 5.2. In general, dissimilar colours indicate greater angular difference, but since this colour system wraps around itself, there occur situations where two grains of very similar orientation are given completely different colours should they lie close to the colour boundary, although this is more pronounced with IPF diagrams.

Near total crystallization is seen across all surfaces with twin sites relatively common. Grain size in the bulk material is consistent between all samples, with grain sizes ranging from 10 µm to 40 µm. Grain size decreases near the top of the surface, revealing the depth of damage caused by each surface finish. The shotblasted surface has the largest band of surface damage at around 10 µm, which is similar to the ground surface at 10 µm. The brushed surface shows very little damage with only around 3 µm of damage at the surface while no grain damage at all can be detected in the rolled surface.

In Figure 5.2b and c, a patterned discolouration within grains can be seen. This is shown with greater magnification in Figure 5.3. This corresponds to the markings seen in the band contrast observed during analysis caused by the polishing process. This shows that small surface scratches will affect and mislead the grain orientation measurement. In Figure 5.2a and d, where the sample surface is more scratched, these erroneous patterns exceed the 7° misorientation required to be identified as grain boundaries and short black lines are drawn. Since these lines are too short to be joined up to form grains they are not counted as grains, and further measurements are not skewed by having an artificially inflated number of grains.

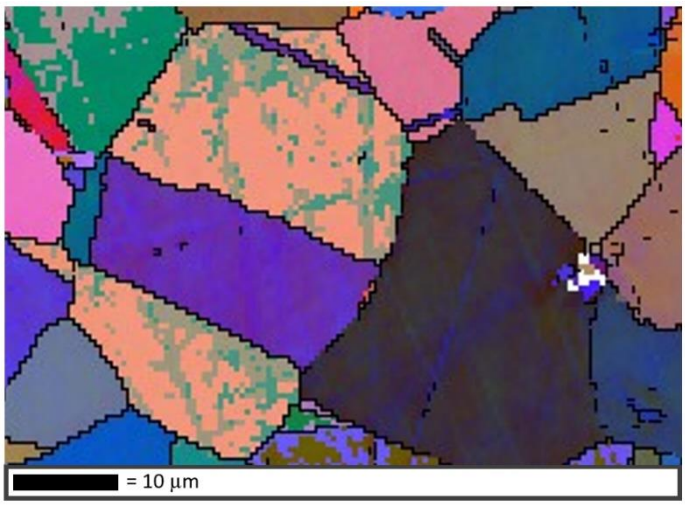

Figure 5.3 Within-grain variance in orientation measurement.

Grains at the edge of any measurement would be expected to have an average grain size of 50% bulk average and 25% at right angled corners due to the measurement area cutting through them. On average grains on the edges will be cut in half and grains in the corners will be cut to a quarter of their original size. This must be taken into account when analysing the distribution of grain sizes near a surface.

The expected rolling direction is into the page, which is also the direction of surface lay. Some within-grain stress misorientation is observable, for example, in Figure 5.4 the central grain shows a gradient of orientation focused at the damaged area on the right side.

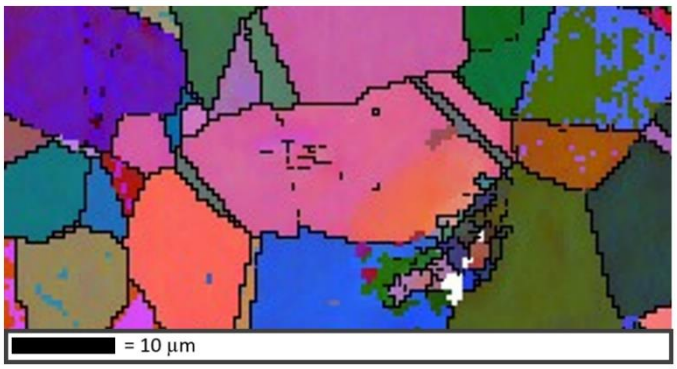

Figure 5.4 An example of a highly stressed grain.

The samples shown in Figure 5.2b and c had lower indexing rates (75-85%) than Figure 5.2a and d (95%+) and thus had higher mis-indexing rates, likely due to surface polishing effects. This considered, the shotblasted surface (Figure 5.2b), showed an especially poor indexing rate near the surface (up to 10 µm deep) and a much smaller average grain size. This is also observed in the ground surface, to a slightly lesser extent. This damage is certainly caused by the surface finishing process, which is known to be more damaging than rolling or brushing. This damage has reduced the grain size, increased local misorientation, worsened the Kikuchi band contrast and decreased the indexing rate near the surface.

5.2.2. Grain Size Distribution

Surface finishing processes have some effect into the bulk material itself; the scale of this effect as a function of depth is quantified in this Section. Manual pattern recognition is prone to experimenter bias and can result in experimenters finding features favourable to their own theories in the areas they expect to find them, whilst missing others. By using an automatic scanning technique that covered the whole of the measured area, as much experimenter bias as possible was removed.

5.2.2.1. Method

Data files were taken from the Tango Software (HKL suit) used in analysis elsewhere in this chapter. For grain size distribution analysis, the noise reduction facility in Tango HKL was utilised, erroneous above-surface measurements were removed, and wild spikes and fill were used consistent with this chapter's method. Additionally, grain detection was completed at 7° with grain boundary completion down to 0°. Since only grain size was to be analysed in this section, this had the effect of simplifying the data without removing any valuable data.

The data was then analysed with a purpose-made Python script that measured the number of grain boundaries in each horizontal line of the measured area, as well as the distance between them. This was done by recording any changes in grain orientation above 7°. From this an average grain intercept distance (AGI) for each line was calculated.

Average grain intercept distance is a 1D measurement indicative of average grain size at a certain depth. It is skewed by the same mechanism that skews 2D grain size measurement when compared with 3D. That is a straight line crossing through a 2D grain is unlikely to pass through the largest cross section. The majority of measurements will go through edge regions, clipping grains and skewing the average to a smaller value. The same effect is observed with 2D grain size measurement as a 2D plane tends to cut through smaller cross sections of grains than their biggest cross-section, also skewing grain size measurement downwards. It is still appropriate and valuable to compare AGI across different samples, and across different areas of a single sample as is done here.

5.2.2.2. Average Grain Intercept Measurements

Figure 5.5 shows the AGI value with increasing depth for the rolled sample next to the Inverse Pole Figure (IPF) image. AGI measurements begin at the highest point that grains appear in the measurement area. The AGI for this sample is ~8 µm. Considering the deviation seen in the bulk, this sample shows no discernible grain size difference near the surface compared with the bulk suggesting that the surface finishing technique of cold rolling does not damage the surface microstructure.

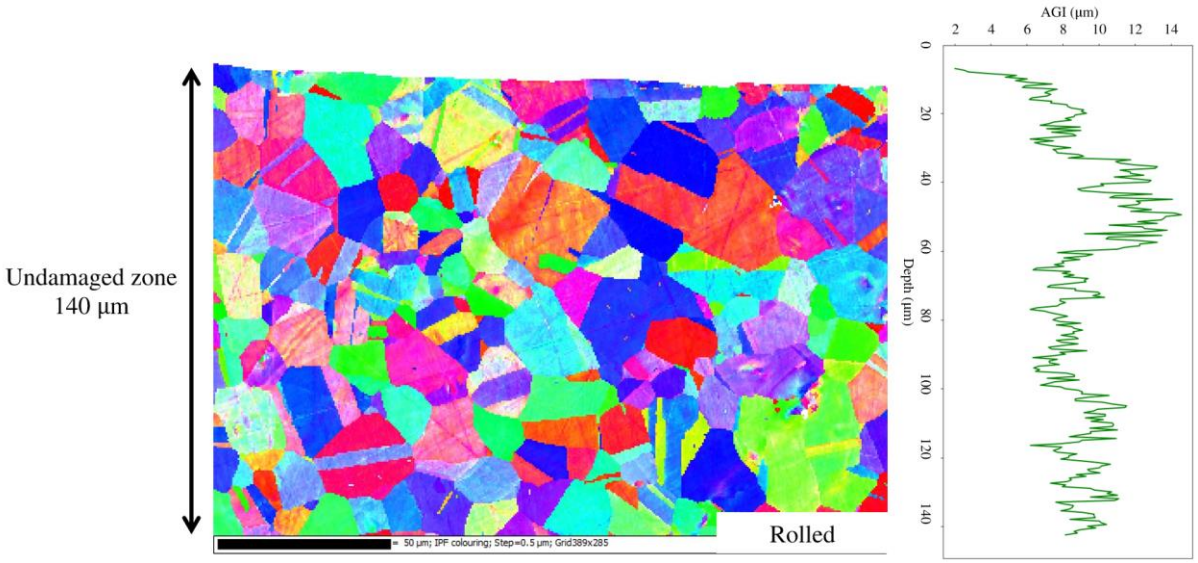

Figure 5.5 A rolled sample. IPF Image alongside AGI with depth.

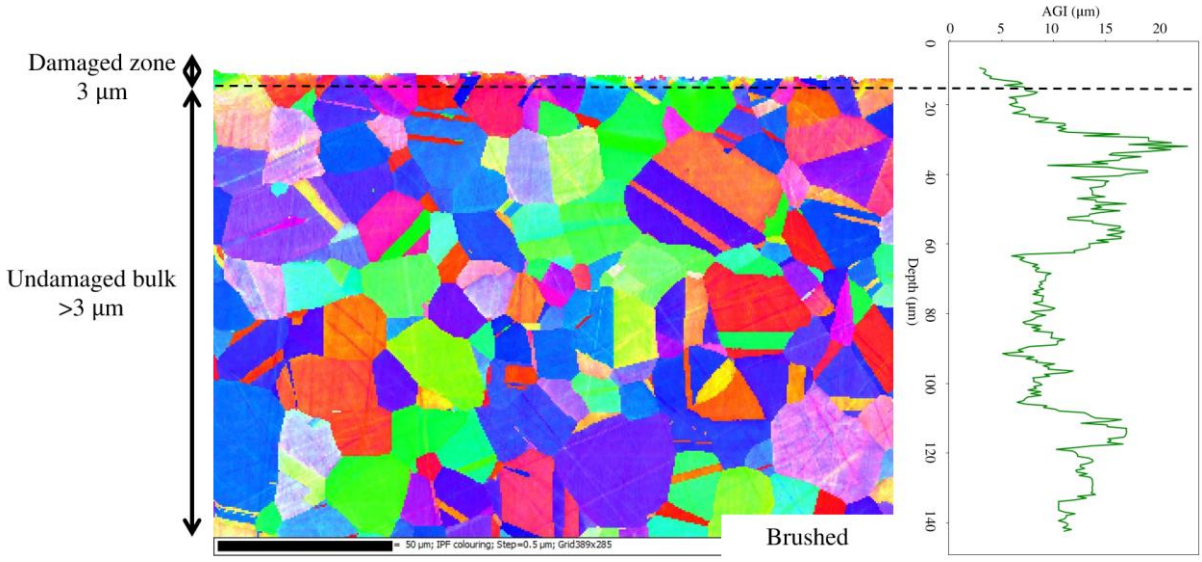

Figure 5.6 A brushed sample. IPF Image alongside AGI with depth.

Figure 5.7 shows the AGI for the shotblasted sample. From the surface of the sample to a depth of 20 µm there is a band with an AGI of around 2 µms. This then increases to 6 µm and remains relatively constant. This shows a clear reduction in grain size distribution near the surface with a highly effected zone in the top 20 µm of the sample.

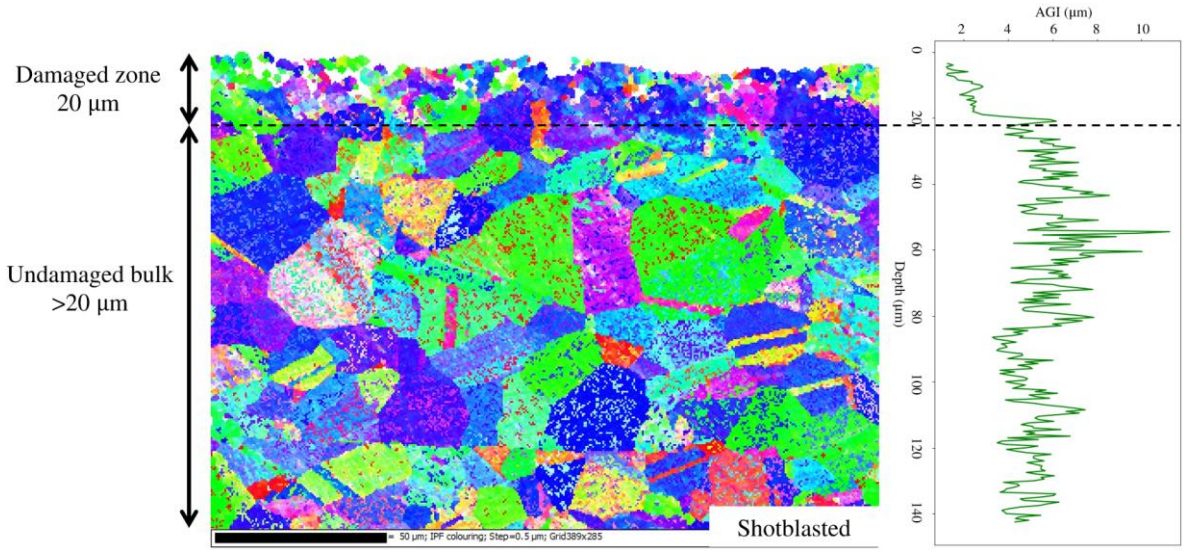

Figure 5.7 A shotblasted sample. IPF Image alongside AGI with depth.

Figure 5.6 shows the AGI for the brushed sample. At the surface there is a shallow, 3 µm deep, zone with an AGI of 3 µm, indicating microstructural damage caused by brushing has been confined to a very shallow surface region.

Figure 5.8 shows the AGI for the ground sample. Within the top 10 µm of the surface, the AGI is <4 µm, showing a relatively deep band of damage caused by the grinding process.

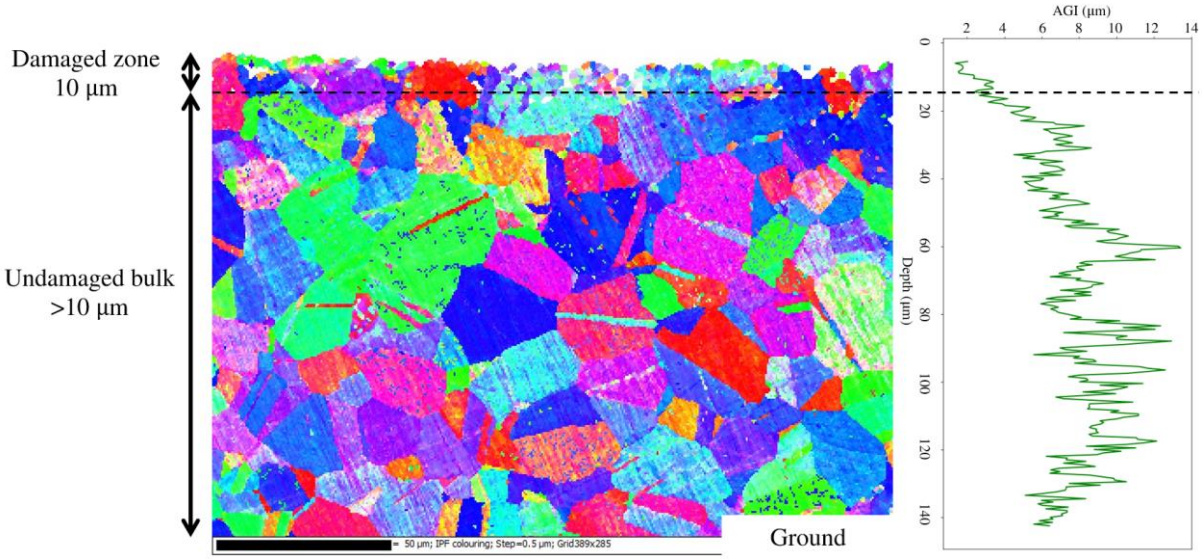

Figure 5.8 A ground sample. IPF Image alongside AGI with depth.

In summary, according the AGI analysis, the depth of damage caused by the surface finishing process, defined here as a clear deviation in grain size from the bulk, was as follows for each surface:

- Rolled sample: no apparent damage or grain size change
- Shotblasted sample: 20 µm deep zone of damage, with a ΔAGI of ~ 4 µm
- Brushed sample: 3 µm deep zone of damage, with a ΔAGI of ~ 7 µm
- Ground sample: 10 µm deep zone of damage, with a ΔAGI of ~ 7 µm

5.3. Residual Stress Analysis

Grain misorientation spread, indicative of strain, can be calculated from EBSD orientation data and is presented in Section 5.3.1. To convert this into a true strain, and therefore be able to make estimations of the residual stress, grain shape must be considered since longer grains would be expected to have higher grain misorientation spreads for a given stress. Section 5.3 presents a method to convert grain misorientation spread into grain stress through the calculation of grain length, width, and shape. This process is summarised in Table 5.2.

Table 5.2 The calculation of grain stress from shape parameters and strain.

Value calculated:	**Used to calculate:**
1. Grain length	Grain shape ratio
2. Grain area	Width
3. Grain width	Grain shape ratio
4. Grain shape ratio	Grain stress
5. Grain strain	Grain stress
6. Grain stress	

5.3.1. Strain Mapping

Figure 5.9 shows strain contour maps of the four surfaces. These were calculated using the Tango HKL software. The software calculates the strain by taking the maximum misorientation between any two points for each grain and designating this value to the centre of the grain [5]. These values are then smoothed out across the measurement area. This method performs poorly with extraneous values and with any errors in grain designation. A new method that uses the full width at half maximum value for the grain orientation spread is presented in Section 5.3.3.

The images shown in Figure 5.9 were normalised such that the maximum stress value on each map was coloured red, and the minimum blue, with all other values linearly distributed linearly along the spectrum colour bar shown at the bottom of the figure. This means that the value denoted by a given colour differs for each map; comparison between maps should be made regarding the location and

distribution of stress, or with direct reference to the scale. For Figure 5.9a these values range from 0.03 - 8.78°, for Figure 5.9b 0.02 - 2.77°, for Figure 5.9c 0.00 - 2.84° and for Figure 5.9d 0.00 - 7.95°.

The highest recorded deformation was measured in the shotblasted surface, with the misorientation measured as 8.78° within 40 µm of the surface. Smaller areas of stress were measured in this sample at a depth of 60 µm. The second highest recorded deformation was measured in the ground surface, which had grain misorientation angle of 7.95° at a single surface location. This sample also contained a second smaller patch of stress at 70 µm depth.

Both the brushed and the shotblasted surface showed a higher strain concentration near the surface. The brushed surface exhibited a consistent band of strain in the upper 20 µm of the sample and the shotblasted surface exhibited an inconsistent, but deeper (40 µm), surface strain band.

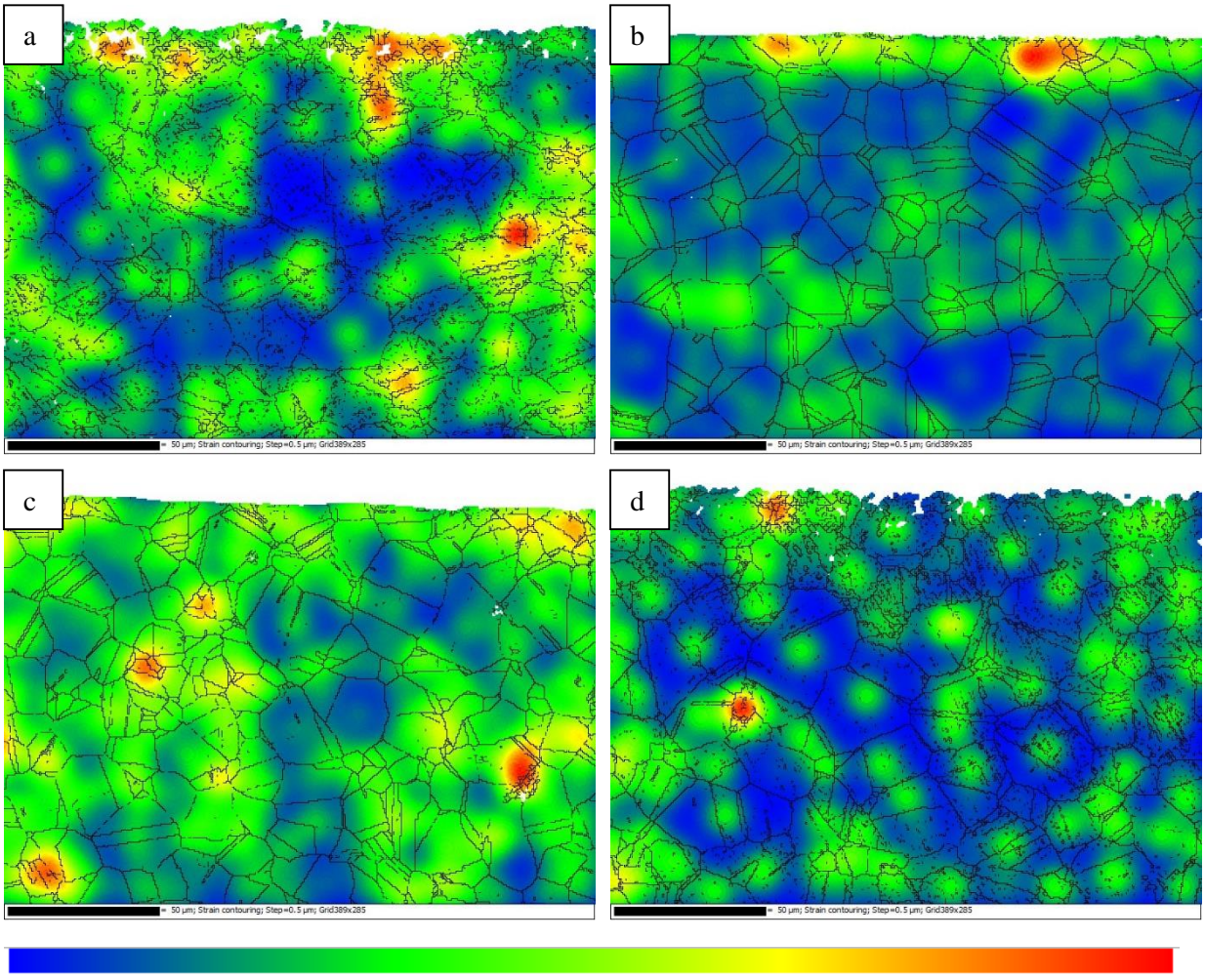

Figure 5.9 Strain maps for: A shotblasted surface, B brushed surface, C rolled surface, D ground surface. Legend below.

5.3.2. Residual Stress Analysis

The method used in Section 5.3.1. of assigning the maximum misorientation of a grain and associating this with the amount of stress the grain exhibits has a number of disadvantages. The amount a grain should be expected to deform under a given stress is dependent on its shape. Size does not play a large factor since the increased width of larger grains compensates for the increase in deformation expected for the length increase by making the grain stiffer. The magnitude of the effect of grain shape on deformation is calculated in this Section, using a model to estimate the flexibility of individual grains. This allows for the estimation of stress from the degree of misorientation.

Additionally, the data shown in Figure 5.9 has likely not been filtered by the HKL software, meaning there could be a high level of erroneous misorientation at the local level that does not represent a strain of the grain, instead being caused by the index quality of the measurement. Taking the maximum misorientation, or the range, is a technique that is particularly vulnerable to individual erroneous points since one abnormally high angle changes the overall range of the data.

To estimate the maximum misorientation angle that could reasonably be attributed to the strain of a grain, a single grain was modelled as a rectangle of sides *2a* and L_o, shown in Figure 5.10. When under stress grains deform such that the crystallographic orientation at one side of the grain is measurably different to that on the other, and there is a gradient of misorientation between them. To estimate the

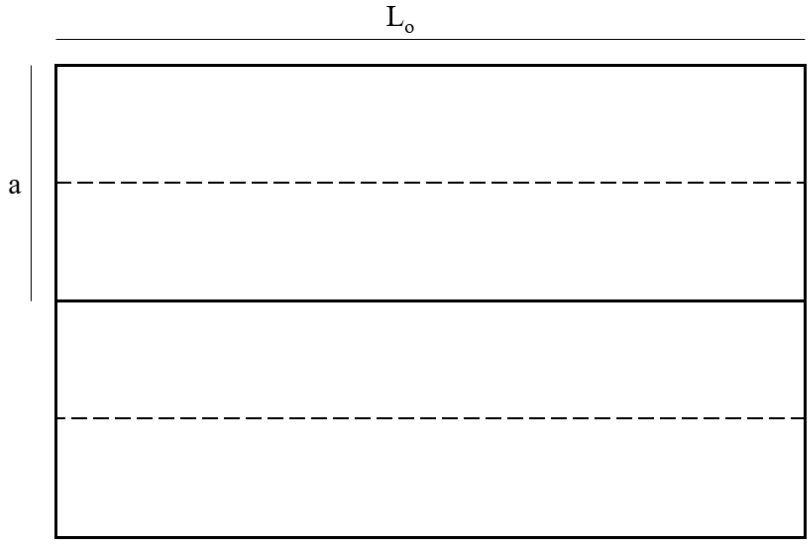

Figure 5.10 Diagram of a single grain with sides 2a and L_o. The solid black line segmenting the grain splits the top and bottom half.

degree of this misorientation a single grain is modelled here that exhibits some bending due to an applied stress.

The bending stress applied to the grain is modelled as a tensile stress in the top half of the grain and a compressive stress in the bottom half. This causes the top half to stretch by ΔL, and the bottom half to compress by ΔL, as shown in Figure 5.11. The distance between the centres of these half grains is a. This forms an angle, θ, which is considered to be the bend angle.

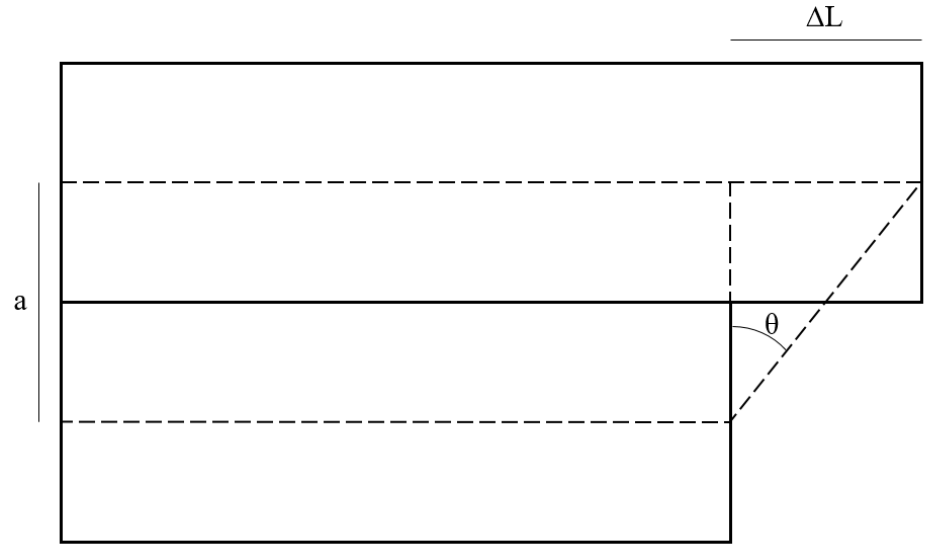

Figure 5.11 Showing an elongated top half under tension and a contracted bottom half under compression.

Equation 5.2 gives the equation for Young's Modulus; it links Stress (σ) with Strain (ε), where F is force, A is area, ΔL is the change in length and L_0 is the initial length.

$$E \equiv \frac{\sigma}{\varepsilon} = \frac{F/A}{\Delta L/L_0} \qquad \textit{Equation 5.2}$$

Re-arranging Equation 5.2 for (σ) gives Equation 5.3 which links stress to deformation:

$$\sigma = \frac{\Delta L}{L_0} E \qquad \textit{Equation 5.3}$$

Equation 5.4 gives the angle (θ) made between the extending top half grain and the compressing bottom half using the properties of a right angled triangle. ΔL Becomes $2\Delta L$ since there is both an expansion and a compression in a bending grain. The terms of Equation 5.4 are given in Figure 5.11.

$$\tan(\theta) = \frac{2\Delta L}{a} \qquad \textit{Equation 5.4}$$

Rearranging Equation 5.4 gives Equation 5.4, which can be substituted into Equation 5.3 to give Equation 5.5:

$$2\Delta L = a\tan(\theta) \qquad \textit{Equation 5.4}$$

$$\sigma = \frac{a\tan(\theta)}{2L_0}E \qquad \textit{Equation 5.5}$$

Equation 5.5 rearranged for (θ) gives Equation 5.6, which describes the maximum misorientation angle expected for an individual grain. It is a product of two variables, the stress applied to the grain (σ) and the ratio between grain length and width; $\frac{2L_0}{\mathrm{a}}$. This shows that the applied stress and the shape ratio are equal factors for bending degree for a given stress.

$$\theta = \tan^{-1}\left(\frac{\sigma 2L_0}{aE}\right) \qquad \textit{Equation 5.6}$$

Interestingly, the stress experienced by a grain should be independent of its size since a larger grain has a larger cross sectional area which distributes the increased force.

Based on this logic, the estimated bending degree for a range of shape ratios and stresses were calculated and displayed in Table 5.3. This Table serves as a useful key to estimate stress from strain contouring maps such as those presented in Section 5.3.1. The Young's modulus used here for 304L stainless steel is 200 GPa [6].

Table 5.3 Calculated bend angle for a grain for a specific shape ratio and applied stress.

Shape Ratio \ Stress (GPa)	0.4	0.8	1.2	1.6	2.0	2.4	2.8	3.2	3.6	4.0	4.4	4.8	5.2	5.6	6.0
1	0.5	0.9	1.4	1.8	2.3	2.7	3.2	3.7	4.1	4.6	5.0	5.5	5.9	6.4	6.8
1.2	0.6	1.1	1.7	2.2	2.7	3.3	3.8	4.4	4.9	5.5	6.0	6.6	7.1	7.7	8.2
1.4	0.6	1.3	1.9	2.6	3.2	3.8	4.5	5.1	5.8	6.4	7.0	7.7	8.3	8.9	9.5
1.6	0.7	1.5	2.2	2.9	3.7	4.4	5.1	5.8	6.6	7.3	8.0	8.7	9.5	10.2	10.9
1.8	0.8	1.7	2.5	3.3	4.1	4.9	5.8	6.6	7.4	8.2	9.0	9.8	10.6	11.4	12.2
2	0.9	1.8	2.7	3.7	4.6	5.5	6.4	7.3	8.2	9.1	10.0	10.9	11.8	12.6	13.5
2.2	1.0	2.0	3.0	4.0	5.0	6.0	7.0	8.0	9.0	10.0	11.0	11.9	12.9	13.8	14.8
2.4	1.1	2.2	3.3	4.4	5.5	6.6	7.7	8.7	9.8	10.9	11.9	13.0	14.0	15.1	16.1
2.6	1.2	2.4	3.6	4.8	5.9	7.1	8.3	9.5	10.6	11.8	12.9	14.0	15.1	16.2	17.3
2.8	1.3	2.6	3.8	5.1	6.4	7.7	8.9	10.2	11.4	12.6	13.8	15.1	16.2	17.4	18.6

Table 5.3 demonstrates the relationship between applied stress, shape ratio, and resultant bend angle. It should be noted that 304L stainless steel has a yield stress of 210 MPa and an ultimate strength of 560 MPa [7]. At calculated values above 210 MPa it is highly likely that material has undergone plastic, rather than elastic, deformation and that given the values of bend angle measured, a large amount of work hardening. It is relatively unwieldy to manually apply the results in Table 5.3 to the strain contour maps shown in Figure 5.9. The next Section demonstrates a computation method for doing so.

In this model, the stress applied to the grain is orthogonal to the grain length, causing maximum strain. In reality this would rarely be the case. Stresses applied at off-angles were not included here. This effect causes the model to underestimate stress from strain. The model further assumes no difference between the Young's modulus of a bulk material and that of an individual grain. In reality the Young's modulus of a single crystal and of a large polycrystalline material would differ. Since the samples examined here are almost entirely crystallized, the assumption that the bulk Young's modulus represents an individual grain is made.

There is likely to be a large source of error in the measurement of bending angle in the strain contouring maps. It is likely that error, which is caused by surface defects, could skew the maximum misorientation measurement. Since it is the maximum misorientation which is measured, isolated individual errors could contribute to the maximum.

Grain shape ratio is a 2D measurement while in reality, grains are 3D. A grain may be much deeper than expected by its 2D appearance and so more affected by a stress than expected; equally a grain could be very shallow into the page and so be more affected by a stress than expected. Care should be taken to use Table 5.3 as a guide and not as an exact reference.

As well as allowing a quantitative estimation of stress to be made, rather than just strain, this method reduces error in the interpretation of strain maps since it provides a way to include the effect of grain shape. While crude, it provides reasonable figures and allows sensible comparisons between samples.

5.3.3. Development and Evaluation of Residual Stress Model Incorporating Grain Shape for Mapping

Using Equation 5.6, orientation data from EBSD scans were used to map the characteristics of individual grains within each of the stainless steel surfaces with depth. Before this could be achieved, firstly it was necessary to obtain realistic values for the grain length, width and area. Section 5.3.3.1 details how these values were obtained, and the results are described in Section 5.3.3.2.

5.3.3.1. Grain Characterisation Calculations

Two datasets were used for each EBSD measurement area. Firstly, the regular EBSD dataset, consisting of orientation by Euler angles, was utilised, as shown in Figure 5.12 for a sample with a rolled surface. The second dataset used was one with each grain filled with its average orientation by the Tango HKL software. The second dataset was used as a reference since it effectively identified whole grains by their orientation.

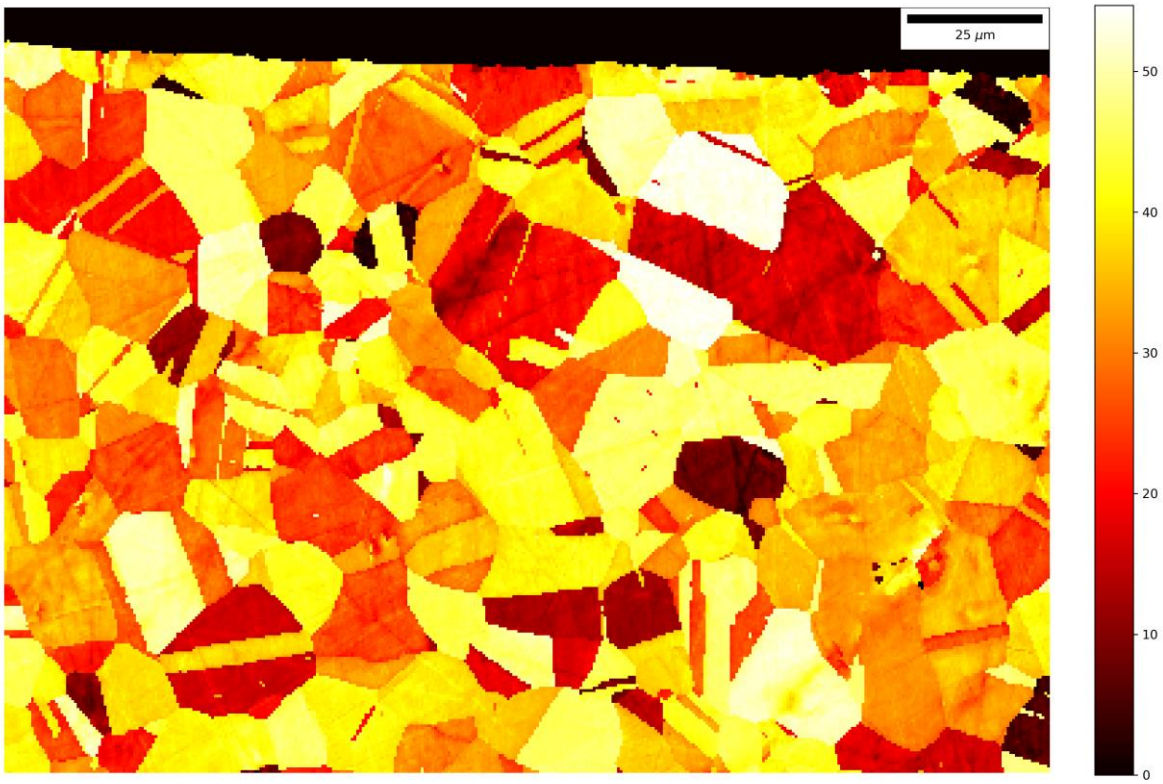

Figure 5.12 Crystallographic orientation map for a rolled surface for the E2 Euler angle. Scale is in degrees.

For the purpose of this analysis, twinned grains were considered to be single grains. For the calculation of misorientation, only values aligned with one orientation were considered for each grain, this is described further in Section Grain Strain and Stress Measurement.

Figure 5.13 shows an example of the second type of dataset used in this analysis, a crystallographic orientation map for a rolled surface. In this map the grains have been filled with their average value, shown by the constant in-grain colour/orientation. As the average grain orientation value for each grain is calculated to 4 significant figures, this map can also be used as a reference map in which grains are indexed since it is highly unlikely two grains will have exactly the same orientation. A purpose-made python script identified and listed each grain in the complete dataset in turn, using the grain filled dataset

as a guide to which points were of the same grain. To increase the identification accuracy, all 3 Euler angles were input to calculate the grain length, width, and area, as discussed in the following sections.

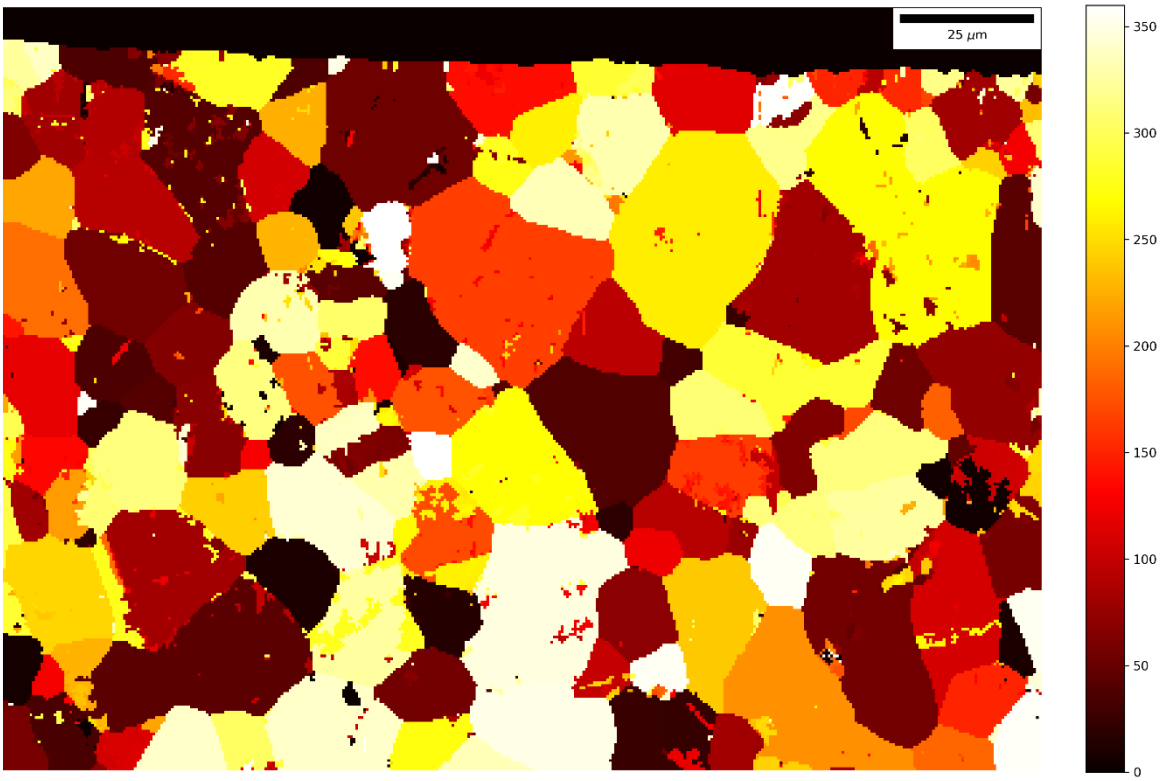

Figure 5.13 Crystallographic orientation map of a rolled surface with depth for the Euler angle, E1. Grains are filled with their average value. Scale is in degrees.

Calculating Grain Length

The length of each grain was initially calculated in python by taking the maximum distance between any two points in a grain. It was found that the same result could be achieved much more efficiently by first identifying pixels that were at the edge of a grain, and then finding the maximum distance between any of these for each grain, since there were far fewer edge pixels. The initial computational method scales with $O(n^2)$ whereas the second method scales with O(n) since the perimeter of an object is proportional to the square root of its area. This means that for the size of the input data, n, (a product of the measurement area and the resolution) the time taken to compute the results is proportional to n^2 for the initial method and n for the second method. For this reason, the second method was used.

Figure 5.14 shows grains of a rolled sample mapped and coloured by grain length. This is the longest distance between any two points of a grain, in any orientation. In the map the longest grains are coloured near white, these are around 50 μm long.

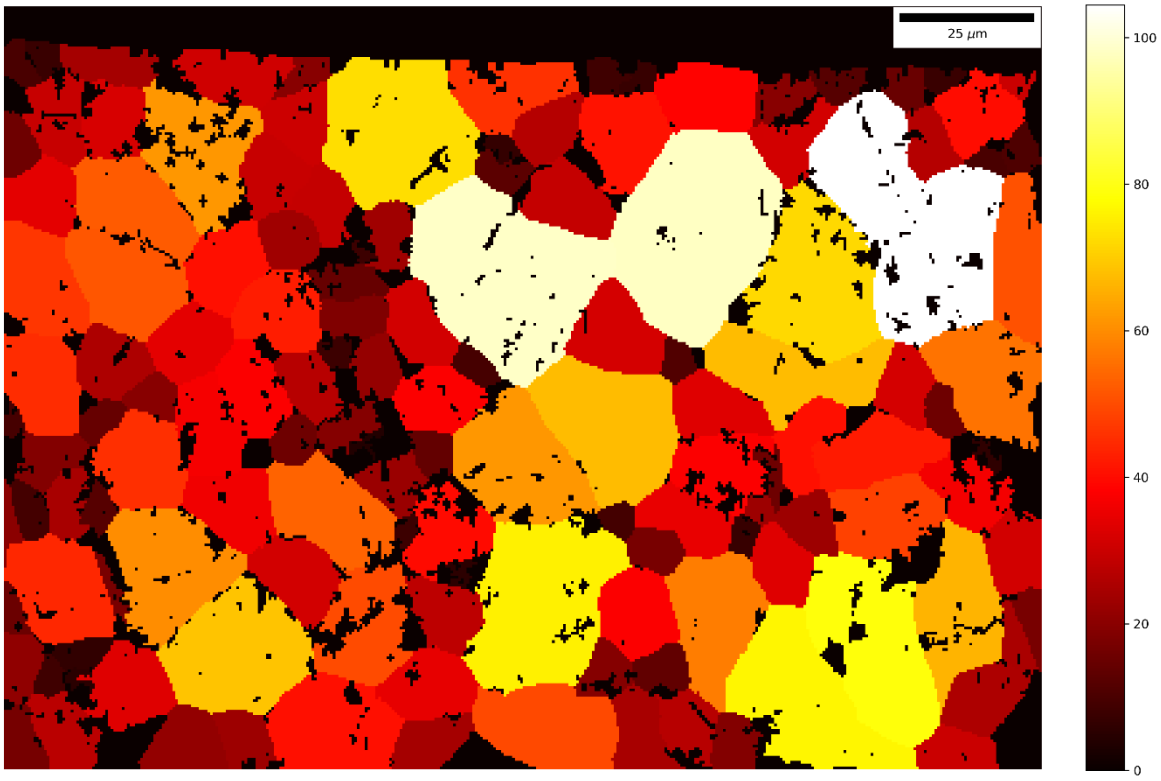

Figure 5.14 Grain mapping by length in any direction for a rolled surface. The length scale is given in pixels (1 pixel = 0.5 μm).

Grain Area Measurement

The area of each grain was calculated by summing the number of pixels occupied by each grain. This was then plotted in colour in Figure 5.15. Once normalised, the area maps largely correlate with the length maps, but where they deviate is significant to the understanding of the shape of grains. If each grain were the same shape, the length and area maps would correlate perfectly. For grains to deviate from the average they must be wider or thinner; this characteristic is described here by the shape ratio (the ratio between the length and width of grains).

Grain Width Measurement

The width of each grain was calculated by dividing the grain area by the length. This was considered a good estimation technique as grains almost entirely took convex shapes that had no concave edges. This also produced a fast method for shape approximation.

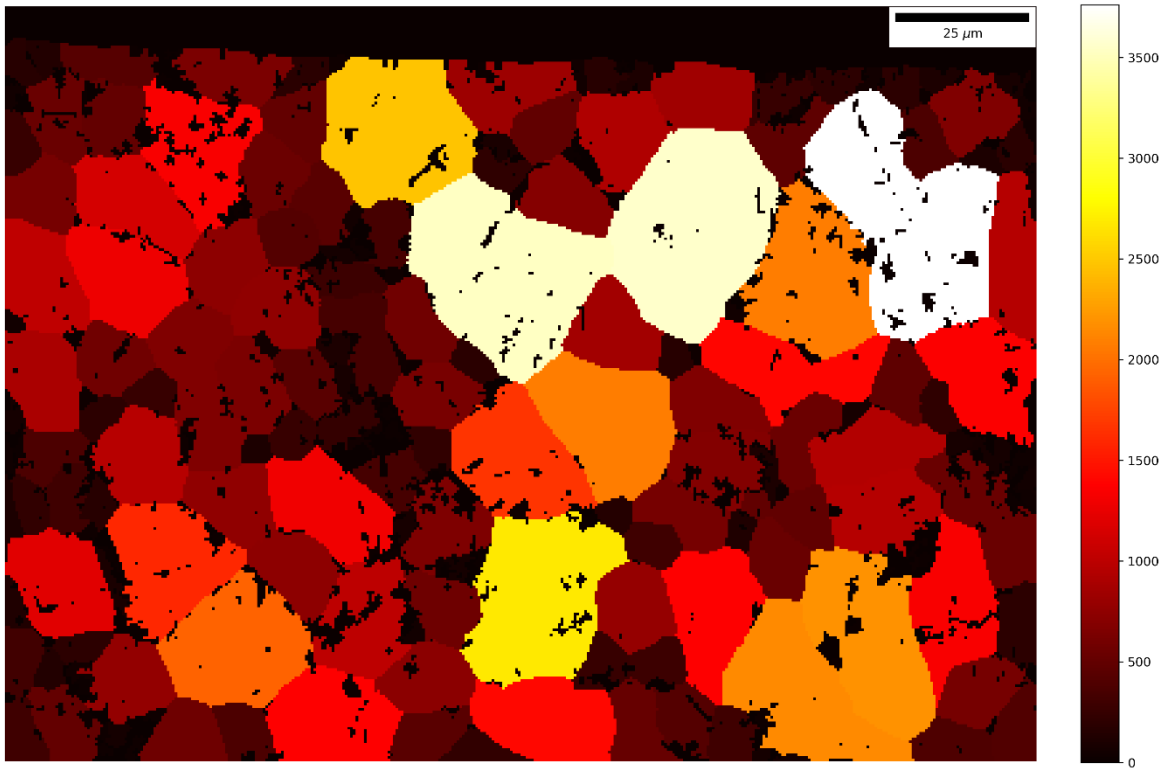

Figure 5.15 Grain area map of a rolled surface. Grain area is given in pixels (1 pixel = 0.25 μm^2).

Width is a difficult dimension to define and measure since it is considered to be the distance "side to side" of an object or the lesser of two dimensions of a shape [8]. While this is intuitive for the human eye, which is able to immediately identify two sides from which to estimate a width, this method is not quickly applicable computationally and so is often done manually [9]. There are around 500 grains in each measurement area, each with areas that include up to 3500 measurement points, so a method that scaled well was required. The width of a grain defined here is not the same as its horizontal span across the measurement area which is used in the ASTM E112-13 [10]. For example, if a grain were long and thin in the horizontal direction its length would be considered to be the longest distance between two points of the grain, whereas the width would be taken as the distance across, edge to edge, perpendicular to the length direction. This makes the exact definition of width difficult.

Algorithmically forming two "callipers" to measure the width of each grain in a range of orientations and pick the smallest was considered, but this method was complicated and scaled badly. Another method that used the known coordinates of the two furthest pixels in a grain to calculate the equation of a line connecting them, before measuring the distance to the edge of the grain from the middle of this line was also considered but found to be overly complex. Instead the area/length definition was chosen. Since width is poorly defined, every method of calculating the width of given shapes will produce

different results. The implications of the chosen method are considered in the Discussion, in Section 5.4.

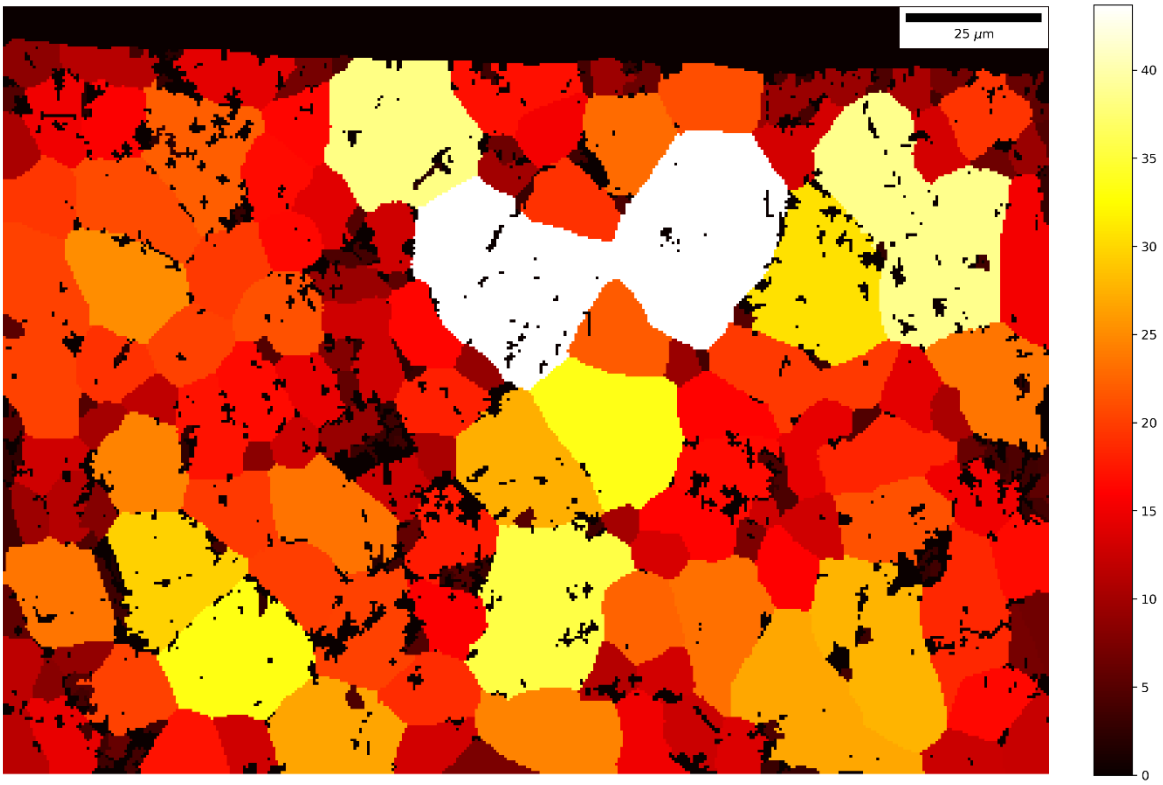

Figure 5.16 Grain width map for a rolled surface. Width is given in pixels (1 pixel = 0.5 µm).

Calculating Grain Shape Ratio

The ratios between the lengths of the grains and their widths were calculated and put into another dataset referred to as shape ratio, or shape. This is shown in Figure 5.17. The factor is similar to grain aspect ratio, which is the longest/ shortest diameter but differs in the calculation of grain width [9]. For grain aspect ratio, the shortest diameter is considered to be the shortest projection of a rotating grain, while the grain area/length is used here.

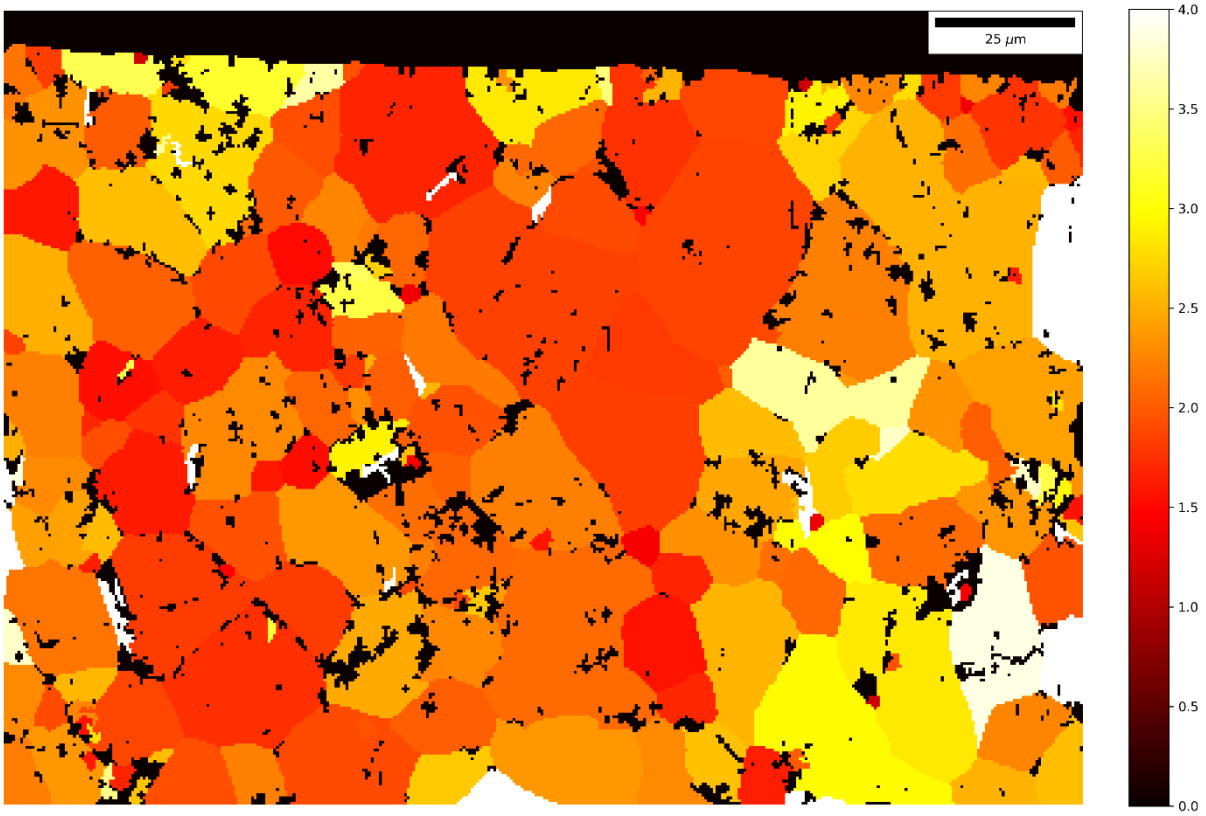

Figure 5.17 Grain shape map for a rolled surface. Showing the ratio of individual grain lengths to widths in colour. Scale bar is the ratio between length and width.

Figure 5.17 shows a grain shape map for a cross-sectionally mounted rolled surface. It shows the brightest grains with a grain shape ratio of around 3.4, indicating they are 3.4 times as long as they are wide. It also shows that for this sample the majority of grains have a grain shape ratio between 1 and 2. This way of viewing the grain structure also provides a map showing that locations will have the greatest discrepancy between the elastic strain measured and their stress, since shape is shown to be a major factor in calculating the bend angle of a grain.

Grain Strain and Stress Measurement

To calculate strain, the orientation spread for each grain was considered. When a crystalline material is under strain the grains bend, meaning that for a single grain the orientation at one end is different to that at the other [11]. The difference in these orientations is known as the orientation spread and indicates how much a grain has elastically, or plastically deformed. A typical method for quantifying the orientation spread is known as the Grain Orientation Spread (GOS) [12]. This is the average misorientation from the average grain orientation value. This has a number of drawbacks, for instance

since it is an average, large extraneous misorientation will influence the value, especially in smaller grains. Additionally, any errors in grain designation can cause wildly inaccurate GOS measurements, since the misorientation recorded in between different grains rather than of a single grain. For these reasons, GOS is typically only recorded for values lower than 2° [11]. The method presented here uses the Full Width at Half Maximum (FWHM) of individual grain orientation spreads to overcome both of these issues.

Figure 5.18 shows a histogram of crystallographic orientation measured for a single grain, which shows two distinct peaks. This is the result of identifying twin grains as single grains or when two adjacent grains are misoriented by less than the threshold value (7°). For the purposes of identifying the orientation spread, only one peak per grain should be assessed [5]. The area under the peak is proportional to the area of the grain and the FWHM of the peak, which is presented as a green line in Figure 5.18, and shows the distribution of orientation, or the amount of bending. It would be expected that longer grains, or more deformed grains, have wider, flatter peaks since they should have a larger GOS. A more deformed grain will contain a greater spread of misorientations and a longer grain, since a uniform misorientation gradient will allow for larger differences in misorientation at the extreme ends. The two peaks shown in Figure 5.18 show that two distinct groups of orientation are seen in what has been (incorrectly) identified as a single grain. This indicates that in fact, two grains have been selected and so to measure the orientation spread one peak must be discarded. This is a good example of where the standard GOS measurement would falsely indicate a value over the allowed threshold [12]. By using the FWHM method and choosing the largest peak, an orientation spread can still be calculated for this grain.

The limits on the orientation axis of Figure 5.18 are the range of orientations of the grain. Orientation of the E1 angle wraps around at 360°, so although the two peaks may look close together by wrapping at the x-axis limit, they are in fact very distinct. Because a minority of grains exhibit multiple peaks, the range of misorientations within a grain such as this would massively exaggerate the bending of the grain and so an algorithm to measure the thickness of the peaks and take the largest one was used. The widest peak was then considered to represent the whole grain since it envelops the majority of the grain and this would not act to obscure high stress areas. This eliminates errors caused by twinned grains being identified as single grains.

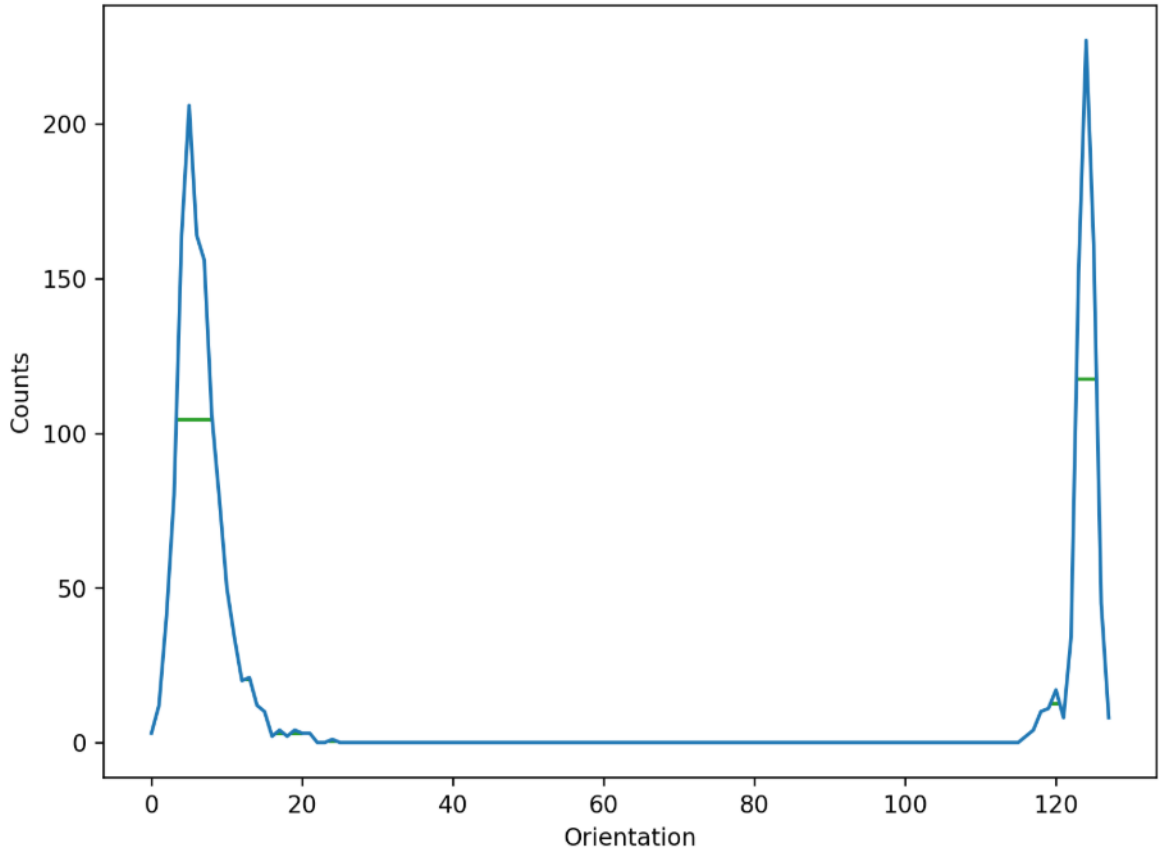

Figure 5.18 The distribution of orientation within a single grain.

Using the strain and grain shape ratio datasets, it was possible to produce a stress estimation dataset that considered the shape of the grains, using Equation 5.6, and a Young's Modulus of 200 GPa, this is presented in Section 5.3.3.4.

5.3.3.2. Grain Characterisation Results

Grain length, area, and width were calculated for measurement areas for each surface finish in order to calculate grain shape ratios. Figure 5.19 shows the grain diagram coloured by the shape ratio of each grain for the four samples. Overall, both high and low shape ratio grains are evenly distributed with regards to depth. Grains tend to be rounded with a shape ratio of between 1 and 2.

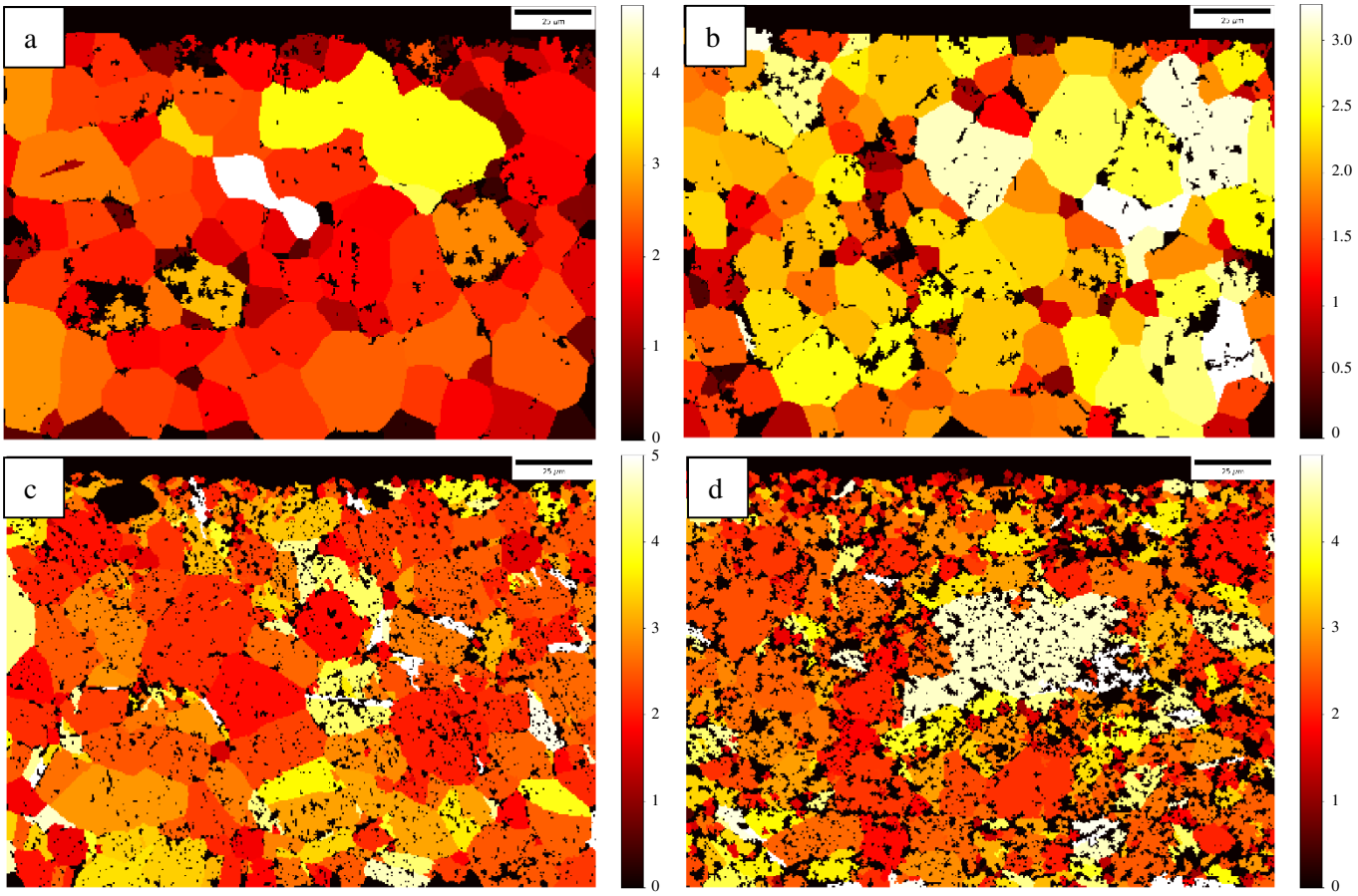

Figure 5.19 Shape maps for: A brushed, B rolled, C ground, D shotblasted surfaces. Scale bar is the ratio between length and width.

5.3.3.3. Strain Mapping

Figure 5.20 shows strain maps in degrees for the four surface finishes. The magnitude of the strain measured (i.e. 0 - 8°) is consistent with that measured by the Tango HKL software presented in Figure 5.9., although the distribution is different.

Should an area of the sample be under uniform stress, some correlation would be expected between strain and grain length since longer grains would deform further under the same stress. This is observed in these diagrams, with larger grains making up the majority of the high strain grains, and smaller grains contributing very little to the observed strain. This effect is a limitation of using strain maps calculated in this manner. A small grain in the sampling area could have the same angular misorientation spread to length ratio, brought about by being under the same stress as neighbouring grains, however the total spread measured would remain low. This highlights the usefulness of considering the flexibility due to the shape and length of grains when converting strain into stress.

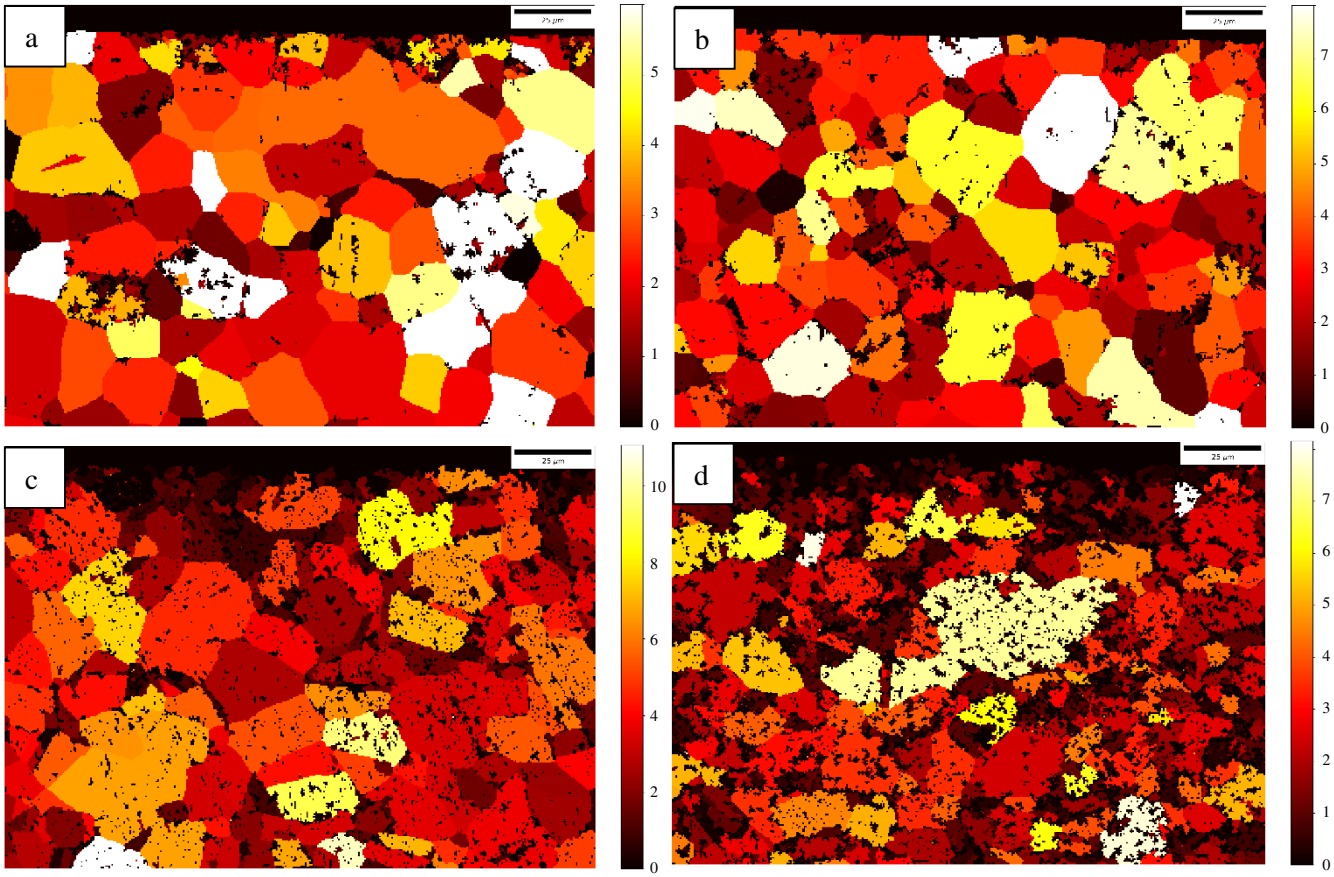

Figure 5.20 Strain maps in degrees into a surface for: A brushed, B rolled, C ground, D shotblasted surfaces.

Figure 5.21 details the relationship between grain shape and strain for the four samples. Each point represents a single grain. Overall grains measuring the highest amounts of strain have grain shape ratios between 2 and 4, at the average shape ratio value. This is the opposite of what would be expected if the bulk material were to deform uniformly in response to a stress. The higher the shape ratio, the longer and thinner a grain is proportionally and therefore the less stiff and more flexible it is. This effect may be visible in these graphs in the lowest value for grain shape ratio for the strain range. This appears to increase with strain leading to an absence of high strain, but very low shape ratio grains.

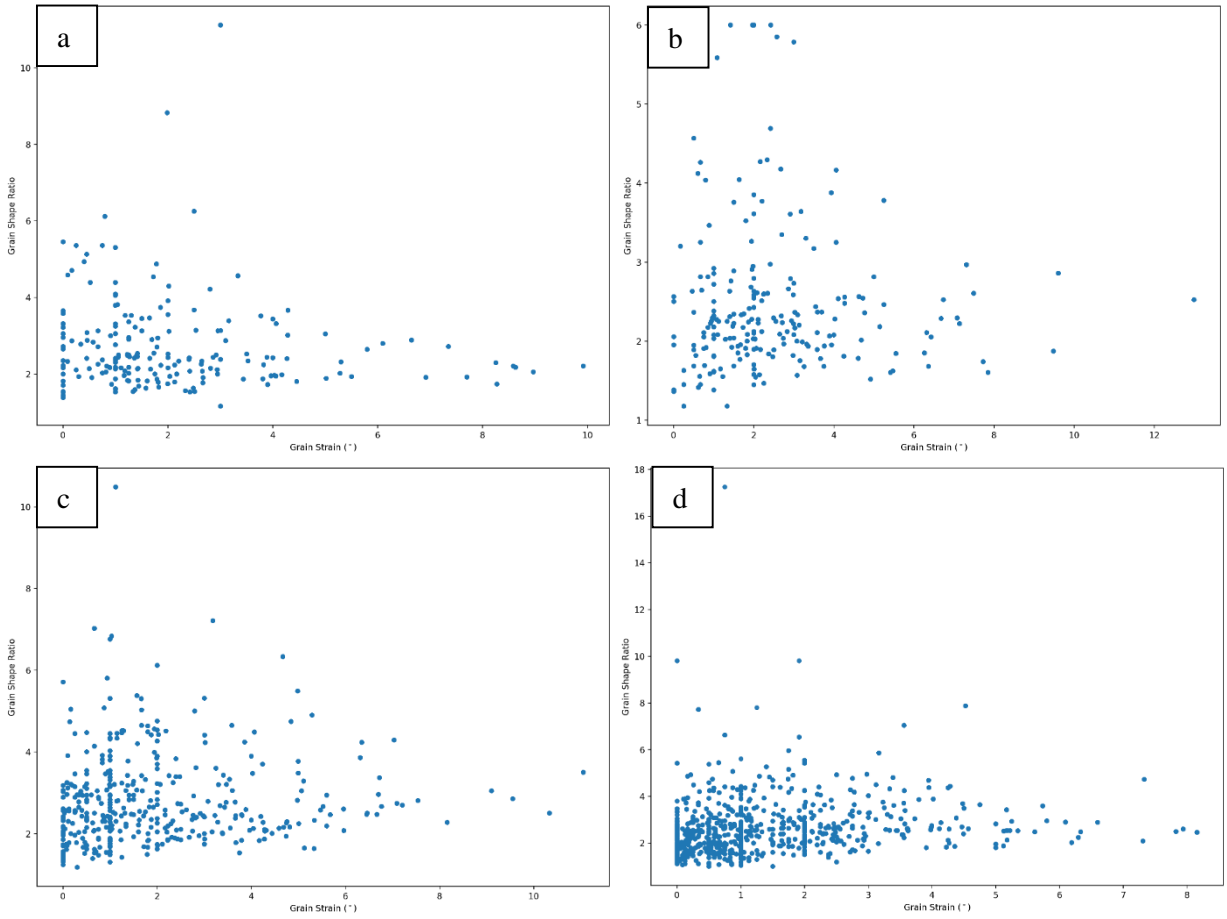

Figure 5.21 The relationship between grain shape and strain for: A brushed, B rolled, C ground, D shotblasted surfaces. Strain is given in degrees and shape is the ratio between length and width. The vertical lines apparent in the plot areas are a product of the analysis procedure.

5.3.3.4. Stress Mapping

Figure 5.22 presents stress maps for cross-sections of samples with four different surface finishes. These have been calculated using the strain calculated from the distribution of crystallographic orientations present in each grain coupled with mechanistic considerations as to how the size and shape of grains affect their response to an applied stress. The calculation method is explained in detail in Section 5.3.2.

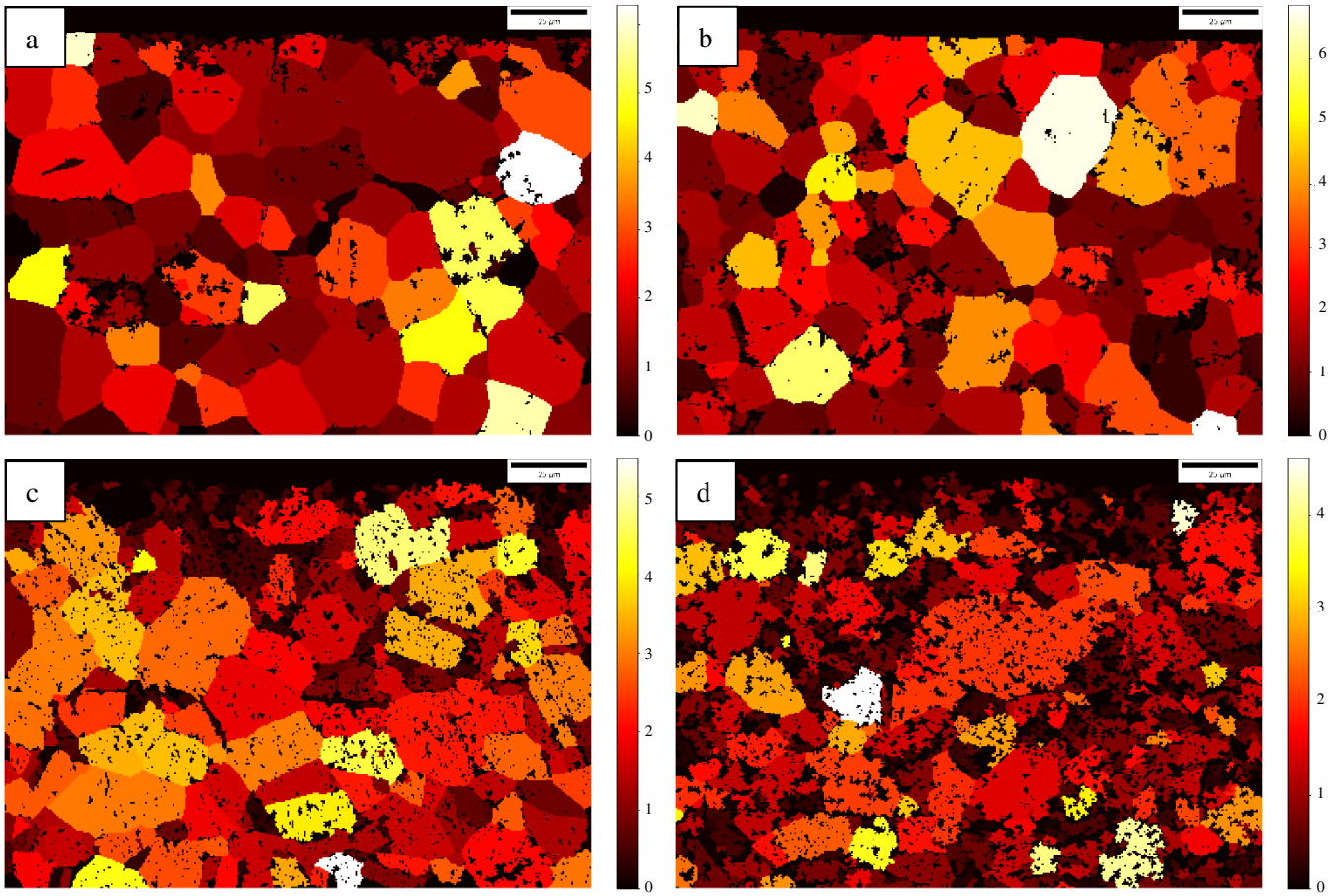

Figure 5.22 Stress maps into a surface for: A brushed, B rolled, C ground, D shotblasted surfaces. Scale is in GPa.

This has shown no detectable stress change with respect to depth of the sample over the 140 µm measurement area; however, it has revealed that individual grains in the material harbour the majority of the residual stress which was previously not detected by plotting strain alone.

The measurement area of the brushed surface (Figure 5.22a) contains 3 high-stress grains with stresses over 5 GPa. This is well above the yield stress of the material and so this is evident of plastic deformation and work hardening, rather than a residual elastic stress. Where stresses in this range are reported by this method, they should be interpreted as indicating deformation. There is little pattern to the distribution of the deformed grains.

When compared with Figure 5.9 (the distribution of strain in the surface) it can be seen that the stress distribution is consistent with the strain distribution in some regards such as magnitude, but deviates in others such as the predominance for smaller grains to bear higher stresses in Figure 5.22. This shows the importance of considering the effects the area, length and shape of each grain have on the flexibility of individual grains and their ability to withstand the effects of an applied stress.

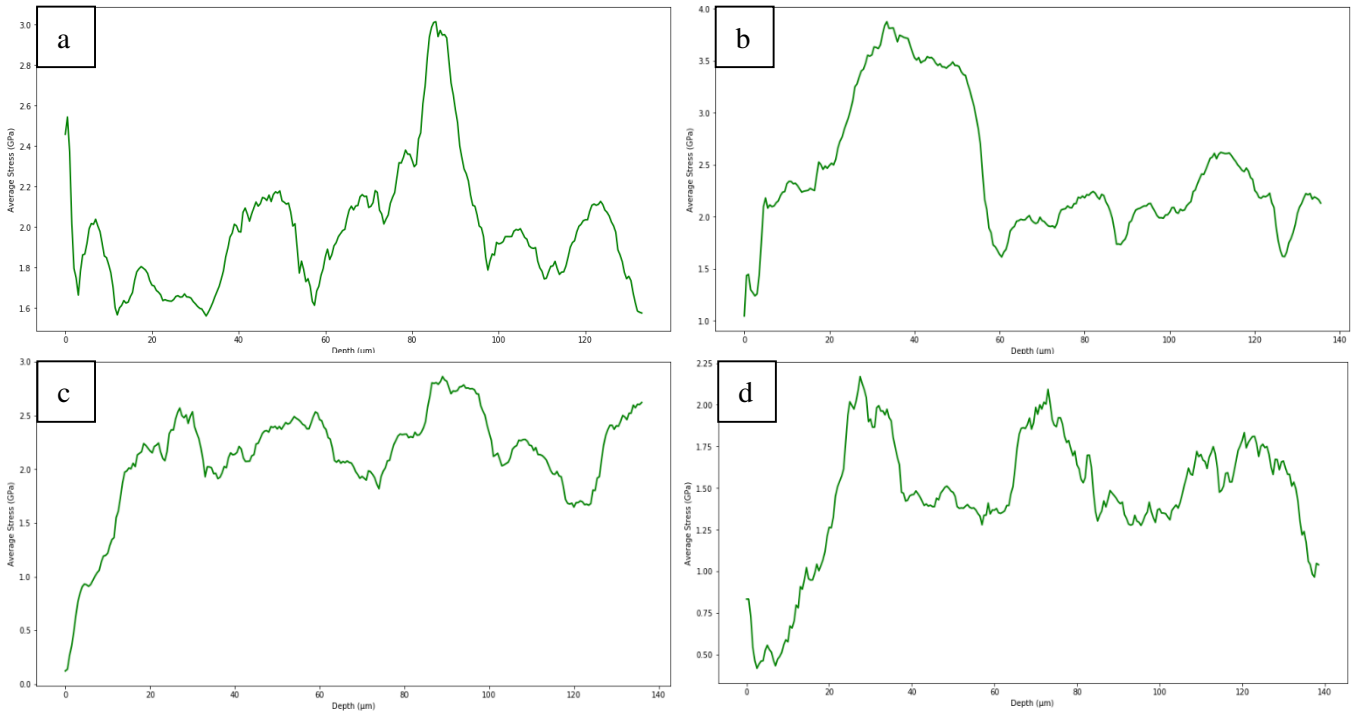

Figure 5.23 Average grain stress with depth for: A brushed, B rolled, C ground, D shotblasted surfaces.

Figure 5.23 shows the average grain stress calculated with respect to depth for four surface finishes. Average stress for depth for a 140 μm wide measurement can be affected by individual grains, leading to a high variation over distances corresponding to grain widths. For all samples, the calculated stress ranged between 1.5 to 3 GPa, evidence of large amount of work hardening near the sample surfaces. Initial rises or falls in stress at the edge of the surface is an artefact due to single grains at these points being the only grains at that initial depth and so dominating the average.

Figure 5.24 shows the relationship between grain stress and area for all four samples. Each point represents a single grain with the size of the point being proportional to the area of the grain. It can be seen that very small grains have a wide distribution of stresses. For the ground and shotblasted samples this distribution narrows for larger grains, with the minimum possible value rising from 0 to 2 GPa, indicating work hardened grains. For the brushed and rolled samples, this narrowing is not as clearly observed.

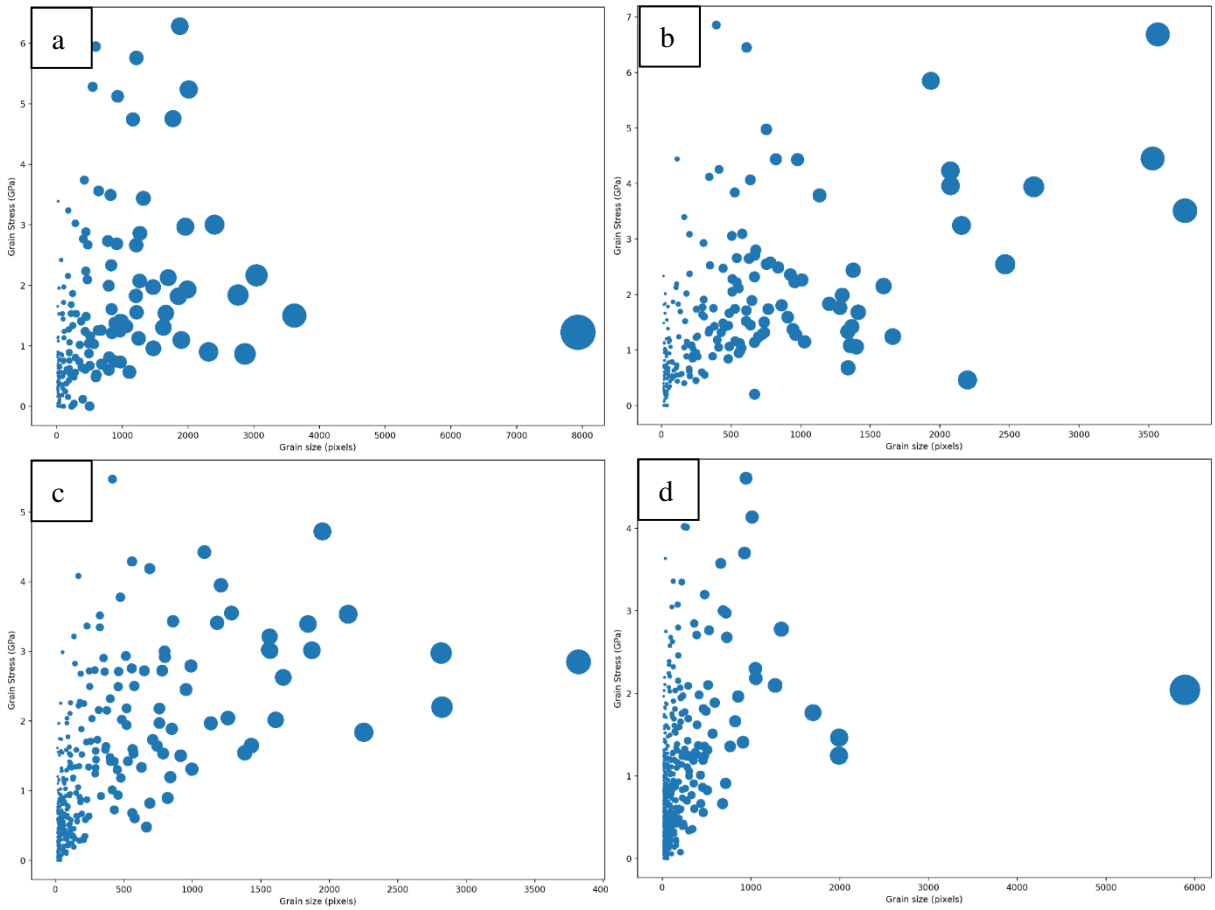

Figure 5.24 The relationship between grain stress and area for: A brushed, B rolled, C ground, D shotblasted surfaces.

By number, Figure 5.24 shows that for all samples, smaller grains are more common than larger grains. Since the grain area is plotted proportionally to the area of the points, it can also be seen that the distribution by total area is more evenly spread out. The larger grains are less common, but they take up more space making the probability for random point to be of a large or small grain more even.

It is interesting that very small grains rarely exhibit the largest stresses. This could be because their size causes them to avoid the process that imparts stress onto grains around them. Stress may be transmitted through the surface specifically through the larger grains, or smaller grains may be more mobile and able to physically move to accommodate an applied stress rather than absorb the stress and deform.

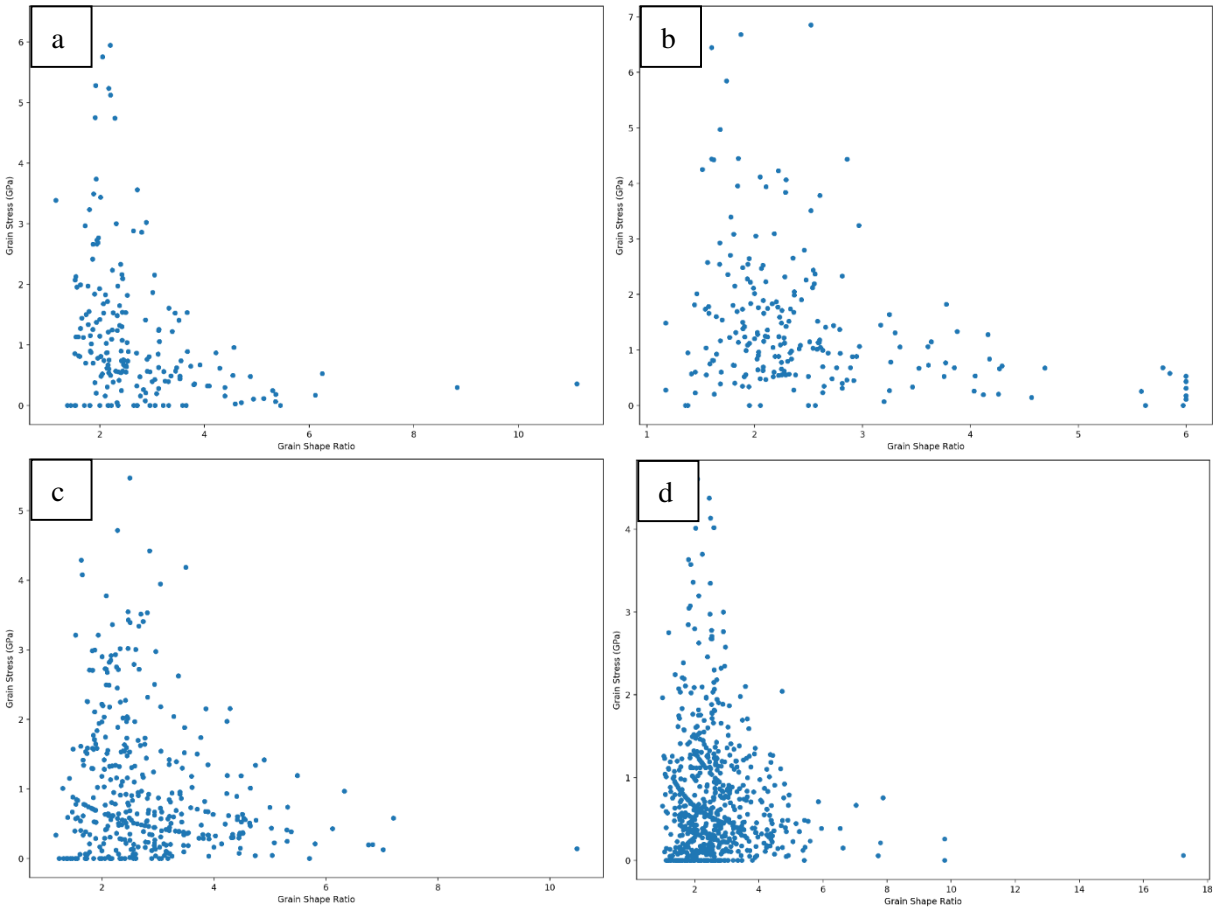

Figure 5.25 The relationship between grain stress and shape for: A brushed, B rolled, C ground, D shotblasted surfaces.

Figure 5.25 shows the relationship between the stress of a grain and its shape for the four surface finishes investigated. A similar distribution is seen across all samples. There is a wide distribution of grain stresses for grains with a low grain shape ratio and a smaller distribution, of lower stresses, for grains with a higher shape ratio. This could be for two reasons. The shape of the grain could influence its ability to withstand stress, with longer thinner grains being quicker to relax and, therefore, having lower residual stresses. There is also the effect that if a long grain is bent in two directions, it will register as being less bent than one that is highly bent in one direction only. Alternatively, because the distribution of the strain of grains is largely uniform across the range of shapes of the grains, and the stress is calculated with the shape as a factor, a negative power shape curve would be expected to match the distribution of grain shapes.

5.4. Discussion

This Chapter has explored the effects of surface finish on the microstructure and residual stress / strain of stainless steel, which will likely impart an effect on the response to corrosion. The following effects were seen for these parameters:

Grain size

- Larger grains show greater strain.
- Smaller grains are much more common.

Grain shape

- Both the most highly strained, and the most highly stressed grains tend to have a shape ratio over 2.

Grain depth

- No clear relationship has been found between grain depth and stress.

The following discussion describes the efficacy of the stress and strain methods utilised and describes the results with respect to the different surface finishing techniques.

5.4.1. Stress and Strain Mapping Technique Evaluation

The misorientation maps developed by application of Equation 5.6 were found to be in disagreement with those produced by the Tango software regarding the distribution of strains, although they were consistent with the magnitude and range of strain. The disagreement regarding distribution does little to confirm the validity of this method, although it does suggest that the results calculated by the Tango HKL software are not reproducible.

One reason for this difference is the method for calculating the grain misorientation spread. The Tango HKL software assigned the maximum misorientation of any two points in a grain to the grain, while the method presented here took the FWHM of the misorientation spread [5].

Stresses were found to be higher than yield stress (0.21 GPa) the tensile strength for the material (0.56 GPa) [13]. Localised plastic deformation and work hardening can be considered to be a major contributor to the stabilisation of high degrees of surface stress [14]. Plastic deformation in all four

surface finishes has been shown here to register over 5°. This strain cannot be maintained elastically and so a large amount of plastic deformation and work hardening is evident.

The Young's modulus for individual grains can vary by ± 25% of the average for the bulk material depending on orientation [15]; it was not within the scope of this Chapter to take this into account, meaning there is a contribution to the final error of around 25%. Additionally, a proportion of the strain measured will consist of that associated with plastic deformation and, therefore, will not scale linearly to stress. Single crystals have been tested to have yield stresses over 60% higher than their polycrystalline counterparts so as a rough estimate, the maximum tensile strength for a single grain is considered to be around 0.8 GPa [16]. This can be used as a cap with all stress measured above this being considered to belong to extensively deformed grains. When plastically deformed, an area can either maintain the maximum yield stress across it or it can relax to a slightly less strained state leaving the area with a residual stress less than the yield stress but still with a degree of plastic strain. This strain is detected in the EBSD measurement and is related to both Type 2 and Type 3 residual stresses [14]. Type 2 residual stresses are attributed to the microscale and are identified by changes in the microstructure such as grain size refinement and texture on the surface. Type 3 residual stresses involve stresses at the atomic scale such as chemical segregations at grain boundaries and small areas of phase change.

Is deformation uniform?

In the 1930s, Taylor[17] proposed a model to describe stress-strain behaviour in polycrystalline materials. It was assumed that strain in a material would be uniform, such that the strain in any grain is equal to the average strain. This assumption is applied to the materials analysed in this work and the implications of this assumption are considered here.

If the material had uniform strain throughout, the method of ascribing the range of misorientation within a grain to its strain would produce different grain orientation spreads for different grains. Orientation spread would be dependent on size since a constant strain over a larger size would lead to a greater deformation and therefore misorientation range. Grain orientation spread would also be independent of shape. Previous literature has found the Taylor models to fail when large strain heterogeneities occur and have highlighted grain shape as a particular cause of this [18].

Are larger grains preferentially stressed?

Smaller grains may be somewhat protected from stresses by the larger grains around them. These larger grains could form a continuous link through the material through which force can be transferred, bypassing the smaller grains. If stress is transferred through the material through the larger grains, these grains would be under higher stresses and exhibit a higher degree of strain. This effect may be observed in Figure 5.24, which shows a positive correlation between area and stress of grains. It is well known that plastic deformation is a heterogeneous process in polycrystalline materials [12]. This supports the results showing that stressed grains do not tend to be grouped together but appear dispersed through the top layer of material.

Higher strains in larger grains has been predicted by modelling [19]. Larger grains have been found to have a low yield strength and high work hardening rate. The topic of the effect of grain size on work hardening behaviour has yet to reach consensus [19]. The effect of larger grains (which work harden at a higher rate and occupy a larger fraction of the total volume), is to raise the overall work hardening rate of the material.

In addition to this, because smaller grains have been shown to have higher yield strengths they deform less and so can be under more stress than the average. Overall, this means that for the same applied deformation, larger grains will deform more, show more grain orientation spread, but exhibit less residual stress than smaller grains.

Weaknesses in the stress calculation method

The lowest grain shape ratio achievable is 1, which is for an object with a width the same as its length. Should its width be greater than its length, its width would be considered to be its length, so the ratio can be no lower than 1. The method used here estimates the width by dividing the area by the length. This is then used to calculate the "grain shape ratio" = $\frac{L^2}{A}$. The largest area that can be found for a given length is with a circle, at $A = \pi r^2$. For length this becomes $A = \frac{1}{4}\pi D^2$. From this, the smallest grain shape ratio that can be achieved, should a grain be perfectly circular, is $\frac{4}{\pi}$ or 1.27, not 1. This difference represents a minor systematic skew that is applied in the shape calculation.

In this model, the stress applied to the grain is assumed to be orthogonal to its longest direction, causing maximum strain. In practice, this would rarely be the case. Stresses applied at off angles were not considered.

This model assumes no difference between the Young's modulus of a material and of an individual grain. In reality the Young's modulus of a single crystal and of a large polycrystalline material would differ. Since this material is almost entirely crystallized the assumption is made that the bulk Young's modulus represents an individual grain.

There is likely to be a large source of error in the measurement of maximum misorientation angle in the strain contouring maps. It is likely that error, which is caused by surface defects, could skew the maximum misorientation measurement. Since it is the maximum misorientation which is measured, isolated individual points of error could contribute to the maximum.

Grain shape ratio is a 2D measurement while grains are 3D. A grain may be much deeper than expected by its 2D appearance and so more affected by a stress than expected, equally a grain could be very shallow into the page and so be more affected by a stress than expected. This model allows some stress prediction to be made from 2D data.

Equation 5.6 can also be calculated using the flexural modulus which would result in a similar equation, with the difference being L and α both become squared [20]. This amplifies the difference between these two values and so has a larger effect when applied to long thin objects such as fibres or sheets. For objects where the length is a similar magnitude to the width, as is the case for the grains of stainless steel the difference in results between the two equations is small.

As well as allowing a quantitative estimation of stress to be made, rather than just strain, this method reduces error in the interpretation of strain maps since it provides a way to include the effect of grain shape. While crude, it provides reasonable figures (±30%) and allows sensible comparisons between samples.

5.4.2. Effect of Surface Finish on Microstructure and Strain

Novel methods for interpreting crystallographic data have been presented such as the measurement of grain width, and the calculation of grain shape ratio. The grain shape ratio has been found to be a useful parameter when estimating grain stress from grain strain since it is responsible for the flexibility of the grain. High levels of residual stress were detected in all surfaces indicating plastic deformation consistent with previous literature [21].

Strain mapping based on maximum grain misorientation or grain orientation spread is insufficient to analyse stress alone. Once grain shape was considered in the form of grain shape ratio, areas previously considered to be of high stress were found to be comparable to those of average stress. Previous studies

have used grain size to normalise grain orientation spread and found it to not be an important factor [12]. Future use of misorientation angle to estimate stress should consider the shape of grains.

The shotblasted and ground surfaces exhibited large amounts of grain deformation, especially within the top 50 μm of the surface, consistent with high levels of residual strain caused by their surface finishing methods. Pockets of strain up to 50 μm deep were identified in the shotblasted and ground samples. This indicates the movement of chains of grain dislocations through the material. Pockets of strain tend to be detected in areas with smaller, fractured grains. These areas of high residual stress have recently been shown to cause SCC [22].

This Chapter has shown that for all four surfaces individual grains in the material harbour the majority of the residual stress showing strong plastic heterogeneity. While this was not identified by plotting strain, this distribution has been found before by studies using similar techniques [12].

Only one sample site was analysed for each surface finish, which reduced the significance and generalisability of the measurements. For each site measured, the characteristics of around 500 grains were calculated. This made it possible to draw conclusions about these specific sites, which were chosen to include features for each surface finish such as ridges and valleys that represented the surface well.

5.4.3. Possible Implications of Grain Area, Strain and Stress on SCC

The large residual stresses found in the shotblasted sample are likely to be compressive and so will mitigate the effect of an applied tensile stress when under SCC conditions [23]. This would be expected to give the shotblasted surface a superior protection against SCC, though this effect would be nullified for uniform, pitting or crevice corrosion.

The large residual stresses found in the ground surface are likely to be tensile in the direction of grinding. This will exacerbate SCC when the applied stress is aligned with the direction of grinding [24]. It would be expected to reduce the required critical applied stress for SCC and cracking would occur at lower stresses, or faster than other surfaces in the same conditions. Additionally, due to the high residual stresses measured, it is possible that this surface could undergo SCC with no applied external stress as has been previously shown [25].

The rolled surface and the brushed surface show extremely low levels of stress by comparison. They are likely to perform better than the ground surface and worse than the shotblasted surface in SCC conditions.

5.5. References

[1] S. Ghosh and V. Kain, "Microstructural changes in AISI 304L stainless steel due to surface machining: Effect on its susceptibility to chloride stress corrosion cracking," *J. Nucl. Mater.*, vol. 403, no. 1–3, pp. 62–67, 2010.

[2] W. Zhang, K. Fang, Y. Hu, S. Wang, and X. Wang, "Effect of machining-induced surface residual stress on initiation of stress corrosion cracking in 316 austenitic stainless steel," *Corros. Sci.*, vol. 108, pp. 173–184, 2016.

[3] Y. F. Al-Obaid, "The effect of shot peening on stress corrosion cracking behaviour of 2205-duplex stainless steel," *Eng. Fract. Mech.*, vol. 51, no. 1, pp. 19–25, 1995.

[4] D. Shiozawa, Y. Nakai, R. Miura, N. Masada, S. Matsuda, and R. Nakao, "4D evaluation of grain shape and fatigue damage of individual grains in polycrystalline alloys by diffraction contrast tomography using ultrabright synchrotron radiation," *Int. J. Fatigue*, vol. 82, pp. 247–255, 2016.

[5] HKL Technology, "Channel5," *(Manual)*, 2001.

[6] S. A. A. Akbari Mousavi and R. Miresmaeili, "Experimental and numerical analyses of residual stress distributions in TIG welding process for 304L stainless steel," *J. Mater. Process. Technol.*, vol. 208, no. 1–3, pp. 383–394, 2008.

[7] D. Peckner and I. M. Bernstein, *Handbook of Stainless Steels*. 1977.

[8] Cambridge University, "Cambridge Dictionary | English Dictionary, Translations & Thesaurus," *Cambridge University Press*. 2018.

[9] R. Heilbronner and N. Keulen, "Grain size and grain shape analysis of fault rocks," *Tectonophysics*, vol. 427, no. 1–4, pp. 199–216, 2006.

[10] A. R. Balachandramurthi, J. Moverare, N. Dixit, D. Deng, and R. Pederson, "Microstructural influence on fatigue crack propagation during high cycle fatigue testing of additively manufactured Alloy 718," *Mater. Charact.*, vol. 149, 2019.

[11] Y. B. Chun, M. Battaini, C. H. J. Davies, and S. K. Hwang, "Distribution characteristics of in-grain misorientation axes in cold-rolled commercially pure titanium and their correlation with active slip modes," *Metall. Mater. Trans. A Phys. Metall. Mater. Sci.*, vol. 41, no. 13, pp.

3473–3487, 2010.

[12] N. Allain-Bonasso, F. Wagner, S. Berbenni, and D. P. Field, “A study of the heterogeneity of plastic deformation in IF steel by EBSD,” *Mater. Sci. Eng. A*, vol. 548, pp. 56–63, 2012.

[13] Outokumpu, “Steel Grades, Properties and Global Standards,” 2004.

[14] S. Ghosh, V. P. S. Rana, V. Kain, V. Mittal, and S. K. Baveja, “Role of residual stresses induced by industrial fabrication on stress corrosion cracking susceptibility of austenitic stainless steel,” *Mater. Des.*, vol. 32, no. 7, pp. 3823–3831, 2011.

[15] R. L. Mullen, R. Ballarini, Y. Yin, and A. H. Heuer, “Monte Carlo simulation of effective elastic constants of polycrystalline thin films,” *Acta Mater*, vol. 45, no. 6, 1996.

[16] S. H. Sun, T. Ishimoto, K. Hagihara, Y. Tsutsumi, T. Hanawa, and T. Nakano, “Excellent mechanical and corrosion properties of austenitic stainless steel with a unique crystallographic lamellar microstructure via selective laser melting,” *Scr. Mater.*, vol. 159, pp. 89–93, 2019.

[17] G. Yang and S. J. Park, “Deformation of single crystals, polycrystalline materials, and thin films: A review,” *Materials (Basel).*, vol. 12, no. 12, 2019.

[18] S. Tiem, M. Berveiller, and G. R. Canova, “Grain shape effects on the slip system activity and on the lattice rotations,” *Acta Metall.*, vol. 34, no. 11, pp. 2139–2149, 1986.

[19] B. Raeisinia, C. W. Sinclair, W. J. Poole, and C. N. Tomé, “On the impact of grain size distribution on the plastic behaviour of polycrystalline metals,” *Model. Simul. Mater. Sci. Eng.*, vol. 16, no. 2, 2008.

[20] C. Zweben, W. S. Smith, and M. W. Wardle, “Test methods for fiber tensile strength, composite flexural modulus, and properties of fabric-reinforced laminates,” 1979.

[21] S. G. Acharyya, A. Khandelwal, V. Kain, A. Kumar, and I. Samajdar, “Surface working of 304L stainless steel: Impact on microstructure, electrochemical behavior and SCC resistance,” *Mater. Charact.*, vol. 72, pp. 68–76, 2012.

[22] J. Kuniya, I. Masaoka, R. Sasaki, Y. Nakagawa, and A. Naruse, “Effects of surface finishing on stress corrosion cracking of austenitic stainless steels in high temperature water,” *Hitachi Res. Lab.*, vol. 1, 1978.

[23] M. Row, “A review of manufacturing processes used in stainless steel intermediate level waste containers to evaluate the presence of residual stresses report to NDA,” *Serco Rep. to NDA*, no.

3, pp. 1–42, 2009.

[24] A. Turnbull *et al.*, “Sensitivity of stress corrosion cracking of stainless steel to surface machining and grinding procedure,” *Corros. Sci.*, vol. 53, no. 10, pp. 3398–3415, 2011.

[25] S. Rahimi, K. Mehrez, and T. J. Marrow, “Effect of surface machining on intergranular stress corrosion cracking (IGSCC) in sensitised type 304 austenitic stainless steel,” *Corros. Eng. Sci. Technol.*, vol. 51, no. 5, pp. 383–391, 2016.

6. The Effect of Surface Morphology on Stress Distribution and its Effect on Atmospheric Stress Corrosion Cracking

6.1. Introduction

6.1.1. Stress Concentration

This Chapter investigates the effects that surface morphology has on the distribution and concentration of stress on a surface. The depth, sharpness, valley radius and openness of concave features affect the concentration of stress at the surface's lowest points [1]. These stress concentrations cause materials to crack under applied stresses that are far below their yield stresses and, in the case of stress corrosion cracking (SCC), can raise local areas of a surface over the stress threshold for SCC. These higher stresses can reduce the time it takes for SCC to occur and can increase the density and rate of cracking [3]. The surface morphology created by the surface finishing process can increase susceptibility to SCC by forming stress concentrations. This Chapter describes this process and assesses how this influences the initiation of corrosion.

The effect of surface morphology on the concentration of stresses and the fracture mechanics of cracks are both well-established fields of study [2]. It is well known that a notch in a steel plate will concentrate stress at its base, which is where cracking will then initiate. Once cracking has begun, the crack tip becomes the site of highest stress and so the crack propagates from the crack tip. This is analogous to how a sharp cut in a piece of paper will serve to initiate a tear.

Multiple analytical models describe stress concentration in 3D surfaces. These tend to describe perfect conditions with analytically derived results which are then tested with finite element analysis or through practical experiments. Some, such as the Neuber and the Arola and Ramulu models have been designed specifically for the consideration of surface roughness values [4][5]. In this Chapter these models are applied to real 3D surfaces and are compared.

6.1.2. Finite Element Analysis

To verify the accuracy and reliability of the application of the Neuber and Arola and Ramulu analytical models presented in this Chapter, surfaces were simulated by a Finite Element Analysis (FEA) technique. This method allowed for the estimation of the concentration of stresses in complex morphologies. The technique involved forming a model of the structure under consideration, and the breaking up of this into many parts, forming a mesh. Instead of calculating the effects of a force or stress on the whole part at once, much simpler calculations can be performed on each mesh segment, which, when combined, can produce very accurate estimations of the of the physics of the larger part. With a good quality model, a fine enough mesh and the sensible application of forces and boundary conditions, software such as Abaqus CAE produces good estimations where otherwise overly complex integration would be required.

Since FEA simulates the real-world behaviour of a material, it can be used to verify other models [6]. While the benefit of these models is their low computational cost, FEA trades this for higher quality results for complex shapes. As described in the literature review (Chapter 2), FEA has been used to estimate the stress concentration caused by some surface finishes [7]. However, this has only been achieved in 3D for surfaces formed by machining or additive manufacturing. This Chapter details a method by which it can be completed in 3D using VSI topographic data of four surfaces and presents the results of the successful application of this model, hence verifying the application of the Neuber and Arola and Ramulu analytical models.

6.1.3. Atmospheric Stress Corrosion Cracking Trial Introduction

To support the investigation and calculation of surface stress concentrations demonstrated in Section 6.5. and the demonstration of stress concentration shown by FEA analysis in Section 6.7., ASCC trials were performed. These trials also provide assessment on the effect of residual stresses computed in Chapter 4. The analytical assessments presented in Section 6.5. were somewhat corroborated by the in-depth 3D FEA analysis of stress concentrations, suggesting the presented theories behind the link between stress concentration and surface finish are correct. The ASCC trials, however, probe the link

between stress concentration and corrosion vulnerability by testing experimentally in laboratory conditions.

The brushed, ground, rolled and shotblasted surfaces of interest to intermediate level waste containers in this Thesis were exposed to under-droplet ASCC conditions and the time to crack, and nature of cracking was assessed. Additionally, the theory that surface finish could concentrate stress and therefore cause stress initiation in some regions was tested by observing orientation effects of the applied stress. For example, for a highly directional ground finish it was be expected that a stress perpendicular to the grinding direction would result in stress concentrations at the bottom of valleys. On the other hand, a stress in the direction of the grinding would not result in these stress concentrations and a difference could be found with different surface finishes. This stress orientation effect was measured by applying stress to surfaces in one of two directions and its performance assessed in ASCC conditions.

6.2. Surface Stress Analysis Methodology

6.2.1. Stress Concentration Theory

Stress concentrations in ideal conditions are discussed in the "Theory of Elasticity and Stress Concentration", where the derived solution for the stress concentration for an elliptical hole is presented [2]. This is shown in Equation 6.1 and Figure 6.1 where t is the depth of the feature, ρ is the root notch radius and σ_0 is an applied stress.

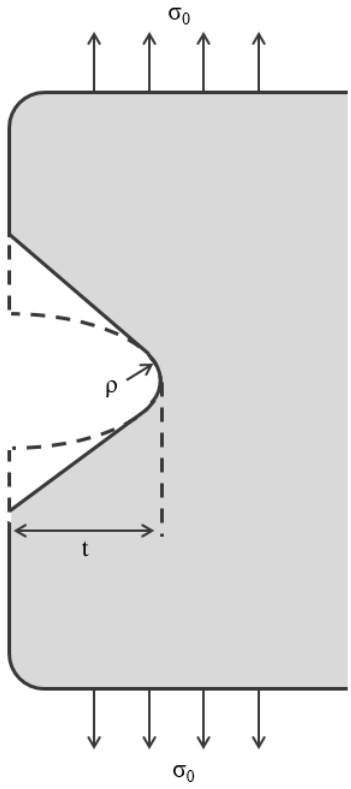

Figure 6.1 The parameters associated with an elliptical hole.

$$K_t = 1 + 2\sqrt{\frac{t}{\rho}} \qquad \textit{Equation 6.1}$$

This equation is commonly used for the estimation of stress concentration at features that are not perfectly elliptical in a method known as the “concept of equivalent ellipse” [2]. These shapes can be approximated as ellipses since they have a characteristic length and root radius. The key component in this equation is the root radius, the ellipse used to measure this is shown in Figure 6.. Although, fortunately, the root radius is well defined, the depth of the feature is far more arbitrary in a real surface with regular deviations, since it is poorly defined at exactly what height a surface starts. The average surface height is used for this in this Chapter.

6.2.2. Notch Root Radius Calculation

The notch root radius was calculated in the same way as the inverse summit curvature (ISsc) in Chapter 4. That is, the notch root radius at a point is the inverse of the second derivative of the height of the surface at that point.

6.2.3. Valley Identification

Only the stress concentrations at valleys were of interest since the stress concentration maximises at the surface minima. The bottoms of valleys were designated as locations where the first derivative of height was 0 and the second was positive, using a sample area of 4 adjacent points in any direction.

6.2.4. Neuber Model Calculation

The stress concentration factor at surface minimas was calculated with the Neuber model as described by Equation 6.2 [4]. The development of this model is detailed further in the literature review (Section 2.3.3.).

$$K_t = 1 + n\sqrt{\lambda \frac{R_z}{\rho}} \qquad \textit{Equation 6.2}$$

In Equation 6.2, ρ is the mean root radius of valleys, n is the state of stress (n = 1 for shear stress, n = 2 for tensile stress), and λ is the ratio between spacing and depth of the features, which is considered to be the openness ratio.

6.2.5. Arola and Ramulu Model Calculation

The stress concentration factor was also calculated using the Arola and Ramulu model presented in Equation 6.3 [5].

$$K_t = 1 + n\left(\frac{R_a}{\rho}\right)\left(\frac{R_y}{R_z}\right) \qquad \textit{Equation 6.3}$$

Similar to the Neuber model, this equation contains the term $\left(\frac{R_a}{\rho}\right)$, showing that an increase in roughness or a decrease in valley radius should be expected to increase the stress concentration factor. Notably, this equation does not contain a factor for the frequency of features, or the openness value as the Neuber model does.

6.3. Finite Element Analysis Methodology

6.3.1. FEA Method

Topographic data was collected on four surface finishes by VSI measurement, as described in Chapter 4. This data was then sectioned to take square sets of size 10 / 10 µm (high magnification) or 200 / 200 µm (larger measurement area). This gave horizontal and vertical resolutions shown in Table 6.1.

Table 6.1 Model Resolutions

	200 / 200 µm area	10 / 10 µm area
Horizontal Resolution	2 µm	0.1 µm
Vertical Resolution	0.02 µm	0.01 µm

These arrays were then processed by a purpose-made python program to convert into a 3D object as an STL (Stereo Lithography/ Standard Triangle Language) file (Appendix 2). To do this, the program utilised the STL ASCII encoding format whereby a 3D object can be represented by a series of triangles; a section of code describing a generic triangle is shown below. The array indexes of each value in the topographic data file, and its z number (representing height), once normalized, supplied the values for the vertices of each triangle. To be a coherent object, rather than just a surface, four sides and a base were constructed by the program, these were also formed of triangles meeting the surface, as shown in Figure 6.2.

facet normal n_i n_j n_k

outer loop

vertex $v1_x$ $v1_y$ $v1_z$

vertex $v2_x$ $v2_y$ $v2_z$

vertex $v3_x$ $v3_y$ $v3_z$

endloop

endfacet

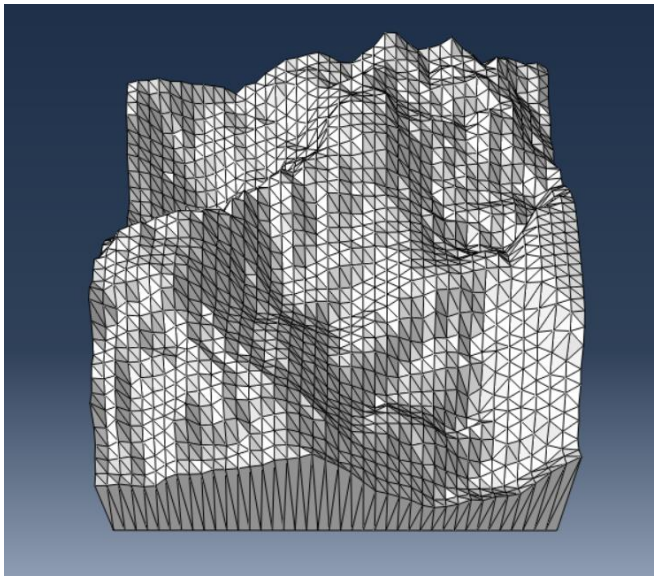

Figure 6.2 The 3D representation of topographic VSI data as an STL file, with sides and a base.

This file was then accessed in MeshLab [8], which was used to delete duplicate faces and vertices. Faces were then reoriented coherently, and any holes filled. This file was then exported as an STL file and opened in Fusion where the mesh was converted to a BRep representation. This step described the object as a solid object based on its boundary representation, rather than a shell, and exported as a .STEP file. This type of file is importable into Abaqus CAE software.

Abaqus CAE was used for the FEA modelling [9]. To mesh the part, it was seeded with mesh size 10. This was then propagated using a tetragonal structure to build a working mesh. The mesh had a coarseness around twice as fine as the resolution of the model, as shown in Figure 6.4. The material properties were defined to match 304L stainless steel with a Young's modulus of 200 GPa and a Poisson's ratio of 0.3.

Boundary conditions were applied. An encastre condition was applied to one side, and a vertical symmetry condition was applied to the base as shown in Figure 6.3. A load of -1 GPa was applied to the opposite side as a uniform pressure, applying tension to the part. The simulation was executed, and the results shown in Section 6.7.

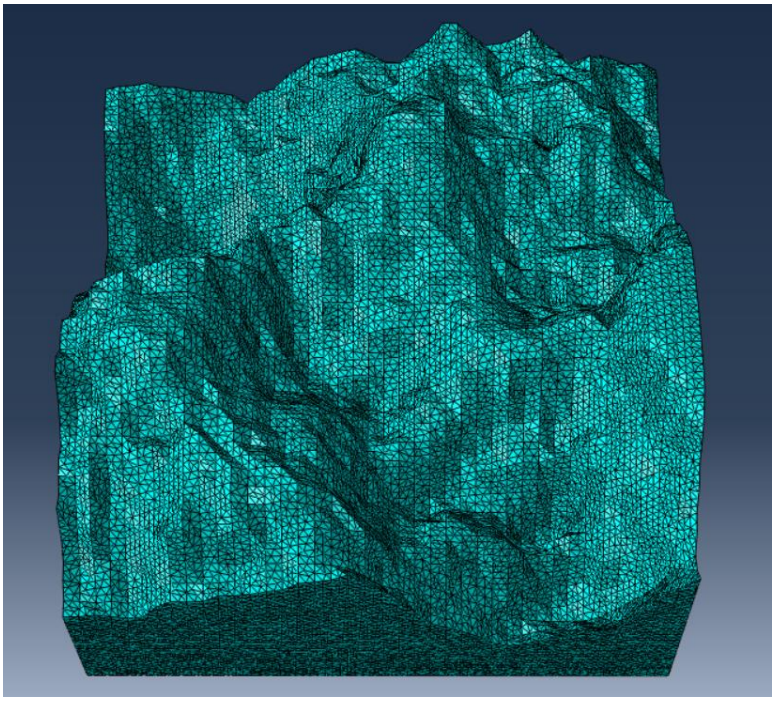

Figure 6.4 A meshed part.

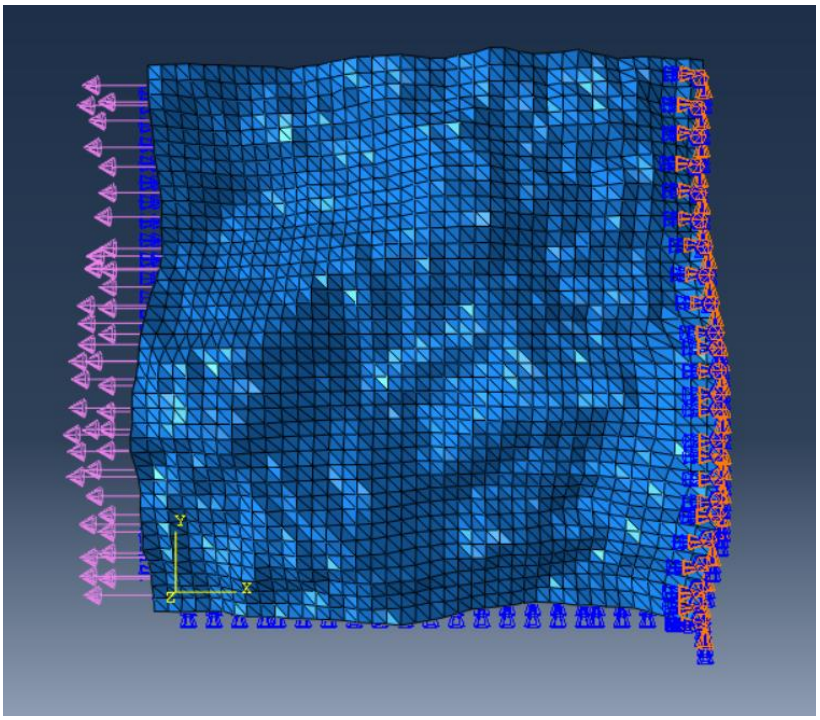

Figure 6.3 The boundary conditions and loading force on the part.

6.4. Atmospheric Stress Corrosion Cracking Experiment Methodology

6.4.1. Decisions on Applied Conditions

The ideal ASCC trial would apply conditions identical to those found in locations where ILW containers exist, such as inside interim storage facilities. The decision to use stainless steel for containers adds an impractically long timescale to such a trial since it resists corrosion relatively well. For this reason, though conditions in this trial are kept as close to ideal as possible, some factors, such as the CDD (Chloride Deposition Density) and the temperature, are raised to create a more aggressive environment. Since the purpose of this experiment is to investigate the effect of stress concentrations on the surface, and not to provide long term predictions on the performance of ILW containers, this accelerated method was deemed to be appropriate.

6.4.2. Stress

As discussed in Chapter 2, the stress state of ILW containers is the summation of a range of different stress sources. The residual stresses imparted by surface finishing range from -800 MPa to 1000 MPa for shotblasting and grinding respectively [10] [11]. Since these are residual, they already exist in the surfaces used in this experiment and so do not need to be applied. Welding can impart stresses of around 400 MPa and operational stresses such as stacking can reach around 7 MPa [12]. This stress exceeds both the yield stress (210 MPa) and is in the vicinity of the ultimate strength (560 MPa) [13]. Therefore, it was decided that applied stresses in this range would provide representative conditions in this trial.

6.4.3. Temperature

The temperature of interim storage facilities range between 1°C and 24°C, and the GDF pre-closure can be expected to reach around 43°C [14][15]. To reduce the timeframe of this experiment, a temperature of 80°C was chosen, since it is well established that this will increase the corrosion rate [16]. This factor

deviates most from container conditions, however, of all the factors, a temperature increase of 40°C will have the lowest impact on corrosion mode since it has been shown that ASCC occurs at both high and low temperatures [16].

6.4.4. Humidity

Below a threshold humidity no ASCC can occur and above this RH, hygroscopic salt deposits on the surface deliquesce [17]. The resulting conductive solution forms droplets that act as electrochemical cells which allow corrosion to begin [18]. At higher humidities still, more H_2O passes into solution and the droplets become dilute, slowing the chemical processes responsible for corrosion. Consequently, the most aggressive humidity for stainless steel is close to the deliquescence point of the hygroscopic contaminant [18]. Additionally, this effect ties the concentration of a deliquesced solution directly to the humidity in the environment, which is the sole determinant in a stable system [19]. Therefore, a completely saturated salt solution can be present on the surface of contaminated containers as long as some salt is present, with the salt deposition density having no effect on the stable concentration.

In interim storage facilities humidity is known to vary between 21% and 94% RH [14]. 33% RH is the humidity at which $MgCl_2$ deliquesces, so this is what was used for this experiment [20][21]. This provides both the most aggressive possible condition, and one that is firmly within the actual measured value in industry.

6.4.5. Chloride

For stainless steel, the development of localised corrosion requires the presence of aggressive ions. Chloride ions are well known to be particularly damaging to the protective passive film [18]. During storage near coastal locations, containers are exposed to dusts, salts, soil, and pollution. Of particular concern is the deposition of atmospheric aerosol salts that originate from the sea [22]. As described in Section 2.2, in current interim storage facilities CDDs of up to 13 $\mu g/cm^2$ have been measured. This is coupled with a yearly deposition rate of 1-5 $\mu g/cm^2/yr$ [23], making CDDs of around 20-25 $\mu g/cm^2$ possible in the near future.

Saturated $MgCl_2$ solution was used in this experiment since it is has been found to be the sea-salt constituent most responsible for low temperature ASCC in 304L stainless steel [24]. A large drop size of 30 µl was used to simulate more aggressive scenarios, such as the formation of larger deposits through the effect of wetting and drying cycles connecting multiple droplets [2]. Over a surface area of 0.5 cm^2, this equated to a CDD of 26 mg/cm^2.

As shown in the previous section, the concentration of salt present in solution on container surfaces is not related to the surface deposition density, since the thickness of film or droplet can change [19]. This means that saturated salt solutions are present on containers in ILW storage facilities, and their application in this experiment is consistent. That being said, it has been shown that the size of chloride deposits do affect the tendency for corrosion since larger salt particles form larger droplets and thicker films which are more conductive, favour mass transport and have a larger surface area to absorb oxygen from the atmosphere [19]. To summarise, the concentration of chloride in solution is consistent with that measured on containers, but the CDD has been increased to accelerate corrosion.

6.4.6. Methodology

To induce ASCC in samples, a U-Bend stress application method, with a saturated salt solution humidity chamber was used in accordance with ASTM G38 [25]. The details of the method used are described in Chapter 3.

6.4.7. Stress Calculation

The area of interest for a U-Bend stress token is the top of the token at the centre of the bend. The circumferential stress runs over the top of the sample, and it should be noted that is not uniform [26]. The stress is largest at the top (as shown in Figure 6.5) and decreases both with thickness through the material and with rotation around the token towards the boltholes. U-Bend tokens exhibit both plastic and elastic deformation. The largest strain, and the largest plastic deformation are found at the centre top point.

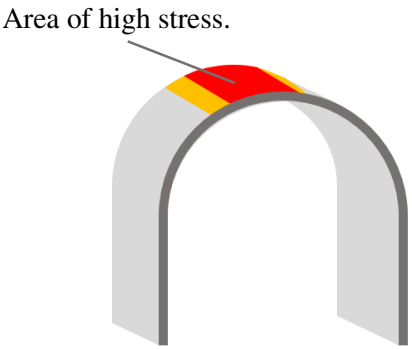

Figure 6.5 U-Bend Stress Distribution

The total strain, ε, on the outside of the bend can be approximated by Equation 6.4. This equation works as a close approximation when the thickness T of the token is much smaller than the radius R of the curved section [26].

$$\varepsilon = \frac{T}{2R} \quad when \quad T \ll R \qquad \textit{Equation 6.4}$$

For all samples used, T = 1 mm and R = 17 mm. This gives an approximate strain of 0.029. This translates to a stress of 5.8 GPa which compares to the ultimate strength of 0.56 GPa. This indicates that a large amount of strain hardening and plastic deformation was present.

The initial section of the stress/strain curve is linear and steep, as shown in Figure 6.6. The application of stress to the material in these tests takes the form of tightening a bolt that controls the bending of the U-Bend token, meaning that the strain is the factor that is controlled. This makes it difficult to reliably achieve a consistent percentage of total elastic pre-strain. For this reason, the tokens are bent beyond the maximum elastic pre-strain into the flatter plastic region. This makes the application of stress more consistent, and more severe. Figure 6.6 shows how a small amount of variation (*a)* in strain in this range gives a smaller, more reliable range of stress (*c*) than in the elastic range, which gives the larger range (*b*).

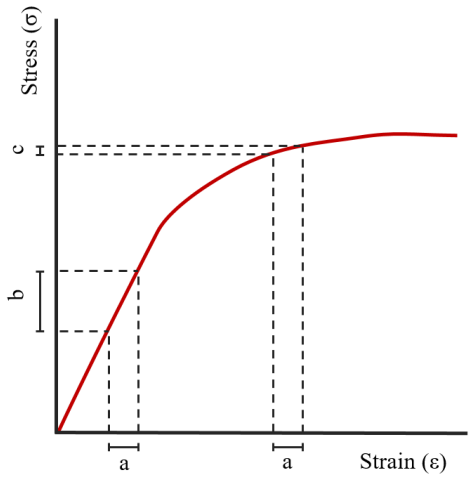

Figure 6.6 Stress/ strain curve of a U-Bend token.

To ensure greater consistency, care was taken to not over-strain the tokens by bending them further than their final form and by preventing relaxation after the bend had been completed. No attempt was made to insulate the stainless-steel restraining bolt from the token to avoid galvanic corrosion. As corrosive media was only placed on the tip of the U-Bend, there were no conditions for corrosion of the bolt.

6.4.8. Surface Finish Application

The tops of some of the U-Bend tokens were ground with P120 silicon carbide grit paper until complete removal of the surface in the area was achieved. Half of the tokens were ground in the direction of applied stress, and half were ground perpendicular to it. This was equivalent to applying stress to a P120 surface finish in two different directions. Tokens were rinsed with water after grinding to remove debris. The remaining tokens retained their pre-applied finishes; brushed, ground, rolled and shotblasted.

6.4.9. Humidity Control

To ensure consistent humidity, exposed saturated $MgCl_2$ solutions inside sealed plastic containers were used. Temperature and humidity logging showed a stable humidity of 33% was reached within 4 hrs. The saturated salt solution buffered the humidity by allowing moisture to evaporate into the air when the humidity dropped below 33% and absorbing water from the air when the humidity was above this amount. Because the solution was saturated with an excess of $MgCl_2$, it could lose or gain a large amount of water without changing the concentration of the salt in solution and remain stable only at 33% RH. Figure 6.7 shows the positioning of tokens and solution within a container.

Figure 6.7 U-Bend stress tokens inside a humidity chamber alongside a saturates $MgCl_2$ solution. $MgCl_2$ droplets have been applied to the tokens.

6.4.10. Chloride Application

Once placed into the humidity chamber, 30 µl of saturated $MgCl_2$ solution was deposited onto the top central area of each U-Bend token using a pipette as shown in Figure 6.7. Since $MgCl_2$ is highly hygroscopic, a volume of saturated solution was used in favour of a weight of dry powder. This was due to the variation in chloride concentration between anhydrous $MgCl_2$ and the hydrated form. This allowed for greater accuracy.

At 20°C, $MgCl_2$ has a solubility of 54.3 g/100ml. A 30 µl aliquot contains 16.3 mg of $MgCl_2$, making the CDD 26 mg/cm^2. Surface tension prevented the droplet from rolling off the token for the duration of the experiment. The tokens were placed into an 80°C oven for 120 hrs checking regularly for visible signs of corrosion.

6.5. The Neuber Model and The Arola and Ramulu Model Results

6.5.1. Valley Radii Distribution

Figure 6.8 details the valley radii distribution for the four surfaces for the data collected with VSI and Figure 6.9 details this for the AFM data. This data was collected, and the radii calculated as in Section 4.4. The VSI and AFM data correlate well with the largest differences between the 8 plots being due to the differences between the surface finishes themselves.

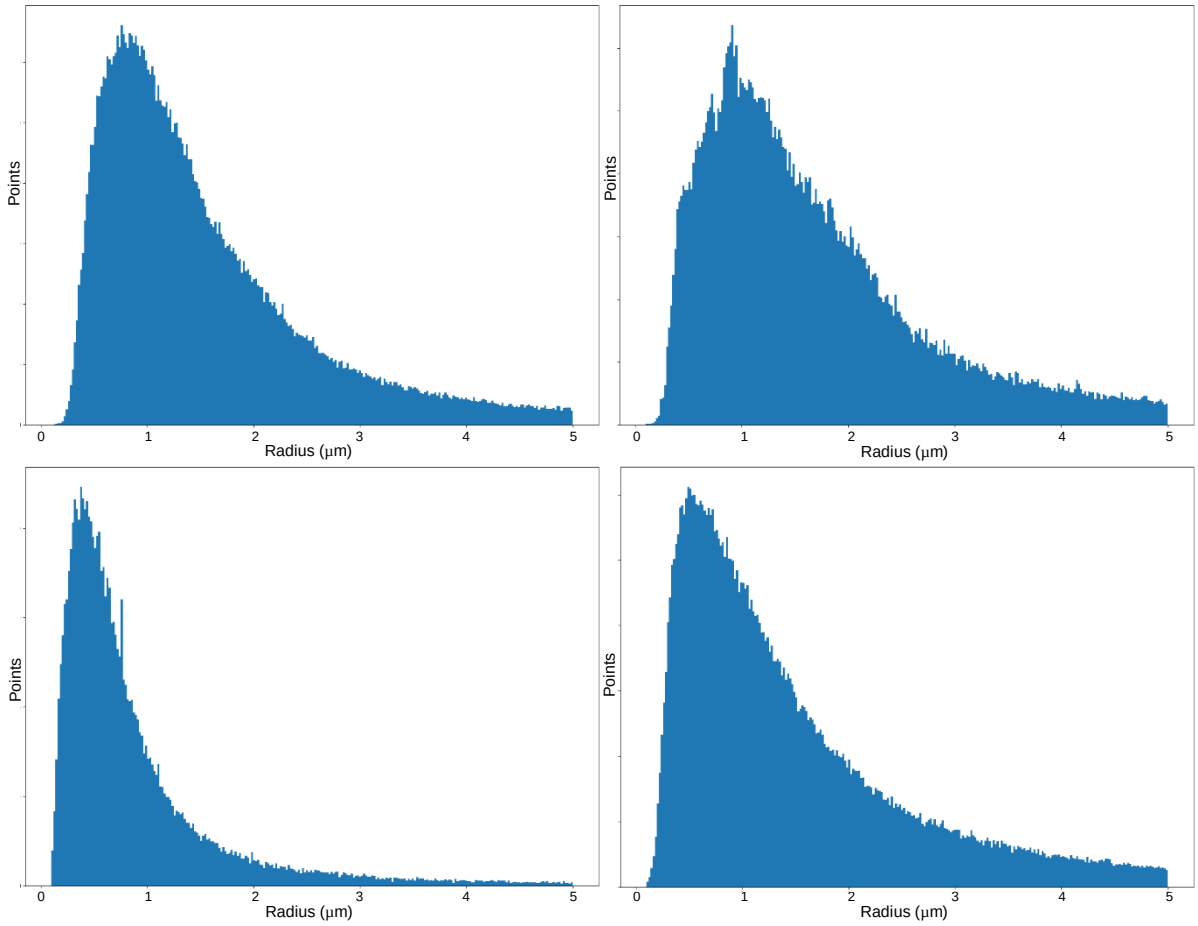

Figure 6.8 Radii distribution across the surface for: A brushed, B ground, C rolled, D shotblasted surfaces. VSI data.

Large radii correspond to large, gradually changing features, while the smaller radii correspond to smaller features. For all surfaces the radii distribution is dominated by smaller radii with the proportion of larger radii tailing off quickly. This is because small inconsistencies in large radii features can be recorded as smaller radii features. For this reason, any noise in the surface will skew the distribution to the left.

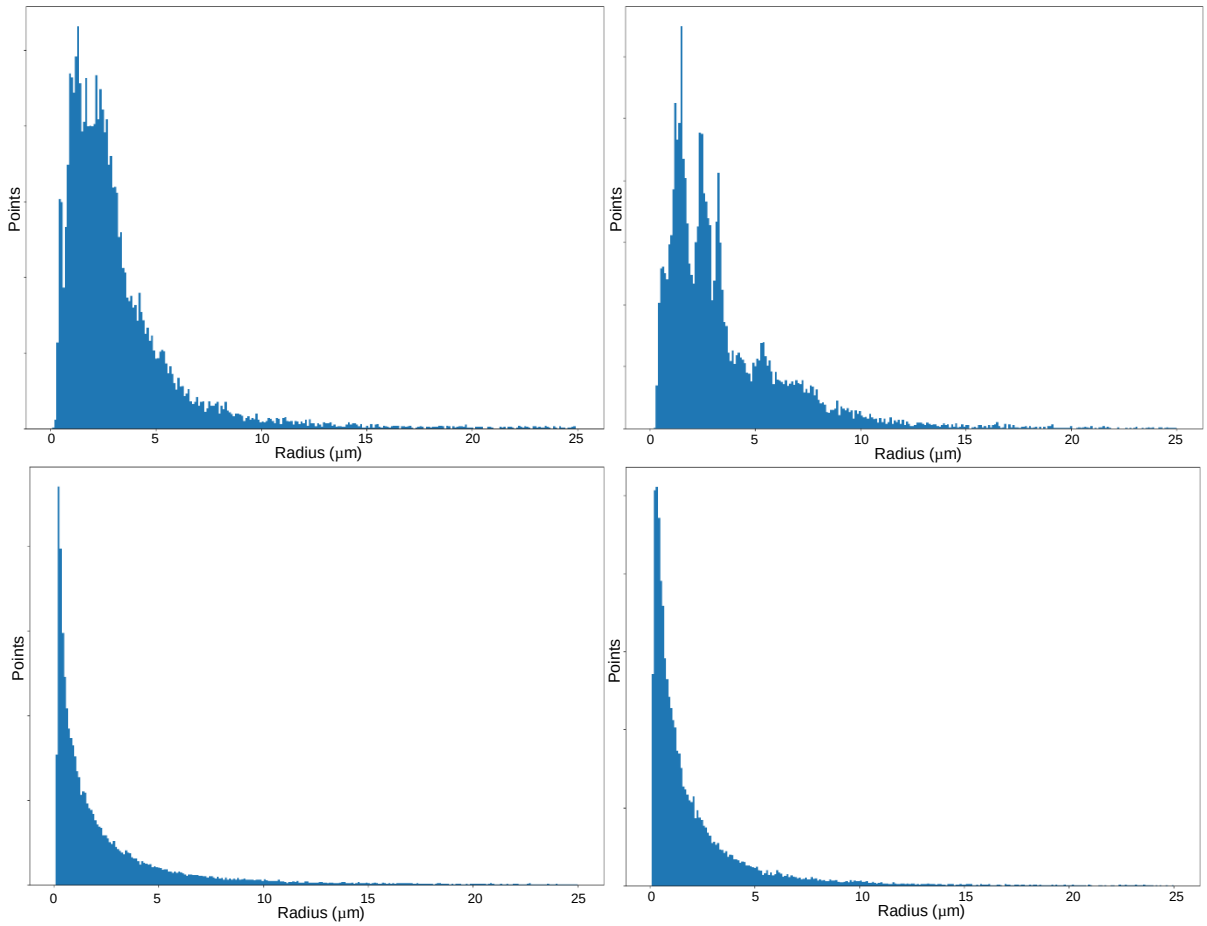

Figure 6.9 Radii distribution across the surface for: A brushed, B ground, C rolled, D shotblasted surfaces. AFM data.

The ground and brushed surfaces have a flatter initial peak. These surfaces are far more regular and ordered than the rolled or shotblasted surfaces and so it is likely that this order can support larger wavelength features. The valleys in these surfaces are deliberately manufactured, whereas the valleys in the rolled surfaces occur as a secondary effect of the finishing process.

6.5.2. Stress Concentration Factor Mapping

In this Section stress concertation factor maps for the two models were produced for the four surfaces. Initially they are shown for the AFM data and are presented next to the corresponding valley radius maps. These maps are shown again when the source of the data changes to VSI, since the measurement technique affects the identification of valleys and their radii.

Using the scale bar to the right of the stress concentration factor maps (Figure 6.10) it can be seen that the stress concentration factor is denoted by colour, ranging from 1 to around 7. The scale starts from 1 (denoted by the colour black) since this represents zero contribution to the stress from the surface shape. Stress concentration factors below 1 exist for structures that alleviate stress, such as mounds that are built up on the surface, however the models utilised in this study are designed for investigating *negative* depth features, so only values above 1 are used.

6.5.3. Neuber Stress Concentration Mapping with AFM Data

Figure 6.10 shows the valley root radius and stress concentration factor maps for a brushed surface. The valley root radii map shows the locations of all minima across the surface. This highlights the bottoms of valleys for the brushed and the ground surfaces. This also gives an indication of the width or frequency of the valleys, and their corresponding ridges. For both the brushed and the ground surfaces this suggests an average valley width of 3 ± 0.2 μm.

The stress concentration factor map shows the factor by which stress is concentrated in the surface. At the bottom of a valley the stress is affected by the root radius of the valley, its depth, and by the proximity of nearby features. The maximum stress concentration is found in the two hole-like features that are apparent in the height map. From the radius map it can be seen that these features have radii smaller than 2.5 μm and from the height map they are also the deepest points on the surface. These factors add up to give a stress concentration around 6. Other valleys that do not have the hole-like features have similar radii but much less depth. Their stress concentration factors range between 1 and 4.

Figure 6.11 shows the valley root radius and stress concentration maps for a ground surface. From the root valley radius map, it is apparent that there is a long range continuity of valley minima in the ground surface that is more broken-up in the brushed surface. This may have implications for minimum feature size for stress concentration, which is discussed in Section 2.4.

Similar to the brushed surface, the highest stress concentration found in the ground surface is around 6 and is found in hole-like features caused by the smearing of material during the grinding process. There is one long valley that has a higher stress concentration due to both its large depth and small radius.

Figure 6.12 shows the valley root radius and stress concentration maps for a rolled surface. The white lines in the root valley radius map show the edges of, and boundaries between, etched grains that register a root radius usually lower than 2.5 μm. These minima join up and outline individual grains. Inside these loops, secondary minima can be seen with less extreme root radii of around 10-15 μm. These are also shallower and so contribute to the creation of smaller stress concentration factors around 3, compared to 4-6 for the grain boundary features.

Figure 6.13 shows the valley root radius and stress concentration maps for a shotblasted surface. Comparing the root valley radius map with the stress concentration map, a large middle section of the stress concentration map appears absent. This area is well above the average surface height and so the comparatively small surface height deviations of the etched grain boundaries don't bring the valley depth below zero, meaning no stress concentration can be calculated in these areas. Elsewhere, the greater depths of this surface lead to the highest stress concentration factor up to 10.

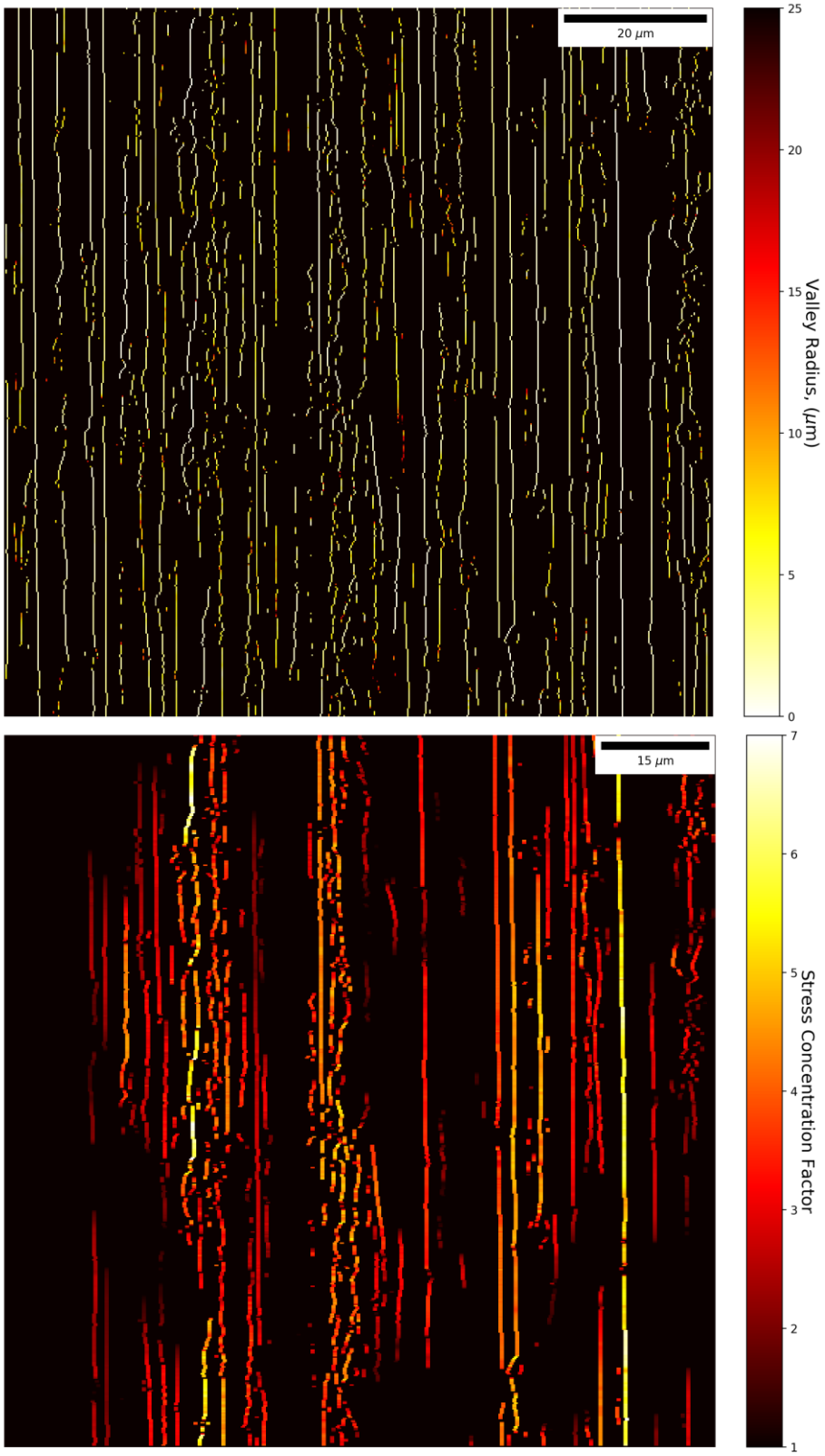

Figure 6.10 Valley root radii and Neuber stress concentration factor maps for a brushed surface. AFM data.

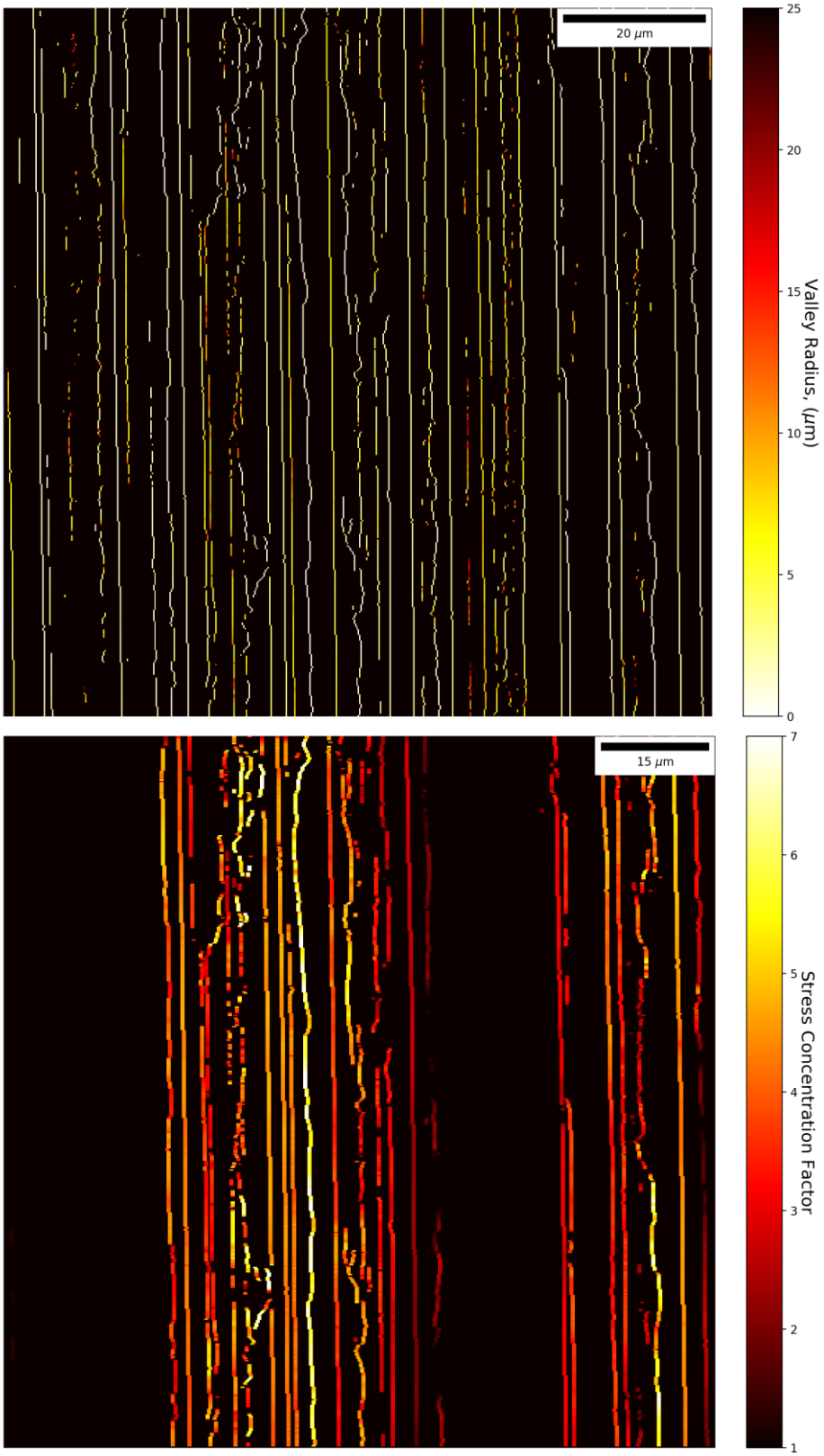

Figure 6.11 Valley root radii and Neuber stress concentration factor maps for a ground surface. AFM data.

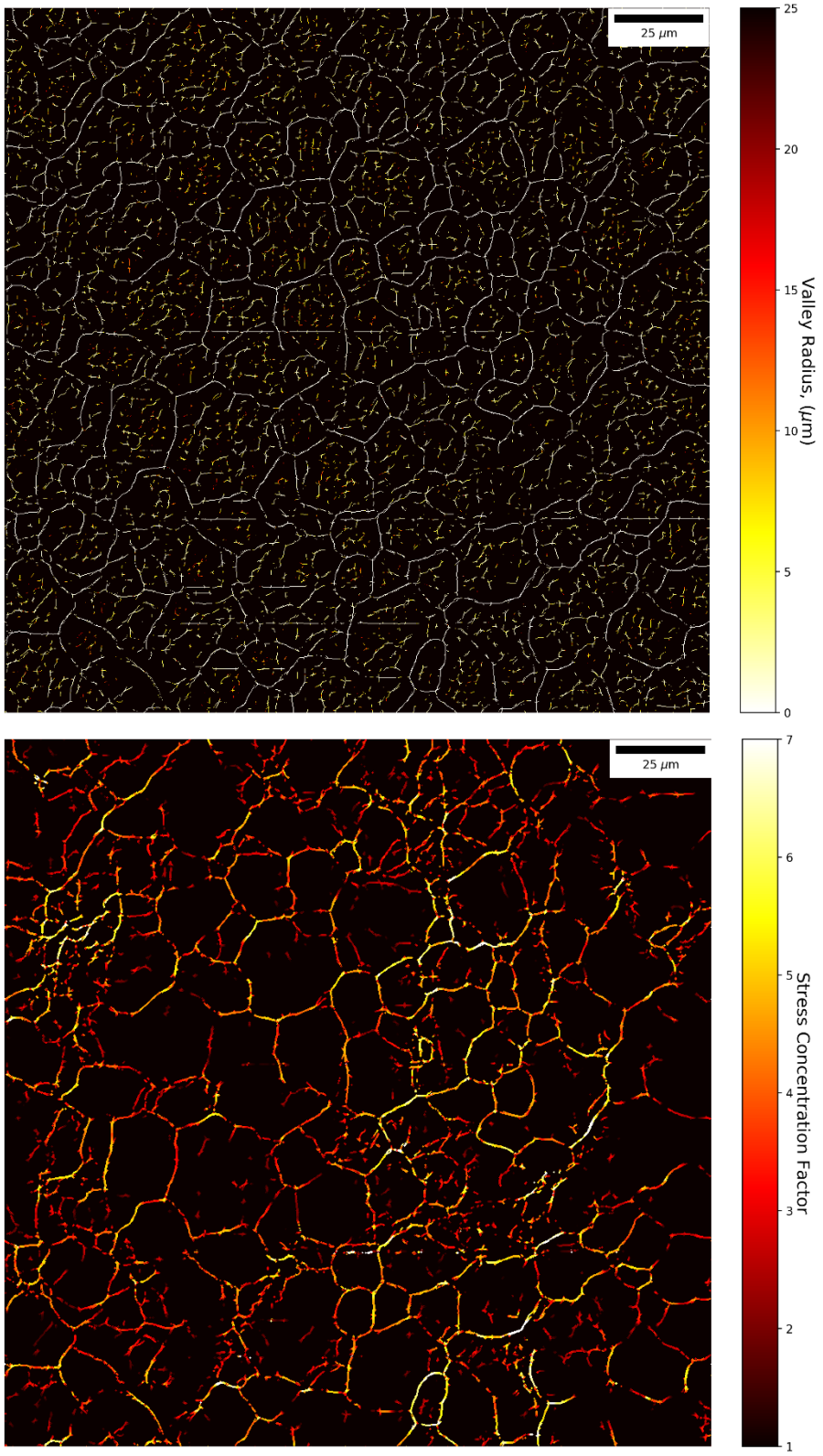

Figure 6.12 Valley root radii and Neuber stress concentration factor maps for a rolled surface. AFM data.

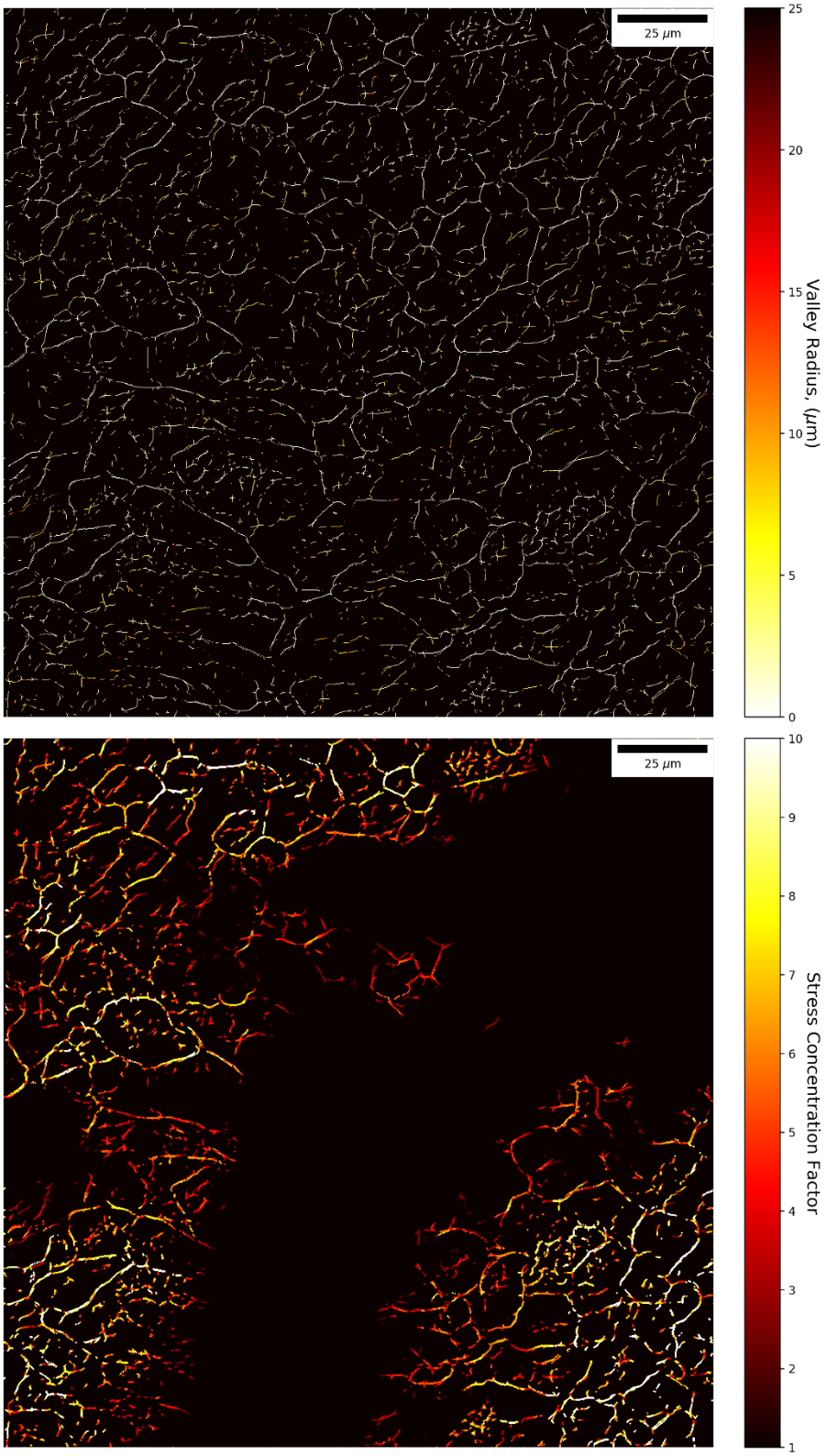

Figure 6.13 Valley root radii and Neuber stress concentration factor maps for a shotblasted surface. AFM data.

6.5.4. Arola and Ramulu Stress Concentration Mapping with AFM Data

Figure 6.14 shows the Arola and Ramulu stress concentration factor distribution for a brushed surface. It should be compared to Figure 6.10, which shows the radii used for both models, and the stress concentration factor distribution predicted by the Neuber model. The Arola and Ramulu stress concentrations are much lower across most points, except on two locations where they are much higher. Most valleys of the brushed surface show an Arola and Ramulu stress concentration factor of 1 – 2.5 whereas they show stress concentrations averaging 4 – 5 for the Neuber stress concentration.

The spacing term (λ) in the Neuber model increases the stress concentration predicted for surfaces that have valley angles less than 90° and decreases it for more open surfaces. For the brushed surface, the valleys are enclosed by an angle lower than 90° and so the Neuber model predicts higher stresses for most valleys, despite the square-rooting of the main term. The Arola and Ramulu model gives more weight to the effect the depth of the feature has on the surface, which means that for the deepest features of the brushed surface, it predicts higher stress concentrations (7+) than the Neuber model. For this surface, the prediction of the location of highest stress is consistent between the two models.

Compared with the brushed surface, the stress concentration factor distribution for the ground surface, shown in Figure 6.14, exhibits much longer, unbroken, lines of stress concentration. This matches what is observable from surface height data, and from SEM. This factor is relevant, given that there is possibly a critical cross sectional surface area required for a feature to cause cracking (as presented in Section 2.2) [5][27]. The models employed here are designed for two dimensional cases. They are applied to the three dimensional surfaces measured here as though a cross section were representative of the whole surface, i.e. as though it were stretched to make a consistent three dimensional surface. For this reason, it underestimates the mechanical support material at the end of a valley could provide into the valley, a factor that could be especially present for the rolled, shotblasted and brushed surfaces.

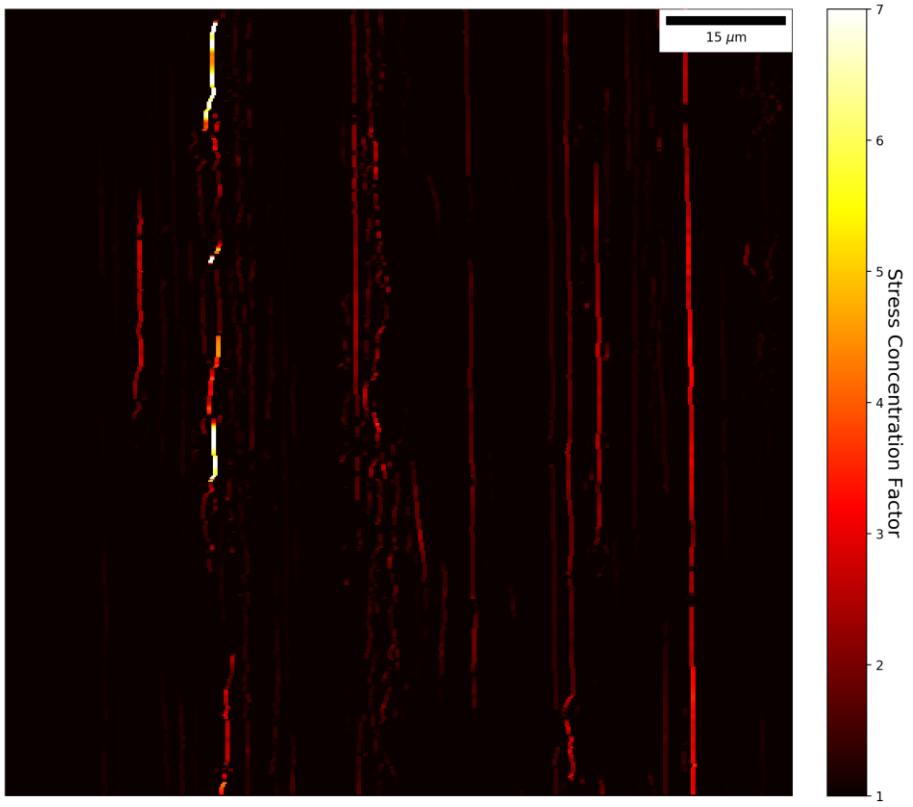

Figure 6.14 Arola and Ramulu stress concentration factor map for a brushed surface. AFM data.

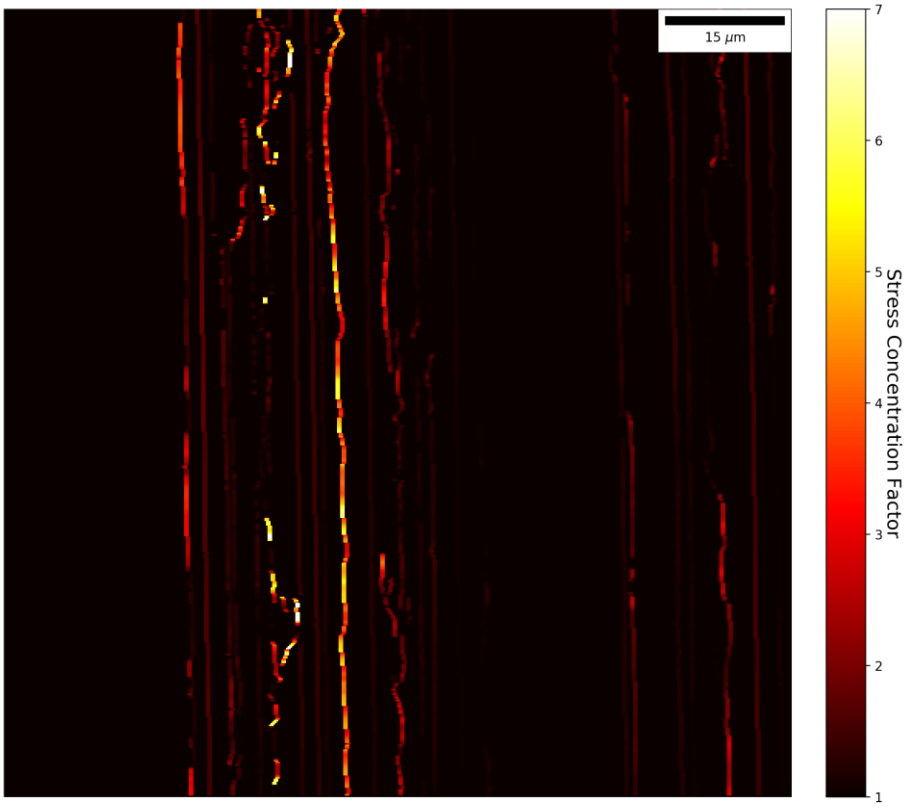

Figure 6.15 Arola and Ramulu stress concentration factor map for a ground surface. AFM data.

Figure 6.16 shows the Arola and Ramulu stress concentration factor distribution for the rolled surface. Comparing it to the Neuber model distribution shown in Figure 6.12, many of the identified minima areas are much darker, indicating a lower predicted stress in the Arola and Ramulu model map. Coupled with this, there are some areas which show much higher stress concentration factors of 7+. The difference between distributions indicates that these areas are either deeper or have smaller valley radii as these features in particular are weighted more heavily by the Arola and Ramulu model. It is highly likely that these areas have much smaller valley radii, since the variation of height across the rolled surface is minimal compared to the other surfaces. This highlights the different factors and weightings the different models ascribe. The more even distribution in the Neuber maps shows that openness is more evenly distributed among the minima features and that this factor obscures the uneven distribution of the valley radii which is then revealed in the Arola and Ramulu model.

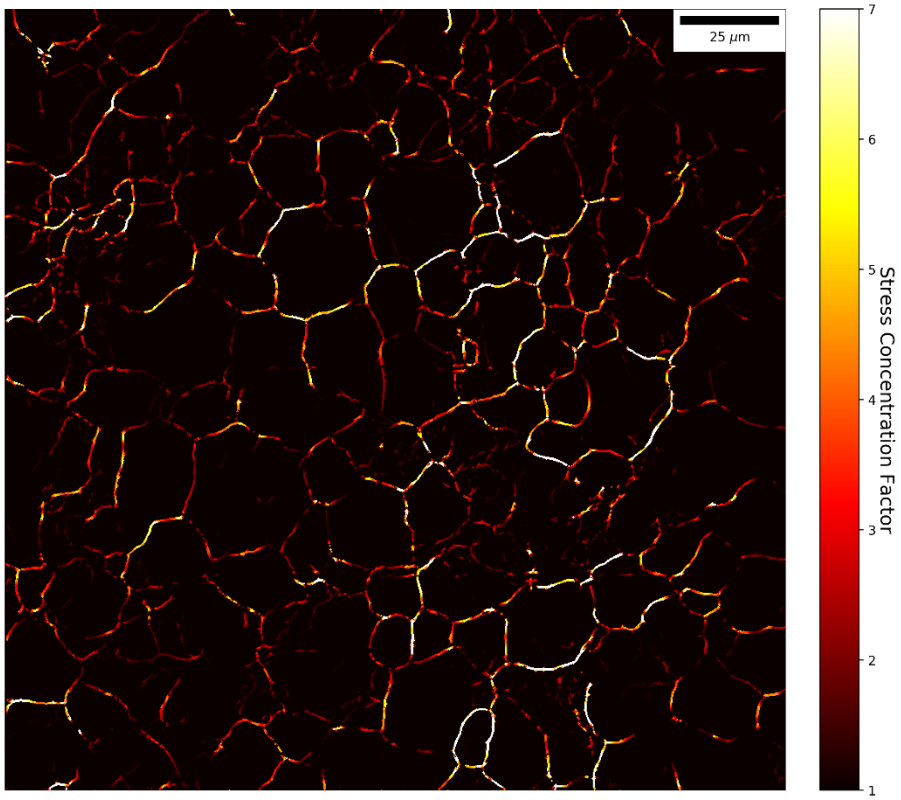

Figure 6.16 Arola and Ramulu stress concentration factor map for a rolled surface. AFM data.

Figure 6.17 shows the Arola and Ramulu stress concentration factor distribution for the shotblasted surface. It is very similar to the corresponding Neuber model representation shown in Figure 6.13. As both models consider depth an important factor, and this surface has the deepest features by far, the depth of the features has the largest impact on the stress concentration factor for this surface. This effect

is illustrated by the large blank regions, where features with positive height are calculated to have no overall stress concentration contribution.

The stress concentrations in the low points of this surface, in the valley-like etched grain boundaries predict the highest stress concentration factor (14) measured across all four surfaces. This is primarily due to the depth of these features. It shows that for this surface, depth of features is the primary factor for determining stress concentration, whereas for the other surface finishes variation in openness and valley radii have a larger relative influence.

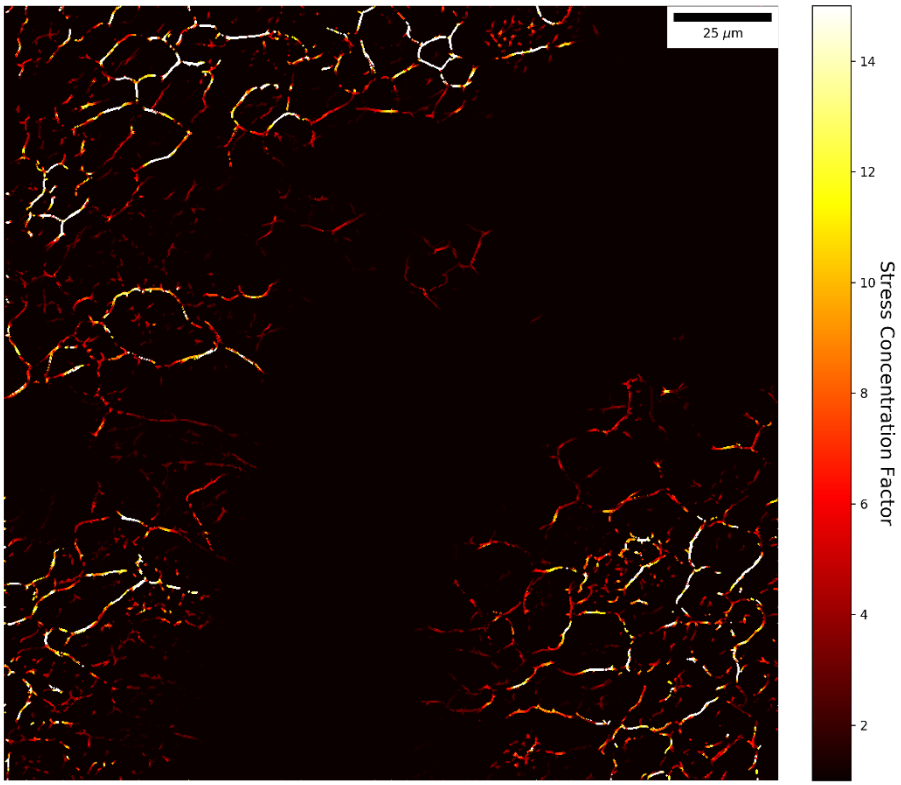

Figure 6.17 Arola and Ramulu stress concentration factor map for a shotblasted surface. AFM data.

6.5.5. Neuber Stress Concentration Mapping with VSI Data

Figure 6.18 shows the valley radius map and the stress concentration map for a brushed surface. The stress concentration factor increases with valley depth and reaches around 5 for the deepest regions of this surface. It is clear that the grooves formed by surface finishing concentrate stress to a high degree, partly by introducing variation in the surface height in the form of depth of valleys and partly by the

formation of low-radii features. It should also be noted that for individual valleys, the stress concentration factors appears to be consistent along the length, indicating that valley radii and depth are characteristic features of valleys and are independent of position along a valley.

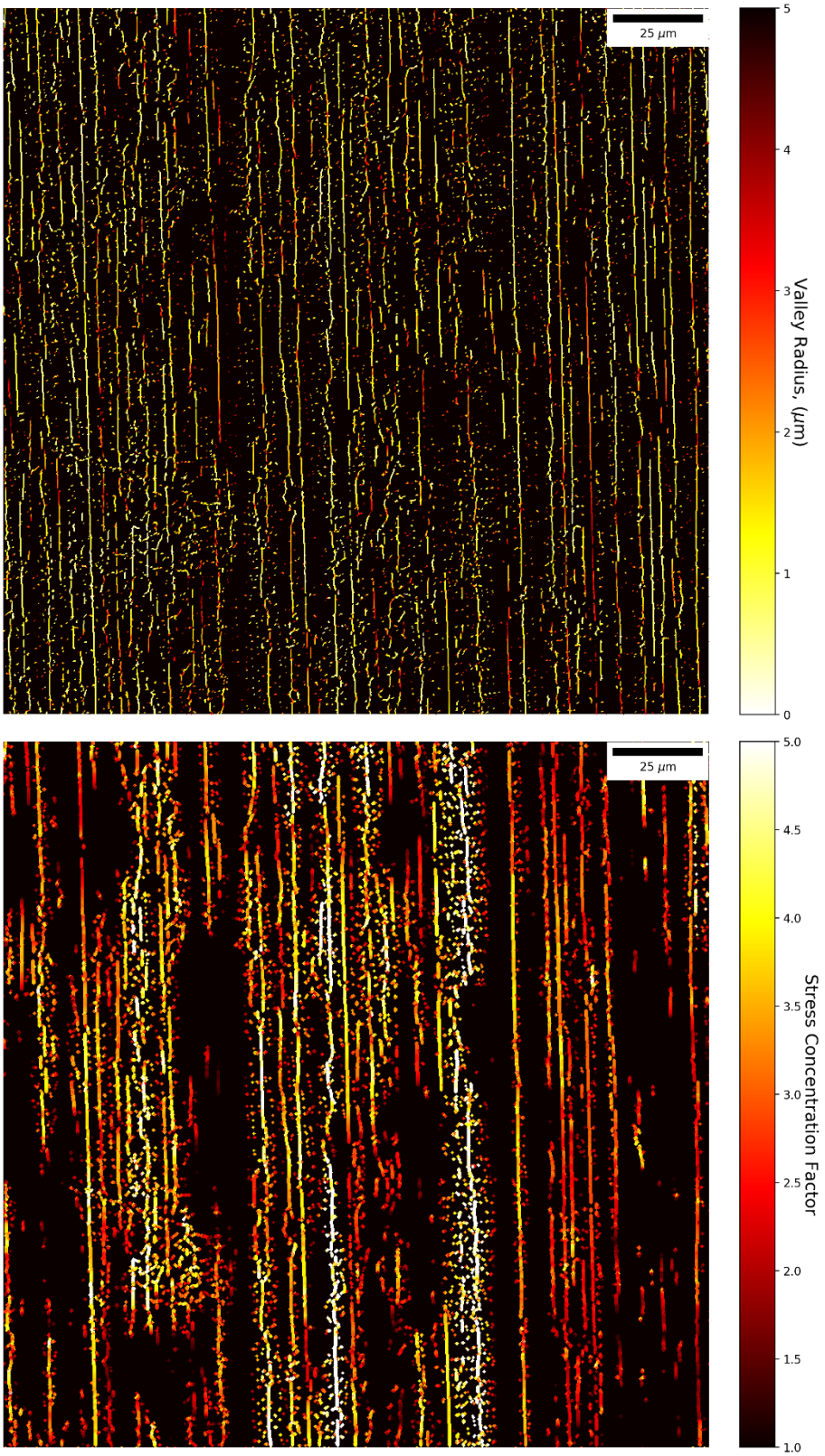

Figure 6.18 Valley root radii and Neuber stress concentration factor maps for a brushed surface. VSI data.

Figure 6.19 shows the valley radius map and the stress concentration factor map for a ground surface. This measurement area has a small scratch running diagonally across it, which is visible in the valley

radius diagram. Interestingly, this scratch is not seen in the corresponding stress concentration factor diagram. This suggests that the depth of the scratch is small in comparison to the height distribution found in the rest of the surface and is not great enough to cause any noticeable stress concentration. The largest stress concentrations found on this surface are around 4, the lowest for this stress concentration model and measurement type.

Figure 6.20 shows the valley radius map and stress concentration factor map for the rolled surface. Stress concentrations in this surface are, consistent with AFM measurements, located at the bottoms of the gaps between grains. This value climbs to around 7, despite features having less depth compared to the brushed and ground surface. This highlights the influence of the smaller valley root radii values that are present between grains on this surface.

Figure 6.21 shows the root valley radius map and stress concentration factor map for the shotblasted surface. The valley radius map looks similar to that of the rolled surface albeit with a greater density of smaller, more extreme, radii, and with fewer closed loops. The lines on the diagram, representing the minima features are more branching in nature. This could be explained by the process of shotblasting flattening some etched grain boundaries so that the gaps between them are too small to register or are non-existent.

Some areas of the radius map are blank; these areas are fairly featureless flat-topped peaks. They appear flat in optical microscopy and in SEM and VSI. Additionally, they register as 180° on the openness maps (see Chapter 4) and have no minima whatsoever on the valley radius maps.

The stress concentration factor map for the shotblasted surface demonstrates the contributions of both valley depth and root radius factors. Areas of the surface over the average height are given a stress concentration factor of 1 as default.

Large stress concentration factors between 7 and 8 are found in the bottoms of shotblasted craters. Here, the depth of the feature is a major contributor to the stress concentration factor, though the small root radii are comparable with the rolled surface.

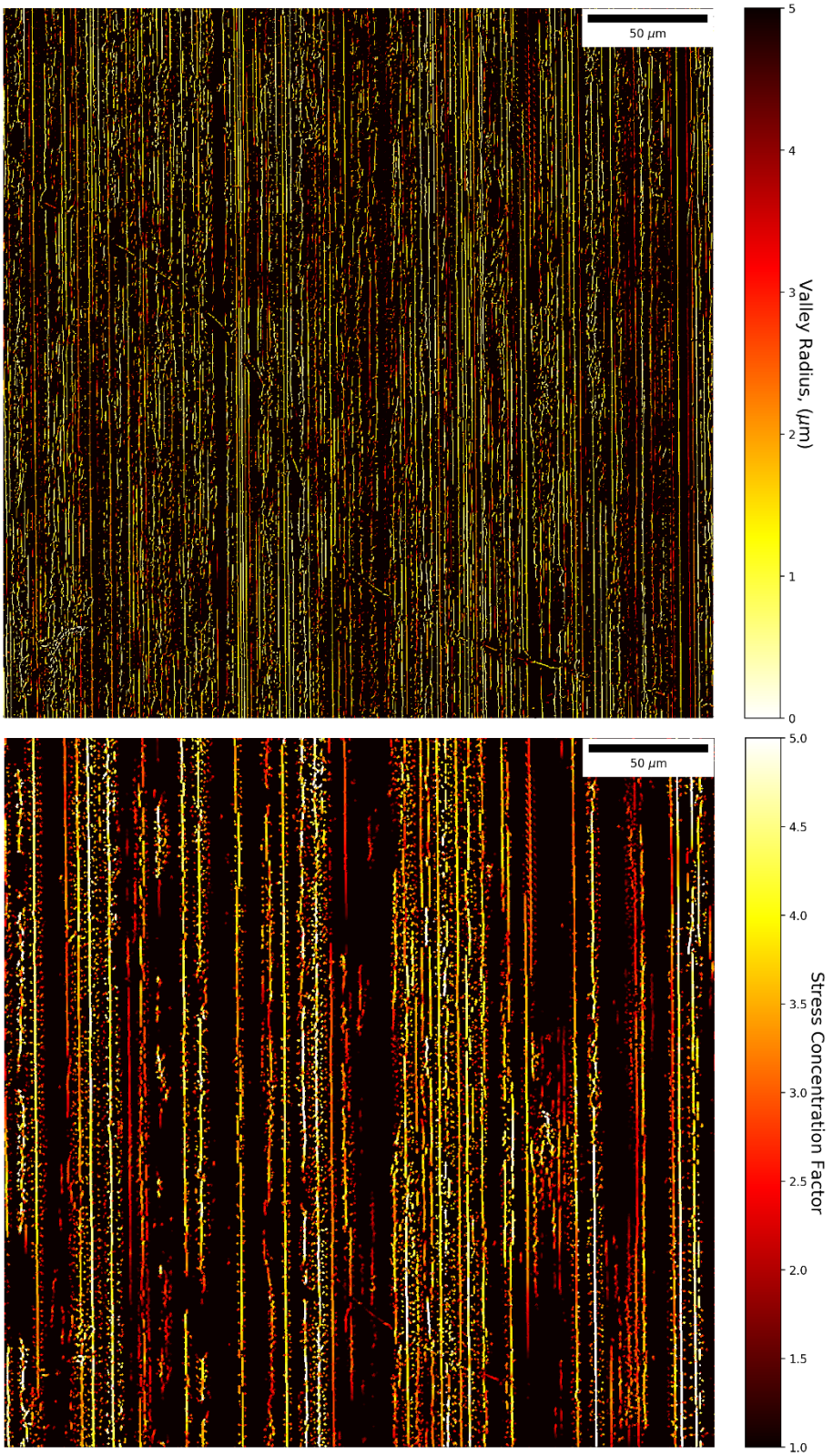

Figure 6.19 Valley root radii and Neuber stress concentration factor maps for a ground surface. VSI data.

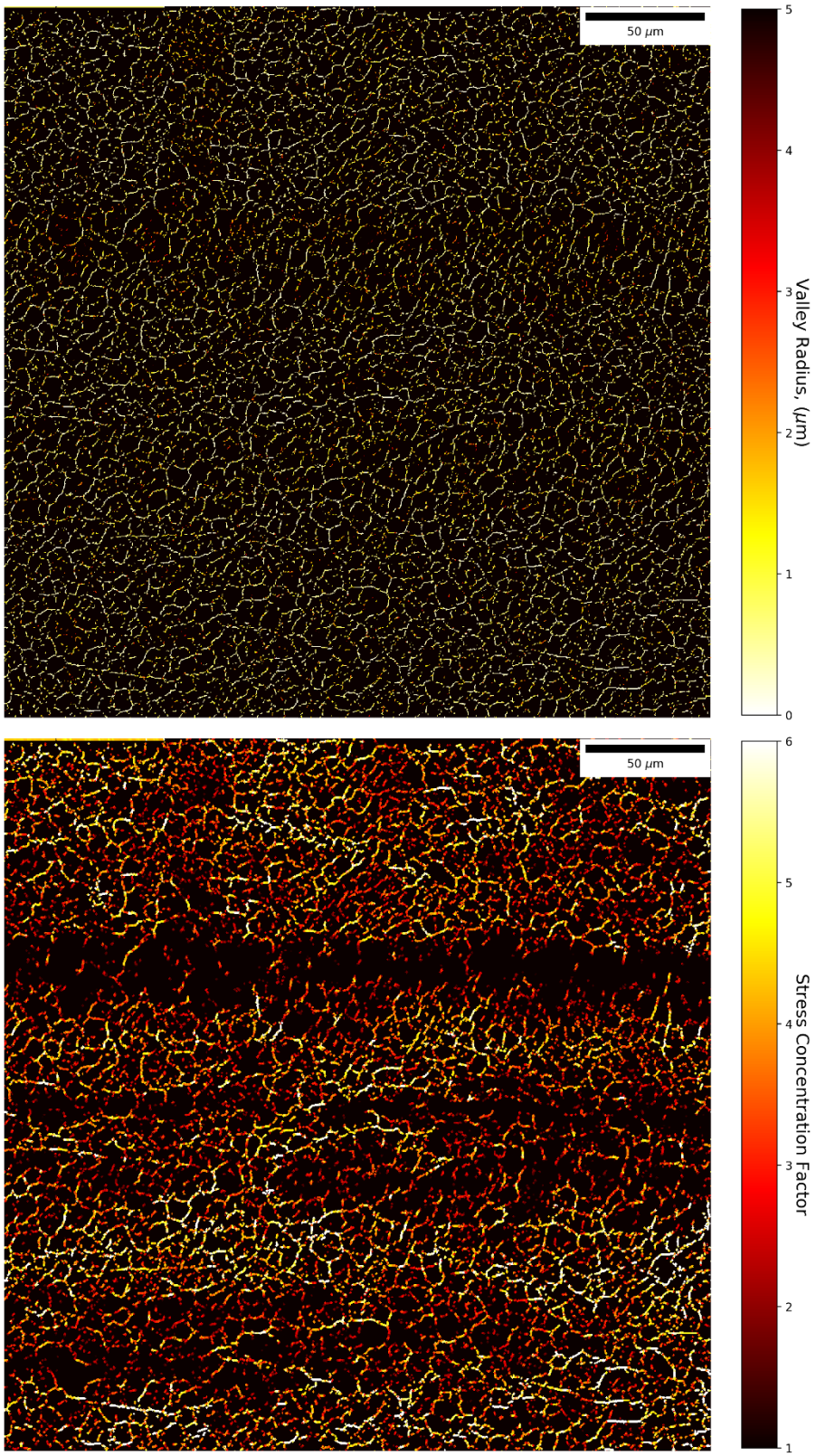

Figure 6.20 Valley root radii and Neuber stress concentration factor maps for a rolled surface. VSI data.

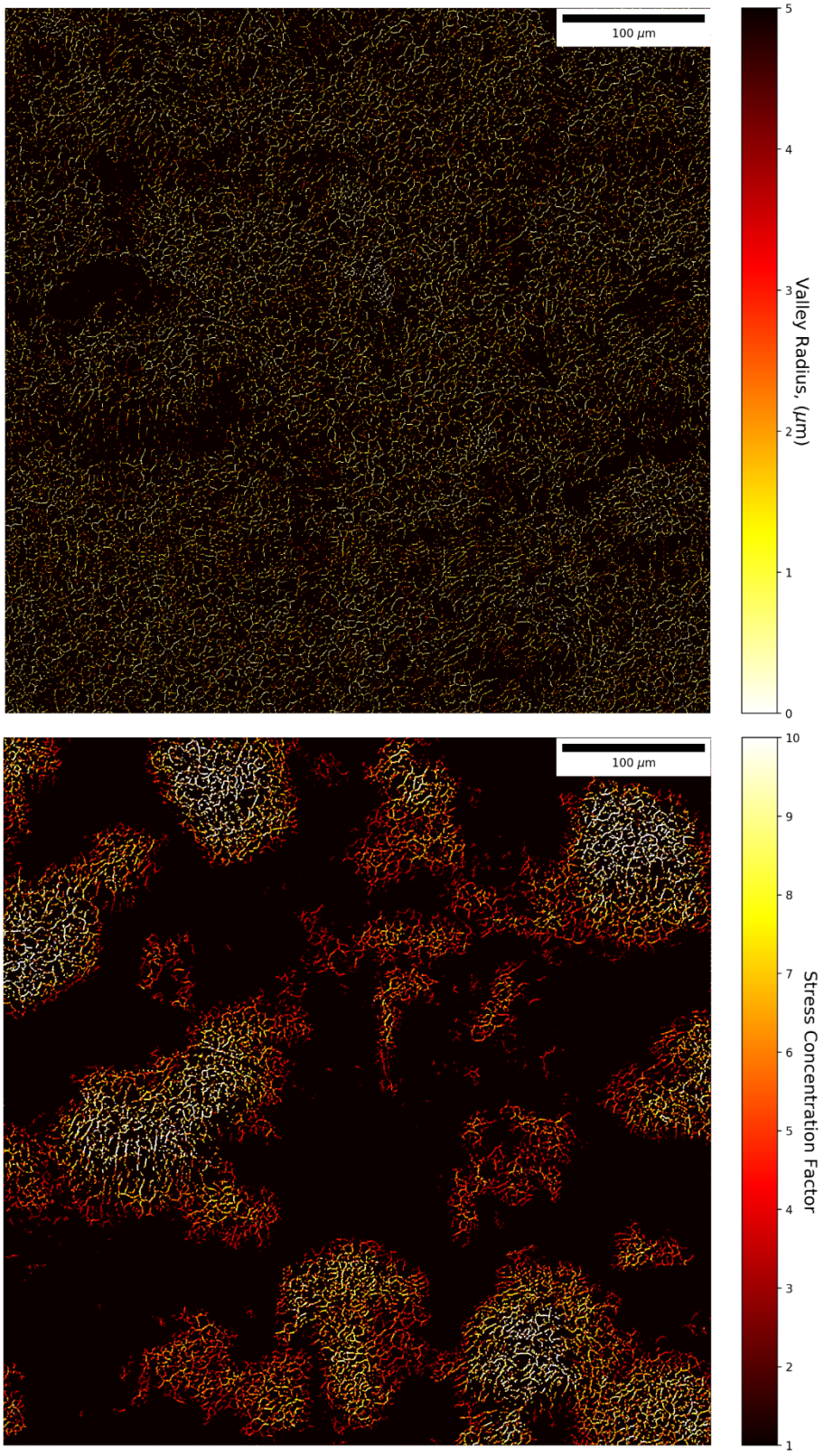

Figure 6.21 Valley root radii and Neuber stress concentration factor maps for a shotblasted surface. VSI data.

6.5.6. Arola and Ramulu Stress Concentration Mapping with VSI Data

The Arola and Ramulu stress concentration factor was also measured using VSI data, across much larger measurement areas than that allowed by AFM. Figure 6.22 shows the Arola and Ramulu stress concentration factor distribution for the brushed surface. Overall, for this surface, the Arola and Ramulu model outputs lower stress concentration factors for most features, but much higher factors for a few select features. This effect is investigated further in this chapter.

A feature of the stress concentration factor distribution for the brushed surface is the discontinuity in regions of high stress concentration factor. This is consistent with the observed shorter valley length previously described.

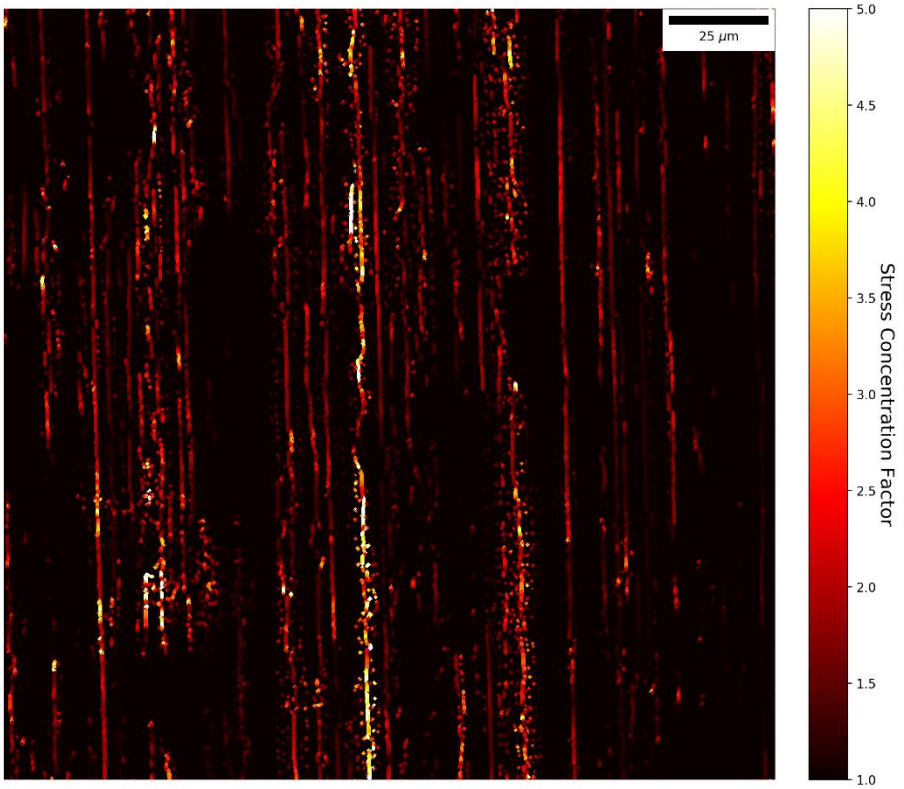

Figure 6.22 Arola and Ramulu stress concentration factor map for a brushed surface. VSI data.

Figure 6.23 shows the Arola and Ramulu stress concentration factor distribution for the ground surface. The full extent of the length of the unbroken stress concentrations caused by the valley structures, that was initially found in the AFM data, can be seen. Some valleys continue for hundreds of microns. The areas with the greatest stress concentration factor (5+) do not continue for as long. This may suggest

that, though a greater stress concentration factor is found at these points, cracking will be more likely to occur at the more continuous features, despite the lower stress concentration, since they will make up a much larger cross-sectional area. Shorter features may be unable to constitute an area over the theorised minimum threshold for cracking that is presented in the Literature Review [5][27][28].

Figure 6.24 shows the Arola and Ramulu stress concentration factor distribution for the rolled surface. A much higher stress concentration factor (10) is seen in this surface compared to those found in the brushed and the ground surfaces of around 5. This is due to the smaller valley radii in the minima features for this surface.

Figure 6.25 shows the Arola and Ramulu stress concentration factor distribution for the shotblasted surface. It shows the greatest stress concentrations of the four surfaces, due to the depth of the craters found on the surface. Once normalised for the craters, the surface would look very similar to the rolled one. It is the grain boundaries characteristic of the rolled surface that are responsible for the locations of the minimas of this surface, since they exist at a much smaller scale to the craters.

The large dark patches are, as is with the AFM data, caused by peak-features well above the average surface height.

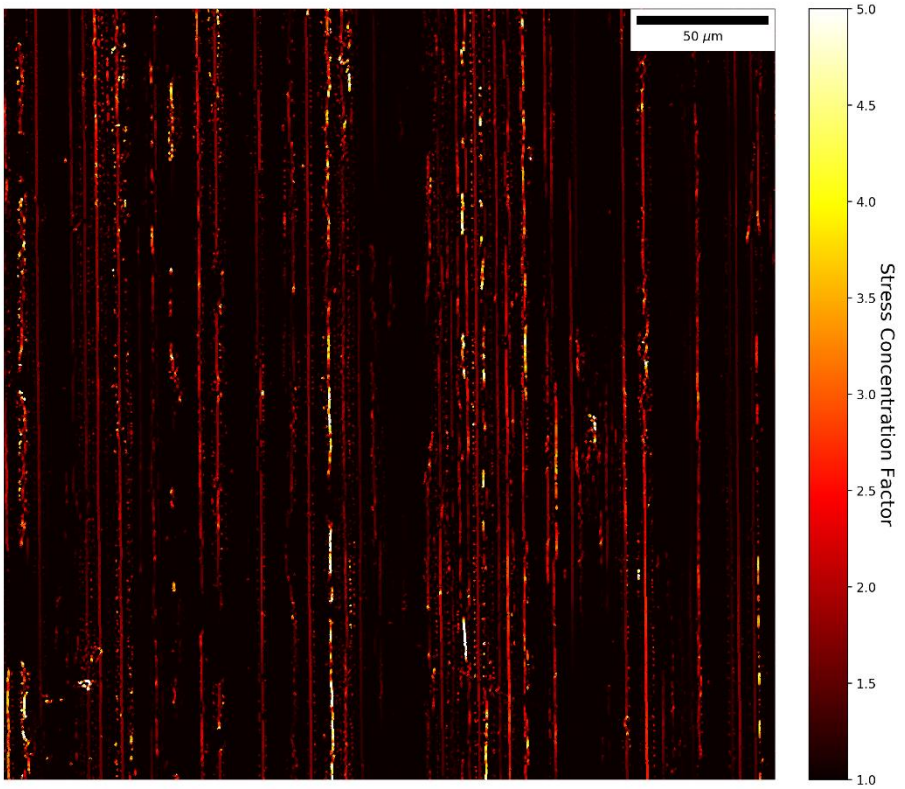

Figure 6.23 Arola and Ramulu stress concentration factor map for a ground surface. VSI data.

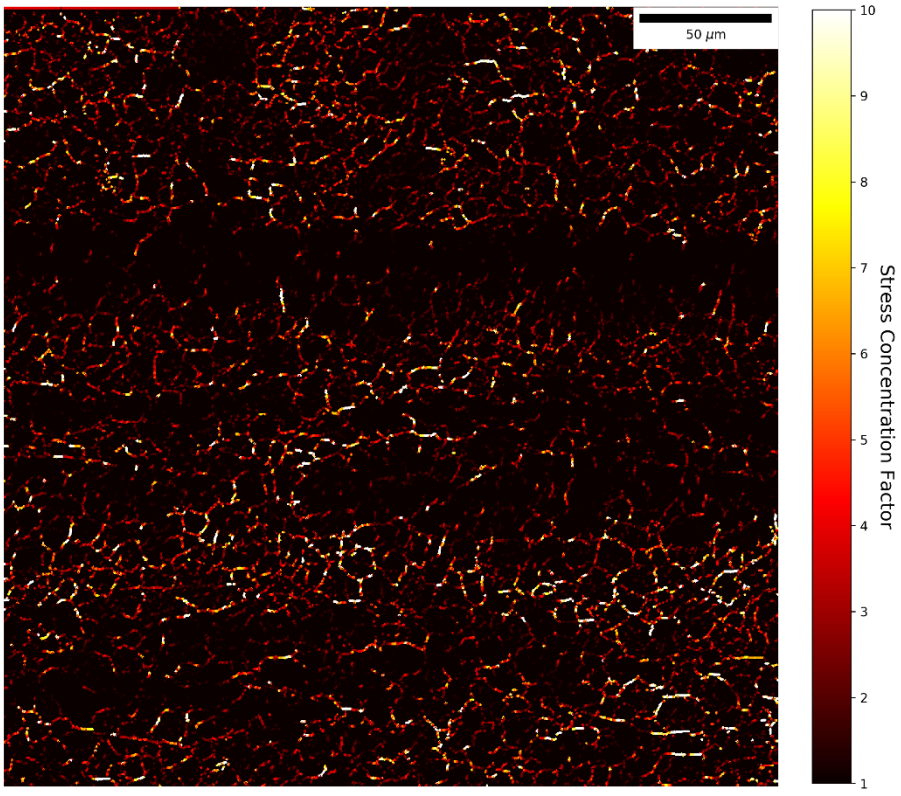

Figure 6.24 Arola and Ramulu stress concentration factor map for a rolled surface. VSI data.

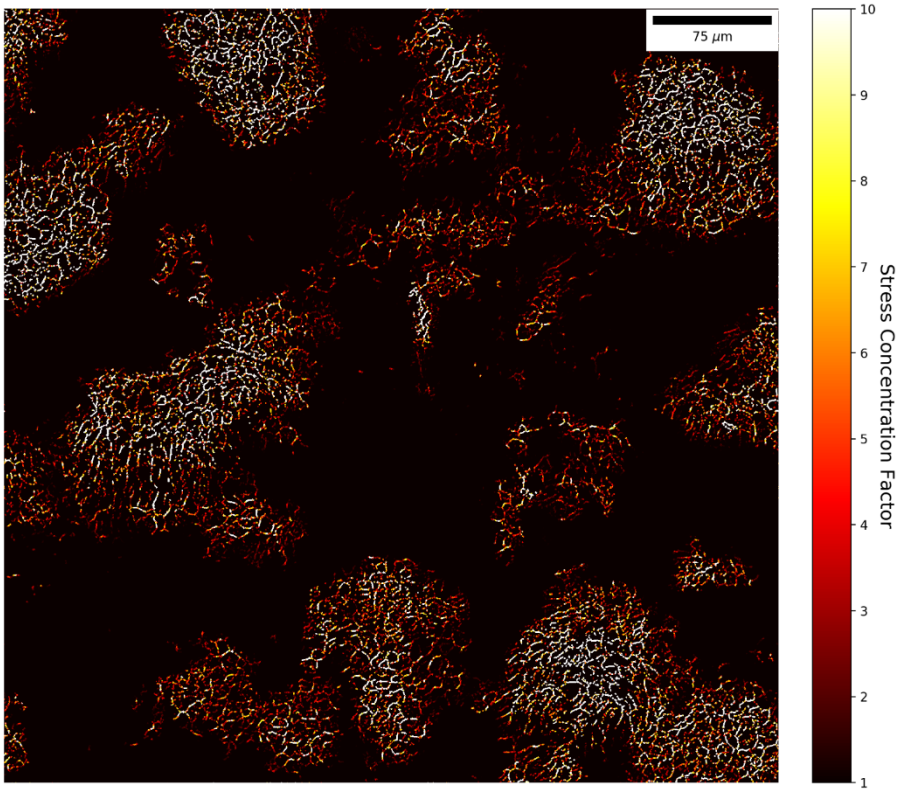

Figure 6.25 Arola and Ramulu stress concentration factor map for a shotblasted surface. VSI data.

6.6. Stress Distribution Comparison

6.6.1. General Stress Distribution Comparison

The proceeding stress concentration distribution graphs show the distribution of the size of stress concentrations found across the minima and valley bottoms of the four different surfaces. These areas are expected to have the highest stress concentrations, so it is for these that stress concentration is calculated for and compared across the different surfaces. Data calculated from the topographic maps produced by AFM are shown here. Analysis was completed for the VSI data and was in close agreement.

6.6.2. Neuber Stress Concentration Distribution

Figure 6.26 shows the stress concentration distributions according to the Neuber model for the four surface finishes. The largest difference lies with the shotblasted surface. This surface has the bulk of its stress concentration at around 5 and is elongated, taking longer to tail off. This means this surface has higher stress concentrations on average, and it has far higher stress concentrations at its top end. This behaviour in the shotblasted surface is seen across all stress concentration distributions for the shotblasted surface, whether the Neuber or Arola and Ramulu models were used. Stress concentration, as predicted by the Neuber model, is distributed in a Gaussian manner for these surfaces.

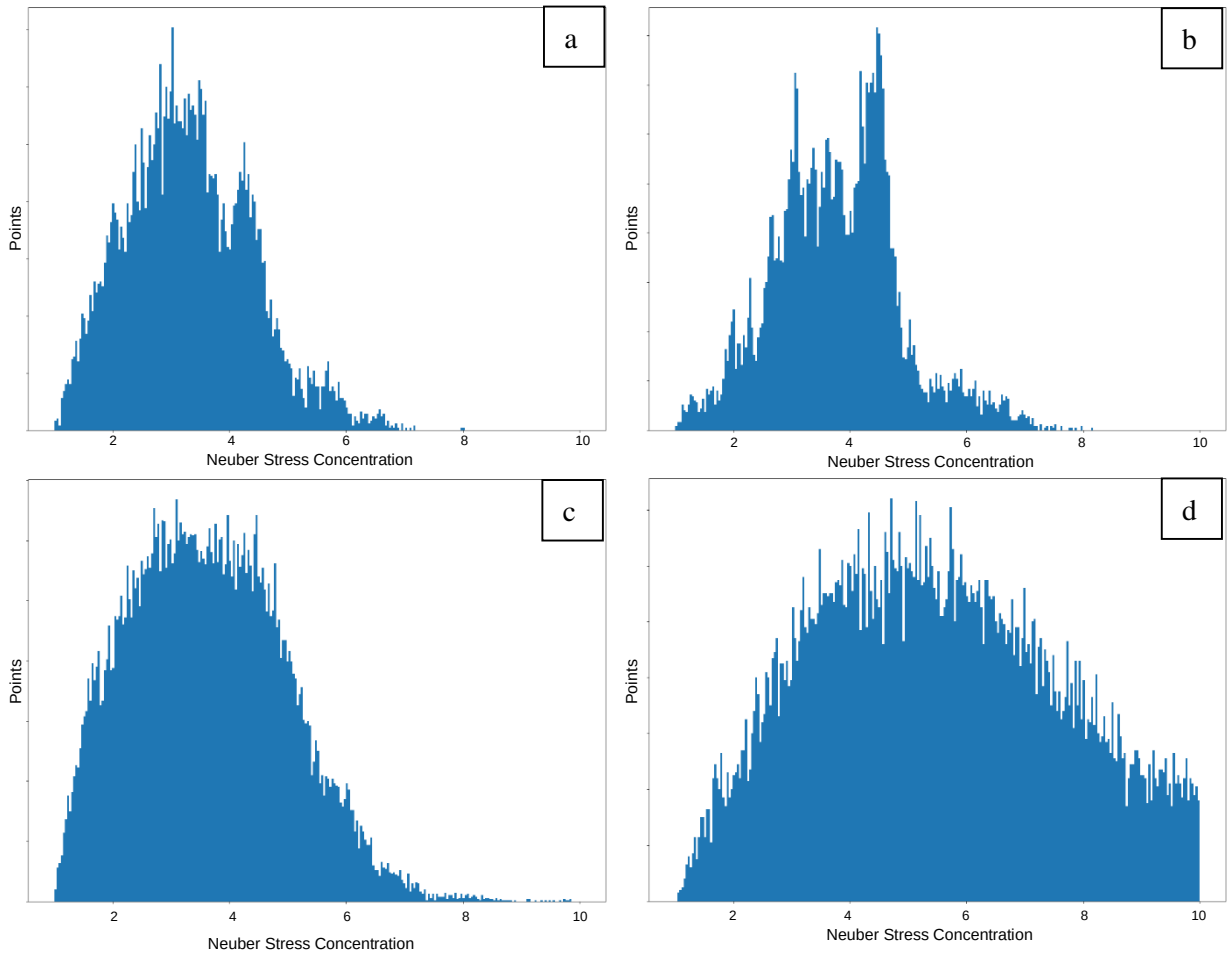

Figure 6.26 Stress concentration distributions according to the Neuber model for: A brushed, B ground, C rolled, D shotblasted surfaces. AFM data.

6.6.3. Arola and Ramulu Stress Concentration Distribution

Figure 6.27 shows the stress concentration distributions according to the Arola and Ramulu model for the four surfaces. The majority of the stress concentrations calculated with this model are at the lower end of the scale. They then tail off exponentially. This is due to the depth of these features being normally distributed, and only the negative depths being included.

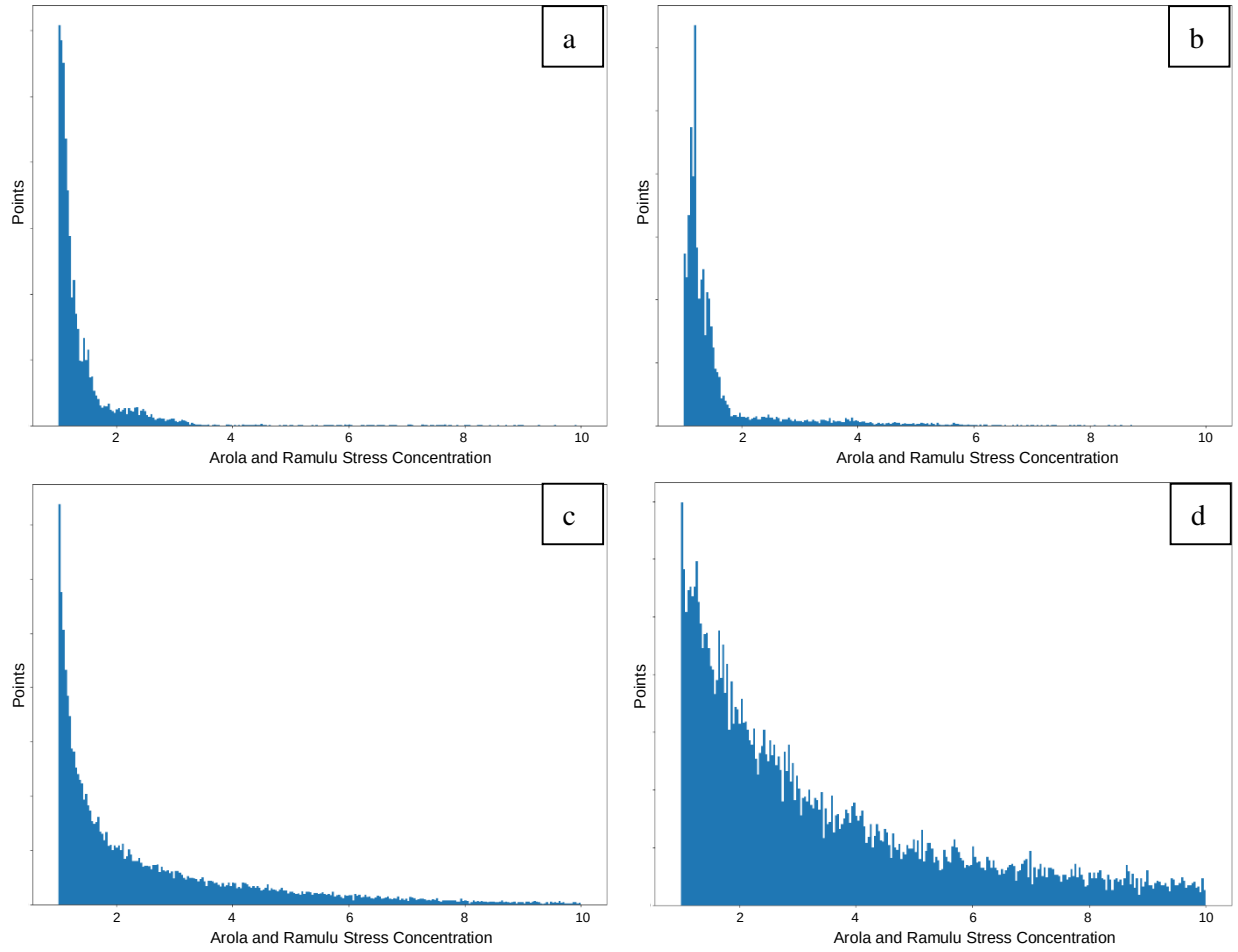

Figure 6.27 Stress concentration distributions according to the Arola and Ramulu model for: A brushed, B ground, C rolled, D shotblasted surfaces. AFM data.

The tails seem much longer, though much thinner, than those plotted with the Neuber model. This is likely to mean that both models predict there to be some high stress features at the higher end of the stress concentration distribution, though the Arola and Ramulu model predicts there to be proportionally fewer.

The stress concentration distribution for the brushed and the ground surfaces are indistinguishable in Figure 6.27. The stress concentration distribution for the rolled surface decays with a wider tail, showing

that it has more high stress regions and again, for the shotblasted surface, the highest stress concentrations are predicted.

6.7. Finite Element Analysis

6.7.1 Finite Element Analysis Results in General

Figure 6.28 shows the stress concentration factor results, mapped onto 3D models of the surfaces, for each of the four surface finishes together, for easy comparison. Topographic relief is represented by the shape (height) of the 3D structure, at a scale consistent between width and height. Stress concentration factor is represented in colour, with the redder end of the spectrum representing higher stress concentration factors. The legends for each map in Figure 6.28 are set to different scales to better see the distribution on a given map.

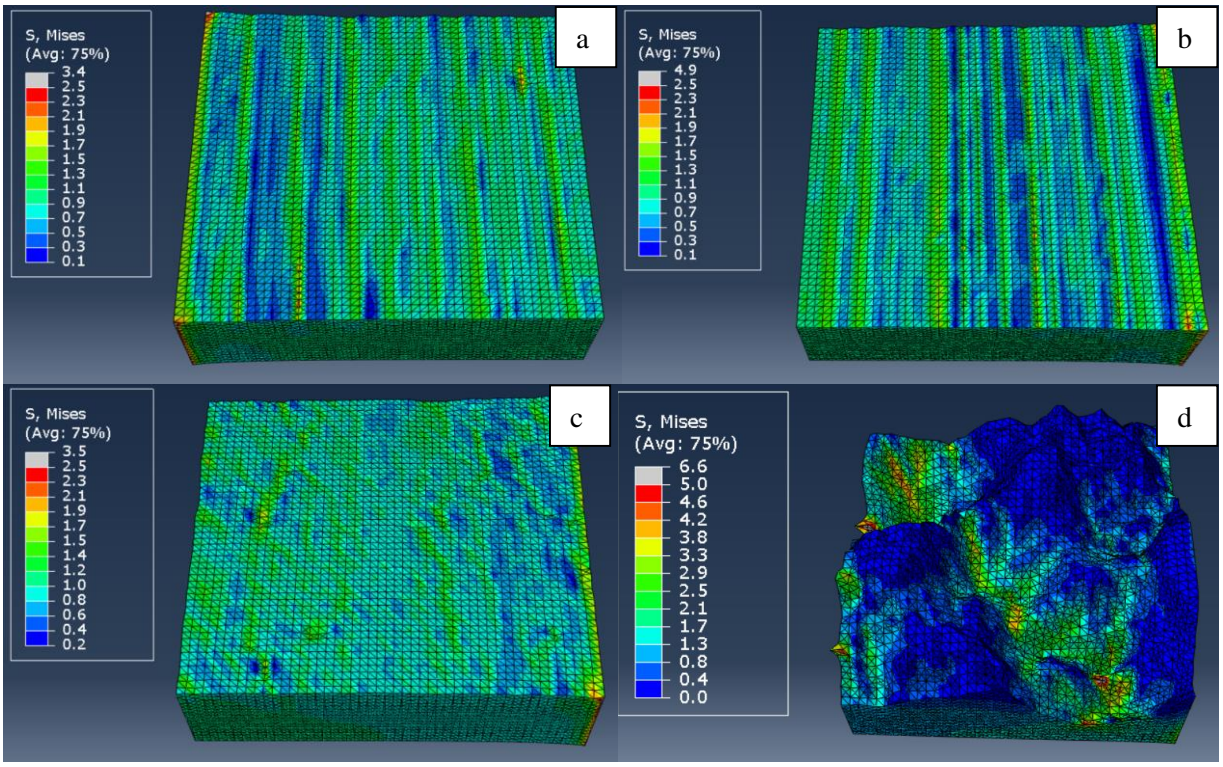

Figure 6.28 Stress concentration ratio mapping by FEA for: A brushed, B ground, C rolled, D shotblasted 200 µm² surfaces.

From these diagrams is can be seen that the shotblasted surface has the highest stress concentration factors at 6.6 at the lowest points of the deepest craters, while the rolled surface has the lowest maximum stress concentration factor at around 2.3, although this is calculated to be higher with better resolution models, as is shown in the next section.

Stress also is distributed differently for each surface. The brushed and the ground surfaces distribute stress in long parallel lines, since the areas of high stress lay at the bottom of valleys. This also mean that the areas of largest stress for these surfaces are themselves very large. This is important when considering the minimum feature size required to initiate cracking as described in the literature review. By comparison, the locations of high stress in the rolled surface are disordered and do not connect. For the shotblasted surface, it is clear that the stress is concentrated at the bottoms of the shotblast craters. With all surfaces, areas of negative surface height tend to concentrate stress whereas areas with positive surface height diminish it. This is consistent with basic stress concentration models such as the ellipsoid model, as well as with more specific surface finish models such as the Neuber model and the Arola and Ramulu model.

6.7.2 High Definition Analysis

Initially, FEA was completed at the highest resolution possible. To do this, only small (10 μm^2) sections of the surface were used, as the Abaqus CAE software became unreliable over 50,000 elements. This allowed for the analysis of the effect of the very small scale surface deviations such as etched grain boundaries on the rolled surfaces but cannot at the same time analyse large scale deviation such as shotblast craters. To do this, further models were constructed that used larger areas at lower resolution, as shown in the next section. With this method, both aspects could be analysed separately.

Figure 6.30 shows the stress concentration distribution for a brushed surface, as calculated by FEA. The stress concentration factor spans between 0 and 4 across the surface. Deep into the material, variation decreases and the value approaches 1. The peaks on the surface (blue) are somewhat protected from the surface stress, with stress levels usually below 0.3, although the minima are largely above 1. Only around half of the minima show large stress concentration, with the average sitting at around 1.5. Some of the minima with particularly small root radii reach stress concentrations of around 2.

Figure 6.29 shows the stress concentration distribution for a ground surface, as calculated by FEA. The effects of long, continuous ridges and troughs can be seen in the measurement area and are more prominent than that seen in the brushed surface.

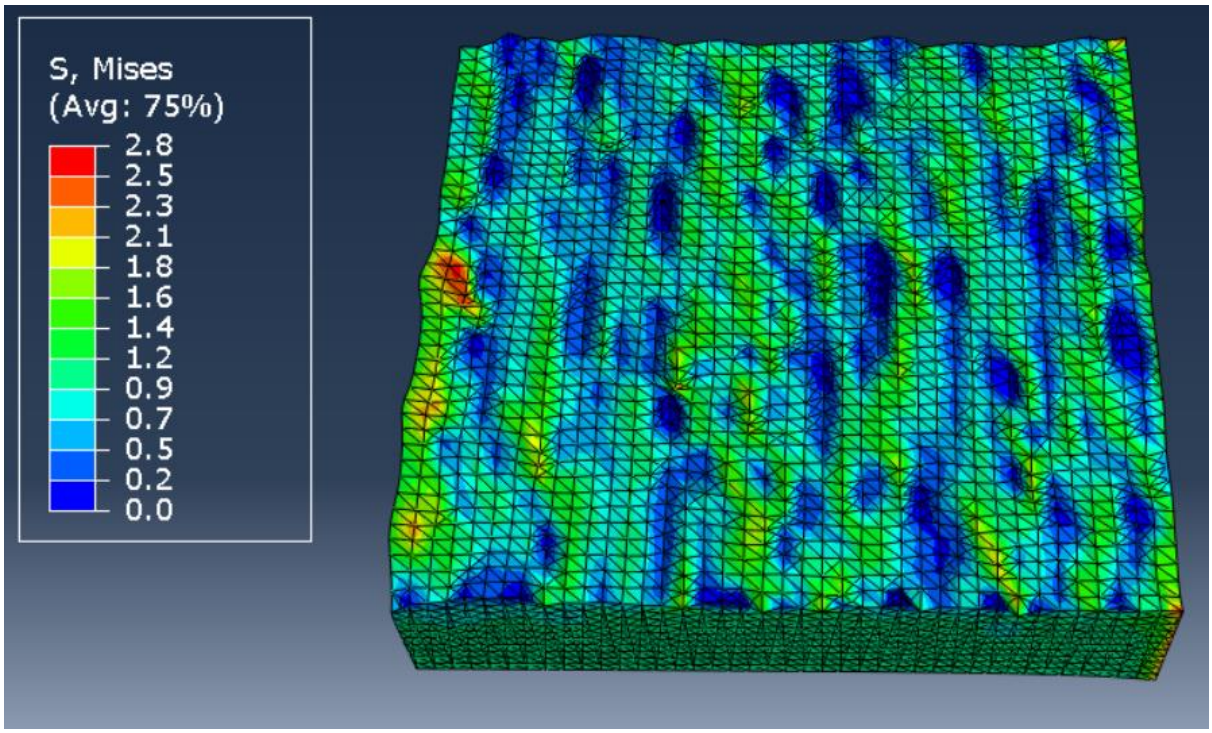

Figure 6.30 FEA analysis of a 10 µm^2 brushed surface, showing stress concentration factor distribution.

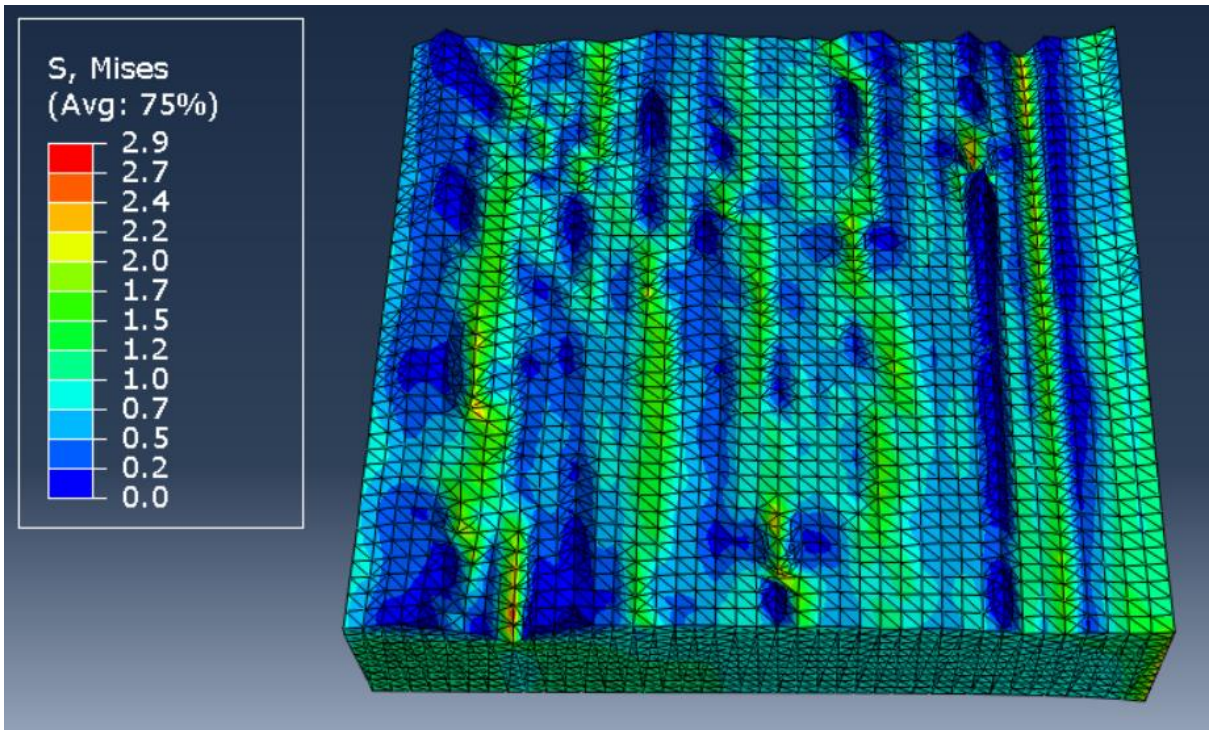

Figure 6.29 FEA analysis of a 10 µm^2 ground surface, showing stress concentration factor distribution.

The dark blue peaks indicate a stress concentration factor well below 0.2, while the green/yellow valleys indicate a stress concentration factor around 1.7-2. As with the other surfaces investigated, the highest stress concentrations are found in the minima. From Section 6.3. it is known that this surface, and the brushed surface, had some of the largest valley radii. From these diagrams it is clear they also have the lower stress concentration factor to go with it. The small height variation in this measurement area also likely keeps the stress concentration factor low.

Figure 6.32 shows the stress concentration distribution for a rolled surface, as calculated by FEA. It is a largely flat surface, with a largely consistent stress distribution. The stress concentration factor sits very close to 1 for the majority of the surface. The minima are not particularly deep compared to the other surfaces, however they do produce comparable stress concentrations, with the deepest features reaching a factor around 3.2. Since this cannot be due to their depth, it is likely due to a small root valley radii or steep valley sides/ low openness, both of which have been presented in this Thesis.

Figure 6.31 shows the stress concentration distribution for a shotblasted surface, as calculated by FEA. The stress concentration factor is seen to increase in the deeper valleys and minima and also in the sharper valleys. A stress concentration factor of 2 is common in most minima on this surface, with 4 found in the deeper, smaller root radii features.

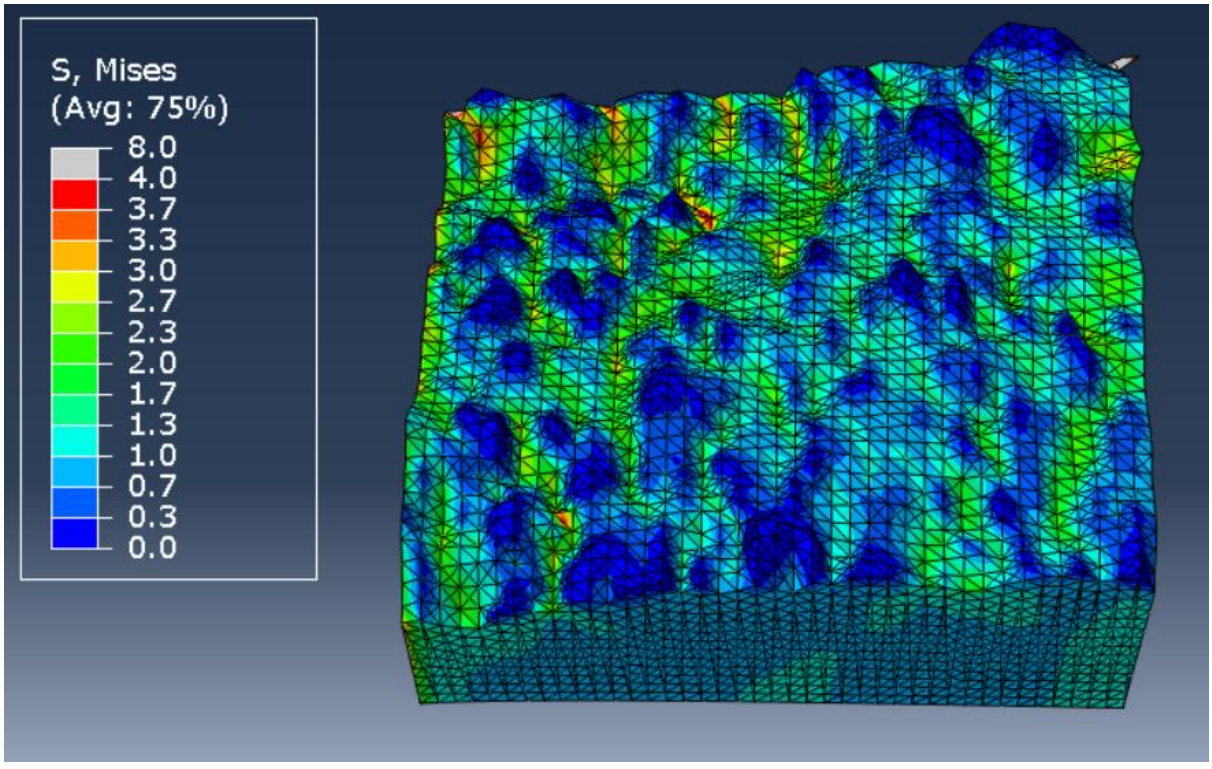

Figure 6.31 FEA analysis of a 10 µm² shotblasted surface, showing stress concentration factor distribution.

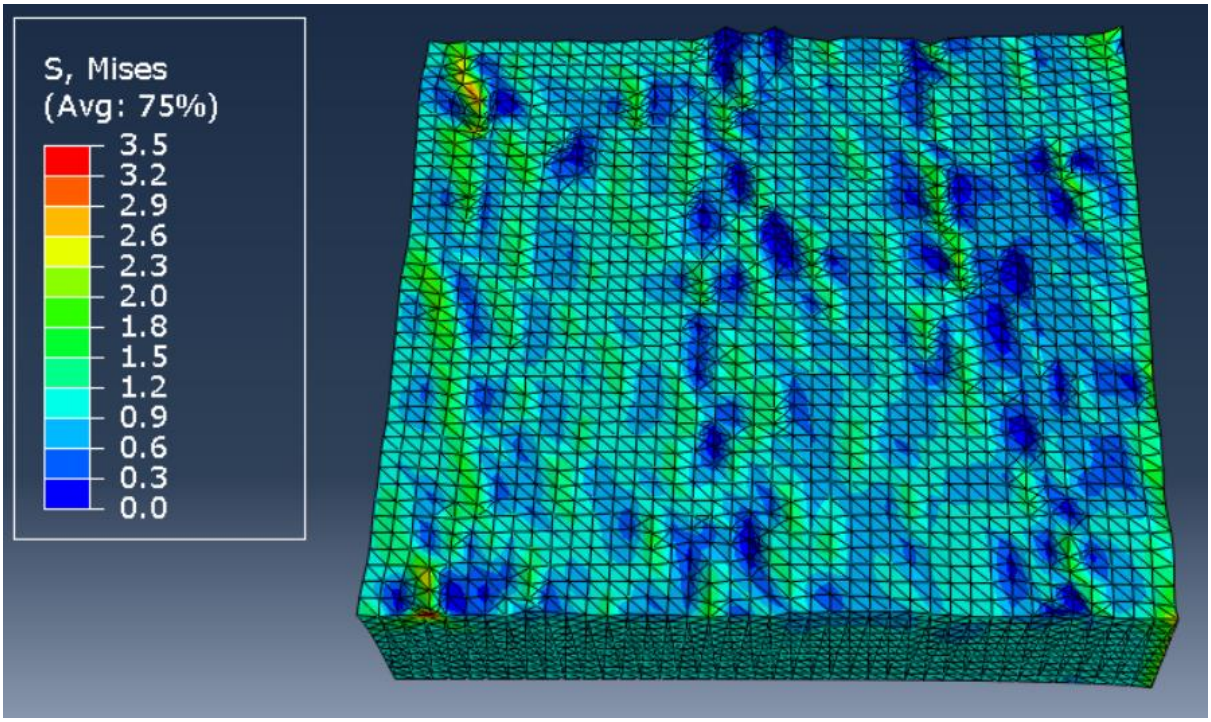

Figure 6.32 FEA analysis of a 10 μm² rolled surface, showing stress concentration factor distribution.

6.7.3 Modelling Larger Areas

The results in this section were produced from 1000 / 1000 pixel areas spanning 200 / 200 μm² from data gathered by VSI measurement. Figure 6.33 shows the stress concentration distribution for a brushed surface, as calculated by FEA. The scale bars for Figure 6.33, Figure 6.34, and Figure 6.35 are standardised such that the colour on each map can be compared directly with the other maps.

The long grinding marks can be seen in Figure 6.33. The stress is distributed consistently with them, with the highest stresses found at the lowest points, as found in the higher resolution models. Compared with the higher resolution model, lower stress concentrations are calculated for this surface. A maximum stress concentration of around 2.3 in Figure 6.33 compares with 2.8 in Figure 6.30. This

highlights the influence of small scale features and demonstrates how the total stress concentration is a function of stress concentration from all scales.

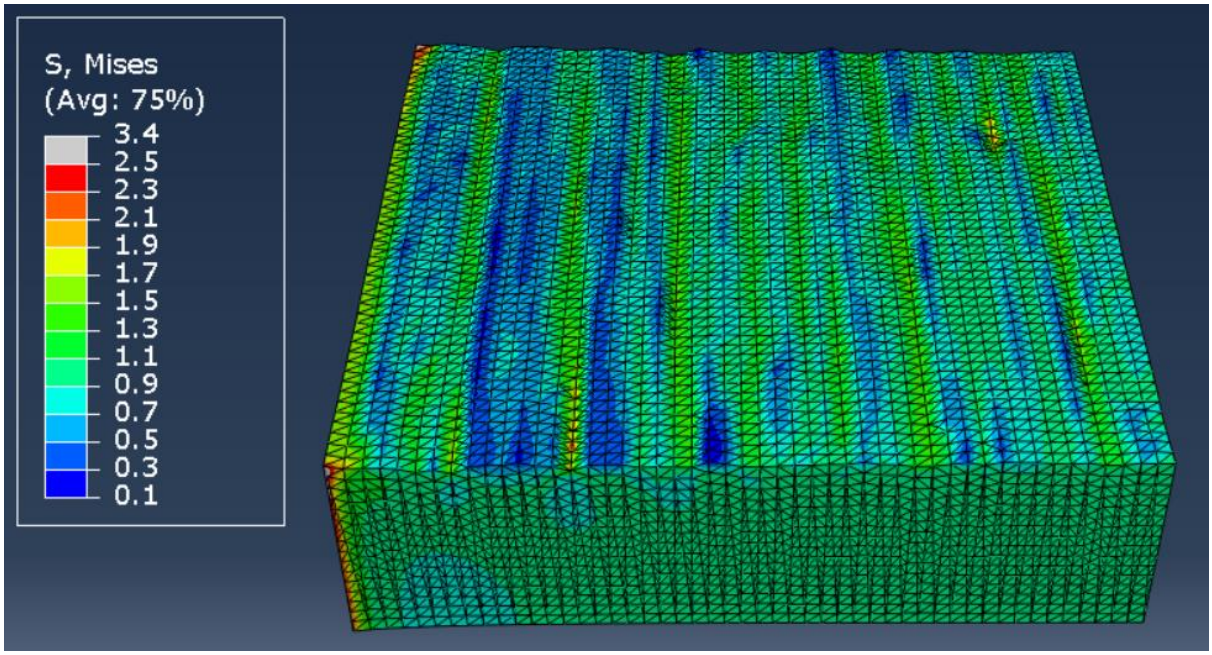

Figure 6.33 FEA analysis of a 200 μm² brushed surface, showing stress concentration factor distribution.

Figure 6.34 shows the stress concentration distribution for a ground surface, as calculated by FEA. The stress distribution on this surface is in accordance with that of the brushed surface, although the grooves are observed to be deeper and harbour greater stress concentrations up to around 2.5. By observing these larger scale models, it can be seen that the stress concentrations found at the bottoms of valleys continue long range.

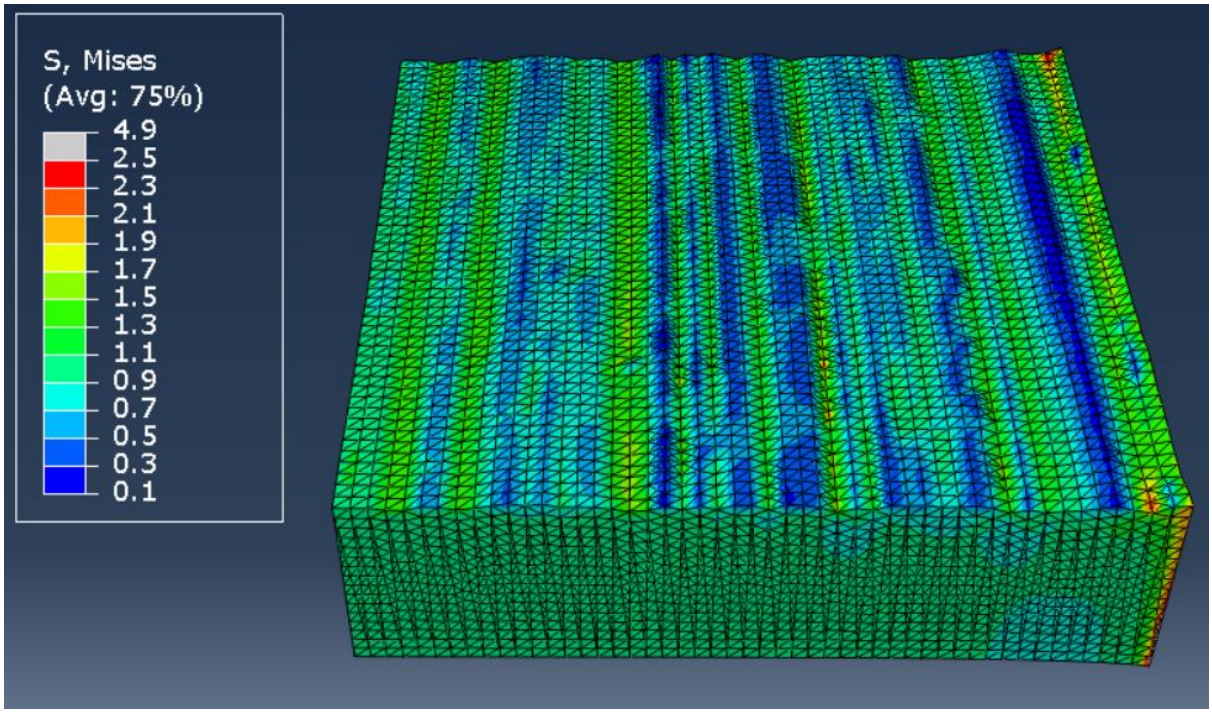

Figure 6.34 FEA analysis of a 200 µm² ground surface, showing stress concentration factor distribution.

Figure 6.35 shows the stress concentration distribution for a rolled surface, as calculated by FEA. Compared with the other surfaces it is very flat, and mostly has no major stress concentrations across the surface at this resolution. There are some small depressions in the surface, and in these the stress concentration reaches around 1.9, however these features tend to be small in size. This indicates that

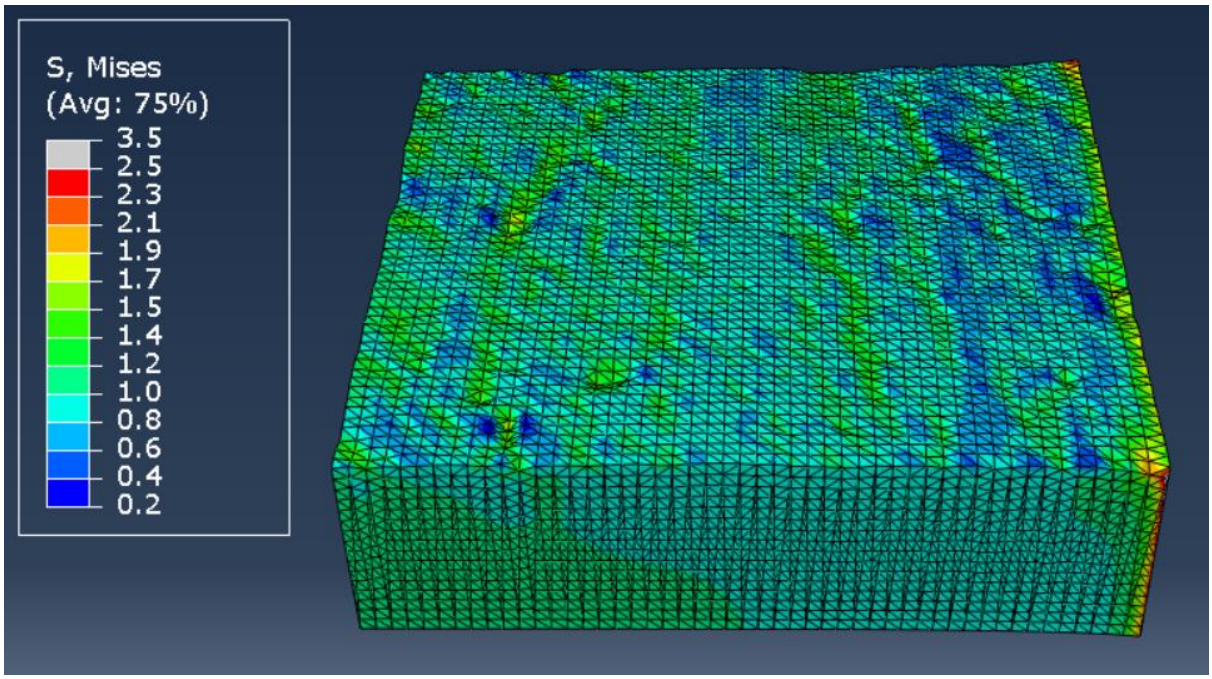

Figure 6.35 FEA analysis of a 200 µm² rolled surface, showing stress concentration factor distribution.

the largest stress concentrations found on this surface are contributed to by unintended features such as small depressions.

Figure 6.36 shows the stress concentration distribution for a shotblasted surface, as calculated by FEA. Most of the visible surface is a dark blue colour, indicating it has a stress concentration factor below 0.8 and mostly below 0.4, meaning it is protected by its height and the morphology of the surface around it. In the bottoms of craters however, stress concentration factors up to 5 are recorded. These are the highest for all the surfaces and, in this model, are almost certainly the result of the depth of these features, since they have relatively large radii.

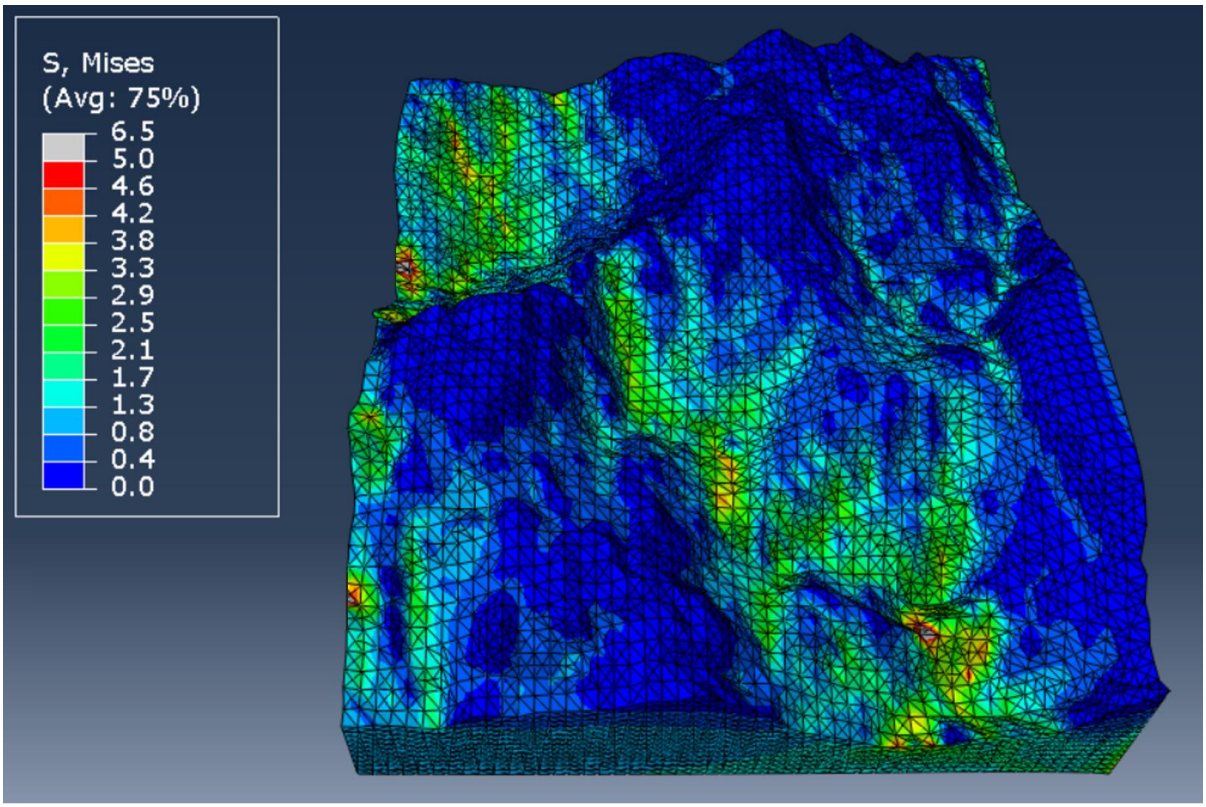

Figure 6.36 FEA analysis of a 200 μm² shotblasted surface, showing stress concentration factor distribution.

6.8. ASCC Trial Results

6.8.1. Immediate Observations

At 120 hrs, the droplets appeared brown/red indicating cracking initiation, as shown in Figure 6.37. They were rinsed with water and imaged by optical microscopy. In Figure 6.37 the characteristic branching cracks of ASCC can be seen by eye.

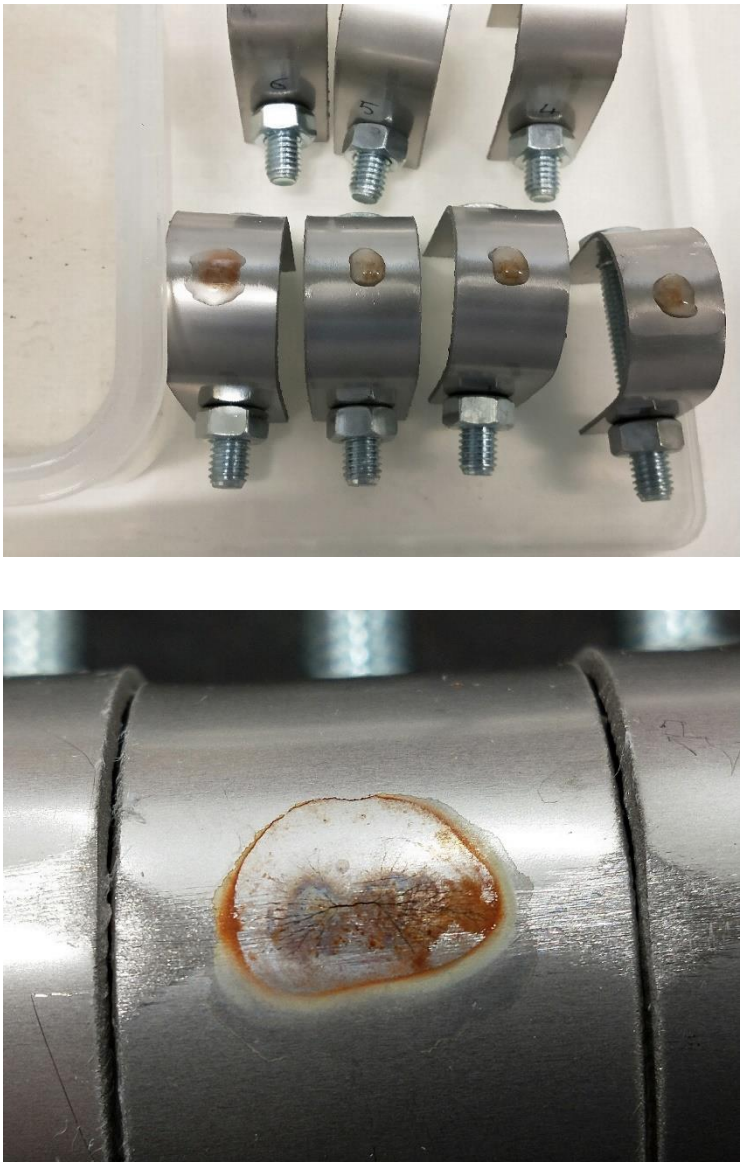

Figure 6.37 Discolouration indicating corrosion has initiated. The branching cracks characteristic of ASCC can be seen.

6.8.2. The Effect of the Direction of Applied Stress

At 120hrs all cracks appeared perpendicular to the applied stress, which in the proceeding optical micrographs is always displayed as vertical. Figure 6.38 shows a representative ASCC crack from a token ground in the direction of applied stress. From matching prominent features on each side of the crack it can be shown that the width of the crack has grown due to the stress pulling and moving the crack apart rather than corrosion eroding it. Red corrosion product can be seen deposited around the crack but not close to it, which is consistent across other cracks. Cracks tended to have a single long crack perpendicular to the direction of stress before branching at either side into 2 or more sub cracks. On occasion, multiple cracks formed concurrently in a parallel manner as can be seen in Figure 6.39.

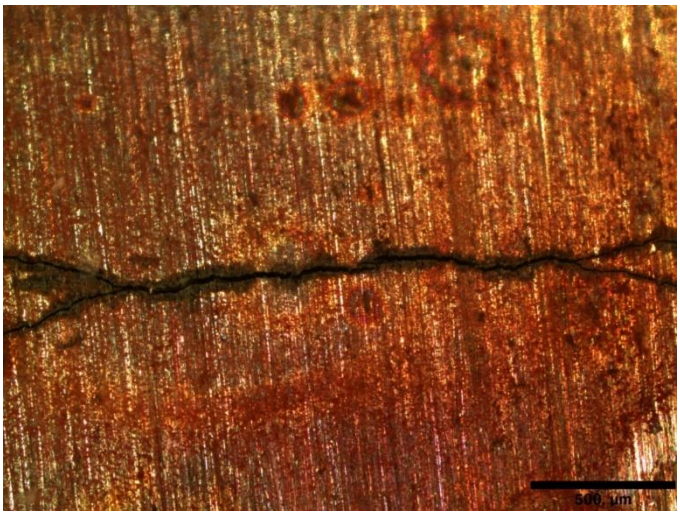

Figure 6.38 Showing a main central crack.

Figure 6.40 shows a crack formed on a sample ground in the direction perpendicular to the applied stress. The thickness of a crack on the surface is a good indication of the depth of the crack, since cracks grown into the material and relax outward, and therefore the thickness can be indicative of the age, suggesting this crack initiated earlier than those ground in the direction of stress.

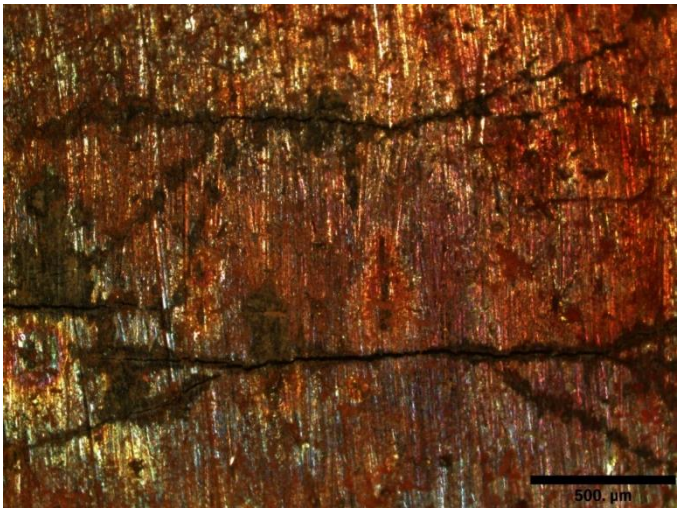

Figure 6.39 Showing two parallel cracks

Figure 6.40 Showing the main central crack branching into multiple sub cracks.

Figure 6.41 shows an ASCC crack formed on a rolled surface. This crack is short and thick and branches quickly into 3, and then many more subbranches. The highly branching nature of this crack is likely the result of there being fewer directional surface features to influence the crack growth.

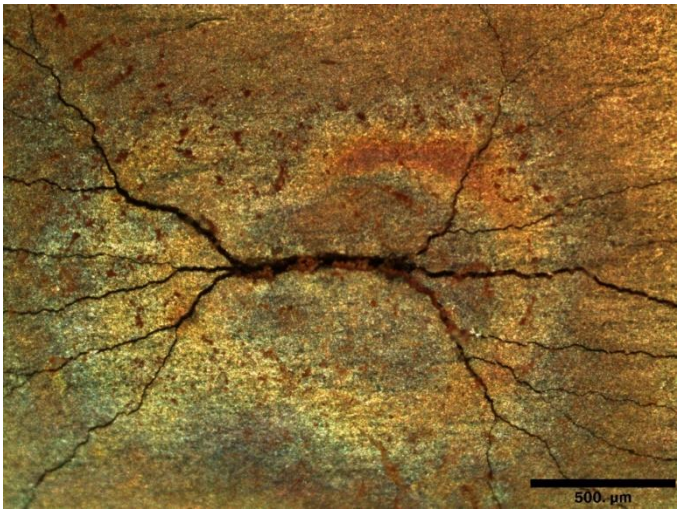

Figure 6.41 Showing an ASCC crack formed on a rolled surface.

A second trial was stopped at 72 hrs to observe the early stage of cracking. The thickness of the cracks was measured in three representative places using a Nikon optical microscope as shown by Figure 6.42. The average crack widths are presented in Table 6.2.

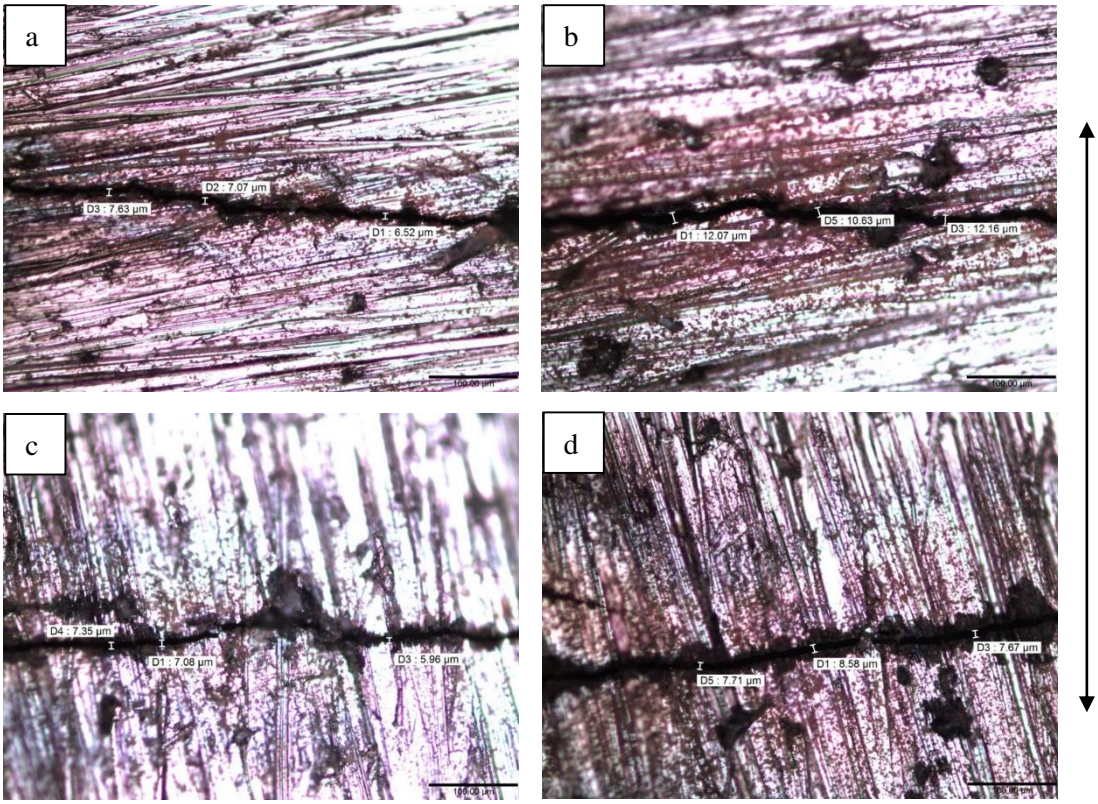

Figure 6.42 Optical micrographs of SCC cracks (72 hr exposure). A, B showing the direction of grinding orthogonal to stress. C, D showing grinding in the direction of the applied stress.

For comparison with the ground surface, Figure 6.43 shows ASCC cracks on a rolled surface. These appeared long and spindly, and they immediately branched into multiple thin cracks. This behaviour is consistent with that seen in trial 1. The cracks found on rolled surfaces exhibited a much less well-defined central crack than that present in all ground samples. The rolled samples show much faster bifurcation. The initial site of cracking was identified as pits for the rolled surfaces. This indicates the existence of a pit before cracking on these samples. Cracks then emanated from the pits, behaviour

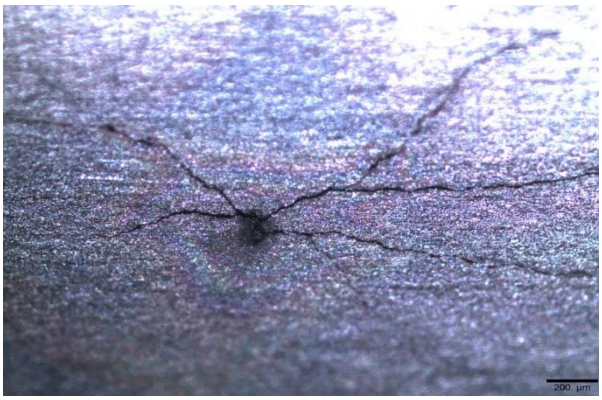

Figure 6.43 ASCC cracks on a rolled surface.

which is not seen in the ground tokens. This suggests that initially, the rolled surface is more vulnerable to pitting than cracking.

6.8.3. The Effect of Surface Finish on Cracking

Figure 6.44 shows representative cracks on the brushed surface. The applied stress for these micrographs is in the vertical direction; this remains consistent for all further figures. The cracks form perpendicularly to the direction of stress, and even at this low magnification, the cracks can be seen to follow the deeper valleys. This behaviour, also seen in the ground surface, is investigated in more detail in the next section. The cracks in the brushed surface tended to be long, averaging at 1.5 mm.

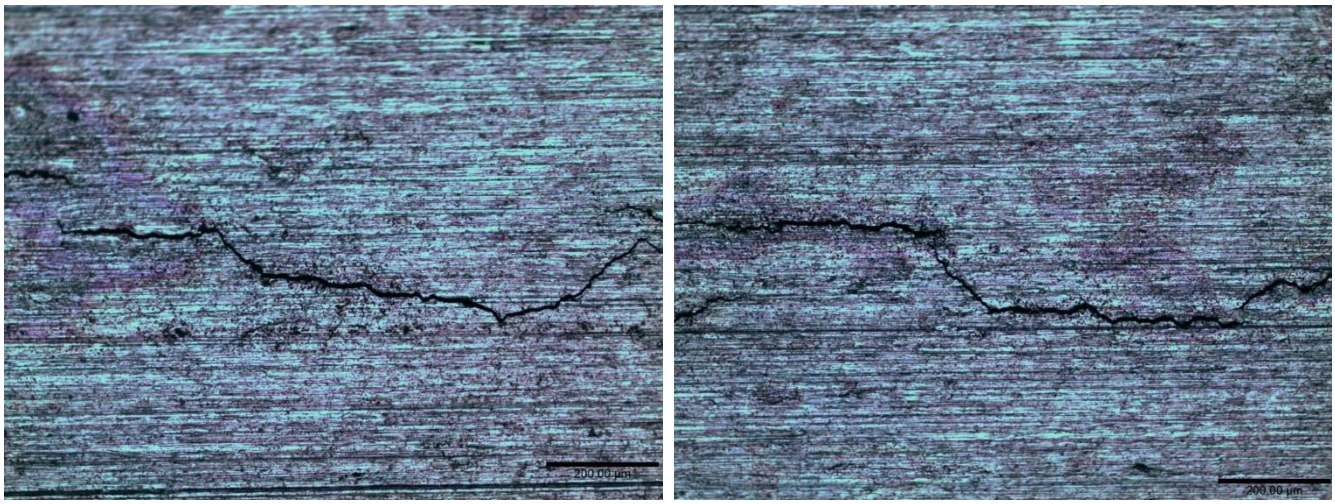

Figure 6.44 Optical micrographs of typical ASCC cracks on a brushed surface.

Figure 6.45 shows representative cracks formed on the ground surface. The cracks on this surface, as was also the case with the brushed surface, always grew perpendicular to the direction of applied stress. The cracks on this surface would follow the deepest valleys for short distances (10 – 100 μm) before deviating briefly. Generally, they followed the valley features less than the brushed surface.

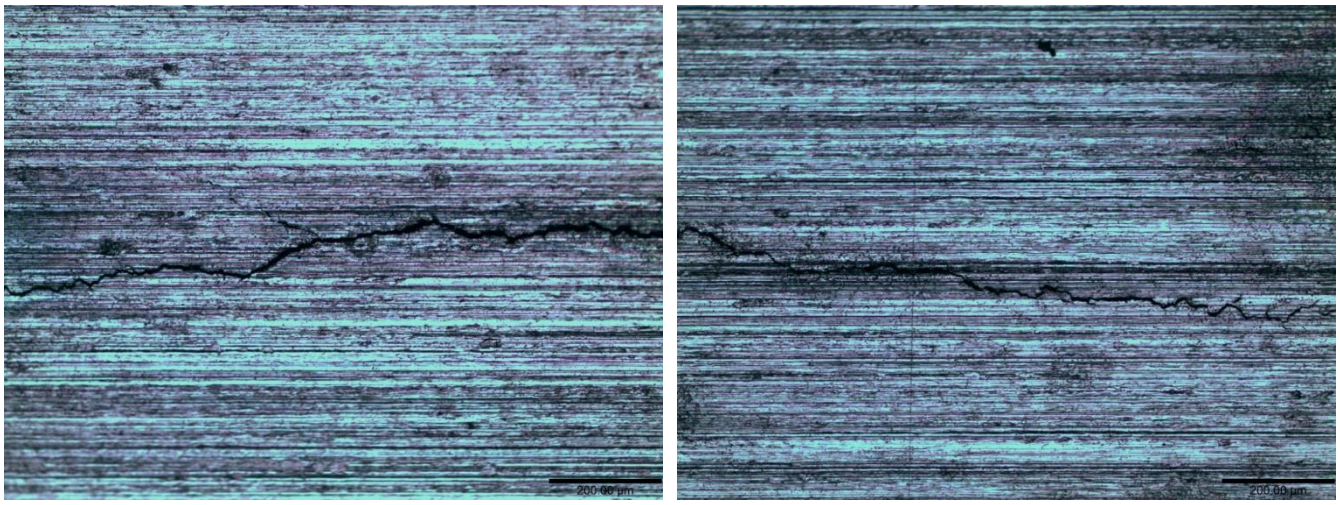

Figure 6.45 Optical micrographs of typical ASCC cracks on a ground surface.

The cracks on the ground surface were similar lengths to that found on the brushed surface, also averaging at 1.5 mm. In addition, crack branching was extremely rare, showing that cracking behaviour was similar between the two valley-dominated surfaces.

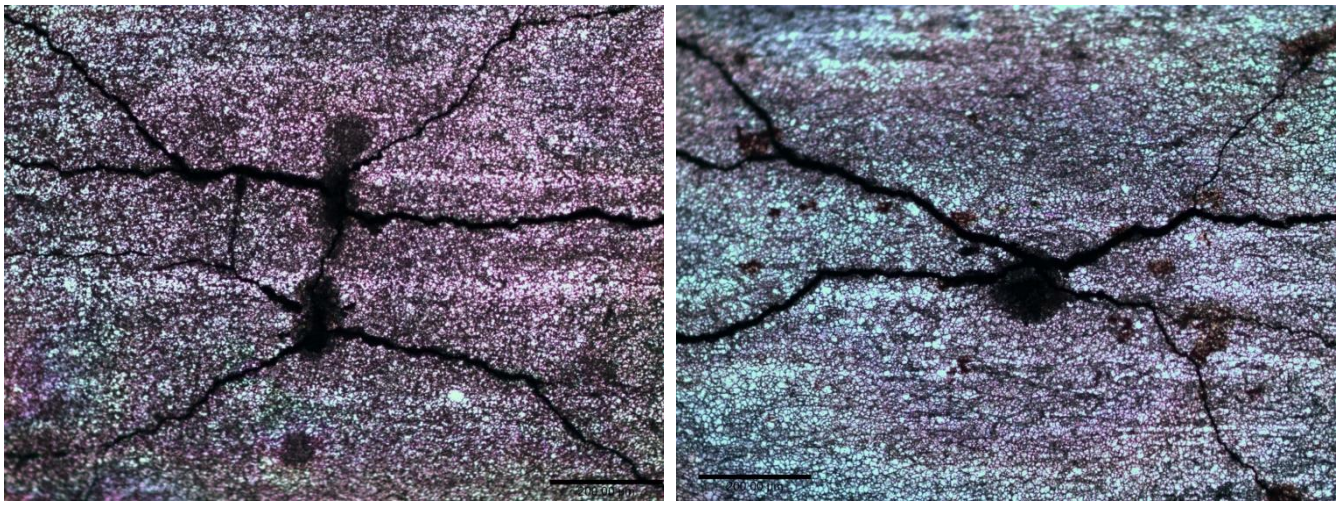

Figure 6.46 Optical micrographs of typical ASCC cracks on a rolled surface.

Figure 6.46 shows representative cracks found on the rolled surface. In general, the cracks grow perpendicular to the direction of applied stress, but they quickly branch and develop cracks at wide angles. The rolled surface produced the longest cracks at 3.1 mm.

Figure 6.47 shows representative cracks formed on the shotblasted surface. Contrary to the other surfaces, these cracks tend to be much shorter (0.6 – 0.8 mm) and also many cracks appeared in parallel. For all other surfaces the tendency was for there to be a single large crack rather than multiple smaller ones.

Cracking was not as straight and horizontal as the brushed and the ground surfaces. Cracks did tend to be horizontal on average but would regularly grow at steep angles for large portions. On the whole, this effect did not seem to follow features, as some cracks were found to pass straight over the tallest regions. Cracks often branched, but not as regularly as that seen in the rolled surface.

From observing the locations of the widest parts of the cracks, it was assessed that cracks tended to initiate at minima sites at the bottoms of shotblast craters. This is collocated with the sites of highest stress concentration.

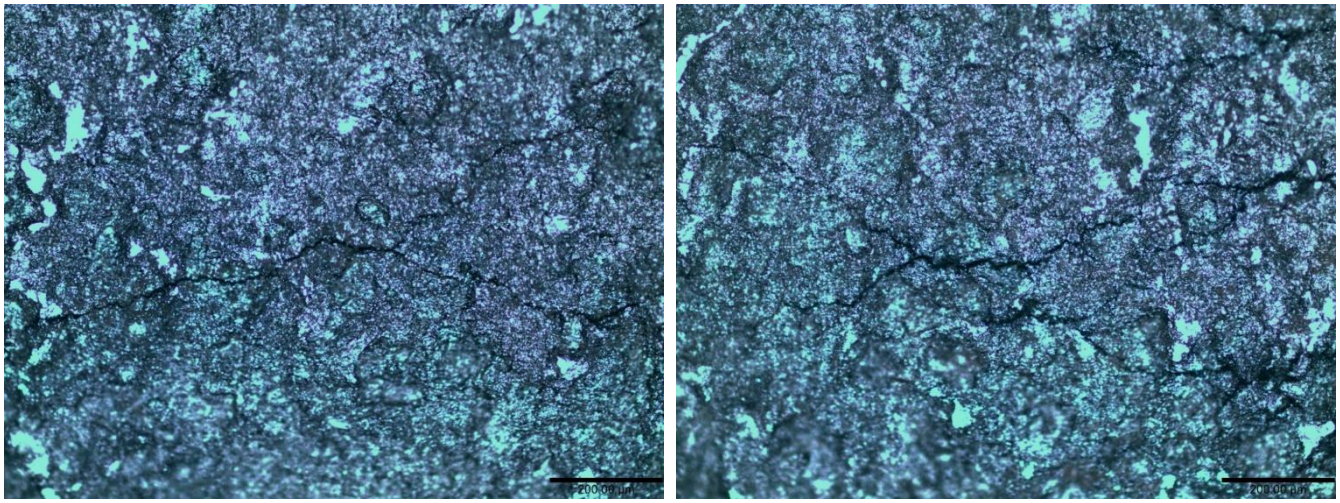

Figure 6.47 Optical micrographs of typical ASCC cracks on a shotblasted surface.

6.8.4. Cracking Rate

Crack length and width was measured for all cracks using the inbuilt measurement tool in the Nikon microscope. The measurement of width was performed using the 50X objective for greater accuracy. Example locations and measurements are shown in Figure 6.48. Each crack was measured at 2 or 3 locations at its thickest region. Most tokens had a single crack, in the case of the few tokens with 2 cracks, both were measured. For the shotblasted surface, which bore many cracks, 3 of the largest cracks for each token were measured.

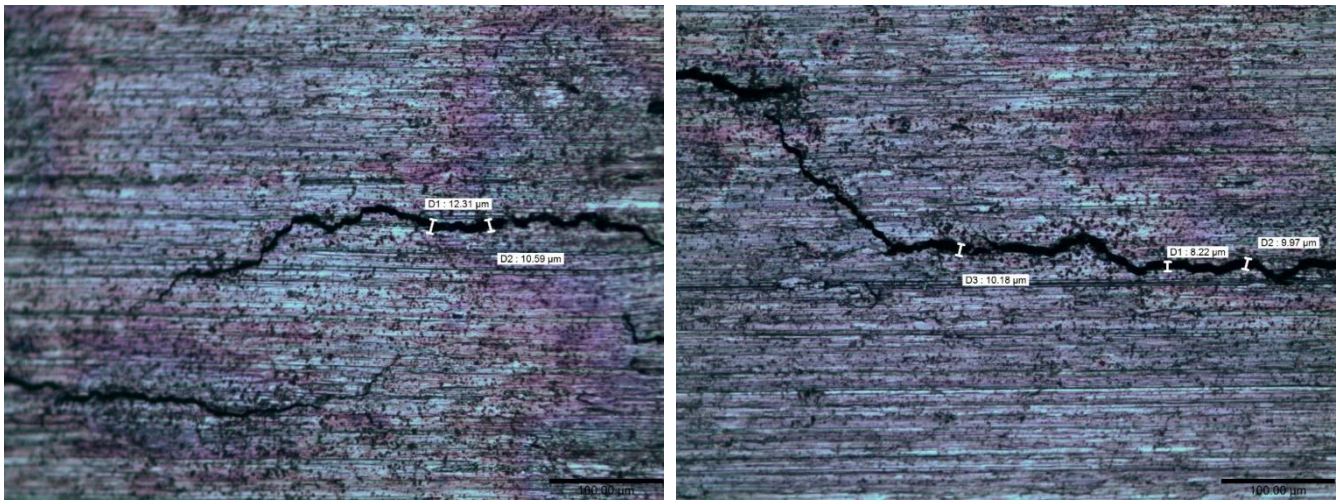

Figure 6.48 Optical micrographs of typical ASCC cracks on a brushed surface, showing method used to measure crack width.

Table 6.2 presents the average crack width measured for each surface. Crack width and crack length correlated positively showing both were related to crack growth, and that either are good indicators of crack size.

Table 6.2 Average crack width and length, with standard deviation (SD)

	Average Crack Width (μm) (SD)	Average Crack Length (mm) (SD)	Number of cracks
Brushed	9.5 ± 1.3	1.5 ± 0.17	14
Ground	7.5 ± 1.2	1.5 ± 0.18	15
Rolled	18 ± 1.4	3.1 ± 0.34	15
Shotblasted	7 ± 1.3	0.7 ± 0.08	14

6.8.5. The Influence of Surface Morphology on Crack Development

The optical micrographs in Figure 6.49 show typical crack behaviour on a brushed surface. They demonstrate how cracks on this surface adhere to some valleys for brief periods. Typically, cracks followed valleys on this surface for between 10 μm and 150 μm. They would often then deviate from the valleys at a 45° angle for similar distances.

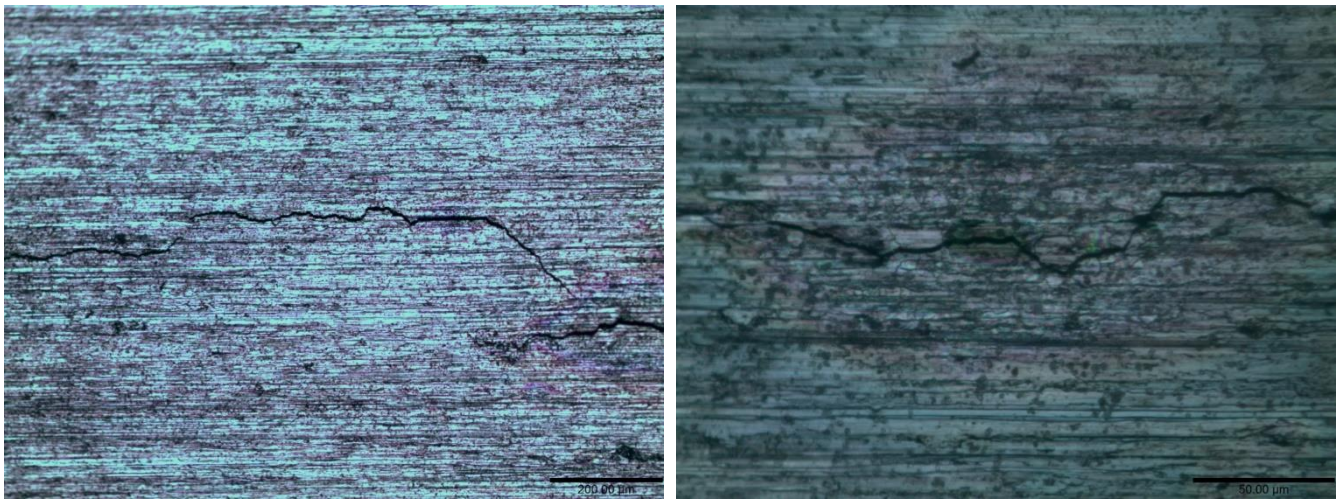

Figure 6.49 Optical micrographs of typical ASCC cracks on a brushed surface, showing the influence of surface features on crack development.

This behaviour indicates that the surface finish influences the route of crack growth with the crack following the deepest parts of the valleys. These areas were found to have the highest stress concentration in the brushed surfaces, and were also found to have the lowest, most aggressive, openness values.

Typical cracking behaviour on the ground surface is shown in Figure 6.50. As with the brushed surface, cracks on the ground surface show a preference for following valley bottoms.

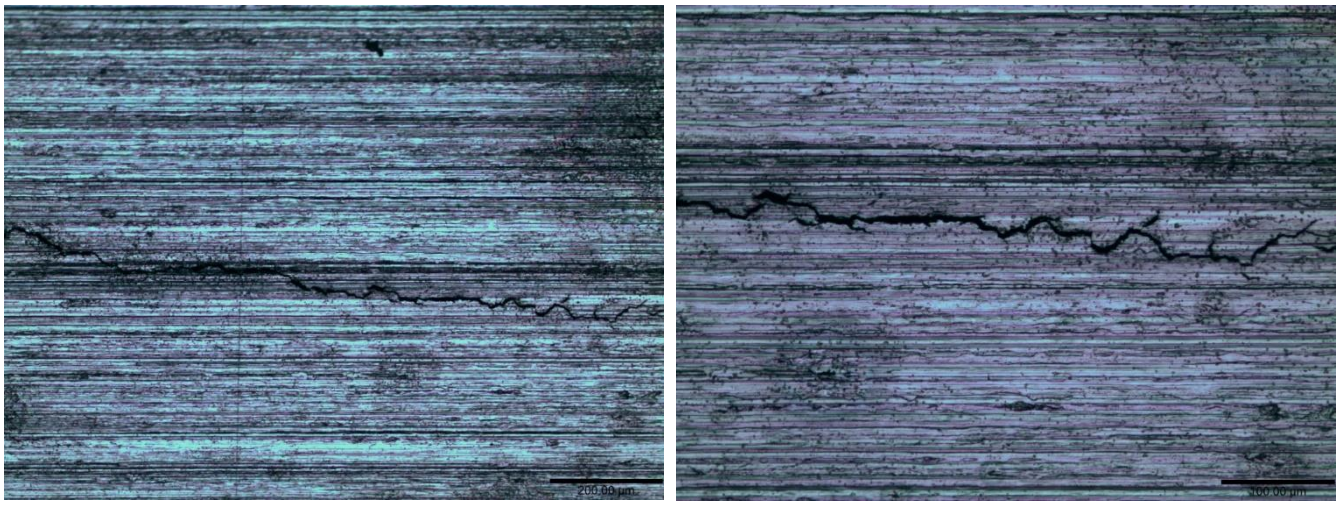

Figure 6.50 Optical micrographs of typical ASCC cracks on a ground surface, showing the influence of surface features on crack development.

Figure 6.51a shows typical cracking behaviour on the rolled surface. The large angles the cracks form from the expected cracking direction are seen. The straight horizontal crack found in both the ground and the brushed surfaces do not appear on the rolled surface indicating that those straight cracks were influenced by surface finish, rather than just forming cracks in the expected horizontal direction.

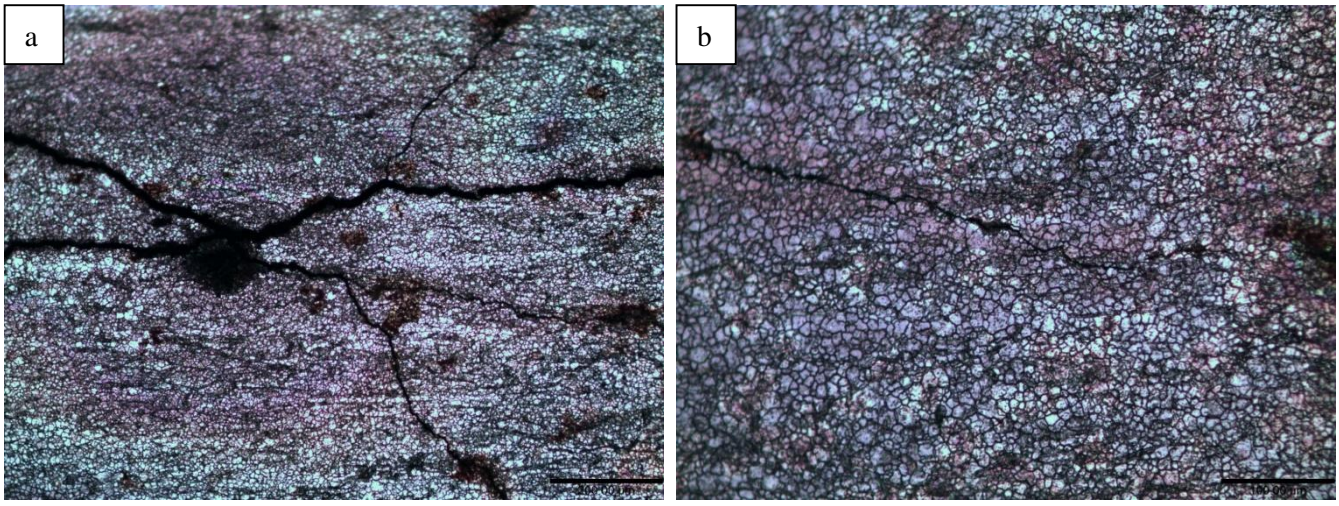

Figure 6.51 Optical micrographs of typical ASCC cracks on a rolled surface, showing the influence of surface features on crack development.

Figure 6.51b shows the edge of a crack at higher magnification. It begins on the left hand side and ends somewhere between the middle and the right hand side of the image. The location of the crack edge is difficult to identify since the crack follows the grain boundaries. Closer to the crack edge, the crack becomes thinner and eventually becomes thinner than the width between grains making its location hidden.

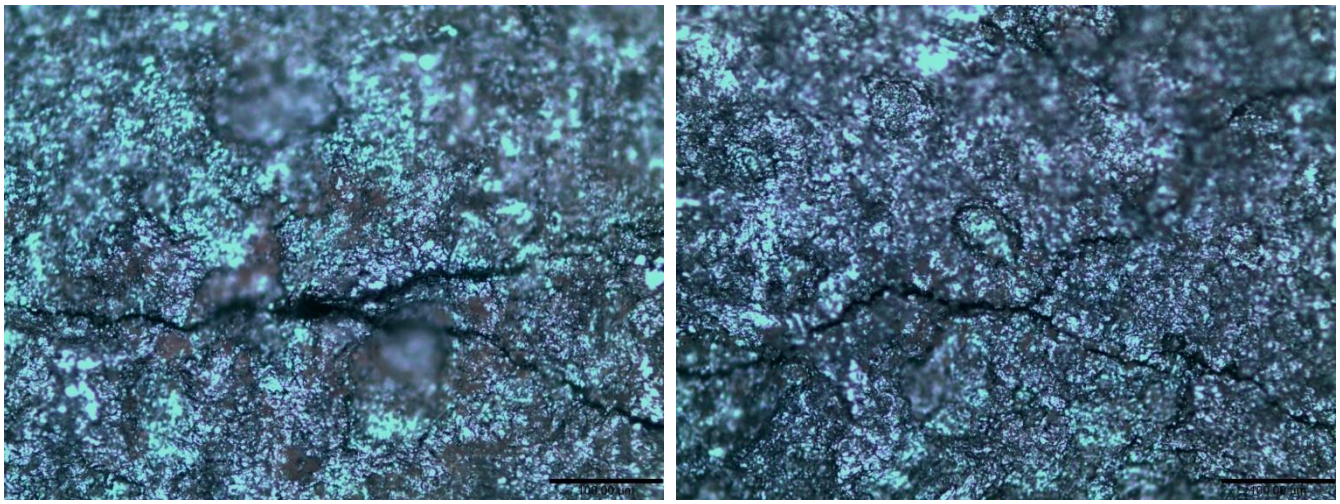

Figure 6.52 Optical micrographs of typical ASCC cracks on a shotblasted surface, showing the influence of surface features on crack development.

Figure 6.52 shows parts of cracks found on the shotblasted surface. Cracking and branching on this surface takes on a different form to that found on the rolled surface, indicating that it is affected by the surface finish. It is not observably affected by surface morphology as cracks pass over high points of the surface with similar regularity to low points.

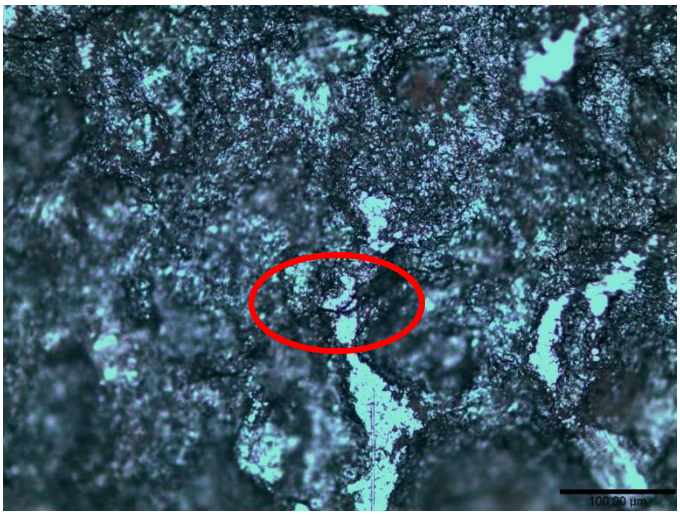

Figure 6.53 Optical micrograph showing an ASCC crack passing over a high peak, indicated by the red oval.

Figure 6.53 shows a thick crack passing over a flat topped peak feature on the shotblasted surface. These features are the highest points on the surface. This indicates that for this surface, crack development is not observably driven by stress concentration distribution (or openness value). Since cracks on this surface do initiate at the minimas of craters, it could be that cracks begin in sites of high stress concentrations (and openness) but propagate through features they otherwise could not initiate on.

6.8.6. Discussion

Crack Branching

The cracks on the brushed surface and the ground surface did not branch at all. This compares with the shotblasted surface that commonly had short cracks with single branches and the rolled surface where each crack had frequent branches. A high degree of branching is considered evidence of a high crack velocity and a high stress concentration [29]. This is supported by the width and length measurements which found that cracks on the rolled surface had grown the most during the trial indicating a higher crack velocity. For the brushed and the ground surfaces, the lack of branches could either be the result of the surface finish slowing the crack velocity to a rate at which branching did not occur, or the surface morphology denying the crack alternative directions with sufficient stress concentration for cracking. The analysis of stress concentrations in this Chapter would suggest the latter is the case, and little evidence is found for the former.

The high degree of branching observed of cracks on the rolled surface has the following possible explanations:

1. Unconstrained by the lack of morphologically directional surface features, cracks develop more freely, directed more by residual stresses and grain structure.
2. The stress concentrations shown analytically and by FEA in this Chapter branch out in a connected network, forming paths of low resistance. Cracks may follow these surface stress concentrations.

Crack Initiation

Cracks on the brushed and the ground surfaces were seen to regularly follow valley bottoms. This is in line with what is known and had been shown for stress concentrations in these regions. This confirms the theory that stress concentrates in these regions, formed by analytical stress concentration modelling, and the FEA modelling. This also implies that, since stress is concentrated in these regions, as well as supporting crack propagation, they encourage crack initiation, since stress concentration has been shown to facilitate crack initiation [30]. A surface which contains features such as valley minimas which have been shown in this chapter to encourage crack development and crack initiation will be more vulnerable to ASCC.

The Shotblasted Surface

Many small cracks formed on the shotblasted surface. This suggests that the formation of a crack on the shotblasted surface does not reduce the likelihood of further crack initiation in the local area. For other surfaces it is known that this can happen mechanically since a large crack will relieve stress across the surface, and, since an ASCC crack tip typically has a higher stress concentration than surface features, crack propagation will be confined to this point [31]. Another effect that limits the number of cracks under a droplet is controlled by the electrochemistry. Anodic corrosion at a main crack imparts a negative charge on the surrounding surface which prevents the formation of positive iron ions and their subsequent dissolution, effectively providing cathodic protection to the surface. By this mechanism, strong corrosion in one area can inhibit corrosion elsewhere. This would be a benefit of this surface since it shows good resistance to large crack generation.

For the shotblasted surface, crack growth may have been interrupted by the steep features on the surface, or by the large residual stress measured in the surface, before growing large enough to relieve stress across the surface or provide cathodic protection. This offers some explanation as to why there were many small cracks on this surface.

Openness and Cracking

It has been shown in Chapter 4 that shotblast craters do not concentrate openness, and it has been shown in this Chapter that they do concentrate stress. Since cracks on this surface do initiate at the minima of craters, it is possible that cracks initiate in sites of high stress concentrations but propagate through

features they otherwise could not initiate on. The large features on this surface show little influence on crack development after crack initiation, despite a strong cracking/surface morphology correlation with the brushed and the ground surfaces. Instead, enclosed features at grain boundaries may have a larger effect since, regarding openness, the surface is very similar to the rolled surface. Although the observed crack behaviour is different, these surfaces were the only ones to exhibit crack branching. This may be due to the branching stress concentrations of the etched grain boundaries on each surface, however the stress concentrations on the shotblasted surface are dominated by the larger scale features which are seen to not influence crack development. Additionally, cracking along grain boundaries on the surface may be indicative of intergranular corrosion. Alternatively, this may be due to the branching nature of the openness distributions on the shotblasted and rolled surface, which are quite similar and may guide the crack by providing a connected path along the surface with a highly localised chemically aggressive environment that is known to exist in enclosed regions [32][33].

6.9. Conclusion

6.9.1. Summary of Conclusions

The stress concentration factor has been mapped across four types of surface finish for two prominent models, the Neuber model and the Arola and Ramulu model. The deductions regarding stress concentration and the implications for SCC have been presented. This method of plotting valley radii and stress concentration factor has shown value in understanding the relative effects of valley radii and depth on stress concentration factor.

Key conclusions:

- Unintended features such as small holes in the surface created by smearing during grinding or brushing are the main cause of some of the most extreme stress concentration factors.
- Features with small valley radii can have large stress concentration factors, despite sometimes lacking in depth. This means the nature of the surface finish can be more important than the overall surface roughness.
- The stress concentration factor lowers the critical applied stress required, and, along with factors that affect the local environment, is a cause of SCC initiation.
- FEA can be used to measure stress concentrations at the micro-scale.
- Surface topography acts to protect the majority of the surface from applied stress, meaning crack initiation is unlikely to occur in high regions.
- Cracks form and propagate along valleys formed by brushing and grinding.

6.9.2. Conclusions in Detail

It is a reoccurring observation that extreme or unintended features are responsible for the highest stress concentration factors. This corroborates existing literature that has found that surface scratches can concentrate stress and decrease fatigue life [34]. These features are generally not a deliberate effect of

finishing but unintended or potentially the result of handling in post. If marks caused by handling were the sole cause of these most vulnerable features, it would suggest that surfaces with different surface finishes would be equally vulnerable to corrosion initiation. This is not the case, suggesting that either the major cause of these features is during the surface finishing process, or that the damage done during handling affects different surfaces differently.

It has been shown that the valley radius has a larger effect on stress concentration than first thought as shown by the larger stress concentration factors found in the rolled surface compared with the brushed and ground surfaces using the Neuber and the Arola and Ramulu models. The brushed and the ground surfaces were expected to be key examples of stress concentration due to surface geometry, since their shape is largely analogous to the notches used in stress concentration studies [35]. Though they had depth and openness, they tended to have larger valley radii which prevented high stress concentrations from forming.

Surface stress concentration factor has been shown to be dependent on surface finishing process. This is in line with existing studies, and has widened the range of surfaces tested [7]. Stress concentration factor influences SCC behaviour, as shown in this Chapter and in existing literature [36]. This effect works alongside the openness effects discussed in Chapter 4 since it has been shown that cracks often originate from pits. In this manner the most vulnerable surface would be one with deep grooves with very sharp, small-radii bases for the maximum stress concentration factor, but that also have very steep sides so as to have the smallest openness value possible. Here, corrosion initiation would be preferable due to the enclosedness of the surface, and crack propagation would occur due to the stress concentration.

Finite element analysis was successfully used to calculate stress concentration factor distribution for surface finishes using real measured 3D data. This successful trial has shown FEA to be a viable and effective method for the calculation of stress concentration factors in 3D surfaces with applied finishes, expanding the use of this method from additive manufacturing to investigate industry standard surface finishes [7]. FEA is an effective method specifically for the analysis of stress concentrations on surfaces at the microscopic scale, should good quality surface data be available from VSI or AFM.

FEA has been used to identify critical regions in each of four surface finishes where crack initiation and fatigue failure are most likely to occur. It has shown that the shotblasted surface concentrates stress the

most, with stress concentrations reaching 5 in the deepest shotblast craters. This compares to 2.8 for the brushed surface and 2.9 for the ground surface and only around 2 for the rolled surface.

The stress concentrations calculated by FEA were much lower than that calculated by either the Arola and Ramulu model or the Neuber model; these are presented for comparison in Table 6.3. Ignoring the absolute values, the two models proportionally match each other well, and match the FEA analysis well for all finishes except rolled. This finish is estimated to be the second highest for stress concentration by the two models due to its small root radii features. These features are not well brought out by the 3D model used in FEA and so the FEA analysis calculates the relatively flat rolled surface to be the least stress-concentrating.

Table 6.3 Comparison of Calculated and Simulated Stress Concentrations

	FEA	Arola and Ramulu	Neuber
Brushed	3 ± 0.5	5 ± 1	5 ± 1
Ground	3 ± 0.5	5 ± 1	5 ± 1
Rolled	2 ± 0.5	9 ± 1	6 ± 1
Shotblasted	5 ± 0.5	10 ± 1	10 ± 1

Topographies for all surfaces tend to protect much more of the surface than they expose; however, it is the state of the more vulnerable features that defines the performance for the whole surface. The higher points on all surfaces exhibit a 5 fold decrease in stress compared to the bulk material, meaning crack initiation is extremely unlikely to occur in these areas.

By FEA and by the analytical methods, the shotblasted surface has been shown to concentrate stress the most, mainly due to its larger-scale morphology. The residual stress present, which for most areas is measured to be of similar magnitude to the yield stress, will counter this effect to some degree. A lower residual stress is expected at crater minimas, which makes the estimation of the combination with stress concentrations more difficult. Further, the stress concentration factor is a multiplying effect whereas the residual stress is an absolute amount making the two difficult to combine.

The direction of grinding has been shown to have no significant impact on the rate of crack initiation in the trials that investigated the direction of stress application. Crack formation reliably occurs

orthogonally to the direction of applied stress, a behaviour already well documented [37]. This indicates that the applied stress is more influential than the residual stress. The cracks formed on the rolled surface took a less uniform route, suggesting they were less constrained by the shape of the surface finish when compared to the cracks on the ground surface.

The rolled surface showed a higher propensity for pitting. It is likely that a lack of stress concentration sites prevented crack initiation, effectively lowering the effective stress and allowing pitting to occur when cracking would have in a ground surface.

Stresses calculated from EBSD data (Chapter 4) showed similar residual stresses at the surface of the rolled and the ground surfaces, but much higher stresses 50 μm deep, with measured values indicating residual stresses of similar magnitude to the yield stress, and with large amounts of plastic deformation in both surfaces. Existing literature has found stresses from machining to reach up to 150 μm into the surface [38]. This is inconsistent with the rate of crack initiation observed in this experiment, where ground samples cracked faster. However, it is likely that the higher residual stresses in the rolled surface may have influenced the direction and spread of the cracking compared to the ground surfaces which were more dominated by the applied stress.

In Section 6.7., FEA analysis showed maximum stress concentration factors to be around 3 for a ground surface and only around 2 for a rolled surface. This somewhat explains the rolled surfaces resistance to cracking and the rolled surface's initial propensity for pitting. Once pitting was initiated, the surface morphology was altered and will have caused the creation of greater stress concentration factors around the pit openings allowing cracking to initiate. This is consistent with previous literature that has shown pitting to cause high stress concentration factors [28].

On brushed and ground surfaces, cracks form and propagate along valleys. It was assessed that the stress concentrations found at the bottoms of valleys provide sites vulnerable to crack initiation and form paths of lower resistance for crack tips to follow. It has previously been shown that the stress concentrations formed by topological features lead to fatigue failures, and that because of this, the influence of surface gradient means that the hybrid features discussed in Chapter 4 could be used to estimate stress behaviour [39].

It was found that cracks tended to form in sites of high stress concentration such as at the bottom of shotblast craters and valleys. The lack of influence of steep features on the shotblasted surface, and the behaviour of cracks on the rolled surface suggested surface openness may play a role in the propagation of the crack tip though no existing literature can be found to support this.

6.9.3. Method Evaluation

The method used here applies models (the Neuber model and the Arola and Ramulu model) usually used for 2D cross sections of surface, to 3D surfaces. This is justified to a degree as, at a very small level, a line drawn across a surface can be considered to be very similar to a line drawn immediately parallel to it. This model loses value when the surface changes quickly in the direction perpendicular to that of the predominant stress causing features. In FEA also, the majority of stress concentration studies use 2D plots taken from real surfaces, which bears the same drawback. This weakness would be removed by using 3D FEA, this makes the FEA study presented in this chapter an effective way to check this issue.

These models (the Neuber model and the Arola and Ramulu model) were also not designed to predict stress for individual points. They contain references to the parameters of the whole surface such as Ra and ρ which were intended to be taken as an average across the surface. Ra has been changed to surface depth for these maps, and ρ has been measured at each point in turn. This technique gives the opportunity to explore what these models might mean for all points across the surface individually, allowing an examination of the effect individual features have on stress concentration. This adds a level of granularity not usually available with these models. This has the likely outcome that the predictions of these models, using the aforementioned parameters, are at the higher limits of what would be experienced by the surface. The maps remain a valid method of comparing different surfaces. It is hoped that the increased granularity and precision of this method of plotting stress concentrations outweighs this drawback.

Another drawback of this stress concentration calculation method is that is can be skewed by surfaces with large peaks. These peaks raise the level of the average surface, making the valleys appear deeper. Svk (presented in Chapter 4) could be used as a way of estimating where the actual surface is instead of using the average surface height. A large peak does not contribute as much to the structural integrity of the surface as much as a large valley reduces it.

Stress concentration factor is affected by the shape of the entire part under consideration and can be the summation of multiple factors. For instance, should the stress concentration factor for a surface be 5 (as it is shown by FEA to be for the shotblasted surface), but this surface is itself on an area of an object that's surrounding structure causes it to have its own stress concentration factor of 2, then the two would combine to give a factor of 10. An example of the consideration of a wider area like this is demonstrated

in Figure 6.54. In this manner the true contribution to stress concentration factor by surface finish will be the combination of stress concentration factors calculated at every scale. It is proposed that, for the surface finishes considered here, the total stress concentration factor is the product of the stress concentration factors at each resolution, with an additional factor to account for the overlap of the ranges of the resolution, as shown in Equation 6.5.

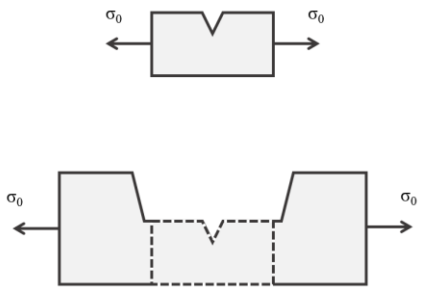

Figure 6.54 Figure demonstrating the influence of a wider area.

$$K_{Total} = (K_{r1} \times K_{r2})^J \qquad \text{Equation 6.5}$$

Where K_{r1} and K_{r2} are the separate stress concentration factor contributions from each resolution and J is an overlap scaling factor which is between ½ and 1 for resolution ranges that overlap and 1+ for those that do not.

In addition to applied stresses, the total stress will include residual stresses which are not concentrated by topography in the same manner. In the centre of shotblast craters, the level of residual stress will be lower, since the residual stress is built up as the superposition of rings of compressive stress with centres of tensile stress. This does not mean that the centre of the creator has a tensile residual stress, since it will also be in the compressive ring region of multiple past craters, but that it may be lower since it is in the tensile region of the final shot in that area. As residual stress is therefore also related to surface shape, future work could attempt to bring together these to estimations.

6.10. References

[1] D. Arola and C. L. Williams, “Estimating the fatigue stress concentration factor of machined surfaces,” *Int. J. Fatigue*, vol. 24, no. 9, pp. 923–930, 2002.

[2] Y. Murakami, *Theory of Elasticity and Stress Concentration*. 2017.

[3] M. Wang, E. Akiyama, and K. Tsuzaki, “Effect of hydrogen and stress concentration on the notch tensile strength of AISI 4135 steel,” *Mater. Sci. Eng. A*, vol. 398, no. 1–2, pp. 37–46, 2005.

[4] H. Neuber, *Kerbspannungslehre: Theorie der Spannungskonzentration. Genaue Berechnung der Festigkeit*. 2001.

[5] Z. Cheng and R. Liao, “Effect of surface topography on stress concentration factor,” *Chinese J. Mech. Eng. (English Ed.*, vol. 28, no. 6, pp. 1141–1148, 2015.

[6] S. A. Meguid, G. Shagal, J. C. Stranart, and J. Daly, “Three-dimensional dynamic finite element analysis of shot-peening induced residual stresses,” *Finite Elem. Anal. Des.*, vol. 31, no. 3, pp. 179–191, 1999.

[7] W. Everhart, E. Sawyer, T. Neidt, J. Dinardo, and B. Brown, “The effect of surface finish on tensile behavior of additively manufactured tensile bars,” *J. Mater. Sci.*, vol. 51, no. 8, pp. 3836–3845, 2016.

[8] P. Cignoni, M. Callieri, M. Corsini, M. Dellepiane, F. Ganovelli, and G. Ranzuglia, “MeshLab: An open-source mesh processing tool,” *6th Eurographics Ital. Chapter Conf. 2008 - Proc.*, pp. 129–136, 2008.

[9] M. Smith, “ABAQUS Version 6.9,” *Dassault Syst. Simulia Corp*, 2009.

[10] M. A. S. Torres and H. J. C. Voorwald, “An evaluation of shot peening, residual stress and stress relaxation on the fatigue life of AISI 4340 steel,” *Int. J. Fatigue*, vol. 24, no. 8, pp. 877–886, 2002.

[11] A. Turnbull *et al.*, “Sensitivity of stress corrosion cracking of stainless steel to surface machining and grinding procedure,” *Corros. Sci.*, vol. 53, no. 10, pp. 3398–3415, 2011.

[12] M. Row, “A review of manufacturing processes used in stainless steel intermediate level waste

containers to evaluate the presence of residual stresses report to NDA," *Serco Rep. to NDA*, no. 3, pp. 1–42, 2009.

[13] D. Peckner and I. M. Bernstein, *Handbook of Stainless Steels*. 1977.

[14] AMEC, "Characterisation of environmental conditions in an ILW store," 2012.

[15] S. C. Boden and G. Hulme, "Nirex phased disposal concept: further analysis of the environment within UILW vaults," 2003.

[16] T. Prosek, A. Iversen, C. Taxén, and D. Thierry, "Low-temperature stress corrosion cracking of stainless steels in the atmosphere in the presence of chloride deposits," vol. 65, no. 2, pp. 105–117, 2009.

[17] Serco, "Literature review of atmospheric stress corrosion cracking of stainless steels report to nirex," no. 01, 2007.

[18] A. J. Davenport *et al.*, "Mechanistic studies of atmospheric pitting corrosion of stainless steel for ILW containers," *Corros. Eng. Sci. Technol.*, vol. 49, no. 6, pp. 514–520, 2014.

[19] A. B. Cook *et al.*, "Atmospheric-induced stress corrosion cracking of austenitic stainless steels under limitted chloride supply," *Proc. 18th Int. Corros. Congr.*, pp. 1–11, 2011.

[20] L. Greenspan, "Humidity fixed points of binary saturated aqueous solutions," *J. Res. Natl. Bur. Stand. Sect. A Phys. Chem.*, vol. 81A, no. 1, p. 89, 1977.

[21] J. Young, "Humidity control in the laboratory using salt solutions – a review," *J. Appl. Chem.*, vol. 17, no. 9, pp. 241–245, 1967.

[22] J. Wintle *et al.*, "Investigations on the susceptibility to atmospheric-induced stress corrosion cracking of austenitic stainless steel nuclear structures," in *SMiRT-22*, 2013.

[23] N. Drew, "Analysis of chloride deposition rates relevant to ILW stores," 2005.

[24] A. B. Cook *et al.*, "Assessing the risk of under-deposit chloride-induced stress corrosion cracking in austenitic stainless steel nuclear waste containers," *Corros. Eng. Sci. Technol.*, vol. 49, no. 6, pp. 529–534, 2014.

[25] ASTM, "ASTM G38: Standard practice for making and using C-ring stress-corrosion test specimens," 2014.

[26] ASTM International, "Standard practice for making and using U-bend stress-corrosion test

specimens," vol. i, pp. 1–8, 2001.

[27] Yukitaka Murakami, *Metal Fatigue: Effects of Small Defects and Nonmetallic Inclusions*. 2002.

[28] J. T. Burns, J. M. Larsen, and R. P. Gangloff, "Driving forces for localized corrosion-to-fatigue crack transition in Al-Zn-Mg-Cu," *Fatigue Fract. Eng. Mater. Struct.*, vol. 34, no. 10, pp. 745–773, 2011.

[29] M. O. Speidel, "Stress corrosion crack growth in austenitic stainless steel.," *Corrosion*, vol. 33, no. 6. pp. 199–203, 1977.

[30] S. Boljanović, "Fatigue strength analysis of a semi-elliptical surface crack," *Sci. Tech. Rev.*, vol. 62, no. 1, pp. 10–16, 2012.

[31] J. W. Dally, W. L. Fourney, and G. R. Irwin, "On the uniqueness of the stress intensity factor - crack velocity relationship," *Int. J. Fract.*, vol. 27, no. 3–4, pp. 159–168, 1985.

[32] Frankel G. S., "Pitting corrosion of metals, a review of the critical factors," *J. Electrochem. Soc.*, vol. 145, no. 6, p. 2186, 1998.

[33] R. T. Loto, "Pitting corrosion evaluation and inhibition of stainless steels: A review," *J. Mater. Environ. Sci.*, vol. 6, no. 10, pp. 2750–2762, 2015.

[34] A. Inchekel and J. E. Talia, "Effect of scratches on the fatigue behaviour of an Al-Li alloy," *Fatigue Fract. Eng. Mater. Struct.*, vol. 17, no. 5, pp. 501–507, 1994.

[35] M. J. Caton, R. John, W. J. Porter, and M. E. Burba, "Stress ratio effects on small fatigue crack growth in Ti-6Al-4V," *Int. J. Fatigue*, vol. 38, pp. 36–45, 2012.

[36] L. Chang, M. G. Burke, and F. Scenini, "Understanding the effect of surface finish on stress corrosion crack initiation in warm-forged stainless steel 304L in high-temperature water," *Scr. Mater.*, vol. 164, pp. 1–5, 2019.

[37] Y. J. Janin, "Characterisation of residual stress and investigation of environmental effects on atmospheric-induced stress corrosion cracking of austenitic stainless steel nuclear waste containers," *PhD Thesis, Univ. Manchester*, 2012.

[38] S. Ghosh and V. Kain, "Microstructural changes in AISI 304L stainless steel due to surface machining: Effect on its susceptibility to chloride stress corrosion cracking," *J. Nucl. Mater.*, vol. 403, no. 1–3, pp. 62–67, 2010.

[39] D. T. Ardi, Y. G. Li, K. H. K. Chan, L. Blunt, and M. R. Bache, “The effects of machined topography on fatigue life of a nickel based superalloy,” *Procedia CIRP*, vol. 13, pp. 19–24, 2014.

Appendix 2

Script to produce STL files from surface height arrays.

```
import numpy as np
import numpy.ma as ma
import math

thefile = open(filename + '.stl', 'w')

sizei = 40 #size of the secition of initial array to be made into STL file
sizej = 40
thefile.write("solid ascii") #STL files start with this


#object is made from the top, four sides and a base

for ii in range(0, sizei):
    for jj in range(0, sizej):
        thefile.write("\n" + " facet normal 0 0 0" + "\n" +"  outer loop" + "\n" + "    vertex " + #this group makes the top, this subgroup makes left handed triangles
                    str(ii)   + " " + str(jj)   + " " + str(grid[ii,jj])   + "\n" + "    vertex " +        #A
                    str(ii)   + " " + str(jj+1) + " " + str(grid[ii,jj+1]) + "\n" + "    vertex " +     #B
                    str(ii+1) + " " + str(jj)   + " " + str(grid[ii+1,jj]) + "\n  endloop \n endfacet" #C

                    "\n" + " facet normal 0 0 0" + "\n" +"  outer loop" + "\n" + "    vertex " +   #this subgroup makes right handed triangles
                    str(ii+1) + " " + str(jj)   + " " + str(grid[ii+1,jj])    + "\n" + "    vertex " +     #C
                    str(ii)   + " " + str(jj+1) + " " + str(grid[ii,jj+1])    + "\n" + "    vertex " +     #B
                    str(ii+1) + " " + str(jj+1) + " " + str(grid[ii+1,jj+1])  + "\n  endloop \n endfacet" +  #D


                    "\n" + " facet normal 0 0 0" + "\n" +"  outer loop" + "\n" + "    vertex " + #makes side 1
                    str(ii)   + " 0 0"     + "\n" + "    vertex " +
                    str(ii)   + " " + "0 " + str(grid[ii,00]) + "\n" + "    vertex " +
                    str(ii+1) + " " +"0 "  + str(grid[ii+1,00]) + "\n  endloop \n endfacet" +

                    "\n" + " facet normal 0 0 0" + "\n" +"  outer loop" + "\n" + "    vertex " +
                    str(ii)   +" 0 0" + "\n"  + "    vertex " +
```

```
str(ii+1) + " "   + "0 "  + str(grid[ii+1,00]) + "\n"+ "   vertex " +
str(ii+1) + " "   +"0 0"  + "\n  endloop \n endfacet" +


"\n" + " facet normal 0 0 0" + "\n" +"  outer loop" + "\n" + "   vertex " + #makes side 2
"0 " + str(jj)   +" 0" + "\n" + "   vertex " +
"0 " + str(jj)   + " " + str(grid[00,jj]) + "\n" +"   vertex " +
"0 " + str(jj+1) + " " + str(grid[00,jj+1]) + "\n  endloop \n endfacet" +

"\n" + " facet normal 0 0 0" + "\n" +"  outer loop" + "\n" + "   vertex " +
"0 " + str(jj+1) + " " + "0" + "\n" + "   vertex " +
"0 " + str(jj)   + " 0" + "\n" + "   vertex " +
"0 " + str(jj+1) + " " + str(grid[00,jj+1]) + "\n  endloop \n endfacet" +


"\n" + " facet normal 0 0 0" + "\n" +"  outer loop" + "\n" + "   vertex " + #makes side 1 opposite
str(ii)   + " " + str(sizej) + " 0"     + "\n" + "   vertex " +
str(ii)   + " " + str(sizej) + " " + str(grid[ii,sizej]) + "\n" + "   vertex " +
str(ii+1) + " " + str(sizej) + " " + str(grid[ii+1,sizej]) + "\n  endloop \n endfacet" +

"\n" + " facet normal 0 0 0" + "\n" +"  outer loop" + "\n" + "   vertex " +
str(ii)   + " " + str(sizej) + " 0" + "\n"  + "   vertex " +
str(ii+1) + " " + str(sizej) + " " + str(grid[ii+1,sizej]) + "\n"+ "   vertex " +
str(ii+1) + " " + str(sizej) + " 0"  + "\n  endloop \n endfacet" +


"\n" + " facet normal 0 0 0" + "\n" +"  outer loop" + "\n" + "   vertex " + #makes side 2 opposite
str(sizei) + " " + str(jj)   +" 0" + "\n" + "   vertex " +
str(sizei) + " " + str(jj)   + " " + str(grid[sizei,jj]) + "\n" +"   vertex " +
str(sizei) + " " + str(jj+1) + " " + str(grid[sizei,jj+1]) + "\n  endloop \n endfacet" +

"\n" + " facet normal 0 0 0" + "\n" +"  outer loop" + "\n" + "   vertex " +
str(sizei) + " " + str(jj+1) + " " + "0" + "\n" + "   vertex " +
str(sizei) + " " + str(jj)   + " 0" + "\n" + "   vertex " +
str(sizei) + " " + str(jj+1) + " " + str(grid[sizei,jj+1]) + "\n  endloop \n endfacet" +


"\n" + " facet normal 0 0 0" + "\n" +"  outer loop" + "\n" + "   vertex " +  #makes base
"0 0 0" + "\n" + "   vertex " +        #A
"0 " + str(sizej) + " 0" + "\n" + "   vertex " +     #B
str(sizei) + " " + str(sizej) + " 0"  + "\n  endloop \n endfacet" +
```

```
"\n" + " facet normal 0 0 0" + "\n" +"  outer loop" + "\n" + "    vertex " +
"0 0 0"+ "\n" + "    vertex " +     #C
str(sizei) + " 0 0"+ "\n" + "    vertex " +     #B
str(sizei) + " " + str(sizej) + " 0"+ "\n  endloop \n endfacet")

# duplicate faces/verticies must be removed using e.g. Meshlab
```

Chapter 7. An Outdoor Atmospheric Corrosion Experiment

7.1. Introduction

For comparison with accelerated laboratory corrosion tests, an atmospheric field test was conducted at the Sellafield site, near Whitehaven, in the NW of the UK. This is site is the location of the majority of ILW containers. Since 1991, Sellafield Ltd have maintained outdoor exposure frames for atmospheric corrosion testing of materials on site [1]. This has enabled analysis of real time corrosion in the absence of accelerating factors normally found in laboratory investigations. As well as facilitating future planning, this approach allows for the paired monitoring of materials in inaccessible locations. The main focus of these tests has been the monitoring of materials for waste containers. Although other materials, paint systems and coatings that either were present or could possibly be used on Sellafield site were also added to the exposure frames.

In this Chapter, the results of an atmospheric field test of the four different stainless steel surface finishes of interest to this Thesis are described.

7.2. Method

The location used in this experiment, “Site 1”, is located 150 m from the sea which exposes the frame and test samples to a large amount of sea aerosol. This is considered a realistic worst case scenario on the Sellafield site, and more aggressive than the conditions that exist within engineered stores on the site (see Section 2.1 for a detailed description of conditions within the ILW waste stores).

The exposure frames held tokens at an angle of 45°, 1 m above the ground as shown in Figure 7.1. A partially covered exposure frame was used in this experiment, where the tokens were held under a corrugated fibreglass cover, exposed to marine environmental conditions but remained unwashed by rain. Studies completed by Sellafield Ltd. have shown that tokens under the covered exposure frame are more prone to corrosion, likely due to the absence of rain to wash off the contaminating aerosol particles. For this experiment, the partially covered exposure frame was chosen due to the presumption

that corrosion would be minimal in a short timescale (8-months). In fact, sufficient corrosion had occurred, allowing examination of the surfaces.

(a) General View of Compound (b) Specimens on Frames

Figure 7.1 Exposure frames at Site 1.

To prepare the samples, 50 mm squares were cut from pristine brushed, ground, rolled and shotblasted surface finishes. They were degreased with isopropanol and mounted on a Perspex frame, designed to fit into the Sellafield Ltd corrosion frame. Figure 7.2 shows the four tokens attached to the custom made Perspex rig and installed at the Sellafield site, in the covered exposure frame on the day of their emplacement, on the 22nd June 2018. The rig was designed to insulate the tokens from the metal bolts to mitigate against galvanic corrosion. To avoid crevice corrosion, the rig was designed to hold the tokens loosely. The tokens had 1 mm of free movement within the test rig to accommodate this. To avoid contamination of the lower tokens by the corrosion products of the upper, there was a gap between the two halves to channel runoff.

During this period, it rained for 163 of the 250 days, averaging around 135 mm per month. It also snowed for 6 days. The average humidity was consistent month to month, always between 81 and 86 % RH, but tended to fluctuate greatly throughout the day/night cycle. The temperature peaked in July, at an average of 17 °C and was lowest in January at an average of 5 °C.

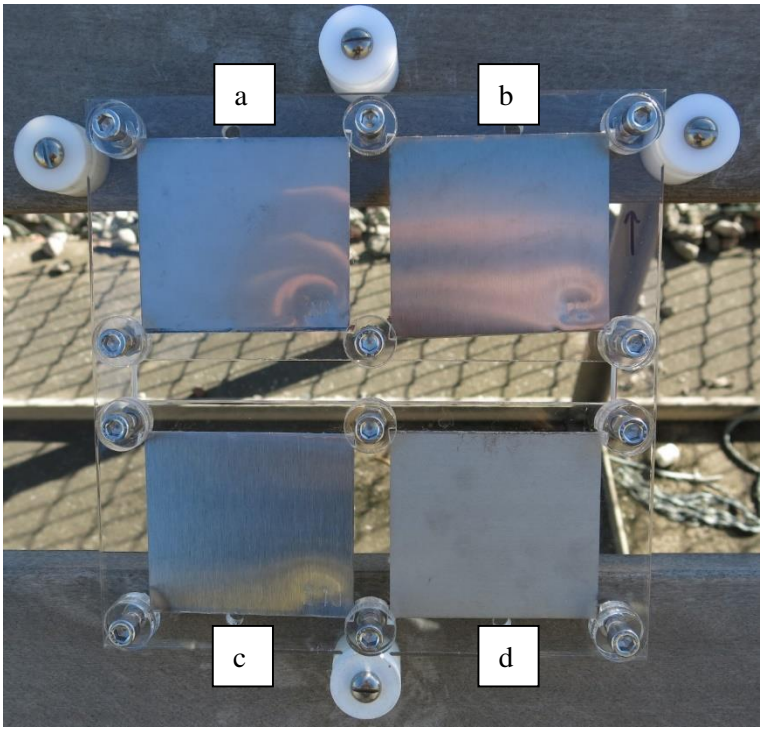

Figure 7.2 Mounted tokens at Site 1. A rolled, B brushed, C ground, D shotblasted. Tokens dimensions were 75 mm by 65 mm.

Figure 7.3 shows the specimens 8 months later on the day of removal, 27th Feb 2019. Corrosion product can be seen on the rolled, brushed and shotblasted surfaces. Once removed, tokens were washed under running water with a soft sponge to remove corrosion product and reveal the corroded surface. Sample surfaces were photographed and then characterised with an optical microscope, SEM and VSI.

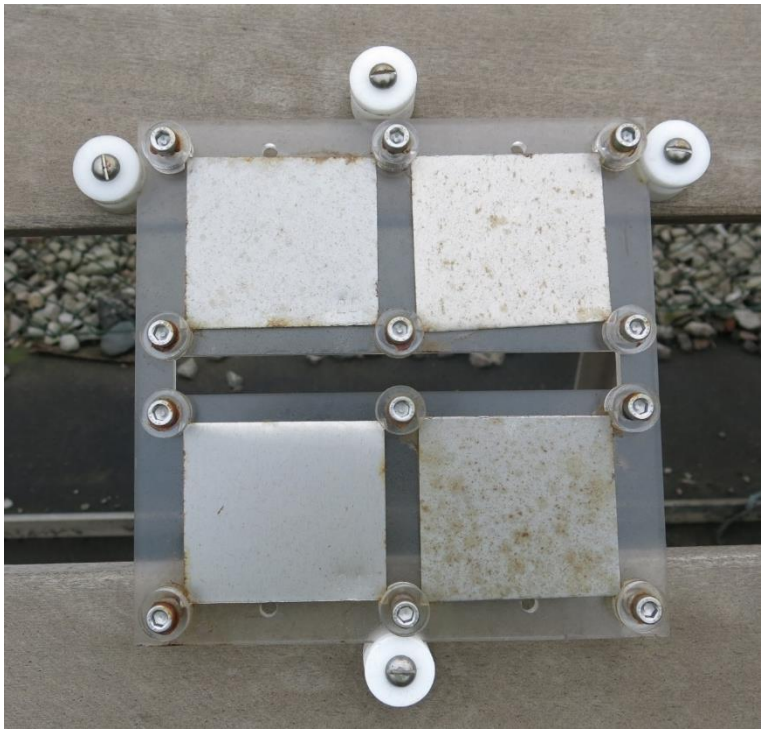

Figure 7.3 Mounted tokens on day of removal.

7.3. Results

7.3.1. Token Photographs

Figure 7.4 shows the brushed surface. Patches of discoloration in areas immediately surrounding pits can be seen, which tended to be the case for all surfaces.

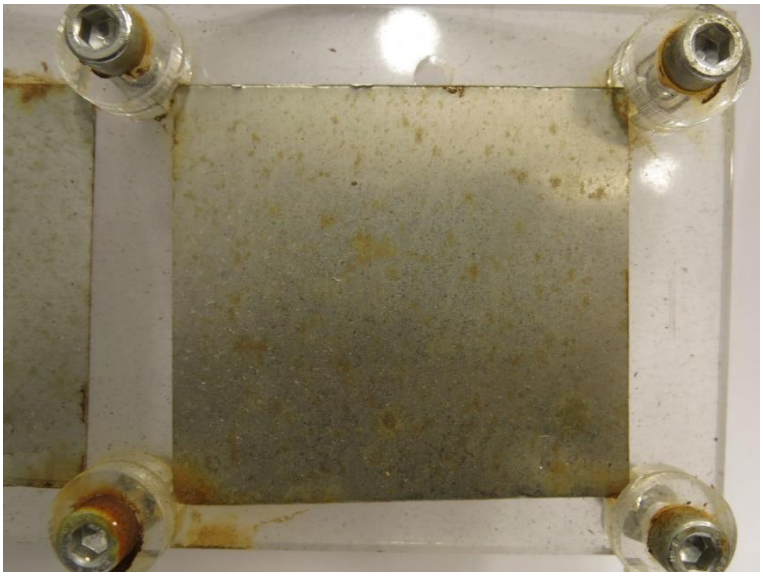

Figure 7.4 Brushed token after 8 month exposure.

Figure 7.5 shows the ground surface. Some discolouration can be seen; however, this surface has fared far better than the other three, showing better corrosion resistance properties under the atmospheric conditions.

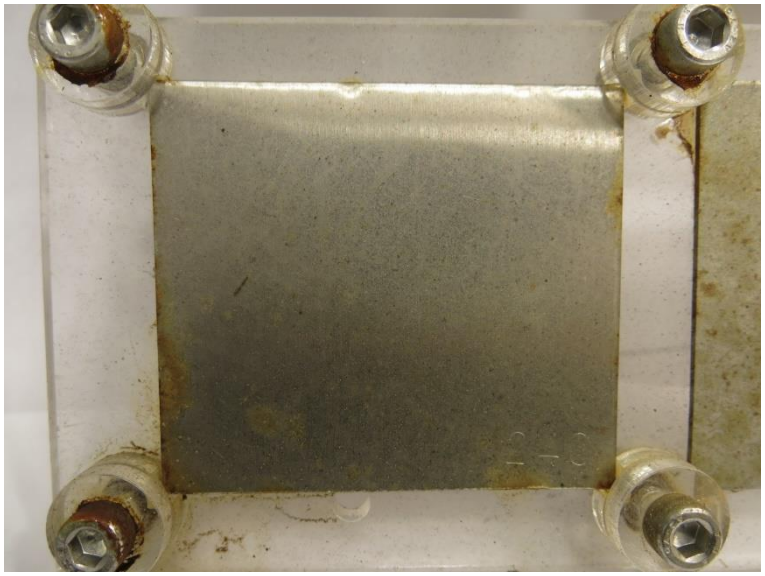

Figure 7.5 Ground token after 8 month exposure.

Figure 7.6 shows the rolled surface. Patches of discolouration and small pits can be seen by eye.

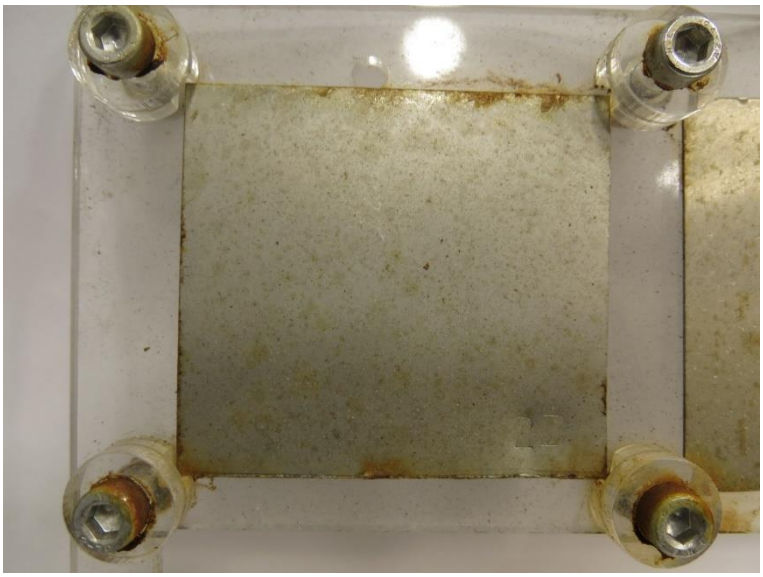

Figure 7.6 Rolled token after 8 month exposure.

Figure 7.7 shows the shotblasted surface. It shows the most discolouration. It is likely that the high degree of roughness on this surface inhibited the routine removal of chlorides from the surface by weather.

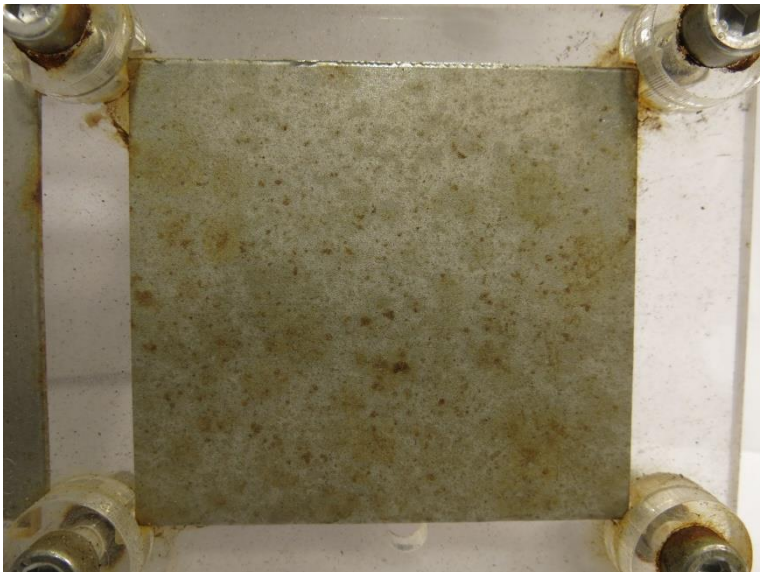

Figure 7.7 Shotblasted token after 8 month exposure.

The tokens were rinsed in water to remove corrosion produce before characterisation by microscopy. The surfaces, post-cleaning, are shown in Figure 7.8, which reveals the extent of the corroded areas for each sample finish. Some large pits are also visible by eye.

A semi-quantitative analysis of the extent of corrosion on each surface was performed using an image thresholding technique. This utilised Dragonfly image analysis software [2]. A Sobel transformation was applied to identify edges, which made it possible to apply thresholding. The initial photographs are shown in the first column of Figure 7.9, the Sobel transformation is shown in the middle column and the results of the thresholding technique is shown in the right column of Figure 7.9. This was used to calculate the percentage of each surface that showed evidence of corrosion which is presented in Table 7.1.

The ground surface showed the least evidence of corrosion at 9.8%, half as much as the next most corroded, which was the brushed surface at 23.9%. The rolled surface and the shotblasted surface had 33.8% and 67.2% of the surface showing evidence of corrosion.

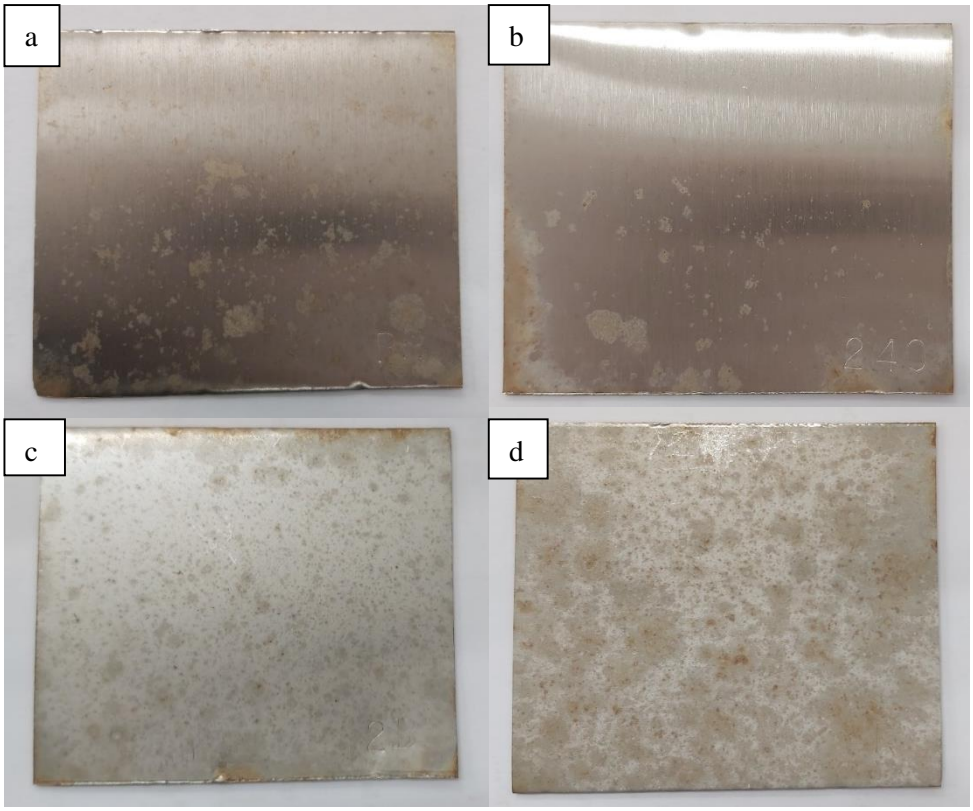

Figure 7.8 Tokens after rinsing with water. A: brushed, B: ground, C: rolled, D: shotblasted.

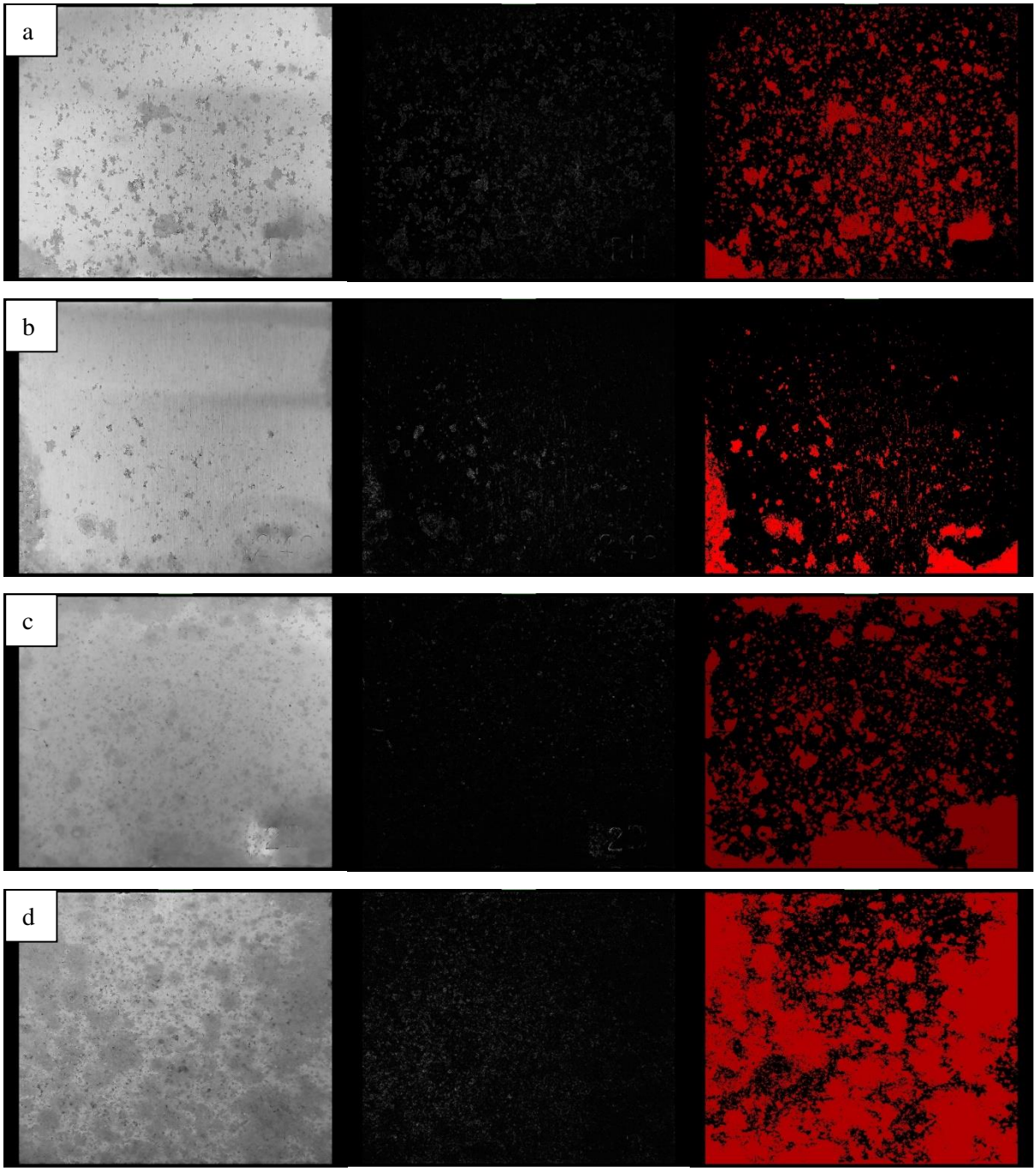

Figure 7.9 Image analysis process. Column 1 shows sample photographs, column 2 shows the Sobel transforms and column 3 shows the threshold images. A brushed, B ground, C rolled, D shotblasted.

Table 7.1 Proportion of surface corroded.

	Brushed	Ground	Rolled	Shotblasted
Corroded Area	23.9% ±5%	9.8% ±5%	33.8% ±5%	67.2% ±5%

7.3.2. Vertical Scanning Interferometry Maps and Height Parameters

Figure 7.10 shows representative VSI data for the four surface finishes, post exposure and after cleaning. Additionally, line profiles of the surfaces before and after exposure are shown in Figure 7.11. The full suite of data collected for these samples are given in Appendix 3. Surface height parameters were calculated from these data and are presented in Table 7.2. Corrosion pits, depicted as black data in the VSI images (due their depth, the VSI laser is not able to penetrate to the bottom of the pit, therefore depth data is not always obtainable) were apparent on all surfaces. It can be seen from Figure 7.10 that the brushed surface (Figure 7.10a) had the highest density of pits followed by the rolled surface (Figure 7.10c). The ground surface had fewer pits, though they tended to be larger. No location preference for pits was discernible from the VSI data. For instance, pits appeared to occur frequently on peaks, craters, valley minima and ridges. It is likely that pit initiation was more selective, as is shown by SEM (Section 7.3.3.), however once a pit has grown, the pit itself can obscure the nature of the initial location.

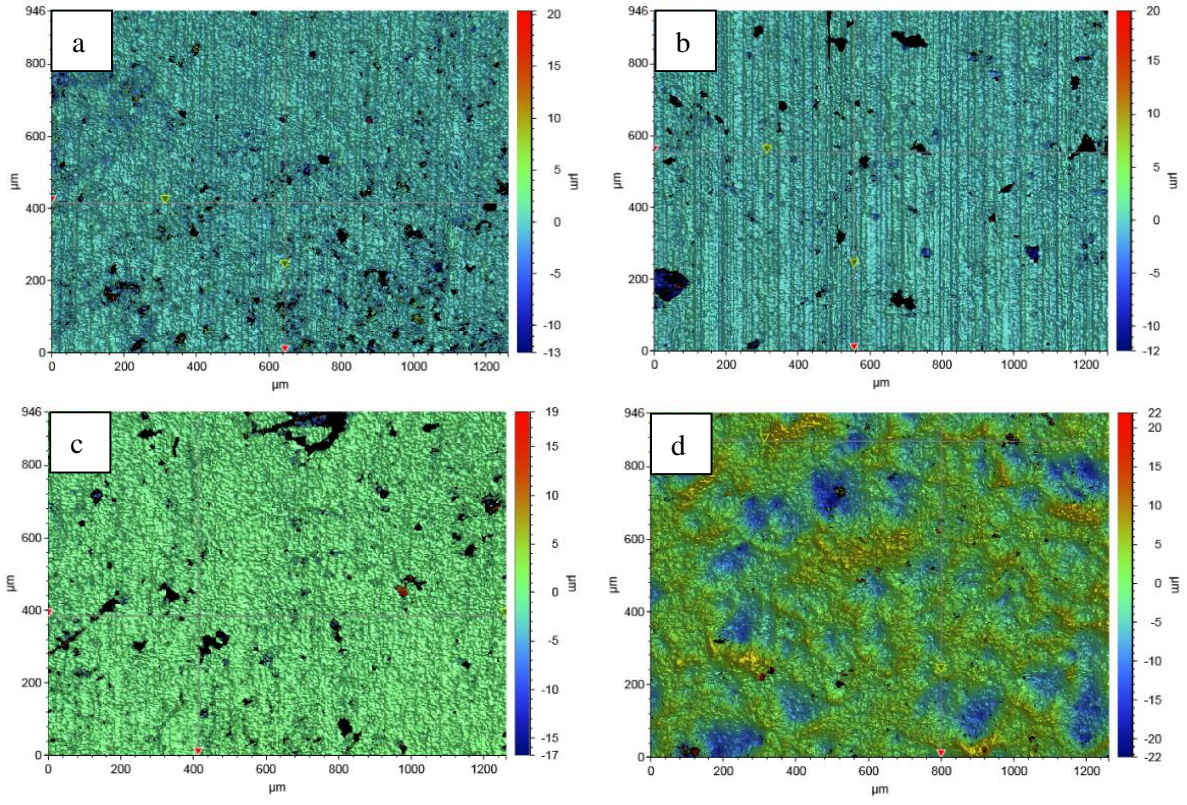

Figure 7.10 VSI height maps, showing pitting. A: brushed, B: ground, C: rolled, D: shotblasted.

The line profiles shown in Figure 7.11 show that the ground surface (Figure 7.11b) changed very little. The brushed surface (Figure 7.11a) and the rolled (Figure 7.11b) surface both show pits in the profiles, which present as the large discontinuities. In these profiles the pit measured on the rolled surface is largest at 10 µm wide compared to the pit on the brushed surface at 5 µm.

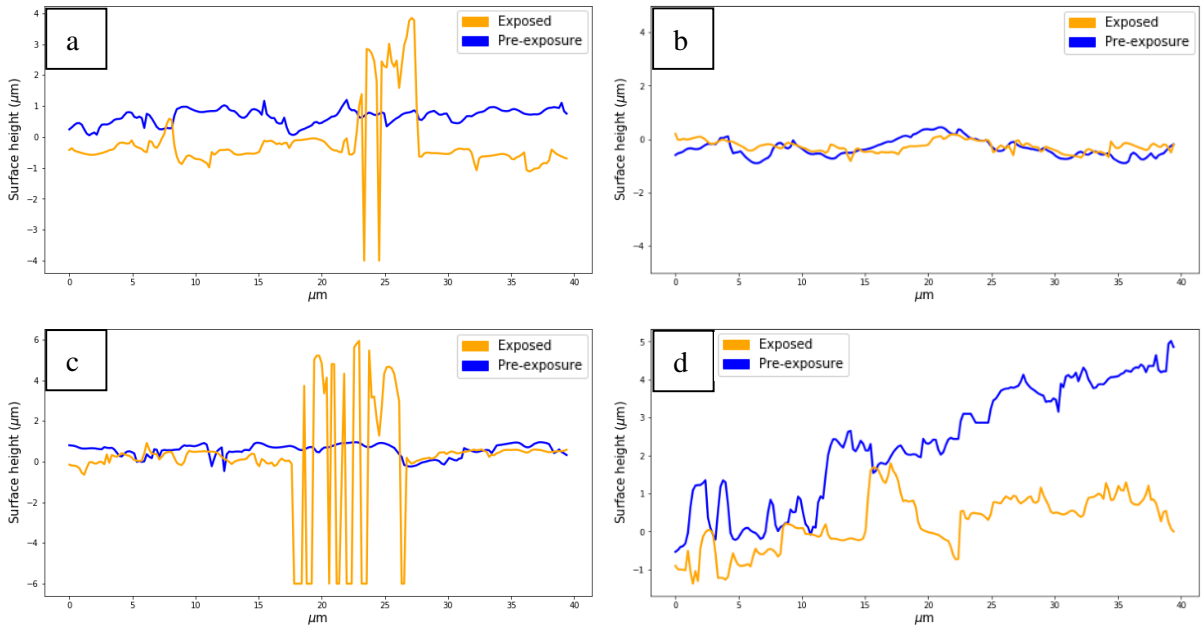

Figure 7.11 Line profiles before and after exposure for: A brushed, B ground, C rolled, D shotblasted.

Table 7.2 Surface height and area parameters for each surface finish, acquired before and after exposure to atmospheric corrosion at Sellafield.

		Brushed	Ground	Rolled	Shotblasted
Ra nm	Initial	232	253	241	2763
	Post Exposure	1992	1283	1877	3382
	Difference	+1760	+1030	+1636	+619
SD/Rq nm	Initial	308	308	317	3602
	Post Exposure	4555	3687	4287	4677
	Difference	+4247	+3379	+3970	+1075
Ssk	Initial	-0.92	-0.12	-1.51	-0.74
	Post Exposure	3.98	5.1	2.32	0.59
	Difference	+4.9	+5.22	+3.83	+1.33
Sku	Initial	8.33	2.5	6.17	3.91
	Post Exposure	17.8	28.5	6.9	7.1
	Difference	+9.47	+26	+0.73	+3.19
Sv nm	Initial	-3752	-1477	-2948	-15677
	Post Exposure	-14397	-13025	-13019	-22583
	Difference	-10645	-11548	-10071	-6906
SAR	Initial	1.06	1.06	1.19	1.42
	Post Exposure	1.91	1.49	2	1.4
	Difference	+0.85	+0.43	+0.81	-0.02

The surface roughness (both Ra and Rq) increased significantly for all surfaces, as shown in Table 7.2. The largest increases in Ra were observed for the brushed and the rolled surfaces, with increases of 1760 nm and 1636 nm, respectively. An increase of 1030 nm and 619 nm were observed for the ground and the shotblasted surfaces. Although the brushed and the ground surfaces started with very similar roughness values, the brushed surface increased in roughness by almost twice the amount. This increase in surface roughness is due to the initiation of a large number of pits and the adherence of corrosion product to the surface.

For all surfaces there was a similarly large increase in Sv, the maximum surface depth. Unfortunately, the Sv values for this dataset are a poor representation of the depth of pits, since the accurate measurement into deep, steep sided pits is unachievable using the VSI technique. Although, a large increase in Sv is a good indication of the presence of pitting. This indicates pitting occurred on all surfaces.

The increase in surface area ratio (SAR, Table 7.2) ranked the surfaces in the same way as the increase in surface roughness for each surface. The brushed surface, which showed the greatest corrosion in during accelerated *in-situ* trials (Chapter 4), had the greatest increase in SAR, with a value of around 2 after exposure. The same was observed for the rolled surface. The ground surface was dramatically different, showing the smallest increase, raising it to around 1.5. The surface area ratio is considered a better measurement of surface roughness since it considers the surface area at the highest possible resolution, including changes of gradient at all surface heights.

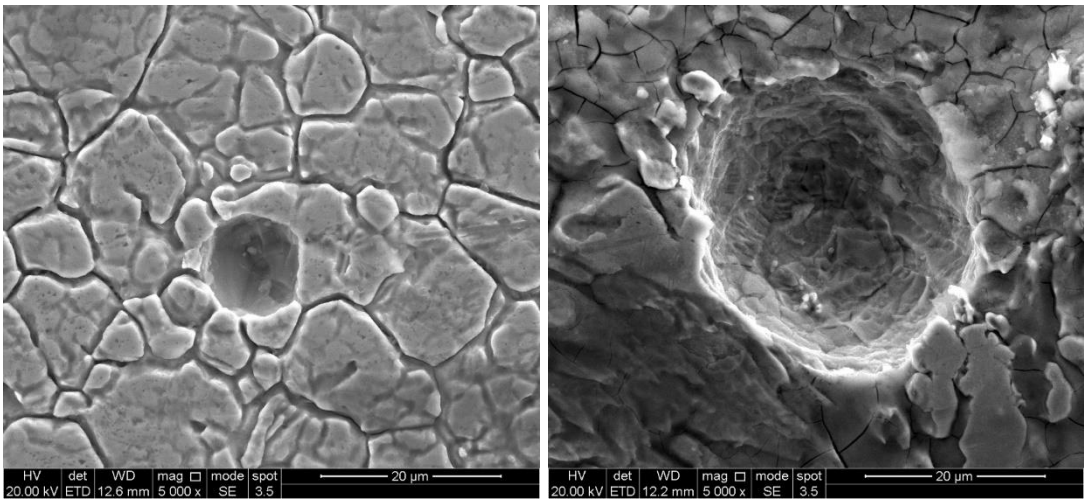

Figure 7.12 Largest pits found on a rolled surface (left) and a shotblasted surface (right).

7.3.3. Scanning Electron Microscope Micrographs

Figure 7.13 shows SEM micrographs that show the representative corrosion behaviour of each of the four surface finishes. As observed for the optical images and the VSI analyses, pits were observed on all surfaces. In agreement with the VSI data, the greatest number of pits were found on the brushed surface (Figure 7.13a). In many cases, these tended to initiate preferentially at the locations of valley minima and were between 0.1 – 2 μm in diameter, according to the SEM images.

Figure 7.14 shows a lower magnification SEM image of the brushed sample shown in Figure 7.13, allowing observation of a wider area. It is clear that a high degree of corrosion occurred, with multiple pits joining to expose subsurface grains. Pit size decreases with distance away from the central area of region (on the left hand side of Figure 7.14), so that the smallest pits are on the right hand side of the

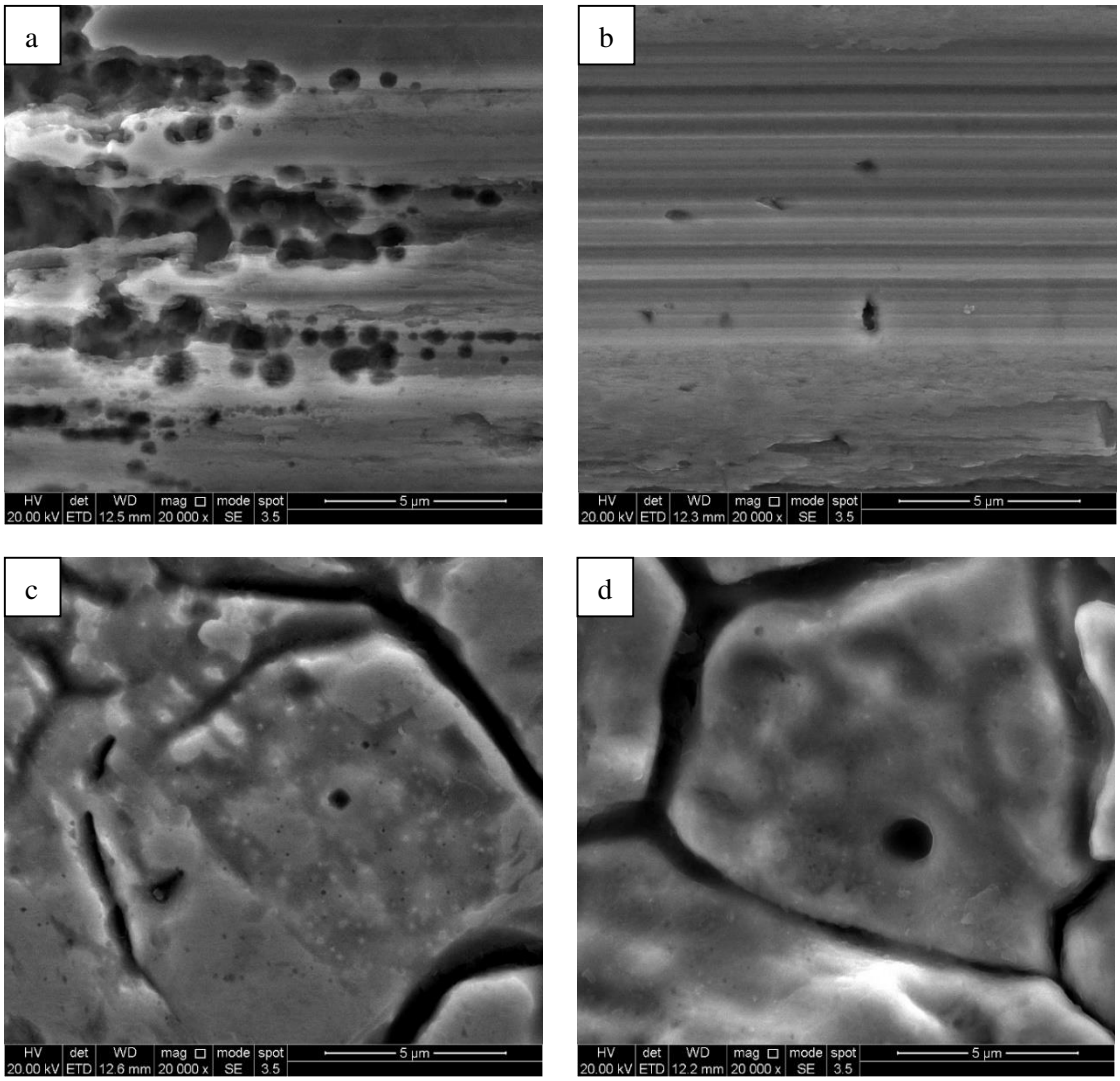

Figure 7.13 SEM micrographs of exposed samples. A: brushed, B: ground, C: rolled, D: shotblasted.

image. The pits in this surface have apparently initiated along valley minima, forming lines of pits in a "string of pearls" fashion.

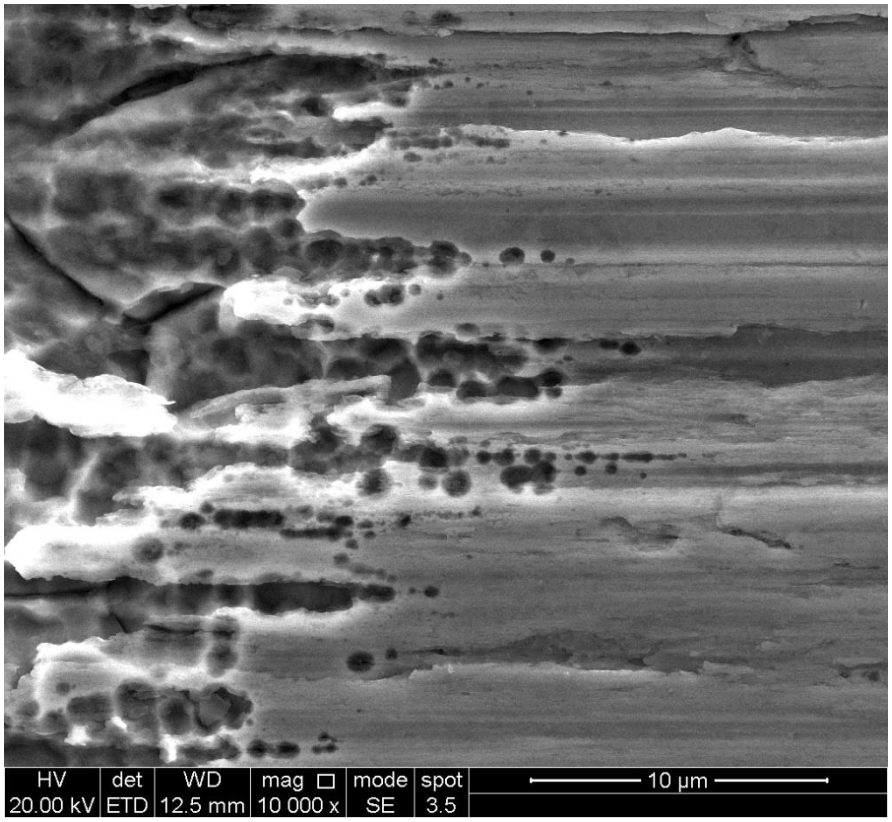

Figure 7.14 SEM micrograph showing pitting along valley minima on a brushed surface.

Figure 7.15 shows a montage of SEM images showing the development of pits on the brushed surface. Pitting was found to initiate across the surface at multiple locations (Figure 7.15a). Pits regularly formed within valley minima and coalesced to form larger pits (Figure 7.15b andFigure 7.15c). The large pit in Figure 7.15c is 15 µm in diameter. Thereafter, more pits form around the outside of the larger pits, often preferentially forming along valley minima. They extend outwards like this, until large shallow areas are corroded, formed of many pits, often with a large pit in the centre (Figure 7.15f). Eventually, the brushed part of the surface is completely corroded away, which exposes the grains below, which then begin to corrode themselves.

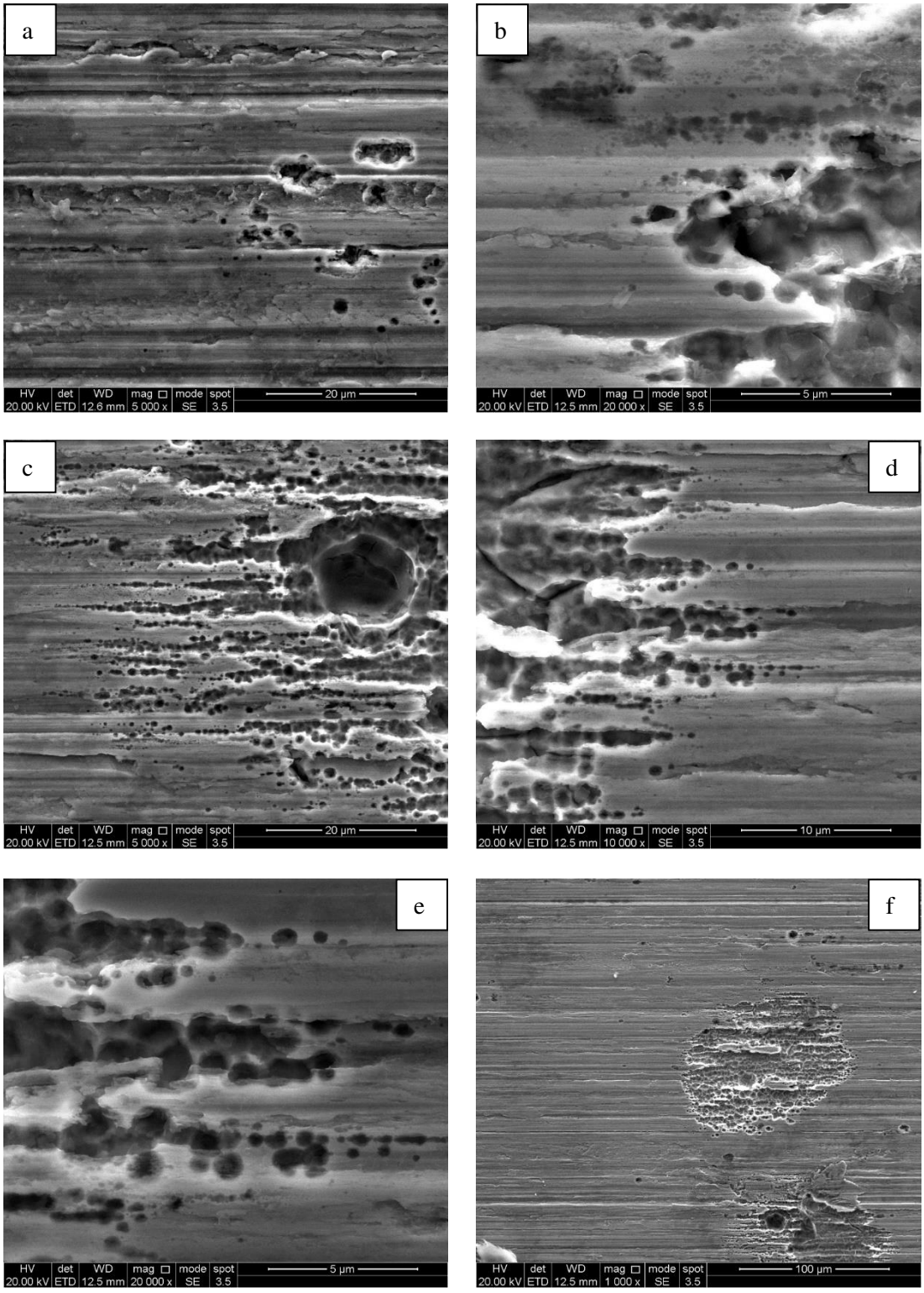

Figure 7.15 SEM micrographs of a brushed surface post exposure.

Figure 7.16 shows a montage of SEM images showing the development of pits on the ground surface. Pitting is far less pervasive than on the brushed surface. Pits initiate mostly at random locations, but with some evidence of preferential pitting along folded-over regions (Figure 7.16b). Occasionally, pits form in lines (Figure 7.16c) indicating a relation to the surface finish. It is not as clear that this is due to openness, as it is clear with the brushed surface, since the majority of pitting appears within rougher bands along the surface. It is likely that the regions which are rougher at small scale are more prone to pitting on this surface.

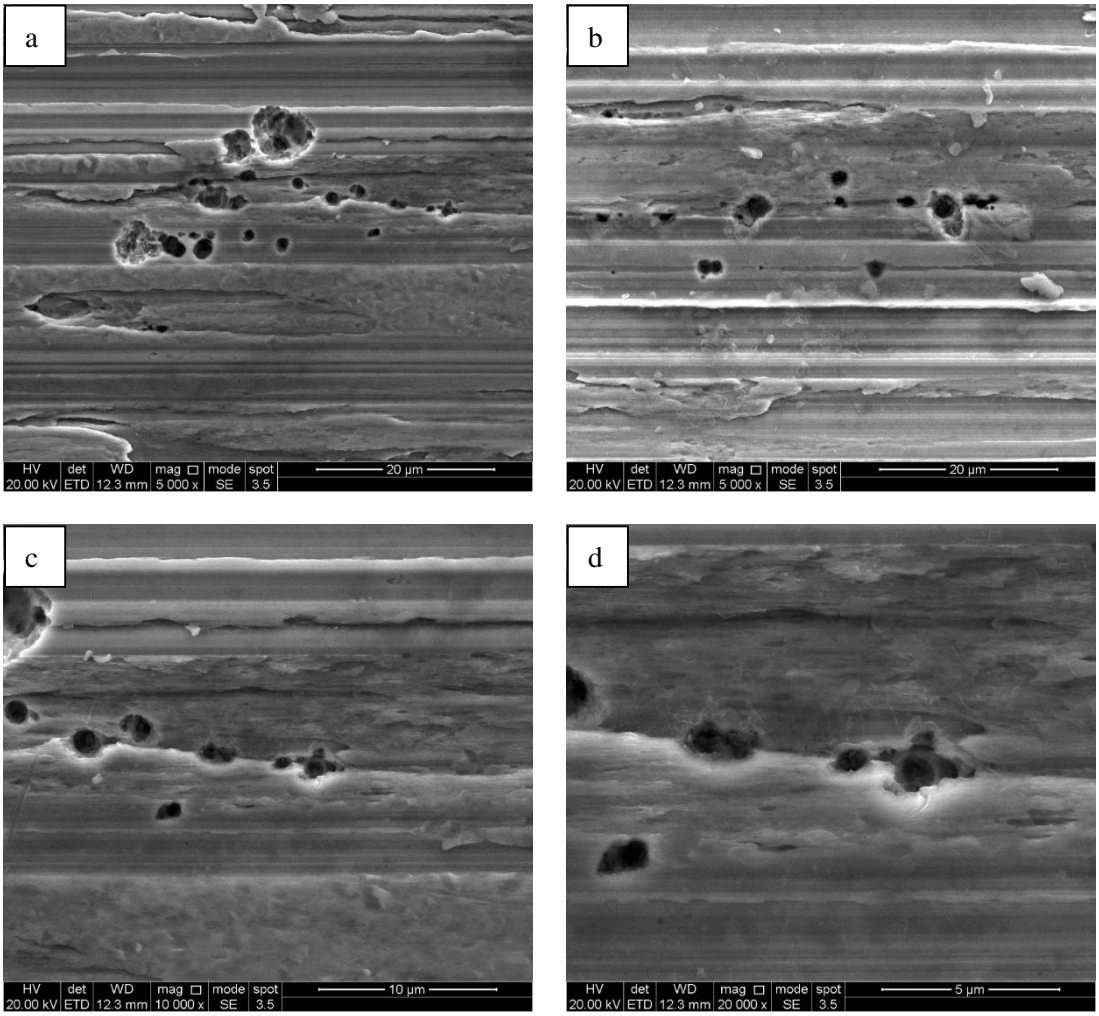

Figure 7.16 SEM micrographs of a ground surface post exposure.

Figure 7.17 shows a montage of SEM images showing the development of pits on the rolled surface. A range of pits from large (10 µm, Figure 7.17b) to small (1 µm, Figure 7.17d) were found randomly distributed on the surface. No preference was found for any particular surface feature such as the grain boundaries.

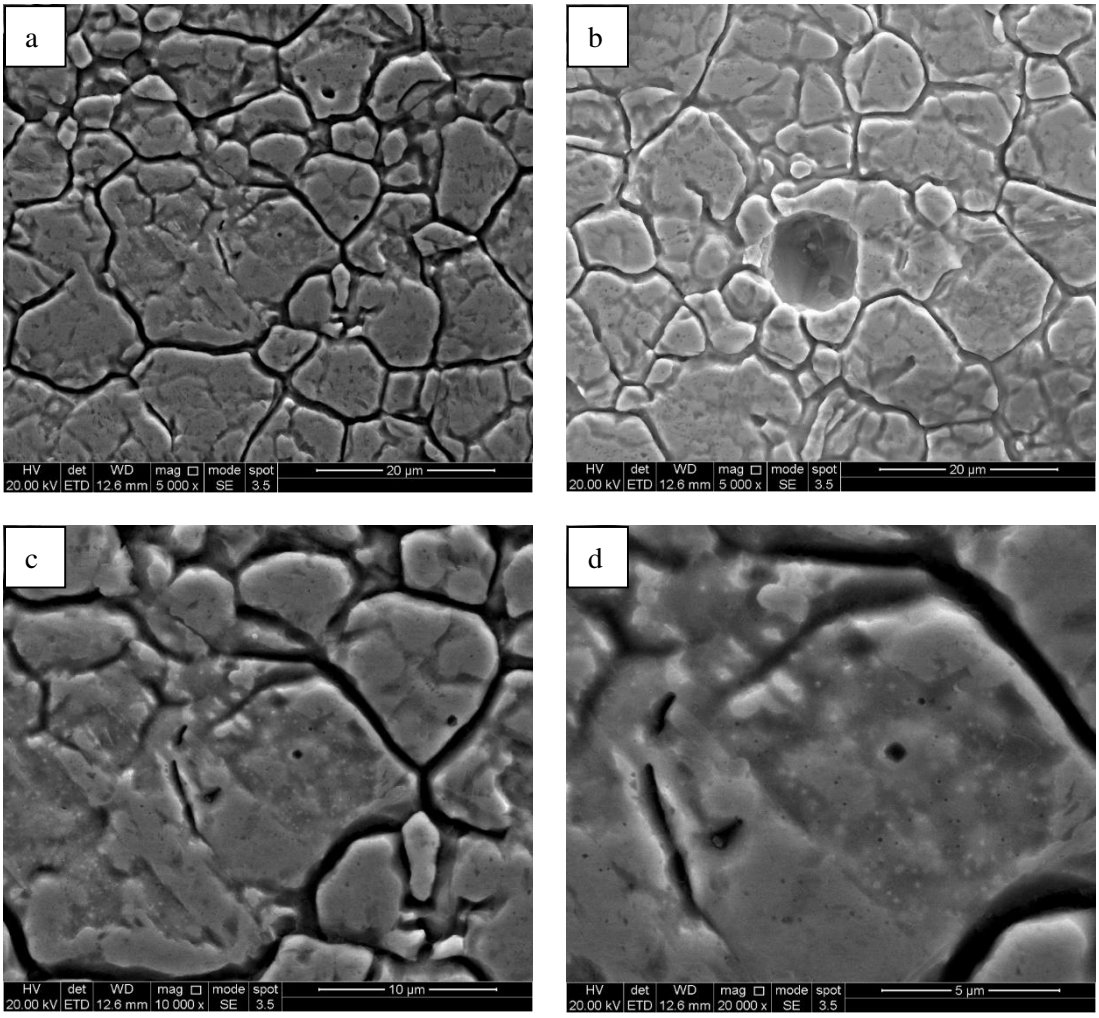

Figure 7.17 SEM micrographs of a rolled surface post exposure.

Figure 7.18 shows a montage of SEM images showing the development of pits on the shotblasted surface. Much like the rolled surface, both small (2 µm, Figure 7.18b) and large (30 µm, Figure 7.18d) pits were found randomly distributed. No preferential locations, such as the bottoms of craters, were found.

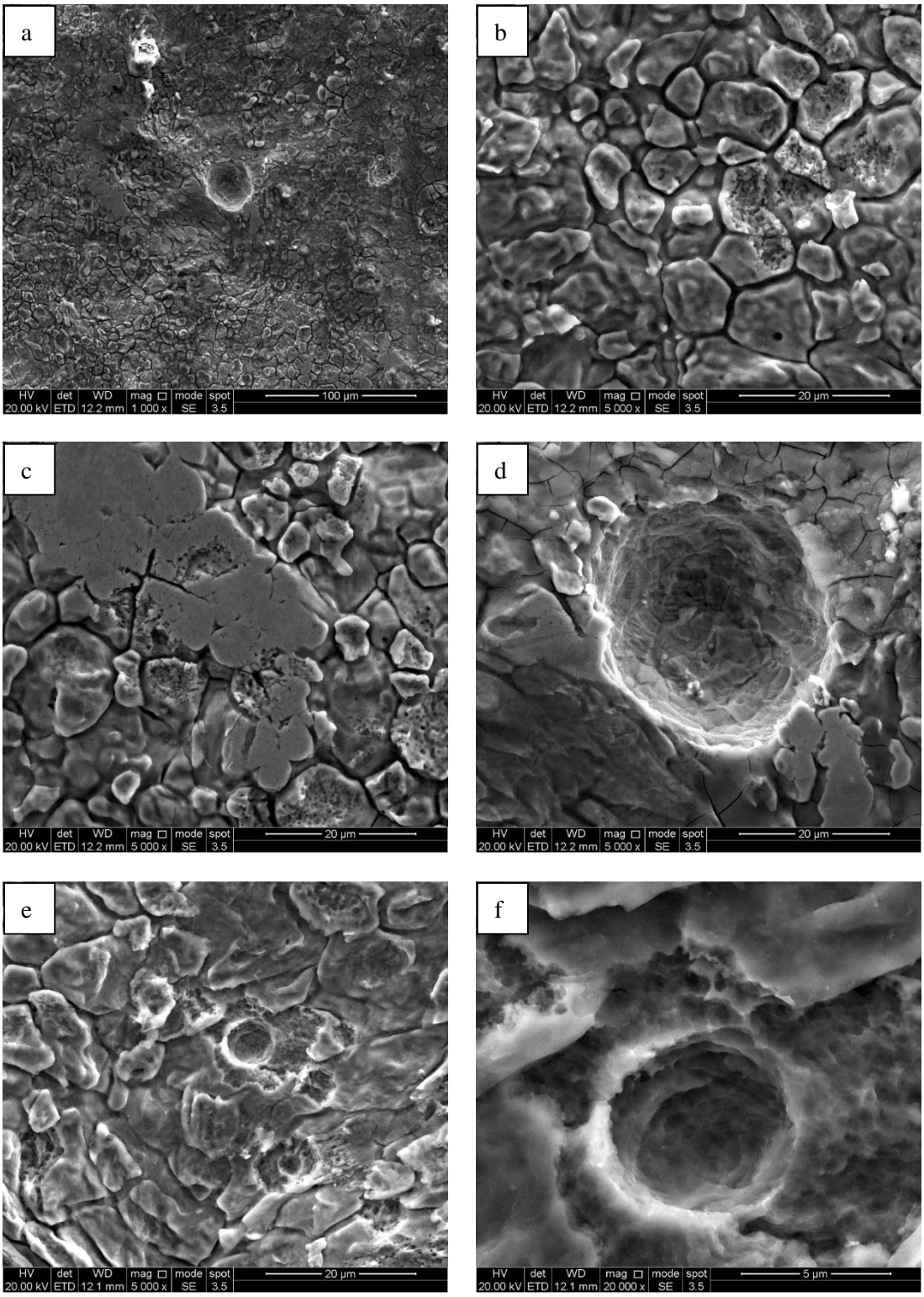

Figure 7.18 SEM micrographs of a shotblasted surface post exposure.

7.4. Discussion

Though there was only one token per surface finish, the surface area of each was large enough for multiple locations of localised corrosion to occur simultaneously and so provide many examples of corrosion on each specimen.

Since the ILW containers currently reside in atmosphere controlled interim storage facilities, the amount of sea-aerosols they are exposed to is much lower than these tokens. Should this system fail, or should containers be exposed during transit, this experiment accurately represents a likely worst case scenario of chloride deposition rate. Additionally, there is the requirement to accelerate corrosion in experiments to be able to make predictive assessments. The conditions used were less aggressive than that used in similar tests conducted in tropical environments [3].

Pitting on stainless steel is widely regarded as stochastic [4]. This study has shown pitting in valley minima and at folded over regions with pits forming along lines, showing that pit initiation is deterministic under certain circumstances. Additionally, rougher bands of the ground surface were more affected by pitting, supporting the link between roughness and pitting that is already seen in the literature [5]. Though overall roughness is a poor indicator of the propensity to form pits, since some studies have found improving surface finish to lead to higher corrosion rates [6], this Chapter has shown that roughness at the micro scale does increase pitting.

The observation of pitting in valleys and folded-over regions supports previous research that has suggested that enclosed features on 304L stainless steel have decreased pitting potential in a 3.5% NaCl solution. This is similar to the atmospheric environment used in this Chapter since droplets formed by humidity will contain mostly NaCl [7]. Galvele has previously found that the deeper a metastable pit, the less current density is required for reactivation [8]. It was found that ion concentration on the surface of steel was dependant on surface geometry, and that current density was also dependent on surface geometry [9] which explains why pits are found to preferentially form at the valley minima.

The ground surface showed the least evidence of corrosion, with a smaller surface area affected, and a less rough surface post exposure. This finding is in line with in-situ corrosion trials presented in Chapter 4. Though a similar initial roughness according to Ra value, at a smaller scale the ground surface is rougher than the brushed surface, which is evident in the SEM images in this chapter, as well as the VSI images in Chapter 4. It is likely that this smooth nature of the ground surface at the micro scale means it has far fewer sites vulnerable to pit initiation when compared to the brushed surface.

In other research, during long term (5 year) exposure to marine environments, shotblasted surfaces have been shown to perform poorly compared to rolled surfaces [10]. This has been attributed to the accumulation of chloride and other contaminates on the rougher surfaces, where regular rainfall was insufficient to effectively clean. This finding is in line with the observation made in this Chapter since the shotblasted surface did show more corrosion, though not by a large amount.

In tests ran by Sellafield Ltd, the effect of 60 and 80 grit grinding was investigated on 304L stainless steel using these exposure frames [11]. These are rougher surfaces produced using grit particles around 5 times larger than that used for the 240 grit ground surfaces in this Thesis. It was found that these grinding areas showed discolouration after one month and evidence of corrosion initiation after just two months. The surfaces were allowed to deteriorate for 16 months. It was found that finishes created by grinding discs corroded faster than those created by flap discs. It was also found that 316L tokens performed slightly better than 304L tokens.

Sellafield Ltd found edges and scratches on some plates to encourage the initiation of corrosion. Chapter 4 of this Thesis showed how scratches caused by handling could create some of the most enclosed and often deepest features on a surface.

7.5. Conclusions

A covered outdoor atmospheric corrosion trial was conducted on four surface finishes on 304L stainless steel. Pitting corrosion occurred within 8 months for all surfaces. The ground surface showed the greatest corrosion resistance as evidenced by the least change in surface roughness and surface area ratio, as well as by visual inspection. Image analysis also showed that the ground surface had the least evidence for corrosion, with less than half (9.8%) that of the brushed surface (23.9%). Surface roughness increased for all surfaces, as has previously been shown using VSI [12]. Surface area ratio was found to be a useful tool to quantify surface roughness since it considers the surface area at the highest possible resolution, including changes of gradient at all surface heights.

SEM analysis found:

- The ground surface resisted corrosion well, this was likely due to its smooth nature at the micro scale.
- Pitting along valley minima and folded over regions, forming lines in the direction of surface finish, was observed on the brushed surface. Other surfaces showed no preferential pitting.

The effect of the enclosed nature of valley minima on the brushed surface combined with ongoing nearby corrosion lead to conditions in valley minima which were aggressive enough to initiate metastable pitting.

It was shown that in some circumstances, valley minima provide sites for pitting initiation, likely due the effect of surface morphology on local diffusion properties as explained in Chapter 4.

7.6. References

[1] B. E. Quayle and L. M. Hartley, “Atmospheric corrosion testing facilities at Sellafield, including summary of testing,” vol. 12754, no. 1, 2013.

[2] Object Research Systems (ORS), “Dragonfly Software Version 3.6.” 2017.

[3] F. Corvo *et al.*, “Outdoor-indoor corrosion of metals in tropical coastal atmospheres,” *Corros. Sci.*, vol. 50, no. 1, pp. 220–230, 2008.

[4] N. Sato, *Basics of Corrosion Chemistry*. 2011.

[5] Y. Zuo, H. Wang, and J. Xiong, “The aspect ratio of surface grooves and metastable pitting of stainless steel,” *Corros. Sci.*, vol. 44, no. 1, pp. 25–35, 2002.

[6] L. Abosrra, A. F. Ashour, S. C. Mitchell, and M. Youseffi, “Corrosion of mild steel and 316L austenitic stainless steel with different surface roughness in sodium chloride saline solutions,” *Electrochem. Process Simul. Iii*, vol. 65, pp. 161–172, 2009.

[7] H. Ezuber, A. Alshater, S. O. Nisar, A. Gonsalvez, and S. Aslam, “Effect of surface finish on the pitting corrosion behavior of sensitized AISI 304 austenitic stainless steel alloys in 3.5% NaCl solutions,” *Surf. Eng. Appl. Electrochem.*, vol. 54, no. 1, pp. 73–80, 2018.

[8] J. R. Galvele, “Transport processes and the mechanism of pitting of metals,” no. April, pp. 464–474, 1976.

[9] P. C. Pistorius and G. T. Burstein, “Growth of corrosion pits on stainless steel in chloride solution containing dilute sulphate,” *Corros. Sci.*, vol. 33, no. 12, pp. 1885–1897, 1992.

[10] A. Burkert, T. Müller, J. Lehmann, and J. Mietz, “Long-term corrosion behaviour of stainless steels in marine atmosphere,” *Mater. Corros.*, vol. 69, no. 1, pp. 20–28, 2018.

[11] L. Hartley, “Technical Memorandum,” *Sellaf. Ltd*, 2017.

[12] J. Dante, “Accelerated dynamic corrosion test method development. SERDP project WP-1673,” no. November, p. 307, 2017.

Appendix 3

Brushed Surface

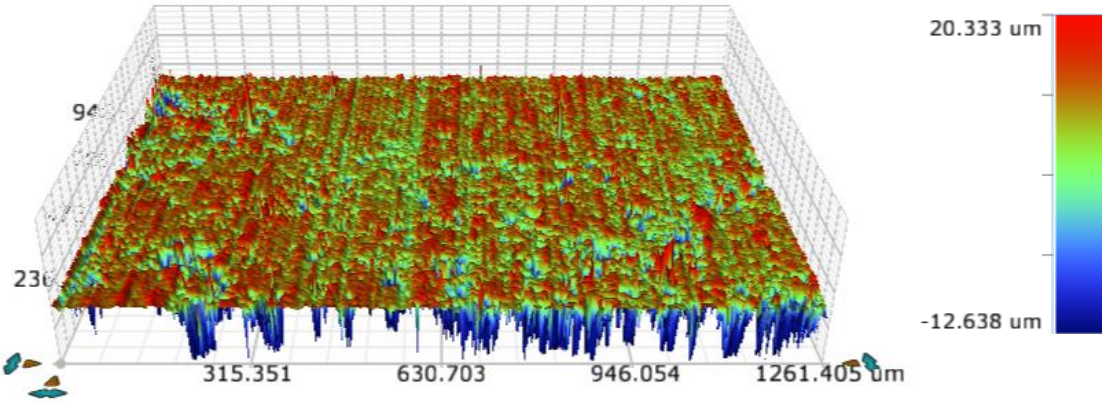

Figure 7.19 3D VSI image of the brushed surface post exposure.

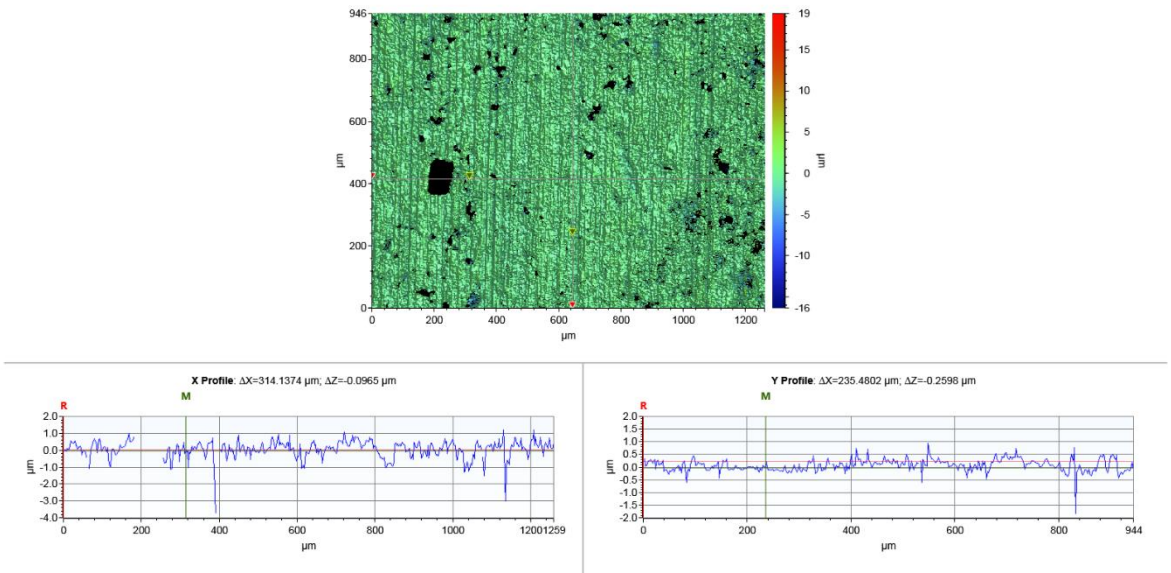

Figure 7.20 VSI image and line profiles of the brushed surface at 5X magnification post exposure.

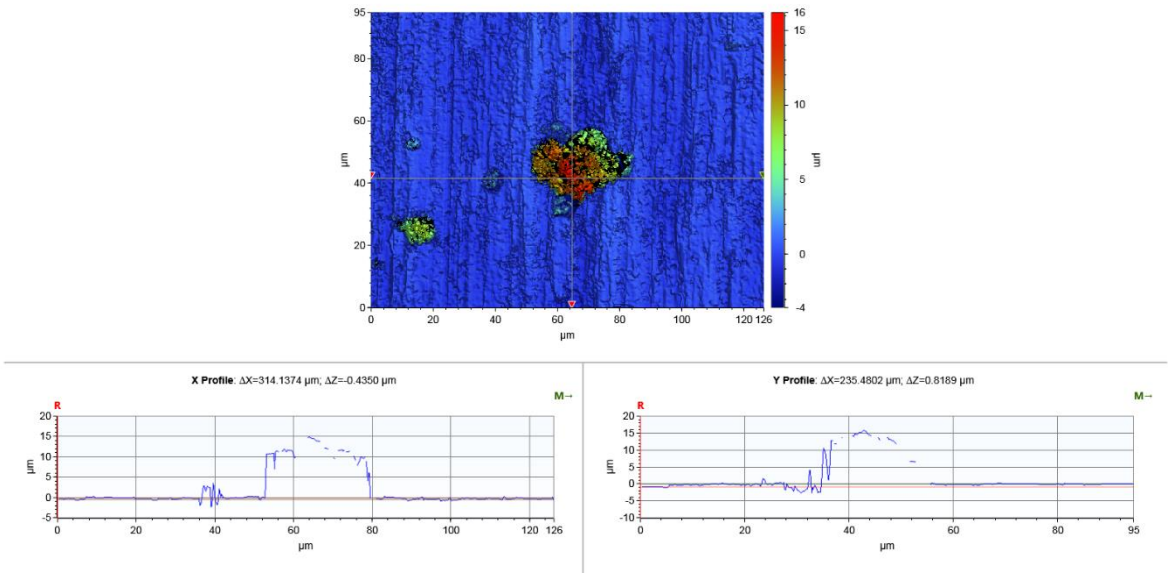

Figure 7.21 VSI image and line profiles of the brushed surface at 50X magnification post exposure.

Ground Surface

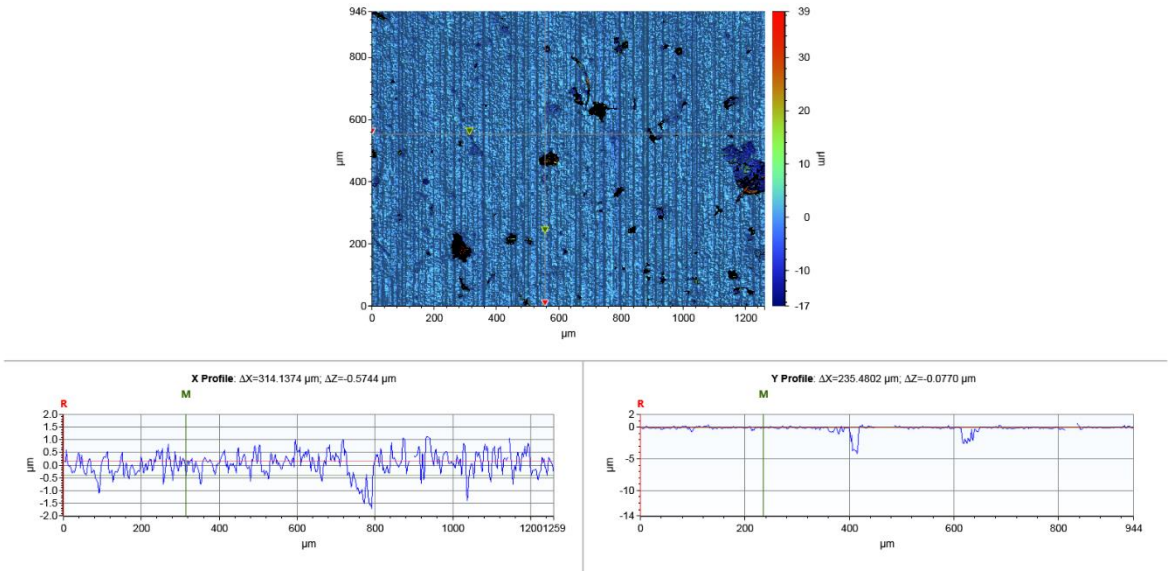

Figure 7.22 VSI image and line profiles of the ground surface at 5X magnification post exposure.

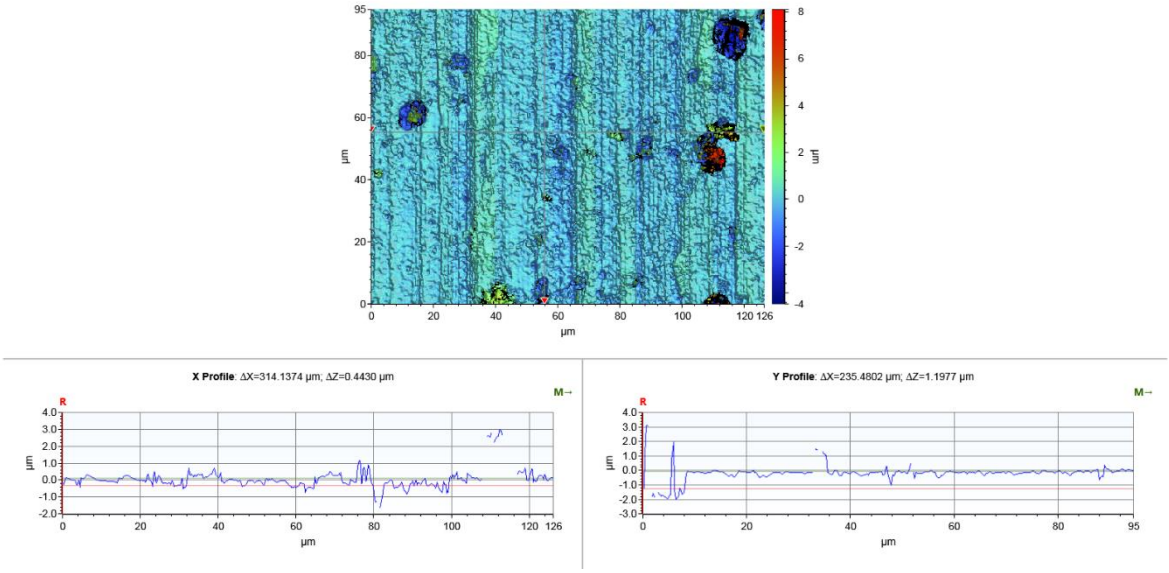

Figure 7.23 VSI image and line profiles of the ground surface at 50X magnification post exposure.

Rolled Surface

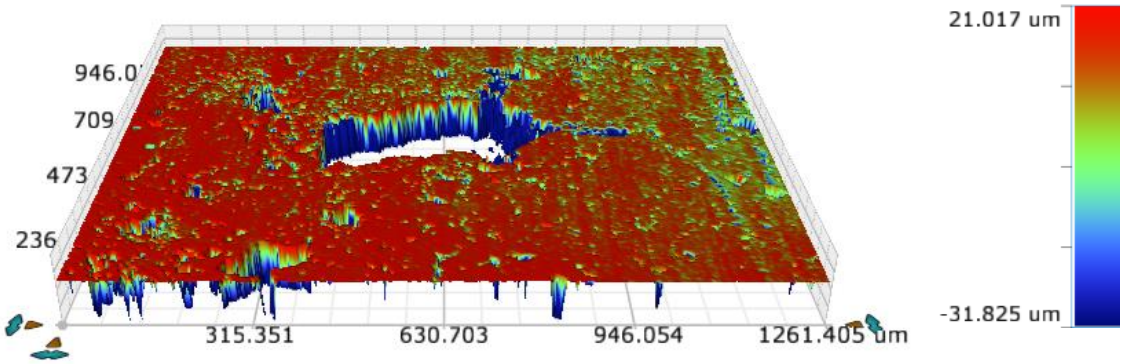

Figure 7.24 3D VSI image of the rolled surface post exposure.

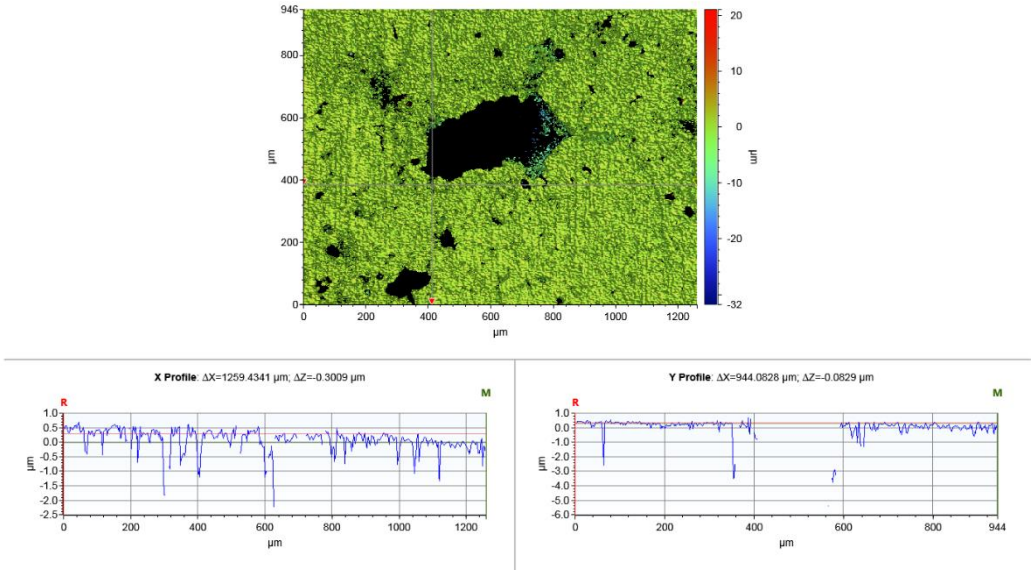

Figure 7.25 VSI image and line profiles of the rolled surface at 5X magnification post exposure.

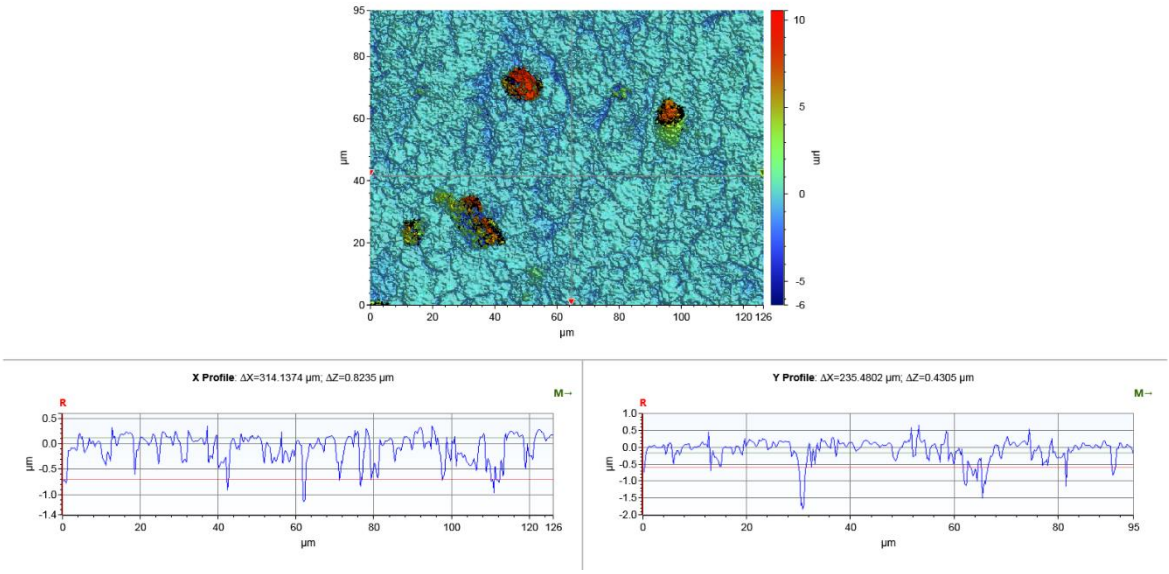

Figure 7.26 VSI image and line profiles of the rolled surface at 50X magnification post exposure.

Shotblasted Surface

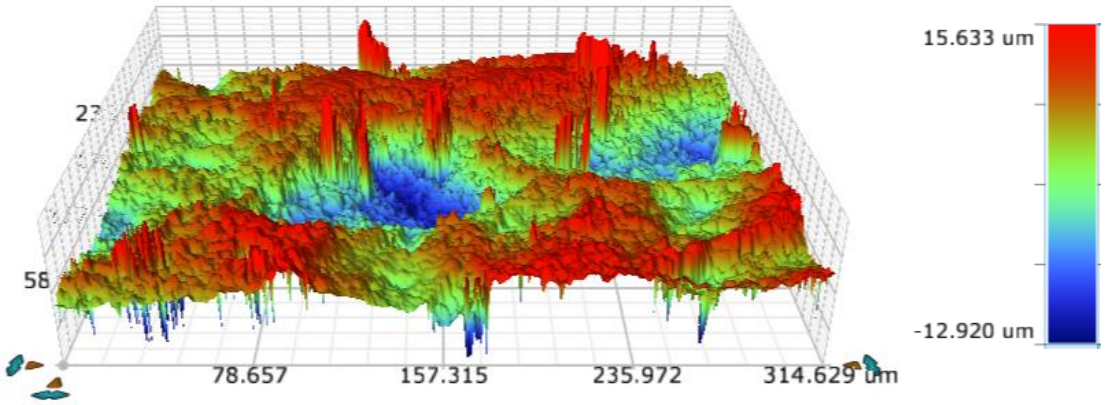

Figure 7.27 3D VSI image of the shotblasted surface post exposure.

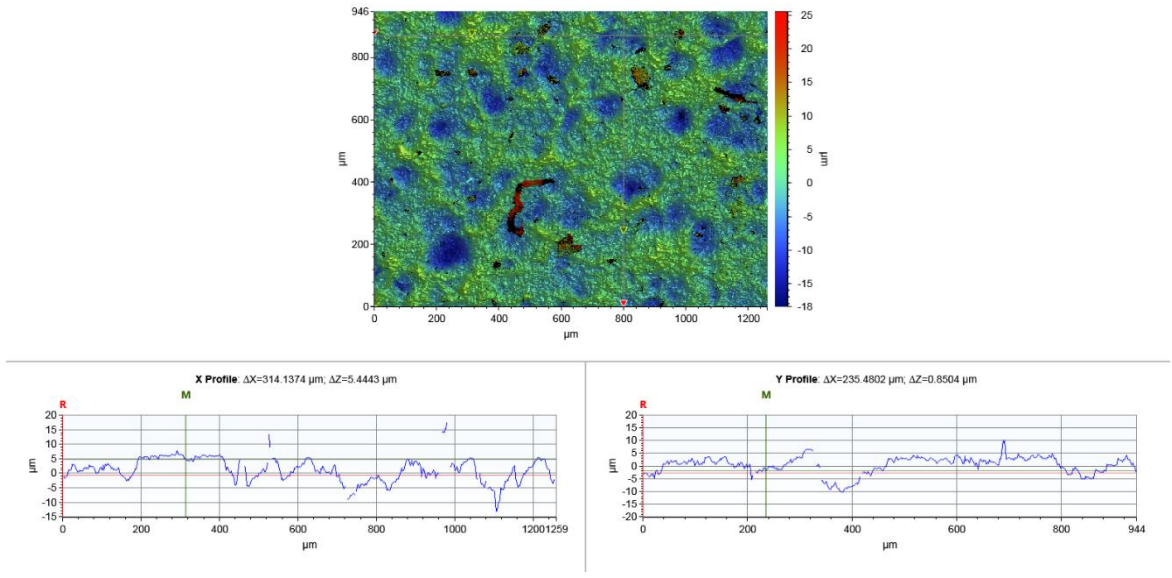

Figure 7.28 VSI image and line profiles of the shotblasted surface at 5X magnification post exposure.

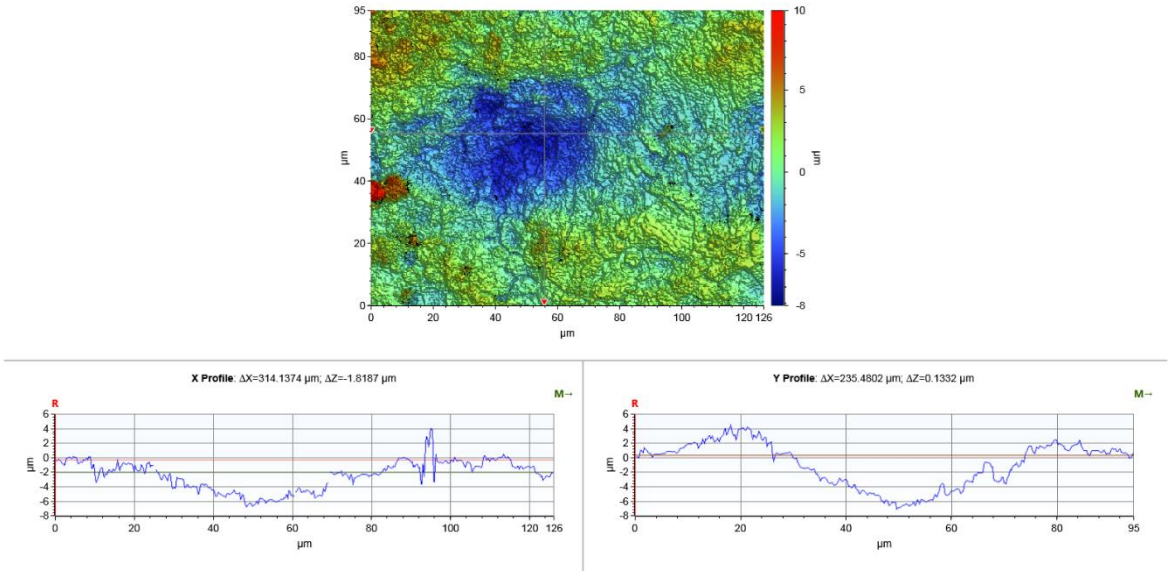

Figure 7.29 VSI image and line profiles of the shotblasted surface at 50X magnification post exposure.

Chapter 8. Discussion and Further Work

The objective of this Thesis was to investigate the effects of surface finish on corrosion initiation of 304L stainless steel, which is the material used in canisters for the storage of intermediate level waste (ILW) in the UK. This investigation was performed with a view to assessing whether a more cost-effective method of surface finishing could be used for future container production.

The four surfaces, brushed, ground, rolled and shot-blasted, were quantified in terms of their morphology and openness, the extent of microstructural damage induced by the finishing method, their residual stress, and stress concentration behaviour. Their corrosion was studied during both in-situ and ex-situ accelerated corrosion experiments, in addition to a "real-life" atmospheric corrosion experiment performed at the Sellafield site, the location at which the majority of intermediate level waste containers are stored. In accordance with previous studies of surface finish in stainless steel materials, the results presented in this Thesis have shown that surface finishing strongly influences the characteristics of the surface, manifest as significant transformations in the morphological and physiochemical nature of the surface. For example, shotblasting was responsible for grain damage and residual stresses that can be detected up to 50 μm deep into the surface, while highly enclosed sites found on untreated rolled surfaces can be vulnerable to corrosion due to their impact on near surface diffusion, but also potentially due to sensitisation.

Because it has been shown that multiple factors are at play, the best performing surface will vary in response to the particular conditions of the environment. For example, in the presence of high concentrations of chloride, the formation of pre-pits in enclosed areas of the surface will be a concern and so the reduction of small-radii features on a given surface should be a goal. For this reason, ground surfaces would be expected to perform better than rolled under conditions of atmospheric corrosion. Indeed, the results of atmospheric corrosion trials in Chapter 7 of this Thesis, where the different surface finishes were exposed to chloride-corrosion from coastal aerosol particles, showed this to be the case, with the ground surfaces undergoing less surface corrosion than the rolled surfaces. Although these findings represent a limited number of measurements.

In high stress environments where SCC is likely, the high compressive residual stress detected in the shotblasted surface will be desirable; in essence, they cancel out the tensile operational and manufacturing stresses, thus making these surfaces less susceptible to SCC. Indeed, the results in

Chapter 6 showed that cracks formed on shotblasted surfaces tended to be much shorter than for other surfaces. Studies showing the good performance of shotblasted surfaces in SCC environments suggest that the physiochemically caused residual compressive stress has the higher impact compared with the morphologically caused high stress concentration. In non-SCC corrosive environments, it was not possible to correlate any of the surface morphology parameters with the corrosion rate; this suggests that the high residual stress imparted on this surface had a greater influence on the corrosion behaviour, at least during the *in-situ* corrosion experiments performed within Chapter 4 of this Thesis, than the surface morphology. The key findings of each Chapter are described herein.

8.1. Surface Finish, Morphology and Corrosion

Chapter 4 presented a thorough characterisation of the morphology of brushed, ground, rolled and shotblasted stainless steel, as well as identifying novel methods of interpreting topographic data. The calculation and comparison of standard parameters and newer, purpose-made parameters, such as openness and inverse summit curvature, were described and compared. This allowed for a correlation analysis of these (and other) surface parameters with the corrosion rates derived from an *in-situ* corrosion study performed using VSI.

Features caused by the smearing of surface material on both the ground and the brushed surfaces were found to be deeper and more enclosed and, as a result, were proven to be more prone to pitting initiation during corrosion. Grain boundaries, etched through pickling, were found to be highly enclosed (<80°) where observable on these surfaces, more so than typical grinding valleys (100°). The etched grain boundaries on the shotblasted surface resulted in a similar openness distribution, highlighting that pickling has an important influence on the openness of the surface.

The openness analysis revealed some features as being potential areas for pitting initiation. For example, the grain boundaries on the rolled and shotblasted surfaces, indent marks on the shotblasted surface, and folded-over regions on the brushed and the ground surfaces, were highlighted as especially enclosed features. *In-situ* corrosion trials in HCl highlighted specific surface features responsible for causing corrosion. Openness was shown to be a good predictor of corrosion location as shown in Section 4.7. Deeper, more enclosed features such as folded over regions on the brushed and ground surfaces and the gaps between grains on the rolled and shotblasted surfaces were seen to increase in both width and

depth, though a limited number of samples were trialled and sensitisation also plays an important role in intergranular corrosion.

The surface area investigation found the parameter of area difficult to define and required a fractal analysis of the surface. Surfaces, especially the shotblasted surface, were found to have a much greater surface area at higher resolutions. The shotblasted surface, which, at a resolution of 0.2 μm, had a 40% larger surface area than its geometric area. Furthermore, the ground and the brushed surfaces were found to be rougher than the rolled surface at larger resolutions but were found to be smoother at very small resolutions. This highlighted a drawback in traditional stylus measurements and in commonly used roughness parameters such as Ra. For the brushed and the rolled surfaces corrosion rate was proportional with surface depth, with deeper areas corroding faster. This showed that surface morphology acts to shelter the surface and can allow aggressive environments to form.

8.2. Influence of Surface Finishing on Grain Damage and Surface Residual Stress

Chapter 5 investigated the grain damage caused by surface finishing processes. Novel methods for interpreting crystallographic data to calculate residual stress, based on the factors of Young's modulus, shape ratio and misorientation profile of grains were developed and presented. The grain shape ratio was found to be a useful parameter when estimating grain stress from grain strain, since it is responsible for the flexibility of the grain in response to the finishing method. The shotblasted and ground surfaces exhibited large amounts of grain deformation, especially within the top 50 μm of the surface, consistent with high levels of residual strain caused by their surface finishing methods. Pockets of strain up to 50 μm deep were identified in the shotblasted and ground samples. Plastic deformation in all four surface finishes was shown to register over 5° which is consistent with previous literature [1]. Although only one measurement area was used per surface type, around 500 grains were measured each time, which made it possible to draw conclusions about these specific sites. These were chosen to include features for each surface finish such as ridges and valleys that represented the surface well.

Results showing that stressed grains do not tend to be grouped together but appeared to be dispersed through the top layer of material supported the theory that plastic deformation is a heterogeneous process in polycrystalline materials [2]. Higher strains were found in larger grains, which has been

predicted by modelling [3]. For all four surfaces, individual grains in the material were found to harbour the majority of the residual stress.

The large residual stresses found in the shotblasted sample were not considered damaging to the corrosion resistance of the material when it is under a tensile stress (i.e., in SCC conditions) since a compressive residual stress protects against SCC, though does not for uniform or pitting corrosion [4]. Interestingly, the shotblasted surface exhibited the lowest extent of pitting corrosion during atmospheric corrosion tests, presented in Chapter 7. The large residual stresses found in the ground surface are likely to be tensile in the direction of grinding. This will exacerbate SCC when the applied stress is aligned with the direction of grinding [5]. It would be expected to reduce the required critical applied stress for SCC, it is possible that this surface could undergo SCC with no applied external stress as has been previously shown [6]. The rolled surface and the brushed surface showed extremely low levels of stress by comparison. They are likely to perform better than the ground surface, but worse than the shotblasted surface, in SCC conditions.

8.3. Surface Finish, Stress Concentration Factor and Relationship to Stress Corrosion Cracking

Chapter 6 mapped the stress concentration factor across the four types of surface finish using two prominent models, the Neuber model and the Arola and Ramulu model. These were then compared with Finite Element Analysis (FEA) modelling and practical SCC trials (Figure 6.18). The use of FEA (Figure 6.29) in this manner showed it to be a viable and effective method for the calculation of stress concentration factors in 3D surfaces with applied finishes. Crack growth behaviour in SCC trials in warm humid conditions was shown to be affected by the unique stress concentration distributions of each surface.

Three major causes of stress concentration were identified. These were: feature depth, root valley radius and feature frequency/openness. The Neuber model gave greater weighting to openness as a factor whereas the Arola and Ramulu model was more affected feature depth and root valley radii. For all 3 models, it was shown that the shotblasted surface concentrates stress the most, with FEA measured stress concentrations reaching a value of 5 in the deepest shotblast craters. This compares to 2.8 for the brushed surface and 2.9 for the ground surface and only around 2 for the rolled surface. The stress

concentrations calculated by FEA were much lower than that calculated by either the Arola and Ramulu model or the Neuber model; these are presented for comparison in Table 8.1. Though only a single measurement area was looked at, the area contained a range of features, for instance for the FEA on the ground surface, 10+ valleys and ridges were measured, modelled, and simulated. Nonetheless, using a single measurement area is a weakness.

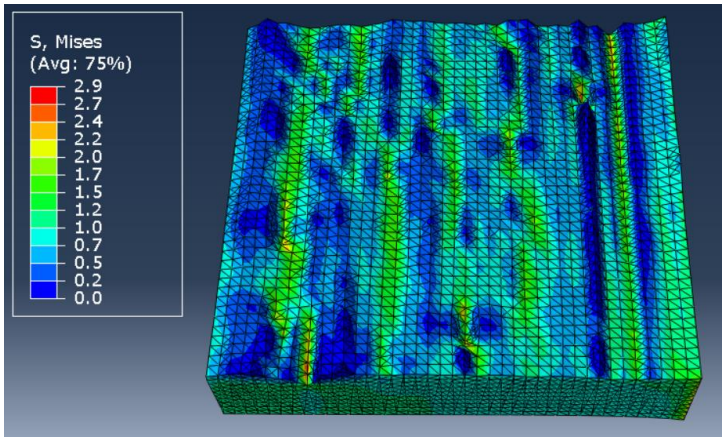

Figure 8.1 FEA analysis of a 10 µm² ground surface, showing stress concentration factor distribution.

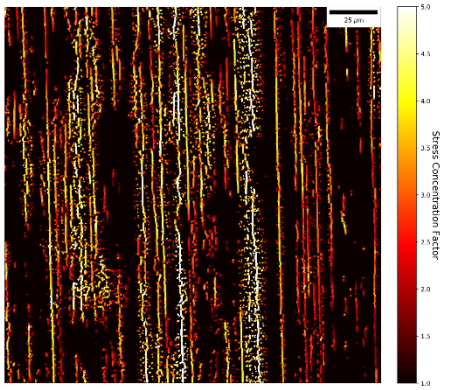

Figure 8.2 Neuber stress concentration factor map for a brushed surface. VSI data.

Table 8.1 Comparison of Calculated and Simulated Stress Concentrations

	FEA	Arola and Ramulu	Neuber
Brushed	3 ± 0.5	5 ± 1	5 ± 1
Ground	3 ± 0.5	5 ± 1	5 ± 1
Rolled	2 ± 0.5	9 ± 1	6 ± 1
Shotblasted	5 ± 0.5	10 ± 1	10 ± 1

Surface finishing features were shown to influence crack development during accelerated SCC investigation. Cracks on the brushed and the ground surfaces regularly followed valley minima. This correlates with the calculated locations of stress concentrations in these regions. It was assessed that the stress concentrations found at valley minima provide sites vulnerable to crack initiation and that they form paths of lower resistance for crack tips to propagate along. Crack behaviour on the shotblasted surface showed that cracks initiate in sites of high stress concentration. Having established within the minima, they were observed to propagate through features of lower stress concentration such as peaks. Surface topography was found to protect the majority of the surface from applied stress, meaning crack initiation is unlikely to occur in high regions.

8.4. Surface Finish and Pitting Corrosion by Coastal Aerosols

Chapter 7 detailed a long term (8 month) outdoor atmospheric corrosion experiment in which pitting occurred on all surfaces. The ground surface performed far better than other surfaces, despite the fact that the brushed surface was morphologically very similar, as described in Chapter 4. This behaviour was attributed to the ground surface being very smooth at the micro scale, compared with the higher micro-roughness of the brushed surface. This supports the well-established theory that rougher surfaces encourage corrosion and supports the results of similar trials ran by Sellafield Ltd [7].

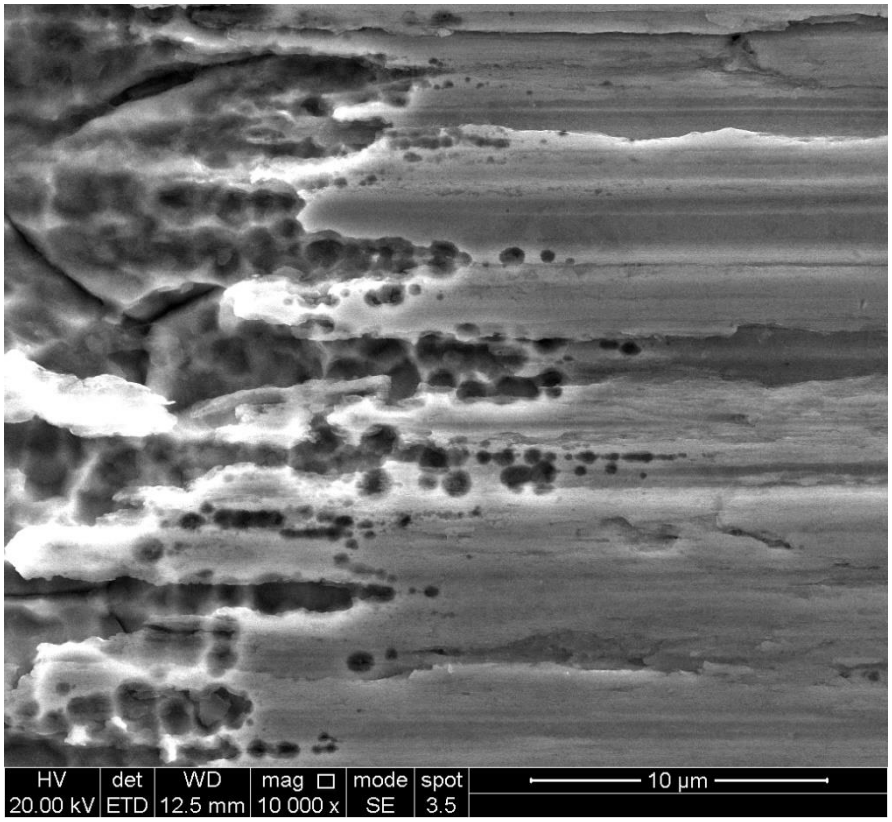

Figure 8.3 SEM micrograph showing pitting along valley minima on a brushed surface after an 8 month exposure to a coastal atmosphere.

Overall, the results from the outdoor experiment, of which constitute a limited number of samples, agree with the accelerated in-situ results in Chapter 4. Deeper, more enclosed, features such as valley minima and folded-over regions showed a higher amount of corrosion in accelerated trials and a prevalence for pitting in the outdoor trial. This is counter to the widely regarded theory that pitting is stochastic since this study has shown that pit initiation is deterministic under certain circumstances [8]. The "string of pearls" pitting behaviour along valley minima is shown in Figure 8.3.

8.5. Considerations in Selection of Surface Finish to Minimise Corrosion

The current surface finish of the body of an ILW container is the result of rolling followed by Vaqua-blasting, which is thought to have similar effects to shotblasting [4]. This study has shown that the deep craters of shotblasted surfaces concentrate stress, and that the etched grain boundaries on this surface are enclosed enough to support aggressive localised environments. This study has found the ground surface performed better than the others at resisting corrosion under aggressive HCl conditions and to have relatively low surface stress concentrations. Additionally, it performed the best in environmental trials at the Sellafield site. This is attributed to the smoothness of the surface at the microscale; though the Ra value of 250 nm indicates a reasonably rough surface, at very high resolution there are few imperfections that form features of low openness. As a result, it is likely that the good corrosion resistance of this surface is due to good diffusion properties near the surface and a failure of aggressive local concentration gradients to stabilise. For this reason, grinding alone would appear to be a suitable method of surface finishing for 304L stainless steel intermediate level waste containers, with respect to corrosion behaviour.

8.6. Future Work

A number of different areas addressed in this Thesis raise further questions and topics for future research that would be pertinent to study in the future. They are briefly described in this Section.

The Nature of Vaqua Blasted Surfaces

Vaqua blasting is currently used to clean the surfaces of ILW containers post manufacture. Although it is used primarily for its cleaning effect, it is known to have similar surface finishing effects to shotblasting [4]. Further research to identify the differences between shotblasted and Vaqua-blasted surfaces would provide justification to apply research conducted on the shotblasted surfaces to ILW containers. It was, unfortunately, not possible to acquire samples of this surface finish for this Thesis.

Inclusions in Stainless Steel

Manganese Sulphide inclusions have, in the literature, been proposed as a major contributor to corrosion initiation [9]. These were not identifiable during this study but given the variation in compositions among individual stainless steel grades they likely appear in some 304L stainless steel. The effect of the combination of MnS inclusions with surface finish could be studied. Specifically, the identification and morphological characterisation of holes left by the dissolution of these inclusions could be carried out by AFM.

EBSD Stress Measurement

Future use of misorientation angle to estimate stress should consider the shape of grains. A development of this method could use diffraction contrast tomography (DCT) to provide a 3D measure of grain shape to greatly improve accuracy.

Wetting Behaviour

Surface finish affects the wetting behaviour which could affect corrosion. It has been observed, for instance, that taller droplets form on some surface finishes. A taller droplet will have a lower ohmic drop but a smaller cathode as the cathode is at edge of drop [10]. Additionally surfaces with higher wettability promote the coalescence of individual non-corrosive droplets, resulting in larger droplets capable of supporting corrosion [11]. The optimal shape of a droplet to cause corrosion will lie in a compromise between the limiting factors of size of cathode and the resistance of the electrolyte. The wettability of stainless steel surface could be assessed by measuring the angle made by the surface of a droplet against the surface of the material. The size and shape of droplets formed could be simply measured using a camera and image analysis and the wettability could be measured by measuring the contact angle. This could be done using a tilt plate and camera setup, with existing contact angle measurement software.

Surface Morphology Applications

A fluid's viscosity acts as though it were proportionally higher at smaller scales [12]. Pitting corrosion relies on the surface geometry slowing the diffusion of corrosion products to maintain a concentration gradient and an aggressive environment. Since diffusion is also proportionally slowed by viscosity, the scale of the diffusion-slowing features is extremely important. As pitting is a major risk in ILW containers, this is a potentially useful application of the surface characterisation techniques presented here [13].

The effect of the openness distribution on flow behaviour across a surface has been alluded to in previous literature [14] and could be investigated further using the openness mapping technique presented in this Thesis. Correlation between openness and the type of flow behaviour seen could be investigated with further FEA modelling.

8.7. References

[1] S. G. Acharyya, A. Khandelwal, V. Kain, A. Kumar, and I. Samajdar, "Surface working of 304L stainless steel: Impact on microstructure, electrochemical behavior and SCC resistance," *Mater. Charact.*, vol. 72, pp. 68–76, 2012.

[2] N. Allain-Bonasso, F. Wagner, S. Berbenni, and D. P. Field, "A study of the heterogeneity of plastic deformation in IF steel by EBSD," *Mater. Sci. Eng. A*, vol. 548, pp. 56–63, 2012.

[3] B. Raeisinia, C. W. Sinclair, W. J. Poole, and C. N. Tomé, "On the impact of grain size distribution on the plastic behaviour of polycrystalline metals," *Model. Simul. Mater. Sci. Eng.*, vol. 16, no. 2, 2008.

[4] M. Row, "A review of manufacturing processes used in stainless steel intermediate level waste containers to evaluate the presence of residual stresses report to NDA," *Serco Rep. to NDA*, no. 3, pp. 1–42, 2009.

[5] A. Turnbull *et al.*, "Sensitivity of stress corrosion cracking of stainless steel to surface machining and grinding procedure," *Corros. Sci.*, vol. 53, no. 10, pp. 3398–3415, 2011.

[6] S. Rahimi, K. Mehrez, and T. J. Marrow, "Effect of surface machining on intergranular stress corrosion cracking (IGSCC) in sensitised type 304 austenitic stainless steel," *Corros. Eng. Sci. Technol.*, vol. 51, no. 5, pp. 383–391, 2016.

[7] L. Hartley, "Technical Memorandum," *Sellaf. Ltd*, 2017.

[8] N. Sato, *Basics of Corrosion Chemistry*. 2011.

[9] A. W. Gjønnes, "Effect of sulfide inclusions in austenitic stainless steel on the initiation of pitting in base metal and heat affected zone after welding," no. June, 2012.

[10] I. S. Cole, T. H. Muster, N. S. Azmat, M. S. Venkatraman, and A. Cook, "Multiscale modelling of the corrosion of metals under atmospheric corrosion," *Electrochim. Acta*, vol. 56, no. 4, pp. 1856–1865, 2011.

[11] A. Cook *et al.*, "Atmospheric-induced stress corrosion cracking of austenitic stainless steels under limited chloride supply," *18th Int. Corros. Congr. 2011*, vol. 2, no. February 2017, pp. 1438–1449, 2011.

[12] A. Kapustin, *Scaling laws in hydrodynamics*. 2016.

[13] F. King, “Container materials for the storage and disposal of nuclear waste,” *Corrosion*, vol. 69, no. 10, pp. 986–1011, 2013.

[14] S. Leonardi, P. Orlandi, and R. A. Antonia, “Properties of d- and k-type roughness in a turbulent channel flow,” *Phys. Fluids*, vol. 19, no. 12, 2007.